DEVELOPMENT OF COMPUTATIONAL CAPABILITIES TO PREDICT THE CORROSION WASTAGE OF BOILER TUBES IN ADVANCED COMBUSTION SYSTEMS

Final Project Technical Report

Reporting Period
August 14, 2007 to August 31, 2014

Prepared by

Steven C. Kung, Ph.D.
Tel: (330) 860-6774
Fax: (330) 860-9949
E-mail: sckung@babcock.com

Consultant
Robert A. Rapp, Professor Emeritus
Tel: (614) 292-6178
E-mail: rapp.4@osu.edu

Submitted by

Babcock & Wilcox Power Generation Group
P. O. Box 351
20 South Van Buren Avenue
Barberton, OH 44203

Report Issued on
November 26, 2014

B&W Contract No.: RCD 1467

DOE Contract No.: DE-FC26-07NT43097

LEGAL NOTICE

Table of Contents

List of Figures

List of Tables

1 ABSTRACT

A comprehensive corrosion research project consisting of pilot-scale combustion testing and long-term laboratory corrosion study has been successfully performed. A pilot-scale combustion facility available at Brigham Young University was selected and modified to enable burning of pulverized coals under the operating conditions typical for advanced coal-fired utility boilers. Eight United States (U.S.) coals were selected for this investigation, with the test conditions for all coals set to have the same heat input to the combustor. In addition, the air/fuel stoichiometric ratio was controlled so that staged combustion was established, with the stoichiometric ratio maintained at 0.85 in the burner zone and 1.15 in the burnout zone. The burner zone represented the lower furnace of utility boilers, while the burnout zone mimicked the upper furnace areas adjacent to the superheaters and reheaters. From this staged combustion, approximately 3% excess oxygen was attained in the combustion gas at the furnace outlet. During each of the pilot-scale combustion tests, extensive online measurements of the flue gas compositions were performed. In addition, deposit samples were collected at the same location for chemical analyses. Such extensive gas and deposit analyses enabled detailed characterization of the actual combustion environments existing at the lower furnace walls under reducing conditions and those adjacent to the superheaters and reheaters under oxidizing conditions in advanced U.S. coal-fired utility boilers. The gas and deposit compositions were then carefully simulated in a series of 1000-hour laboratory corrosion tests, in which the corrosion performances of different commercial candidate alloys and weld overlays were evaluated at various temperatures for advanced boiler systems. Results of this laboratory study led to significant improvement in understanding of the corrosion mechanisms operating on the furnace walls as well as superheaters and reheaters in coal-fired boilers resulting from the coexistence of sulfur and chlorine in the fuel. A new corrosion mechanism, i.e., “Active Sulfidation Corrosion Mechanism,” has been proposed to account for the accelerated corrosion wastage observed on the furnace walls of utility boilers burning coals containing sulfur and chlorine. In addition, a second corrosion mechanism, i.e., “Active Sulfide-to-Oxide Corrosion Mechanism,” has been identified to account for the rapid corrosion attack on superheaters and reheaters. Both of the newly discovered corrosion mechanisms involve the formation of iron chloride ($FeCl_2$) vapor from iron sulfide (FeS) and HCl, followed by the decomposition of $FeCl_2$ via self-sustaining cycling reactions. For higher alloys containing sufficient chromium, the attack on superheaters and reheaters is dominated by Hot Corrosion in the presence of a fused salt. Furthermore, two stages of the hot corrosion mechanism have been identified and characterized in detail. The initiation of hot corrosion attack induced by molten sulfate leads to Stage 1 “acidic” fluxing and re-precipitation of the protective scale formed initially on the deposit-covered alloy surfaces. Once the protective scale is penetrated, Stage 2 Hot Corrosion is initiated, which is dominated by “basic” fluxing and re-precipitation of the scale in the fused salt. Based on the extensive corrosion information generated from this project, corrosion modeling was performed using non-linear regression analysis. As a result of the modeling efforts, two predictive equations have been formulated, one for furnace walls and the other for superheaters and reheaters. These first-of-the-kind equations can be used to estimate the corrosion rates of boiler tubes based on coal chemistry, alloy compositions, and boiler operating conditions for advanced boiler systems.

2 EXECUTIVE SUMMARY

The recent development of high efficiency, low emission coal-fired utility boilers has led to the implementation of higher steam temperatures and pressures. The design strategies for these boilers often involve staged combustion, which generates corrosive combustion gases in the lower furnace and requires the use of high-strength corrosion-resistant superheater/reheater alloys in the upper furnace. Examples include recent development of the ultrasupercritical (USC) boiler systems, with the potential of combining oxy combustion technologies, pushing the steam outlet temperatures up to 760^{o}C (1400^{o}F) and steam pressures up to 35 MPa (5000 psi). While higher efficiencies and lower emissions can be realized from these advanced combustion systems, fireside corrosion is also expected to increase on the boiler tubes. For instance, low-NO_X combustion tends to produce high concentrations of H_2S in the flue gas and FeS in the deposit due to incomplete combustion of the sulfur-bearing species in coal. Both of these species are known to cause fireside corrosion on the furnace walls via sulfidation, although the respective corrosion mechanisms are quite different. Utility boilers retrofitted with low-NO_X burners and NOx ports for staged combustion in recent years have indeed experienced accelerated boiler tube wastage in the lower furnace. Consequently, application of a coating or weld overlays is often required on at least portions of the lower furnace walls to combat the fireside corrosion. In the upper furnace, the presence of higher steam temperatures and pressures inevitably raise the tube surface temperatures of superheaters and reheaters, thus potentially increasing the tendency for coal ash corrosion.

While the boiler operating conditions are important variables, the coal chemistry also plays a pivotal role in fireside corrosion. Some impurity constituents of coal are well known to accelerate corrosion wastage. For example, high sulfur and chlorine contents in coal have long been recognized as major causes for boiler tube corrosion on both the waterwall and superheater/reheater surfaces. The effects of other constituents in coal on corrosion, such as the presence of alkali and alkaline earth metals as well as the total ash content, are also important but less understood. Indeed, operating experiences indicate that the corrosivity of coal is not simply determined by individual impurities. Rather, it is the result of a complex, synergistic interaction of all impurities with each other simultaneously. There have been attempts to link coal corrosivity to its impurities based on empirical correlation and indexing. However, the results proved to be less reliable and often coal-specific due to oversimplification of the interaction and/or significant variation in the coal chemistry from seam to seam and mine to mine.

Therefore, it was the objective of this multi-year project to develop comprehensive corrosion models that can be used to predict the corrosion rates of boiler tubes under staged combustion conditions in the lower furnace and coal ash corrosion conditions in the upper furnace. To this goal, B&W has down-selected eight popular U.S. coals with a wide range of coal ranks and compositions commonly burned in modern utility boilers for power generation. These coals were tested in a pilot-scale combustion facility to closely simulate the actual staged combustion conditions existing in utility boilers. During each of the combustion tests performed, in-situ gas and deposit samples were obtained and analyzed at selected locations representing the waterwall and superheater of typical utility boilers. Such efforts have allowed better understanding of the realistic combustion environments and corrosive species present in the boilers. Once the conditions were determined, a series of long-term laboratory corrosion tests,

1000 hours each, were performed. These corrosion tests involve exposure of different alloys and weld overlay coatings in a wide range of compositions to the laboratory conditions simulating the actual boiler environments. As a result of the laboratory tests, a fireside corrosion database was generated and used for the intended fireside corrosion modeling efforts. The modeling efforts led to two predictive equations, one for the lower furnace walls and one for superheaters/reheaters. These equations could be used to estimate the corrosion rates of boiler tubes as a function of several key variables, such as sulfur, chlorine, alkali, alkaline, ash, FeS_2, metal temperature, gas temperature, etc. Application of these predictive equations is relatively versatile for both advanced and conventional combustion systems and not coal-specific.

The project award was announced in December 2006, and the contract was fully executed between DOE-NETL and B&W on August 21, 2007. The project kickoff meeting was held on January 23, 2008 to officially start the planned work. Task 1 on the selection of eight US coals suitable for fireside corrosion modeling was completed in 2009. A change in the combustion testing facility for Tasks 2 and 3 from B&W's Small Boiler Simulator (SBS-II) to Brigham Young University's Burner Flow Reactor (BFR) was made in Q3 2008 after receiving the official approval from DOE-NETL. The change was necessary due to an unexpected delay of the SBS-II construction at the B&W Research Center. In 2009, the capability of BFR in producing realistic combustion conditions was evaluated and demonstrated for the project. It was concluded that fireside conditions generated in the BFR were closely representative of those expected in utility boilers burning coals in staged combustion mode. Therefore, the original objectives set forth for this project have been preserved without any deleterious impact from the change of the test facility. Tasks 2 and 3 have generated invaluable combustion/corrosion information that helped better understand the environments leading to fireside corrosion in coal-fired utility boilers. The laboratory corrosion testing for Task 4 was started in early 2010 and has also generated valuable corrosion data. The laboratory tests for Task 4 and corrosion modeling for Task 5 were completed in 2014. Results of each of the tasks are discussed in detail in this final project report.

Key accomplishments from this project are summarized below:

(1) Bituminous and sub-bituminous coals from eight U.S. mines were selected and acquired for investigation in this project. The coals, commonly burned in utility boilers, consisted of a wide range of sulfur and chlorine contents suitable for fireside corrosion modeling. Because of significant variation in the coal compositions, the selected coals offered unique opportunities for a detailed and in-depth parametric study utilizing both pilot-scale combustion and laboratory corrosion testing facilities, which led to much better understanding of the corrosion mechanisms and the roles of impurities in fireside corrosion.

(2) A total of 12 alloys was evaluated in the laboratory fireside corrosion tests under the reducing conditions of lower furnace walls, while another set of 12 alloys total was investigated under the oxidizing conditions of superheaters and reheaters. This number of alloys for both conditions exceeded that originally proposed (i.e., 10 alloys each) because additional alloy compositions were deemed necessary to adequately perform Task 5,

Corrosion Modeling. However, no additional cost was incurred to NETL for the increased testing scope of additional alloys.

(3) Because the needs for additional corrosion data at different temperatures were identified, a total of 14 laboratory corrosion tests were performed during which the alloys were exposed to the upper furnace conditions in an expanded range of temperatures. This number of upper furnace tests again exceeded the 10 tests originally proposed for this project but without a cost increase to NETL.

(4) As a deliverable of this project, a corrosion model has been developed for furnace wall corrosion under the conditions of low-NOx combustion of U.S. coals. The comprehensive model is capable of predicting the corrosion rate of furnace walls based on the metal temperature, coal chemistry, and alloy composition. Details of the furnace wall corrosion model are discussed in Section 3.5.1.4.

(5) A second corrosion model utilizing the unique approach of Gaussian distribution has been proposed to describe the behavior of the bell-shape curve for the high-temperature fireside corrosion of superheaters and reheaters as a function of metal temperature. Details of the superheater/reheater corrosion model are discussed in Section 3.5.2.10. The Goodness of Fit for this model is less satisfactory because of the lack of laboratory corrosion data generated for the coals other than OH Mahoning 7A as a function of temperature.

(6) The role of chlorine in fireside corrosion has been identified from this project, which is a significant accomplishment by itself. For decades, it has been speculated that chlorine in coal attacked alloys independently of sulfur. From this research, it was determined that chlorine, in the concentration range of coals, can accelerate fireside corrosion by assisting sulfidation attack via the formation and cycling reactions of $FeCl_2$ vapor.

(7) A total of eleven technical papers have been published in reputable journals and presented at various conferences. A complete list of the publications is shown in Section 6.

3 TECHNICAL APPROACHES

A literature and web review on coal quality database was performed in Task 1. This effort included a thorough search to identify available coal analyses (including ultimate, proximate, heating value, ash analysis, sulfur content, chlorine content, etc.) and sourcing information that would aid in proper coal selection to meet the task objectives. Multiple coal databases have been reviewed, which include B&W Coal Database, Penn State Coal Database, U.S. Geological Survey Coal Database, and information from the Argonne Premium Coal Sample (APCS) Program. Among them, information contained in the Argonne Premium Coal Sample (APCS) Program, although for a limited number of coals, was deemed to be the most detailed and up to date, followed by the Penn State Coal Database. The two databases are also structured to be the most user-friendly for coal property search. In addition, the Keystone Coal Industry Manual was consulted for coal availability and comparative usage in the US utility industry.

Due to a long delay of the SBS-II construction at B&W Research Center, an alternate pilot-scale combustion facility available at BYU was identified. The BYU facility, i.e., Burner Flow Reactor (BFR), has been evaluated and deemed to be capable of generating the needed corrosion information for this project. Subsequently, a request for the facility change was submitted to DOE-NETL and approval was received. Associated with this request for approval, several contract documents were revised, which included the Statement of Project Objectives (SOPO), Project Management Plan (PMP), and Gantt chart showing the updated task schedules and milestones proposed at that time. In addition, the workscope and cost to BYU's participation in this project were integrated into the project documentation. A further revision of the project schedules was made in the Continuation Application for Budget Period 3, which was submitted to DOE-NETL in June 2010.

The BFR at BYU has been successfully utilized as a pilot-scale combustion facility to generate the necessary information for this project on fireside corrosion environments resulting from burning the selected eight US coals. The environments were determined through extensive in-furnace gas sampling and deposit collection. Based on this information, a series of laboratory corrosion tests were designed and performed to simulate the fireside conditions produced from the combustion of the eight coals in the BFR. Extensive thermodynamic calculations have also been carried out to help design the laboratory testing conditions adequately. Different alloys and weld overlays have been exposed to the simulated fireside conditions during each of the laboratory tests. Results of the laboratory tests led to the generation of a comprehensive corrosion database useful for modeling the materials performance of furnace walls and superheaters/reheaters in advanced coal-fired utility boilers. The database was also useful in formulating the fireside corrosion predictive equations as part of the project deliverables.

4 RESULTS AND DISCUSSION

4.1 Task 1 - Coal Selection, Procurement, and Handling

Several coal databases were utilized in the selection process to narrow the coal choices to eight groups. These databases included the Penn State Coal Database, the USGS Coal Quality Database, the Keystone Coal Industry Manual, and the coal analyses from the Argonne Premium Coal Sample (APCS) Program. Based on these databases, a number of coals have been identified as potential candidates for the project. For high sulfur bituminous coals, multiple choices are available. For example, the Ohio #5 coal seam has a sulfur content, on a dry basis, at as high as 9 wt.%. Specifically, the Empire mine (hvAb) contains a sulfur content at approximately 4%, the East Fairfield County mine (hvAb) at 5%, and the Holmes County (hvBb) mine at 6%. In Kentucky, the Camp #1 mine (hvBb) of Kentucky #9 seam has a sulfur concentration at 4%, Paradise mine (hvBb) of the Kentucky #11 seam at 5%, and Homestead mine (hvCb) of the Kentucky #11 seam at 6%.

Since chlorine also plays an important role in fireside corrosion, various chlorine-bearing coals have been considered along with their sulfur contents. In Illinois, the Will Scarlett mine (hvAb) of Top Dekoven seam has a chlorine content of 0.27% and sulfur of 4.69% on a dry basis. Similarly, the Eagle #2 mine (hvAb) of Illinois #5 seam has 0.27% chlorine and 4.72% sulfur. Furthermore, the Orient #3 mine (hvBb) of Illinois #6 seam has a combination of lower sulfur content of 1.35% but higher chlorine of 0.45%. This Illinois coal was considered a strong candidate for this study to isolate the effect of chlorine on fireside corrosion.

For additional selection of medium-sulfur bituminous coals, the Hillsville mine (hvBb) of Middle Kittanning seam, which consists of 2.77% sulfur and 0.16% chlorine, and the O'Donnell #1 mine (hvAb) of Pittsburgh seam, which consists of 3.07% sulfur and 0.06% chlorine, were considered. The Stinson #3 mine (hvAb) of Elkhorn #3 seam, having 0.98 % sulfur and 0.33 % chlorine, were also a good choice for this coal group.

In addition to individual impurities, the base/acid ratio (BAR) was also used as a selection criterion to identify bituminous coals that have a relatively high calcium and magnesium content in the ash. Several coals have been identified as candidates for this study. For example, the Stahlman mine (3500 Pit) (hvAb) of Clarion seam, with a BAR of 3.58, and the Bokoshe #10 mine (hvAb) of Upper Hartshorne seam, with a BAR of 7.0, are among the possibilities for coals with a high alkaline earth metal content. There are bituminous coals, such as the Michigan #5 mine (hvCb) in Iowa, which contain an even higher BAR ratio at 12-78. Such a high BAR is attributed to an unusually high calcium concentration, i.e., 20-30%, in the ash. Typically, these coals also have a high sulfur contents, ranging from 9 to 10%, with pyritic sulfur being the main constituent at approximately 7%.

For sub-bituminous coals, the Spring Creek mine (subB) in Montana has a sulfur content of 0.5% and chlorine content of 0.07%. Similarly, the Black Thunder mine in Wyoming has a relatively low sulfur content at 0.43% and a very low chlorine content. Both of these sub-bituminous mines are from the Powder River Basin (PRB). On the other hand, North Dakota lignite at the Beulah mine was considered a unique candidate for its high ash content at ~9% and

extremely high moisture content at nearly 30% as-received (A.R.). This coal has a sulfur concentration of typically less than 1%.

Due to its unique characteristics and popularity, the Powder River Basin (PRB) coal, a Wyoming coal from the Black Thunder mine, was included in the test matrix as one of the eight final coals. In general, the PRB coal is considered non-corrosive based on utility experiences. However, this coal exhibits a very high (Ca+Mg)/S ratio, which has been linked to possible mechanisms for high fireside corrosion found in some utility boilers, especially those implementing fuel blending. Therefore, this coal is of great interest to this study.

Final selection of the eight U.S. model coals for this project has been completed. Special considerations were given to the various coal properties and impurity concentrations mentioned above. Understandably, it was extremely challenging to narrow the coal selection to just eight mines that would cover all of the coal properties important to fireside corrosion. However, the selected coals are believed to represent a wide range of coal ranks and properties relevant to the fireside corrosion mechanisms of interest. As mentioned above, these properties include the sulfur content and its forms, chlorine content, BAR (the base/acid ratio calculated from the elemental ash analysis of coal), and ash content. Concentrating mainly on the steam coals for fireside corrosion modeling and down-selecting the large number of U.S. coals to eight, it was decided not to consider the low or medium volatile bituminous coals.

4.1.1 Consideration of Coal Properties

Some specific properties of each coal group and rationale for its selection are given below. The ranking of each coal is classified per ASTM D388, Standard Classification of Coals by Rank.

Coal Group 1 - In general, Illinois coals are highly enriched with trace elemental chlorine. The Galatia Mine located in SE Illinois produces both washed Illinois #5 and #6 seams. The ASTM coal rank is hvBb. For the sulfur content, it is considered a medium sulfur coal. The sulfur forms for these coals are a close balance of pyritic and organic, with the sulfate sulfur being very low to negligible. The primary reason for selecting this coal is its relatively high chlorine content (0.39 %, on a dry basis) and medium sulfur content.

Coal Group 2 - B&W has previously tested the Mahoning No. 7A Stoker coal in the CEDF (Clean Environment Development Facility) in Alliance, OH, for a separate project. The coal is mined near Lisbon, OH, and ranked as hvAb with a medium sulfur content. This coal was mainly selected for its relatively high chlorine percentage (0.20 %, dry basis), representing a medium chlorine content in the study.

Coal Group 3 - Currently, Powder River Basin (PRB) coal is the most used coal for utility electricity production in the U.S. For this reason, Wyoming is currently the largest coal producing state. Part of the Wyodak PRB seam for the Black Thunder mine is located in NE Wyoming. The coal rank is sub-bituminous

(subB). Since PRB is a compliance coal, it is characterized as having low sulfur (< 1.0 %, as-received basis) and chlorine (< 0.01 %, dry basis) contents. Therefore, it was selected for this study. The majority of sulfur in this coal is in the form of organic, and the BAR value of 0.64 for this coal is considered moderately high. Sub-bituminous coals typically have lower calorific values than bituminous coals.

Coal Group 4 - The Beulah Zap lignite seam is located in Mercer County in west central North Dakota. The coal rank is lignite, which is characterized as having high moisture, ash, and BAR, but a low calorific value. The sulfur content can vary from low to medium and almost exclusively in the form of organic. The Beulah Zap lignite was selected mainly for these reasons.

Coal Group 5 - The Gatling Mine is located in Meigs County in southeast Ohio. This mine is a source of coal specifically for the AEP Mountaineer Plant located in New Haven, WV. The ASTM coal rank is hvBb. In general, high volatile eastern bituminous coals are characterized as having a low chlorine content with a varying sulfur content ranging from low to high. Specifically, the chlorine percentage of this coal is relatively low (0.04%, dry basis), and the sulfur content (4.5%, as-received basis) is considered quite high. For these reasons this coal was selected for the study.

Coal Group 6 - The Indiana #6 seam mined in Gibson County is located in southwest Indiana. The coal rank is hvCb. The chlorine percentage in this coal (0.21%, % dry) is medium, and is similar to the Group 2 and Group 8 coals. The sulfur content of this coal is considered low to medium, its sulfur percentage (1.1%, as-received basis) is lower than that of the Group 2 coal (2.0%, as-received basis) and the Group 8 coal (3.8%, as-received basis). Since sulfur in coal is one of the key contributors to corrosion, a number of coals having varying sulfur contents were selected for this study, and the Indiana #6 coal was considered one of the candidates of interest.

Coal Group 7 - The Pittsburgh #8 seam is located in Greene County in southwest Pennsylvania. The coal rank is hvAb. The sulfur content of this coal is ranked medium, and the chlorine percentage (< 0.01%, dry basis) is considered very low. The pyritic to organic sulfur ratio can vary significantly in this coal, but the sulfate sulfur is very low (i.e. ~0.08%, dry basis). This is a low to medium sulfur coal selected for this study.

Coal Group 8 - The Kentucky #11 seam is located in Union County of southwest Kentucky. The coal rank is hvBb. The sulfur content of this coal is ranked high, and the chlorine percentage (0.21%, dry basis) is considered medium. Minimum fusion temperatures of the coal ash typically occur at a BAR of 0.7 to 0.8. A ratio in the range of 0.5 to 1.2 is generally an indication of high slagging potential.[1] The BAR for this coal is 0.81, on the fringe where the minimum fusion temperatures

occur. Compared to the bituminous coals selected for this study, the Kentucky #11 coal has a relatively high BAR.

These coals represent a wide range of coal properties. Table 1 and Figure 1 list the coal supplier information, some coal properties, and coal geographic locations for each of the eight coals. Additional coal and ash analyses are provided later in Section 3.2. All of the coals in Table 1 are of high usage in the utility industry. Coal usage was another consideration taken into consideration in the coal selection process for Task 1.

Approximately two tons of each coal were initially purchased, pulverized, and shipped to BYU for the pilot-scale combustion testing of Task 2. However, the amounts of PRB and Illinois #6 coals proved to be insufficient for all the combustion testing planned, including test burns and instrument calibrations. Therefore, additional tonnages of these coals were procured and processed to complete the respective tests.

It should be mentioned that the sulfur, chloride, and ash values in Table 1 come from the actual analyses of the eight coals reported in Section 3.2. The proximate (ASTM Method D 5142), ultimate (ASTM Methods D 5142 and D 5373), elemental ash analysis (ASTM Method D 4326), chloride (ASTM Method D 4326 Modified), and heating value (ASTM Method D 5865) for each coal is shown in Appendix A. Sulfur forms (ASTM Method D 2492) for each coal are discussed in the following section.

Table 1 - Final Coal Selection.

Group	Coal Company	ASTM Rank	State	County	Mine	Seam	Sulfur, % A.R.	Chlorine, % dry	Ash , % dry	BAR	Comments	2006 Annual Production, M short tons
1	**American Coal Co.**	hvBb	IL	Saline	Galatia	#6 Seam Washed	2.7	0.39	9.1	0.39	Med to High S, High Cl	7.20
2	**Buckeye Industrial**	hvAb	OH	Columbiana	-	Mahoning 7A	2.0	0.20	7.3	0.34	Med S, Med Cl	0.40
3	**Thunder Basin Coal Co.**	subB	WY	Campbell	Black Thunder	Wyodak	0.3	0.0012	6.8	0.64	Low S, Low Cl	92.60
4	**Dakota Westmoreland**	lig	ND	Mercer	Freedom	Beulah	0.7	0.0010	11.9	0.84	High OS, High BAR,	15.20
5	**Gatling Coal Co. for AEP/Mountaineer**	hvBb	OH	Meigs	Gatling	-	4.5	0.04	10.4	0.52	High S, Equal PS and OS, Low Cl	-
6	**Black Beauty Coal Co.**	hvCb	IN	Gibson	-	Indiana #6	1.1	0.21	7.8	0.26	Low to Med S,	3.10
7	**Penn Keystone Coal**	hvBb	PA	Greene	-	Pittsburgh Seam	1.0	0.0045	10.6	0.13	Low to Med S, Low Cl	4.30
8	**Alliance Coal, LLC**	hvBb	KY	Webster	Dotiki	Kentucky #11	3.8	0.21	8.8	0.57	High S, Lower PS	3.70

*** USGS criteria for ranking sulfur in coal, % sulfur reported on an as-received basis, low < 1%, medium 1 to 3%, high > 3%.**

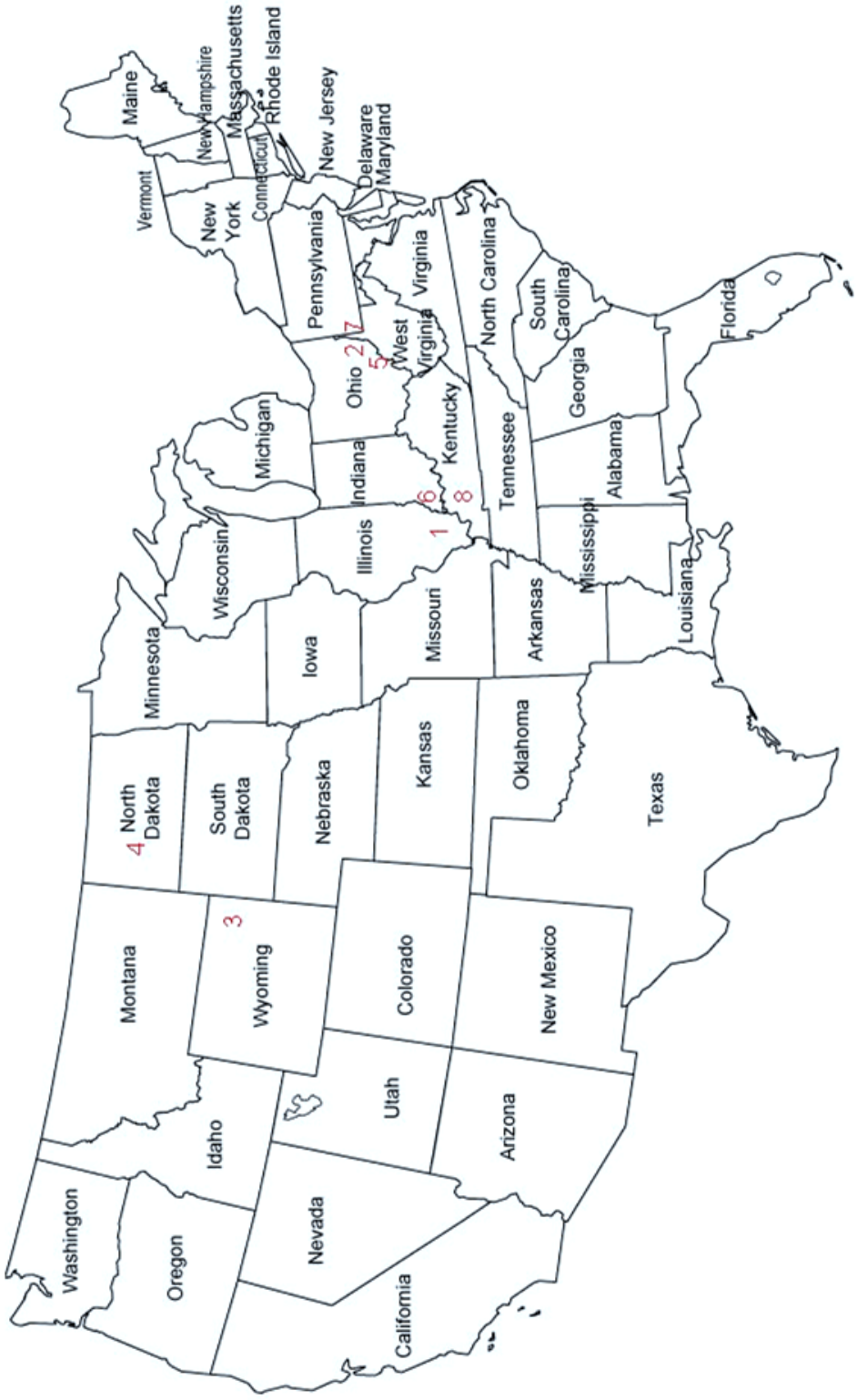

Figure 1 - Geographical Locations of Selected U.S. Coal Groups.

4.1.2 Sulfur Forms in Selected Eight U.S. Coals

The weight percentage of sulfur in a coal can have a strong impact on the fireside corrosion of boiler tubes. More specifically, the pyritic to organic sulfur ratio was believed to be a key parameter that may affect coal corrosivity. For this reason, sulfur forms were determined for each of the eight coals. As mentioned previously, ASTM Method D 2492 was used to determine the sulfur forms, which is a fairly lengthy analytical procedure. Sulfate sulfur was determined gravimetrically after precipitation with a $BaCl_2$ solution. Pyritic sulfur was determined from the iron analysis of the ashed precipitate collected on a filter paper following aqueous ammonium hydroxide addition and separation. Pyritic sulfur was calculated as a stoichiometric ratio of the molecular weight of sulfur (S_2) to that of iron (Fe) (i.e., 64.14/55.85), which is equivalent to multiplying the determined iron value by 1.148. The organic sulfur in coal was determined by the difference after subtracting the sulfatic sulfur and pyritic sulfur from the total sulfur in coal. Therefore, any error associated with the analysis of sulfatic sulfur and/or pyritic sulfur was carried over to the organic sulfur value.

Listed in Table 2 are the results of sulfur forms for each of the eight model coals investigated. The Black Thunder PRB coal has the lowest pyritic/organic sulfur ratio (PS/OS). Even though the Mahoning 7A coal has a relatively lower total sulfur percentage than several of the other coals, it has the highest PS/OS. Figure 2 summarizes the measured sulfur forms for the eight coals. Figure 3 also shows the sulfur forms but as a relative percentage of each sulfur form to the total sulfur in each coal. Finally, Figure 4 is a plot of pyritic sulfur vs. organic sulfur for each of the eight coals.

Table 2 - Results of Sulfur Forms for the Eight Model Coals

Coal Sulfur Forms	PRB, Black Thunder	Illinois #6 Galatia	North Dakota lignite	Gatling Mine Coal AEP Mountaineer	Mahoning 7A OH	Indiana #6 Gibson	Pittsburgh #8 PA	Kentucky #11 Warrior
Pyritic	0.05	1.05	0.28	1.92	1.03	0.48	0.18	1.46
Organic	0.36	1.78	0.50	1.82	0.71	0.59	0.73	2.15
Sulfate	0.02	0.11	0.06	0.43	0.12	0.10	0.08	0.08
Total Sulfur	0.43	2.94	0.84	4.17	1.86	1.17	0.99	3.69
Pyritic/Organic Ratio	0.14	0.59	0.56	1.05	1.45	0.81	0.25	0.68

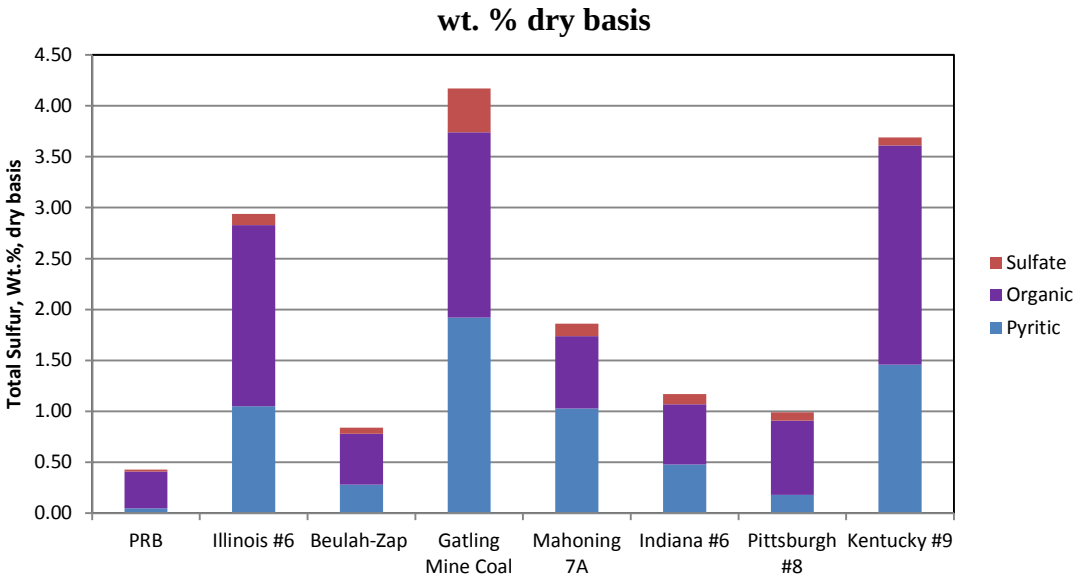

Figure 2 - Sulfur Forms for Eight Model Coals.

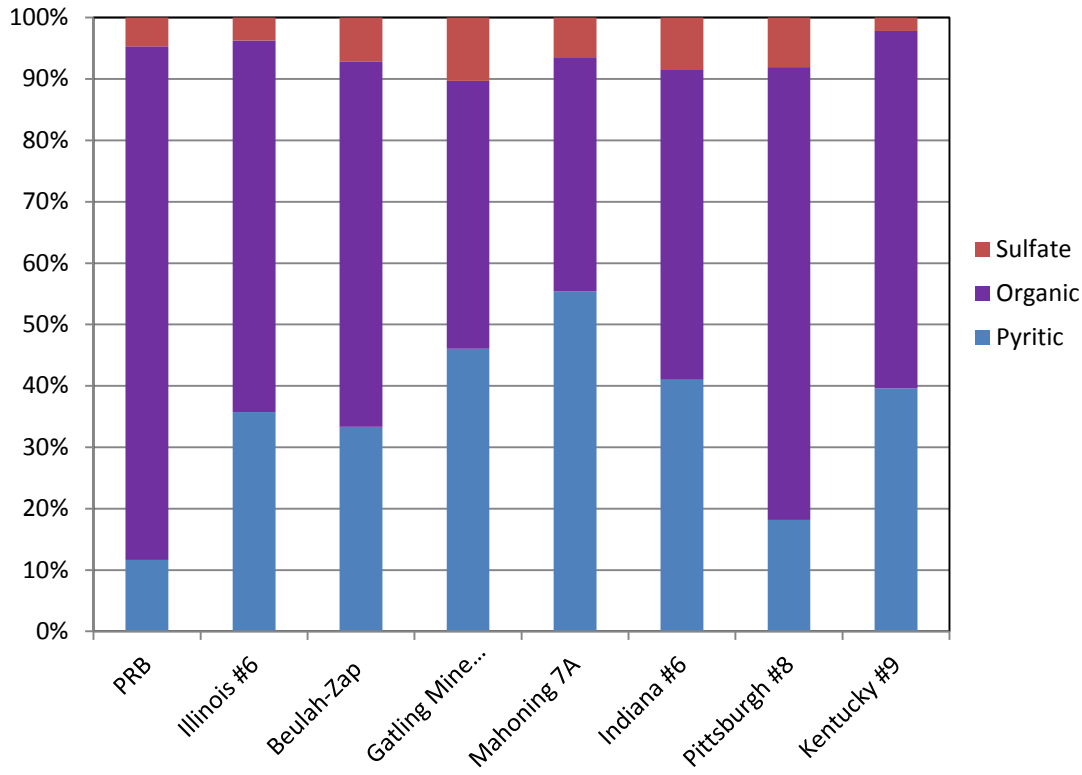

Figure 3 - Comparison of Sulfur Forms to Total Sulfur in Coals.

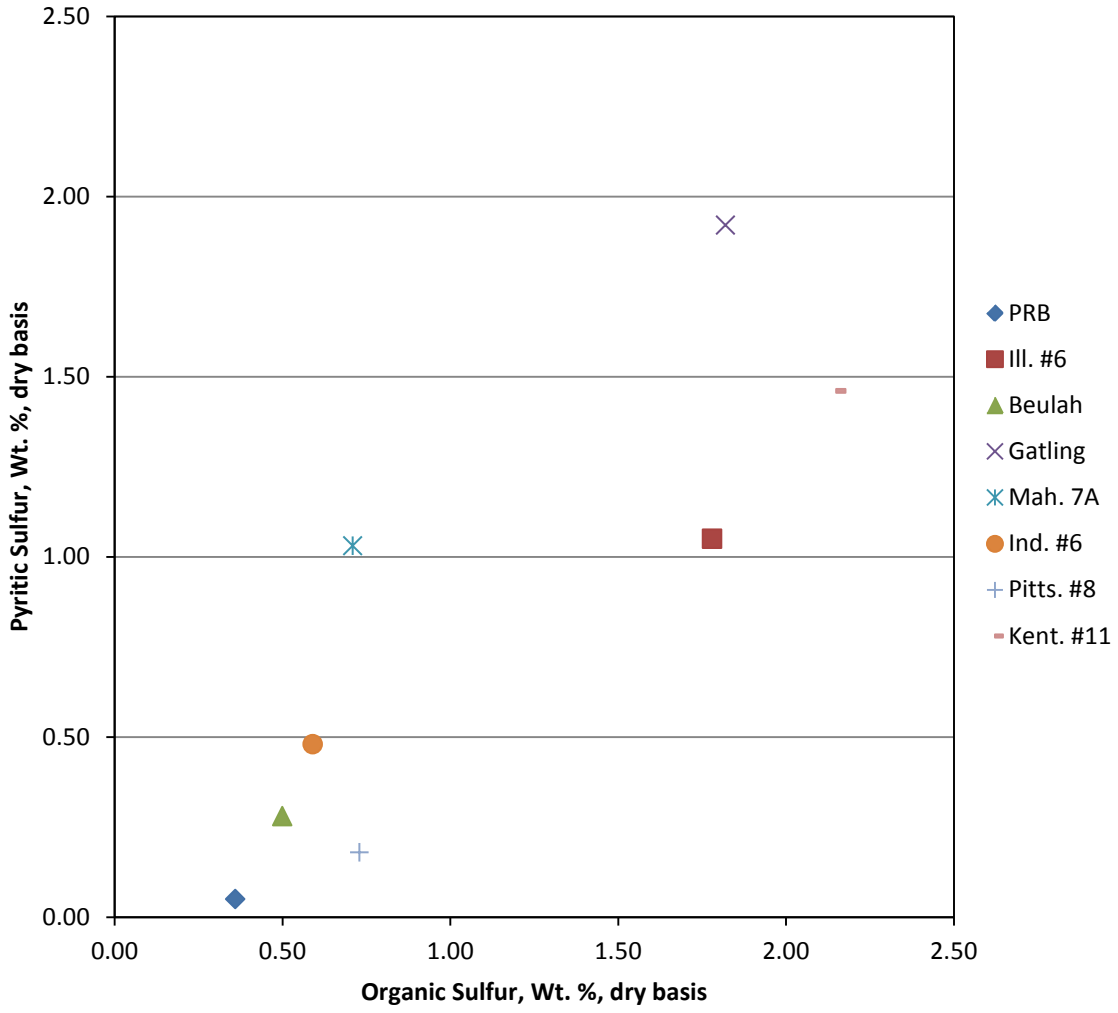

Figure 4 - Pyritic vs. Organic Sulfur for Different Coals.

4.1.3 Chloride in Selected Eight U.S. Coals

The presence of chloride in coal can also lead to increased fireside corrosion on boiler tubes. For this reason, chloride was determined for each of the eight coals. Even though the reported values are typically in wt.% dry basis as chloride, the measured chloride can be a combination of the chlorides present in inorganic minerals and elemental chlorine chemically bonded in an organic matrix. A modified version of ASTM Method D 4326-04, Major and Minor Elements in Coal and Coke Ash by X-ray Fluorescence (XRF), was used to measure the chlorine in coal. It is considered a modified version because the current ASTM method does not include chloride as one of the listed elements for coal analyses. Additional elements, including chloride, can be measured by XRF as long as the accuracy and precision of the method can be demonstrated for each analyte. Also, chloride standards must be available for calibration, and it is required that the range of concentrations represented by the standards exceeds that of any unknown. The Kα line used for the analysis of chlorine in XRF is 2.621Å.

Figure 5 shows the measured values of chloride, expressed in mg/kg (or ppm) on a dry basis, for the eight U.S. coals selected. The Illinois #6 Galatia coal has the highest chloride content, while the Black Thunder PRB, Beulah-Zap lignite, and Pittsburgh #8 coals have relatively low chloride contents. The Gatling Mine bituminous coal also has a low chloride content, although it is higher than the previous three coals mentioned. The Mahoning 7A, Indiana #6, Gibson, and Kentucky #11 Warrior coals have medium chloride contents that are at similar values.

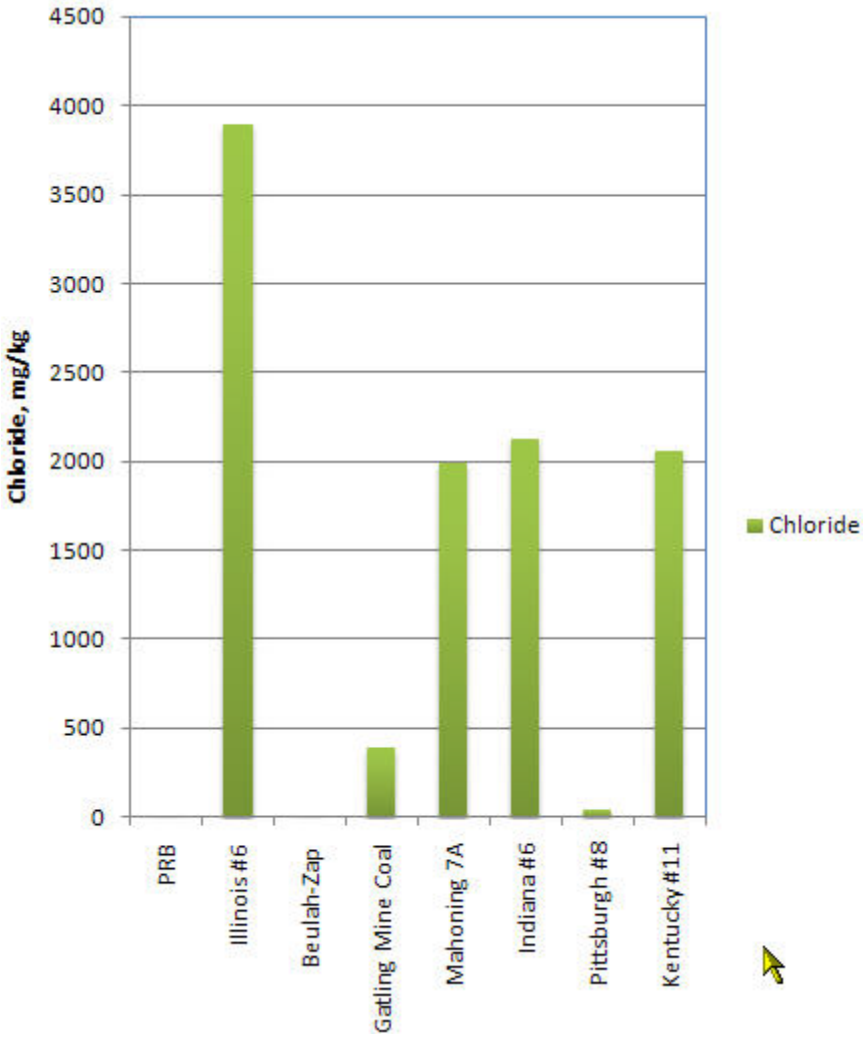

Figure 5 - Comparison of Chloride Content in Coals.

Figure 6 shows the measured values of chloride on a % dry basis versus the as-received sulfur contents for the eight coals. This figure helps point out the relative ranges of chloride and sulfur tested for the coals.

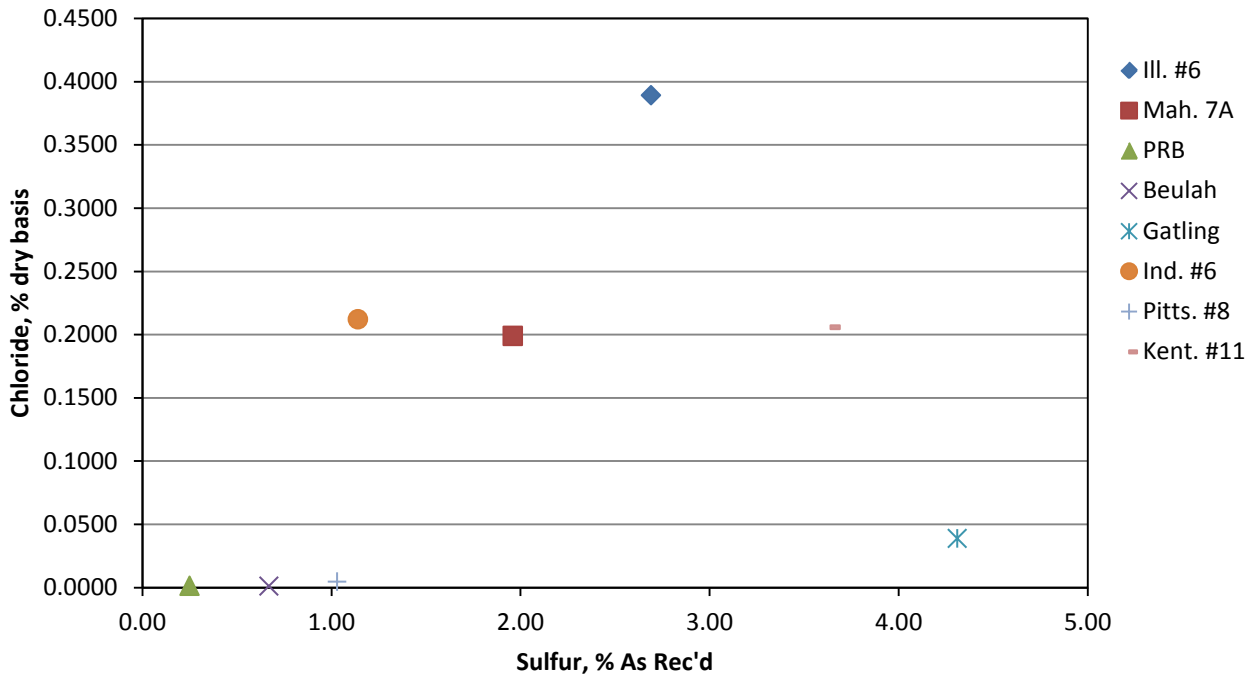

Figure 6 - Final Coal Group Selection: Comparing Chlorine vs. Sulfur.

4.1.4 Fouling Potential of Selected Eight U.S. Coals

The combination of clay minerals and quartz accounts for nearly all mineral matters in coal.[1] Minor minerals found in coal are carbonates and sulfur-containing phases. The more common sulfur-containing phases include disulfides, pyrite, marcasite, sulfides, and sulfates. During the combustion process of coal, the minerals originally in the coal are converted into ash. The high temperature of the furnace can decompose less stable coal minerals. Vapors of these decomposed minerals, fine particles, and gaseous elements are carried up to the convective pass of a boiler where condensation and deposition may occur on cooler surfaces. From continuous operation of a boiler, part of the coal ash is deposited onto the boiler tube surfaces. Specifically, the propensity of coal ash deposits accumulated on the convective heat-transfer surfaces, e.g., superheater and reheater tubes, is related to its fouling potential. In addition to the reduction of heat transfer, the ash deposited on the tube surfaces can lead to severe fireside (coal ash) corrosion.

The fouling index of a coal can be calculated from its elemental ash analysis. However, an analysis must be made first to determine whether the coal ash is bituminous or lignitic, as different correlations are used for different coal ash designations. By definition, lignitic ash has a combined CaO+MgO content that is greater than Fe_2O_3, and bituminous ash is the opposite.[2]

Elemental ash analysis for each coal has been performed in accordance with ASTM Method D 4326-04, Major and Minor Elements in Coal and Coal Ash by X-ray Fluorescence. Although the ash constituents are reported only as oxides, they actually occur in the ash predominately as a mixture of silicates, oxides, and sulfates, with smaller quantities of other phases or compounds. Phases, different from those in the original coal minerals, can also form from the ash analysis.

4.1.4.1 Fouling Index – Bituminous Ash (R_f)

B&W's approach for determining the fouling index of a bituminous coal is derived from sintering strength characteristics of its ash using the sodium content of the coal ash and the base to acid ratio,[3] i.e.,

$$R_f = \frac{B}{A} \times Na_2O$$

where

$B = CaO + MgO + Fe_2O_3 + Na_2O + K_2O$

$A = SiO_2 + Al_2O_3 + TiO_2$

Na_2O = wt. % from coal ash analysis

Classification of the fouling potential for a bituminous coal based on the value of R_f is:

$R_f < 0.2$	= low
$0.2 < R_f < 0.5$	= medium
$0.5 < R_f < 1.0$	= high
$R_f > 1.0$	= severe

4.1.4.2 Fouling Index – Lignitic Ash

B&W's approach for determining the fouling classification for lignite ash is based solely on the sodium content in the ash,[3] i.e.,

When $CaO + MgO + Fe_2O_3 > 20\%$ by weight of coal ash:

$Na_2O < 3$	= low to medium
$3 < Na_2O < 6$	= high
$Na_2O > 6$	= severe

When $CaO + MgO + Fe_2O_3 < 20\%$ by weight of coal ash:

$Na_2O < 1.2$	= low to medium
$1.2 < Na_2O < 3$	= high
$Na_2O > 3$	= severe

4.1.4.3 Comparison of Fouling potential for Selected Eight U.S. Coals

Listed in Table 3 are the elemental ash analyses for the eight U.S. coals selected. The coal ash of Black Thunder PRB and Beulah-Zap lignite is considered lignitic, and that of the other six coals is bituminous. Comparing the two lignitic ash coals, both have a combined concentration of $CaO+MgO+Fe_2O_3$ greater than 20wt.%. However, the Beulah-Zap lignite has a much higher sodium content. As a result, the fouling potential classification for the Beulah-Zap lignite is high and the Black Thunder PRB is low to medium. In low rank coals, a major portion of the alkali and alkaline earth metals is organically bound to the coal. It is believed that alkalis, especially sodium in organic forms, are readily vaporized during combustion and thus play a dominant role in fouling.

The BAR for the Beulah-Zap lignite coal is higher than PRB, which would also suggest a higher fouling potential for the Beulah Zap lignite. However, the BAR is not used to calculate the fouling potential for lignitic ash.

The calculated fouling index (R_f) for each of the six bituminous coals is listed in Table 3. Based on the calculated R_f values, the order of decreasing fouling potential for the six coals is:

(1) Illinois #6, Galatia
(2) Indiana #6, Gibson
(3) Kentucky #11, Warrior
(4) Gatling Mine, AEP Mountaineer
(5) Mahoning 7A, Ohio
(6) Pittsburgh #8, PA

Table 3 - Calculated Fouling Potentials for Eight Model Coals

Coal Ash Analysis	PRB, Black Thunder WY	Illinois #6, Galatia	Beulah-Zap North Dakota Lignite	Gatling Mine Mountaineer AEP	Mahoning 7A OH	Indiana #6 Gibson	Pitts #8 PA	Kentucky #11 Warrior
Silicon Dioxide % as SiO_2	36.04	48.12	32.25	40.35	42.65	55.14	56.77	41.70
Aluminum Oxide % as Al_2O_3	16.84	19.65	12.23	22.56	29.07	21.10	29.28	18.40
Iron Oxide % as Fe_2O_3	5.86	17.64	7.45	28.33	20.45	12.93	6.63	26.09
Calcium Oxide % as CaO	21.61	4.28	19.91	2.62	1.76	2.48	0.90	4.80
Magnesium Oxide % as MgO	5.06	0.95	6.47	0.69	0.52	0.86	0.56	0.90
Sodium Oxide % as Na_2O	1.69	1.08	3.29	0.41	0.34	1.25	0.65	0.53
Potassium Oxide % as K_2O	0.50	2.59	0.82	1.28	1.61	2.40	2.30	2.43
Titanium Oxide % as TiO_2	1.32	1.05	0.65	1.04	1.41	1.30	1.53	0.96
Manganese Oxide % as MnO_2	0.02	0.07	0.08	0.05	0.00	0.03	0.05	0.03
Phosphorus Pentoxide % as P_2O_5	1.00	0.08	0.27	0.22	0.76	0.35	0.56	0.31
Strontium Oxide % as SrO	0.35	0.03	0.64	0.09	0.12	0.08	0.12	0.05
Barium Oxide % as BaO	0.62	0.05	0.73	0.11	0.07	0.06	0.12	0.18
Sulfur Trioxide % as SO_3	9.09	4.41	15.21	2.25	1.24	2.02	0.53	3.62
Coal Ash Designation	Lignitic	Eastern	Lignitic	Eastern	Eastern	Eastern	Eastern	Eastern
Base to Acid Ratio	0.64	0.39	0.84	0.52	0.34	0.26	0.13	0.57
Fouling Potential R_f	**N/D***	**0.42**	**N/D**	**0.21**	**0.11**	**0.32**	**0.08**	**0.30**
Classification of Fouling Potential	**Low to Med**	**Med**	**High**	**Med**	**Low**	**Med**	**Low**	**Med**

*** A value is not calculated for lignitic coal ash.**

4.2 Task 2 – BFR Pilot Scale Combustion Testing

The Burner Flow Reactor (BFR) pilot-scale facility at BYU was used to collect the combustion data required for this project. Modifications to the BFR were initiated after approval received from DOE-NETL for the change of testing facility. This section describes the BFR facility and the gas sampling system implemented for Task 2. The deposit collection and analysis will be discussed separately in Section 3.3 for Task 3. Details of the improvements and modifications made to the BFR for staged combustion are highlighted here. Highlights of the improvements made to the BFR included (1) installing a staged combustion system (i.e., NO_x port) that produces the required fuel-rich and fuel-lean combustion zones, (2) testing two burners to investigate their ability to produce an appropriate fuel-rich region, and (3) extending the test duration of the BFR up to 30 hours for each coal.

4.2.1 Description of the BFR

The BFR is a down-fired, pulverized-coal, swirl-stabilized combustor with a nominal coal feed rate of 22.5 kg/hour (50 lb/hour). The BFR, shown in Figure 7, has access ports allowing gas and deposit sampling probes to be inserted at many axial position between the 15 and 235 cm (5.9 and 92.5”) positions below the primary fuel inlet tube of the burner. The BFR is supplied with compressed air for the primary, secondary, and tertiary (NO_x port) air. The secondary air is heated to 204°C (400°F) by an electric heater controlled by a temperature controller. Fuel is supplied by a twin screw auger and loss-in-weight feeder. Flue gas is cooled by a wet spray scrubber and moved through the stack using an induction draft fan. The pressure in the BFR can be increased by opening a bypass valve which allows the exhaust fan to draw additional room air to the BFR flue through the fan. Opening the bypass valve produces a positive pressure in the BFR. The BFR is run at a slightly positive pressure (0.1-0.5” H_2O) in order to eliminate air in-leakage.

Flows of natural gas, primary air, secondary air, and NO_x port air to the BFR are measured and controlled. Natural gas is used only to preheat the BFR and is turned off when the coal feed starts. All of the air flows are measured using choked flow orifice plates. The orifices plates have been calibrated and compared to the choked flow equation. An example of the primary air (the smallest orifice) calibration results are shown in Figure 8. The data exhibit good linearity as is expected for chocked flow. The ratio of actual flow to theoretical flow for the primary flow orifice, represented by the ratio of the slopes of the two lines (i.e., the discharge coefficient, C_D) shown in Figure 8, was found to be 0.967.

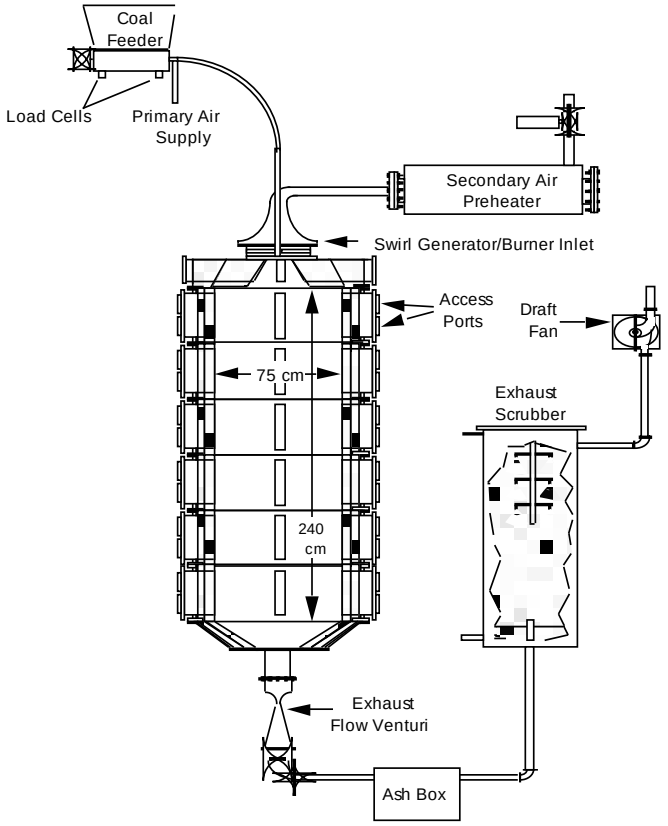

Figure 7 - Diagram of the BFR Showing Feed and Exhaust Systems.

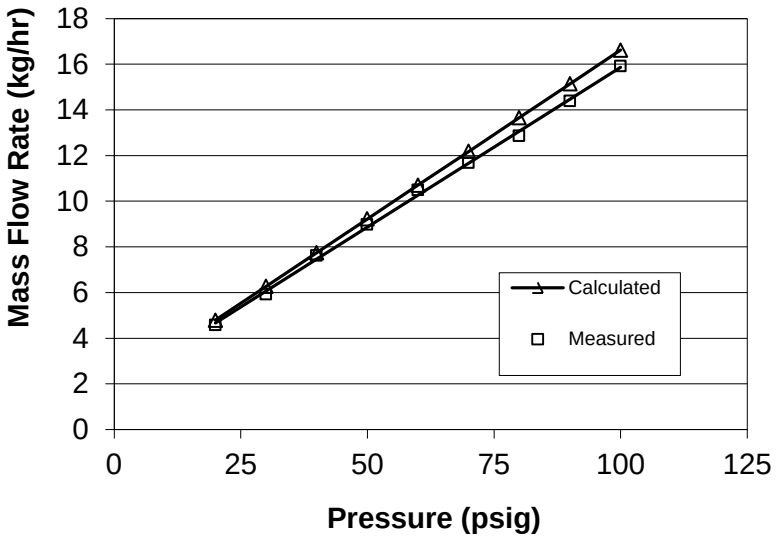

Figure 8 - Measured and Calculated Mass Flow Rates as a Function of Upstream Pressure for 1.8 mm Primary Air Flow Orifice.

The air/fuel stoichiometric ratio is calculated according to Eq. 1, where (A/F) is the air to fuel ratio and the subscripts "actual" and "stoich" refer to the actual and stoichiometric air fuel ratios, respectively. The stoichiometric ratio is calculated from a molar balance of the coal by assuming complete combustion to fully oxidized products as given by Eq. 2. Therefore, it is also referred to as theoretical air. The equation assumes that all of the coal nitrogen is converted to N_2. The molar coefficients *a, b, c, d,* and *e* are determined from the dry ash-free (DAF) ultimate analysis of the coal on a 100 gram basis by dividing the mass percentage of each element in the coal with its molecular weight. Once A_{th} is calculated, the stoichiometric mass of air required to burn the 100 gram of dry ash-free coal is determined by Eq. 3. The as-received mass of the 100 grams of DAF coal is then calculated according to Eq. 4, where X_{moist} and X_{ash} represent the mass fractions of moisture and ash in the as-received coal, respectively. Finally, the as-received stoichiometric air fuel ratio is determined by Eq. 5.

$$S.R. = \frac{(A/F)_{actual}}{(A/F)_{stoich}} \qquad \text{Eq. 1}$$

$$C_a H_b O_c S_d N_e + A_{th}(O_2 + 3.76N_2) = aCO_2 + \frac{b}{2}H_2O + dSO_2 + (3.76A_{th} + \frac{e}{2})N_2 \qquad \text{Eq. 2}$$

$$A_{th} = a + d + \frac{b}{4} - \frac{c}{2}$$

$$A_{s,100,DAF} = A_{s,as-rec} = A_{th}(32.0 + 3.76 * 28.02) \qquad \text{Eq. 3}$$

$$F_{s,as-rec} = \frac{F_{s,100,DAF}}{1 - X_{moist} - X_{ash}} \qquad \text{Eq. 4}$$

$$(A/F)_{stoich} = \frac{A_{s,as-rec}}{F_{s,as-rec}} \qquad \text{Eq. 5}$$

An example of the calculations for Illinois #6-1 Galatia coal is given in Table 4. The results show an air/fuel stoichiometric ratio of 9.2 for this coal.

At the beginning of each coal test, a mass balance is calculated for oxygen, which is required for the fuel and air flows to be controlled correctly. This is done by calculating the excess oxygen in the system under the condition of complete combustion. Using natural gas as an example, methane and air flows are set to a S.R. of 1.15. The appropriate oxygen concentration for the mixture, assuming complete conversion of natural gas to CO_2 and H_2O, is therefore determined. Agreement between the measured and calculated O_2 concentrations is generally within 0.4%, which means that the S.R. was controlled within approximately 0.02 (or

2%). The small difference can be caused by a combined uncertainty of 2% from the fuel and air flows. This is also within the uncertainty of the rotometer used to measure the natural gas flow. When the difference in O_2 concentrations is greater than 0.4%, the source of error must be determined. The most common sources of error are (1) the BFR pressure is maintained slightly positive and thus air is allowed to leak into the BFR, (2) there is a leak in the sampling line, and (3) the gas analyzer is out of calibration.

Table 4 - Stoichiometry Calculated for Illinois #6-1 Coal

	MAF (100 g basis)	Mole per 100 g
Carbon	81.26	6.7661
Hydrogen	4.35	4.3155
Nitrogen	1.21	0.0864
Sulfur	3.13	0.0976
Oxygen	9.69	0.6056
Moisture (%)	5.4	
Ash (%)	8.65	
A_{th}	7.64	
$A_{s,\ 100,\ DAF}$ (g)	1048.78	
$F_{s,\ as\text{-}rec}$ (g)	116.34	
$(A/F)_{stoich}$	9.014	

A similar procedure was performed on pulverized coal combustion for this project at the beginning of fuel flow. The overall stoichiometry of the air/fuel mixture was set to 1.15, and the oxygen concentration at furnace exit was measured and compared to the expected value of ~3% O_2. If the O_2 concentration was not within 0.5%, the sources of error were investigated. In addition to the most common sources identified above for natural gas, additional errors were caused by the mass flow rate of coal, primary air flow, and incomplete combustion of the coal.

4.2.2 BFR Modifications

Several modifications of the BFR were required in order to measure the gas species in a staged combustion configuration representative of full-scale utility boilers. Furthermore, upgrade of the fuel feed system was needed to produce a steady and repeatable fuel flow rate over a long period of time.

4.2.2.1 Air Staging (NOx port design)

Gas and deposit sampling was performed in both fuel-rich and fuel-lean combustion zones of the BFR during staged combustion. The two zones were created by running the primary and secondary air of the burner at reduced flow rates and then adding tertiary or burnout air downstream of the burner. Staged combustion is widely implemented for NO_x control in commercial utility boilers. The BFR had been previously used in separate reburning projects that required the staging of natural gas combustion using a water-cooled air injection port. This port was available and therefore used for this project. A schematic diagram of the original water-

cooled injection port is shown in Figure 9. However, the flow rates used previously for natural gas reburning proved to be much lower than those required for this project.

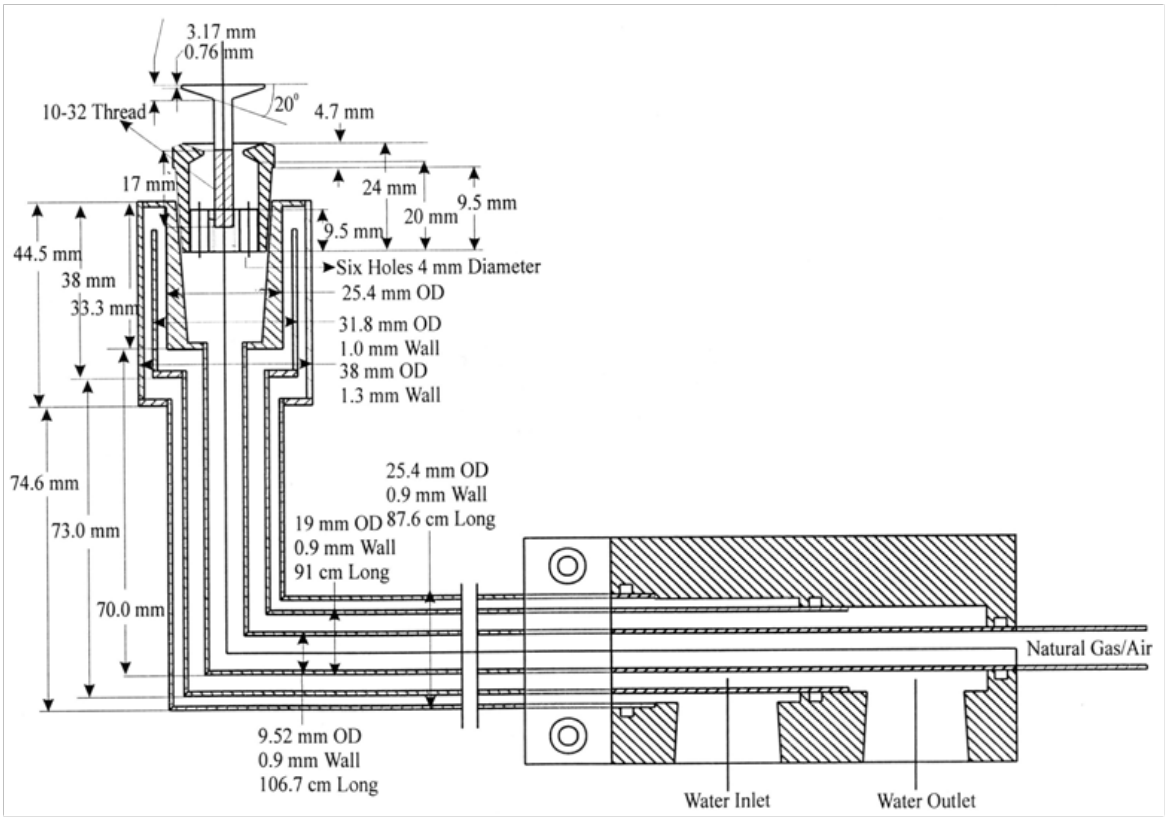

Figure 9 - Drawing of the Existing NOx Port Device for Staged Combustion (Ref. 4).

To support the Task 2 effort, B&W performed a CFD study to (1) review the aerodynamics and combustion process in the BFR and (2) suggest modifications to the NO_x port design. Since the mid-1970s, B&W has invested considerable amount of resources in the development of numerical modeling as a cost-effective method for design and development of burners, boilers, and other related components. This investment has led to the creation of a computer program, COMO (COmbustion MOdel). In this model, furnace geometry is approximated using a collection of control volumes, also called a computational grid or mesh. Fundamental conservation principles (i.e., conservation of mass, momentum, and energy) are then applied to each of these control volumes, resulting in a coupled set of governing equations that are subsequently solved to predict the steady-state furnace performance. This model has been extensively augmented with empirical data, such as the rate parameters for coal pyrolysis, coal devolatilization, and char oxidation. For Task 2 of this project, COMO was utilized to predict the flow, heat transfer, and combustion processes in the BFR. The key parameters essential for modeling of the BFR, including the ultimate analysis of the coal and furnace operating conditions, were input to the COMO code.

A parametric study was first performed to determine the burner settings of two swirler blocks required for a well-mixed primary combustion zone and optimized swirl in the BFR furnace. The maximum adjustment angle between the swirler blocks is 21.5°. Nine different

cases were set-up by gradually varying the angle between the swirler blocks to control the tangential and axial flow split, which helped characterize its effect on the swirl number of the flow. The secondary airflow entered through the plenum section above the swirl device at the location of the porous media to get a uniform flow, which was then distributed through the flow channels formed between the swirler blocks below. The flow continued into the diverging quarl section before entering to the furnace that was modeled separately.

For the numerical analysis, the entire computational domain was approximated using a volumetric mesh for the burner, as shown in Figure 10. Based on the BFR operating conditions, a mass flow of 44 g/s at 350°C was used for the secondary airflow through the plenum inlet. The turbulence kinetic energy was calculated using a turbulence intensity of 4%. A mass flow of 0.38 g/s was applied for the primary airflow through the fuel core pipe with a length scale of 0.2 cm used to calculate the turbulence dissipation rate. An outflow boundary condition was used to define the model outlet that is located beyond the burner outlet. Figure 11 shows the airflow path through the burner that houses the movable block type swirl device.

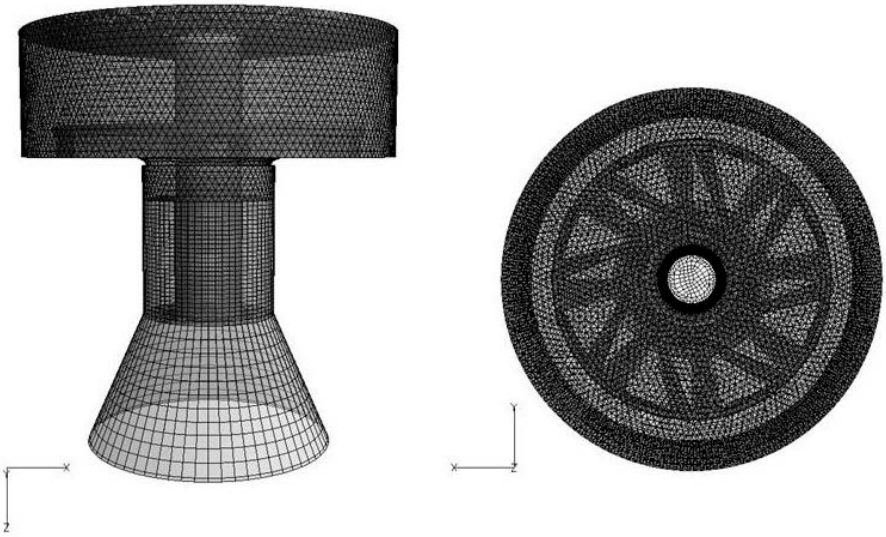

Figure 10 - Mesh Generated for the BFR Burner Geometry.

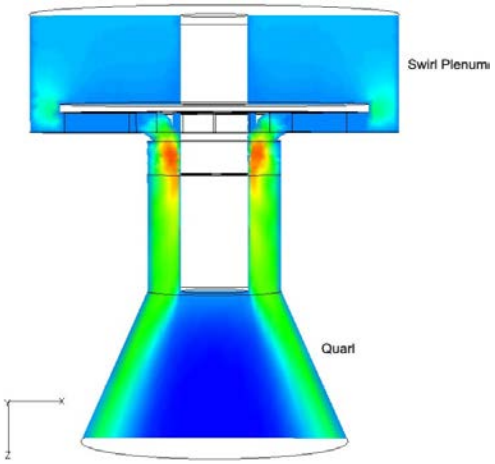

Figure 11 - Contour Plot of Z-Velocity Showing Air Flow Path for BFR Burner Geometry.

The COMO numerical model was able to create steady-state simulations of the flow. The flow distribution at two different sections of the burner for a high swirl number case of 0.833 is shown in Figure 12.

As the angle between the blocks was varied, increasing the tangential component of airflow increased the swirl number. A plot of the swirl number as a function of the swirler block setting determined from the simulations of the nine cases is shown in Figure 13. These results are in good agreement with the swirl numbers obtained by Leuckel[5] who conducted experiments on similar movable block-type swirl generators at the International Flame Research Foundation (IFRF) of Holland.

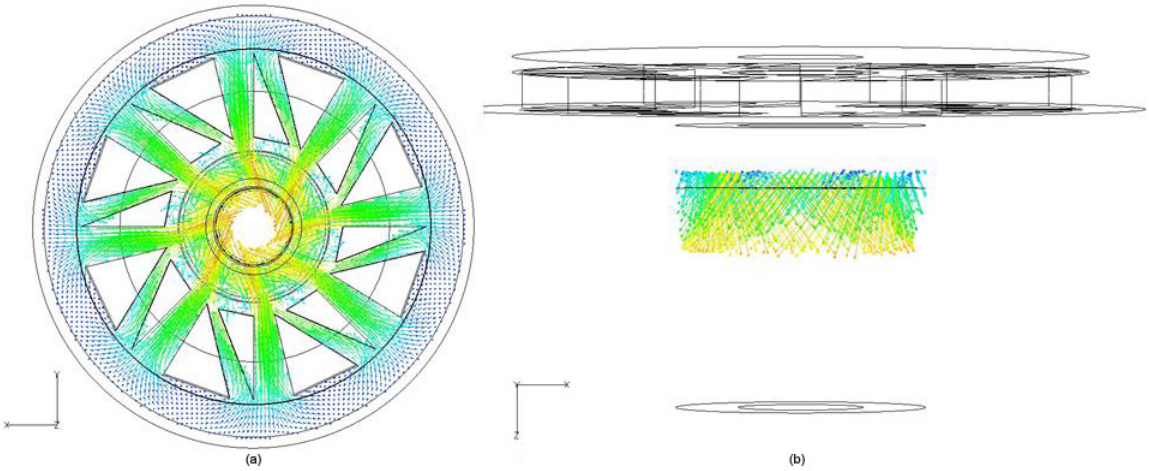

Figure 12 - Plot of Velocity Vectors at Swirl Number of 0.833 Showing Flow Pattern of (a) Plane Cut Through the Swirler Block and (b) Side View of Location Below the Swirler Block Entering the Quarl.

From the results of the individual burner model simulation, the velocity profile of the burner was mapped to the inlet of the furnace model to generate the nine cases. The inlet of the furnace model started at the beginning of the quarl. A coal flow rate of 6.3 g/s was used with a fuel rich near-burner stoichiometry of 0.85.

As the second objective of this CFD work, the NOx port design has also been investigated. Based on the BFR operating conditions, a mass flow of 44 g/s was used for the secondary airflow through the plenum inlet. The turbulence kinetic energy was calculated using a turbulence intensity of 4%. The mass flow of 13.44 g/s was used for the secondary air through the NOx port at 86000 Pa and 293K. The mass flow of 0.38 g/s was applied for the primary airflow through the coal pipe, with a length scale of 0.2 cm used to calculate the turbulence dissipation rate. An outflow boundary condition defined the model outlet. Coal properties of the Illinois #6-1 Galatia coal were used, while a coal flow rate of 6.3 g/s was maintained.

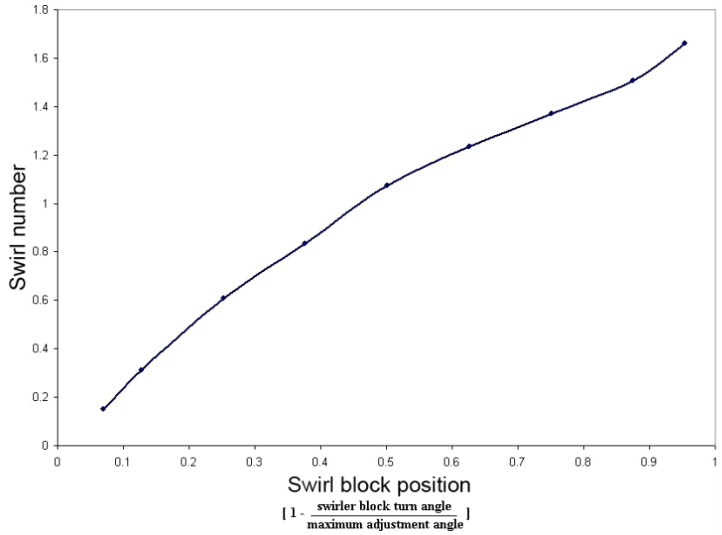

Figure 13 - Variation of Swirl Number of Gas Flow with Swirler Block Setting.

Eight different cases were set-up by varying the diameter of the NOx port while keeping the rest of the geometry constant, as shown in Table 5. The results of these simulations are summarized in Figure 14 in the form of contour plots of mixture fraction near the NOx port region. The distribution of the secondary and tertiary air comes through the plenum and NOx port inlets, respectively. It can be seen from Figure 14 that, for the smaller diameter NOx ports, the velocity is very high, thus causing the air flow to behave like a jet and negatively impacting the staged combustion conditions intended.

Table 5 - NOx Port Design Cases Investigated by CFD Modeling.

	NO_x Port OD		**Spindle OD**		**Spindle Height**
	cm	in	cm	in	cm
case 1	1.905	0.75	0.635	0.25	0.423
case 2	2.540	1.00	0.635	0.25	0.595
case 3	3.175	1.25	0.635	0.25	0.762
case 4	3.810	1.50	0.635	0.25	0.926
case 5	4.445	1.75	0.635	0.25	1.089
case 6	5.080	2.00	0.635	0.25	1.250
case 7	5.715	2.25	0.635	0.25	1.411
case 8	6.350	2.50	0.635	0.25	1.572

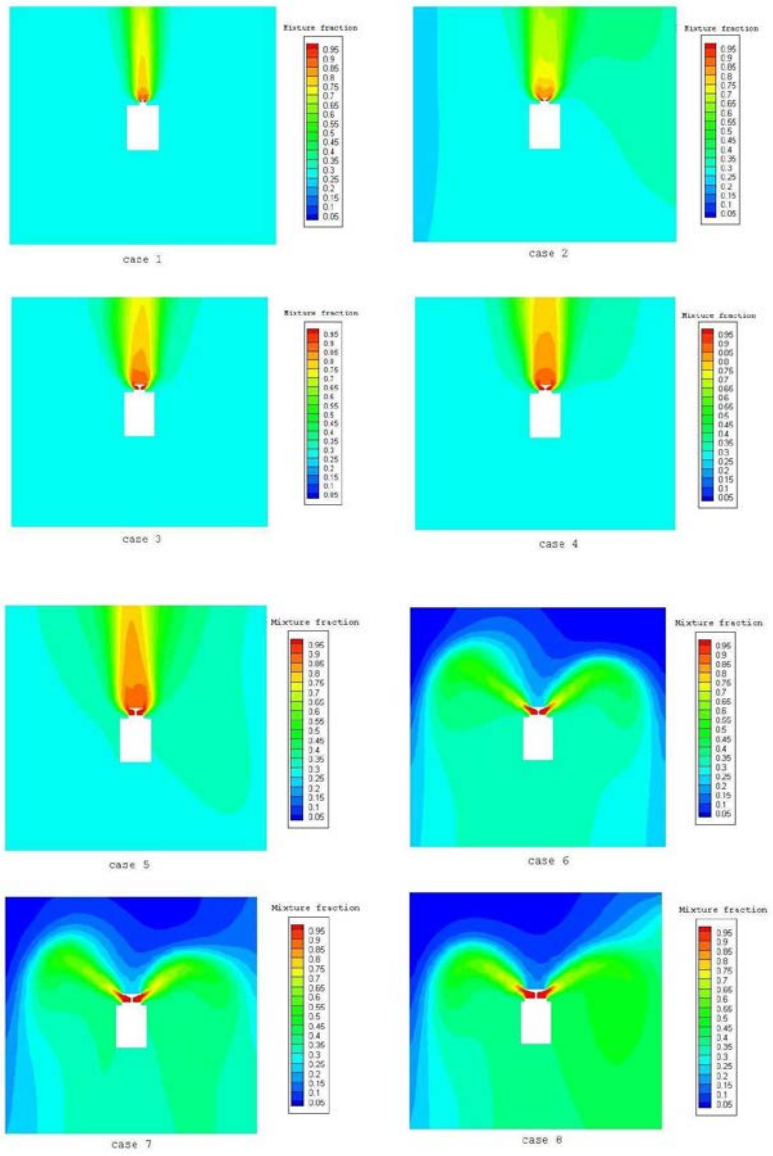

Figure 14 - Contour Plots of Mixture Fraction near NOx Port for Cases in Table 5.

An additional set of eight cases were set-up to extend the diameter of the spindle head and to better match the diameter of the water jacket around the NO_x port. These cases would help direct the air flow exiting the NO_x port downward, thus maintaining a lower stoichiometric ratio in the burner zone. Table 6 lists these geometries investigated.

Figure 15 shows that the air flow through the NO_x port can be directed towards the bottom half of the furnace using a larger diameter spindle, thus producing better staged combustion conditions in the furnace. Based on these CFD results, the geometry of Case 6 was selected for the NO_x port design due to an enhanced air flow structure and less recirculation near the walls.

Table 5 - Additional NOx Port Design Cases Investigated by CFD Modeling

	NOx Port OD		Spindle OD		Spindle Height
	cm	in	cm	in	cm
case 1	1.905	0.75	2.705	1.06	0.423
case 2	2.540	1.00	3.340	1.31	0.595
case 3	3.175	1.25	3.975	1.56	0.762
case 4	3.810	1.50	4.610	1.81	0.926
case 5	4.445	1.75	5.245	2.06	1.089
case 6	**5.080**	**2.00**	**5.880**	**2.31**	**1.250**
case 7	5.715	2.25	6.515	2.56	1.411
case 8	6.350	2.50	7.150	2.81	1.572
Outer jacket thickness = 0.8 cm					

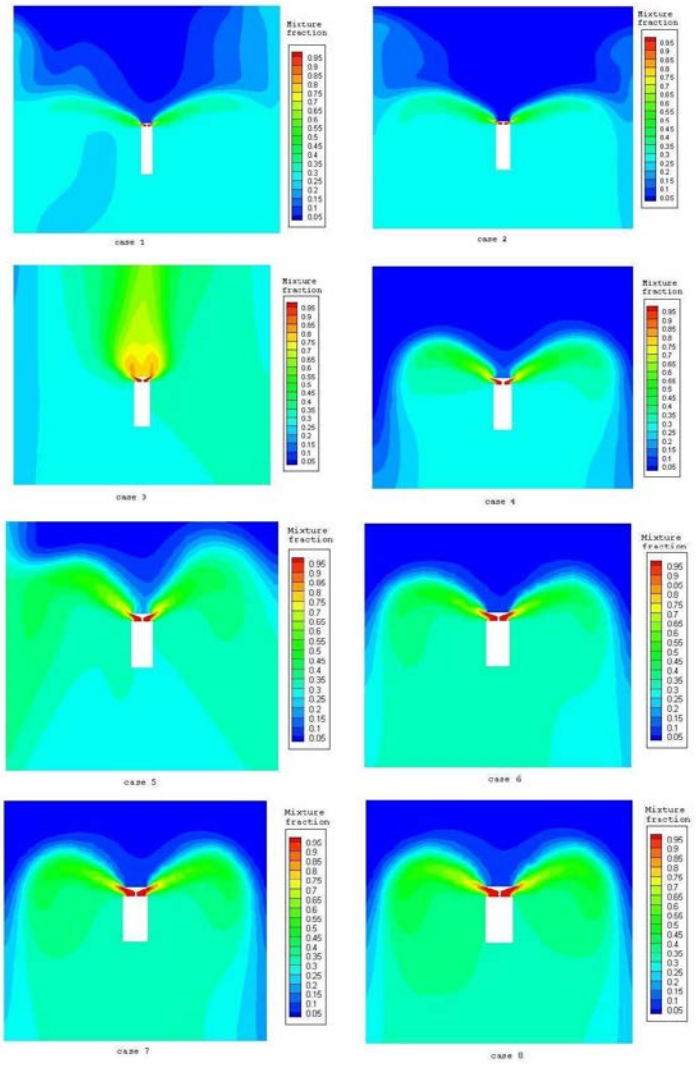

Figure 15 - Additional Contour Plots of Mixture Fraction near NOx Port for Cases in Table 6.

The original NO_x port shown in Figure 16 was tested in the BFR while burning a pulverized Utah sub-bituminous coal. This Utah coal is not part of the eight U.S. coals selected from Task 1 but was available prior to the arrival of the test coals. Therefore, it was used to facilitate the evaluation of the NO_x port. The original NO_x port nozzle outlet proved to be too small to work with the choked flow orifice that was used to measure the flow rate. This problem, along with the CFD predictions indicating interference of the NO_x port flow from the original nozzle with the reducing zone, led to a modified geometry of the spindle. However, it was not possible to implement the optimum spindle and NO_x port OD's proposed by the COMO results using the existing water cooled housing. Therefore, the largest diameter possible was selected as shown in Figure 16. The diameter of the spindle was increased from 0.34" to 1.73".

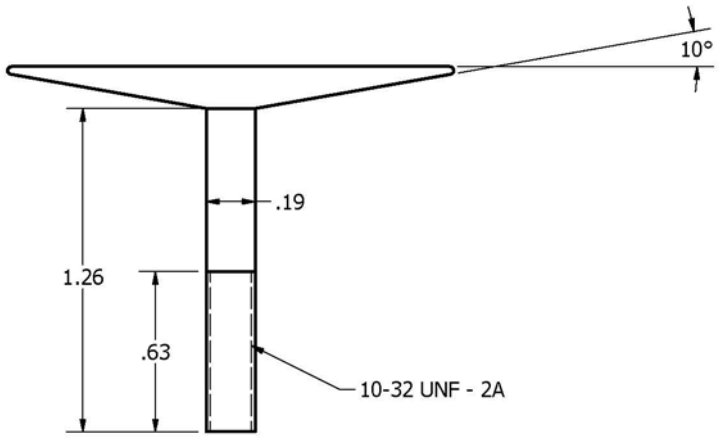

Figure 16 - Diagram of Spindle Used to Modify the Original Air Injection Probe.

Using the modified NO_x port, reducing combustion gases in the near burner zone and oxidizing gases at the furnace exit were successfully demonstrated in the BFR test runs, as shown in Table 7. With the Utah sub-bituminous coal, the BFR was able to maintain these combustion conditions during the test periods.

Table 6 - Gas Species Measured in the Burner Zone and Convection Pass of BFR

Gas	Burner Zone	Convection Pass
CO	> 5000 ppm	300 – 500 ppm
O_2	< 0.5%	1-2 %

4.2.2.2 Burner Characteristics and Selection

Two burners, both being a movable block swirl type, were available for use for this task. One of the burners was designed for a single coal feed, while the second was built to co-fire two fuels. The burners are referred to as the single and the dual-fuel burners in this report. Both of the burners consist of the components shown in Figure 17. Coal is conveyed by primary air into the injection tube at the center of the burner. For the dual-fuel burner, there are concentric tubes, referred to as the center and annular tubes. For the single-fuel burner, there is only a single tube.

Secondary air enters the upper plenum and is directed downward into the swirl plenum. The air is then directed toward the center fuel tube(s) through a set of triangular blocks, as shown by the top view in Figure 12a. One path through the blocks directs the air at the centerline of the burner without generating swirl, while the second path through the blocks directs the air off-axis or tangentially around the center of the burner. Moving the blocks changes the fraction of air in each passage, thus producing a different amount of swirl.

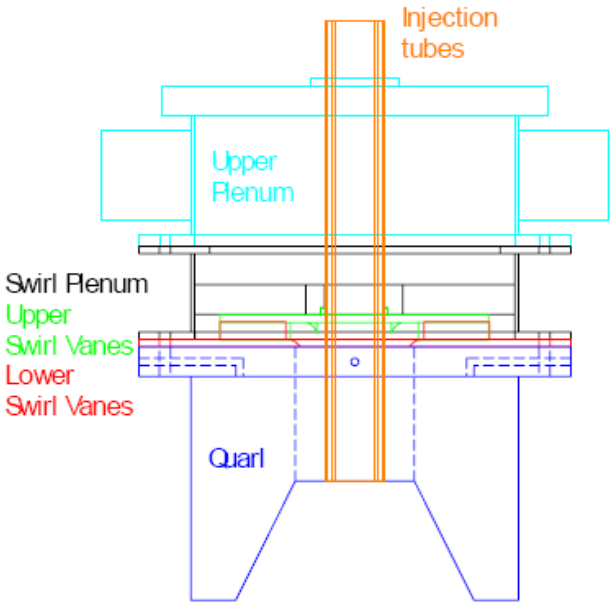

Figure 17 - Components of Variable Swirl Burner.

Some key geometric dimensions of the two burners are given in Table 8. Both the center and annular tube cross-sectional areas in the dual-fuel burner are larger than that of the primary tube in the single-fuel burner. The annular tube, which has a 14% larger cross sectional area, was selected for use in this project. A larger area can produce a slightly lower momentum of the fuel flow at the tube exit. A lower momentum and the absence of swirling in the center tube are expected to produce less mixing between the fuel and the secondary air stream, thus producing a lower stoichiometry in the dual-fuel burner. During testing, the single-fuel burner appeared visually to have a shorter and more compact flame with higher mixing between the primary fuel and secondary air.

The upper plenum of the dual-fuel feeder is designed with secondary air entering from opposing sides of the burner, while the single-fuel burner has secondary air entering from only one side. The two inlets result in a more even distribution of air in the dual-fuel feeder, thus reducing the tendency for flame asymmetry. As swirl is increased from 0.0 to 0.25 the flame transitions from straight down the BFR to a flow that is initially outward and recirculating up along the centerline. Above 0.25 the flame remains in the same recirculating structure but the recirculation zone becomes smaller and closer to the top of the BFR. At higher swirl the flame has a lower tendency to be asymmetric.

Table 7 - Differences in the Geometry of the Single and Dual-Fuel Burners

Burner Geometry	Single-Fuel Burner	Dual-Fuel Burner
Center tube I.D. (in)	1.0	1.342
Annulus Inner I.D. (in)	N/A	1.50
Annulus Outer I.D. (in)	N/A	1.842
Secondary Air Inner I.D. (in)	1.158	2.00
Secondary Air Outer I.D. (in)	3.543	3.68
Center Tube Area (in^2)	0.7854	1.414
Annulus Tube Area (in^2)	N/A	0.8977
Secondary Air Tube Area (in^2)	8.806	7.495
Swirl Plate Thickness	0.157	0.25

The dual-fuel burner has been used extensively in the literature by Damstedt[6] who mapped the gas species in the BFR burning different fuels, including coal, straw and three co-firing cases. An example of the CO concentration map from burning a Utah Blind-Canyon sub-bituminous coal at S.R. = 1.25 and swirl number = 1.0 is shown in Figure 18. This figure shows a high concentration of CO along the centerline of the BFR. The high CO concentration marks the fuel-rich combustion products extending to about an axial distance of 100 cm before being consumed by air. These data show a relatively narrow, symmetric reducing zone at overall fuel-lean conditions, which would be broadened under the fuel-rich conditions (at S.R. = 0.85) for the current project.

The single-fuel burner has been used extensively in the past for reburning measurements by mapping the gas species and temperature.[7-9] A map of CO at two operating conditions, i.e., fuel lean and fuel lean with natural gas addition (reburning), are shown in Figure 19. Both contour maps show that recirculation and high swirl produced a toroidal fuel-rich zone closer to the burner. Under overall air-rich conditions (e.g., S.R. = 1.12), shown in Figure 19(a), the CO concentrations produced by the single-fuel burner are lower than those by the dual-fuel burner at the same stoichiometric ratio. However, the fuel-rich zone of the single-fuel burner is shorter and combustion is more complete. The addition of natural gas injected from the NO_x port to produce an overall S.R. = 1.25 caused the size of the fuel-rich zone to increase and also greatly increased the concentrations of CO.

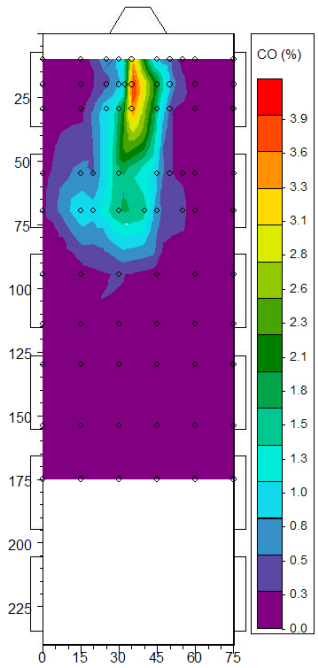

Figure 18 - Measured CO Concentrations for Blind Canyon Coal, S.R.=1.25, Swirl=1.0.

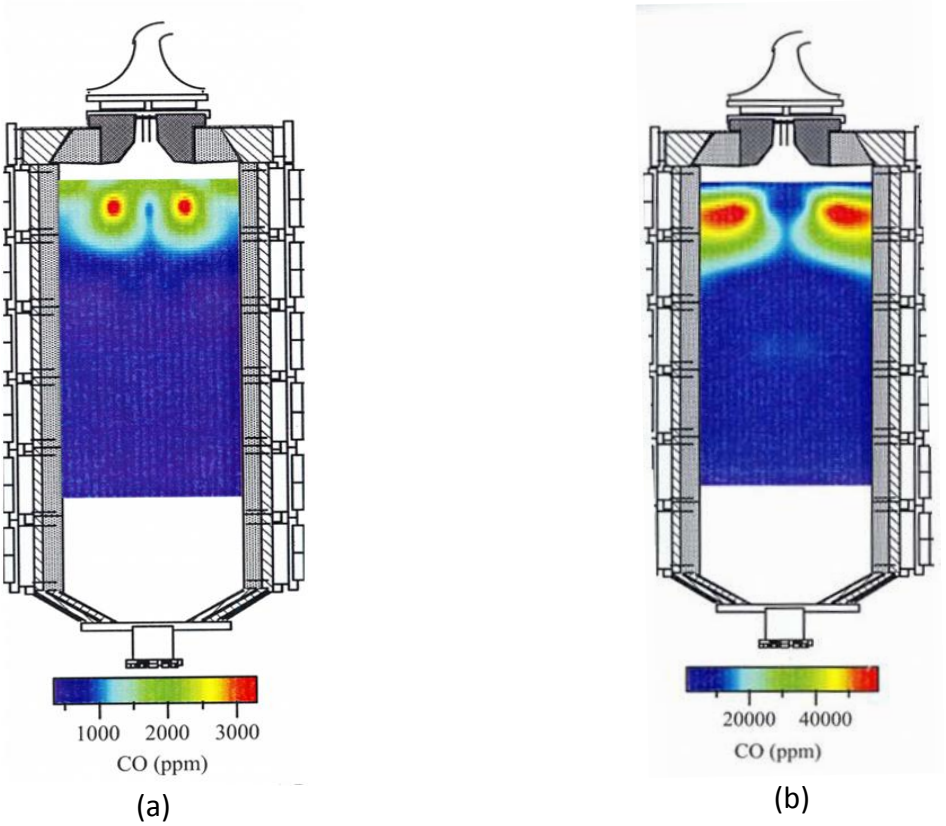

Figure 19 - Maps of CO Concentration for Single Fuel Burner at 1.5 Swirl, (a) without Natural Gas Injection and (b) with Natural Gas Addition.

Both the single and dual fuel-burners have been tested for this project. Based on the previous experiments, the dual-fuel burner has the advantage of creating a deeper reducing zone and thus behaves more like a commercial low-NO_x burner in producing a longer, less vigorously mixed flame. The single-fuel burner has the advantage of producing a shorter flame, which is advantageous for staged combustion of a smaller scale combustor. The shorter flame can also reduce flame impingement and increase carbon burnout.

A plot of CO concentrations at various radial positions and at the axial position of 70 cm is shown in Figure 20 for the dual-fuel burner. The data, obtained with the PRB coal during the first 30 hour test, show that a maximum CO concentration was present near the center of the BFR and became lower near the walls. As expected, the fuel-rich region is broader from this study comparing to that measured by Damstedt[6] (see Figure 18). The conditions produced with the dual-fuel burner were considered suitable for the gas and deposit sampling of Task 3, as similar variation in CO concentration has been found in actual commercial boilers. The flame, however, appeared to be lazy and occasionally impinged on the deposit collection probe.

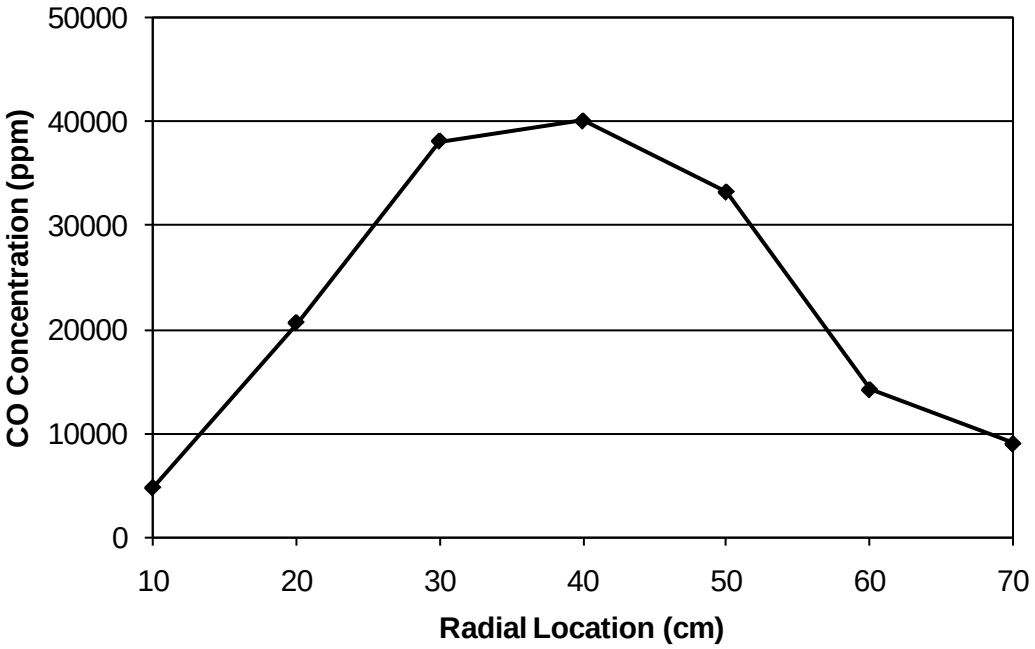

Figure 20 - Profile of CO Concentration for Dual Fuel Burner at Axial Distance of 70 cm from Burner at S.R.=0.85.

The use of the single-fuel burner was also investigated for the current project. The Illinois #6 Galatia bituminous coal was burned in the BFR to reveal the flame structure produced from the burner. During this test, the swirl number (1-1.5), probe location (z = 22-70 cm), and S.R. (0.70-0.90) were varied coarsely over a wide range of conditions to identify the flame shape as well as the size and intensity of the reducing zone. Results of the CO concentration measurements are shown in Figure 21. Each dark-lined rectangular section represents one of the top three sections (or modules) of the BFR. The CO concentrations were measured at the

approximate locations of the BFR indicated in the figure. The data reveal that a reducing zone was created near the center of the BFR but became less reducing toward the left side (i.e., south side) of the combustor.

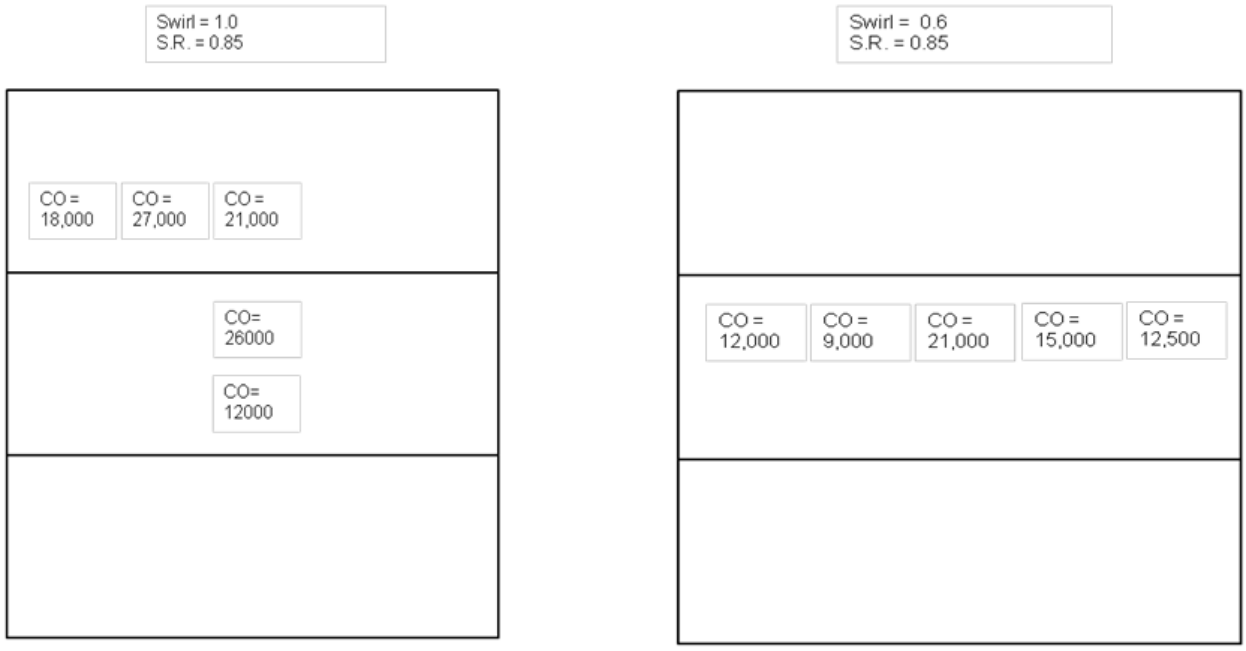

Figure 21 - CO Concentration in ppm for Single Fuel Burner at Two Swirl Ratios.

Although the single-fuel burner can create a stronger reducing zone near the burner, it was decided that the dual fuel-burner would produce the combustion environments in the BFR representing those in commercial utility boilers better and was therefore selected for Task 2 of this project.

4.2.2.3 Coal Delivery System and Improvements

The original coal delivery system of the BFR consisted of an Acrison variable speed SCR-DC motor controller, a Baldor DC electric motor, and an Acrison 105x-f volumetric feeder. An acceptable coal flow rate was accomplished by partially filling the fluted region of the ½" auger in the existing feeder with steel wires. The wires filled the fluted area sufficiently to reduce the coal flow to a desired level. The fuel feeder was found to have a linear relationship between the fuel flow rate and controller load, as shown in Figure 22, which indicates a linear relationship between the mass flow and voltage control position. However, this feed system had a very small coal hopper capacity, thus requiring constant attention of operators to manually fill the hopper.

To facilitate the coal combustion tests planned for Task 2, a new coal feed system was purchased by BYU and installed as part of the BFR. This system consists of a bulk bag unloader and loss-in-weight feeder, as shown in Figure 23. The new system also includes a platform to hold a bulk bag in place and pneumatic massage paddles to help discharge the coal. The bulk bag is approximately 49"x38"x38" in dimension and can hold up to 1500 lbs of pulverized coal.

After discharge, the coal is fed through an agitator hopper that fills the feeder hopper on demand. A pneumatic line was installed to convey the pulverized coal from the feeder to the burner. This integrated system allows the coal feed rate to be held constant for an extended period of testing time.

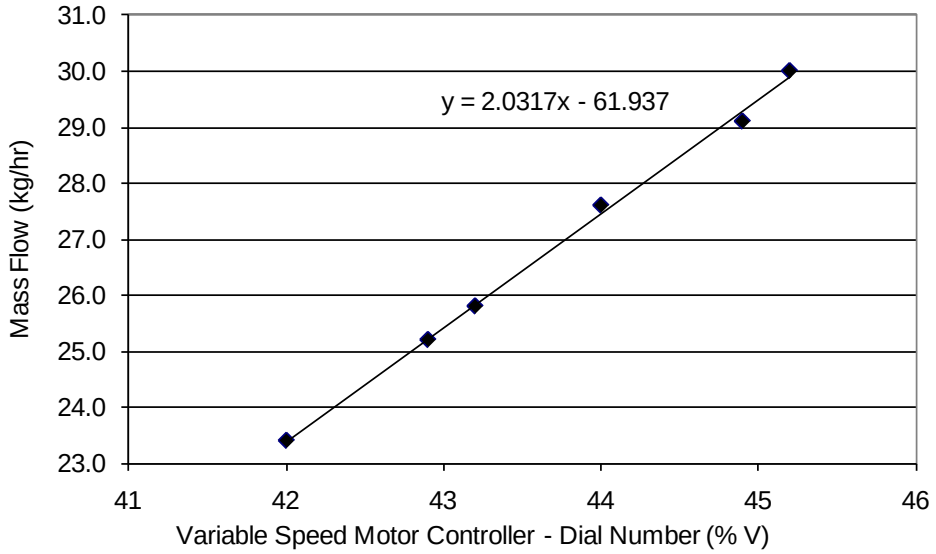

Figure 22 - Mass Flow Rate as a Function of Motor Speed Controller Dial Position.

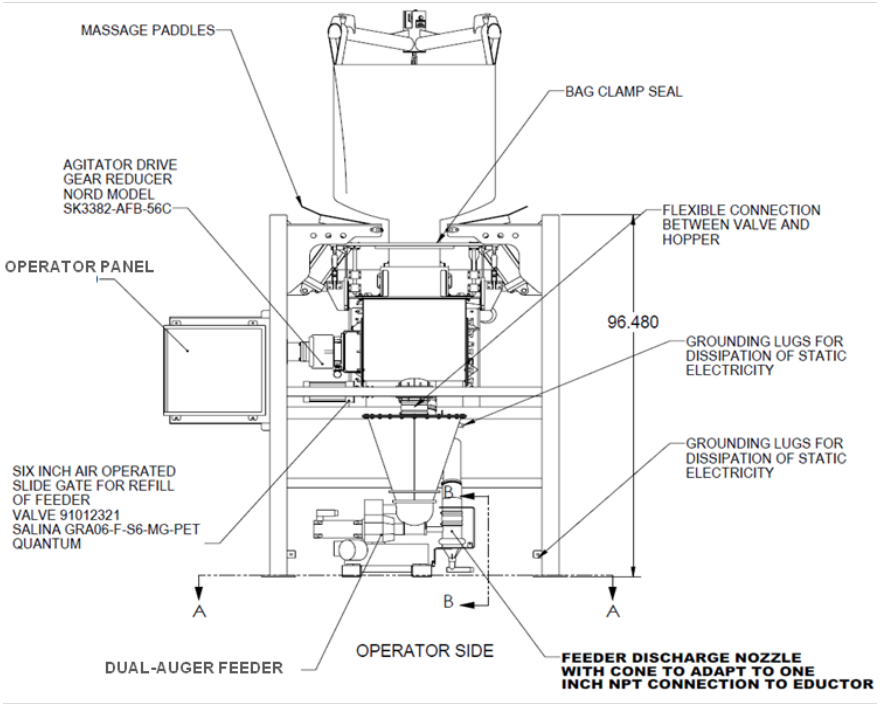

Figure 23 - Schematic of Bulk Bag Unloader and Coal Feeder.

Following installation of the new coal feed system, shakedown was performed in 2009 during which the feeder demonstrated a steady coal flow rate. The new feed system has since been integrated to the BFR and successfully operated. The system typically held the feed rate to within 5% of the set point over a period of 1 minute and to within 1% over a period of an hour. The feeder was also able to maintain the coal flow rate to within 5% of the set point during a refill.

Coal exit the feeder as it was pushed out of a feed tube by the twin augers. As with all auger systems, the coal tended to exit in clumps, which was further exaggerated by coal with a high moisture content. It was found to be effective that placing a wire mesh screen over the exit of the feeder tube helped break up the coal clumps. However, the wire mesh also behaved like a collector for foreign materials mixed in the coal. On two occasions, testing was interrupted by pluggage of the wire mesh, leading to very labor-intensive maintenance and repair work. For this reason, a decision was made to remove the wire mesh. Instead, a larger mesh with approximately 1-cm^2 openings was tested on the feeder exit, which proved to work better. The use of the larger mesh screen has since been implemented for this project.

Another problem encountered with the feed system was caking of the coal powder to the feeder hopper wall surfaces. Although the hopper walls have a slope of approximately 62^o, moist coal powder is still able to stick to them, thus preventing the coal from reaching the auger and ultimately the burner. The problem was minimized by the installation of mechanical vibrators mounted to the outside surfaces of the hopper walls.

4.2.3 Coal Procurement and Analysis

In preparation for combustion testing of the eight U.S. coals selected from Task 1, a vendor who is capable of procuring and processing small coal quantities (2-10 tons) required for the BFR testing was identified. Subsequently, all eight coals have been purchased, pulverized, and delivered to BYU. Following the delivery, proximate, ultimate, and ash analyses have also been performed for each coal, with results summarized in Table 9. The specified particle size of the pulverized coals was 75% passing through 200 mesh screen, identical to the typical specifications for coal-fired utility boilers.

The initial delivery of Illinois #6 and Powder River Basin (PRB) coals was consumed in 2009 before planned testing was complete. Therefore, additional coals were ordered and received in late 2009. Results of the coal analyses on the second batches are also included in Table 9. Although similar, some noticeable differences in the coal compositions existed between the two batches. For clarity, the first batch of Illinois coal is labeled as Illinois #6-1 and the second batch as Illinois #6-2. Likewise, the two batches of PRB coal are designated as PRB-1 and PRB-2, respectively. Consequently, Task 2 (and thus Task 3) involved a total of ten coals tested in the BFR, two coals more than those originally proposed for this project.

Table 8 - Proximate and Ultimate Analyses of Test Coals.

Proximate Analysis, As Received	Ill. #6-1	Ill. #6-2	PRB-1	PRB-2	Beulah Zap	Mahoning	Indiana	Gatling	Pitt 8	Kentucky
Moisture	5.40	3.68	24.59	21.23	27.33	2.22	7.25	3.77	1.05	3.39
Ash	8.65	10.45	5.14	5.53	8.66	9.92	7.20	11.34	10.45	8.46
Vol. Matter	35.68	33.70	37.00	33.76	33.77	40.79	30.87	40.73	18.61	36.97
Fixed Carbon	50.27	52.17	33.27	39.48	30.24	47.07	54.68	44.16	69.89	51.18
Total	100.00	100.00	100.00	100.00	100.00	100.00	100.00	100.00	100.00	100.00
Ultimate Analysis										
Moisture (%)	5.40	3.68	24.59	21.23	27.33	2.22	7.25	3.77	1.05	3.39
Hydrogen (%)	3.74	3.14	2.55	2.06	2.03	4.18	4.02	4.07	3.86	4.34
Carbon (%)	70.16	67.66	54.75	54.39	46.56	74.67	69.48	67.11	77.37	70.89
Nitrogen (%)	1.04	0.95	0.83	0.86	0.86	0.93	1.36	0.94	1.44	1.23
Sulfur (%)	2.69	2.96	0.25	0.26	0.67	1.96	1.14	4.31	1.03	3.64
Oxygen (%)	8.32	11.16	11.89	15.67	13.89	6.12	9.55	8.46	4.80	8.05
Ash (%)	8.65	10.45	5.14	5.53	8.66	9.92	7.20	11.34	10.45	8.46
Total (%)	100.00	100.00	100.00	100.00	100.00	100.00	100.00	100.00	100.00	100.00
Chloride (%) (dry basis)	0.3892	0.283	0.0012	0.001	0.001	0.1989	0.2121	0.0387	0.0045	0.2057
Heating Value (Btu/lb)	12,575	12,464	9,156	9,479	7,792	13,404	12,400	12,191	13,715	12,905
Ash Analysis										
Silicon Dioxide, % as SiO2	48.12	49.13	36.04	37.42	32.25	42.65	55.14	40.35	56.77	41.70
Aluminum Oxide, % as Al2O3	19.65	18.55	16.84	17.18	12.23	29.07	21.10	22.56	29.28	18.40
Iron Oxide, % as Fe2O3	17.64	16.38	5.86	5.50	7.45	20.45	12.93	28.33	6.63	26.09
Calcium Oxide, % as CaO	4.28	5.49	21.61	17.41	19.91	1.76	2.48	2.62	0.90	4.80
Magnesium Oxide, % as MgO	0.95	1.07	5.06	3.94	6.47	0.52	0.86	0.69	0.56	0.90
Sodium Oxide, % as Na2O	1.08	0.66	1.69	1.08	3.29	0.34	1.25	0.41	0.65	0.53
Potassium Oxide, % as K2O	2.59	2.34	0.50	0.57	0.82	1.61	2.40	1.28	2.30	2.43
Titanium Dioxide, % as TiO2	1.05	0.93	1.32	1.20	0.65	1.41	1.30	1.04	1.53	0.96
Manganese Dioxide, % as MnO2	0.07	0.04	0.02	0.02	0.08	0.00	0.03	0.05	0.05	0.03
Phosphorus Pentoxide, % as P2O5	0.08	0.09	1.00	0.54	0.27	0.76	0.35	0.22	0.56	0.31
Strontium Oxide, % as SrO	0.03	0.03	0.35	0.25	0.64	0.12	0.08	0.09	0.12	0.05
Barium Oxide, % as BaO	0.05	0.05	0.62	0.43	0.73	0.07	0.06	0.11	0.12	0.18
Sulfur Trioxide, % as SO3	4.41	5.24	9.09	14.46	15.21	1.24	2.02	2.25	0.53	3.62
Alkalies as Na20	2.79	2.20	2.02	1.46	3.83	1.40	2.83	1.25	2.17	2.13
Base to Acid Ratio	0.39	0.38	0.64	0.51	0.84	0.34	0.26	0.52	0.13	0.57
Silica Ratio	0.68	0.68	0.53	0.58	0.49	0.65	0.77	0.56	0.88	0.57
T250, °F	2429	2439	2228	2302	2130	2497	2624	2295	> 2900	2263

4.3 Task 3 – Gas and Deposit Sampling

This section describes the deposit and gas sampling methods and results for Task 3. It begins with a description of the probes and analyzers used for online gas measurements and a discussion of the calibration and accuracy of these measurements. The delivery of gas samples to the analyzers without condensation or reactions in the sampling line proved to be quite a difficult task. Efforts to develop a sampling system that can produce accurate measurements are also detailed here.

4.3.1 Gas Sampling – FTIR Theory

An FTIR spectrometer, model number MG2030 manufactured by MKS Online Instruments, was used to measure the CO, CO_2, H_2O, H_2S, COS, HCl, NO, SO_2, and SO_3 concentrations in the combustion gas. Although not the focus of this project, additional gases, such as HCN, NH_3, and CH_4, were also measured. The FTIR has a 5.11-m long optical gas cell with a maximum resolution of 0.5 cm^{-1}. The instrument transmits an infrared light through the sampled gases and analyzes the absorption of light as a function of wave numbers (WN). Each gas has a known spectral absorption pattern which can be quantified when compared to the calibration spectra taken at the same temperature and pressure.

The absorption of gases follows Beer's law[10] that relates the amount of transmitted light through a gas to the product of absorption coefficient κ_η, and the path length through the gas, s, according to Eq. 6. Per convention used by MKS, absorbance is defined as the negative logarithm of τ, as shown in Eq. 7.[11]

$$\tau = \frac{I}{I_0} = 10^{-\kappa_\eta s} \qquad \text{Eq. 6}$$

$$A_\eta = -\log_{10}(I / I_0). \qquad \text{Eq. 7}$$

Combining Eqs. 6 and 7, it can be seen that the absorbance is a function of the absorption coefficient and path length and therefore the absorptivity ε_η, concentration c, and path length s, as shown in Eq. 8.

$$A_\eta = \kappa_\eta s = \varepsilon_\eta c s \qquad \text{Eq. 8}$$

When measuring combustion products, the total absorbance is the sum of absorbance of all gases in the mixture. Although each gas may absorb over a large range of wave numbers, an analysis band is specified for each measured gas, from which its concentration can be calculated. The analysis band is selected in a way to avoid interference from other gases. For example, even though H_2S has a spectrum range spanning from 400 to 3000 cm^{-1}, a band of 2670-2700 cm^{-1} was chosen to minimize the overlapping with water bands. When other gases have a signal in the analysis band of a gas being measured, that signal becomes noise interfering with the desired

measured signal. The MKS software determines the concentration of the measured gas by comparing the measured absorbance with the absorbance of the calibration gas absorbance signal. In the H_2S example, the data between 2670-2700 cm^{-1} are used to calculate the H_2S concentration while the rest of the H_2S spectrum are used to determine the absorption contribution from H_2S as noise to the signals of other gases.

An advantage of measuring H_2S with FTIR is that the instrument can collect data continuously and simultaneously with other gases. The FTIR is also an online measurement allowing sampling from numerous locations without the need of performing chemical analysis in the lab following gas sampling. However, H_2S is a difficult gas to measure because of its low absorbance signal relative to interfering gases. The poor signal to noise ratio can lead to lower accuracy in the measured concentrations. Therefore, special effort was made to quantify the uncertainty of H_2S measurement. The FTIR spectral absorption pattern for 1000 ppm of H_2S is shown in Figure 24. Note that the maximum absorption is only about 0.012 absorbance units (AU), as determined from Equation 8. This low absorption corresponds to a transmitted IR intensity of $0.973I_0$, indicating that at this specific wave number (1292.8 cm^{-1}), only 2.7% of the IR light was absorbed by H_2S.

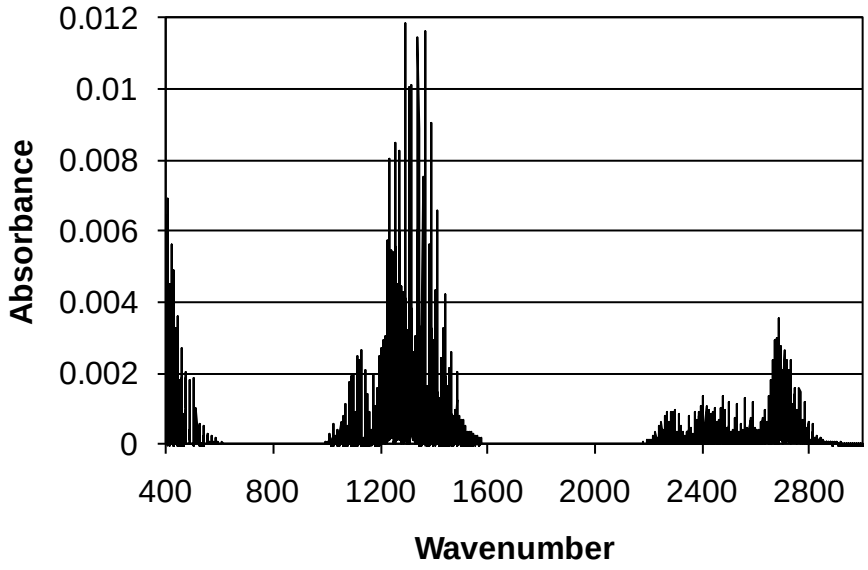

Figure 24 - H_2S Absorption Spectrum for 1000 ppm H_2S in Nitrogen.

As mentioned above, the FTIR software produces a calculated spectrum that best matches the measured spectrum from a set of calibration spectra in the software library. The match between the measured and calculated spectra is determined by minimizing the error E, as given by Eq. 9,[11] where the index *i* represents each wave number measured in the analysis band.

$$E = \frac{\sqrt{\sum_{0}^{n}\left(meas_i - calc_i\right)^2}}{\sum_{0}^{n} calc_i} \times conc \qquad \text{Eq. } \mathbf{9}$$

where *meas* and *calc* refer to the absorbance values of the measured spectra and calculated calibration spectra, respectively, and *conc* is the measured concentration of the gas.

The calculation assumes that the difference between the measured and calculated spectra, or residual, is the only source of noise. Therefore, it is strictly an indication of precision but not the total error. Comparison between the measured and calculated H_2S values showed that the uncertainty of a single 300 ppm H_2S measurement was on the order of 100% on a relative basis. Averaging several data points reduced the error, as the magnitude of reduction is inversely proportional to the square root of the number of data points averaged.

Interference of water with the H_2S spectra is inevitable. The level of interference on the measured H_2S concentration depends on the relative amount of water and H_2S in the gas sample, the change in the FTIR emission source signal strength over time, and the change in the gas cell window transmittance. With clean optics and a strong signal, water interference from typical coal combustion appears to produce approximately ±125 ppm of uncertainty in the H_2S measurement. Averaging six measurements was typically done in the data reported, leading to an uncertainty of ±50 ppm under clean operating conditions. However, the gas cell can rapidly become dirty during testing, thus increasing the uncertainty. In general, when the H_2S average uncertainty increased above ±125 ppm, as noted by negative readings, the FTIR was cleaned before proceeding. There are some data, however, taken under noisier signal conditions due to a shortage of fuel or time constrain.

4.3.2 Gas Sampling System

It was necessary to deliver the combustion gases from the BFR chamber to the analyzers through a gas sampling system free of condensation and chemical reactions. Particulate in the gas samples had to be removed upstream of the analyzers to protect the instrument optics. Gas samples were rapidly quenched to 180°C at the tip of the sampling probe to prevent further chemical reactions among the sampled gases. However, this temperature was sufficiently high to avoid acid condensation. A total of ten gas species of interest were investigated, including CO, CO_2, H_2, H_2O, H_2S, HCl, NO, O_2, SO_2, and SO_3. The use of three different gas analyzers was required for measuring all of these gases.

A five-gas analyzer, Horiba PG-250, is capable of measuring common combustion gases, including NO, CO, SO_2, CO_2, and O_2. Three of the gases, CO, SO_2 and CO_2, are measured using infrared absorption. The NO concentration is measured using chemiluminescence, and O_2 is measured using a zirconium oxide cell. Prior experience indicates that the desiccant and water trap used at the gas inlet would influence the SO_2 measurement and therefore, this gas was not analyzed with the Horiba for this study. The CO readings were limited to a maximum of 5000 ppm on the Horiba analyzer, which is too low for most substoichiometric coal combustion.

Therefore, this gas was not measured with the Horiba either. Instead, both SO_2 and CO were analyzed with the FTIR instead.

A micro GC, Model 3000 manufactured by Agilent Technologies, was used for the H_2 and O_2 measurements. The GC operates by separating the combustion gases in a capillary column. Once separated, the thermal conductivity of the gases at the column exit was measured to determine the gas concentrations. Only H_2 and O_2 were analyzed with the GC for this project, although the instrument is also capable of measuring N_2 and CO.

A schematic diagram of the gas sampling system is shown in Figure 25, where all bolded components were heated to 180°C to prevent acid condensation. A water cooled probe was inserted into the BFR chamber through a circular port in an access door. The probe housed an electrically heated sampling line. The heating element of the sampling line within the probe was connected to a temperature controller to maintain a constant temperature of 180°C. This sampling line made of either Teflon or stainless steel is available commercially. Both line materials were evaluated in this study, but the use of Teflon was chosen due to its chemical stability with the combustion gases (to be discussed shortly). The water-cooled probe and heated sampling line were nominally 5 ft long, sufficient to traverse through the inner diameter of the BFR.

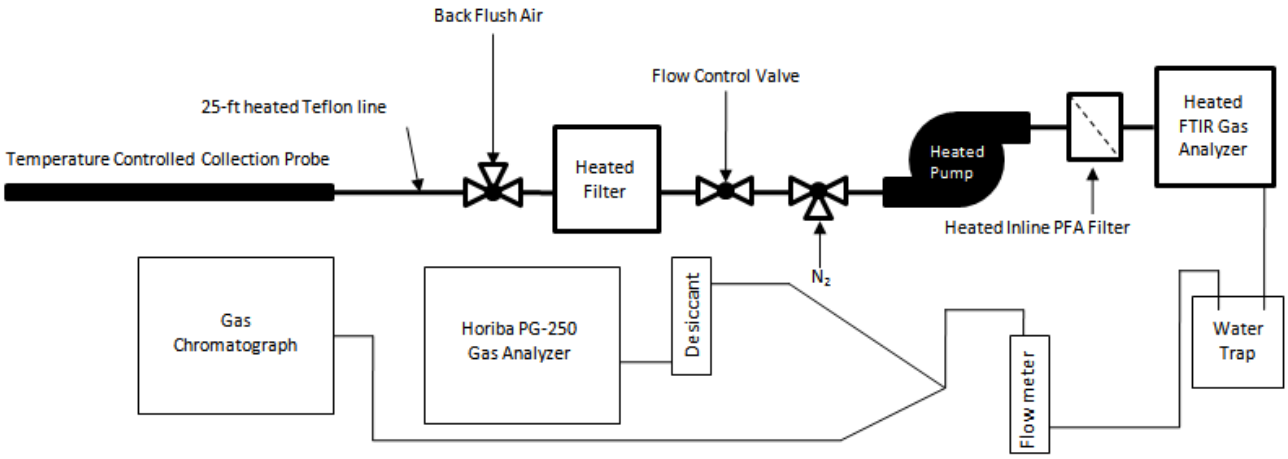

Figure 25 - Schematic Diagram of Components and Analyzers of Gas Sampling System.

Although the majority of the heated sampling line is made of Teflon, the line tip in the probe exposed directly to the combustion gases was made of stainless steel to withstand the high gas temperatures. A quartz tube was later tested because it was concerned that the small piece of stainless steel tip could have reacted with some of the corrosive gases, especially HCl. Quartz is often used in the online measurements of combustion products due to its high melting point and chemical stability. After numerous tests with both quartz and stainless steel tube tips, both materials appeared to provide accurate gas measurements. The stainless steel tip allowed compression fittings to be used and thus minimized air leakage into the sample line. The Teflon tube tip often melted at the connection between the stainless and Teflon tubes. The quartz eliminates the melting problem but it was more fragile and more easily plugged. There are also

no compression fittings available to connect the quartz and Teflon tubing, resulting in more frequent air leakage.

Outside the BFR, a second heated line, 25 ft in length, was used to carry the gases from the probe exit to the analyzers. Before reaching the analyzers, the gas samples went through a series of heated components. The first was a 3-way valve that allowed either the samples to travel toward the analyzers or pressurized air to back-flush the probe. During flushing, air traveled back through the 25-ft heated line and probe to clear out any particulates accumulated in the system. After the 3-way valve, the gas sample passed through a heated Teflon filter that was controlled at 180°C. No metallic components were present in the heated filter in contact with the sampled gases.

Upon exiting the heated filter, the gas traveled through two additional valves. The first was a needle valve for the control of the sample flow through the system. When the valve was closed, the heated line was inaccessible to the pump. Conversely, as the valve was opened, the pump was allowed to draw gas from the BFR. The second valve, a three-way valve, controlled the source of gases flowing into the gas analyzers. When turned one direction, the combustion gases were allowed to flow to the FTIR; while turned the other direction, dry nitrogen was allowed to flow into the FTIR. The nitrogen was used as a calibration gas for the FTIR and Horiba. The gas subsequently traveled through a heated pump that was oil-less and contained a Teflon diaphragm. The pump head and valve body were constructed of 316 stainless steel but were Teflon coated. The final component before the FTIR was an inline Teflon-PFA (perfluoroalkoxy) filter with a single 47 mm-diameter Whatman qualitative grade 5 filter paper (No. 1005 047).

While in the FTIR, the gas samples were maintained at a temperature of 150°C and pressure close to one atm. The FTIR can accurately compensate for pressure variations that are within ±10% of atmospheric pressure. Upon exiting the FTIR, the gases passed through a water trap housed in an ice bath maintained at 0°C, thus eliminating most of the water in the line prior to the analyzers. After the water trap, the gas samples passed through a rotometer containing a needle valve used to control the FTIR pressure. The flow was then split into two lines, with one going to the GC and the other going to Horiba PG-250.

Several important modifications have been made to the gas sampling system developed for this project, which is summarized below.

1. A heated Teflon filter with a temperature controller was added to the system. Originally, a metal filter surrounded by heat tapes was used between the probe and 25-ft heated line. The filter became plugged often and required frequent replacement. The filter replacement was time consuming because the heat tapes and filter housing must be disassembled first. A commercial Teflon filter was identified and integrated into the gas sampling system. The filter was prone to leak due to a threaded Teflon connection. However, in spite of this challenge, the use of the Teflon filter was deemed necessary to prevent particulate from entering the gas analyzers.

2. A needle valve was added downstream of the FTIP to reduce the total flow rate through the sampling line. This valve served two important purposes. First it reduced the total flow of flue gas (and particulate) through the line and thus reduced the frequency of filter replacement. Consequently, gas sampling could be performed continuously for four hours before filter replacement became necessary. The second benefit was associated with reduced heat loading on the sampling line. Teflon melts at 190°C. The additional heat introduced from a high gas flow through the sampling line increased the temperature and thus melted the Teflon. By using the flow control valve, the temperature of the sampling line was more easily controlled. However, the lower gas flow rate in the sampling line might have created another issue, as the concentrations of some combustion gases, especially HCl, appeared to decrease with decreasing flow rate. More discussion on this topic is given in Section 3.3.6.1.

3. The back-flush valve was useful in clearing the sampling line without the need to disassemble any components. Prior to the use of a back-flush valve, line fittings wrapped in heat tapes had to be disconnected in order to clear the line, which was time consuming.

4. Although both the GC and Horiba consisted of separate desiccants, the addition of a water trap was very effective in preventing acid condensation in the rotometer, thus prolonging the desiccant use life.

5. The tip of the gas sampling line that protruded out of the water-cooled probe in direct contact with the combustion gases was originally made of stainless steel. Quartz has been tested recently but it did not appear to produce a different result from the stainless steel. A quartz tube was used for the gas sampling of last three coals.

6. The additions of the metallic valves and fittings mentioned above were found to reduce the HCl concentration proportional to the contact time with the combustion gases. Cold fittings produced exaggerated reductions in HCl compared to well insulated fittings. In order to obtain repeatable HCl measurements, all metal fittings were removed. This meant that the sample line lacked flow control, plugged rapidly and was not easily cleaned or calibrated. The difficulty of obtaining data was significantly increased. As a result, special fittings and valves coated with Teflon were used.

A detailed drawing of the sampling probe designed by Damstedt[12] is shown in Figure 26, which was initially used for this project. The flow of water in the cooling jacket is indicated by the arrows with the heating element shown as the shaded area. Combustion gases enter the probe from the left into a Teflon tube inside the heating jacket. Two problems have been encountered with this probe design: (1) the end of the Teflon tube often melted due to the high temperatures of combustion gases and (2) air in-leakage occurred via the spacing between the heating element and cooling jacket, thus diluting the compositions of sampled gases.

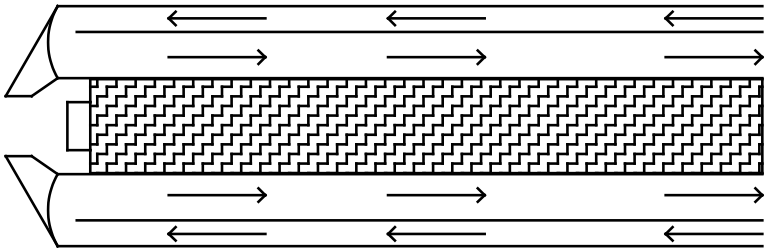

Figure 26 - Schematic Diagram of Sample Line Inlet Showing Water-Cooled Tube and Heated Sample Line (Dark Region), after Damstedt (Ref. 12).

In consultation with the manufacturer of the heated sampling line, a new design was implemented, as shown in Figure 27. The new heated line consisted of two modifications: (1) the heating element is surrounded by a smooth outer surface and (2) the center tube is a larger 3/8"-OD stainless steel tubing. The 3/8"-OD tubing allowed a ¼"-OD Teflon tubing to be inserted into the line ID. The Teflon tubing could be easily replaced when damaged from overheating without the need to change the entire heating element.

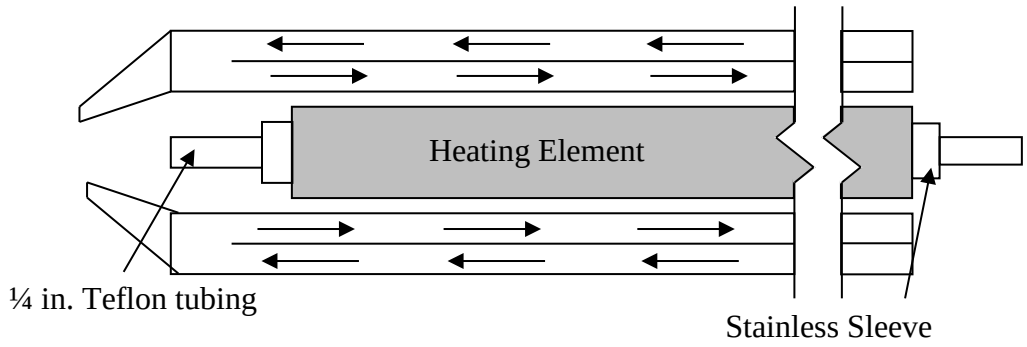

Figure 27 - New Heated Probe Design with Replaceable 1/4 Inch Teflon Tubing and Smooth Surface Heating Element.

This modified probe design also included a short stainless steel tube tip coupled with the Teflon line by a compression fitting, as shown in Figure 28. The metal tip protruded approximately 1" from the probe opening into the BFR chamber. The pressure inside the BFR was maintained slightly positive, thus minimizing significant leaks from the interface between the heated sampling line and cooling jacket.

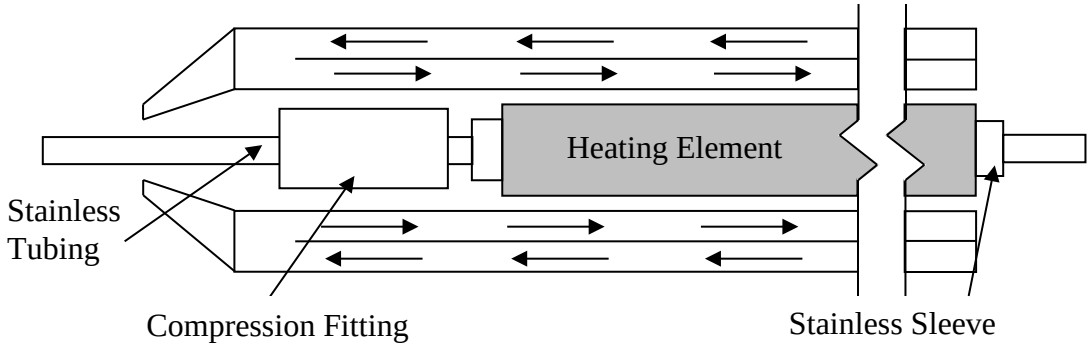

Figure 28 - Heated Probe Design with 1" Long Stainless Steel Tubing Exposed to Hot Combustion Gas.

In the most recent measurements (the last three coals tested), both the stainless steel and Teflon tubes inside the heating element were replaced with a ¼ inch diameter tube.

4.3.3 Sampling Line Checks and Calibration

A schematic diagram of the gas sampling system is shown in Figure 25 and the components have been discussed in Section 3.3.2. It was imperative to eliminate any leak and prevent acid condensation in the sampling train. The analyzers must also be well calibrated.

4.3.3.1 Leak Test

Leak test was performed when the BFR was running on natural gas prior to each of the coals. The natural gas and air flow rates to the BFR were very stable and thus produced a constant combustion environment in term of gas temperatures and compositions. The Horiba analyzer was used to measure the O_2, CO, and CO_2 through a short piece of stainless steel and unheated Teflon tubing. Although this line would condense HCl and H_2S, it allowed an accurate measurement of the O_2 concentration. The O_2 measurement was then repeated through the use of entire heated sampling line, including the heated filter and pump. An agreement on the O_2 concentrations from both measurements was an indication of no leak in the sampling train.

4.3.3.2 Analyzer Comparison and Calibration

Various certified calibration gases were used to calibrate the Horiba, GC, and FTIR. The calibrations were done routinely, usually in the morning of each day before data collection. The calibration gases used to calibrate the Horiba and GC are listed in Table 10. It should be mentioned that the GC was only calibrated with a high CO concentration expected in fuel-lean regions, as the Horiba analyzer cannot measure CO more than 5000 ppm.

Table 9 - Calibration Gases Used for the Analyzers.

Analyzer	Gas	Concentration (Nominal)
GC	O_2	0, 0.1, 22 (%)
	H_2	0, 0.1(%)
	CO	0, 0.1 (%)
Horiba	O_2	0, 22 (%)
	CO_2	0, 18 (%)
	CO	0, 4500 (ppm)
	NO	0, 1000 (ppm)
FTIR	H_2S	800 (ppm)
	HCl	100 (ppm)

The FTIR utilizes spectra supplied by the manufacturer. In order to check the accuracy of the FTIR spectra, calibration gases of known concentration were delivered to the analyzer and the measured results were compared to the known gas concentrations. Figure 29 shows the setup of these calibration tests with results of the gas measurements for H_2S and HCl shown in Table 10. The results show an excellent agreement between the measured and actual concentrations, with a less than 3% deviation. The SO_3 spectra could not be compared to a known standard because of the unavailability of SO_3 calibration gases. MKS was contacted for assistance in evaluating the accuracy of the SO_3 measurement. It was learned that the MKS spectra for SO_3 were produced by reaction and not by using a certified gas mixture. Therefore, the manufacturer expressed confidence only in the spectral shape but not the absolute values. An uncertainty of ±50% for the measured SO_3 concentrations was suggested.

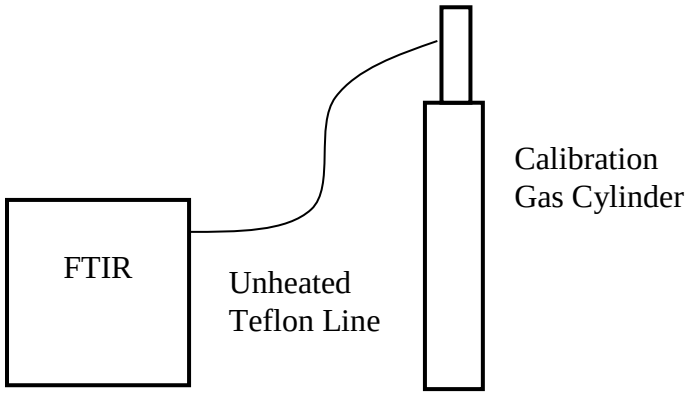

Figure 29 - Calibration Setup for the FTIR.

Table 10 - Results of HCl and H_2S Calibrations.

Gas	Cylinder Concentration (ppm)	FTIR Measurement (ppm)	Error
H_2S	817	827	+ 2%
HCl	96	93	- 3%

4.3.3.3 Reactivity Testing

Several combustion gases of interest, including H_2S, HCl, and SO_3, are chemically reactive and can condense out with water in the sampling line when the temperatures fall below their dew points. In order to determine the loss of H_2S and HCl in the sampling line due to acid condensation, calibration gases were passed through individual and multiple line components. A diagram of the sampling line used for the reactivity testing is shown in Figure 30. This sampling system differed from the one used for Task 3, shown in Figure 25, because the reactivity testing was done prior to the final setup. Specific components of interest for this study included (1) a 2-m heated stainless steel sampling line, (2) a heated stainless steel filter, (3) a 25-ft heated Teflon sampling line, (4) a 10-ft unheated Teflon line, and (5) a heated pump.

Results of the measured gas concentrations with the FTIR after passing the calibration gases through various components are listed in Table 12. These results are also compared to those by feeding the gases directly into the FTIR through a short 2-m Teflon line (see Table 11). Although not all of the components were tested, a trend was evident. When either of the calibration gases were passed through the Teflon lines (Components 3 and 4), losses were negligible. However, when the gases were passed through stainless steel tubing (Component 1), the loss was approximately 10%. The losses in the heated filter that was housed in a stainless steel enclosure were also significantly at approximately 10%. Following these tests, it was decided that the use of stainless steel components in the sampling train must be eliminated.

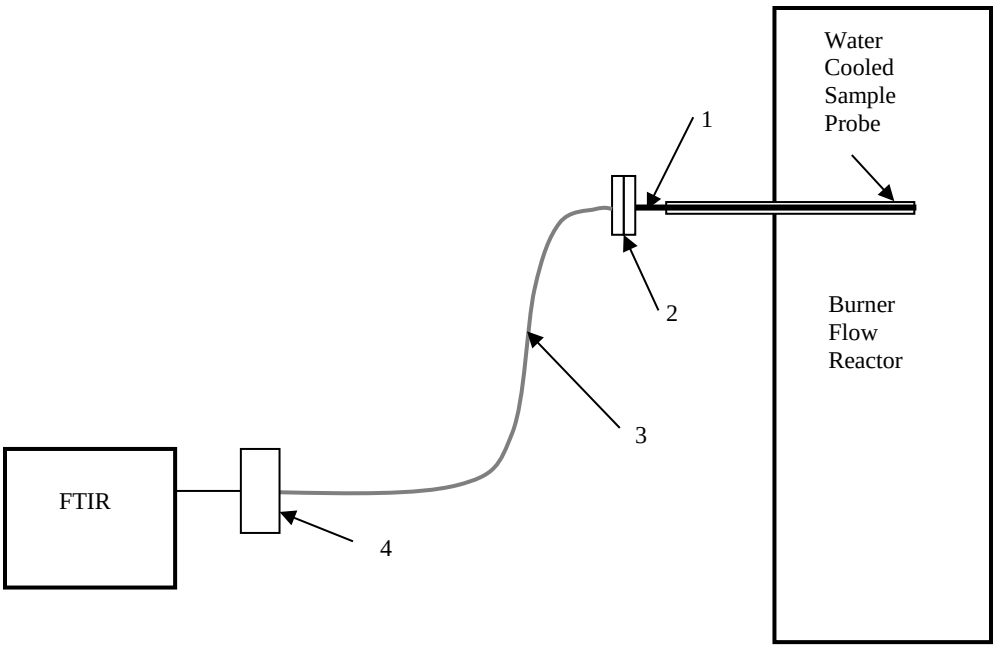

Figure 30 - Diagram of Gas Sampling System Showing (1) 2-m Heater Sample Line, (2) Heated Filter, (3) 7.6-m Heated Teflon Sample Line, and (4) Heated Pump.

Table 11 - Results of Measured Gas Concentrations after Passing the Calibration Gas Through One or More of the Components in Sampling Line.

Gas (concentration)	Components	FTIR Measurement	Difference From Direct Delivery (%)
H_2S (817 ppm)	3	821 ppm	- 6 ppm (-0.7%)
H_2S (817 ppm)	1, 2, 3, 4	744 ppm	- 83 ppm (-10%)
HCl (96 ppm)	3	91 ppm	- 2 ppm (-2%)
HCl (96 ppm)	5	91 ppm	-2 ppm (-2%)
HCl (96 ppm)	2, 5	80 ppm	-13 ppm (-14%)
HCl (96 ppm)	1, 4, 5	80 ppm	-13 ppm (-14%)

Also of interest was the variability seen in the concentration data for H_2S. Although the averages of measured H_2S concentration were in good agreement with the actual concentration of the calibration gas, a scattering of ~100 ppm was observed from sample to sample, as shown in Figure 31. The scattering of H_2S was greater than that of the other gases. Possible reasons for the variability in H_2S are discussed in section 3.3.1. However, in this case, there was no water to interfere with the H_2S measurement. Therefore, the scattering was attributed only to the low absorbance of H_2S. Averaging the data based on 16 data points from 4 minutes of gas sampling has produced an average value of 744 ppm for the H_2S, with a 95% confidence interval at $\pm$20 ppm.

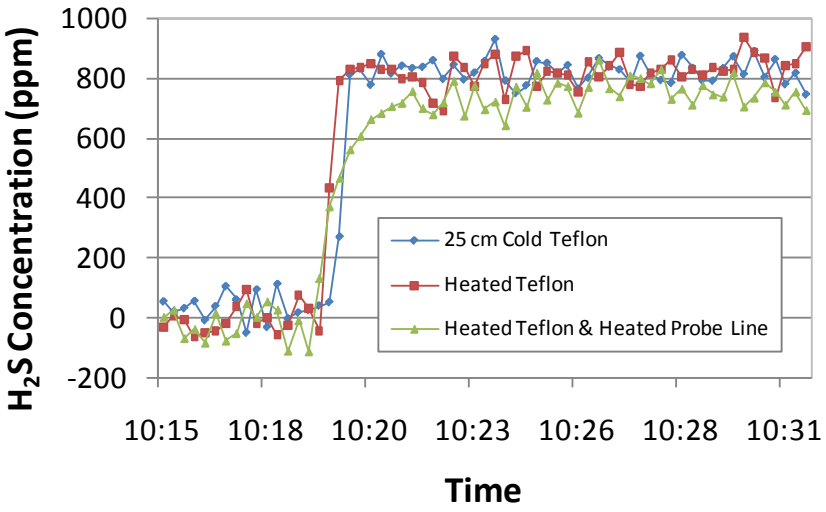

Figure 31 - FTIR Measurement of 817 ppm H_2S Calibration Gas.

Although initial measurements for the Illinois #6-1 and Beulah Zap lignite coals were completed with no stainless steel components in the sampling line except for the stainless-steel tip inserted into the combustion gas, the need for better control of the gas sampling line became obvious. The sampling line would plug after a brief period of approximately 5 – 10 minutes of sampling. In order to reduce plugging problems, a back-flush system was added, which required a three way valve and fitting made of stainless steel. A stainless steel needle valve was also added to reduce the flow rate of the sampled gases and therefore reduce the particle loading on

the filter. The Teflon fittings on the heated filter would frequently leak and were replaced with stainless fittings.

The coals tested when the stainless components were used in the sampling line (i.e., PRB and Beulah Zap) showed no change in H_2S. The chlorine contents of these coals were so low that the calculated highest possible HCl was near the measurement limit of 1 ppm. Therefore, impact on these coals from the stainless steel components was not noticeable. However, the Mahoning and Illinois 6-2 coals were subsequently tested, and the measured HCl concentrations were found to be unexpectedly low. Following the test of Indiana coal and a low HCl concentration was again observed. A series of experiments were thus performed to examine the accuracy of the measured HCl concentrations. Results of these experiments showed that when stainless steel components were used in the sampling line, the measured HCl concentration would respond slowly to changes in the operating conditions. With the steady-state value being approached, the HCl concentration would increase with increasing flow rate and temperature. These results indicated adsorption of HCl in the stainless steel surfaces, which increased with increasing contact time (i.e., at lower flow rates). The adsorption also increased with lower stainless steel metal temperatures. When the stainless steel components were removed, the measured HCl concentration increased rapidly to a steady value and was no longer dependent on the flow rate. After these phenomena were discovered, the gas sampling was repeated for the Mahoning, Indiana, and Illinois 6-2 coals. Gas sampling for the remainder of the coals, i.e., Gatling, Pittsburg and Kentucky, was performed with the stainless steel components were completely removed from the sampling line.

It was noted that the concentrations of other gas species, with the exception of HCl, exhibited negligible changes during testing with and without the stainless steel components. Such results indicate that the stainless steel surfaces in the sampling line had little impact on their measured values. It has been noticed however that if the sampling line temperature dropped well below the target temperature of 180^{o}C, the measured H_2S concentration decreased with decreasing temperature.

4.3.4 Deposit Sampling in BFR

Two sampling probes have been designed, fabricated, and tested for this project to collect deposit samples in the fuel-rich and fuel-lean regions of the BFR. The targeted surface temperatures for the fuel-rich region were 750-1100°F (400-600°C), simulating the temperatures of lower furnace walls. The targeted temperatures for the fuel-lean region were 1100-1500°F (600- 800°C) to simulate the conditions of superheaters. Initial testing showed that air was insufficient to cool the probe surface temperatures in the near-burner reducing zone but was sufficient in the oxidizing region. Therefore, an air-cooled probe was built for the oxidizing region, and a water-cooled probe was developed for the reducing zone. Each probe contained multiple sleeves mounted to the OD surface for deposit collection. For the water-cooled probe, a series of experiments were performed to determine the thickness of the sleeves that would produce the desired sleeve surface temperatures.

Drawings for the air and water-cooled deposition probes are shown in Figure 32 and Figure 33, respectively. The air-cooled probe is a 0.50”-OD tube inserted through the BFR walls

with air entering from one side and exiting from the other. Six, 3” long and 0.625”-OD deposition sleeves with 0.065” wall thickness were mounted to the probe. The sleeves were made of 304 stainless steel and were cut into two halves along the axial direction to provide good thermal contact with the probe surface. The split also allowed easy removal of the sleeves from the probe body after testing. Three of the six sleeves had slots cut on the outside surfaces parallel to the probe body to create channels for the insertion of 0.032”-OD Type-K thermocouples.

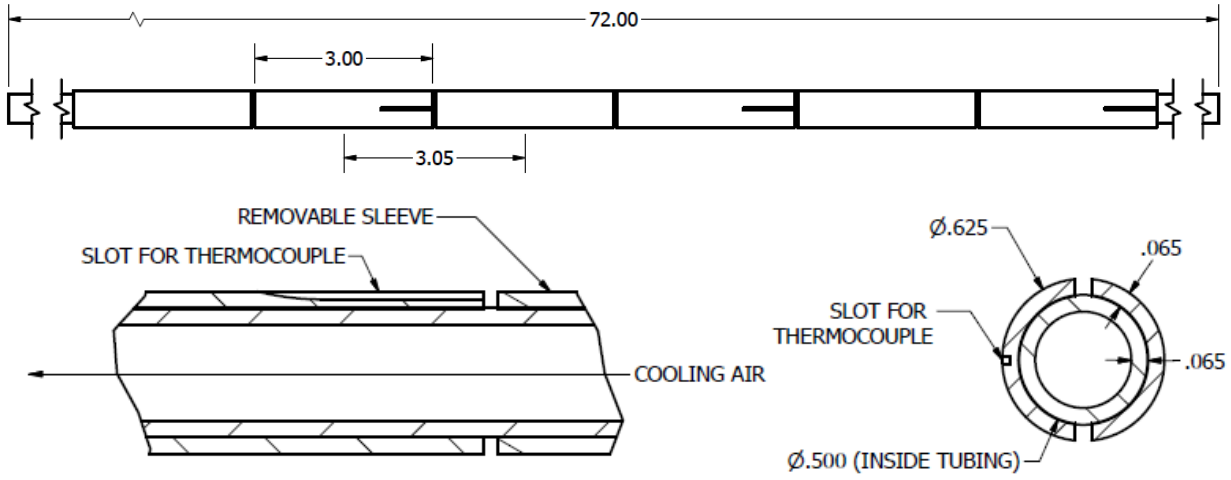

Figure 32 - Drawing of Air-Cooled Deposition Collection Probe.

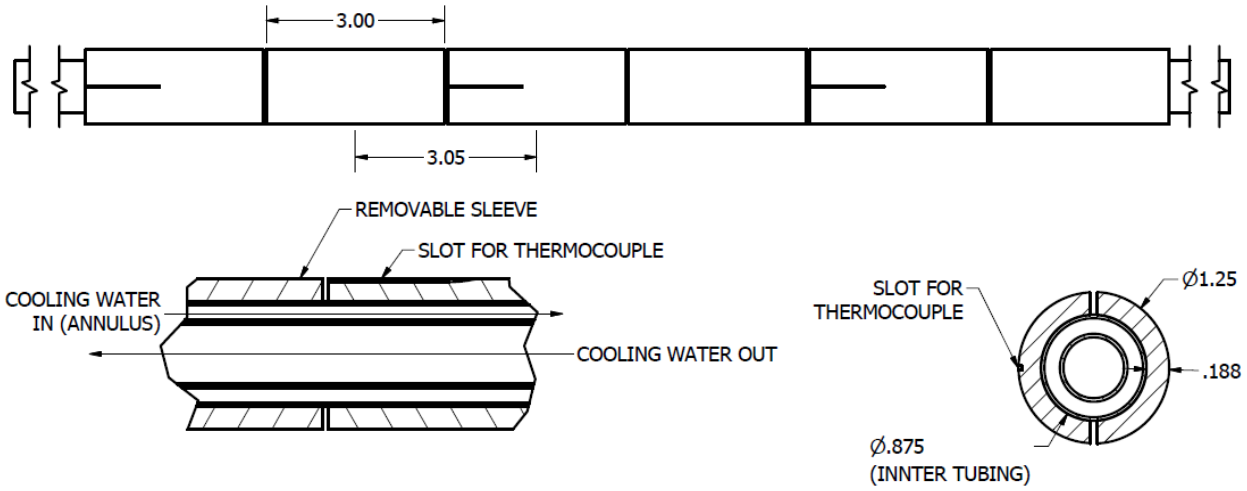

Figure 33 - Drawing of Water-Cooled Deposit Collection Probe.

The water-cooled probe is constructed of 1”-OD stainless steel. Water entered the probe, recirculated through a cooling jacket, and exited from the same side of the probe. As with the air cooled probe, six 304 stainless steel sleeves were mounted to the tube, and three of the six sleeves had thermocouples positioned in the slots on the outside surfaces. The water cooled sleeves were machined from1.25”-OD and 0.188” MW 304 stainless steel.

4.3.5 Deposit Preparation for SEM Analysis

A process for preparing the sleeves containing the deposit samples for SEM analysis has previously been developed at BYU.[13] This process was implemented for this project, which involved mounting the deposit-covered sleeves in a tray and carefully filling the tray with a low viscosity (2 m^2/s) epoxy consisting of EPOES resin (Struers M1201025) and EPOAR hardener (Struers M1201026), as shown in Figure 34. The tray surfaces were coated with a high vacuum grease so that the hardened epoxy could be easily removed. After drying, the mounted samples were cross-sectioned and polished. To preserve water-soluble compounds that might be present in the deposits, the sleeve samples were polished with an oil-based medium (Leco No. 811-004) consisting of ethylene glycol, monobutyl ether, and methyl alcohol.

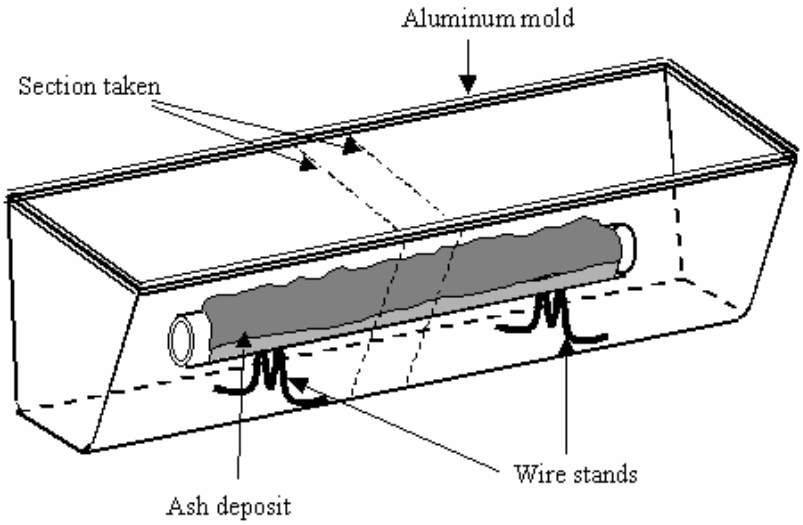

Figure 34 - Aluminum Tray Used to Create SEM Samples, after Lokare et al. (Ref. 11).

4.3.6 Results of Gas Sampling for Selected Eight U.S. Coals

This section summarizes the results of online gas sampling from the BFR. As discussed earlier, there were two shipments of the Illinois #6 Galatia and WY PRB coals. For clarity, the first delivery is referred to as Illinois #6-1 and PRB-1, while the second delivery is Illinois #6-2 and PRB-2. To correct errors in the HCl measurements, repeat tests were necessary for several coals, as discussed in Section 3.3.3.3, and have also been completed.

The coal and air flow rates used for each of the coals tested are listed in Table 13. The coal feed rates were selected to produce a heat input of 150 kW to the BFR, which was required to maintain the reactor interior sufficiently hot for combustion. The air flow rates were calculated based on staged combustion of the eight U.S. coals, i.e., at a SR of 0.85 in the fuel-rich reducing zone and 1.15 in the oxidizing zone. The ultimate and proximate analyses of each coal were used to determine the air-fuel stoichiometric ratios, as described in Section 3.2.1. Due to an error in the program used to calculate the stoichiometric air-fuel ratios, the air flow rates implemented in the experiments were slightly higher than what were needed to produce a target S.R. of 0.85 in

the reducing zone. The uncertainty of fuel and air flow rates was estimated to be approximately ±2%, while the uncertainty of the calculated stoichiometric ratio was ±2% due primarily to the uncertainty of moisture content. Therefore, the overall uncertainty of the implemented S.R. would be on the order of ±3%, which is considered small.

Table 12 - Coal and Air Flow Rates Used in the Coal Combustion Tests.

	Ill. #6-1	PRB	Beulah Zap	Mahoning	Indiana	IL #6-2	Gatling	KY #11	Pitt. #8
Coal (kg/hour)	20	30	32	19.30	20.28	20.18	20.63	19.5	18.3
Primary Air (kg/hour)	18.8	27	22	28.54	28.94	27.28	28.07	34.5	34.4
Secondary Air (kg/hour)	139.8	148	135	132.8	124.09	119.8	127.13	118.5	122.8
Tertiary Air (kg/hour)	50.4	62.2	51.8	45.7	54.37	51.72	54.84	54.0	53.6
Sec. Air Temp. (°C)	138	138	138	138	138	138	138	121.7	122.8
Swirl No.	0.77	1.21	1.70	0.89	0.89	0.89	0.89	0.89	0.89
Stoich. A/F	9.01	6.63	5.46	9.80	8.97	8.47	8.90	9.41	10.0
Red. Zone, Actual Avg. S.R.	0.88	0.88	0.89	0.85	0.84	0.86	0.85	0.85	0.86
Ox. Zone, Actual Avg. S.R.	1.16	1.19	1.19	1.14	1.14	1.16	1.14	1.15	1.15

The swirl number of each test was chosen based on a sparse matrix of preliminary gas data and visual observations of the flame. The O_2 concentrations at the BFR exit were measured as the swirl ratio was changed. For example, at zero swirl, the Illinois #6-1 coal produced a lifted flame that shifted slightly off-axis from the centerline and extended to almost the entire length of the BFR. The flame shortened and the O_2 concentrations at the BFR exit decreased as the swirl number was increased. After reaching a swirl of 0.6 or higher, the flame shape appeared stable and the measured O_2 concentrations no longer decreased with increasing swirl. Regions of high CO, along with H_2S and SO_2, were found in the near-burner regions. Subsequently, a swirl number of 0.77 was selected for Illinois #6-1, which is considered the minimum value for a stable and attached flame.

A similar process was used to determine the swirl numbers for the other coals. The lower rank PRB and Beulah Zap coals required a higher swirl number to produce a stable and recirculating flame. This is evident by the higher ratios of primary to secondary air flows required for these coals. As can be seen in Table 13, the lower rank coals required approximately the same total air flow to complete the combustion, but the primary flow rates were increased due to both higher coal and primary air flow rates to carry the coals to the burner. Thus the swirl ratio of PRB was 1.21 and Beulah Zap, 1.70.

4.3.6.1 Reducing Zone Gas Sampling Results

The measured concentrations of different gas species for the reducing zones of each coal are shown in Table 14. The test data are shown chronologically from which they were taken. The concentrations were taken from the axial positions through the port closest to the deposit sampling probe. The radial positions given were measured from the north wall of the BFR. The

inner diameter of the BFR is 75 cm, thus making the center point at 37.5 cm from the walls. General trends of the test data are discussed in this section.

Table 13 - Measured Gas Species in the Reducing Zone.

Illinois #6-1 – Axial Distance 77 cm

Dist. (cm)	CO (ppm)	CO_2 (%)	H_2O (%)	H_2S (ppm)	HCl (ppm)	NO (ppm)	SO_2 (ppm)	SO_3 (ppm)	COS (ppm)	H_2 (%)	O_2 (%)
10	642	15.44	7.35	18	180	296	2129	44	0	0.95	4.07
20	1574	16.29	7.78	20	224	275	2253	36	4	0.33	3.31
30	7619	15.85	8.91	10	244	230	2529	39	-7	0.04	1.35
40	22414	14.76	9.77	788	157	96	1773	37	57	0.17	0.69
50	17264	15.07	9.88	376	187	141	2258	37	41	0.65	0.10
60	32254	14.40	10.47	991	144	99	1497	23	132	0.89	0.07
70	22070	14.47	10.12	671	129	148	1828	33	118	0.67	0.06

PRB-1 – Axial Distance 90 cm

Dist. (cm)	CO (ppm)	CO_2 (%)	H_2O (%)	H_2S (ppm)	HCl (ppm)	NO (ppm)	SO_2 (ppm)	SO_3 (ppm)	COS (ppm)	H_2 (%)	O_2 (%)
10	5130	14.17	12.16	-41	1	301	190	11	7	0.03	4.35
20	5116	13.96	11.20	-81	1	311	179	12	6	0.08	4.08
30	6642	14.04	11.43	-27	0	321	171	11	7	0.12	3.46
40	38487	14.11	15.17	203	0	215	149	6	13	1.32	0.41
50	34866	14.48	14.32	180	0	288	141	7	13	1.13	0.66
60	15135	15.24	12.58	53	0	311	168	9	11	0.35	1.85
70	1835	13.72	10.65	-35	0	360	149	10	7	0.03	4.33

Beulah Zap – Axial Distance 77 cm

Dist. (cm)	CO (ppm)	CO_2 (%)	H_2O (%)	H_2S (ppm)	HCl (ppm)	NO (ppm)	SO_2 (ppm)	SO_3 (ppm)	COS (ppm)	H_2 (%)	O_2 (%)
10	11617	17.79	16.94	54	4	454	781	12	20	0.32	2.89
20	39181	17.86	18.91	170	3	227	629	15	71	1.51	0.90
30	47406	16.21	20.50	571	3	174	298	13	108	2.07	0.96
40	42536	16.05	21.29	465	2	211	419	10	75	2.06	0.86
50	29380	17.39	19.14	98	2	287	666	19	45	0.90	1.26
60	6640	17.24	16.64	-43	1	410	719	18	21	0.18	3.01
70	1030	16.25	15.01	-32	1	510	668	19	11	0.07	3.36

Indiana #6 – Axial Distance 70 cm

Dist. (cm)	CO (ppm)	CO_2 (%)	H_2O (%)	H_2S (ppm)	HCl (ppm)	NO (ppm)	SO_2 (ppm)	SO_3 (ppm)	COS* (ppm)	H_2 (%)	O_2 (%)
10	652	11.69	6.79	-41	44	375	800	29	-9	0.00	4.44
20	17225	11.79	9.27	93	66	212	910	23	16	0.87	0.81
30	42635	10.63	10.56	303	188	76	522	8	42	2.56	0.59
40	39253	10.75	10.46	423	184	66	436	7	13	3.18	0.56
50	30262	11.22	10.13	318	132	80	432	14	19	2.19	0.56
60*	16239	14.42	9.44	-27	16	280	1237	30	0	0.10	0.80
70*	10105	14.46	8.49	-76	12	349	1133	26	-2	0.19	0.73

* Data recorded on different day.

Illinois #6-2 – Axial Distance 84 cm

Dist. (cm)	CO (ppm)	CO_2 (%)	H_2O (%)	H_2S (ppm)	HCl (ppm)	NO (ppm)	SO_2 (ppm)	SO_3 (ppm)	COS (ppm)	H_2 (%)	O_2 (%)
10	8256	15.82	9.20	-1	30	213	2402	53	15	1.10	0.53
20	23505	14.85	9.77	491	262	49	1098	30	93	1.04	0.50
30	28591	14.63	9.81	578	255	36	748	22	108	1.16	0.53
40	25197	14.71	9.83	646	242	42	802	25	109	1.32	0.52
50	13365	15.46	9.62	477	177	83	2049	47	101	0.61	0.52
60	6764	15.93	8.63	20	90	192	3456	68	14	0.23	0.54
70	6993	15.98	7.82	43	44	227	2675	64	1	0.07	0.74

Gatling – Axial Distance 97 cm

Dist. (cm)	CO (ppm)	CO_2 (%)	H_2O (%)	H_2S (ppm)	HCl (ppm)	NO (ppm)	SO_2 (ppm)	SO_3 (ppm)	COS (ppm)	H_2 (%)	O_2 (%)
10	18168	16.79	10.43	353	15	164	2861	54	98	0.30	0.77
20	20853	16.73	10.15	404	53	115	2614	58	124	0.40	1.62
30	27136	14.65	10.49	760	15	92	2154	52	57	2.24	0.02
40	21515	16.66	10.23	680	10	107	2606	57	71	2.32	0.02
50	13377	17.22	10.20	307	5	125	3112	62	53	0.23	0.34
60	10594	17.39	10.49	305	4	127	3146	64	4	0.07	0.92
70	6111	17.66	9.43	-69	3	190	3643	80	4	0.03	1.59

Kentucky #11 – Axial Distance 83 cm

Dist. (cm)	CO (ppm)	CO_2 (%)	H_2O (%)	H_2S (ppm)	HCl (ppm)	NO (ppm)	SO_2 (ppm)	SO_3 (ppm)	COS (ppm)	H_2 (%)	O_2 (%)
10	867	13.90	7.98	-118	65	255	2436	53	0	0.00	3.80
20	4142	16.74	9.02	-124	78	257	2736	53	4	0.08	2.25
30	16892	16.52	9.89	-8	113	229	2954	48	58	0.62	0.46

40	37095	13.81	9.94	958	370	84	1166	23	278	2.35	0.15
50	23652	16.20	10.36	100	160	257	2702	46	100	0.91	0.18
60	10825	16.83	9.74	-175	93	254	3036	42	21	0.35	0.42
70	4405	17.02	8.94	-141	85	247	2842	54	5	0.11	1.01

Mahoning – Axial Distance 77 cm

Dist. (cm)	CO (ppm)	CO_2 (%)	H_2O (%)	H_2S (ppm)	HCl (ppm)	NO (ppm)	SO_2 (ppm)	SO_3 (ppm)	COS (ppm)	H_2 (%)	O_2 (%)
10	2388	14.08	7.87	-18	65	304	1233	36	-5	0.02	3.33
20	5272	14.30	8.46	44	85	311	1323	34	5	0.08	2.34
30	24549	13.91	10.08	-28	117	298	1465	33	2	0.76	0.55
40	27844	13.82	10.16	50	109	303	1473	36	-27	1.44	0.40
50	9230	14.47	8.44	-54	81	334	1360	38	-17	0.23	1.72
60	4303	15.71	8.34	-27	80	240	1396	35	0	0.10	1.06
70	3430	15.85	8.29	-8	79	231	1388	29	0	0.04	1.06

Pittsburgh #8 – Axial Distance 243 cm

Dist. (cm)	CO (ppm)	CO_2 (%)	H_2O (%)	H_2S (ppm)	HCl (ppm)	NO (ppm)	SO_2 (ppm)	SO_3 (ppm)	COS (ppm)	H_2 (%)	O_2 (%)
10	4630	14.51	9.32	89	13	226	851	16	8	0.00	1.94
20	10738	15.83	10.82	140	17	184	914	11	11	0.00	0.41
30	16073	13.68	10.75	180	12	198	999	-6	9	0.00	0.17
40	12904	14.53	10.84	200	13	210	964	13	8	0.00	0.38
50	4895	15.08	9.54	203	11	242	838	5	4	0.00	1.29
60	1251	14.77	8.36	-7	5	290	737	8	6	0.00	2.28
70	595	14.48	7.76	57	6	318	715	6	7	0.00	2.97

The first column of Table 14 contains the measured CO concentrations, which shows that a similar stoichiometry was produced in the near burner fuel-rich zone for each coal. The CO concentrations peaked in the center of the reactor directly below the burner and lowered near the walls. This trend is expected, as the coal was injected through the burner down the centerline of the BFR surrounded by swirling secondary air. The CO concentrations can be used to show the extent of symmetry (or asymmetry) of the flames. For the Illinois #6-1 and PRB-1 coals, the flame was richest south of the centerline at 50-60 cm. The asymmetry does not create a significant problem for the objectives of this work but it does make comparison with the modeling results more difficult. Following the PRB-1 test, attempts were made to produce a more symmetric gas distribution by adjusting the primary air/fuel tube location and removing a baffle in the swirl plenum. Centering the flame was accomplished by visual observation of the flame and measurements of CO at the centerline during operation. The flame centering improved symmetry for all of the tests following PRB-1.

Upon the completion of all coals, it was noted that some coals produced higher CO concentrations than the others even though the overall S.R. was nominally constant. The data show that coals with high volatile content and high oxygen concentrations produced higher CO concentrations in the reducing zone. The presence of volatiles and high oxygen concentration of

the coal are expected to increase the rate of oxygen consumption relative to the mixing of oxygen from air into the primary fuel stream and therefore create a richer mixture near the burner. The coal with the highest volatiles and oxygen was Beulah Zap lignite, with an average CO concentration of 25,398 ppm (or 2.5%), while Pittsburgh #8 contains the lowest volatiles and oxygen, with an average CO concentration of 7,298 ppm (or 0.7%). Thus, the Beulah Zap lignite coal produced a stronger reducing zone in the near burner region than the other coals under the same overall S.R value.

The second and third columns show the measured CO_2 and H_2O concentrations. These gaseous species provided indication of the completeness of combustion and mixing between air and fuel. The highest values of CO_2 and H_2O should and did occur in regions where carbon was burned out and the mixture was near stoichiometric (S.R. =1.0). In general, the CO_2 concentrations were lower in regions of high CO.

Staying with the major species, the O_2 concentrations are shown in the last column of Table 14. The O_2 values obtained from the GC are reported here because the GC sampling time was more in sync with that of the FTIR. The Horiba produced readings that were time averaged over a period of approximately 2 minutes while the FTIR sampling time was less than 1 second. As expected, the O_2 concentration generally varied inversely with CO, as the reading was higher near the walls where CO was low. Conversely, the O_2 concentration became lowest near the center of the BFR where CO was the highest. The O_2 concentration was very low (less than 0.5%) in the most reducing zone where CO was above 25,000 ppm. The O_2 readings became significantly higher near the walls with values >1%. Such a variation is expected and suggests that the secondary air was directed downward and radially outward towards the walls.

The O_2 values of Beulah Zap lignite in the reducing and oxidizing zones were slightly higher than those of the other coals. It was initially thought the higher readings were caused by a leak in the sampling line. However, it was later determined that the leak was in the primary air line. This leak was later corrected, as evidenced by the O_2 results for the following coal runs. Because of the leak, however, the S.R. value of the reducing zone for Beulah Zap was slightly higher than the targeted value, i.e., 0.89 vs. 0.85. In spite of this higher S.R. value, the CO concentrations for Beulah Zap were high, suggesting a strong reducing zone.

Measurements of the sulfur-bearing species of H_2S, SO_2, and SO_3 are critically important to fireside corrosion and therefore are of particular interest. COS was found to exist in significant amounts and was measureable with the FTIR. COS was therefore added to the species being measured. H_2S and COS followed the same trend as the CO, i.e., highest in the reducing zone and lowest near the walls where O_2 is present. At the same locations where H_2S and COS were high, the concentration of SO_2 was low. Mahoning and Pittsburgh #8 showed lower fraction of H_2S and COS relative to total sulfur in the coal. This would appear to be related to the lower values of CO produced for these coals as discussed above. It will be shown that the trend of increasing H_2S and COS with decreasing S.R. is consistent with equilibrium where sulfur is preferentially formed as H_2S and COS under reducing conditions.[14] The concentration of SO_2 deceased slightly near the walls where oxygen was present because of dilution with the secondary air. The concentration of SO_3 was very low compared to the other sulfur-bearing species, typically on the order of 1-2 percent of the total coal sulfur.

The sum of H_2S, SO_2, SO_3, and COS for each coal as a function of radial position in the reducing zone is shown in Figure 35. The sum is relatively constant across the chamber of the BFR with a deviation of typically less than 10 percent. The less steady trend seems to be associated with the Illinois #6-1 and Gatling coals. The lack of uniformity might have been caused by incomplete combustion, non-steady conditions in the BFR operation during the measurement, or measurement uncertainty. The overall measurement uncertainty was dominated by the uncertainty of H_2S data, which was considered to be approximately ±125 ppm. The sulfur data are discussed more thoroughly in Section 3.3.6.3 where the trends are compared with results of thermodynamic equilibrium and the correlations are discussed between measured and forms of sulfur in coal.

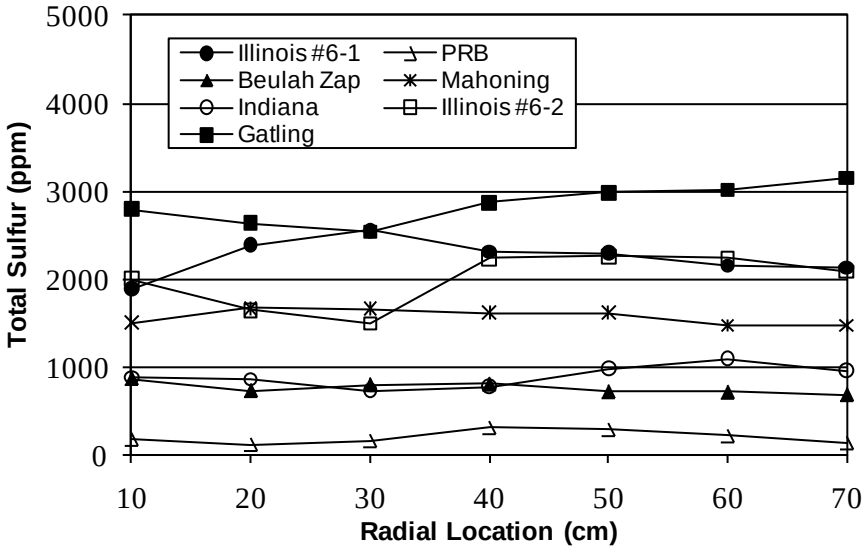

Figure 35 - Sum of H_2S, SO_2, SO_3, and COS Measured for Different Coals.

HCl is another species pivotal to fireside corrosion. Looking at the HCl data, several trends can be readily recognized. First, coals with a low chlorine content, such as Black Thunder PRB and Beulah Zap lignite, produced very low values of HCl, typically near or below the measurement limit of 1 ppm for FTIR. On the other hand, high chlorine coals, such as Illinois #6-1 and Illinois #6-2, produced measureable quantities of HCl in several hundred ppm. Another noticeable trend is that HCl values are higher in the center of the BFR where CO is the highest and lower near the walls where O_2 is present. A more detailed discussion of chlorine is provided in section 3.3.6.4 where the equilibrium trends as well as the fraction of coal chlorine being measured as HCl are discussed.

4.3.6.2 Oxidizing Region Gas Sampling Results

Results of the online gas measurements in the oxidizing zone of BFR are summarized in Table 15. Under oxidizing conditions, almost all CO was oxidized and converted to CO_2, as evidenced by the large decrease in CO concentrations and increase in CO_2. Because of the addition of burnout air from the NOx port to the combustion mixture, on the order of ~30% by

volume, the concentration of CO_2 would decrease due to a relatively insignificant conversion of CO to CO_2.

As discussed previously, the H_2S formed in the reducing zone was expected to convert to SO_2 in the oxidizing zone. Such a conversion was observed in the data where H_2S typically fell within a range of ±50 ppm for each coal, or essentially zero when the measurement uncertainty for H_2S is considered.

The SO_2 values in the oxidizing zone were similar in magnitude to those in the reducing zone. If no additional SO_2 were formed between the reducing and oxidizing zone measurements, the SO_2 concentration would decrease by approximately 30% due to the addition of tertiary air. The SO_2 decrease was less than 30% for all coals except Beulah Zap, indicating that SO_2 was still forming between the reducing zone and oxidizing zone, although most of the sulfur in coal was released to the gas phase in the reducing zone. Similar results were also found for SO_3; as it traveled from the reducing to oxidizing zone, the average concentration decreased by only about 10%. The SO_3 appeared to exist as a small fraction of the total SO_2 concentration at all times. A more complete discussion on SO_2 is given in Section 3.3.6.3.

Table 14 - Measured Gas Species in the Oxidizing Zone.

Illinois #6-1 – Axial Position 217 cm

Dist. (cm)	CO (ppm)	CO_2 (%)	H_2O (%)	H_2S (ppm)	HCl (ppm)	NO (ppm)	SO_2 (ppm)	SO_3 (ppm)	H_2 (%)	O_2 (%)
10	95	13.75	6.16	58	153	149	1841	37	0.00	4.81
20	161	15.90	6.82	2	180	153	2110	43	0.00	3.31
30	2159	16.45	7.84	-23	247	146	2384	47	0.00	1.46
40	97	16.98	7.68	-55	187	131	2282	39	0.00	1.81
50	304	17.05	7.93	-19	191	140	2338	41	0.00	1.92
60	427	16.24	7.77	-14	182	153	2237	40	0.00	2.45
70	705	13.41	6.81	29	199	170	1904	35	0.00	2.92

PRB – Axial Position 243 cm

Dist. (cm)	CO (ppm)	CO_2 (%)	H_2O (%)	H_2S (ppm)	HCl (ppm)	NO (ppm)	SO_2 (ppm)	SO_3 (ppm)	H_2 (%)	O_2 (%)
10	11	15.08	10.96	26	2	273	116	5	0.0000	3.52
20	14	16.12	11.80	37	1	236	139	6	0.0005	2.73
30	21	17.04	12.63	6	2	252	180	10	0.0003	2.36
40	31	17.08	13.07	26	2	249	184	8	0.0017	1.41
50	46	17.53	12.99	29	3	255	191	7	0.0006	1.80
60	21	16.78	12.61	-2	3	271	163	8	0.0002	2.41
70	18	13.08	10.87	15	3	256	100	7	0.0003	3.82

Beulah Zap – Axial Position 243 cm

Dist. (cm)	CO (ppm)	CO_2 (%)	H_2O (%)	H_2S (ppm)	HCl (ppm)	NO (ppm)	SO_2 (ppm)	SO_3 (ppm)	H_2 (%)	O_2 (%)
10	9	10.67	8.57	59	2	304	273	2	0.00	5.31
20	22	13.69	11.03	178	2	264	458	9	0.00	7.33
30	20	13.74	11.20	172	2	269	481	11	0.00	5.18

40	16	13.64	11.28	191	2	264	494	12	0.00	5.31
50	15	13.26	11.17	162	2	261	476	10	0.00	5.97
60	23	12.85	11.17	135	1	253	453	7	0.00	6.69
70	40	12.46	12.68	201	1	250	402	7	0.00	6.69

Mahoning – Axial Distance 243 cm

Dist. (cm)	CO (ppm)	CO_2 (%)	H_2O (%)	H_2S (ppm)	HCl (ppm)	NO (ppm)	SO_2 (ppm)	SO_3 (ppm)	H_2 (%)	O_2 (%)
10	324	16.36	7.88	-56	7	234	1546	37	0.00	2.54
20	193	16.39	10.52	-10	9	229	1692	38	0.00	2.70
30	321	16.58	11.61	72	10	230	1668	35	0.00	2.86
40	83	15.43	10.03	-50	12	251	1501	31	0.00	4.55
50	82	15.31	8.50	-48	11	254	1434	34	0.00	3.89
60	220	15.89	7.81	-31	13	266	1466	37	0.00	4.05
70	149	15.41	6.94	-11	14	282	1374	33	0.00	4.89

Indiana #6– Axial Distance 250 cm

Dist. (cm)	CO (ppm)	CO_2 (%)	H_2O (%)	H_2S (ppm)	HCl (ppm)	NO (ppm)	SO_2 (ppm)	SO_3 (ppm)	H_2 (%)	O_2 (%)
10	244	14.61	7.91	-4*	104	111	980	26	0.00	2.39
20	266	14.83	8.12	-13	108	115	1010	32	0.00	2.42
30	330	14.32	7.62	-5	100	111	937	29	0.00	3.08
40	185	14.73	8.00	-27	111	106	980	31	0.00	2.30
50	187	14.76	8.02	35	111	100	980	28	0.00	2.48
60	280	14.83	8.11	-47	113	103	991	27	0.00	2.27
70	345	14.80	8.13	-5	111	109	986	33	0.00	2.14

*These H2S data were taken on a different day than the other data.

Illinois #6-2 – Axial Distance 257 cm

Dist. (cm)	CO (ppm)	CO_2 (%)	H_2O (%)	H_2S (ppm)	HCl (ppm)	NO (ppm)	SO_2 (ppm)	SO_3 (ppm)	H_2 (%)	O_2 (%)
10	493	14.76	6.77	7	136	182	2094	54	0.00	2.63
20	95	14.43	6.29	-91	128	154	1989	49	0.00	3.55
30	152	14.22	6.45	28	146	192	1970	46	0.00	3.62
40	237	14.18	6.44	-11	146	177	1962	54	0.00	3.53
50	608	13.96	6.64	-33	148	174	1949	54	0.00	3.31
60	464	15.45	6.88	-15	134	186	2208	46	0.00	1.88
70	1300	15.80	7.41	14	158	177	2284	54	0.00	1.39

Gatling – Axial Distance 257 cm

Dist. (cm)	CO (ppm)	CO_2 (%)	H_2O (%)	H_2S (ppm)	HCl (ppm)	NO (ppm)	SO_2 (ppm)	SO_3 (ppm)	H_2 (%)	O_2 (%)
10	74	15.00	6.83	59	-2	113	2788	54	0.00	3.79
20	74	14.96	6.97	59	1	108	2823	60	0.00	3.68
30	106	15.09	7.00	52	5	112	2828	56	0.00	3.86
40	74	14.36	6.74	26	6	118	2650	53	0.00	4.83
50	73	13.79	6.55	36	6	115	2497	46	0.00	5.42
60	93	14.82	6.85	97	6	109	2711	50	0.00	4.22

70	71	14.26	6.71	58	7	116	2574	52	0.00	4.67

Kentucky #11 – Axial Distance 243 cm

Dist. (cm)	CO (ppm)	CO_2 (%)	H_2O (%)	H_2S (ppm)	HCl (ppm)	NO (ppm)	SO_2 (ppm)	SO_3 (ppm)	H_2 (%)	O_2 (%)
10	557	17.01	7.76	23	113	98	2655	58	0.00	2.52
20	615	16.80	7.60	33	115	100	2610	55	0.00	2.56
30	409	16.59	7.47	15	116	100	2571	52	0.00	3.03
40	474	16.96	7.74	28	115	103	2656	55	0.00	2.47
50	498	17.09	7.67	30	110	104	2611	49	0.00	2.58
60	244	15.81	7.55	-18	98	96	2397	48	0.00	4.38
70	84	14.82	7.98	-9	71	90	2299	51	0.00	4.01

Mahoning – Axial Distance 243 cm

Dist. (cm)	CO (ppm)	CO_2 (%)	H_2O (%)	H_2S (ppm)	HCl (ppm)	NO (ppm)	SO_2 (ppm)	SO_3 (ppm)	H_2 (%)	O_2 (%)
10	156	13.37	6.81	-131	98	87	1261	35	0	3.15
20	159	14.49	7.56	-201	108	74	1337	29	0.00	3.10
30	149	14.54	7.47	-82	109	76	1333	27	0.00	3.40
40	134	14.39	7.37	-98	110	78	1311	32	0.00	3.40
50	142	14.22	7.19	23	108	80	1301	33	0.00	3.40
60	143	14.33	7.24	-45	108	82	1309	32	0.00	3.60
70	176	14.53	7.31	-158	109	91	1333	30	0.00	3.10

Pittsburgh #8 – Axial Distance 243 cm

Dist. (cm)	CO (ppm)	CO_2 (%)	H_2O (%)	H_2S (ppm)	HCl (ppm)	NO (ppm)	SO_2 (ppm)	SO_3 (ppm)	H_2 (%)	O_2 (%)
10	574	15.28	6.53	78	8	96	711	23	0	3.03
20	596	14.89	6.46	92	7	90	710	11	0.00	3.23
30	546	14.61	6.36	-80	5	88	696	19	0.00	3.60
40	600	14.44	6.40	51	3	89	684	11	0.00	3.59
50	568	14.30	6.24	-122	6	90	678	14	0.00	3.90
60	533	14.40	6.21	-151	6	90	671	13	0.00	3.97
70	338	14.42	6.08	-271	7	87	671	18	0.00	3.93

Similar to the reducing zone, the HCl concentrations measured in the gas phase were proportional to the chlorine concentrations in these coals. The PRB, Beulah Zap and Pittsburgh coals contain very small amounts of chlorine. As a result, they produced HCl concentrations only slightly above the FTIR measurement limit. The HCl concentrations measured in the oxidizing zone for all coals were similar to the average concentrations in the reducing zone. A more complete discussion on HCl is given in Section 3.3.6.4.

4.3.6.3 Discussion of the Fate of Coal Sulfur

The gas measurements presented above can be used to help understand the fate of coal sulfur during combustion. Sulfur originates in coal in one of three forms, i.e., organic, pyritic, and sulfatic. The total sulfur and distribution of the sulfur for each coal studied are listed in Table 2. It is of interest to determine if the distribution of the coal sulfur can be used to determine the amount of sulfur species formed, which are important to fireside corrosion.

Thermodynamic calculations were performed to identify the potential sulfur species produced from coal combustion and indicate the most stable products. A commercial equilibrium code, HSC Chemistry 7.0, was used to determine the equilibrium compositions for each of the U.S. coals at the S.R. values of 0.85 and 1.15 over a temperature range of 500-1400^{o}C. The predicted concentrations of gas species for Illinois #6-1 at concentrations greater than 1 ppm are shown in Figures 36 and 37.

The reducing conditions produced four sulfur-bearing species of importance, including SO_2, H_2S, COS and S_2. At higher temperatures, SO_2 would exist as the most stable form of sulfur. As the temperature is decreased, SO_2 decreases and H_2S and COS increase. The crossover temperature where H_2S becomes greater than SO_2 is approximately 1150^{o}C. At this temperature, the S_2 concentration is at a maximum, whereas COS is near maximum. As the temperature is further decreased, H_2S continues to dominate until ~700^{o}C, below which the sulfur begins to form different condensed compounds, including $CaSO_4$, $KAl(SO_2)_4$, $Fe_2(SO_4)_3$, Na_2SO_4, K_2SO_4*2$MgSO_4$, $Al_2(SO_4)_3$, and $FeSO_4$. The trends shown here for Illinois #6-1 are representative of all the coals studied, even though the total amounts of sulfur vary.

Gas temperatures in the reducing zone are estimated to be 1300–1400^{o}C, which is below the adiabatic flame temperature. In this temperature range, SO_2 is expected to be the dominant form of sulfur species, with H_2S, COS, and S_2 also present in significant amounts. This equilibrium result is in general agreement with the measured data. The precise amounts of H_2S, COS, and SO_2 are highly dependent on the gas temperatures, which could not be accurately measured form the combustion tests and therefore, a definitive conclusion on whether the sulfur species are near equilibrium is not possible. Since the adiabatic flame temperatures are similar, the expected temperatures of combustion gases for all coals are expected to be similar. Based on the equilibrium calculations, the ratio of H_2S to SO_2 would be similar for all coals at a given temperature. However, the measured data indicate that the ratio of H_2S to SO_2 was very different among coals. Such differences suggest that, while the measured data followed the equilibrium trends, thermodynamic equilibrium of the sulfur-bearing gaseous species was not reached in the reducing zone.

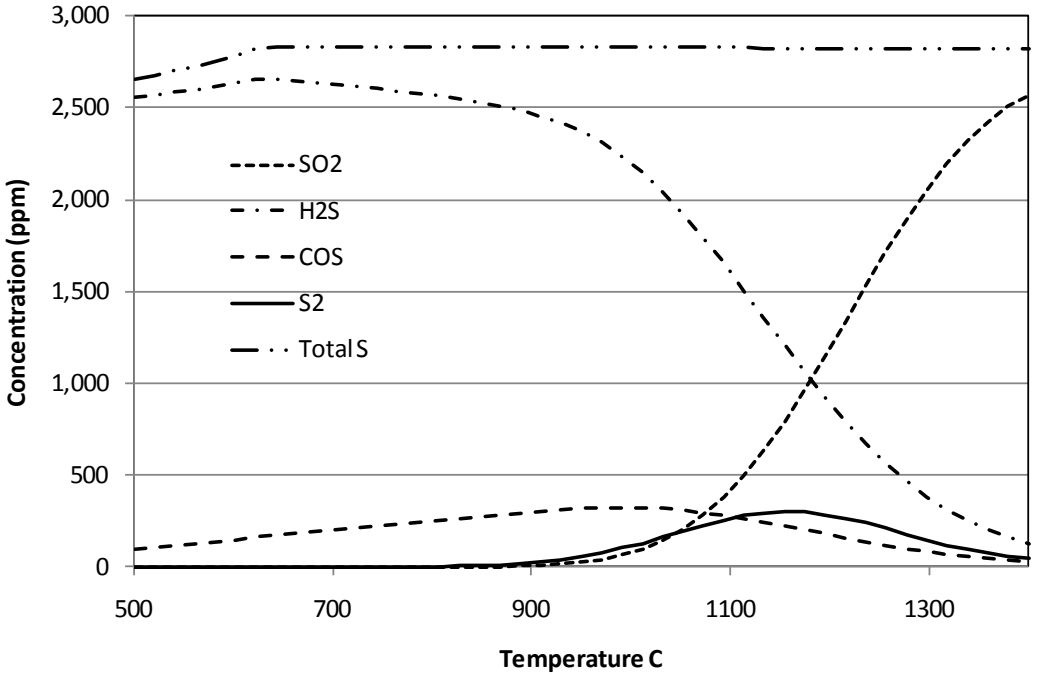

Figure 36 - Sulfur Gas Phase Equilibrium Results for IL #6-1 Coal under Reducing Conditions at S.R.=0.85.

In the oxidizing zone, results of the equilibrium calculations indicated that the significant sulfur-bearing gaseous species consisted of SO_2 and some SO_3 in the temperature range of coal combustion. The SO_3 concentration increased with decreasing gas temperature and peaked at approximately 550^{o}C, below which both SO_3 and SO_2 started to decrease due to the formation of condensed sulfur compounds. Similar equilibrium predictions were performed for all of the coals studied, which differed mainly in the total amount of sulfur present. The measured data were in reasonable agreement with the equilibrium predictions at higher temperatures, with the measured combustion products consisting primarily of SO_2 and a small amount of SO_3. However, a precise comparison between the measured and equilibrium concentrations were not possible due to uncertainty of the gas temperatures. It did appear that the measured SO_3 concentrations were higher than those predicted by equilibrium at all gas temperatures.

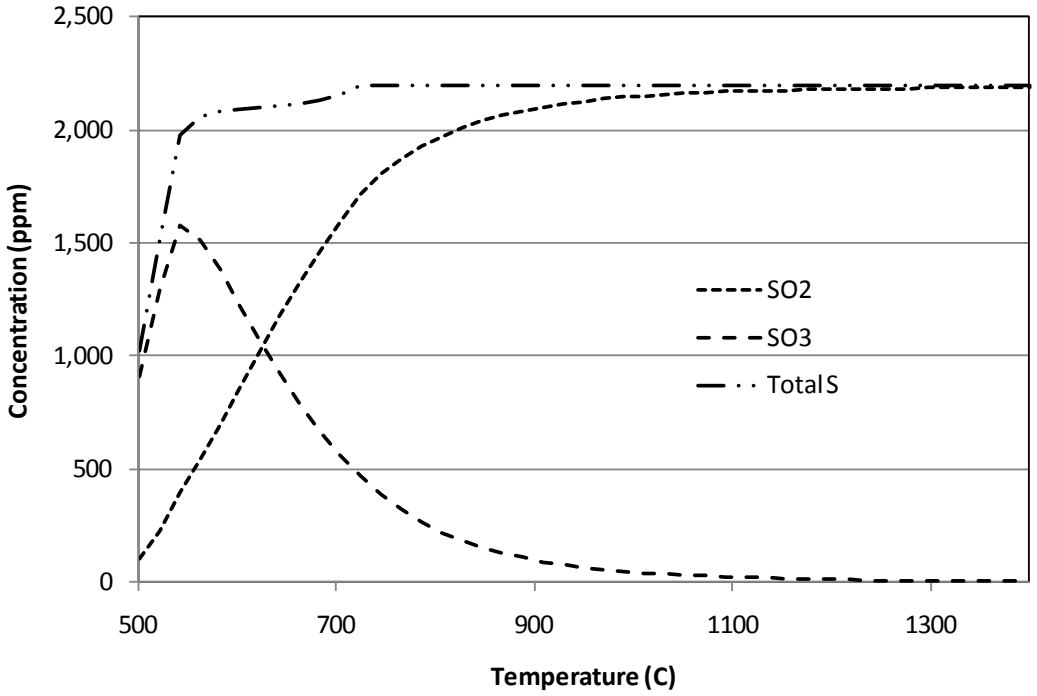

Figure 37 - Sulfur Gas Phase Equilibrium Results for IL #6-1 Coal under Oxidizing Conditions at S.R.=1.15.

Results of the equilibrium calculations were used to determine the total moles of sulfur-bearing gaseous products for each coal under the reducing and oxidizing conditions. The total moles of sulfur in the coal divided by the total moles of all combustion products provided an estimate for the maximum possible concentration of sulfur species in the gas phase. Figures 38 and 39 compare the concentrations of total maximum possible sulfur species as a function of coal sulfur for each coal. On the same figures, the total concentrations of the four sulfur-bearing species (SO_2 + H_2S + COS + SO_3) measured are compared to the maximum possible sulfur concentrations. For both reducing and oxidizing conditions, the total concentrations of measured sulfur species increase linearly with coal sulfur. Linear regression analysis generated an R^2 value of 0.97 for the measured data under both reducing and oxidizing conditions.

The slope of the measured and maximum concentration lines can be used to estimate the fraction of the coal sulfur in the measured gases. In the reducing zone, the measured sulfur is 75% of the total coal sulfur. In the oxidizing zone, the measured sulfur is 86% of the total sulfur. Clearly, a fraction of the sulfur was rapidly released from coal combustion, thus forming sulfur-bearing gaseous species. While a linear relationship has been used to approximate the average fraction of sulfur release for all the coals investigated, the ratios of measured to maximum possible sulfur are higher for the low-sulfur coals and lower for the high-sulfur coals. This variation might have been caused by the higher fraction of pyritic sulfur in the high sulfur coals where sulfur may be released slowly during combustion compared to organic sulfur. Such a difference is not observed in the oxidizing data.

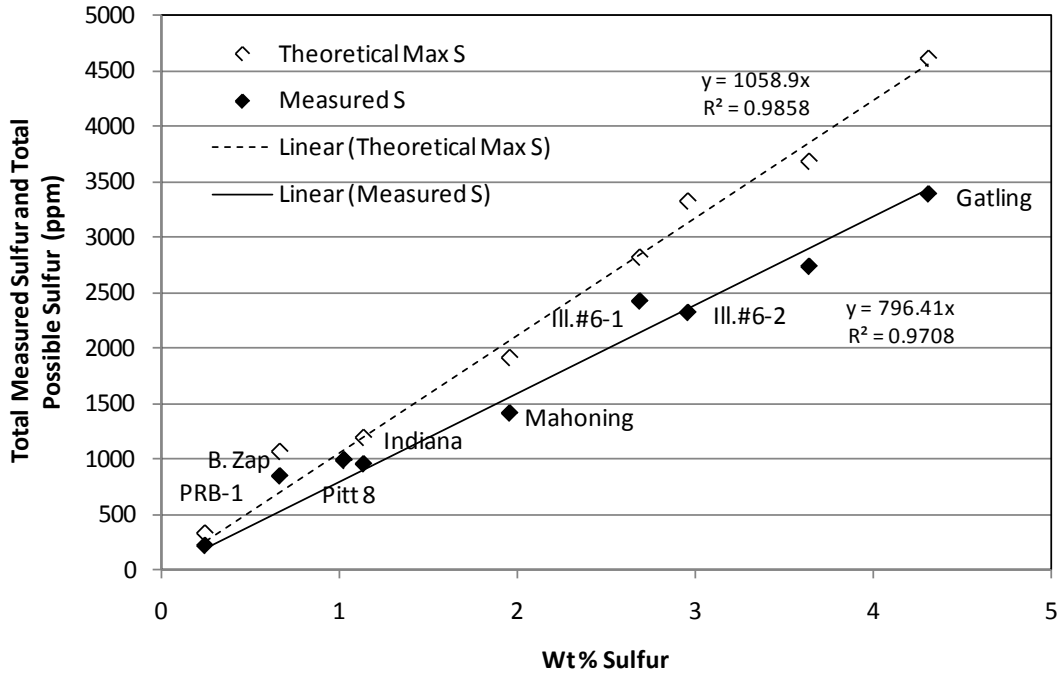

Figure 38 - Total Possible Sulfur Concentration and Sum of Four Measured Sulfur-Bearing Species for Different Coals under Reducing Conditions.

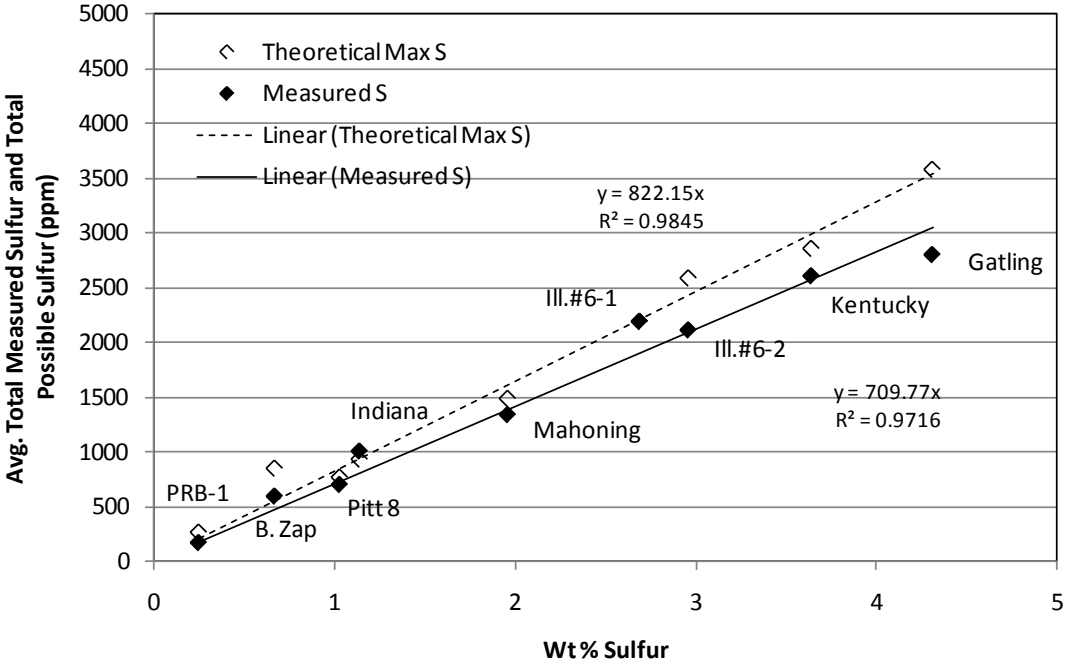

Figure 39 - Total Possible Sulfur Concentration and Sum of Four Measured Sulfur-Bearing Species for Different Coals under Oxidizing Conditions.

Additional reasons for the difference in the measured and maximum possible sulfur might be attributed to (1) the gaseous species of sulfur not measured, (2) sulfur not released from the coal, and (3) condensed sulfur species. The equilibrium results shown in Figure 36 indicated that under reducing conditions, a significant amount of sulfur may be present as S_2 and would therefore remain unaccounted for in the gas phase. The S_2 concentration from the equilibrium calculations could account for as much as approximately 20% of the total sulfur. Therefore, in the reducing zone, 20% of the fuel sulfur may be in the form of S_2.The increase in total sulfur of 9% in the gas phase from 75 to 86% might likely be attributed to the conversion of S_2 to SO_2 between the reducing and oxidizing zones.

The remaining sulfur, not accounted for by the measured gas species and S_2, was likely to be contained in condensed phases. If so, sulfur should be found in the deposit samples. Using Illinois #6-1 coal as an example, if 14% of the coal sulfur remained in the deposit, the fraction of coal remaining as sulfur would be 14% of the total sulfur in coal , i.e., 2.69% x 0.14 = 0.37%. The ash fraction of Illinois #6-1 was 8.65%; therefore the fraction of sulfur remaining in the deposit would be approximately 0.37 of 8.65 or 4.3%. This amount seems to be consistent with the chemical analysis of the deposit samples where a total sulfur of 8.95% was reported as SO_3 from the reducing zone (see Table 22).

The relationship between the measured SO_2 and H_2S and the amount of sulfur in coal are shown in Figures 40 and 41. The SO_2 exhibits a very strong linear relationship with the total coal sulfur, with an R^2 value of 0.99; while H_2S is poorly correlated, with only an R^2 value of 0.36. It was noted in the original discussion of the data in Table 14 that H_2S was strongly correlated with CO that is an indicator for reducing environments. The equilibrium trends shown in Figure 36 also show that H_2S was formed in the reducing environments. After numerous parameters explored, the strongest correlation for H_2S was found to be the product of coal organic sulfur fraction and the measured CO mole fraction, as shown in Figure 42. In other words, the combination of a high organic sulfur fraction and reducing conditions produces a high H_2S concentration. Coals with high volatile and oxygen concentrations tended to produce high CO concentrations in the reducing zone at a given S.R. value. The trend of COS concentration was found to follow that of H_2S.

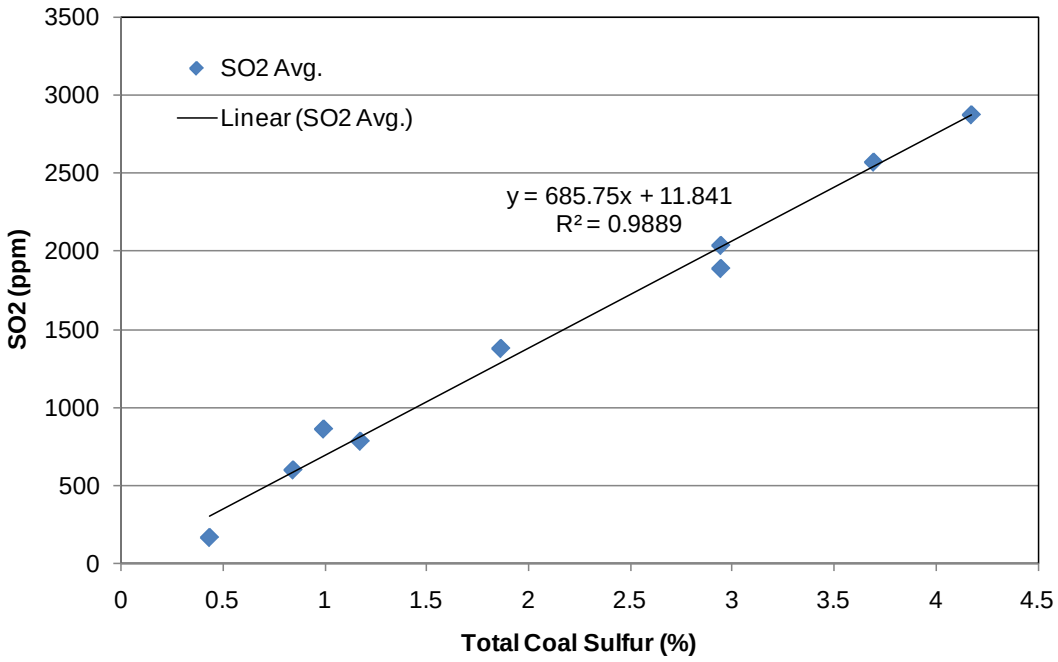

Figure 40 - Correlation of Average Measured SO_2 with Total Coal Sulfur in Reducing Zone of BFR.

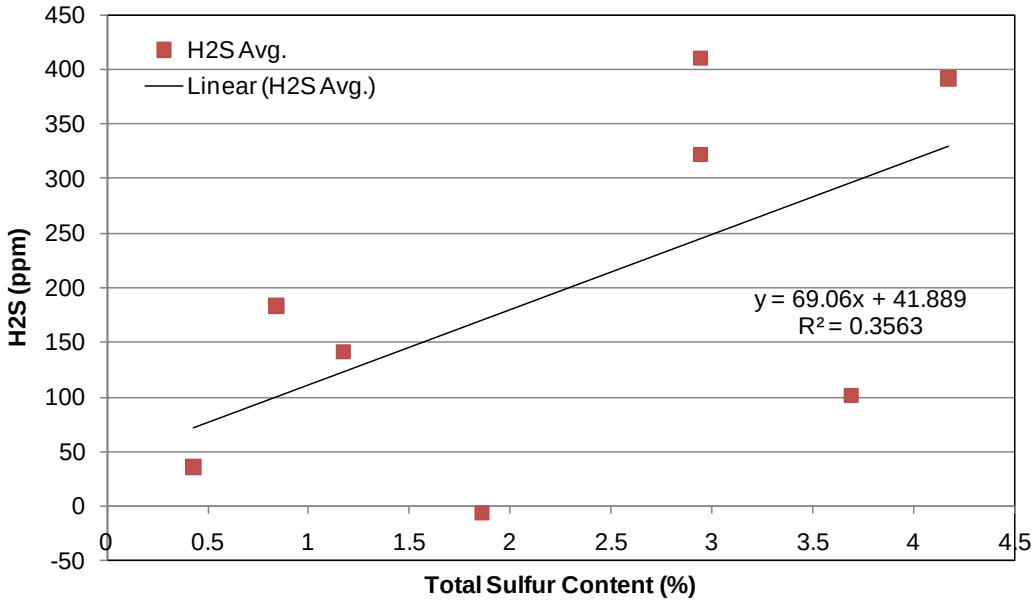

Figure 41 - Correlation of H_2S with Total Coal Sulfur under Reducing Conditions.

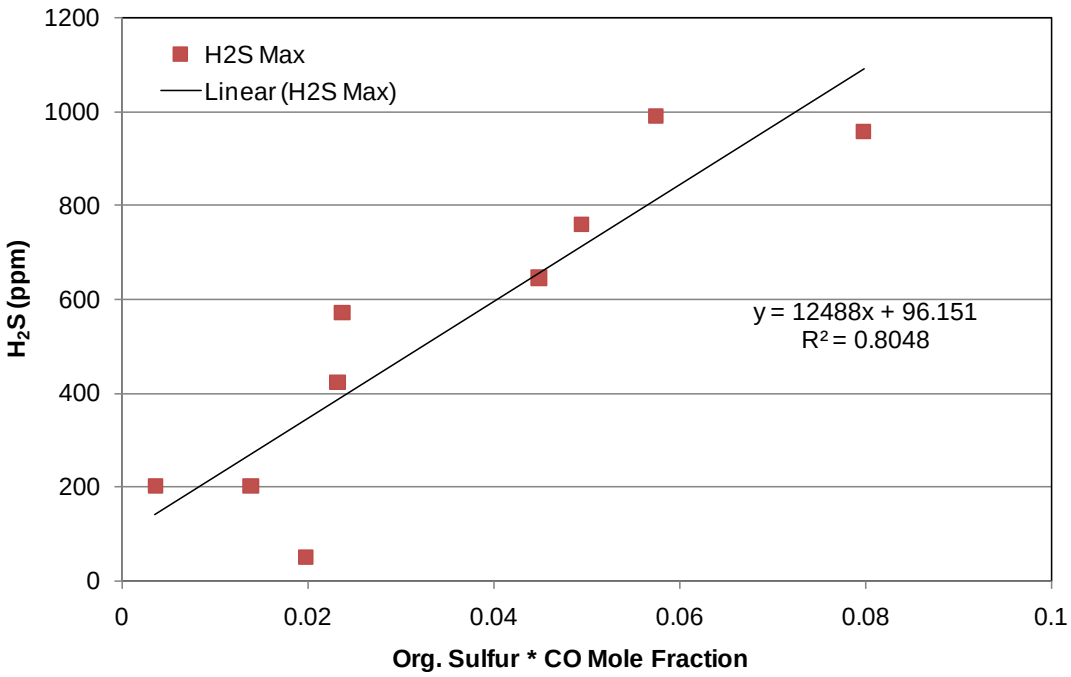

Figure 42 - Correlation of Measured H_2S Concentrations with Product of Organic Sulfur Mass Fractions in Coal and Measured CO Concentrations.

Since the H_2S concentration was found to increase with increasing CO concentration, an attempt was made to determine what coal properties would have produced a high CO concentration at a fixed S.R. The best correlation was found between H_2S and the product of organic sulfur and fuel oxygen fractions, as shown in Figure 43. The organic mass of sulfur provides the source of sulfur for the formation of H_2S while the coal oxygen fraction correlated with reducing conditions. The reason for a correlation of coal oxygen fraction with CO is not yet understood. Other coal properties that were investigated for a correlation with H_2S included: the coal pyritic sulfur content, ASTM volatile yield, coal hydrogen fraction, and the inverse of coal hydrogen fraction. In addition to these individual parameters, products of these parameters were investigated. The product of organic sulfur and coal oxygen fraction still produced the best correlation. A more accurate prediction of the volatile release using a coal devolatilization model could provide a better understanding of the correlation.

Given the data presented, a process of sulfur evolution has been postulated. Approximately 85% of the sulfur in the coal is rapidly released and converted to gas phase species in the fuel rich burner zone. Organic sulfur appears to preferentially form H_2S, COS, and S_2 under fuel rich conditions. As oxygen becomes available, H_2S and COS are converted to SO_2 and SO_3. Pyritic sulfur is more likely to burn heterogeneously and form SO_2 and SO_3. Thus, there is a stronger correlation of SO_2 and SO_3 with pyritic sulfur as well as a stronger correlation of H_2S and COS with organic sulfur. The S_2, H_2S, and COS gases can further react with the deposit condensed on boiler tubes to form sulfides in the burner zone. However, under oxidizing conditions, the H_2S, COS and S_2 are converted to primarily SO_2. The SO_3 gas exists in both the

oxidizing and reducing zones, which accounts for about 1% of the total coal sulfur. The SO_3 and SO_2 concentrations scale linearly in the oxidizing zone with the total coal sulfur content.

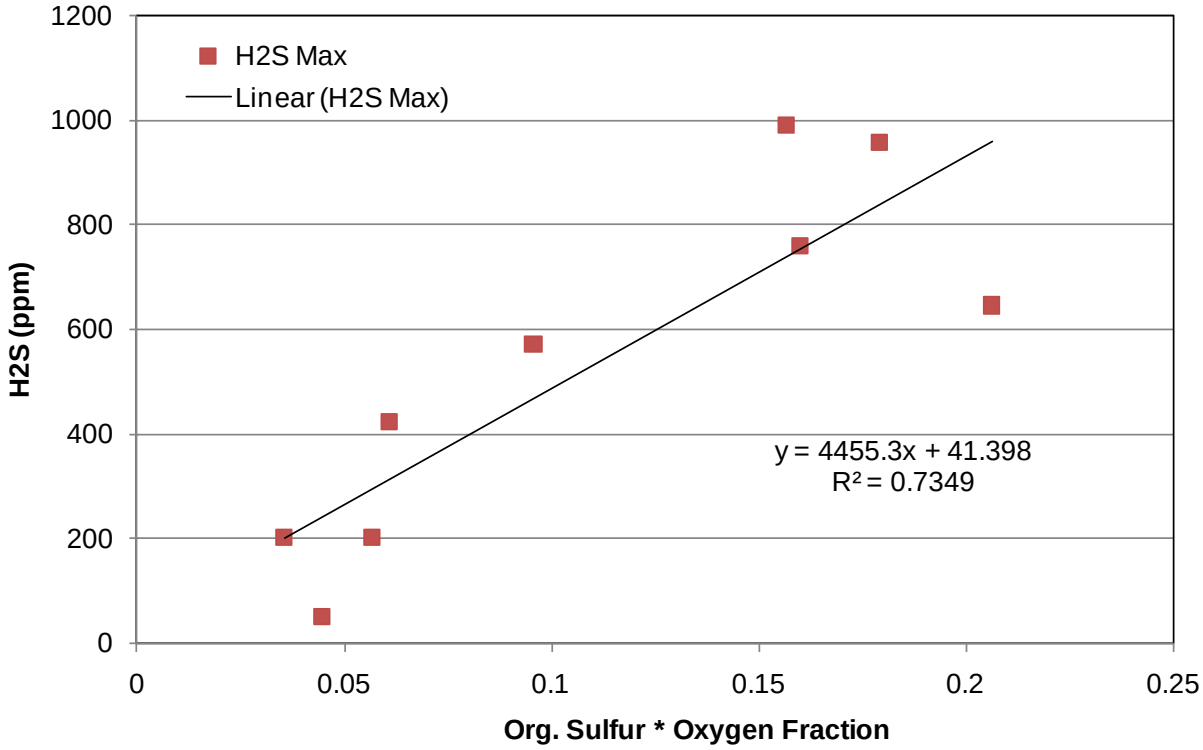

Figure 43 - Correlation of Measured H2S with Product of Organic Sulfur Mass and Coal Oxygen Fractions.

4.3.6.4 Discussion on the Fate of Coal Chlorine

Coal chorine is present in a variety of concentrations as shown in Table 9. The equilibrium software, HSC Chemistry 7.0, was used to investigate the stable forms of chlorine under combustion conditions. Results of the equilibrium calculations were obtained for the S.R. of 0.85 and 1.15 at temperatures ranging from 500 to 2000^{o}C. The results, shown in Figures 44 and 45, were similar for all the coals that contain a significant amount of chlorine (i.e., coals that produced gaseous chlorine species greater than 1 ppm). HCl was determined to be the most predominant species, with a small amount of Cl and NaCl becoming more stable at very high temperatures. The temperature range was extended in the calculations beyond what is considered a feasible gas temperature in order to investigate the decrease in HCl at high temperatures. The formation of NaCl at high temperatures and the lack of formation of NaCl at low temperatures are counterintuitive and will be further discussed later.

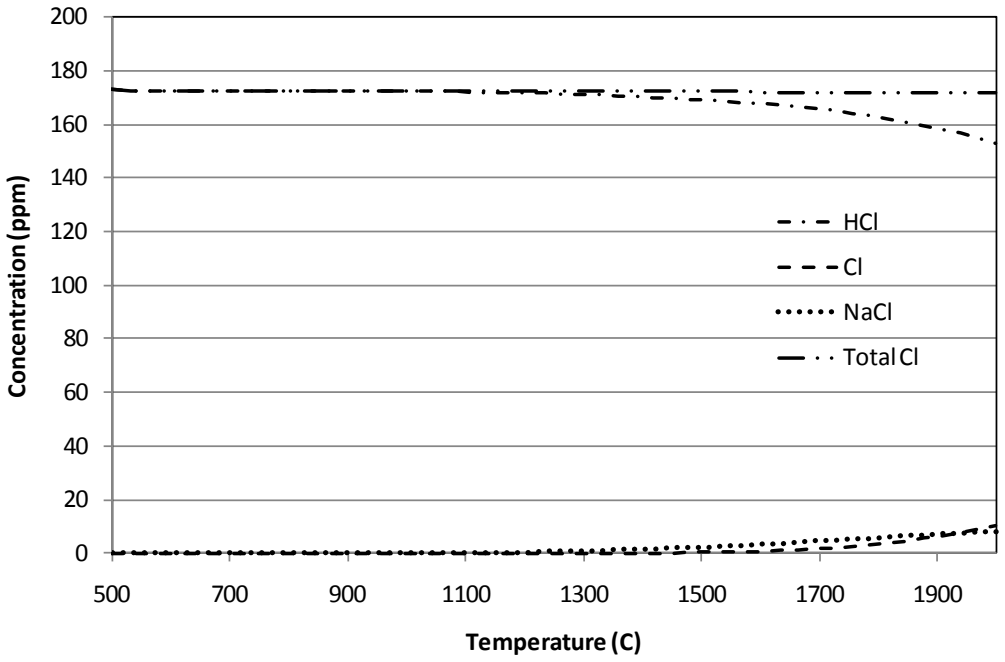

Figure 44 - Equilibrium of Chloride Species for OH Mahoning Coal under Reducing Conditions at S.R.=0.85.

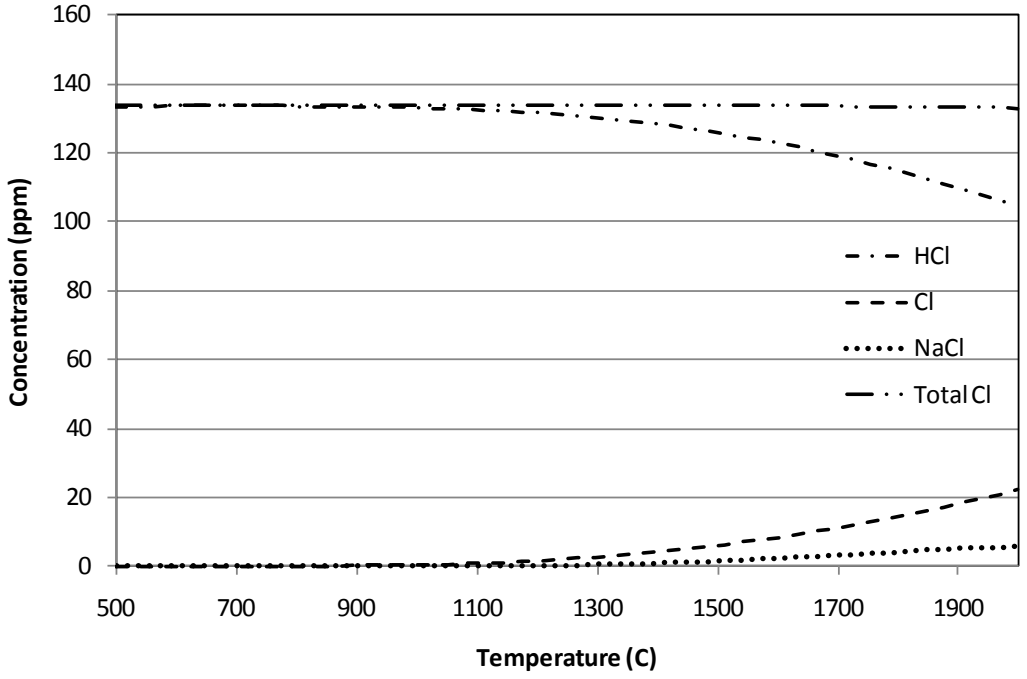

Figure 45 - Equilibrium of Chloride Species for OH Mahoning Coal under Oxidizing Conditions at S.R.=1.15.

Using the total number of moles in the gas phase for all species predicted by the equilibrium program and the total moles of chlorine in coal, the maximum possible HCl concentration could be estimated for each coal and compared to the average of measured chlorine concentration in the reducing and oxidizing zones, as shown in Figures 46 and 47. The measured HCl concentration shows a strong linear relationship between the measured HCl and the chlorine content in coal. The ratio of the slopes of the measured and maximum chlorine lines was used to estimate the fraction of the coal chlorine that is released as HCl. The data show that approximately 55% of the coal chlorine has formed HCl in the reducing zone and 71% in the oxidizing zone. The increase of HCl between the reducing and oxidizing zones indicates that HCl continued to form during char oxidation.

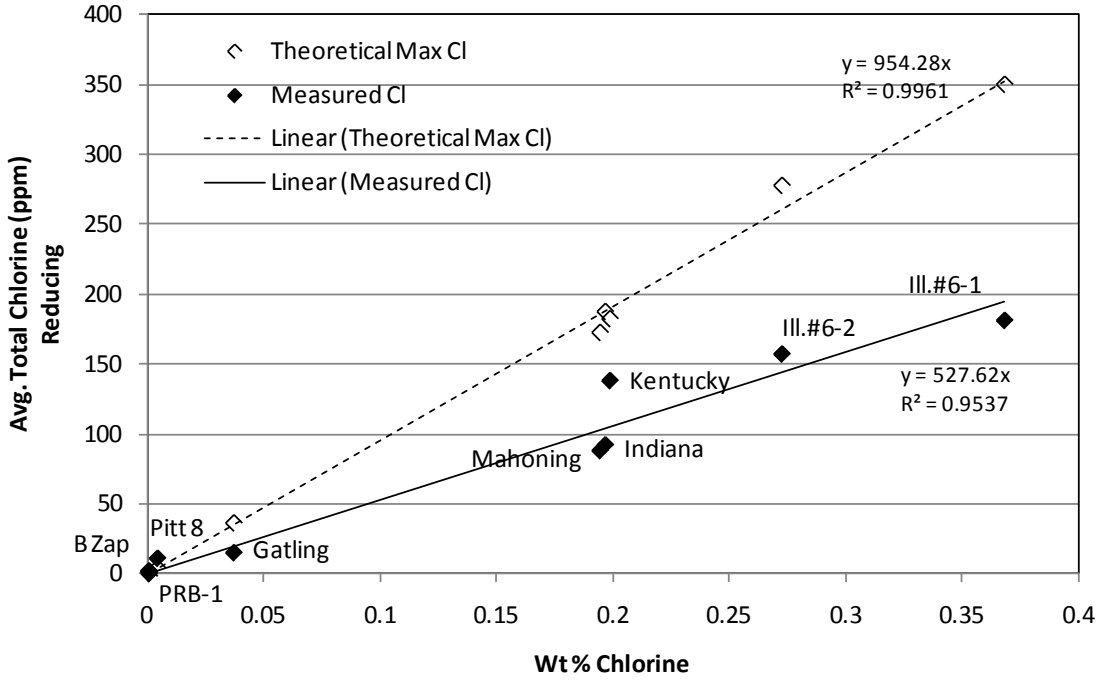

Figure 46 - Comparison of Measured and Maximum Possible HCl Concentrations as a Function of Coal Chlorine Content under Reducing Conditions.

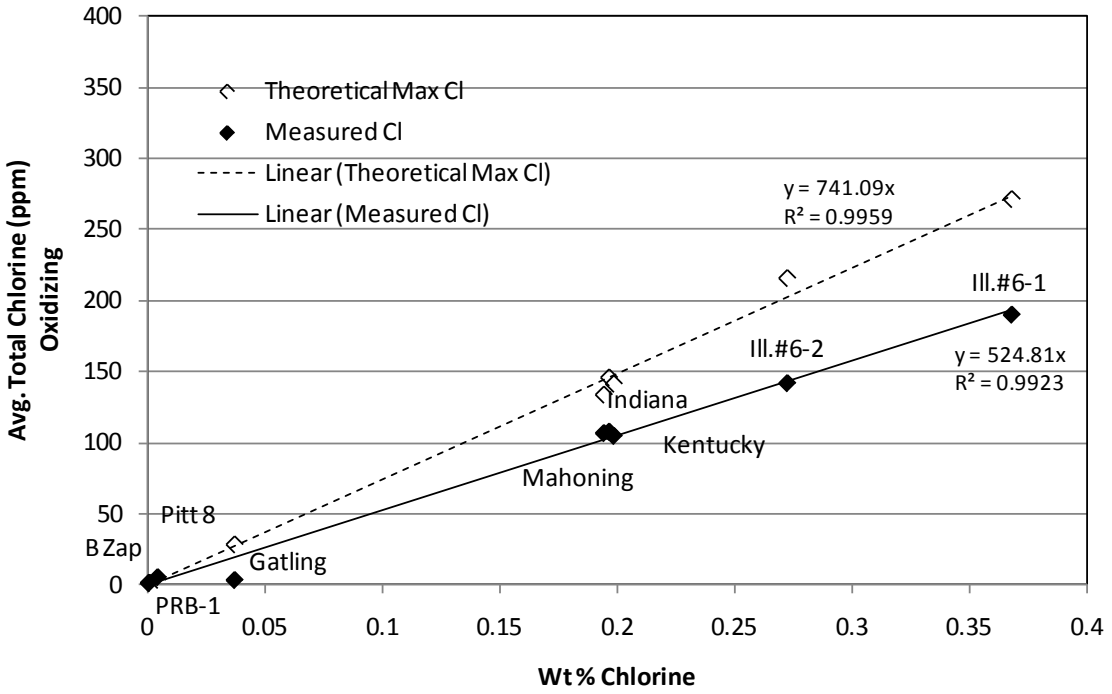

Figure 47 - Comparison of Measured and Maximum Possible HCl Concentrations as a Function of Coal Chlorine Content under Oxidizing Conditions.

The fate of chlorine that is not in the form of HCl gas is unknown. If the remaining chlorine was still in the unburned coal, char, or condensed phase, it would have appeared in the deposit samples. For Illinois #6-1 the fraction of chlorine in the coal is 0.389% and the ash fraction is 8.65%. If 45% of this chlorine was not released in the reducing zone and remained in the solid phase, followed by deposition in the deposit, the chlorine should have been approximately 2% of the ash. To date, chlorine concentrations in the deposits have been well below 2%, in fact essentially negligible. A second possibility is that the measured HCl concentrations contained errors. The possibility for measurement errors was attributed to the difficulty of keeping HCl from being adsorbed in the sampling line. It seems unlikely, however, that a sampling error would have created a consistent fractional bias for all coals. Recall that the FTIR was successful used to produce the correct HCl concentration for a calibration gas (see Table 12). Another possibility is that the HCl was removed slowly from the ash, and once the ash is deposited, chlorine continued to be released and entered the gas stream. In other words, chlorine in the deposit collected on the deposition probe had reached equilibrium because of the long residence time. Ash particles in the gas stream exiting the BFR are not in equilibrium and continued to release chlorine beyond the location of the oxidizing zone. If this is true, the ash deposits quenched rapidly at the reactor exit should contain a measureable amount of chlorine. However, this postulation was not supported by analyses of the exit deposit samples.

4.3.7 Deposit Sampling for Selected Eight U.S. Coals

4.3.7.1 Collection of Deposit Samples

Deposit samples were collected on two collection probes performed simultaneously with the online gas measurements described in Section 3.3.4. The water-cooled probe was employed in the reducing zone at the axial location of ~50 cm below the burner outlet. Six 5-cm long sleeves (cut in half, top and bottom) machined from 3.175 cm (1.25”)-OD 304 stainless steel tubing, were mounted to the water-cooled probe in three groups of two. As mentioned previously, thermocouples were mounted on three of these sleeves. The sleeve positions are shown in Figure 48(a) measured from the north wall of the BFR. These sleeves were labeled north, middle, and south after removal from the probe for easy identification. Similarly, six sleeves, consisting of three groups of two 5-cm sleeves, were placed on the air-cooled tube for the oxidizing zone, ~190 cm below the burner fuel outlet. The corresponding sleeve positions on this probe are shown in Figure 48(b).

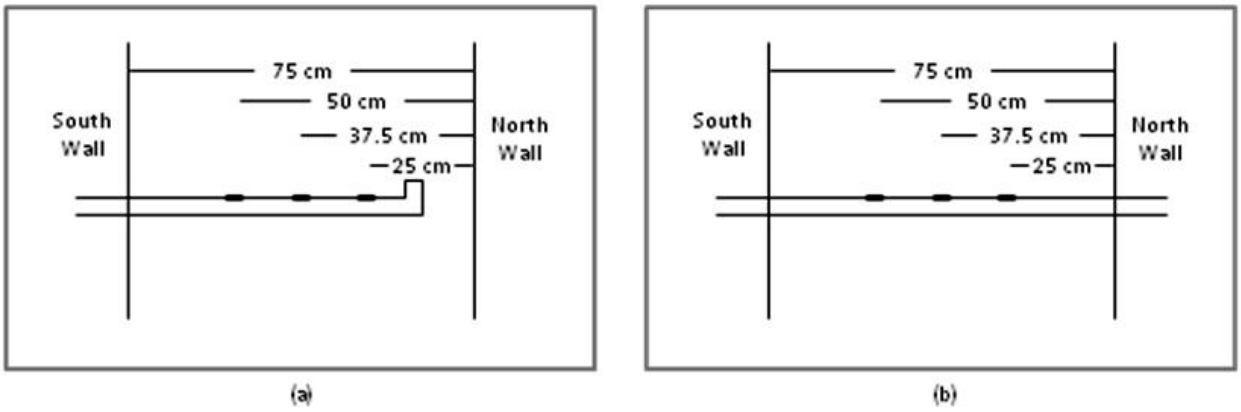

Figure 48 - Sleeve Positions on (a) the Water-Cooled Sampling Probe in the Reducing Zone and (b) Air-Cooled Sampling Probe in the Oxidizing Zone.

As an example, a photograph of the water-cooled deposit probe removed from the reducing zone after the Illinois #6-1 coal run is shown in Figure 49. The sleeves were secured to the probe with stainless steel hose clamps. The sleeves have been annotated on the figure as south, middle, and north according to their relative locations to the BFR. The deposit sample had a dark black color on the center sleeves and light brown/beige on the north and south ends. In comparison, the color was darker on the south deposit than that of the north, which was consistent with the results of the gas measurements summarized in Table 14, as a higher CO concentration (~3.5%) was present near the south end and lower near the north end. All of the sleeves appeared to have been exposed to different degrees of reducing combustion conditions.

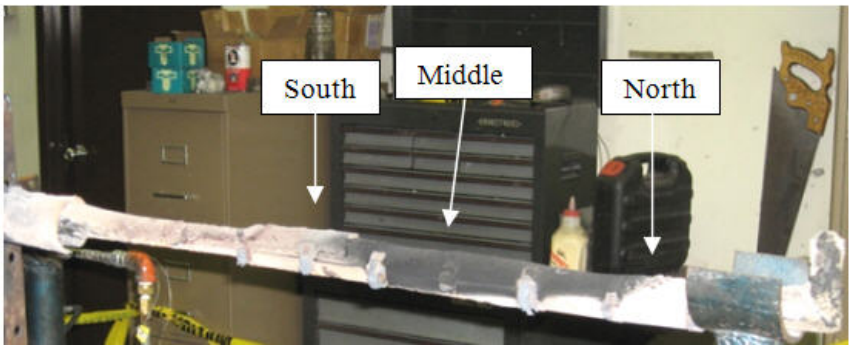

Figure 49 – Water-Cooled Deposition Probe Removed from the Reducing Zone of IL #6-1 Test.

A photograph of the air-cooled deposition probe removed from the oxidizing region after exposure to the Illinois #6-1 Galatia test is shown in Figure 50. It can be seen that all of the deposits appeared to be well burned out and uniform in color. The deposition rate on these sleeves was clearly slower than that in the reducing zone. Deposition is primarily governed by the impaction of particles on the sleeve surface. The ash particles in this oxidizing zone should have been completely burned out and therefore the particle size would be smaller as they approached the probe surface. Smaller particles were more likely to follow the flow contour around the probe, while larger particles maintained their momentum to impact on the surface. The deposit samples shown in these examples are representative of all coals investigated.

Figure 50– Air-Cooled Deposition Probe Removed from the Oxidizing Zone of Illinois #6-1 Test.

4.3.7.2 SEM/EDS Analysis of Deposit Samples

The deposit samples were collected as discussed in Section 3.3.4. Adjacent samples were examined using a SEM equipped with EDS. The SEM/EDS examinations included (1) BSE imaging of the sleeve cross-sections to identify general features of the deposit and deposit

morphology, (2) EDS analyses to quantify the deposit compositions on the sleeves, and (3) dot mapping to reveal the distribution of key elements in the deposit samples.

The SEM/EDS system used for this study was an FEI model XL30 ESEM, FEG with an EDAX Genesis detector processing package. Images obtained were in a 256 x 200 array with a dwell time on each pixel of 2 seconds. The detector collected spectral energy counts for each pixel location, while the associated software was used to identify key elements based on the energy spectra. The EDAX Genesis software was able to identify regions within the image of similar compositions and make suggestions of the condensed phases/compounds. The spectral compositions of all pixel locations were saved to an electronic file server for subsequent detailed analysis.

Figure 51 shows a labeling scheme established for the deposit samples to associate their probe and sleeve locations. For example, “RB5” represents Reducing, Bottom, and Sleeve #5. The location of RB5 relative to the other deposit samples on the reducing probe is shown. The sleeves positioned on the top of the reducing deposition probe were marked with RT, where T stands for top. The same naming system was also used for the oxidizing deposit samples, except where “R” for reducing was replaced with “O” for oxidizing.

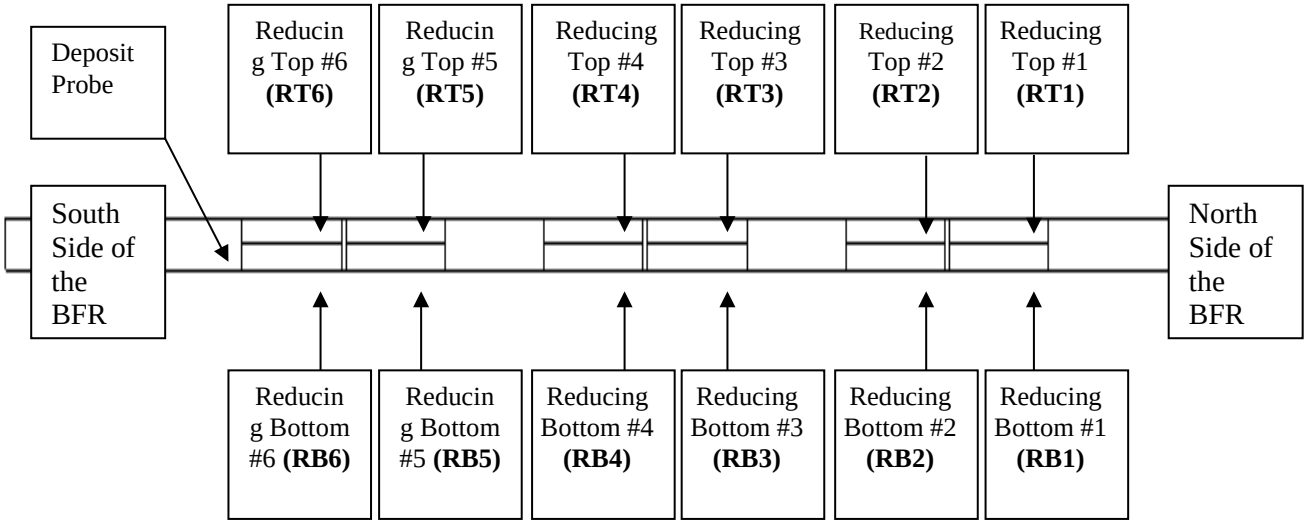

Figure 51 - Nomenclature for Probe Deposition Sleeve Locations.

Using SEM images to obtain quantitative and non-biased information is always challenging. The nature of the SEM imaging is to investigate a very small cross section of the deposit which may or may not be representative of the average or important subset of the entire sample. The choice of where to collect the image within a sample for this project was further complicated by the fact that for some samples, most of the deposit had separated from the probe surface before it was encased in epoxy. In these cases, the only deposit remaining was a thin layer next to the sleeve. In other cases, the deposit was several mm thick. Another issue of complication was related to the selection of SEM/EDS resolution. By increasing the image

resolution, thus focusing on a smaller subset of the deposit, the captured image might no longer be fully representative of the deposit. Also, the resolution of the image would impact the average composition of the particles analyzed. Finally, the EDS software used for the particle and composition analyses required an arbitrary intensity cut-off to determine which pixels within an image were considered particles and which were the substrate material (i.e., epoxy). In spite of these limitations, significant insight to the deposit chemistry was obtained from the image analysis.

As an example, the backscattered SEM image of Illinois #6-2 OB5 sample is shown in Figure 52. Backscattered electron micrographs produce images with light intensity proportional to the atomic numbers of elements. Therefore, the bright band near the bottom of the image represents the cross-section of the metal sleeve, and the dark region at top is the low-density epoxy mounting material. The porous layer in the middle section, approximately 200 μm thick, is the deposit collected on this probe sleeve. In this case, the deposit appears to be relatively uniform in size, shape, and intensity throughout. A higher resolution (1200x) image near the probe surface is shown in Figure 53 to allow analysis of the smaller ash particles. The selection of the image resolution was arbitrary based on the thickness of the deposit layer. Therefore, a higher resolution was used for thicker deposit and lower resolution for thinner deposit.

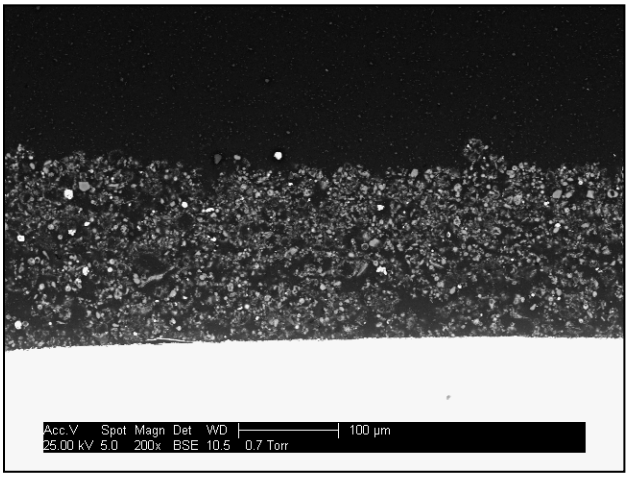

Figure 52 - Backscattered Electron SEM Image on the IL#6-2 OB5 Sleeve Cross-Section.

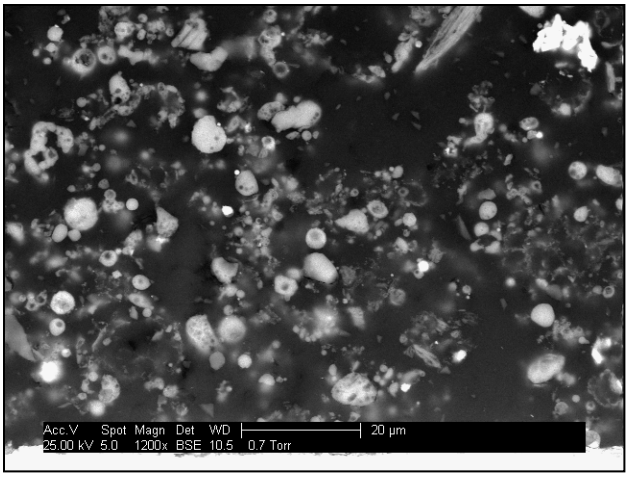

Figure 53 - Backscattered Electron SEM Image on the IL#6-2 OB5 Sleeve Cross-Section.

The EDAX software, Genesis Particle Analysis, used the backscatter image to identify particles in the deposit samples. Only pixel intensity higher than a threshold was analyzed. An example of the software selection process is shown in Figure 54. The histogram at the right shows the number of particle as a function of pixel intensity. The blue line on the histogram indicates a threshold limit of 175. When X-ray analysis was performed, the signal collection time for each particle was typically 4 seconds.

Proper selection of the threshold limit is critical. If the limit is set too low, the adjacent epoxy material is included as part of the particles. On the other hand, if the limit is set too high, the particles with low density are excluded from the analysis. Typically, the intensity limit is adjusted until the particle count is near 1000 and the majority of the lighter, shaded particles are included.

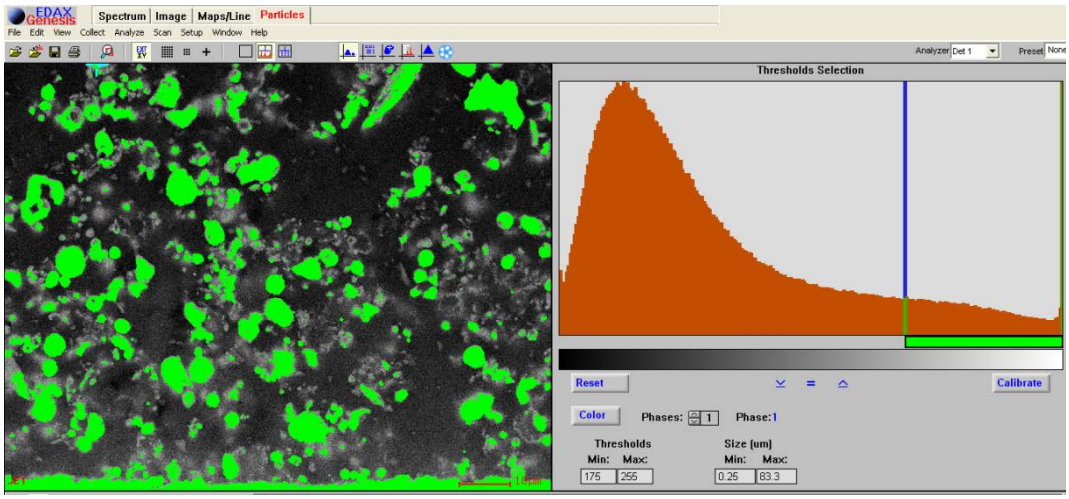

Figure 54 - Screen Shot of EDAX Genesis Particle Analysis Software with a Threshold Minimum of 175 and Maximum of 256.

Once identified, the particles were analyzed for sizes, shapes, and compositions. For the Illinois #6-2 OB5 deposit particles, shown in Figure 54, the size minimum was 0.24 μm and the total number of particles analyzed was 864.

The morphology data supplied by the software included the following information for each particle:

- Area (μm^2)
- Diameter (μm) (assuming the particle is circular)
- Perimeter (μm)
- Aspect ratio
- Shape (roundness)
- Elemental Composition (elements selected by the user)

As an example of the morphology and composition information produced by the EDAX software, results for fifteen of the 864 particles present in the Illinois #6-2 OB5 deposit are given in Tables 16 and 17. Several particles at the minimum resolution size of 0.24 μm were found. Carbon is by far the richest element in each particle due primarily to the carbon coating applied. The second most abundant element is oxygen that is associated with the oxides of various ash elements. The results of EDS analysis are compared to those of the coal ash analysis and the XRF elemental analysis in the next section.

Table 15 - First 15 Particles of Illinois #6-2 OB5 Analyzed for Size and Shape.

Particle Number	Average Diameter (μm)	Area (μm^2)	Perimeter (μm)	Shape	Aspect Ratio
1	0.62	0.30	4.48	5.25	4.15
2	0.24	0.04	0.73	0.97	2.55
3	2.73	5.85	38.13	19.78	3.68
4	0.68	0.36	3.44	2.63	4.24
5	2.85	6.38	19.38	4.68	2.62
6	0.35	0.10	1.25	1.27	1.75
7	0.33	0.09	1.04	0.99	3.63
8	0.24	0.04	0.73	0.97	1.96
9	0.44	0.15	1.56	1.28	2.08
10	0.24	0.04	0.73	0.97	1.96
11	0.53	0.22	3.02	3.35	2.87
12	0.41	0.13	1.67	1.70	3.27
13	0.62	0.30	2.40	1.50	2.52
14	0.24	0.04	0.73	0.97	1.96
15	0.55	0.24	2.08	1.45	2.64

Table 16 - First 15 Particles of Illinois #6-2 OB5 Analyzed for Compositions.

#	C	O	Na	Mg	Al	Si	P	S	Cl	K	Ca	Ba	Ti	Cr	Mn	Fe	Ni
1	60.48	16.07	0.66	0.50	5.63	8.09	0.00	0.58	0.00	1.46	0.65	0.00	0.00	1.40	0.00	4.47	0.00
2	71.22	8.38	0.00	0.00	2.70	10.16	0.00	0.00	0.00	1.01	0.46	0.00	0.00	1.22	0.34	4.51	0.00
3	56.42	14.50	0.56	0.43	8.21	10.21	0.00	0.00	0.42	3.25	0.43	0.00	0.00	1.17	0.00	4.39	0.00
4	64.05	11.59	0.54	0.29	6.06	8.64	0.00	0.00	0.54	2.08	0.50	0.00	0.00	1.16	0.34	3.42	0.78
5	53.04	18.06	0.00	0.00	2.28	18.10	0.00	0.00	0.00	0.94	0.41	0.00	0.55	1.10	0.34	5.19	0.00
6	56.93	15.94	0.38	0.00	6.29	9.98	0.00	0.37	0.64	1.51	0.50	0.00	0.66	1.04	0.00	5.22	0.54
7	58.51	17.13	0.00	0.00	6.09	8.84	0.00	0.00	0.32	1.45	0.53	0.00	0.50	1.05	0.32	4.75	0.51
8	70.26	8.74	0.00	0.37	5.57	7.29	0.00	0.00	0.46	1.19	0.00	0.00	0.00	1.32	0.35	4.45	0.00
9	61.03	15.76	0.76	0.36	6.04	7.25	0.00	0.00	0.54	1.45	0.49	0.00	0.00	1.48	0.33	4.00	0.50
10	71.49	7.83	0.00	0.00	2.69	9.67	0.00	0.00	0.00	0.98	0.00	0.00	0.00	1.52	0.00	5.10	0.71
11	63.22	15.83	0.00	0.00	2.93	8.79	0.00	0.29	0.64	0.96	0.24	0.97	0.00	1.07	0.31	4.09	0.66
12	63.77	15.50	0.59	0.00	2.72	9.03	0.00	0.00	0.55	0.92	0.47	0.00	0.37	1.34	0.44	4.29	0.00
13	68.23	8.68	0.39	0.00	4.86	7.29	0.00	0.00	0.58	1.66	0.52	0.00	0.36	1.12	0.29	5.34	0.69
14	59.86	14.43	0.65	0.49	5.59	7.19	0.00	0.50	0.64	1.52	0.75	0.86	0.40	1.05	0.43	5.07	0.58
15	70.79	8.05	0.43	0.00	4.92	6.48	0.00	0.41	0.69	1.25	0.39	0.00	0.23	1.06	0.45	4.28	0.58

Results of the SEM/EDS analyses for the deposit samples collected in the BFR during the combustion of the eight coals are summarized in Section 3.3.10.

4.3.7.3 Deposit Morphology

Using Illinois #6-2 as an example, the distribution functions of ash particles in a deposit are demonstrated in Figures 57 and 58 by showing the equivalent diameter of the particles on the top and bottom sides of the probe, respectively. The median particle size of the top side ranged from 2.5 to 7 μm, while that of the bottom ranged from 1 to 5 μm. The particles were generally smaller on the bottom side due to the deposition mechanism of eddy impaction or condensation.[13] On the other hand, the particles on the top sleeves were deposited mostly by direct impaction. Furthermore, the ash particles collected in the reducing zone were generally larger than those in the oxidizing zone. This difference could be attributed to incomplete combustion of coal in the reducing zone, thus allowing larger unburned coal particles to deposit, as discussed previously.

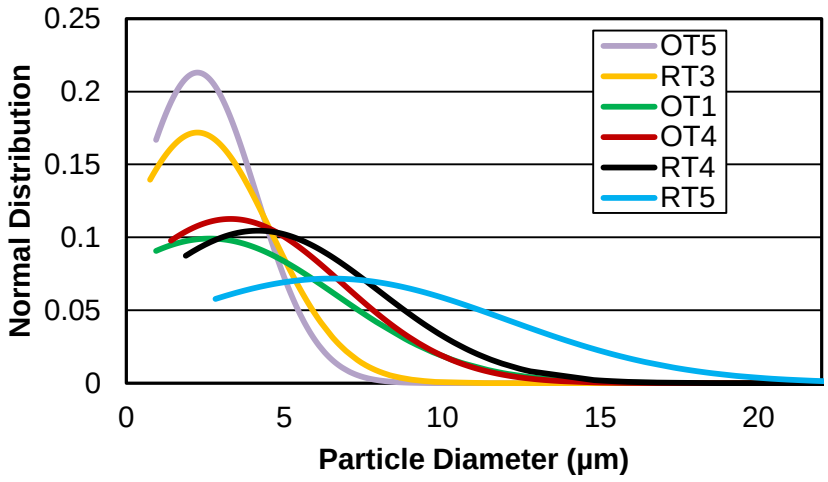

Figure 55 - Normal Distribution of Particle Diameter in the Top Deposit for the IL #6-2 Coal.

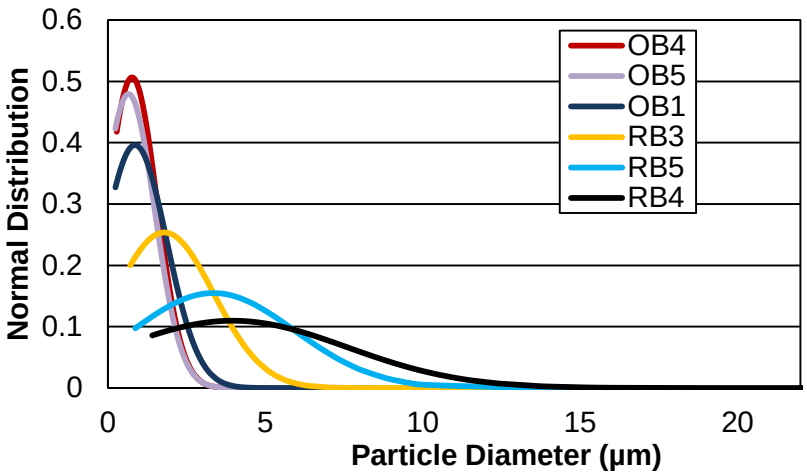

Figure 56 - Normal Distribution of Particle Diameter in the Bottom Deposit for the IL #6-2 Coal.

Based on the elemental analysis for each particle, the average compositions of the deposit were determined. These elemental compositions were then converted to oxides as typically done per ASTM ash analysis. Results of the average of all particles analyzed in the reducing top and reducing bottom deposits as well as the oxidizing top and oxidizing bottom deposits for Illinois 6-2 are shown in Figure 59. The deposit particles appear to have only minor differences in the locations. A good agreement between the deposit particle compositions and that of the XRF ash analysis (labeled as WAL) is also evident. While a significant amount of chlorine was detected in the deposit by SEM/EDS, it was not measurable by means of XRF analysis. The chlorine signal was likely picked up from the epoxy used for mounting the deposit/sleeve sample. Therefore, it should be ignored from the SEM/EDS results.

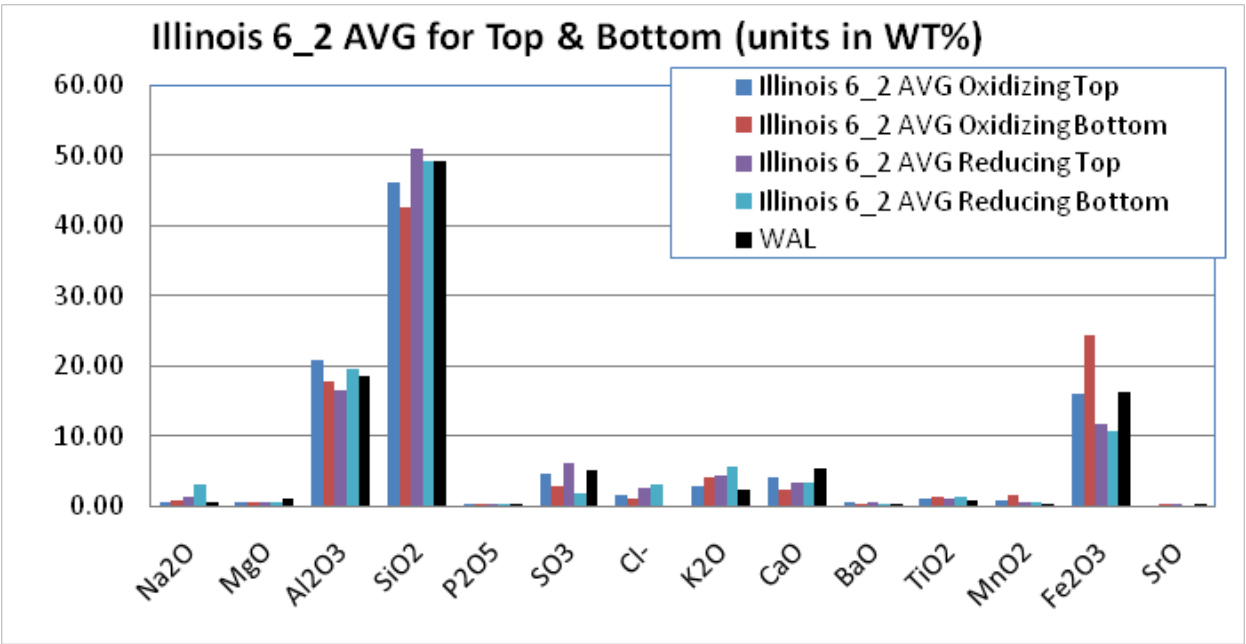

Figure 57 - Comparison of the Elemental Analysis of the Coal Deposits with the Ash Composition.

4.3.7.4 Probe Sleeve Temperatures

Results of the measured sleeve temperatures in the reducing and oxidizing zones are summarized in Figures 60 and 61, respectively, with the upper and lower targeted sleeve temperatures defined by the horizontal lines. The desired temperature was maintained most of the time in the oxidizing zone, while some temperature variations in the reducing zone were experienced. Heat flux to the probe surface was expected to be dominated by radiative heat transfer in the reducing zone. The radiative heat flux varied drastically from one sleeve location to another, as the center sleeve is positioned directly below the flame while the outer sleeves are further away from the flame. The temperature variations were attributed to different levels of deposit build-up and removal. The sleeve temperatures in the reducing zone typically started out in the desired range but rapidly reduced with time. The reduction in temperature was attributed to the deposit build-up, thus acting as an thermal insulator to the sleeve surfaces. Periodically, some deposit layer fell off the probe, causing a rapid increase in the sleeve temperature.

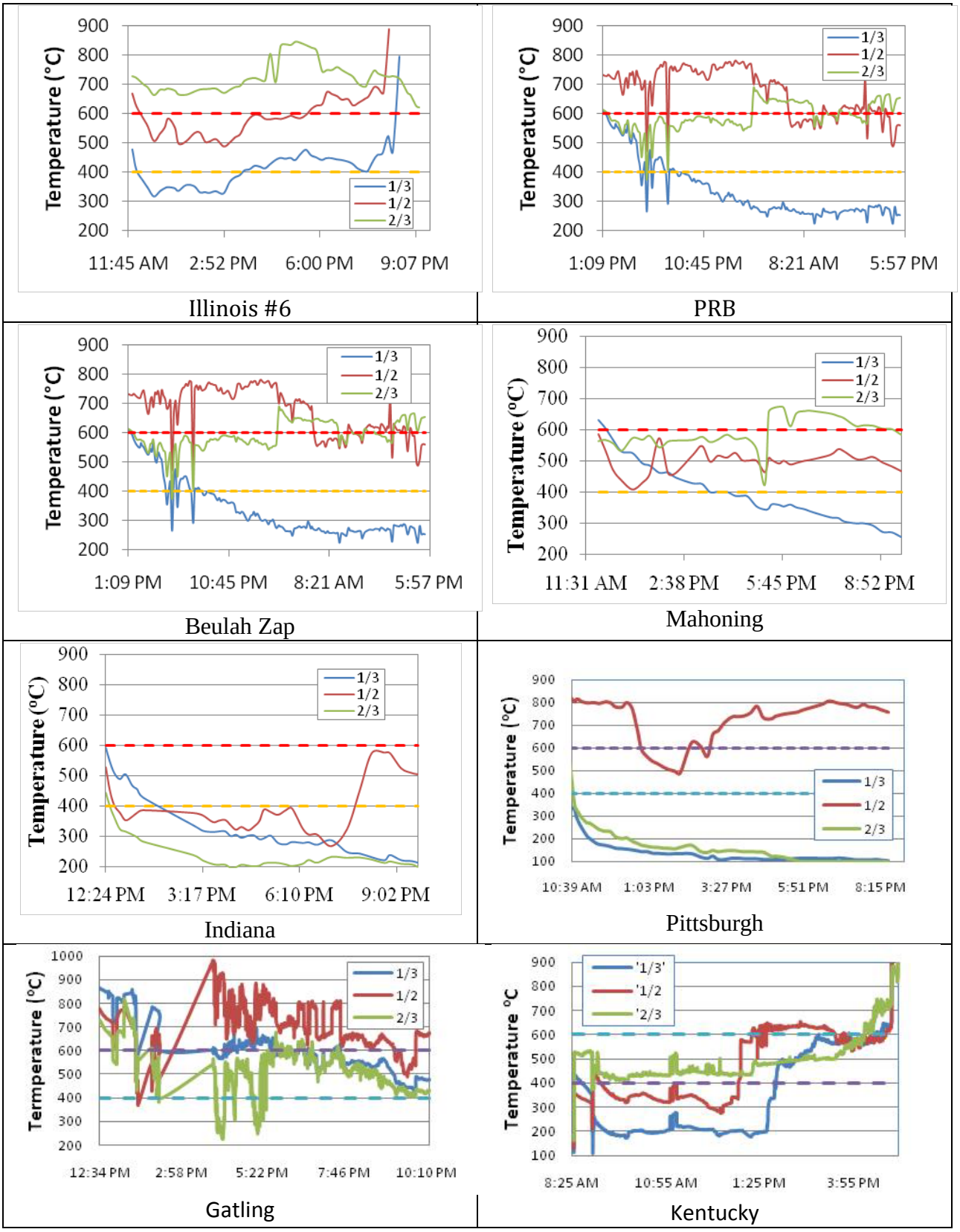

Figure 58 - Deposit Collection Sleeve Temperature in Reducing Zone.

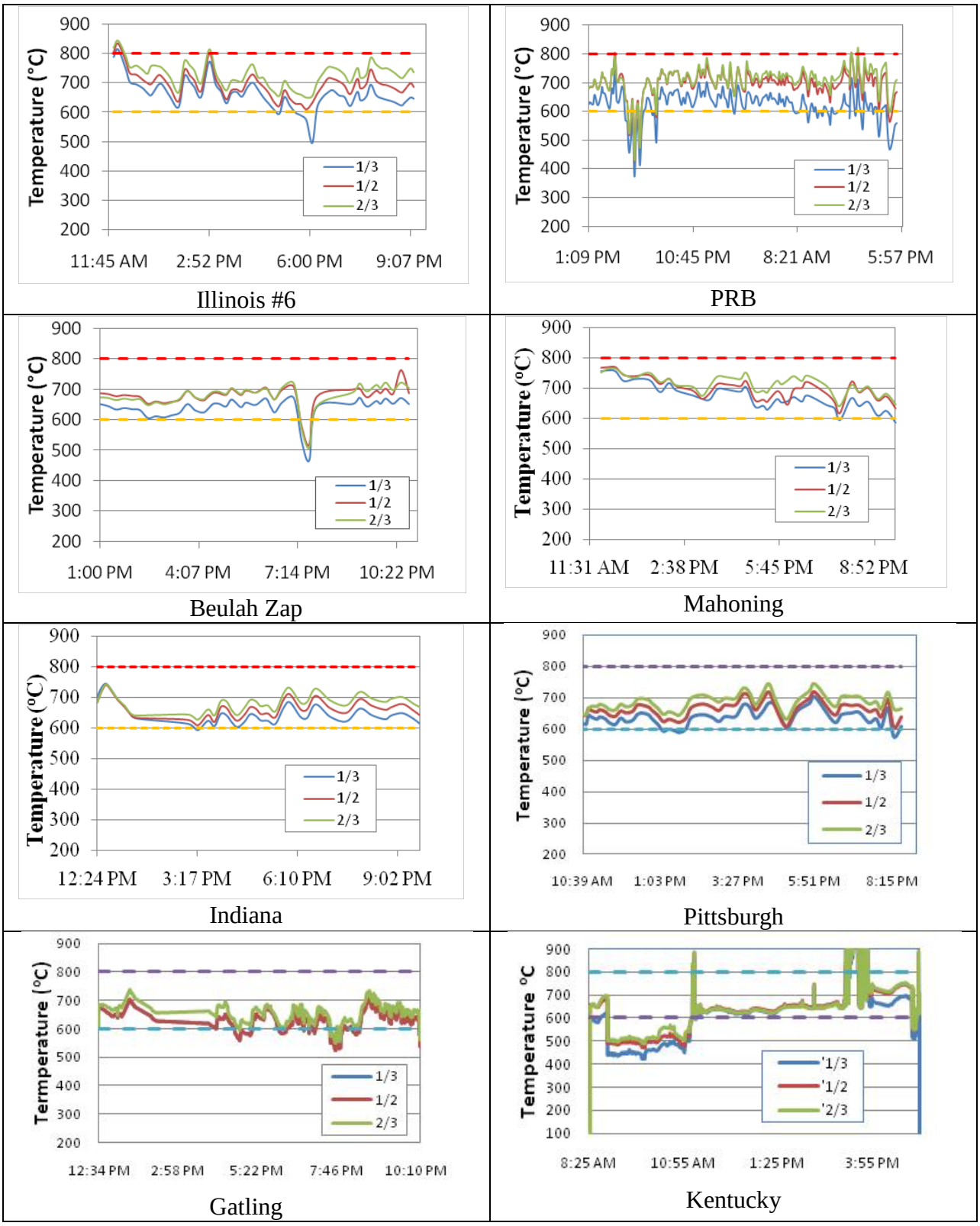

Figure 59 - Deposition Collection Sleeve Temperature in Oxidizing Zone.

4.3.8 Chemical Analyses of Deposit Samples Collected from Coal Combustion

Furnace probe deposits were collected for each coal test using sampling probes at both the oxidizing and reducing zones of the BFR. A schematic diagram of the sampling location for the reducing probe is shown in Figure 51, and the methodology for sample identifications is discussed in Section 3.3.7.2. There were three probe positions across the sampling zones, and each with two rows of sampling surfaces (i.e., top and bottom).

A removable stainless-steel sleeve was placed at each location/surface on which the deposit was collected. As discussion in Section 3.3.4, the sleeves were curved, longitudinally spliced in half tubing, and were positioned on the probe so that deposit was collected on the extrados surfaces. Due to the different probe diameters, the sleeves (1-3/8" OD) in the reducing region had approximately twice the surface area as the sleeves (5/8" OD) in the oxidizing region. After testing, each sleeve was carefully removed from the sampling probe, and was labeled and placed in a Ziploc bag for chemical analysis. During the operation of removing a sleeve, any loosely adhering deposit that had fallen off the sleeve was collected and placed in a labeled container, and identified as "loose deposit" for that sleeve.

Table 19 lists the locations of sleeve deposits from the oxidizing and reducing zones submitted for chemical analysis. A total of six sleeves from both the oxidizing and reducing zones, i.e., three sampling positions and two rows (top and bottom), were obtained from each coal test. In order to be consistent with the sampling position, the middle sleeves, i.e., Position 3 or 4, at the top row was selected for the chemical analysis. Based on the appearance, these middle positions have yielded the most representative deposit samples from the pilot-scale combustion testing. However, if the amount of sample from the top row was insufficient for chemical analyses, i.e., less than 0.1 g, the bottom row at the same position was also included. This was the case with several of the coals, and is denoted in Table 18. In some instances, the loose deposits collected at the same position were also included with both sleeve deposits in order to have enough ash samples.

As discussed previously for sleeve identifications, the deposit removed from the #3 position top sleeve in the oxidizing zone is labeled OT3. In the reducing zone at the #3 position top sleeve position, the deposit was labeled RT3. For a loose deposit, if the material can be tied to just an individual sleeve, the loose deposit was given the same identification as the sleeve. Otherwise, the designation for the loose material at a given position is labeled as top and bottom rows of the corresponding position (i.e., OT3+OB3).

Table 17 – Locations of Furnace Probe Deposit Samples for Chemical Analyses.

Coal	Oxidizing Zone			Reducing Zone		
	Location	Location	Location	Location	Location	Location
Illinois #6, Galatia	2	4	6	2	4	6
PRB, Black Thunder, WY	1	3	5	1	3	6
Beulah-Zap Lignite, ND	2	4	6	2	4*	6
Mahoning 7A, OH	2	3*	6	1	4*	5
Indiana #6, Gibson	3*	5	6	1	2	4
Gatling, WV	2	4	6	1	3	6
Pittsburgh #8, PA	2	3*	6	2	3	6
Kentucky #11	1	4	6	2	3	6

* Denotes that both the top and bottom probe deposits were needed and combined for the analyses.

Photographs were taken from all the as-received sleeve samples for each coal test. Shown in the following sections are the pictures of the sleeve deposits selected for the chemical analyses. Each sleeve was removed from its Ziploc bag, and was handled with nitrile gloves to minimize contamination. The deposit was removed from its sleeve by lightly brushing the extrados surface with a stiff short-hair brush and was carefully collected on a sheet of clean paper. The reason for light brushing was to minimize the potential of removing the scale (or corrosion products) formed on the sleeve surfaces, as characterization of just the deposit was the primary goal. Furthermore, any deposit that may have separated from the sleeve in the Ziploc bag during shipping was retrieved and combined with that collected on the paper. Similarly, any loose material collected in a bottle for that sleeve was combined with that collected on the paper. The deposit was accurately weighed to 0.1 mg using a digital analytical balance. After weighing each deposit sample, it was ground with an agate mortar and pestle until 100% passed through a 200 mesh (75 micron) SS screen. The deposit was then transferred to a labeled sample bottle. The numbers in red in Table 19 denote that those deposit samples have been submitted for chemical analysis, while those in black at the other locations were archived.

4.3.8.1 X-ray diffraction phase identification analysis

The amount of sample for each deposit remaining on the sleeve was limited due to the fact that spallation occurred when retrieving the sampling probe from the BFR. When the quantity was over 0.1 g, selected chemical analyses could be performed. The sequence in performing the chemical analyses for each of the deposit samples was (1) X-ray diffraction phase identification analysis (non-destructive), (2) wavelength dispersive X-ray fluorescence (destructive), and (3) carbon/sulfur analysis.

The instrument used for performing X-ray diffraction phase identification analysis was a PANalytical X'Pert Pro, equipped with a small sample holder. Samples were analyzed as packed powders that were first dried at 45^{o}C, followed by mounting on an off-axis PANalytical low background Si-Schiff wafer sample holder. The mounting diameter of the wafer was 15mm with a depth of approximately 0.5mm. This wafer allows very small samples to be analyzed using the

sample changer and spinner by means of signal averaging. The X-ray diffraction system was equipped with a PW3050 goniometry, sample spinner, x'celerator detector, PANalytical electronics, and search/match software. The X-ray diffraction patterns (diffractograms) were generated using Cu Kα radiation at a tube power setting of 45kV and 40mA. The samples were scanned from 5 to 65^{o} 2θ.

The X-ray diffraction phase identification analysis provided information of the phases or compounds present in a deposit sample. In addition, it provided relative concentrations of the phases present in a sample based on peak intensities with consideration given to the elemental analysis, which were ranked as major (>25%), medium (10 to 25%), minor (5 to 10%), and trace (detection limit to 5%) phases.

4.3.8.2 X-ray fluorescence elemental analysis

Following the XRD analysis, the sample was placed on a boric acid backing media, and compressed to a disc under a 50,000 psig pressure. The diameter of the formed disc was 32 mm. The instrument used for performing the wavelength dispersive X-ray fluorescence elemental analysis was a PANalytical Axios spectrometer, Model PW4400. The PANalytical IQ+ Software was used for the elemental analysis. IQ+ was a standardless software package based on an advanced fundamental parameters algorithm. It had the flexibility to handle a wide variety of materials with accurate results over a wide range of concentrations (detection limit to 100%). However, the use of this technique was destructive, and did not allow recovery of the sample for other testing.

In some cases, there was interference for magnesium due to the presence of arsenic in the probe deposit. The Lα line for arsenic was located at 1.282 Å, and was very near the Kα line for magnesium at 1.253 Å. Also, the presence of lead in a probe deposit could interfere with magnesium, as the M4 line for lead was very close to the Kα line for magnesium. Since the concentrations of arsenic and lead were at trace levels relative to the magnesium concentrations in the deposit samples from coal combustion, these two elements were ignored in the XRF elemental analysis software calculations to generate the more abundant magnesium readings.

Table 20 shows an example of an XRF elemental analysis for a probe deposit sample. In this report, the compounds in the sample were calculated as oxides. The IQ+ software determined the oxygen based on the stoichiometry of the compounds and the peak intensities of the analyte elements that the oxygen was bonded to. For example, the oxygen in the compound CaO is calculated based on the Ca peak intensity and the fact that there is one O atom for every Ca atom.

The compound list can vary for each probe deposit sample depending on the elements present and the detection limit for each element. In general, the higher the atomic number is, the greater the sensitivity is. In the "Weight %" column, all the detected elements, expressed as compound oxides, were normalized to 100 %. This was accomplished by dividing each compound by the "Sum before normalization" percentage in decimal form. The "As-received Weight %" for each element was calculated by first subtracting the "LOI" percentage from 100, converting that percent value to decimal form, and then multiplying the decimal value by the

wt.% value. The accuracy of the XRF elemental analysis was ±10 % for compounds with higher weight percentages. However, as the detection limit for an element was approached, the uncertainty of the result would increase.

Table 18 - Example of XRF Elemental Analysis for a Probe Deposit Sample.

Sample Description: Furnace Probe Deposit, Beulah-Zap Lignite, Reducing, Top, Position 4

REPORT of ANALYSIS
(Powdered X-ray Semi-quantitative)

Sum before normalization:	85.30%
Normalised to:	100.00%
Sample type:	Pressed powder
Correction applied for medium:	No
Correction applied for film:	None
Used Compound list:	OXIDES
Results database:	iq+ 4kw 27mm
LECO Carbon	1.02
LOI	2.15

Analyte	Compound	Weight %	As Received Weight %
Na	Na2O	5.72	5.60
Mg	MgO	7.29	7.13
Al	Al2O3	16.27	15.92
Si	SiO2	32.95	32.24
P	P2O5	0.37	0.36
S	SO3	3.12	3.06
K	K2O	1.30	1.27
Ca	CaO	22.95	22.45
Ti	TiO2	0.85	0.83
Cr	Cr2O3	0.05	0.05
Mn	MnO	0.06	0.06
Fe	Fe2O3	8.39	8.21
Ni	NiO	0.02	0.02
Cu	CuO	0.04	0.04
Zn	ZnO	0.09	0.09
Ga	Ga2O3	0.01	0.01
As	As2O3	0.01	0.01
Rb	Rb2O	0.02	0.01
Sr	SrO	0.37	0.36
Ba	BaO	0.13	0.12
Cl	Cl	0.02	0.02
Total		100.00	

Notes:
1. This analysis represents specifically the sample submitted.
2. Sample results reported on an as received weight basis.
3. Oxide analysis by X-ray fluorescence spectrometry using PANalytical IQ+ Quantification program.
4. This report may not be reproduced except in its entirety.

4.3.8.3 Total carbon and sulfur analysis

When Loss on Ignition (LOI) of the deposit samples could not be determined by using TGA due to insufficient sample quantity, the UBC value was determined with a LECO carbon/sulfur analyzer. The principle of detection for both carbon and sulfur was the use of

individual IR cells measuring CO_2 and SO_2 absorbances, respectively. ASTM Method D 4239-08, Method B, High Temperature Combustion Method with Infrared Absorption Procedure, was followed. Total of the as-received weight % was therefore the difference between 100% and the carbon and other volatile species in a sample lost during heat up of the sample to 1000^{o}C in air, as determined by the analyzer.

4.3.9 Results of Chemical Analyses of Deposit Samples

4.3.9.1 Illinois #6 - Galatia, Group 1

The Illinois #6 Galatia is a medium to high sulfur and high chlorine bituminous coal. Shown in Figures 62-65 are the photographs taken of the sleeves containing the deposit samples used for chemical analyses. The majority of the deposit in the oxidizing zone, top, position #4, had fallen off the sleeve and was present loose in the Ziploc bag. Comparing the appearances of the top and bottom sleeves at position #4 from both the oxidizing and reducing zones, a more tightly adhering deposit on the reducing bottom sleeve and a less carbon-rich deposit on the oxidizing bottom sleeve are shown in the photographs.

Figure 60 - Photo of the Illinois #6 Galatia Sleeve from Oxidizing Zone, Top, Position #4.

Figure 61 - Photo of the Illinois #6 Galatia Sleeve from the Reducing Zone, Top, Position #4.

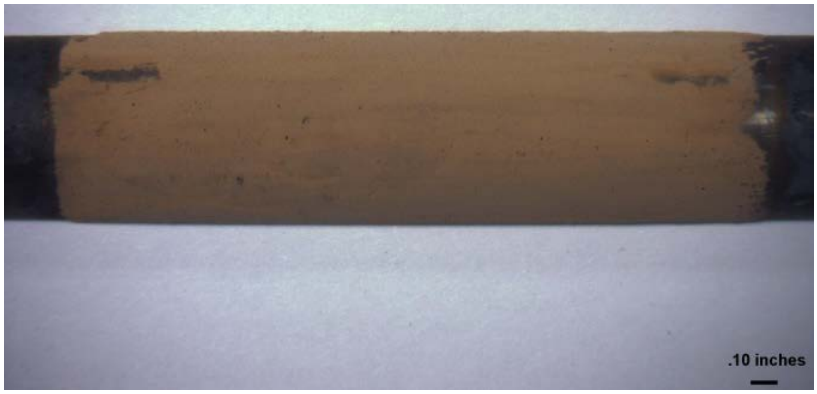

Figure 62 - Photo of the Illinois #6 Galatia Sleeve from the Oxidizing Zone, Bottom, Position #4.

Figure 63 - Photo of the Illinois #6 Galatia Sleeve from the Reducing Zone, Bottom, Position #4.

The XRF elemental analysis for Illinois #6-1 Galatia, Oxidizing, Top, Position #4 is shown in Table 21. The table compares the original coal ash elemental analysis to the elemental analyses for the oxidizing and reducing zone probe deposits. The totals for the elemental analyses of the probe deposit samples were less than 100% because trace elements were not included. Since sulfur was analyzed by two different methods, i.e., XRF and LECO, the sulfur values could be compared for a cross-check. This was important because obtaining an accurate sulfur percentage for the deposit was critical to the intended corrosion modeling effort. The as-determined SO3 wt.% comparative values were 2.87 by LECO vs. 2.66 by XRF for the oxidizing probe deposit. For the reducing zone probe deposit, the as-determined SO3 wt.% comparative values were 8.95 by LECO vs.11.62 by XRF. However, the LECO sulfur value was considered more accurate.

The chloride concentration in the Illinois #6-1 coal was measured at 3892 mg/kg or ppm on a dry weight % basis. This chloride concentration was considered high for typical U.S. coals.

The chloride concentration measured in the oxidizing zone deposit was < 100 ppm, and for the reducing zone deposit, the chloride concentration was 500 ppm. Even though the chloride concentration was higher in the reducing zone deposit than that in the oxidizing zone, both were considerably less than the chloride concentration in the original coal.

As expected, the percentage of unburned carbon (UBC) in the reducing zone deposit was much higher than the oxidizing zone deposit, i.e., 26.95 vs. 0.32 wt.%.

Figure 66 compares the major elements measured in the original coal ash to those in both the oxidizing and reducing zone deposit samples. Emphasis was placed on the elements believed to be the main contributors to ash deposition and thus corrosion, as well as their fate during the combustion process. There were several distinct differences in the comparison of these ash analyses. The iron content was lower in the reducing zone deposit compared to the original coal ash and oxidizing zone deposit. The calcium and sulfur values were higher in the reducing zone deposit compared to the original coal ash and oxidizing zone probe deposit.

Table 19 - Comparison of Elemental Ash Analyses between Original Coal Ash and Probe Deposit for IL #6 Galatia.

Coal Description	Illinois #6, Galatia	Illinois #6, Galatia	Illinois #6, Galatia
	Coal Ash	Probe Deposit - Ox	Probe Deposit - Red
Coal Ash Analysis			
Silicon Dioxide, % as SiO2	48.12	47.23	41.85
Aluminum Oxide, % as Al2O3	19.65	20.99	18.52
Iron Oxide, % as Fe2O3	17.64	19.68	3.98
Calcium Oxide, % as CaO	4.28	4.09	9.69
Magnesium Oxide, % as MgO	0.95	0.90	1.17
Sodium Oxide, % as Na2O	1.08	1.12	2.76
Potassium Oxide, % as K2O	2.59	2.05	3.95
Titanium Oxide, % as TiO2	1.05	0.78	0.7
Manganese Oxide, % as MnO2	0.07	0.05	0.05
Phosphorus Pentoxide, % as P2O5	0.08	0.10	0.96
Strontium Oxide, % as SrO	0.03	0.10	N/D
Barium Oxide, % as BaO	0.05	N/D	N/D
Sulfur Trioxide, % as SO3	4.41	2.67	15.9
Chloride, ppm as Cl	3892.00	< 100	500.00
LECO Total Carbon, %	N/A	0.32	26.95
LECO Sulfur, % SO3	N/A	2.87	8.95

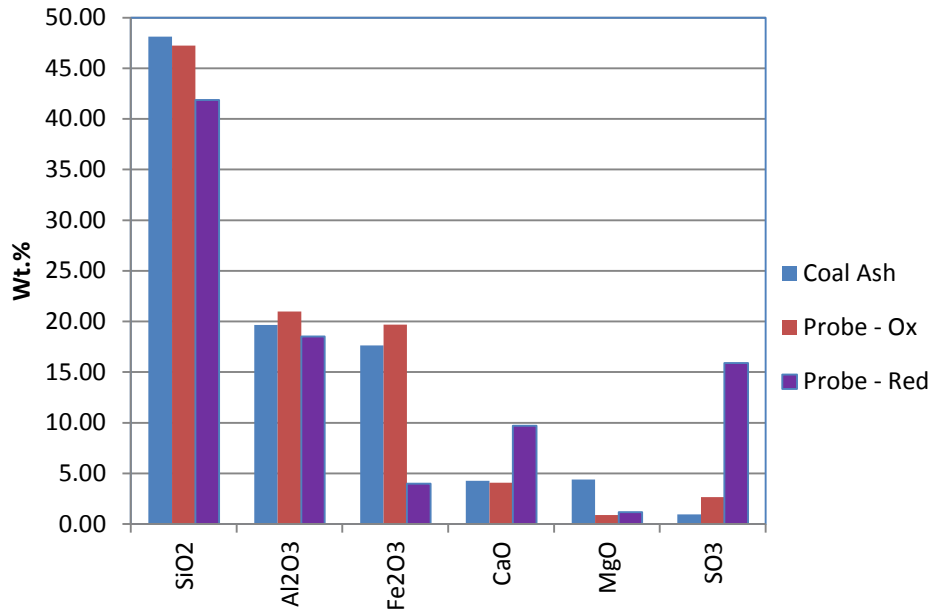

Figure 64 - Comparison of Major Elements in Coal Ash with Probe Deposit for IL #6 Galatia Coal in Oxidizing and Reducing Conditions.

Figure 67 compares the minor elements measured in the original coal ash to those in both the oxidizing and reducing zone deposit samples. Interestingly, the sodium, potassium, and phosphorus values were higher in the reducing zone deposit compared to the original coal ash and oxidizing zone probe deposit.

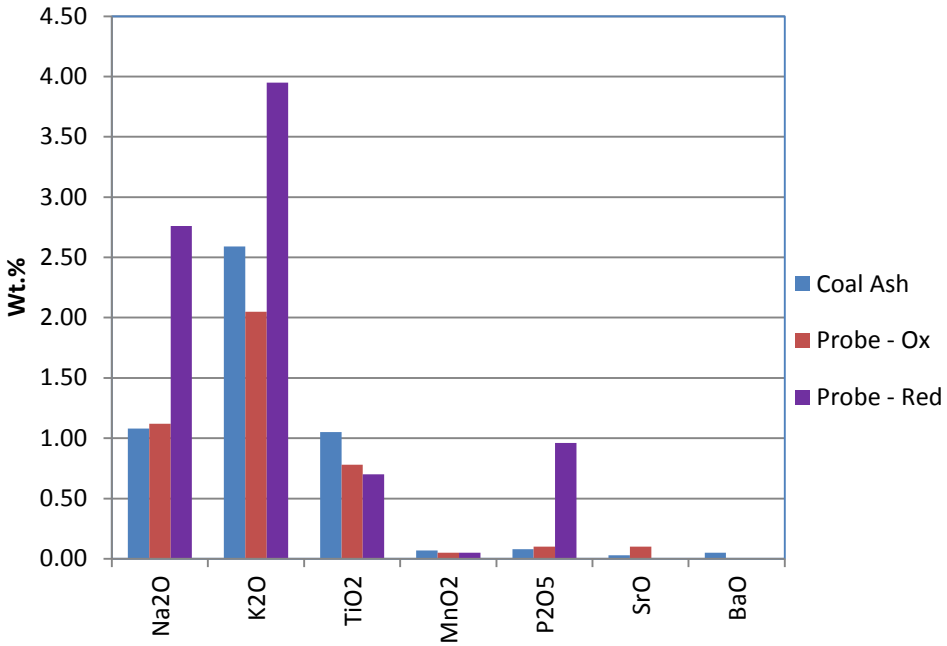

Figure 65 - Comparison of Minor Elements in Coal Ash with Probe Deposit for IL #6 Galatia Coal in Oxidizing and Reducing Conditions.

Based on the coal ash analysis of Illinois #6-1 Galatia shown in Table 21 and Appendix B, the silicon percentage was high, and the calculated BAR (base to acid ratio) was 0.39. For the oxidizing zone probe deposit, X-ray diffraction (XRD) in Appendix C showed the major phase being Quartz (low, syn, SiO_2) with smaller amounts of other silicon-containing compounds, including Mullite (syn, $Al_6Si_2O_{13}$) and Albite (ordered, $NaAlSi_3O_8$). Also, Hematite (syn, Fe_2O_3) was identified as a medium phase with a trace amount of Anhydrite (syn, $CaSO_4$). It is mentioned in Section 3.1.4 that the combination of clay minerals and quartz accounts for nearly all of the mineral matter in coal.[1]

For the reducing zone deposit, the results of XRD showed the major phase also being Quartz (low, syn, SiO_2). There were also two iron-containing phases, i.e., hematite (syn, Fe_2O_3) and magnetite (syn, $FeFe_2O_4$). A trace phase of Sylvite (syn, KCl) was identified, suggesting chlorine in the coal under reducing conditions had interacted with potassium. The reducing zone deposit consisted of 26.95% carbon which created an amorphous "hump" in the diffractogram between 20 to 30^o 2θ, thus making it more difficult to identify the less abundant phases. Also, the high carbon percentage tends to dilute the signals from the other phases present in the sample. As a result, a lower quality diffractogram was generated from the reducing zone deposit compared to that from the oxidizing zone deposit.

It should be mentioned that drying was only conducted at 45^{o}C on each deposit sample prior to performing the XRD phase identification. The purpose of a low drying temperature was to minimize any changes of the original phases in the probe deposit samples.

4.3.9.2 PRB – Black Thunder, Group 3

PRB is a low sulfur and low chlorine sub-bituminous coal. Figures 68 and 69 show the photographs of oxidizing and reducing sleeves, respectively, containing the deposit samples for chemical analysis.

Figure 66 - Photo of the Black Thunder PRB Sleeve from the Oxidizing Zone, Top, Position #3.

Figure 67 - Photo of the Black Thunder PRB Sleeve from the Reducing Zone, Top, Position #3.

Results of the XRF elemental analysis for the PRB deposit sample from the oxidizing zone, Top Position #3, are shown in Table 22. The table compares the original coal ash elemental analysis to those from the oxidizing and reducing zone probe deposits. Again, totals of the elemental analyses for the deposits are less than 100 % because the trace elements are not included. Since sulfur was analyzed by two different methods, i.e., XRF and LECO, the sulfur values can be compared for a cross-check. The as-determined wt.% SO3 comparative values were 8.78 by LECO vs. 11.03 by XRF for the oxidizing zone probe deposit. For the reducing zone probe deposit, the as-determined wt.% SO3 comparative values were 1.04 by LECO vs. 1.50 by XRF. Again, the LECO sulfur value is considered more accurate. The chloride concentration in the original coal was measured at 12 mg/kg or ppm on a dry wt.% basis. This is considered a very low concentration of chloride for a coal. The chloride concentration measured for both the oxidizing and reducing zone probe deposits was < 100 ppm, and is below the detection limit for the XRF method. As expected the % unburned carbon in the reducing zone probe deposit was much higher than the oxidizing zone probe deposit, i.e., 16.00 vs. 1.08 wt.%.

Figure 70 compares the major elements measured in the original coal ash with those in both the oxidizing and reducing zone deposits. The sulfur value is higher in the reducing zone deposit compared to the original coal ash and oxidizing zone deposit.

Table 20 - Comparison of Elemental Ash Analyses between Original Coal Ash and Probe Deposit for Black Thunder PRB.

Coal Description	PRB, Black Thunder WY	PRB, Black Thunder WY	PRB, Black Thunder WY
	Coal Ash	Probe Deposit - Ox	Probe Deposit - Red
Coal Ash Analysis			
Silicon Dioxide, % as SiO2	36.04	32.52	32.78
Aluminum Oxide, % as Al2O3	16.84	17.84	20.28
Iron Oxide, % as Fe2O3	5.86	5.37	7.67
Calcium Oxide, % as CaO	21.61	21.16	25.19
Magnesium Oxide, % as MgO	5.06	4.71	5.92
Sodium Oxide, % as Na2O	1.69	2.36	2.46
Potassium Oxide, % as K2O	0.50	0.59	0.31
Titanium Oxide, % as TiO2	1.32	1.31	1.60
Manganese Oxide, % as MnO2	0.02	0.08	0.03
Phosphorus Pentoxide, % as P2O5	1.00	1.53	1.50
Strontium Oxide, % as SrO	0.35	0.10	0.13
Barium Oxide, % as BaO	0.62	0.75	0.10
Sulfur Trioxide, % as SO3	9.09	11.15	1.79
Chloride, ppm as Cl	12.00	< 100	< 100
LECO Total Carbon, %	N/A	1.08	16.00
LECO Sulfur, % SO3	N/A	8.78	1.04

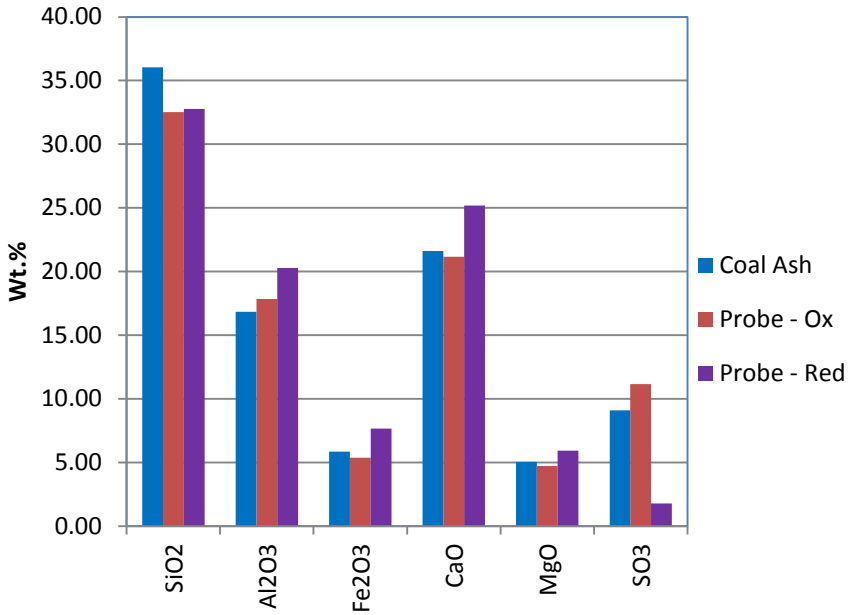

Figure 68 - Comparison of Major Elements in Coal Ash with Probe Analyses for PRB Black Thunder Coal in Oxidizing and Reducing Conditions.

Figure 71 compares the minor elements measured in the original coal ash to those in both the oxidizing and reducing zone deposits. The sodium and phosphorus values are higher in both the oxidizing and reducing zone probe deposits compared to those in the original coal ash. Also, the potassium is lower in the reducing zone probe deposit compared to those in the original coal ash and oxidizing zone deposit.

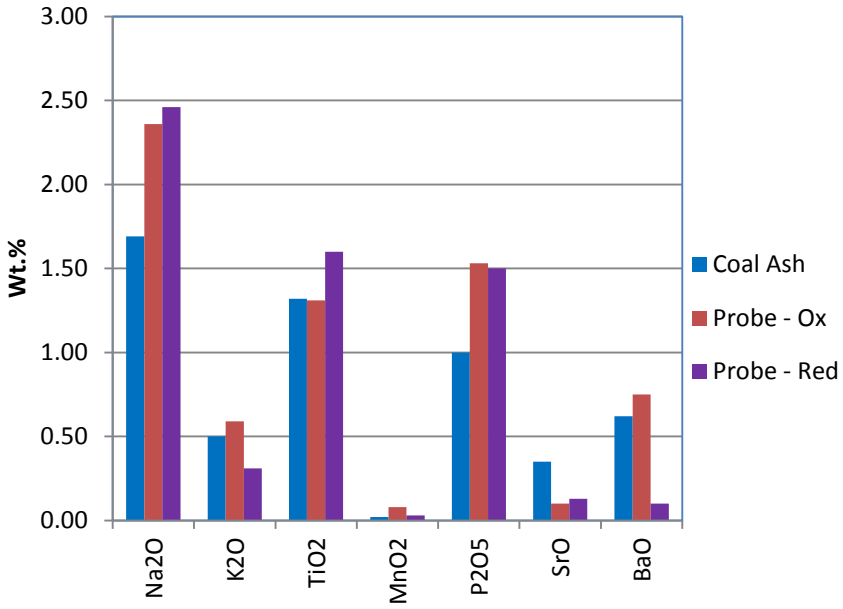

Figure 69 - Comparison of Minor Elements in Coal Ash with Probe Deposit for PRB Black Thunder Coal in Oxidizing and Reducing Conditions.

The Black Thunder PRB is a low sulfur (0.25% A.R.) and low chlorine (0.0012% dry Cl) sub-bituminous coal. Based on the coal ash analysis in Table 22 and also in Appendix B, the silicon and calcium (21.61% as CaO) concentrations are relatively high, with a calculated BAR of 0.64. For the oxidizing zone deposit, the XRD phase identification in Appendix C showed the major phase being Quartz, low, syn, SiO_2 with smaller amounts of other silicon-containing phases, i.e., alcium sodium magnesium aluminum iron silicate and nepheline. Also, anhydrite, syn, $CaSO_4$ was identified as a medium phase.

For the reducing zone deposit, the XRD phase identification showed the major phase also being Quartz, low, syn, SiO2. There were other less abundant silicate-bearing phases, i.e., calcium aluminum silicate trioxide, nepheline, and cristobalite. Calcium sulfate was just a trace phase in this deposit as compared to that in the oxidizing zone deposit. Since there is 16% carbon in the reducing zone deposit, this could contribute to diluting or weakening the signals from the calcium sulfate diffraction patterns. Another trace phase identified was mackinawite, syn, FeS, a reduced sulfur species, which is consistent with the deposit originating from the reducing zone.

4.3.9.3 Beulah-Zap lignite, Group 4

This is a low sulfur and chlorine and high moisture and ash lignite coal. Figures 72-74 show the photographs taken of the sleeves containing the deposit samples submitted for chemical analysis. There was not sufficient sample, only 0.03 gram, for the reducing zone deposit. For this reason, the Bottom, Position #4 deposit sample (RB4) was combined with the Top, Position #4 deposit (RT4). Visually, the top deposit appeared to contain a higher carbon percentage than the bottom deposit.

Figure 70 - Photo of the Beulah Zap Lignite Sleeve from the Oxidizing Zone, Top, Position #4.

Figure 71 - Photo of the Beulah Zap Lignite Sleeve from the Reducing Zone, Top, Position #4.

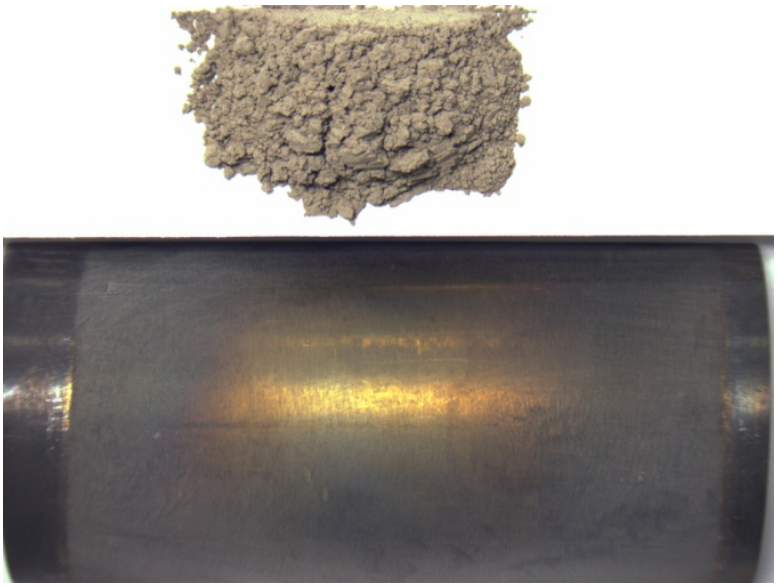

Figure 72 - Photo of the Beulah Zap Lignite Sleeve from the Reducing Zone, Bottom, Position #4.

Results of the XRF elemental analysis for Beulah-Zap lignite, Oxidizing, Top, Position #4, are summarized in Table 23, which compares the original coal ash elemental analysis to those for the oxidizing and reducing zone deposits. Totals of the elemental analyses for the probe deposits are less than 100 %, because the trace elements are not included. Since sulfur was analyzed by two different methods, i.e., XRF and LECO, the sulfur values can be compared for a cross-check. The as-determined wt.% SO3 comparative values were 15.26 by LECO vs. 19.66 by XRF for the oxidizing zone deposit. For the reducing zone deposit, the as-determined wt.% SO3 comparative values were 2.71 by LECO vs. 3.06 by XRF. However, the LECO sulfur value is considered more accurate. The chloride concentration in the original coal was measured at 10 mg/kg or ppm on a weight % dry basis, which is considered a very low concentration of chloride for a coal. The chloride concentration measured for the oxidizing zone probe deposit was 100 ppm, and for the reducing zone deposit, the chloride concentration was 200 ppm. The chloride concentrations are higher in both the oxidizing and reducing zone probe deposits than that in the original coal. As expected the % unburned carbon in the reducing zone probe deposit was higher than the oxidizing zone probe deposit, 1.02 vs. 0.05 %, but is not much of a difference.

Figure 75 compares the major elements measured in the original coal ash with those in both the oxidizing and reducing zone deposits. The sulfur content is lower in the reducing zone probe deposit compared to those in the original coal ash and oxidizing zone probe deposits.

Table 21 - Comparison of Elemental Ash Analyses between the Original Coal Ash and Probe Deposit for ND Beulah-Zap Lignite.

Coal Description	Beulah-Zap North Dakota Lignite Coal Ash	Beulah-Zap North Dakota Lignite Probe Deposit - Ox	Beulah-Zap North Dakota Lignite Probe Deposit - Red
Coal Ash Analysis			
Silicon Dioxide, % as SiO2	32.25	31.74	32.95
Aluminum Oxide, % as Al2O3	12.23	12.34	16.27
Iron Oxide, % as Fe2O3	7.45	9.24	8.39
Calcium Oxide, % as CaO	19.91	16.43	22.95
Magnesium Oxide, % as MgO	6.47	4.30	7.29
Sodium Oxide, % as Na2O	3.29	2.95	5.72
Potassium Oxide, % as K2O	0.82	0.97	1.30
Titanium Oxide, % as TiO2	0.65	0.69	0.85
Manganese Oxide, % as MnO2	0.08	0.06	0.06
Phosphorus Pentoxide, % as P2O5	0.27	0.28	0.40
Strontium Oxide, % as SrO	0.64	0.27	0.37
Barium Oxide, % as BaO	0.73	0.11	0.13
Sulfur Trioxide, % as SO3	15.21	20.32	3.12
Chloride, ppm as Cl	10.00	100.00	200.00
LECO Total Carbon, %	N/A	0.05	1.02
LECO Sulfur, % SO3	N/A	15.26	2.71

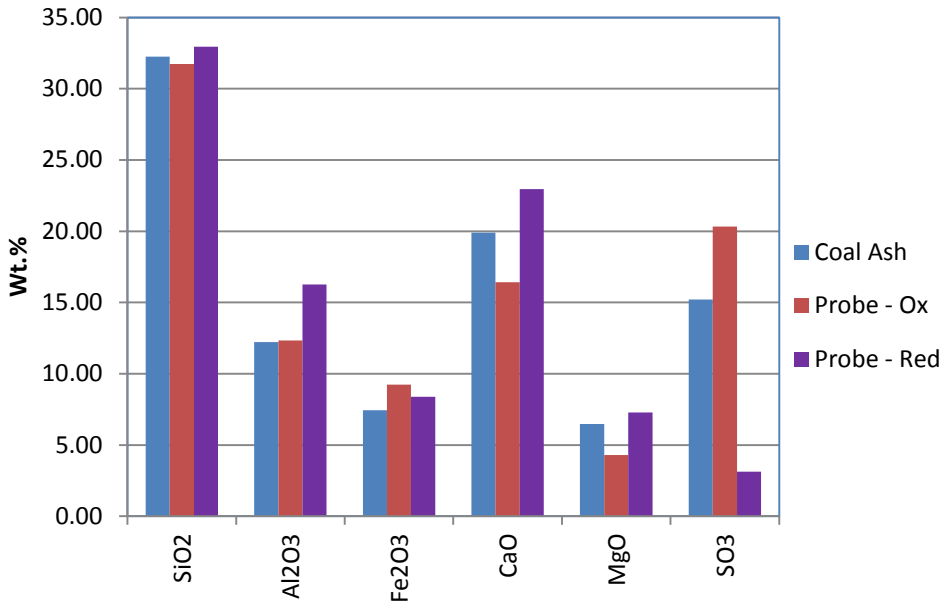

Figure 73 - Comparison of Major Elements in Coal Ash with Probe Deposit for Beulah Zap Lignite coal in Oxidizing and Reducing Conditions.

Figure 76 compares the minor elements measured in the original coal ash to those in both the oxidizing and reducing zone deposits. Especially for sodium, but also for potassium and phosphorus, the values are higher in the reducing zone probe deposit than those in the oxidizing zone probe deposit and original coal ash.

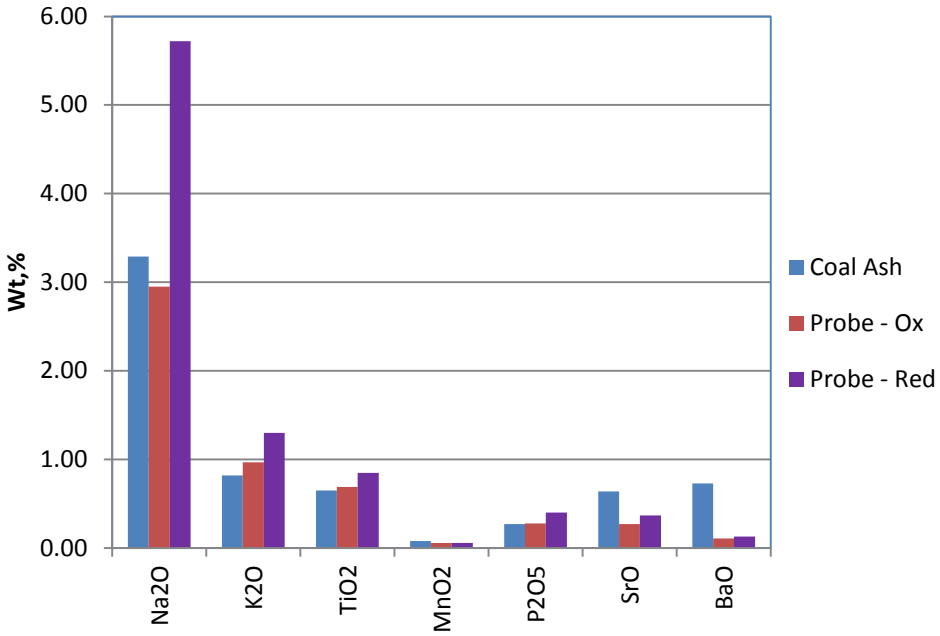

Figure 74 - Comparison of Minor Elements in Coal Ash with Probe Deposit for Beulah Zap Lignite coal in Oxidizing and Reducing Conditions.

The Beulah-Zap North Dakota lignite is a low sulfur (0.67 % A.R.) and low chlorine (0.0010 % dry Cl) coal. Based on the coal ash analysis in Table 23 and also in Appendix B, the silicon and calcium (19.91 wt.% as CaO) concentrations are relatively high, with a calculated BAR of 0.84. For the oxidizing zone deposit, results of the XRD phase identification in Appendix C showed the major phase being Quartz, low, syn, SiO_2 with smaller amounts of other silicon-containing phases, i.e., akermanite and calcium titanium magnesium aluminum catena-alumosilicate. Also, anhydrite, syn, $CaSO_4$ was identified as a medium phase with a minor phase of hematite. For the reducing zone deposit, the XRD phase identification showed the major phase being akermanite. There were other less abundant silicate-bearing phases, i.e., nepheline, and quartz. Another minor phase identified was hematite, syn, Fe_2O_3.

4.3.9.4 Mahoning 7A, Ohio, Group 2

Mahoning 7A is a medium sulfur and medium chlorine bituminous coal. Figures 77 and 78 show the photographs of the sleeves containing the deposit samples for chemical analysis. There was insufficient sample for either the oxidizing or reducing zone deposit at the top position. For the oxidizing zone sample, the Bottom, Position #3 deposit (OB3) was combined with the Top, Position #3 deposit (OT3). Similarly, for the reducing zone sample, the Bottom, Position #4 deposit (RB4) was combined with the Top, Position #4 deposit (RT4).

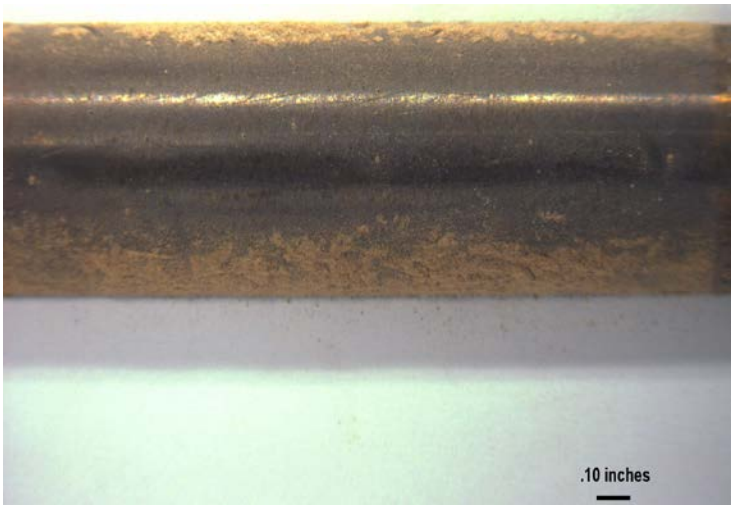

Figure 75 - Photo of the Mahoning 7A Sleeve from the Oxidizing Zone, Top, Position #3.

Figure 76 - Photo of the Mahoning 7A Sleeve from the Reducing Zone, Top, Position #4.

Results of the XRF elemental analysis for Mahoning 7A, Oxidizing, Top and Bottom Combined, Position #3, are shown in Table 24. The table compares the original coal ash elemental analysis with those for the oxidizing and reducing zone probe deposits. Again, totals of the elemental analyses for the probe deposits are less than 100% because the trace elements are not included. Since sulfur was analyzed by two different methods, i.e., XRF and LECO, the sulfur values can serve as a cross-check. The as-determined wt.% SO3 comparative values were 2.90 by LECO vs. 1.63 by XRF for the oxidizing zone probe deposit. For the reducing zone

deposit, the as-determined wt.% SO3 comparative values were 1.25 by LECO vs. 0.77 by XRF. However, the LECO sulfur value is considered more accurate.

Table 22 - Comparison of Elemental Ash Analyses between Original Coal Ash and Probe Deposit for Ohio Mahoning 7A.

Coal Description	Mahoning 7A	Mahoning 7A	Mahoning 7A
	OH	OH	OH
	Coal Ash	Probe Deposit - Ox	Probe Deposit - Red
Coal Ash Analysis			
Silicon Dioxide, % as SiO2	42.65	43.79	37.27
Aluminum Oxide, % as Al2O3	29.07	32.47	27.51
Iron Oxide, % as Fe2O3	20.45	14.91	25.51
Calcium Oxide, % as CaO	1.76	1.70	1.43
Magnesium Oxide, % as MgO	0.52	0.55	0.42
Sodium Oxide, % as Na2O	0.34	0.62	0.76
Potassium Oxide, % as K2O	1.61	1.64	2.37
Titanium Oxide, % as TiO2	1.41	1.19	1.14
Manganese Oxide, % as MnO2	0.00	0.08	0.15
Phosphorus Pentoxide, % as P2O5	0.76	0.82	0.85
Strontium Oxide, % as SrO	0.12	0.03	0.07
Barium Oxide, % as BaO	0.07	< 0.01	0.04
Sulfur Trioxide, % as SO3	1.24	1.64	0.78
Chloride, ppm as Cl	1989.00	< 100	< 100
LECO Total Carbon, %	N/A	0.45	2.14
LECO Sulfur, % SO3	N/A	2.90	1.25

The chloride concentration in the original coal was measured at 1989 mg/kg or ppm on a weight % dry basis, which is considered a medium concentration of chloride for a coal. The chloride concentration measured for the oxidizing zone probe deposit was < 100 ppm, and for the reducing zone deposit, the chloride concentration was also < 100 ppm. As expected, the % unburned carbon in the reducing zone probe deposit was higher than that in the oxidizing zone deposit, i.e., 2.14 vs. 0.45 %. However, the difference is not considered significant.

Figure 79 compares the major elements measured in the original coal ash with those in both the oxidizing and reducing zone deposits. Though there are small differences in the elemental concentrations, nothing stands out as being significant.

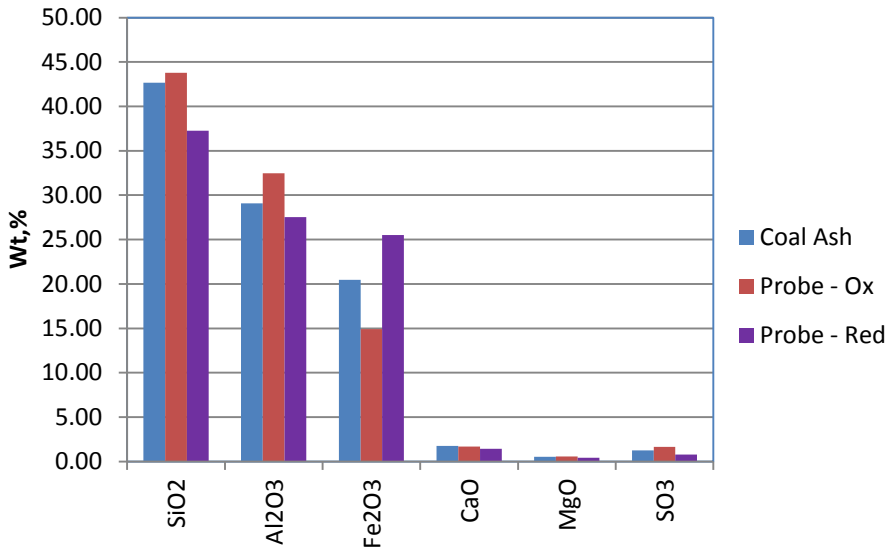

Figure 77 - Comparison of Major Elements in Coal Ash with Probe Deposit for OH Mahoning 7A coal in Oxidizing and Reducing Conditions.

Figure 80 compares the minor elements measured in the original coal ash with those in both the oxidizing and reducing zone deposits. Especially for potassium, but also for sodium, the values are higher in the reducing zone deposit than those in the oxidizing zone deposit and original coal ash.

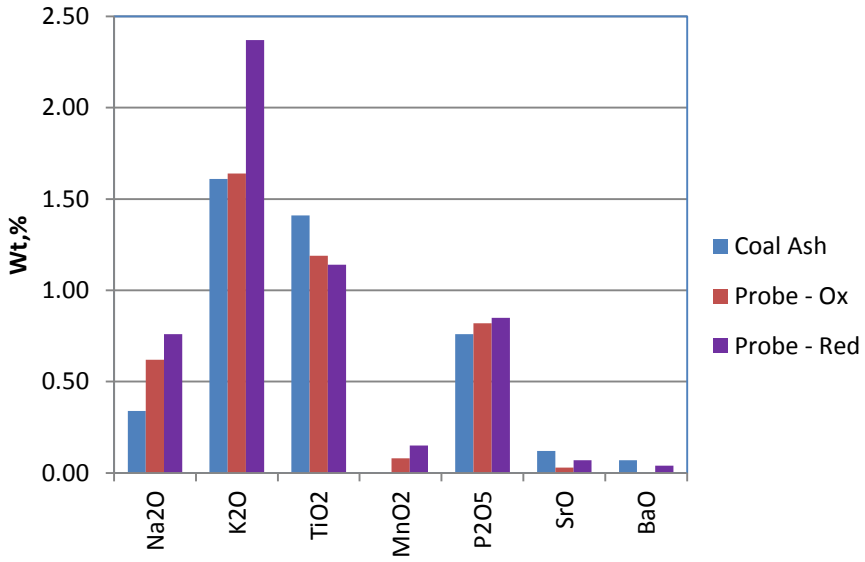

Figure 78 - Comparison of Minor Elements in Coal Ash with Probe Deposit for OH Mahoning 7A coal in Oxidizing and Reducing Conditions.

The Mahoning 7A is a medium sulfur (1.96% A.R.) and medium chlorine (0.1989% dry Cl) bituminous coal. Based on the coal ash analysis in Table 24 and also in Appendix B, the

silicon, aluminum, and iron concentrations are relatively high, with a calculated BAR of 0.34. For the oxidizing zone deposit, the XRD phase identification in Appendix C showed the major phases being Quartz, low, syn, SiO_2 and Mullite, syn, $Al_6Si_2O_{13}$. Hematite, syn, Fe2O3 was also identified as a medium phase with a trace phase of Anhydrite, syn, $CaSO_4$. For the reducing zone deposit, the XRD phase identification showed the major phase being Mullite, syn, $Al_6Si_2O_{13}$. There was another less abundant silicate-bearing phase identified as silimanite. Both magnetite and hematite were also identified as medium phases.

4.3.9.5 Indiana #6, Gibson, Group 6

Indiana #6 Gibson is a low to medium sulfur and medium chlorine bituminous coal. Figures 81 and 82 show the photographs of the sleeves containing the deposit samples submitted for chemical analysis. There was insufficient sample for the oxidizing zone probe deposit at the top position. Therefore, for the oxidizing zone, the Bottom, Position #3 deposit (OB3) was combined with the Top, Position #3 deposit (OT3).

Figure 79 - Photo of the IN#6 Gibson Sleeve from the Oxidizing Zone, Top, Position #3.

Figure 80 - Photo of the IN#6 Gibson Sleeve from the Reducing Zone, Top, Position #4.

Results of the XRF elemental analysis for Indiana #6, Gibson, Oxidizing, Top and Bottom Combined, Position #3 are shown in Table 25. The table compares the original coal ash elemental analysis to those for the oxidizing and reducing zone probe deposits. Totals of the elemental analyses for the probe deposits are less than 100 % because the trace elements are not

included. Since sulfur was analyzed by two different methods, i.e., XRF and LECO, the sulfur values can be used as a cross-check. The as-determined wt.% SO3 comparative values were 2.19 by LECO vs. 1.39 by XRF for the oxidizing zone probe deposit. For the reducing zone deposit, the as-determined wt.% SO3 comparative values were 3.41 by LECO vs. 5.01 by XRF. However, the LECO sulfur value is considered more accurate.

Table 23 - Comparison of Elemental Ash Analyses between Original Coal Ash and Probe Deposit for Indiana #6 Gibson Coal.

Coal Description	Indiana #6 Gibson	Indiana #6 Gibson	Indiana #6 Gibson
	Coal Ash	Probe Deposit - Ox	Probe Deposit - Red
Coal Ash Analysis			
Silicon Dioxide, % as SiO2	55.14	50.77	47.27
Aluminum Oxide, % as Al2O3	21.10	24.46	20.98
Iron Oxide, % as Fe2O3	12.93	14.31	13.55
Calcium Oxide, % as CaO	2.48	2.64	2.54
Magnesium Oxide, % as MgO	0.86	0.88	0.45
Sodium Oxide, % as Na2O	1.25	1.15	1.39
Potassium Oxide, % as K2O	2.40	2.31	4.27
Titanium Oxide, % as TiO2	1.30	1.11	1.33
Manganese Oxide, % as MnO2	0.03	0.09	0.03
Phosphorus Pentoxide, % as P2O5	0.35	0.47	0.35
Strontium Oxide, % as SrO	0.08	0.05	0.02
Barium Oxide, % as BaO	0.06	< 0.01	N/D
Sulfur Trioxide, % as SO3	2.02	1.39	6.85
Chloride, ppm as Cl	2121.00	< 100	200
LECO Total Carbon, %	N/A	0.07	26.91
LECO Sulfur, % SO3	N/A	2.19	3.41

The chloride concentration in the original coal was measured at 2121 mg/kg or ppm on a weight % dry basis. This chloride concentration is considered medium for a coal. The chloride concentration measured for the oxidizing zone probe deposit was < 100 ppm, and for the reducing zone deposit, the chloride concentration was 200 ppm. As expected, the % unburned carbon in the reducing zone probe deposit was higher than the oxidizing zone deposit, i.e., 26.91 vs. 0.07 wt.%.

Figure 83 compares the major elements measured in the original coal ash to the major elements measured in both the oxidizing and reducing zone deposits. The emphasis here is to look at the elements believed to be the main contributors to ash deposition and subsequent corrosion, and their fate during the combustion process. The sulfur content is higher in the reducing zone probe deposit compared to the original coal ash and oxidizing zone probe deposit.

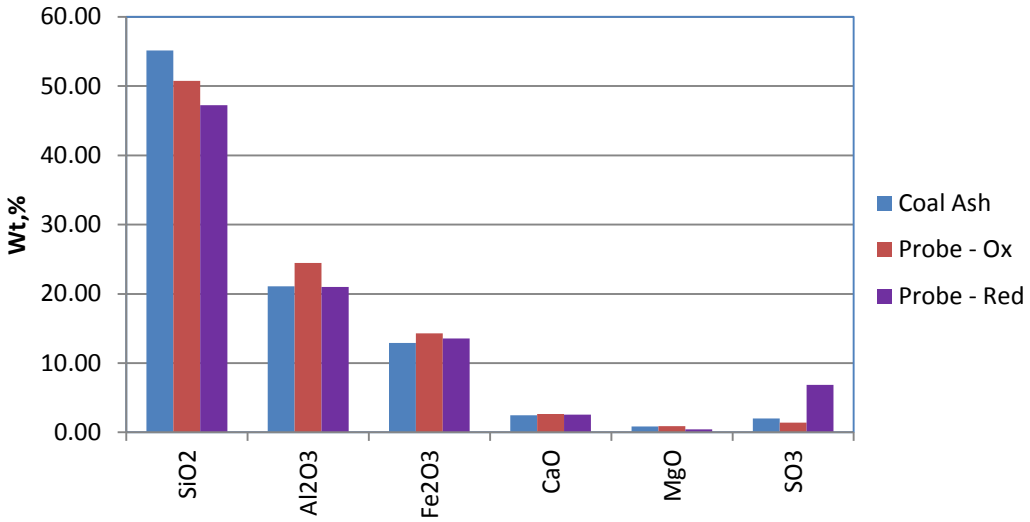

Figure 81 - Comparison of Major Elements in Coal Ash with Probe Deposit for IN#6 Gibson Coal in Oxidizing and Reducing Conditions.

Figure 84 compares the minor elements measured in the original coal ash with those in both the oxidizing and reducing zone deposits. The potassium value is higher in the reducing zone deposit than those in the oxidizing zone probe deposit and original coal ash. The Indiana #6, Gibson, is a low to medium sulfur (1.14% A.R.) and medium chlorine (0.2121% dry Cl) bituminous coal. Based on the coal ash analysis in Table 25 and also in Appendix B, the silicon, aluminum, and iron concentrations are relatively high, with a calculated BAR of 0.26. For the oxidizing zone deposit, the results of XRD phase identification in Appendix C showed the major phase being Quartz, syn, SiO_2. Mullite, syn, $Al_6Si_2O_{13}$, and Hematite, syn, Fe2O3 were identified as a medium phases with trace phases of Anhydrite, syn, $CaSO_4$, and Rutile, syn, TiO_2. For the reducing zone deposit, results of the XRD phase identification showed the major phase Quartz, syn, SiO_2. Mullite, syn, $Al_6Si_2O_{13}$ was identified as a medium phase, and both magnetite and hematite were identified as minor phases.

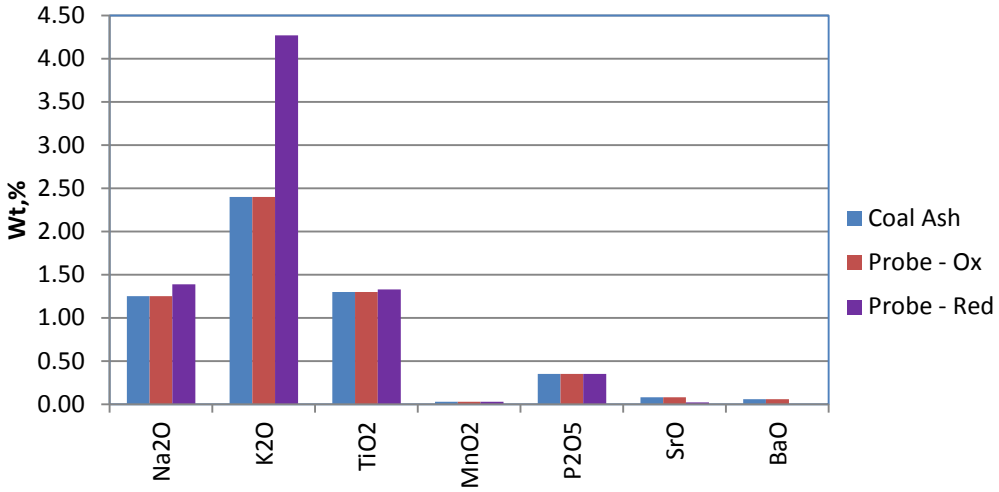

Figure 82 - Comparison of Minor Elements in Coal Ash with Probe Deposit for IN#6 Gibson Coal in Oxidizing and Reducing Conditions.

4.3.9.6 Gatling Mine Coal, AEP/Mountaineer, Group 5

Gatling Mine coal is a source of coal specifically for the AEP Mountaineer Plant and is a high sulfur and low chlorine bituminous coal. Figures 85 and 86 show the photographs of the sleeves containing the deposit samples submitted for chemical analysis. The sleeve locations selected for analysis were OT4 and RT3.

Figure 83 - Photo of OH Gatling Coal Sleeve from Oxidizing Zone, Top Position #4.

Figure 84 - Photo of OH Gatling Coal from Reducing Zone, Top Position #3.

Results of the XRF elemental analysis for Gatling Mine Coal, Oxidizing, Top, Position #4 and Reducing, Top, Position #3 probe deposits are shown in Table 26. The table compares the original coal ash elemental analysis to those for the oxidizing and reducing zone probe deposits. Totals of the elemental analyses for the probe deposits are less than 100 % because the trace elements are not included. Since sulfur was analyzed by two different methods, i.e., XRF and LECO, the sulfur values can be used as a cross-check. The as-determined SO_3 wt.% comparative values were 3.86 by LECO vs. 2.49 by XRF for the oxidizing zone probe deposit. For the reducing zone deposit, the as-determined SO_3 wt.% comparative values were 19.47 by LECO vs. 14.91 by XRF. However, the LECO sulfur value is considered more accurate.

The chloride concentration in the original coal was measured at 387 mg/kg or ppm on a weight % dry basis. This chloride concentration is considered low for a coal. The chloride concentration measured for the oxidizing zone probe deposit was 100 ppm, and for the reducing zone deposit the chloride concentration was 400 ppm. As expected, the % unburned carbon in

the reducing zone probe deposit was higher than the oxidizing zone deposit, i.e., 30.79 vs. 0.21wt.%, respectively.

Table 24 - Comparison of Elemental Ash Analyses between Original Coal Ash and Probe Deposit for Gatling Mine Coal.

Coal Description	Gatling Coal OH	Gatling Coal OH	Gatling Coal OH
	Coal Ash	Probe Deposit - Ox	Probe Deposit - Red
Coal Ash Analysis			
Silicon Dioxide, % as SiO2	40.35	39.67	35.77
Aluminum Oxide, % as Al2O3	22.56	24.95	21.09
Iron Oxide, % as Fe2O3	28.33	26.10	15.61
Calcium Oxide, % as CaO	2.62	2.02	2.19
Magnesium Oxide, % as MgO	0.69	0.38	0.32
Sodium Oxide, % as Na2O	0.41	0.35	0.32
Potassium Oxide, % as K2O	1.28	2.14	1.45
Titanium Oxide, % as TiO2	1.04	0.77	0.78
Manganese Oxide, % as MnO2	0.05	0.05	0.03
Phosphorus Pentoxide, % as P2O5	0.22	0.15	0.19
Strontium Oxide, % as SrO	0.09	0.04	0.02
Barium Oxide, % as BaO	0.11	N/D	N/D
Sulfur Trioxide, % as SO3	2.25	2.50	21.54
Chloride, ppm as Cl	387.00	100.0	400
LECO Total Carbon, %	N/A	0.21	30.79
LECO Sulfur, % SO3	N/A	3.86	19.47

Figure 87 compares the major elements measured in the original coal ash to the those measured in both the oxidizing and reducing zone deposits. The emphasis here is to look at the elements believed to be the main contributors to ash deposition and subsequent fireside corrosion, and their fate during the combustion process. The sulfur content is higher in the reducing zone probe deposit compared to the original coal ash and oxidizing zone probe deposit. This trend was also observed in the Illinois #6, Galatia, and Indiana #6, Gibson, bituminous coals, but not to the same extent. The iron content is lower in the reducing zone deposit.

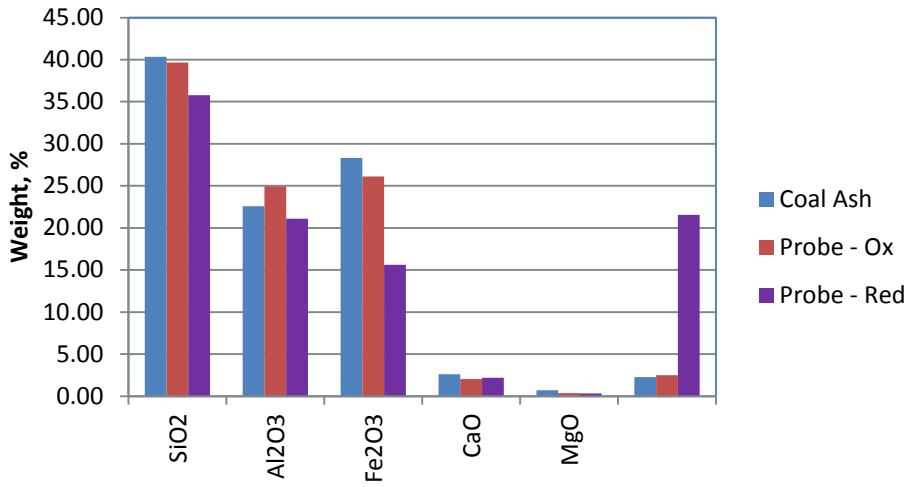

Figure 85 - Comparison of Major Elements in Coal Ash with Probe Deposit for OH Gatling Coal in Oxidizing and Reducing Conditions.

Figure 88 compares the minor elements measured in the original coal ash with those in both the oxidizing and reducing zone deposits. The potassium value is higher in the oxidizing zone deposit than that in the reducing zone probe deposit and original coal ash. The Gatling Mine Coal is a high sulfur (4.31% A.R.) and low chlorine (0.04 % dry Cl) bituminous coal. Based on the coal ash analysis in Table 26 and also in Appendix B, the silicon, aluminum, and iron concentrations are relatively high, with a calculated BAR of 0.52. For the oxidizing zone deposit, the results of XRD phase identification showed the major phase being Quartz low, syn, SiO_2. Iron (III) Oxide, Fe_2O_3 was identified as a medium phase with Mullite, syn, $Al_6Si_2O_{13}$, as a minor phase and a trace phase of Calcium Sulfate, $CaSO_4$. For the reducing zone deposit, results of the XRD phase identification showed the major phase being Quartz low, syn, SiO_2. Iron (III) Oxide, Fe_2O_3, was identified as a medium phase, with Mullite, syn, $Al_2(Al_{2.8}Si_{1.2})O_{9.6}$, a minor phase and Pyrrhotite 4C, Fe_7S_8 and Calcium Magnesium bis (catena-Silicate), $CaMg(SiO_3)_2$ trace phases.

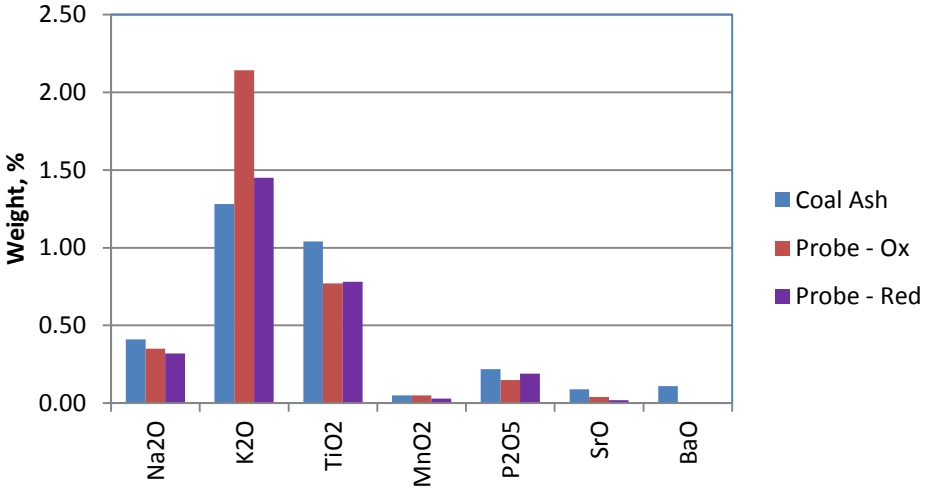

Figure 86 - Comparison of Minor Elements in Coal Ash and Probe Deposit for OH Gatling Coal in Oxidizing and Reducing Conditions.

4.3.9.7 Kentucky #11, Webster County, Group 8

The Kentucky #11 seam coal is located in Webster County of southwest Kentucky (Dotiki Mine). The coal rank is hvBb, and is a high sulfur and medium chlorine (0.21 %, dry basis) bituminous coal. Figures 89 and 90 show the photographs of the sleeves containing the deposit samples submitted for chemical analysis. The sleeve locations selected for analysis were OT4 and RB3.

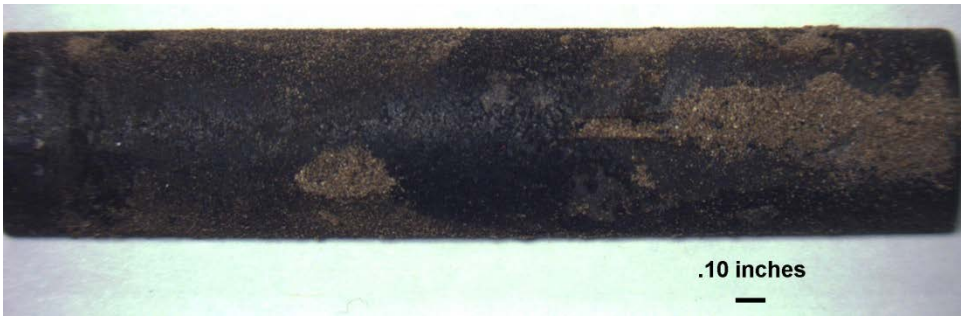

Figure 87 - Photo of KY #11 Coal Sleeve from Oxidizing Zone, Top Position #4.

Figure 88 - Photo of KY #11 Coal Sleeve from Reducing Zone, Bottom Position #3.

Results of the XRF elemental analysis for Kentucky #11 Coal, Oxidizing, Top, Position #4 and Reducing, Top, Position #3 probe deposits are shown in Table 27. The table compares the original coal ash elemental analysis to those for the oxidizing and reducing zone probe deposits. Totals of the elemental analyses for the probe deposits are less than 100 % because the trace elements are not included. Since sulfur was analyzed by two different methods, i.e., XRF and LECO, the sulfur values can be used as a cross-check. The as-determined wt. % SO_3 comparative values were 6.30 by LECO vs. 6.65 by XRF for the oxidizing zone probe deposit. The % SO_3 results are in close agreement.

Table 25 - Comparison of Elemental Ash Analyses between Original Coal Ash and Probe Deposit for Kentucky #11 Coal.

Coal Description	Kentucky #11 Dotiki	Kentucky #11 Dotiki	Kentucky #11 Dotiki
	Coal Ash	Probe Deposit - Ox	Probe Deposit - Red
Coal Ash Analysis			
Silicon Dioxide, % as SiO2	41.70	38.04	41.79
Aluminum Oxide, % as Al2O3	18.40	18.66	20.55
Iron Oxide, % as Fe2O3	26.09	26.56	17.90
Calcium Oxide, % as CaO	4.80	5.03	3.51
Magnesium Oxide, % as MgO	0.90	0.84	0.77
Sodium Oxide, % as Na2O	0.53	0.53	1.22
Potassium Oxide, % as K2O	2.43	1.93	3.52
Titanium Oxide, % as TiO2	0.96	0.66	1.07
Manganese Oxide, % as MnO2	0.03	0.08	0.06
Phosphorus Pentoxide, % as P2O5	0.31	0.53	0.28
Strontium Oxide, % as SrO	0.05	0.02	0.02
Barium Oxide, % as BaO	0.18	0.08	N/D
Sulfur Trioxide, % as SO3	3.62	4.62	7.83
Chloride, ppm as Cl	2057.00	< 100	100.00
LECO Total Carbon, %	N/A	0.08	15.60
LECO Sulfur, % SO3	N/A	4.70	6.30

The chloride concentration in the original coal was measured at 2057 mg/kg or ppm on a weight % dry basis. This chloride concentration is considered medium for a coal. The chloride concentration measured for the oxidizing zone probe deposit was < 100 ppm, and for the reducing zone deposit the chloride concentration was 100 ppm. As expected, the % unburned carbon in the reducing zone probe deposit was higher than the oxidizing zone deposit, i.e., 15.60 vs. 0.08 wt.%.

Figure 91 compares the major elements measured in the original coal ash to the major elements measured in both the oxidizing and reducing zone deposits. The emphasis here is to look at the elements believed to be the main contributors to ash deposition and subsequent corrosion, and their fate during the combustion process. The sulfur content is much higher in the reducing zone probe deposit compared to the original coal ash and oxidizing zone probe deposit. This trend was also observed in the Illinois #6, Galatia, Indiana #6, Gibson, and Gatling bituminous coals. The iron content is lower in the reducing zone deposit.

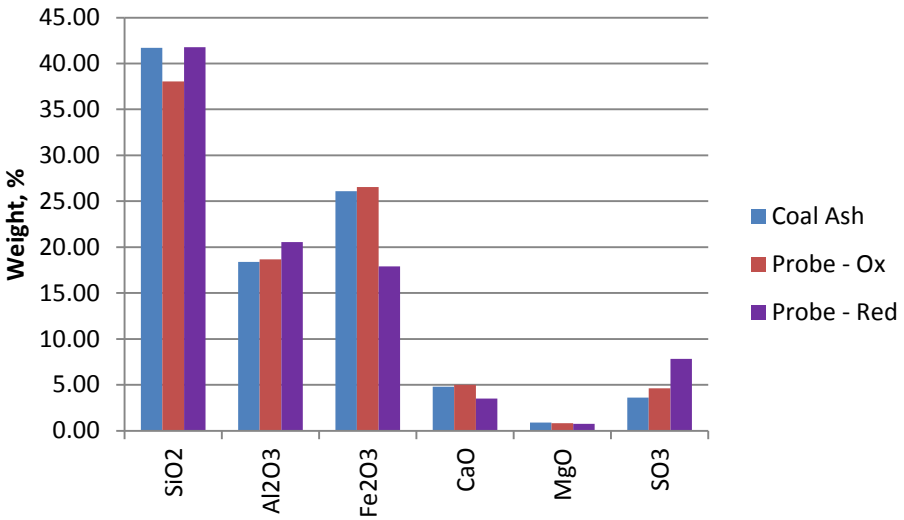

Figure 89 - Comparison of Major Elements in Coal Ash with Probe Deposit for KY #11 Coal in Oxidizing and Reducing Conditions.

Figure 92 compares the minor elements measured in the original coal ash with those in both the oxidizing and reducing zone deposits. The sodium and potassium values are higher in the reducing zone deposit than those in the oxidizing zone probe deposit and original coal ash. Kentucky #11 is a high sulfur (3.64 % A.R.) and medium chlorine (0.2057 % dry Cl) bituminous coal. Based on the coal ash analysis in Table 27 and also in Appendix B, the silicon, aluminum, and iron concentrations are relatively high, with a calculated BAR of 0.57. For the oxidizing zone deposit, the results of XRD phase identification showed the major phases being Quartz, SiO_2, and Iron (III) Oxide, Fe_2O_3. Anhydrite, $CaSO_4$ was identified as a minor phase. For the reducing zone deposit, results of the XRD phase identification showed the major phase being Quartz, SiO_2. Magnetite, syn, $FeFe_2O_4$ was identified as a medium phase.

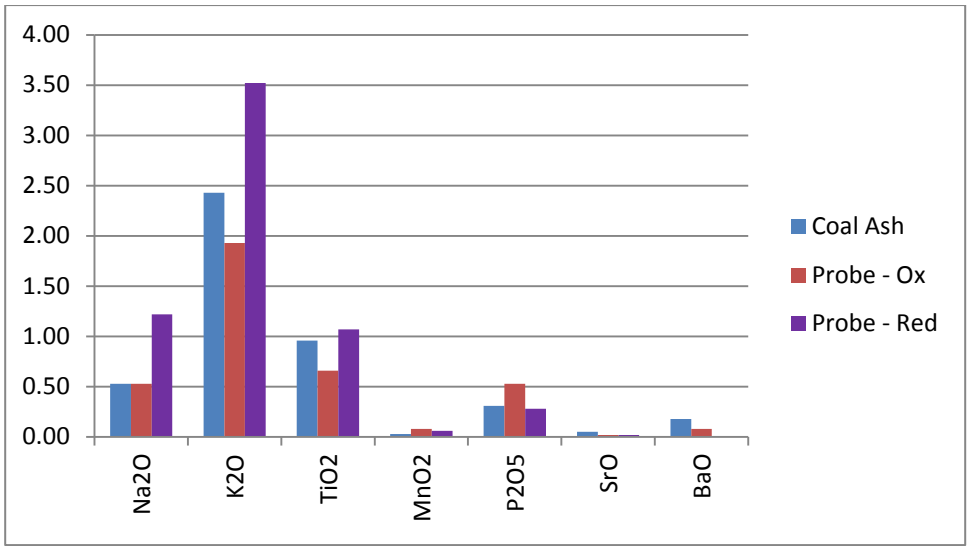

Figure 90 - Comparison of Minor Elements in Coal Ash with Probe Deposit for KY #11 Coal in Oxidizing and Reducing Conditions.

4.3.9.8 Pittsburgh Seam Coal, Greene County, Group 7

The Pittsburgh #8 seam is located in Greene County in southwest Pennsylvania. The coal rank is hvAb. The sulfur content of this coal is ranked medium, and the chlorine percentage (<0.01 %, dry basis) is considered very low. Figures 93 and 94 show the photographs of the sleeves containing the deposit samples submitted for chemical analysis. The sleeve locations selected for analysis were OT3 and RT3.

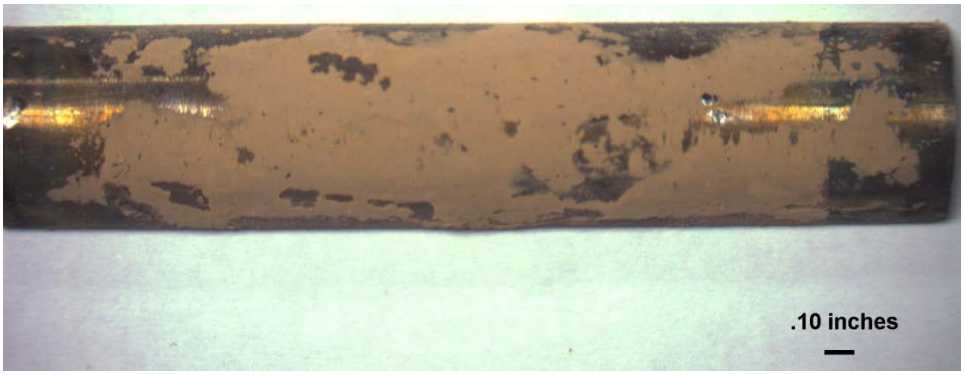

Figure 91 - Photo of Pittsburg #8 Coal from Oxidizing Zone, Top Position #3.

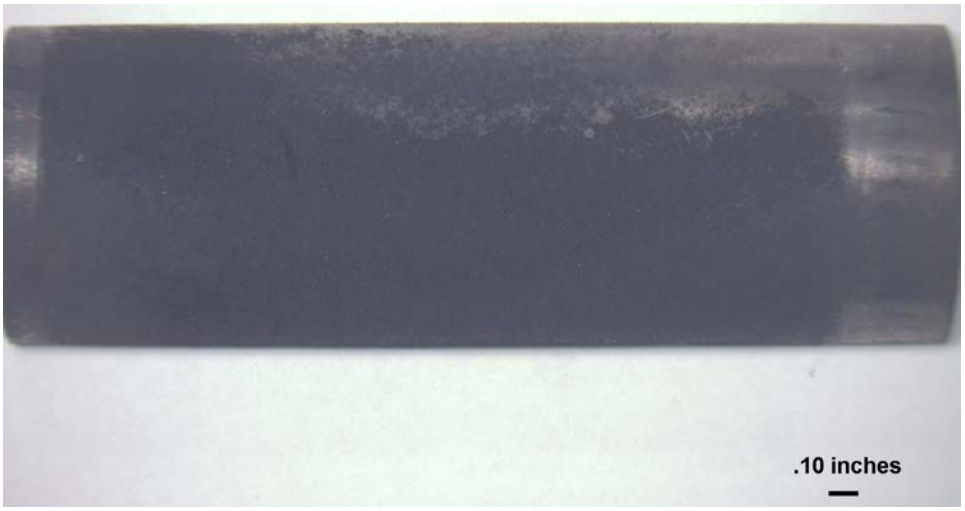

Figure 92 - Photo of Pittsburgh #8 Coal from Reducing Zone, Top Position #3.

Results of the XRF elemental analysis for Pittsburgh #8 Coal, Oxidizing, Top, Position #3 and Reducing, Top, Position #3 probe deposits are shown in Table 28. The table compares the original coal ash elemental analysis to those for the oxidizing and reducing zone probe deposits. Totals of the elemental analyses for the probe deposits are less than 100% because the trace elements are not included. Since sulfur was analyzed by two different methods, i.e., XRF and LECO, the sulfur values can be used as a cross-check. The as-determined wt. % SO3

comparative values were 3.79 by LECO vs. 3.84 by XRF for the reducing zone probe deposit. The cross-check was very close. There was insufficient sample to perform the LECO sulfur analysis on the oxidizing zone probe deposit.

The chloride concentration in the original coal was measured at 45 mg/kg or ppm on a weight % dry basis. This chloride concentration is considered very low for a coal. The chloride concentration measured for the oxidizing and reducing zone probe deposits was < 100 ppm. As expected, the % unburned carbon in the reducing zone probe deposit was higher than the oxidizing zone deposit, i.e., 59.10 vs. 2.10 wt.%.

Figure 95 compares the major elements measured in the original coal ash to the major elements measured in both the oxidizing and reducing zone deposits. The emphasis here is to look at the elements believed to be the main contributors to ash deposition and subsequent corrosion, and their fate during the combustion process. The sulfur content is much higher in the reducing zone probe deposit compared to the original coal ash and oxidizing zone probe deposit. This trend was also observed in the Kentucky #11, Illinois #6, Galatia, Indiana #6, Gibson, and Gatling bituminous coals.

Table 26 - Comparison of Elemental Ash Analyses between Original Coal Ash and Probe Deposit for Pittsburgh #8 Coal.

Coal Description	Pittsburgh #8 PA	Pittsburgh #8 PA	Pittsburgh #8 PA
	Coal Ash	Probe Deposit - Ox	Probe Deposit - Red
Coal Ash Analysis			
Silicon Dioxide, % as SiO2	56.77	47.87	42.54
Aluminum Oxide, % as Al2O3	29.28	30.77	22.81
Iron Oxide, % as Fe2O3	6.63	12.20	11.93
Calcium Oxide, % as CaO	0.90	0.96	1.41
Magnesium Oxide, % as MgO	0.56	0.51	0.44
Sodium Oxide, % as Na2O	0.65	1.04	1.51
Potassium Oxide, % as K2O	2.30	1.81	2.48
Titanium Oxide, % as TiO2	1.53	1.34	1.96
Manganese Oxide, % as MnO2	0.05	0.11	0.04
Phosphorus Pentoxide, % as P2O5	0.56	1.39	1.90
Strontium Oxide, % as SrO	0.12	0.05	0.07
Barium Oxide, % as BaO	0.12	0.05	N.D.
Sulfur Trioxide, % as SO3	0.53	0.54	13.70
Chloride, ppm as Cl	45.00	< 100	< 100
LECO Total Carbon, %	N/A	2.10	59.10
LECO Sulfur, % SO3	N/A	Insufficient sample	3.79

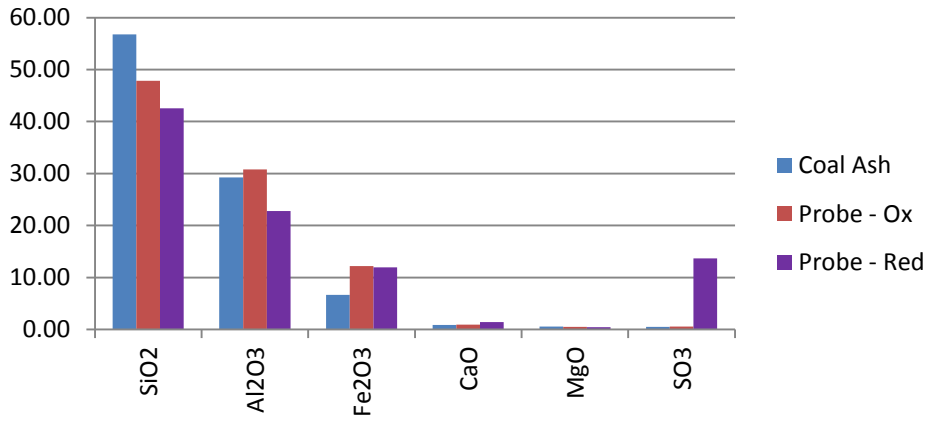

Figure 93 - Comparison of Major Elements in Coal Ash with Probe Deposit for Pittsburgh #8 Coal in Oxidizing and Reducing Conditions.

Figure 96 compares the minor elements measured in the original coal ash with those in both the oxidizing and reducing zone deposits. The sodium and phosphorus values are higher in the reducing zone deposit than those in the oxidizing zone probe deposit and original coal ash. Pittsburgh #8 is a medium sulfur (1.03 % A.R.) and low chlorine (0.0045 % dry Cl) bituminous coal. Based on the coal ash analysis in Table 28 and also in Appendix B, the silicon, aluminum, and iron concentrations are relatively high, with a calculated BAR of 0.52. For the oxidizing zone deposit, the results of XRD phase identification showed the major phase being Quartz, SiO_2, with Mullite, syn, $Al_6Si_2O_{13}$ as a medium phase, Iron (III) Oxide, Fe_2O_3 and Magnetite, Fe_3O_4 as minor phases, and Anhydrite, $CaSO_4$ was identified as a trace phase. For the reducing zone deposit, results of the XRD phase identification showed the major phase being Quartz low, SiO_2. Mullite, syn, $Al_6Si_2O_{13}$ and Iron Oxide, Fe_2O_3 were identified as medium phases.

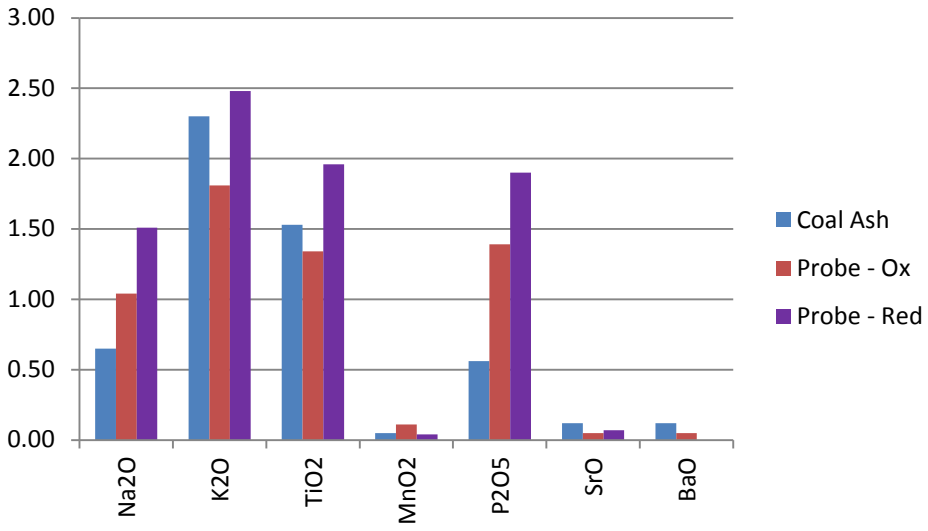

Figure 94 - Comparison of Minor Elements in Coal Ash with Probe Deposit for Pittsburgh #8 Coal in Oxidizing and Reducing conditions.

4.3.10 Average Results of SEM/EDS Analyses on Deposit Samples

The averages of deposit composition are presented in this section and compared to the results of standard coal analysis. It is important to distinguish among different sources of ash samples, which consisted of: (1) ash that was formed and analyzed during an ASTM standard analysis of the original coal, (2) fly ash that was formed as a result of a boiler combustion process, and (3) fly ash or partially burned coal particles that were deposited on the deposition probes. In order to clearly differentiate among these types of ash, they are referred to as ASTM ash (or coal ash), fly ash, and deposit ash in this report, respectively. The ASTM ash composition was readily available from standard coal analysis for each coal but was not necessarily an accurate representation of the fly ash in boilers. The ASTM analysis procedures do not replicate a boiler combustion process that typically has a much higher heating rate. The boiler combustion operation may also be staged, thus creating reducing conditions, while the ASTM process is not. As a result, the deposition process in boilers may be relatively selective to ash particles of certain compositions. After deposition, the particles may continue to react with the combustion gases and result in further changes of composition.

In this and subsequent sections, the deposit ash compositions collected from the BFR are compared to the ASTM ash composition of the original coals. In order to do this, the elemental composition measured with EDS must be converted to the oxides, similar to the common practice per ASTM ash analysis.

The first step to producing oxides from the measured EDS composition was to remove the C and O mass fractions (X_C, X_O). Small amount of Ni and Cr were also found in the deposit samples, which were likely introduced from the 304SS sleeves during sample polishing. These mass fractions and the associated Fe (X_{Fe} ~3.5X_{Cr} for 304SS) mass fraction were removed to produce a corrected mass fraction for each element $X_{i,cf}$, as shown in Eq. 10. The adjusted weight percent of each elemental was then converted to its highest oxidation state.

$$X_{i,cf} = \frac{X_i}{1 - X_c - X_o - X_{Ni} - X_{Cr} - 3.5X_{Cr}} \qquad \text{Eq. 10}$$

Discussion of the average elemental composition measured for each coal is given below. A detailed discussion is made for the Beulah Zap lignite coal, of which many observations were applicable to all of the eight coals investigated. Therefore, the remaining coals are only discussed briefly.

4.3.10.1 Beulah Zap Lignite Deposit and Ash Comparison

Results of the SEM/EDS analyses of the probe deposit sample, XRF chemical analysis of the probe deposit sample from the oxidizing zone, and coal ash analyses of the original Beulah Zap coal are shown in Figure 97. The first three bars on the left of each oxide were calculated from the deposits on the top of the probe. The fourth bar from the left was from the deposit on the bottom of the probe. The last two bars are the XRF analysis of the probe deposit and coal ash

analysis, respectively. A similar graph is shown in Figure 98 for locations on the top of the reducing probe and in Figure 99 for locations on the bottom of the reducing probe.

It is noted that the results of SEM/EDS analyses in most cases are in good agreement with the standard coal ash analysis. There are, however, considerable differences observed for several deposit samples.

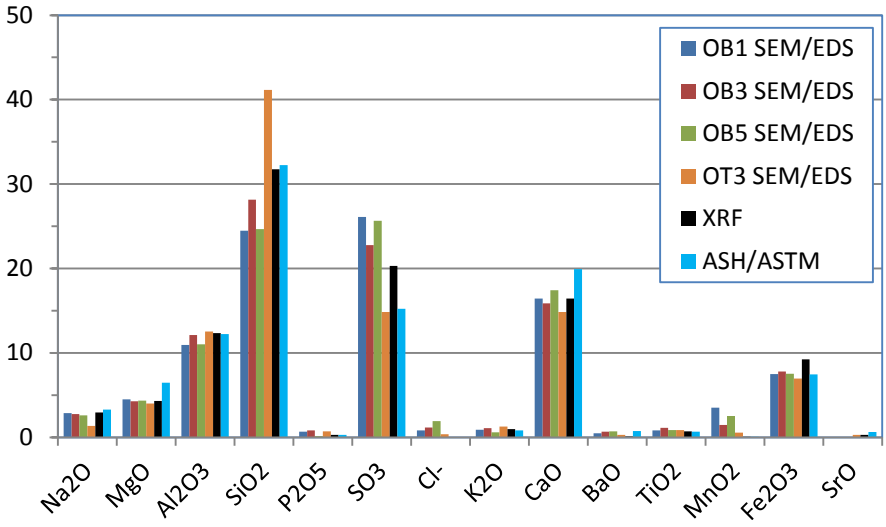

Figure 95 - Oxide Graph of ND Beulah Zap Coal in Oxidizing Zone.

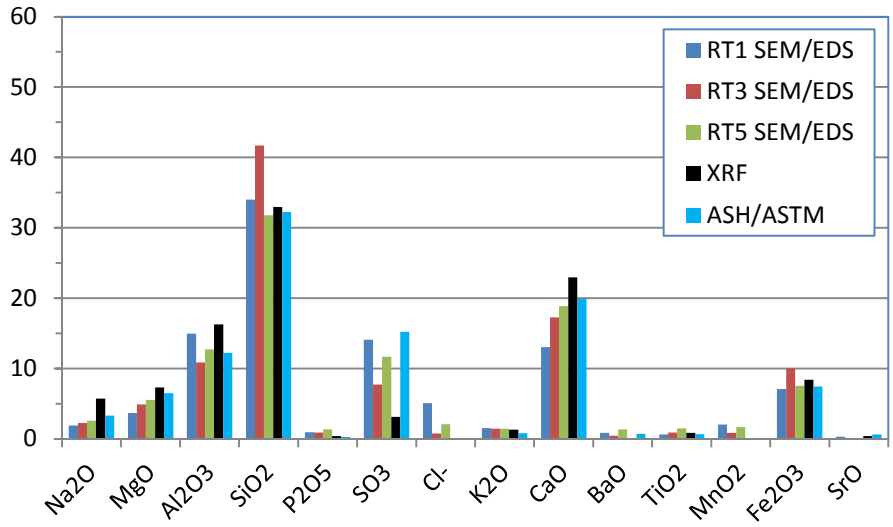

Figure 96 - Oxide Graph of ND Beulah Zap Coal in Reducing Zone, Top Position.

In the oxidizing deposits, the calculated SO_3 concentrations from SEM/EDS exhibited higher values than those of the coal ash analysis; whereas in the reducing zone, the SO_3 concentrations tended to be lower.

A key element of interest is chlorine. Unfortunately, a significant amount of chlorine was present in the epoxy used for mounting the deposit/sleeve samples for cross-sectional examinations. As a result, the chlorine in ash particles could not be reliably separated from the chlorine in the epoxy, thus making the chlorine data unreliable.

The deposit samples of OT3, RT3, and RB5 consisted of unusually high Si concentrations relative to the coal ash analysis. The high concentrations of Si inevitably reduced the concentrations of other oxides. It is unclear why high concentrations of Si were found in some of the deposit samples.

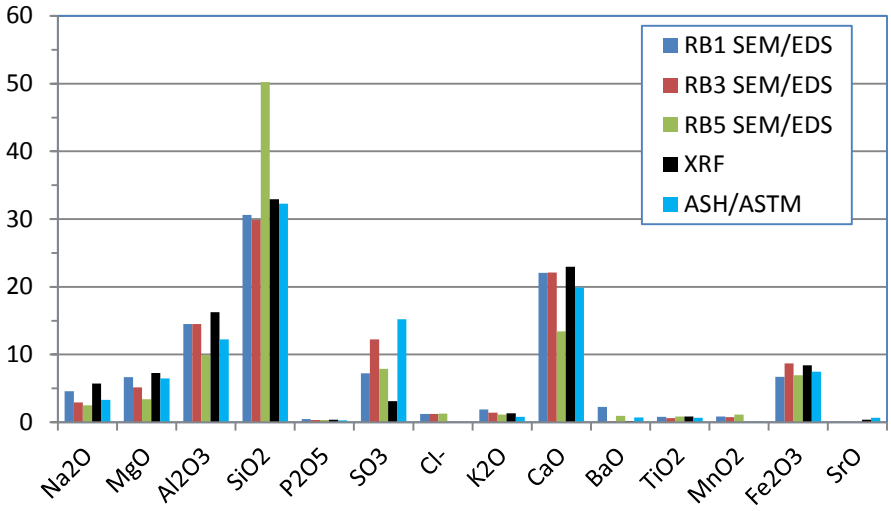

Figure 97 - Oxide Graph of ND Beulah Zap Coal in Reducing Zone, Bottom Position.

4.3.10.2 Mahoning 7A Deposit and Ash Comparison

Figures 100-102 show the average elemental compositions of the BFR deposit samples determined by the SEM/EDS, XRF chemical analysis, and coal ash analysis. Comparing this coal ash to Beulah Zap, the Al, Si, and Fe concentrations were significantly higher, and Na, Mg, S, and Ca were significantly lower. Again, the deposit composition was often in agreement with the coal ash composition.

Sulfur in the oxidizing deposit was slightly enriched or comparable to that determined by coal ash analysis, whereas sulfur in the reducing deposit was slightly lower. This trend was consistent with that found in the Beulah Zap deposit samples. Chlorine was significantly higher in the oxidizing zone than the reducing zone. However, as mentioned previously, the chlorine results were unreliable due to a significant amount of chlorine present in the mounting epoxy. It appeared that Na, Mg, and P were slightly enriched in the oxidizing deposit samples, as they were generally higher than those of the reducing samples.

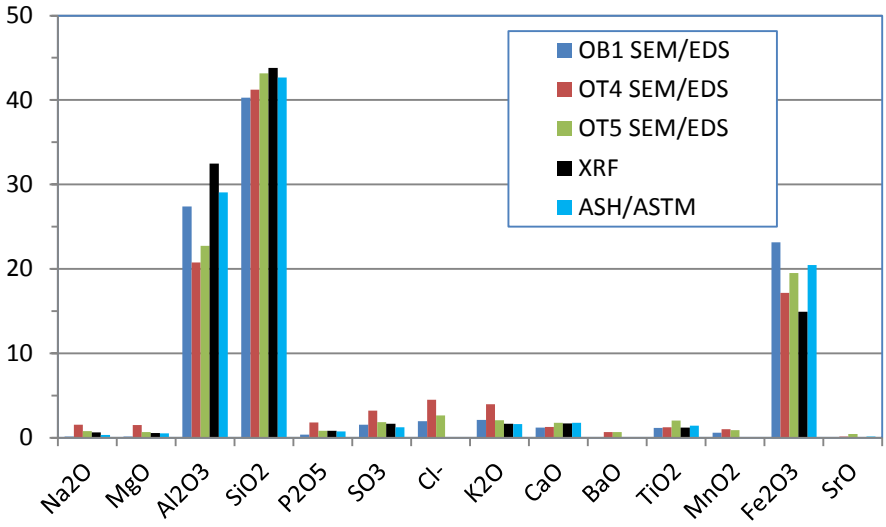

Figure 98 - Oxide Graph of OH Mahoning Coal in Oxidizing Zone.

The results show that little difference existed between the top and bottom reducing samples, except that Fe was perhaps lower on the bottom side of the probe. A combined top and bottom sample was analyzed with XRF. As a result, a variation in the compositions between these two locations could not be quantified. Based on the results of SEM/EDS analysis, a lower concentration of Fe was typically observed on the bottom of the probe. Such a variation between the two locations might have been attributed to a difference in the deposition process. Particles deposited on the bottom of the probe were dominated by impaction after transport in turbulent eddies and therefore were smaller in size and less dense. Iron was one of the heavier constituents in the ash deposit and therefore was more likely to be deposited on the top sleeve.

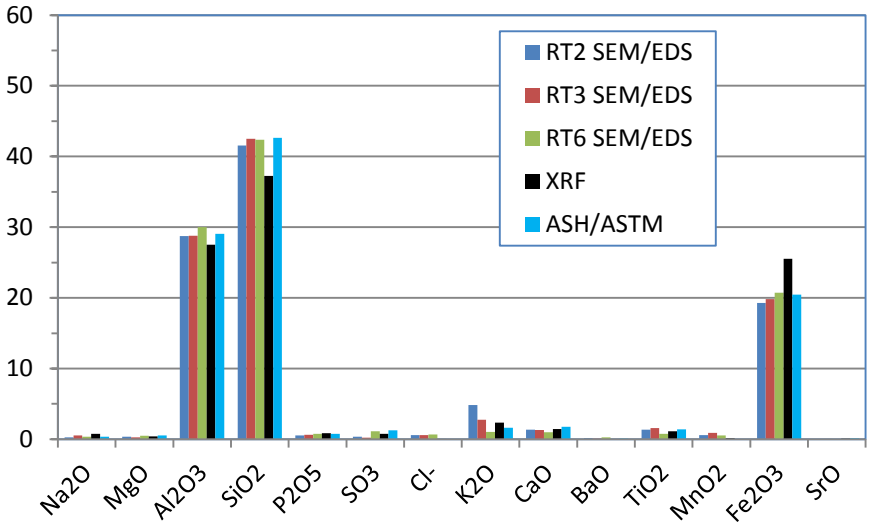

Figure 99 - Oxide Graph of OH Mahoning Coal in Reducing Zone, Top Position.

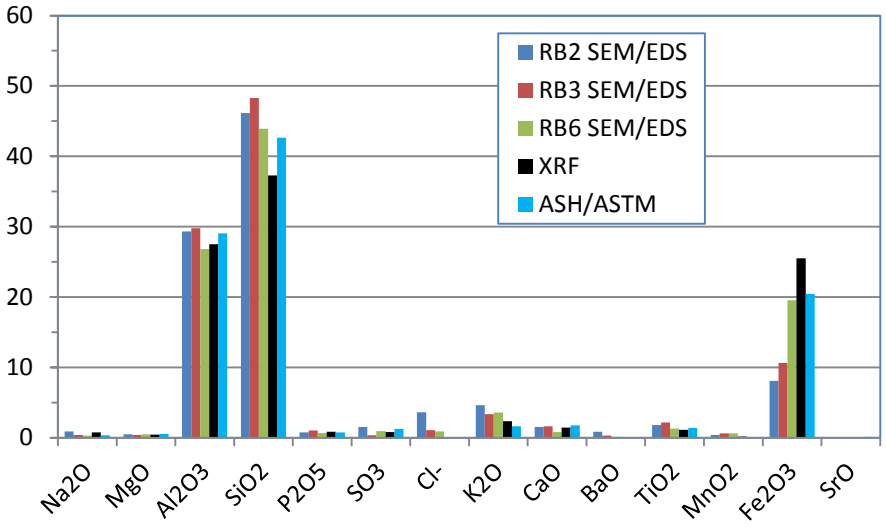

Figure 100 - Oxide Graph of OH Mahoning Coal in Reducing Zone, Bottom Position.

4.3.10.3 PRB Deposit and Coal Ash Comparison

Results of the PRB deposit samples collected from different locations of the probe are shown in Figures 103-106. The PRB deposit compositions are similar to those of the Beulah Zap coal, except for lower sulfur and calcium contents and higher Al, Si, and Fe contents. Again, the deposit compositions are generally in agreement with the coal ash composition. When comparing the top and bottom of the deposition probe, the most noticeable difference appears to be two of the top deposit samples that are high in Si and low in Al. After examining the SEM micrographs from which the EDS analyses were performed, it was found that the high silicon concentration was attributed to the presence of a few large Si-rich particles. Such results might not be representative of all of the particles present on the probe. The Na, Mg, P, and S concentrations appear to have been slightly enriched on the bottom side of the oxidizing probe.

Comparing the oxidizing and reducing deposit samples, the top of the deposition probe generally contained less sulfur. These results are similar to those seen in the Beulah Zap samples. The Beulah Zap and PRB coal ash are both high in calcium, which may promote the formation of $CaSO_4$ and result in a higher sulfur content in the oxidizing deposit. Individual particles high in Ca, S, and O are discussed in the next section.

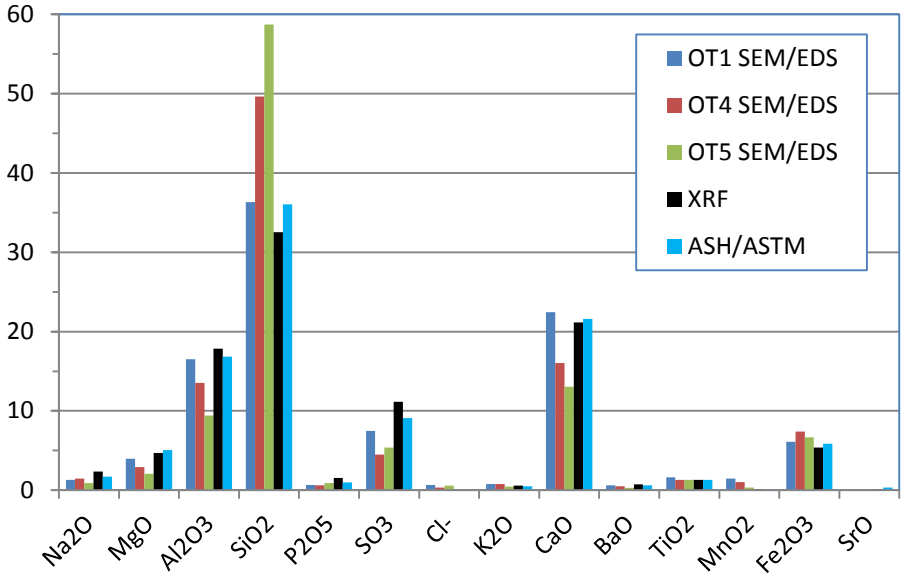

Figure 101Oxide Graph of WY PRB-1 in Oxidizing Zone, Top Position.

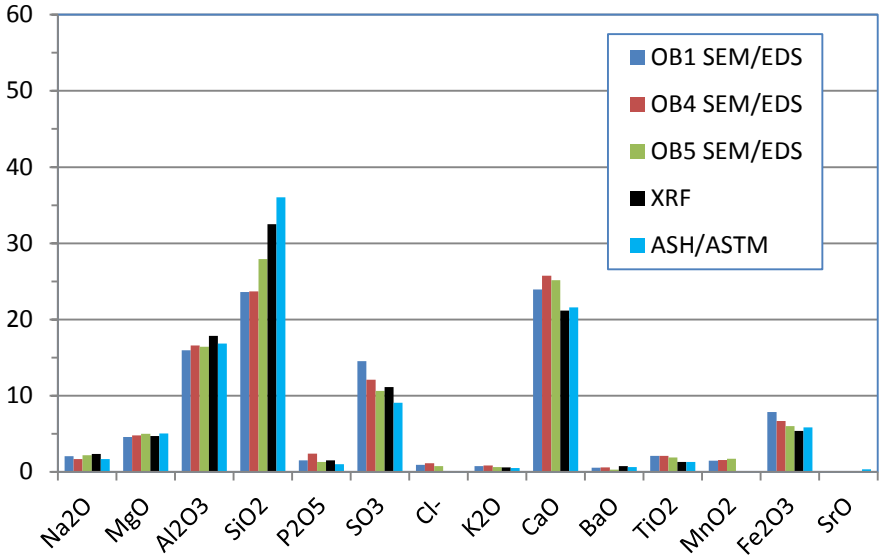

Figure 102 - Oxide Graph of WY PRB-1 in Oxidizing Zone, Bottom Position.

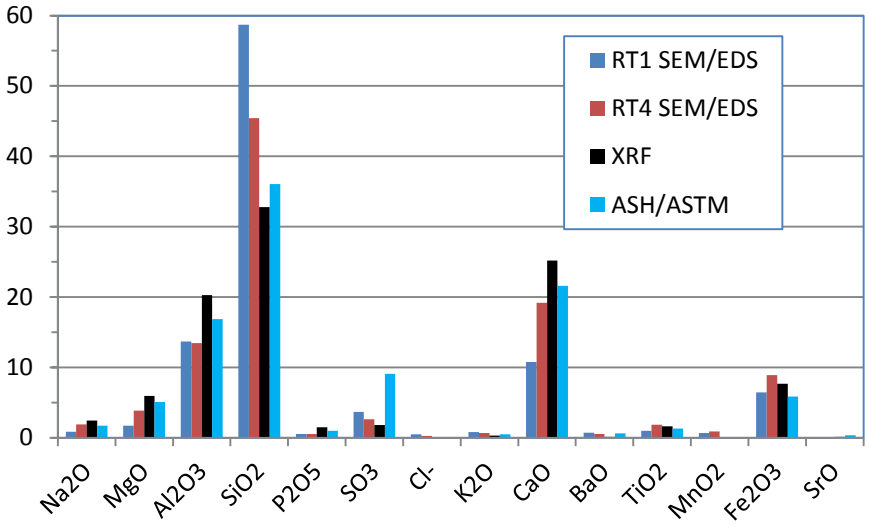

Figure 103 - Oxide Graph of WY PRB-1 in Reducing Zone, Top Position.

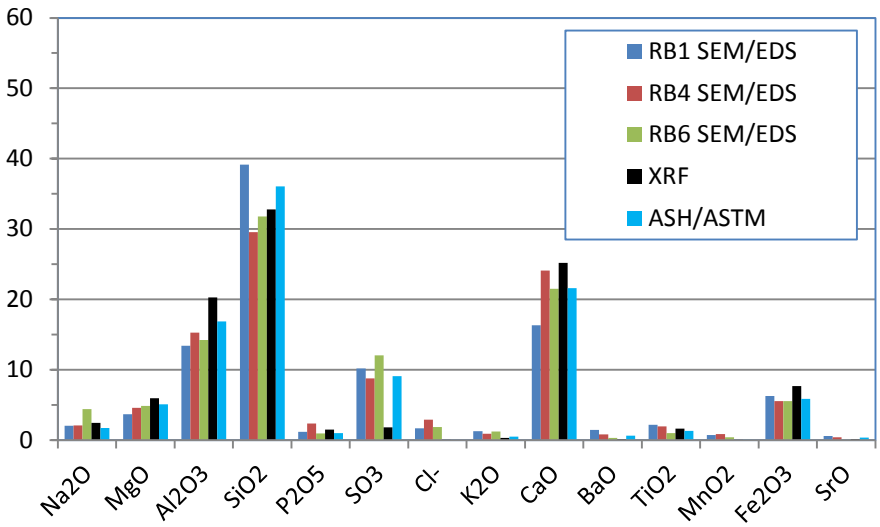

Figure 104 - Oxide Graph of WY PRB-1 in Reducing Zone, Bottom Position.

4.3.10.4 Illinois #6-2 Deposit and Coal Ash Comparison

The deposit and coal ash compositions for the Illinois #6-2 coal formed under reducing and oxidizing conditions are compared in Figures 107-110. Illinois #6-2 has the highest Cl content of all the coals studied and is relatively high in sulfur and iron. Illinois #6 contains the highest amount of Ca among the bituminous coals. Like the other coals, the deposit compositions are similar to the coal ash.

All of the Illinois #6-2 deposit samples exhibit higher concentrations of S, Na, and K in the reducing zone compared to those of coal ash analysis. The Na concentrations in three of the

seven deposit samples are more than three times of that from the coal ash analysis. K is enriched in all seven of the reducing zone deposit samples. The S content is lower in the oxidizing zone. Six of the seven deposit samples in the oxidizing zone have less sulfur than the coal ash produced from the ASTM analysis, while four of the seven deposits in the reducing zone have more sulfur than the coal ash. The Illinois #6-2 therefore appears to follow an opposite pattern for sulfur compared to the other coals discussed above.

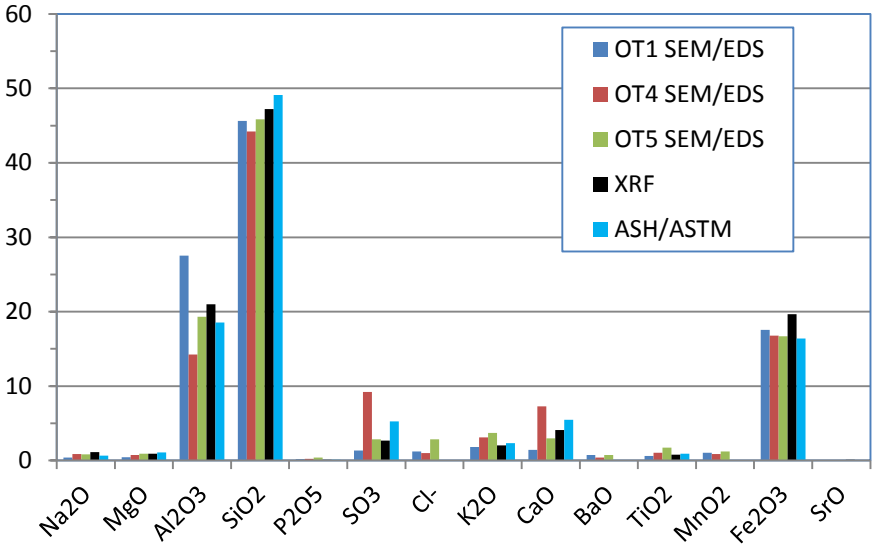

Figure 105 - Oxide Graph of IL #6-2 Coal in Oxidizing Zone, Top Position.

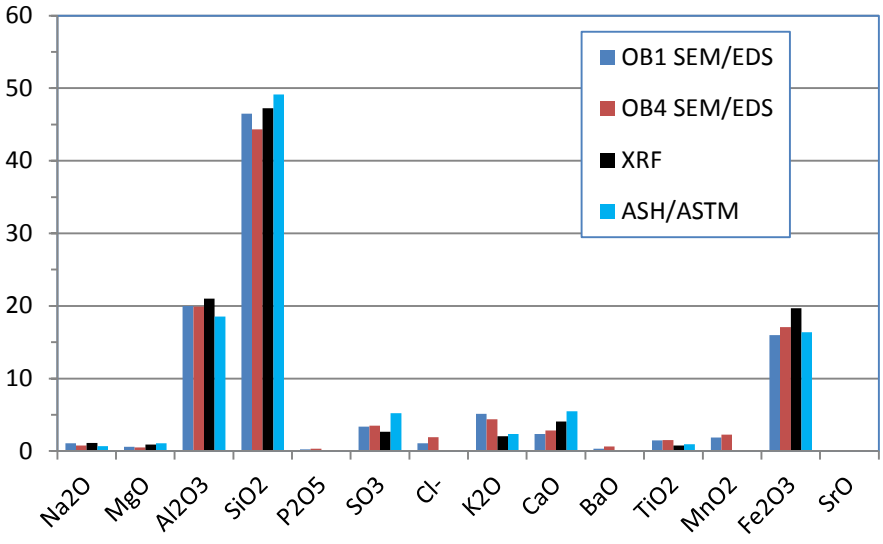

Figure 106 - Oxide Graph of IL #6-2 Coal in Oxidizing Zone, Bottom Position.

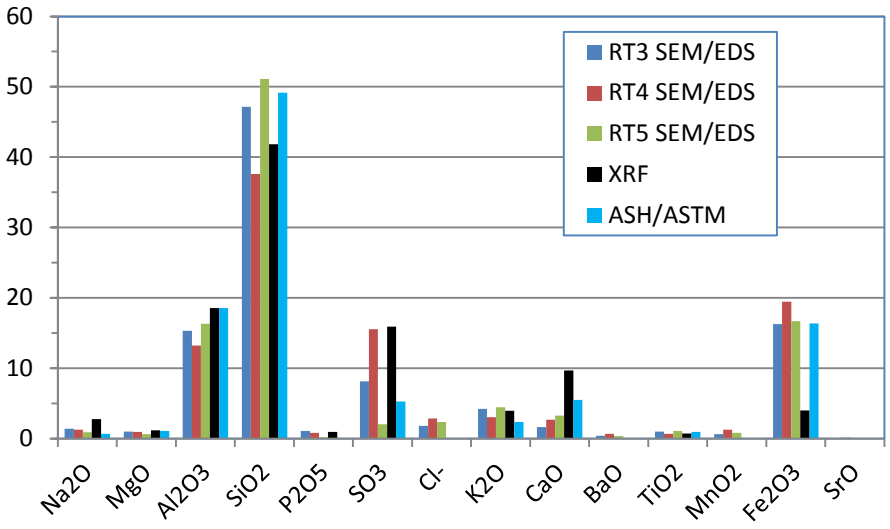

Figure 107 - Oxide Graph of IL #6-2 Coal in Reducing Zone, Top Position.

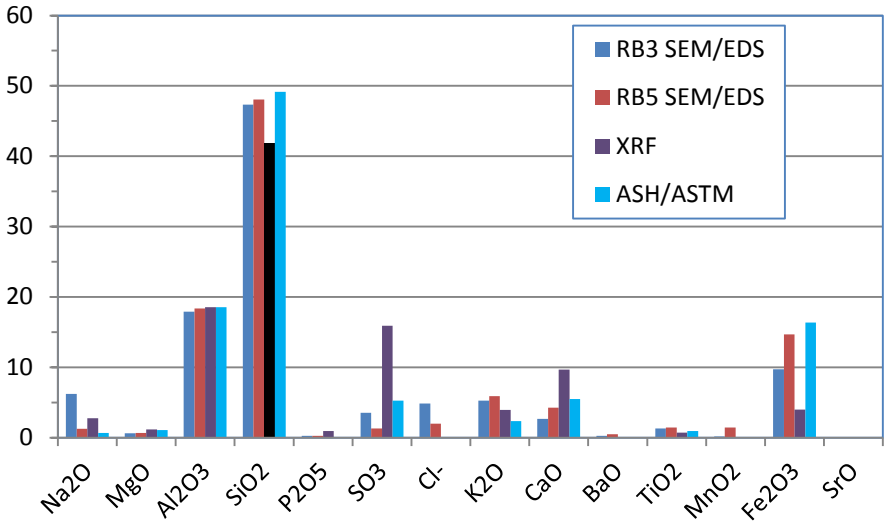

Figure 108 - Oxide Graph of IL #6-2 Coal in Reducing Condition, Bottom Position.

4.3.10.5 Gatling Deposit and Coal Ash Comparison

The coal ash and deposit compositions of Gatling coal collected from the reducing and oxidizing zones of the BFR are compared in Figures 111-113. The Gatling coal ash from the ASTM coal analysis is relatively high in Si, Al, and Fe but low in S, Ca, K and other elements. The Gatling deposit samples do not appear to be either enriched or depleted in these elements, perhaps with the exception for S, K, and Fe. Sulfur is significantly higher in three of the fours

deposit samples on the reducing top. Thus, the sulfur in Gatling deposit samples follows the same trend as Illinois #6, i.e., rich in the reducing top deposits. The XRF analysis of the reducing deposit was from a combined top and bottom sample. As a result, the high sulfur content shown represents an average of both top and bottom deposits. Potassium in the deposit sample is higher than that in the coal ash from the ASTM coal analysis for all of the reducing samples, and in some cases, more than doubled. The potassium concentration in two of the three deposit samples is slightly higher than that in the coal ash from ASTM analysis.

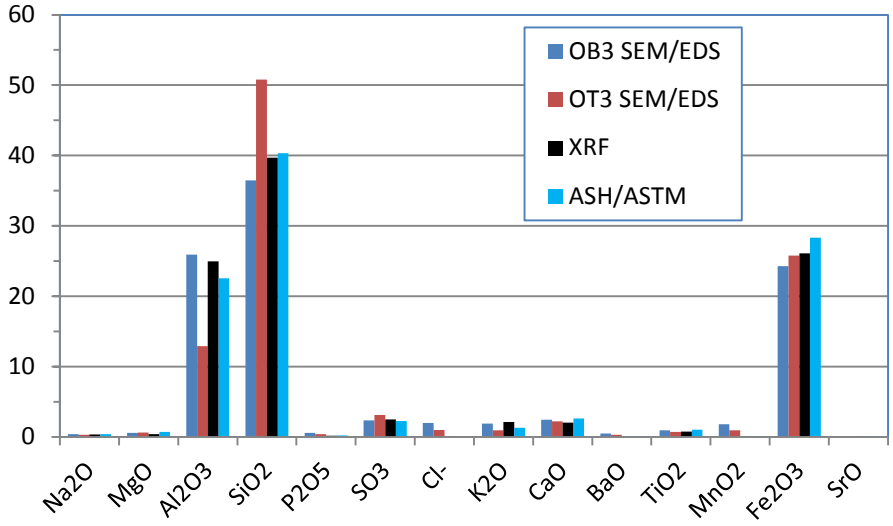

Figure 109 - Oxide Graph of OH Gatling Coal in Oxidizing Zone.

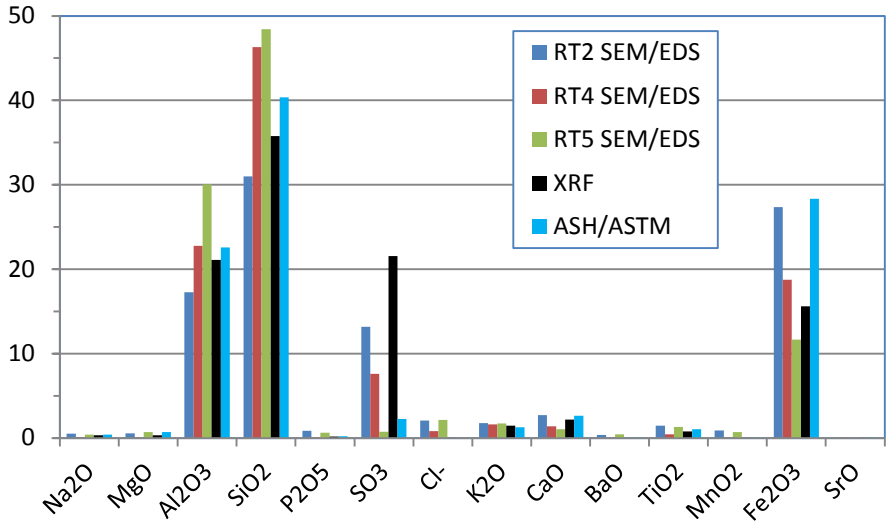

Figure 110 - Oxide Graph of OH Gatling Coal in Reducing Zone, Top Position.

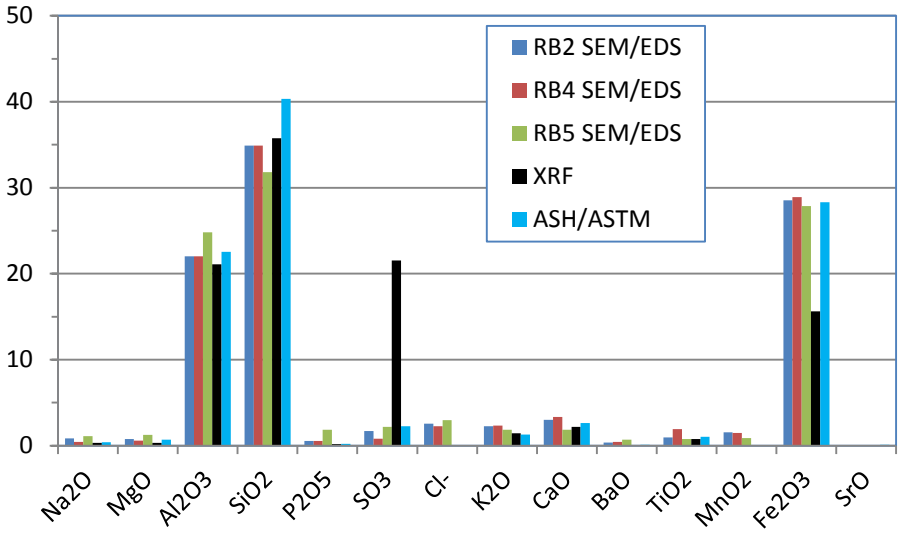

Figure 111 - Oxide Graph of OH Gatling Coal in Reducing Zone, Bottom Position.

4.3.10.6 Indiana Deposit and Coal Ash Comparison

The coal ash and deposit compositions for the Indiana coal under reducing and oxidizing conditions are compared in Figures 114-116. As in most of the bituminous coals, the Indiana coal ash is high in Al, Si, and Fe. In general, a good agreement in composition was observed between the deposit samples from both the reducing and oxidizing deposits and the coal ash from ASTM coal analysis. The RT3 sample is quite unique compared to the other samples, i.e., low in Al and high in P, S, and Fe. The Na concentration is lower in the deposit than in the coal ash under both oxidizing and reducing conditions, although it is near the detection limit of 1%. Potassium is higher in seven of the eight reducing deposit samples and even more so in the reducing-top deposit. Potassium is therefore enriched in the Indiana reducing deposits as for many other coals. Sulfur is lower in the oxidizing deposit samples; while about half of the reducing deposits show high sulfur, consistent with most of the bituminous coals.

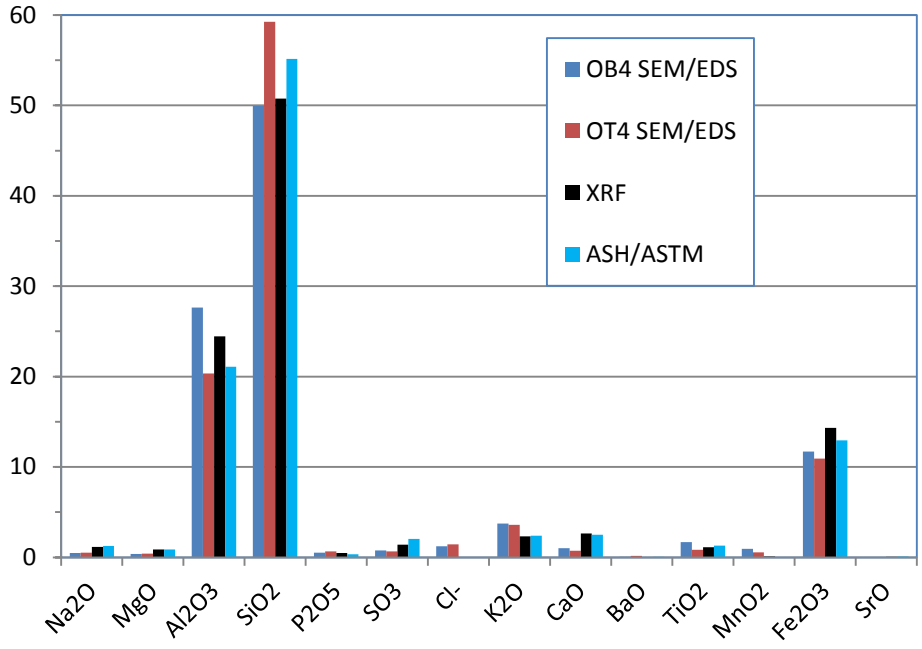

Figure 112 - Oxide Graph of IN #6 Coal in Oxidizing Zone.

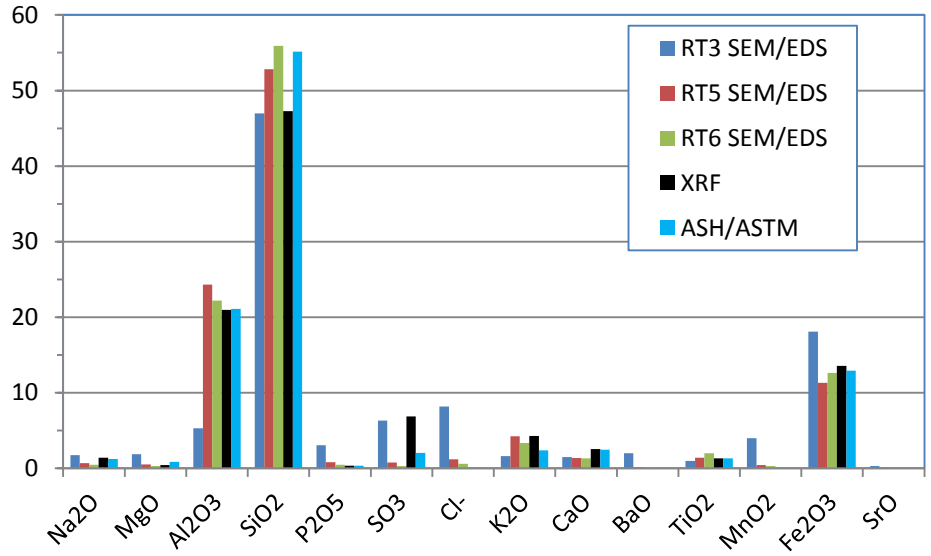

Figure 113 - Oxide Graph of IN #6 Coal in Reducing Zone, Top Position.

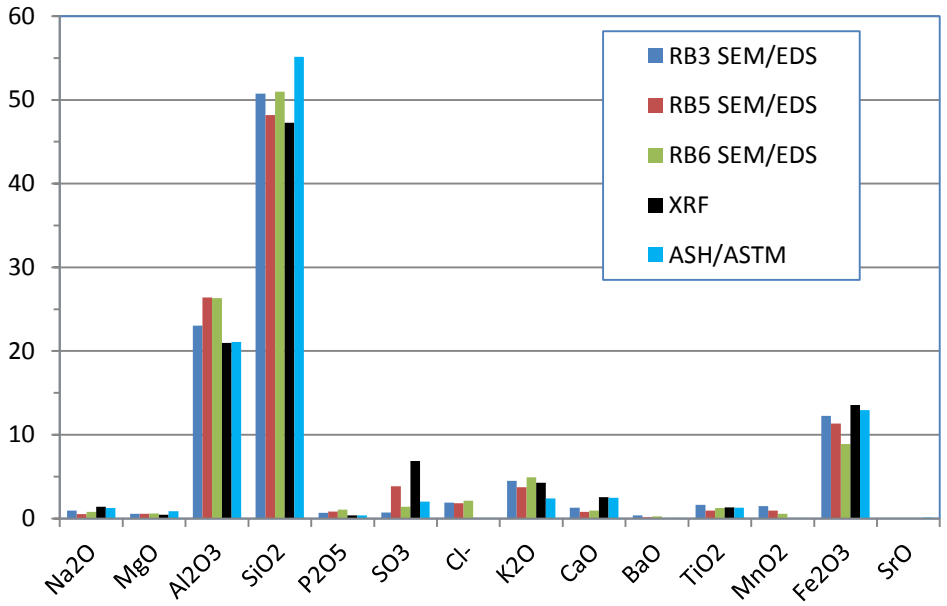

Figure 114Oxide Graph of IN #6 Coal in Reducing Zone, Bottom Position.

4.3.10.7Kentucky Deposit and Coal Ash Comparison

The coal ash and deposit compositions for the Kentucky #11 coal under reducing and oxidizing conditions are compared in Figures 117-119. The coal ash from ASTM coal analysis is high in Al and Si and very high in Fe. This coal has the second highest Fe concentration among the eight coals studied. As with the other coals, the deposit compositions are in general agreement with the ASTM coal ash composition. There are a few exceptions, however. Very little Na was found in any of the deposit samples. The K concentrations are similar when comparing the oxidizing and reducing top deposits with the ASTM coal ash. However, as with the other coals, K is enriched in the reducing-bottom deposits. Sulfur is relatively low in the oxidizing deposits but is significantly higher in the reducing-top deposits. These general observations are again consistent with the other bituminous coals.

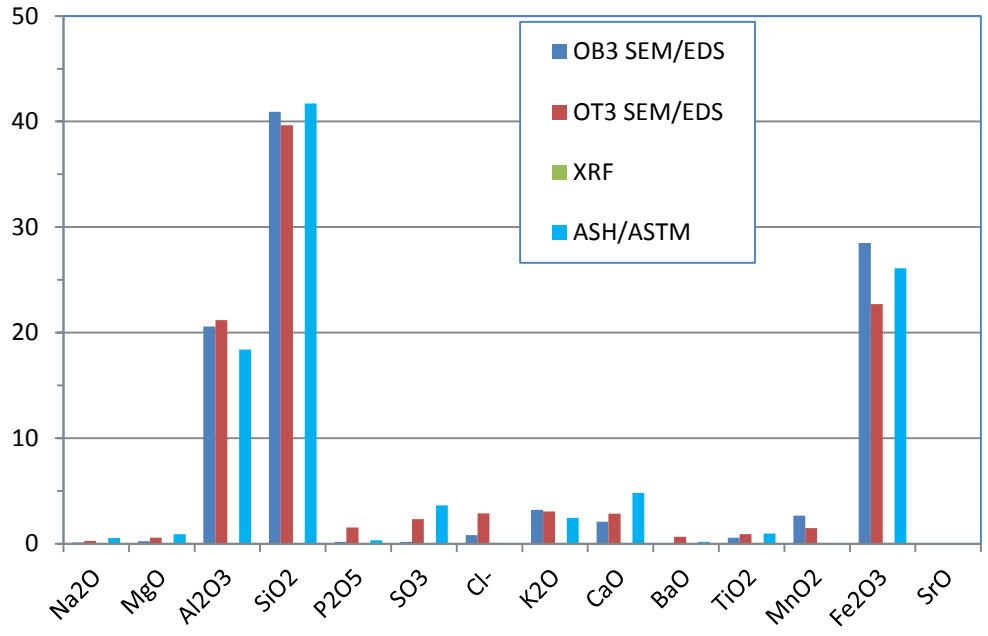

Figure 115 - Oxide Graph of KY #11 Coal in Oxidizing Zone.

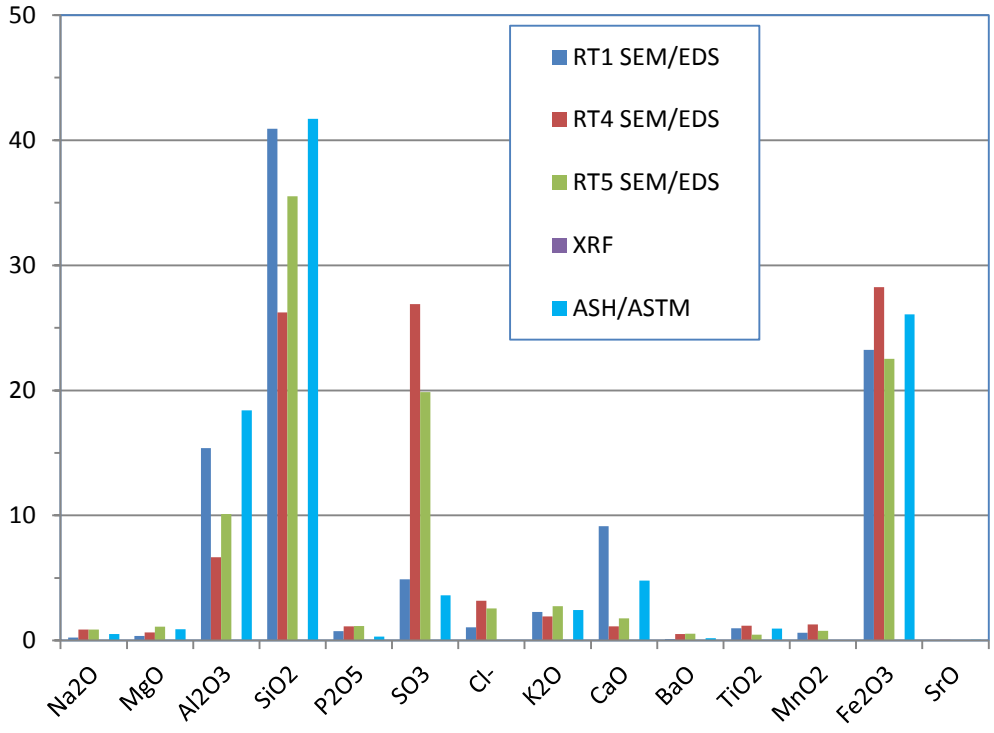

Figure 116 - Oxide Graph of KY #11 Coal in Reducing Zone, Top Position.

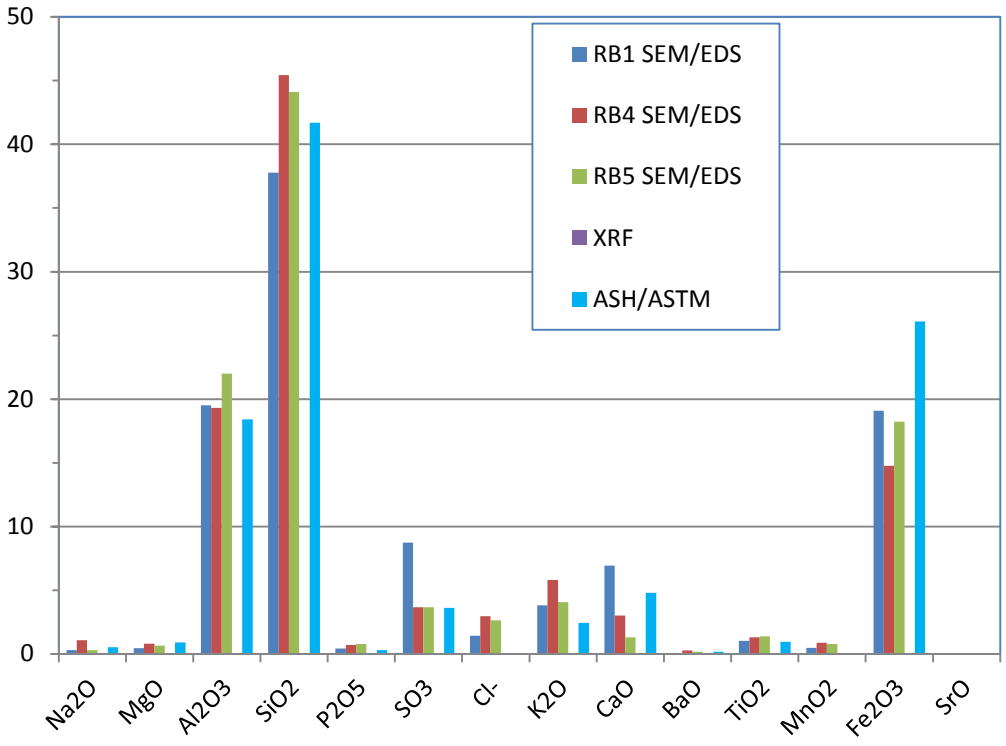

Figure 117 - Oxide Graph of KY #11 Coal in Reducing Zone, Bottom Position.

4.3.10.8Pittsburgh Deposit and Coal Ash Comparison

The coal ash and deposit compositions for the Pittsburgh #8 coal under reducing and oxidizing conditions are compared in Figures 120-122. This coal has the highest combined concentration of Al and Si among the eight coals studied but is relatively low in Fe (6.6%) and even lower in all other elements. Of all the coals, the deposit compositions of Pittsburgh #8 are closest to the coal ash composition from ASTM coal analysis. No elements are significantly enriched or depleted in either reducing or oxidizing deposit samples compared to those of the coal ash. This agreement might be in part due to some elements, such as Na, S, and K, being in such small quantities. Thus, the deposit and coal ash compositions are dominated by the more abundant inert oxides.

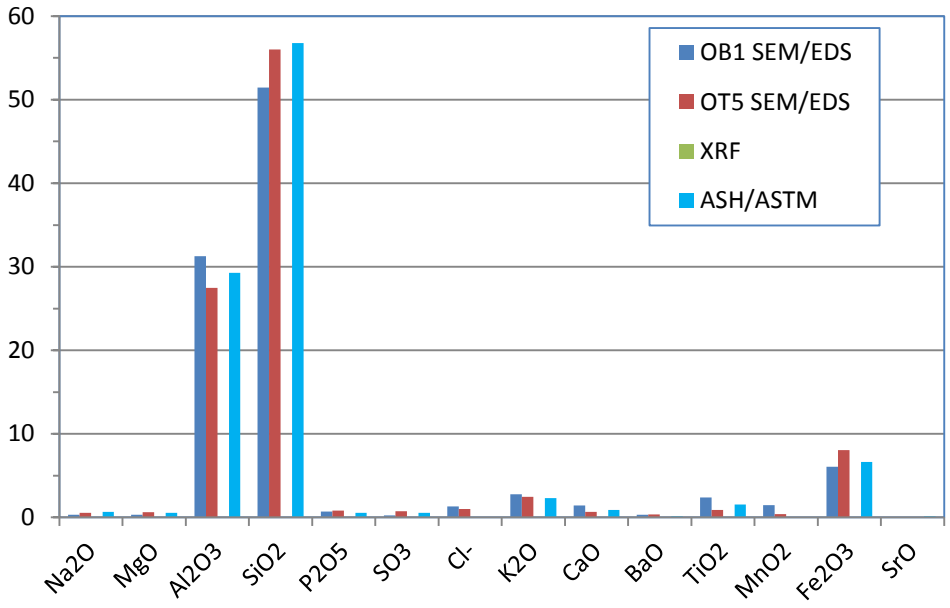

Figure 118 - Oxide Graph of Pittsburgh #8 Coal in Oxidizing Zone.

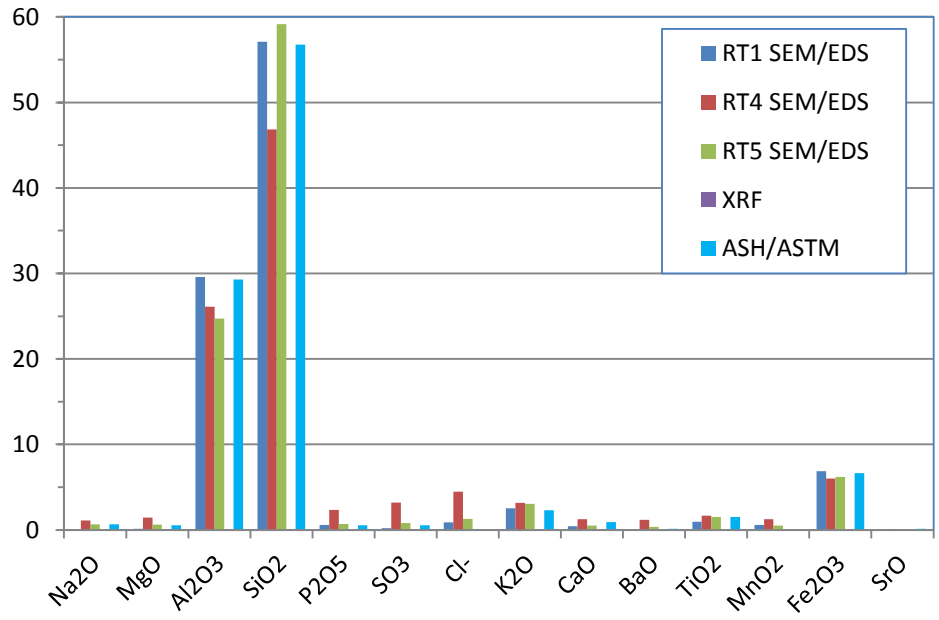

Figure 119 - Oxide Graph of Pittsburgh #8 Coal in Reducing Zone, Top Position.

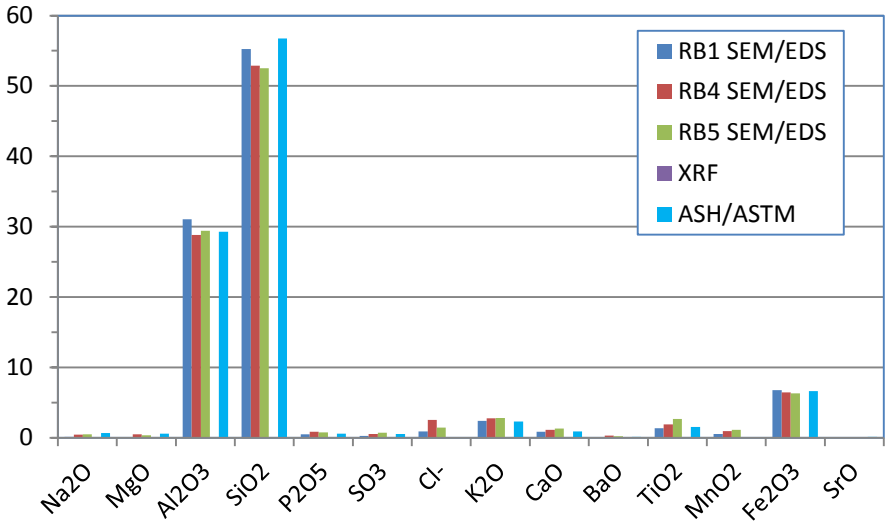

Figure 120 - Oxide Graph of Pittsburgh #8 Coal in Reducing Zone, Bottom Position.

4.3.11 Results of SEM/EDS Analyses of Individual Deposit Particles

This section details the backscattered SEM electron micrographs and EDS analyses of the ash particles present in the deposit samples collected from the BFR for each coal. As with Section 3.3.10, discussion on the Beulah Zap lignite coal is given in more detail, and much of it is applicable to the other coals as well.

4.3.11.1 Beulah Zap - Individual Particle Analysis

The backscattered electron SEM micrographs of Beulah Zap deposit samples collected from the oxidizing and reducing zones of the BFR are shown in Figures 123 and 124. All images in this section are arranged in such a way so that they are in sync with the probe locations from which the deposit samples were retrieved, i.e., the top samples on top row, etc. Each image is denoted by the sample location and the number of particles that were analyzed for elemental compositions. The brightness of backscattered electron images is proportional to the atomic numbers of elements. Therefore, the mounting epoxy appears black in the background.

In general, the particles in the top deposit sample were larger in size and more irregular in shape, whereas those in the bottom samples were smaller and more spherical. Note that, due to smaller particle sizes, the images of the bottom deposit samples were typically taken at higher magnifications. A micron bar is provided on each micrograph to help determine the particle sizes. Some particles in the top deposit sample of OT3 are as large as 100 μm, and some in the 20-50 μm range are present in the top samples of RT3 and RT5. On the other hand, the particles in the bottom deposit samples are mostly below 5 μm.

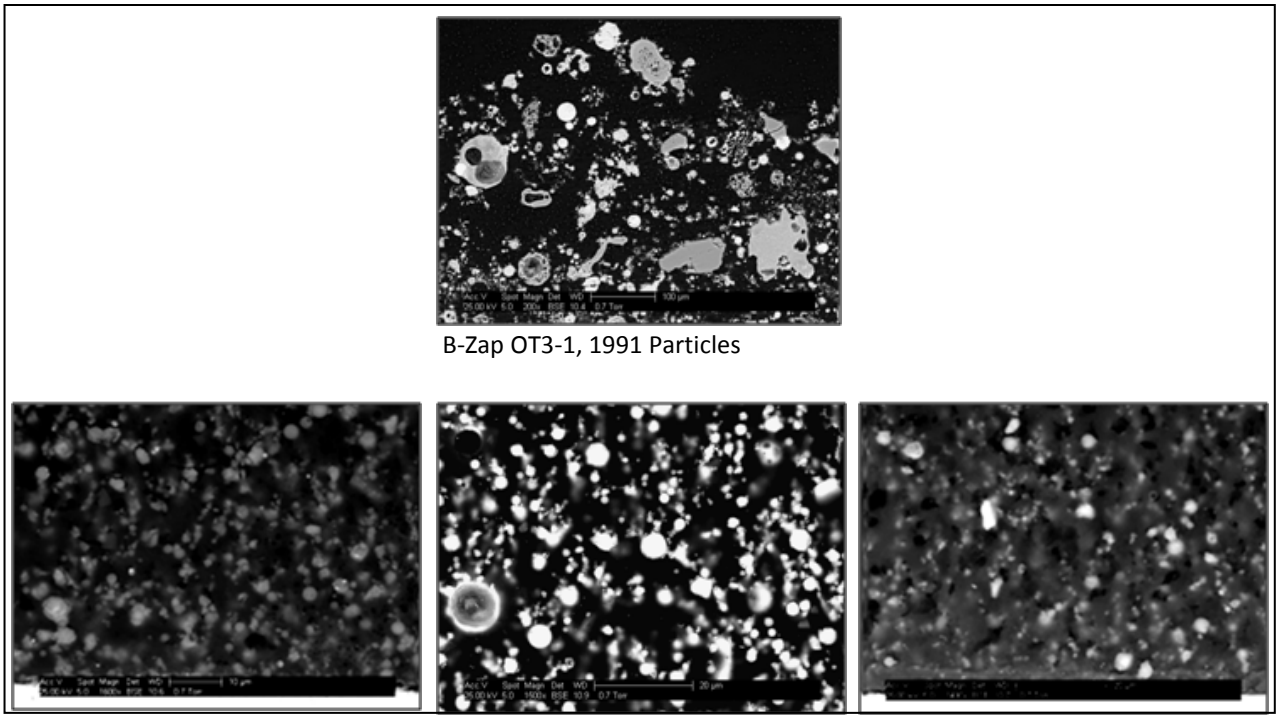

B-Zap OT3-1, 1991 Particles

B- Zap OB1, 322 Particles. B-Zap OB3, 1951 Particles. B-Zap OB5, 308 Particles.

Figure 121 - Backscattered Electron SEM images of Oxidizing Deposits for Beulah Zap.

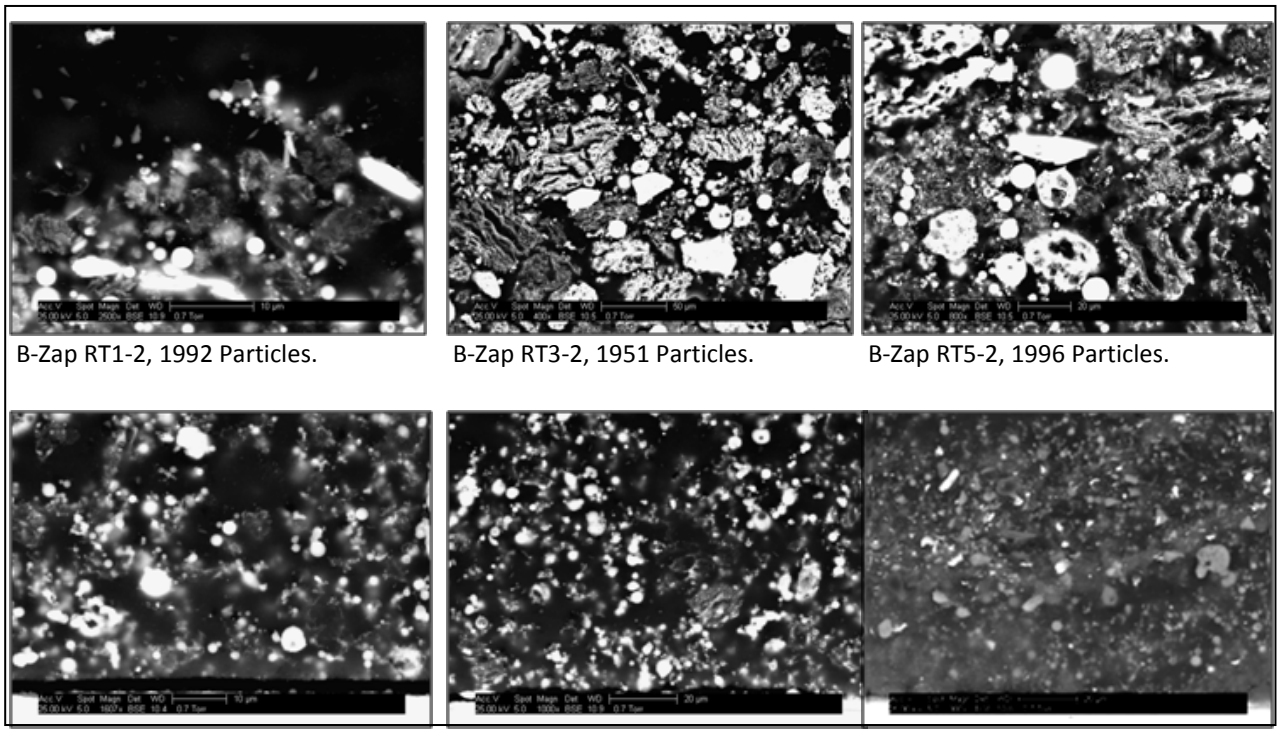

B-Zap RT1-2, 1992 Particles. B-Zap RT3-2, 1951 Particles. B-Zap RT5-2, 1996 Particles.

B-Zap RB1, 1865 Particles. B-Zap RB3, 1863 Particles. B-Zap RB5, 485 Particles.

Figure 122 - Backscattered Electron SEM images of Reducing Deposits for Beulah Zap.

As discussed previously, a difference in particle size between the top and bottom of the probe was expected due to a difference in the deposition mechanism. Deposit on the top of the deposition probe was formed by impaction of the ash particles when having sufficient momentum to penetrate through the boundary layer. Conversely, smaller particles tended to be entrained in the combustion gases and flow around the probe. Therefore, the deposit on the bottom of the probe was formed by way of eddy impaction. Particles that appear to be spherical in the deposit samples were likely molten in the combustion gases prior to deposition, whereas large particles (>20 μm) that are irregular in shape probably remained solid throughout the deposition process.

Additional SEM images for the Beulah Zap deposits are given in Figures 125-128. In the oxidizing deposit of OB3, Particle A, which contains 40.9% Ca, 32.2% S, and 21.9% O, is an example of the presence of $CaSO_4$. Particles D and E in the deposit are relatively high in Cl. As mentioned previously, the chlorine signal was likely produced from the mounting epoxy that contains a significant amount of chlorine.

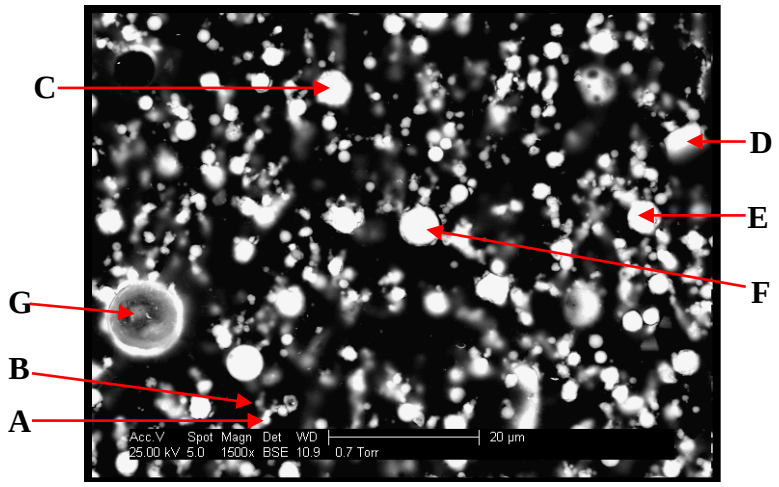

Coal: BEULAH ZAP							
Sleeve Location: OXIDZING BOTTOM #3 (OB3)							
	A	B	C	D	E	F	G
Particle No.	1798	1816	83	136	192	266	347
Area (μm^2)	0.03	0.05	16.02	12.40	18.00	39.63	21.98
O	11.1	18.0	31.89	31.6	32.8	32.96	31
Na	0.0	1.4	0	1.3	2.3	2.433	3.242
Mg	4.3	3.4	5.8	1.2	4.0	3.796	3.121
Al	6.5	6.1	6.427	2.7	4.9	9.195	7.394
Si	12.0	11.0	8.486	40.7	9.9	15.13	19.82
P	0.0	0.0	0	1.2	0.0	0	0
S	22.8	20.4	12.48	3.4	12.4	9.249	8.576
Cl	0.0	1.6	0	1.5	1.2	0	0
K	0.0	1.1	0	2.0	0.9	0	0
Ca	26.0	22.4	24.4	3.9	17.4	14.25	9.182
Ba	3.5	0.0	0	2.0	1.5	0	0
Ti	0.0	1.0	0	0.0	1.2	1.069	1.333
Cr	3.1	2.5	0	2.4	2.4	2.165	2.394
Mn	1.0	1.2	0	1.0	1.0	0	1.333
Fe	9.7	8.3	9.201	5.0	8.1	9.715	10.19
Ni	0.0	1.7	1.306	0.0	0.0	0	2.455
Sr	0.0	0.0	0	0.0	0.0	0	0

Figure 123 - Beulah Zap OB3, 25 kV, Spot Size 5.0, Backscattered Electron (BSE).

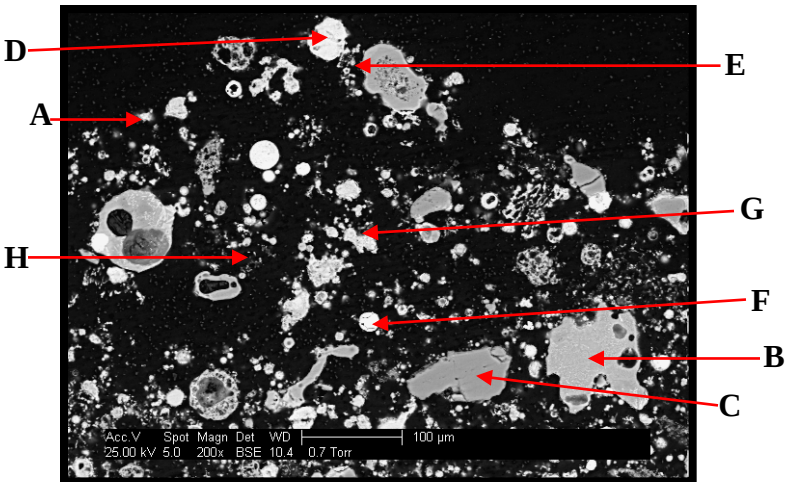

Coal: BEULAH ZAP								
Sleeve Location: OXIDZING TOP #3 (OT3)								
	Label A	Label B	Label C	Label D	Label E	Label F	Label G	Label H
Particle No.	75	845	1071	3	1	935	501	641
Area (μm^2)	100.8	6718	3734	1264	0.4	309.9	492.7	2.8
O	21.9	22.7	25.2	15.3	9.0	13.3	17.6	8.1
Na	0.0	0.0	0.0	1.6	3.3	0.0	1.4	2.3
Mg	0.0	0.0	0.0	8.7	3.2	1.2	7.0	3.3
Al	0.0	19.6	1.2	13.9	4.8	1.9	6.3	5.8
Si	2.7	42.0	69.5	9.3	6.0	3.0	6.1	9.2
P	0.0	0.0	0.0	1.6	4.6	0.0	1.5	3.7
S	32.3	0.0	0.0	6.8	4.6	1.5	19.0	10.2
Cl	0.0	0.0	0.0	0.0	13.5	0.0	1.3	8.8
K	0.0	3.6	0.0	0.0	3.5	0.0	1.1	3.3
Ca	40.9	2.3	0.0	32.1	4.4	2.0	21.2	9.9
Ba	0.0	0.0	0.0	0.0	8.6	0.0	1.4	0.8
Ti	0.0	2.1	0.0	0.0	1.2	0.0	2.9	3.1
Cr	0.0	0.0	1.0	0.0	2.6	0.0	1.2	5.8
Mn	0.0	0.0	0.0	0.0	3.8	0.0	1.1	3.2
Fe	2.1	6.5	1.9	10.8	6.1	77.2	9.7	11.4
Ni	0.0	1.1	1.1	0.0	3.1	0.0	1.1	4.0
Sr	0.0	0.0	0.0	0.0	17.8	0.0	0.0	7.0

Figure 124 - Beulah Zap OT3, 25 kV, Spot Size 5.0, Backscattered Electron (BSE).

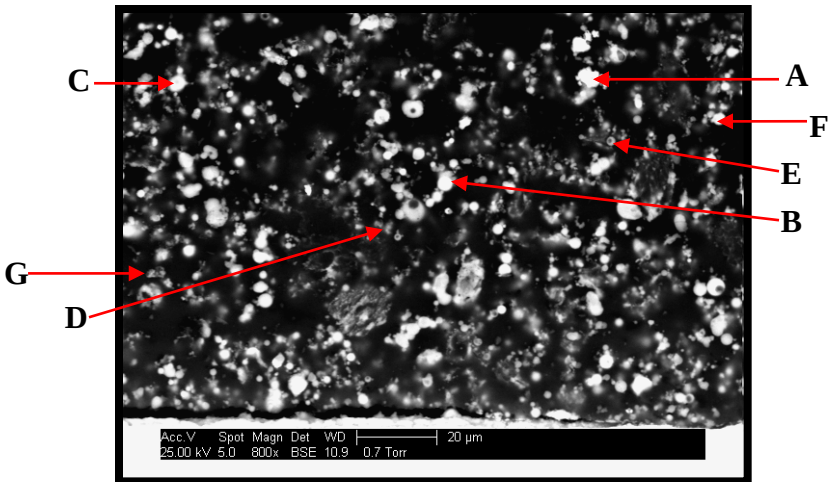

Coal: BEULAH ZAP							
Sleeve Location: REDUCING BOTTOM #3 (RB3)							
	Label A	Label B	Label C	Label D	Label E	Label F	Label G
Particle No.	84	197	83	1351	942	145	1402
Area (μm^2)	36.72	25.85	15.05	0.516	0.629	0.64	0.113
O	29.1	32.6	30.4	21.4	24.0	25.0	37.9
Na	0.0	3.8	1.9	2.7	0.0	0.0	0.0
Mg	3.6	3.7	4.3	2.7	5.6	0.0	0.0
Al	4.6	8.3	6.8	11.1	3.4	2.7	3.6
Si	9.6	14.5	12.7	14.7	5.6	4.7	6.4
P	0.0	0.0	0.0	0.0	0.0	0.0	0.0
S	8.1	0.0	2.8	8.2	18.9	23.0	2.9
Cl	0.0	0.0	0.0	0.0	0.0	0.0	8.7
K	0.0	0.0	0.0	3.1	0.0	0.0	0.0
Ca	23.5	17.6	26.0	16.9	31.5	33.2	7.2
Ba	0.0	0.0	0.0	0.0	0.0	0.0	0.0
Ti	1.5	0.0	0.0	0.0	0.0	0.0	0.0
Cr	3.5	3.2	2.8	3.6	2.0	2.8	6.1
Mn	1.4	0.0	0.0	0.0	0.0	0.0	1.6
Fe	12.1	14.1	12.3	13.8	7.5	8.6	22.3
Ni	3.0	2.2	0.0	1.9	1.5	0.0	3.3
Sr	0.0	0.0	0.0	0.0	0.0	0.0	0.0

Figure 125 - Beulah Zap RB3, 25 kV, Spot Size 5.0, Backscattered Electron (BSE).

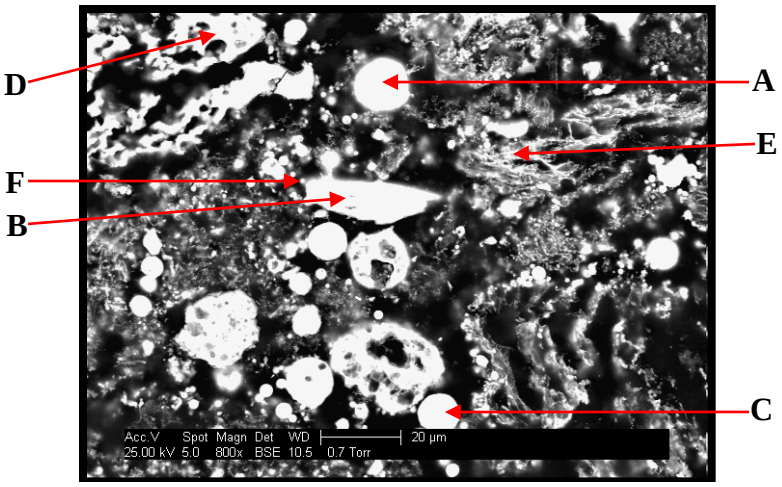

Coal: BEULAH ZAP						
Sleeve Location: REDUCING TOP #5 (RT5)						
	Label A	Label B	Label C	Label D	Label E	Label F
Particle No.	192	388	940	72	1391	1481
Area (μm^2)	137.1	256	92.62	181.9	199.7	0.787
O	24.3	22.1	26.7	27.8	24.8	40.6
Na	0.0	0.0	5.5	3.3	0.0	2.4
Mg	1.7	6.2	0.0	1.8	3.5	2.4
Al	3.5	6.2	25.2	6.2	3.1	5.2
Si	5.4	21.5	29.7	40.8	3.7	26.9
P	0.0	0.0	0.0	0.0	0.0	0.0
S	8.5	1.9	0.0	0.0	10.5	0.0
Cl	1.7	1.7	0.0	0.0	0.0	1.6
K	0.0	1.1	3.5	2.5	0.0	2.8
Ca	7.3	28.3	3.4	10.9	7.8	7.6
Ba	33.2	0.0	0.0	0.0	34.4	0.0
Ti	8.8	0.0	0.0	2.9	6.3	1.2
Cr	0.0	1.8	1.0	0.8	0.0	2.1
Mn	1.9	1.1	0.7	0.0	0.0	1.4
Fe	3.7	6.6	3.1	3.1	3.9	5.8
Ni	0.0	1.5	1.1	0.0	2.0	0.0
Sr	0.0	0.0	0.0	0.0	0.0	0.0

Figure 126 - Beulah Zap RT5, 25 kV, Spot Size 5.0, Backscattered Electron (BSE).

4.3.11.2 Mahoning7A - Individual Particle Analysis

Backscattered electron images of the deposit samples collected from the reducing and oxidizing zones of the BFR burning Mahoning 7A are shown in Figures 129 and 130. The particles in the top probe samples are larger than those in the bottom samples. A higher number of large, non-spherical particles can be found in the bottom deposit samples compared to those at the same location from the Beulah Zap coal. In the reducing samples, the particle size observed on top and bottom of the deposition probe is similar. The layered structure near the center of RB3 and RB6 may be an example of a particle which has oxidized within the porous coal structure under diffusion controlled combustion. This is the dominant mode of combustion when particles oxidize at lower combustion temperatures as would occur after deposition.

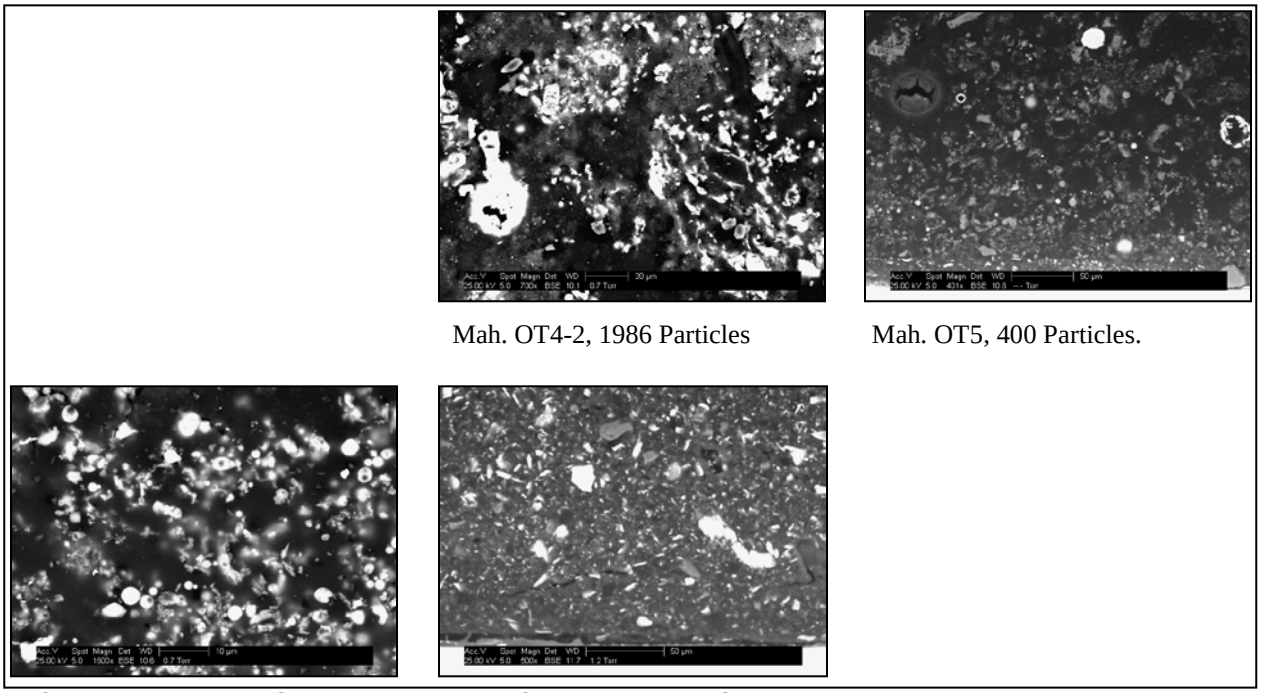

Figure 127 - Backscattered Electron (BSE) Images of Mahoning Oxidizing Deposit Samples.

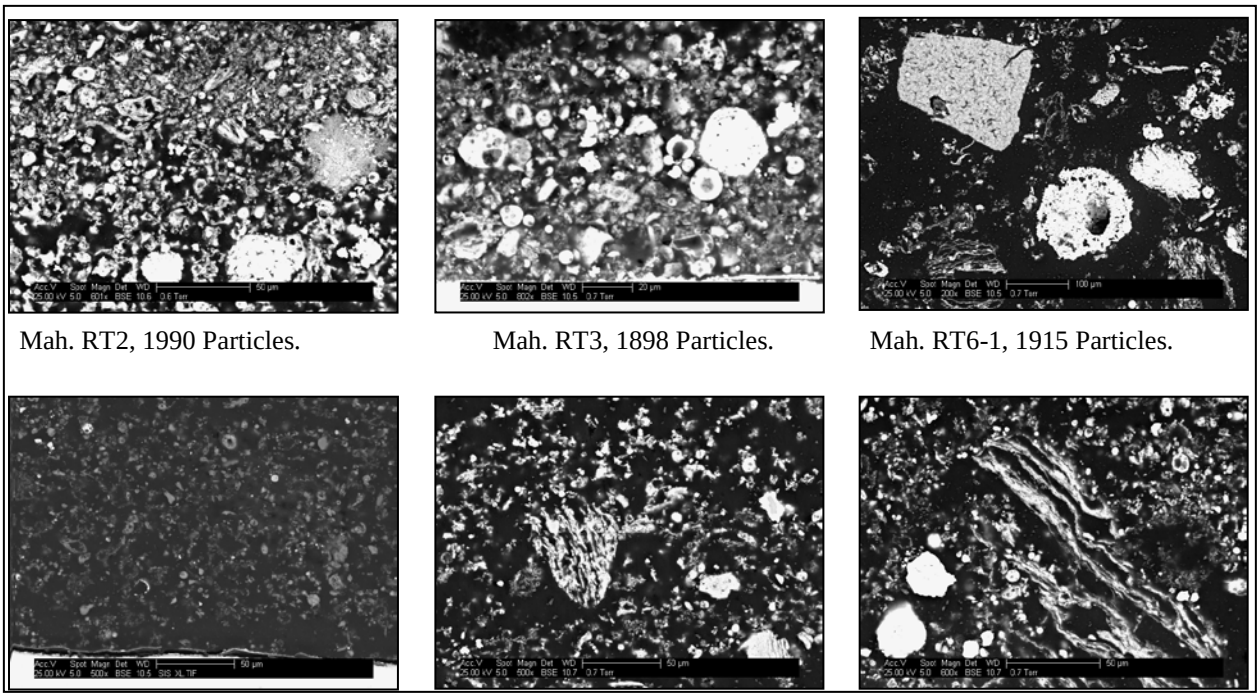

Mah. RT2, 1990 Particles. Mah. RT3, 1898 Particles. Mah. RT6-1, 1915 Particles.

Mah. RB2, 794 Particles. Mah. RB3, 1979 Particles Mah. RB6, 1911 Particles.

Figure 128 - Backscattered Electron (BSE) Images of Mahoning Reducing Deposit Samples.

Individual particles have been analyzed for their compositions as identified in Figures 131-134. The large particle in OT4, labeled as F, is primarily Fe and contains no Cr and little nickel. Particles B and G in OT4 contain relatively large amounts of K (7.4 and 5.8%, respectively). In the deposit sample of RB3, several particles (e.g., G, H, and C) appear to be pieces of a larger particle containing high concentrations of Al and Si. Particle A in the RT3 image adjacent to the surface of the metal sleeve contains sulfur in addition to a large fraction of Fe. Note that the only sulfur-bearing particle in RT3 also contains a significant amount of calcium, indicating a close association of these two elements.

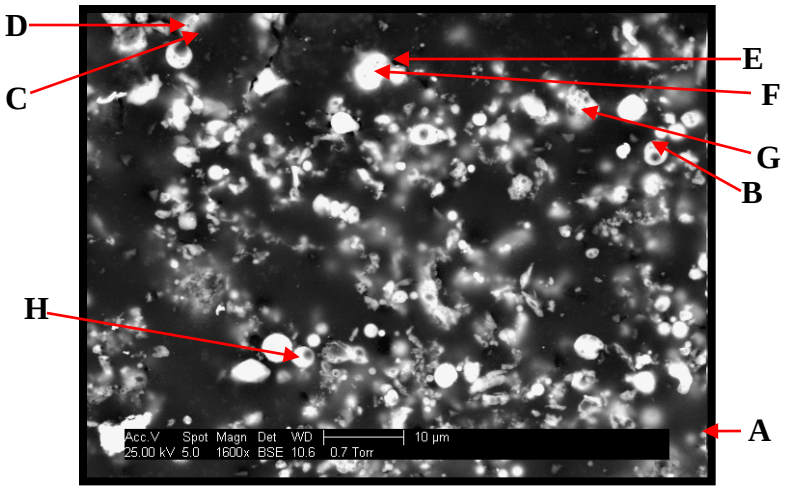

Coal: MAHONING 7A								
Sleeve Location: OXIDZING BOTTOM #1 (OB1)								
	Label A	Label B	Label C	Label D	Label E	Label F	Label G	Label H
Particle No.	1215	1475	2	1	642	36	58	1723
Area (μm^2)	0.046	0.024	0.009	7.2	5.3	18.9	9.9	8.1
O	26.8	12.7	25.9	26.5	27.4	36.9	32.4	28.8
Na	0.0	0.0	0.0	0.0	0.0	0.0	0.0	0.0
Mg	0.0	0.0	0.0	0.0	0.0	0.0	0.0	0.0
Al	18.0	22.0	21.6	16.2	20.6	20.1	25.1	20.3
Si	14.6	30.6	27.7	21.2	24.9	24.6	27.7	26.1
P	0.0	0.0	0.0	0.0	0.0	0.0	0.0	0.0
S	6.7	5.2	0.0	2.0	0.0	0.0	0.0	0.0
Cl	0.0	0.0	5.1	6.3	1.9	0.0	0.0	2.3
K	0.0	3.6	3.2	2.0	3.0	2.4	2.5	2.6
Ca	6.6	6.3	0.0	0.0	0.0	0.0	0.0	0.0
Ba	0.0	0.0	0.0	0.0	0.0	0.0	0.0	0.0
Ti	3.7	2.3	0.0	0.0	1.7	0.0	0.0	0.0
Cr	4.1	2.8	2.6	2.9	2.7	0.0	2.3	4.1
Mn	0.0	0.0	0.0	0.0	0.0	0.0	0.0	0.0
Fe	19.5	13.0	11.4	20.8	16.1	14.9	10.0	13.1
Ni	0.0	1.6	2.5	2.1	1.7	1.2	0.0	2.7
Sr	0.0	0.0	0.0	0.0	0.0	0.0	0.0	0.0

Figure 129 - Mahoning OB1, 25 kV, Spot Size 5.0, Backscattered Electron (BSE).

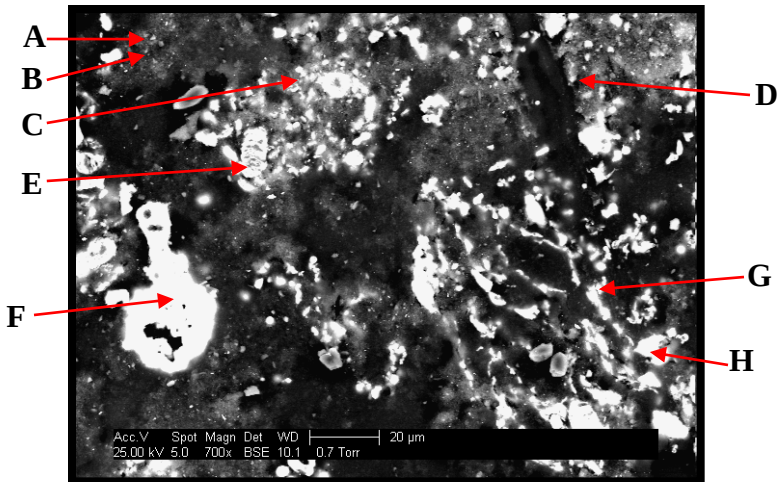

Coal: MAHONING 7A								
Sleeve Location: OXIDZING TOP #4 (OT4)								
	Label A	Label B	Label C	Label D	Label E	Label F	Label G	Label H
Particle No.	898	907	203	197	298	387	467	532
Area (μm^2)	0.131	0.116	0.093	1.48	1.25	705.6	28.88	51.92
O	7.8	4.4	13.1	24.5	57.1	26.6	31.0	43.3
Na	1.4	1.5	3.5	3.4	3.2	1.5	1.8	1.9
Mg	2.4	2.4	0.0	0.0	1.9	1.3	1.7	1.5
Al	10.3	11.4	13.3	11.7	5.5	3.2	16.7	15.3
Si	34.3	36.0	36.9	45.7	11.6	5.0	25.2	25.8
P	4.0	3.4	0.0	0.0	1.6	1.0	1.7	0.0
S	9.8	7.9	4.6	0.0	2.6	1.4	2.5	0.0
Cl	4.3	2.8	11.0	8.5	6.2	2.0	5.1	3.8
K	5.6	7.4	4.8	0.0	2.3	1.3	5.8	5.0
Ca	8.2	8.9	0.0	0.0	1.5	1.2	1.4	0.0
Ba	0.0	0.0	0.0	0.0	0.0	1.4	0.0	0.0
Ti	0.0	0.0	3.2	0.0	1.4	0.6	2.9	0.0
Cr	0.0	0.0	2.2	0.0	1.6	0.7	0.8	0.0
Mn	0.0	0.0	1.8	0.0	0.0	0.0	0.0	0.0
Fe	11.0	12.6	5.7	6.2	3.7	51.8	3.4	3.5
Ni	1.0	1.2	0.0	0.0	0.0	1.0	0.0	0.0
Sr	0.0	0.0	0.0	0.0	0.0	0.0	0.0	0.0

Figure 130 - Mahoning OT4, 25 kV, Spot Size 5.0, Backscattered Electron (BSE).

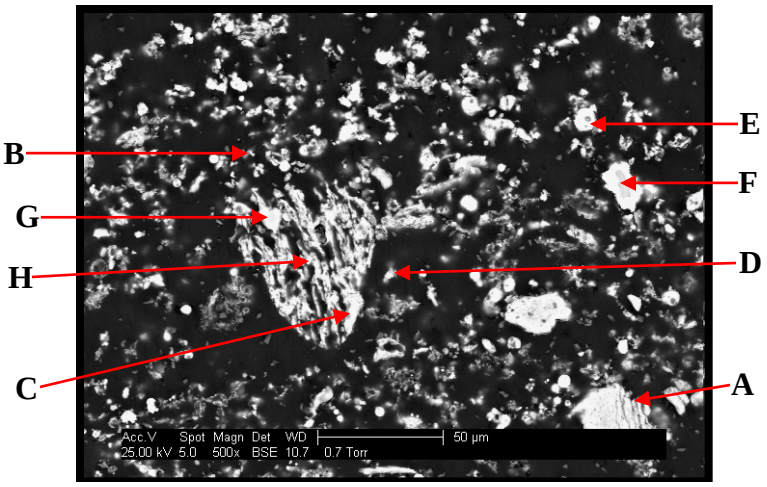

Coal: MAHONING 7A								
Sleeve Location: REDUCING BOTTOM #3 (RB3)								
	Label A	Label B	Label C	Label D	Label E	Label F	Label G	Label H
Particle No.	1016	1527	562	550	196	310	348	435
Area (μm^2)	4.12	0.51	122.9	14.63	73.72	222.7	648.9	365.1
O	29.7	39.4	35.5	42.4	33.3	27.3	38.6	32.3
Na	1.4	0.0	0.8	0.0	0.0	0.0	0.0	1.1
Mg	1.1	0.0	1.3	0.0	0.0	0.0	0.0	1.1
Al	18.6	9.9	21.0	19.7	17.5	1.7	12.0	20.6
Si	20.1	12.1	31.6	23.3	27.9	28.5	40.6	30.6
P	2.2	1.6	0.0	0.0	1.5	0.0	0.0	0.0
S	2.8	1.1	0.0	0.0	0.0	0.0	0.0	0.0
Cl	1.9	11.8	0.0	0.0	0.7	0.0	0.9	0.0
K	4.4	2.6	4.8	3.6	3.9	0.0	2.9	4.5
Ca	5.1	2.3	0.0	0.0	1.2	0.8	0.7	1.0
Ba	3.5	0.0	0.0	0.0	0.0	0.0	0.0	0.0
Ti	1.8	2.0	1.7	0.0	0.6	0.0	2.0	4.9
Cr	1.3	1.6	0.0	0.0	0.0	0.0	0.0	0.0
Mn	0.8	0.0	0.0	0.0	0.0	0.0	0.0	0.8
Fe	5.5	15.6	3.2	11.0	13.2	41.8	2.2	3.2
Ni	0.0	0.0	0.0	0.0	0.0	0.0	0.0	0.0
Sr	0.0	0.0	0.0	0.0	0.0	0.0	0.0	0.0

Figure 131 - Mahoning RB3, 25 kV, Spot Size 5.0, Backscatter Electron (BSE).

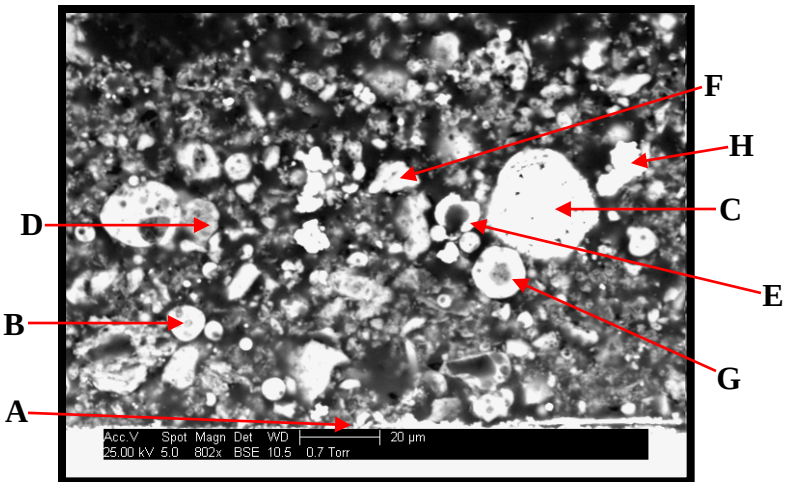

Coal: MAHONING 7A								
Sleeve Location: REDUCING TOP #3 (RT3)								
	Label A	Label B	Label C	Label D	Label E	Label F	Label G	Label H
Particle No.	1327	273	137	790	172	146	212	132
Area (μm^2)	0.035	51.10	535.1	69.11	56.28	53.7	102.9	99.18
O	17.0	33.7	18.5	27.0	31.4	38.8	23.7	22.4
Na	0.0	0.0	1.2	0.0	1.3	0.0	0.0	1.3
Mg	0.0	0.0	0.0	0.0	0.0	0.0	0.0	1.0
Al	10.8	17.3	3.1	26.6	11.7	7.2	16.6	10.5
Si	23.9	22.6	3.2	27.2	23.3	36.8	15.9	10.0
P	0.0	0.0	0.7	0.0	0.0	0.0	0.0	0.7
S	4.5	0.0	0.0	0.0	0.0	0.0	0.0	0.7
Cl	0.0	0.0	0.0	0.0	0.0	0.0	0.0	0.9
K	0.0	3.1	0.0	2.7	2.3	2.4	2.0	1.2
Ca	7.4	0.9	0.0	0.0	0.0	0.0	1.0	1.4
Ba	0.0	0.0	0.0	0.0	0.0	0.0	0.0	0.0
Ti	0.0	1.6	0.0	0.0	0.9	1.8	1.4	1.0
Cr	6.2	2.7	1.5	2.6	2.3	2.1	1.8	1.4
Mn	1.3	0.0	0.9	0.0	0.0	0.0	0.9	0.0
Fe	26.4	16.5	69.7	12.2	26.9	9.7	35.8	46.3
Ni	2.4	1.6	1.3	1.8	0.0	1.2	0.9	1.3
Sr	0.0	0.0	0.0	0.0	0.0	0.0	0.0	0.0

Figure 132 - Mahoning RT3, 25 kV, Spot Size 5.0, Backscatter Electron (BSE).

4.3.11.3 PRB - Deposit Images and Individual Particle Analysis

SEM images of the deposit samples collected from the reducing and oxidizing zones of the BFR burning PRB are shown in Figures 135 and 136. In the oxidizing samples, the particle sizes on top and bottom of the collection probe are similar, suggesting that deposition was fairly uniform. However, the particle sizes of reducing deposit samples are different. The particles are generally larger on the top surface and smaller on the bottom. The RB1 deposit consists of small particles, consistent with the other bottom deposit samples, with the exception of two large particles observed. This deposit also appears to have separated from the metal sleeve, as evident by the gap in this region.

In RT4, two distinct layers of deposit are present. A relatively dense layer, approximately 30 mm thick, covers the metal sleeve. A second layer is present on top, which consists of particles in similar shape and size to the inner layer but apparently of less density. It is speculated that portions of the deposit might have exfoliated from the sleeve surface, followed by re-deposition, resulting in a layered structure.

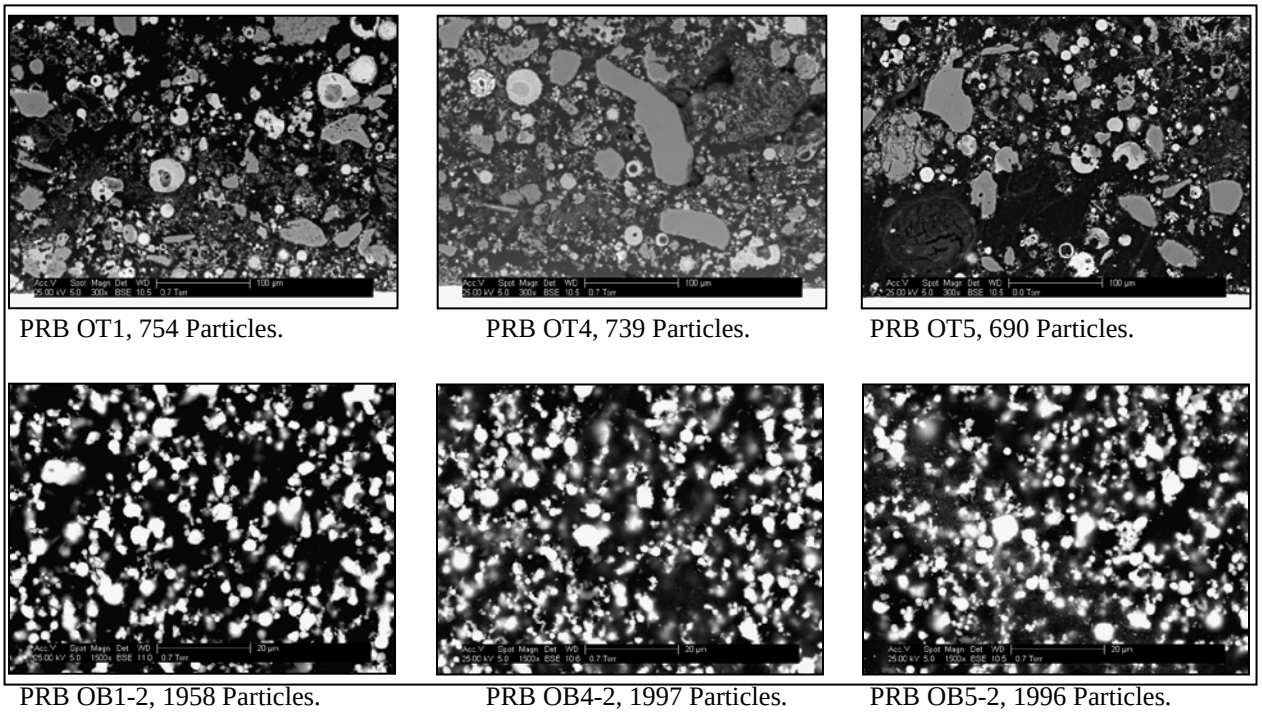

PRB OT1, 754 Particles. PRB OT4, 739 Particles. PRB OT5, 690 Particles.

PRB OB1-2, 1958 Particles. PRB OB4-2, 1997 Particles. PRB OB5-2, 1996 Particles.

Figure 133 - Backscattered Electron (BSE) Images of PRB Oxidizing Deposit Samples.

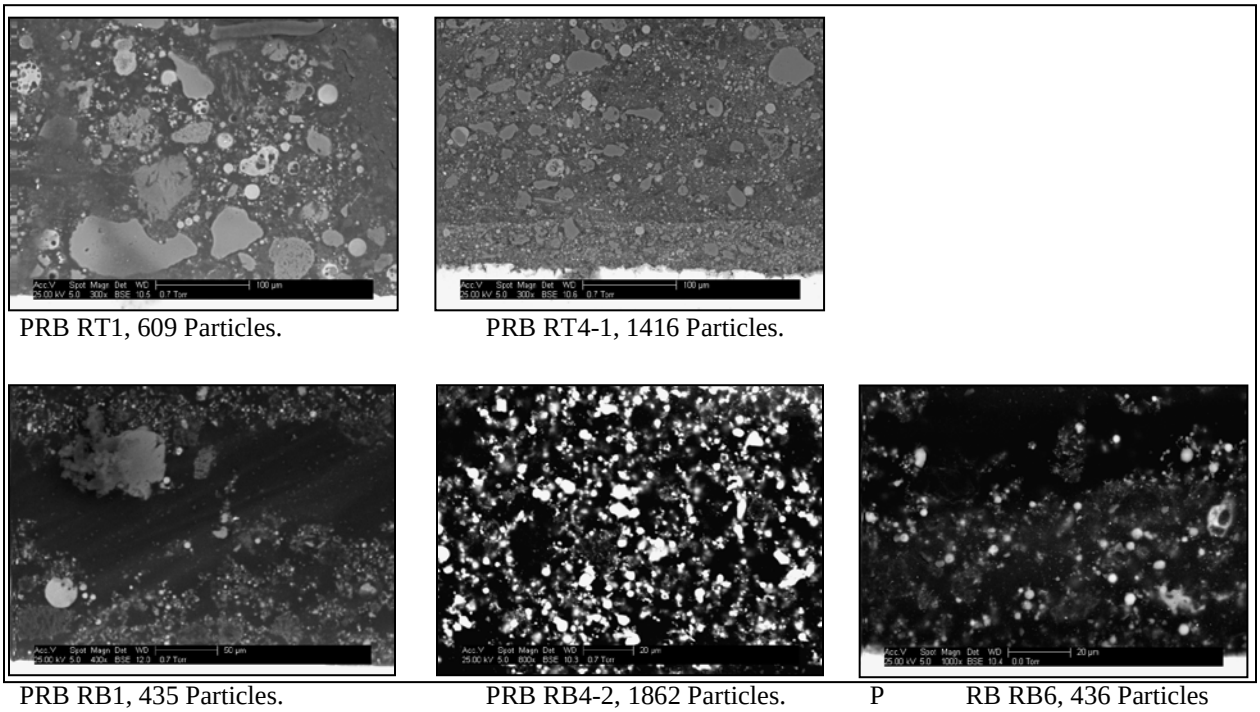

Figure 134 - Backscattered Electron (BSE) Images of PRB Reducing Deposit Samples.

Additional SEM images and elemental analyses of the deposit samples collected from the BFR burning PRB are shown in Figures 137-140. Numerous particles in the oxidizing deposit samples, such as Particles A and B in OB4, show a large amount of sulfur, calcium, and oxygen. Once again, these compositions suggest the presence of $CaSO_4$. The particle with the lowest Ca concentration identified in OB4, i.e., Particle C, is also low in S but high in Si. The large irregular shape of particle B in the top oxidizing sample (OT4) is almost exclusively Si and O. Particles E and F from OT4 are high in signal intensity due to a high concentration of Fe.

In the top reducing sample, most particles are high in Ca. Si, and Fe but low in S, as evident in Particle F. The darkest particles, such as Particle E in RT4, are primarily Si. The medium dark particles, such as Particle D, are a mixture of many different elements, including large Fe, Ca, Si, Al, and Mg.

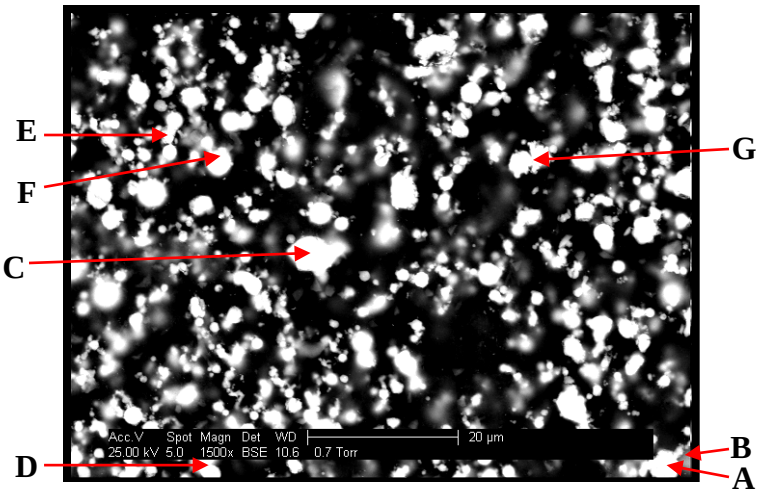

Coal: POWDER RIVER BASIN (PRB-1)								
Sleeve Location: OXIDIZING BOTTOM #4 (OB4)								
	Label A	Label B	Label C	Label D	Label E	Label F	Label G	Label H
Particle No.	491	1148	267	478	135	158	161	301
Area (μm^2)	15.02	0.347	26.74	26.48	10.71	12.46	16.34	13.56
O	24.8	17.2	22.3	25.7	30.2	23.1	30.5	21.8
Na	1.7	0.0	1.7	2.2	2.7	1.3	0.0	2.3
Mg	3.8	5.9	2.2	4.0	4.7	4.6	2.6	3.0
Al	6.5	6.4	6.5	10.7	13.1	8.8	12.2	5.8
Si	6.4	4.9	27.5	8.5	14.4	10.3	5.8	24.0
P	1.4	0.0	1.2	3.2	0.0	1.9	4.1	0.0
S	13.6	21.9	2.0	6.1	3.6	6.0	5.9	2.2
Cl	2.6	0.0	1.5	2.2	0.0	2.2	0.0	1.4
K	2.1	0.0	2.7	1.5	0.0	1.0	0.0	2.2
Ca	21.8	29.0	16.6	21.4	19.1	23.6	22.6	24.4
Ba	0.0	0.0	2.0	0.0	0.0	3.0	2.2	0.0
Ti	1.8	0.0	2.1	2.4	2.3	1.7	1.3	2.1
Cr	2.1	1.3	1.4	2.1	1.4	1.3	1.4	1.6
Mn	1.9	0.0	1.6	0.9	0.0	1.2	1.1	0.9
Fe	9.5	11.9	7.4	9.0	8.5	9.9	8.7	8.3
Ni	0.0	1.6	1.2	0.0	0.0	0.0	1.5	0.0
Sr	0.0	0.0	0.0	0.0	0.0	0.0	0.0	0.0

Figure 135 - PRB OB4-2, 25 kV, Spot Size 5.0, Backscattered Electron (BSE).

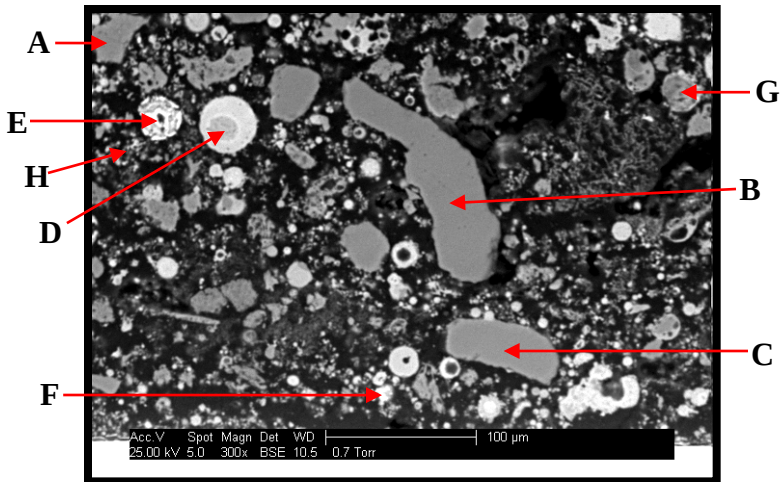

Coal: POWDER RIVER BASIN (PRB-1)								
Sleeve Location: OXIDIZING TOP #4 (OT4)								
	Label A	Label B	Label C	Label D	Label E	Label F	Label G	Label H
Particle No.	1	111	493	138	134	614	129	178
Area (μm^2)	834.7	4738	2390	1306	693.1	208.3	245.1	39.58
O	34.2	34.3	34.9	21.0	21.9	17.4	29.8	24.9
Na	0.7	0.5	0.7	0.5	2.1	1.4	0.9	0.0
Mg	0.8	0.5	0.6	4.3	0.0	1.9	10.1	3.3
Al	2.2	1.2	1.3	10.3	5.7	3.6	4.1	7.4
Si	48.0	53.3	49.1	11.8	8.6	4.8	5.9	7.6
P	0.0	0.0	0.0	1.1	0.0	0.0	0.0	0.0
S	1.3	1.0	0.0	1.1	1.0	3.4	13.8	12.0
Cl	0.0	0.0	0.0	0.7	0.0	0.0	0.0	0.0
K	0.8	0.0	0.7	0.8	0.9	0.0	0.0	0.0
Ca	5.5	1.6	2.5	32.2	4.4	9.7	26.9	27.3
Ba	0.0	1.2	0.0	0.0	1.6	0.0	0.0	0.0
Ti	0.8	0.4	0.6	1.8	0.6	0.0	0.9	0.0
Cr	1.2	1.4	1.9	1.5	1.8	3.9	1.8	1.7
Mn	0.7	0.6	0.6	0.9	0.5	1.1	1.0	0.0
Fe	3.7	3.1	6.3	10.9	50.7	50.8	4.9	14.3
Ni	0.0	1.0	1.0	1.3	0.0	2.0	0.0	1.6
Sr	0.0	0.0	0.0	0.0	0.0	0.0	0.0	0.0

Figure 136 - PRB OT4, 25 kV, Spot Size 5.0, Backscattered Electron (BSE).

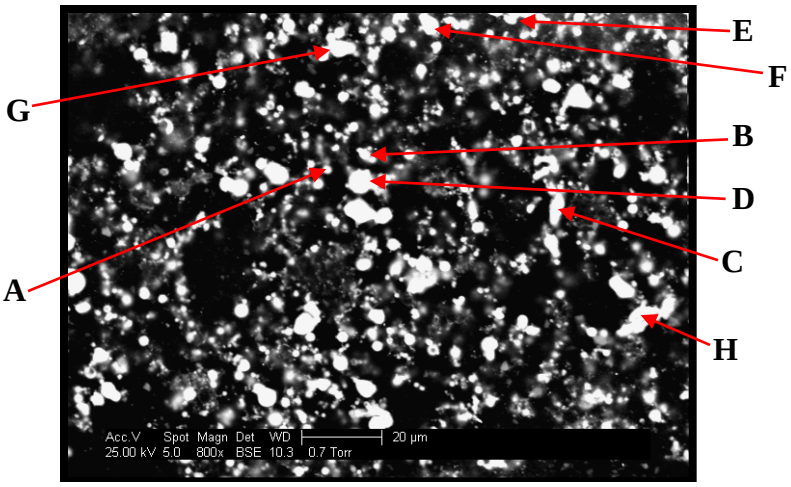

Coal: POWDER RIVER BASIN (PRB-1)								
Sleeve Location: REDUCING BOTTOM #4 (RB4)								
	Label A	Label B	Label C	Label D	Label E	Label F	Label G	Label H
Particle No.	307	277	331	313	9	42	82	525
Area (μm^2)	0.201	10.50	32.05	48.38	84.58	27.53	40.60	64.50
O	16.5	26.1	35.9	30.2	36.5	56.3	39.9	32.0
Na	1.4	1.4	2.2	2.0	2.9	0.0	2.2	2.0
Mg	5.0	4.7	5.1	3.5	1.9	2.5	2.0	2.2
Al	10.5	10.8	9.9	7.9	5.7	7.0	6.7	9.6
Si	9.6	7.8	11.0	8.1	20.9	16.8	20.4	13.7
P	2.5	0.0	1.7	2.0	0.0	0.0	0.0	1.4
S	12.6	13.1	5.9	10.0	1.8	0.0	2.6	3.3
Cl	1.7	0.0	4.3	2.9	1.0	0.0	1.9	2.7
K	1.2	0.0	1.2	1.3	0.7	0.0	0.0	1.5
Ca	24.5	23.9	11.9	19.7	20.4	13.0	18.1	20.0
Ba	1.2	0.0	0.0	1.8	0.0	0.0	0.0	3.1
Ti	1.1	0.0	2.8	1.0	2.8	0.0	1.4	1.3
Cr	0.9	1.2	1.1	1.1	0.6	0.0	0.0	0.9
Mn	0.8	1.1	0.0	0.9	0.7	0.0	0.9	0.0
Fe	9.1	9.9	7.0	7.6	4.1	4.5	3.9	6.2
Ni	1.3	0.0	0.0	0.0	0.0	0.0	0.0	0.0
Sr	0.0	0.0	0.0	0.0	0.0	0.0	0.0	0.0

Figure 137 - PRB RB4-2, 25 kV, Spot Size 5.0, Backscattered Electron (BSE).

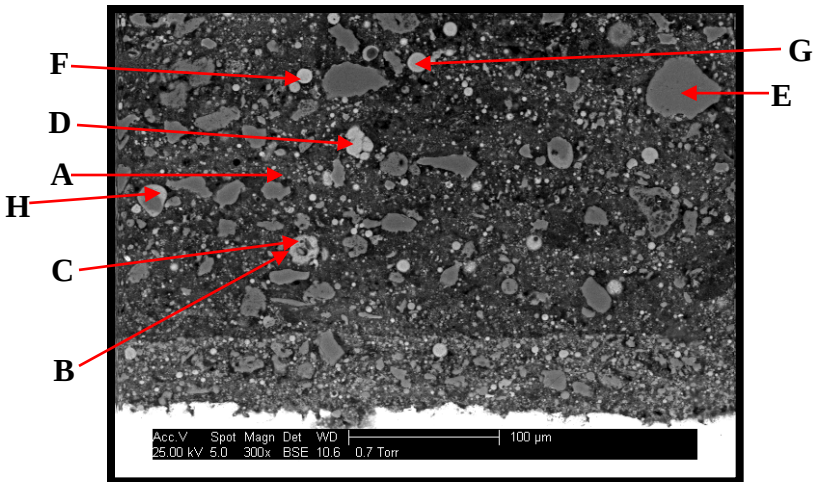

Coal: POWDER RIVER BASIN (PRB-1)								
Sleeve Location: REDUCING TOP #4 (RT4)								
	Label A	Label B	Label C	Label D	Label E	Label F	Label G	Label H
Particle No.	483	697	665	351	267	197	169	531
Area (μm^2)	5.556	9.722	234.0	303.5	923.0	94.44	143.8	93.75
O	18.1	19.4	24.4	20.2	34.0	24.1	26.8	35.6
Na	0.0	0.0	0.0	0.9	0.7	0.0	2.3	0.0
Mg	1.4	1.2	2.0	6.0	0.0	5.0	3.4	4.7
Al	0.0	1.4	4.7	9.5	1.8	7.1	7.1	5.2
Si	5.1	8.6	19.3	9.8	54.2	15.6	15.7	20.3
P	0.0	0.0	0.0	1.3	0.0	0.0	0.0	0.0
S	22.2	17.0	5.1	1.9	0.0	1.4	1.1	0.0
Cl	0.0	0.0	0.0	0.9	0.0	1.1	0.0	0.0
K	0.0	0.0	0.0	0.9	0.0	1.0	0.9	0.8
Ca	44.5	41.7	31.7	30.7	2.9	28.8	17.4	19.1
Ba	0.0	0.0	0.0	0.0	0.0	0.0	0.0	0.0
Ti	0.0	0.0	0.0	2.7	0.6	3.4	15.4	1.7
Cr	1.4	2.0	2.6	1.5	1.6	1.3	1.5	2.9
Mn	0.0	1.0	0.9	0.8	0.0	1.0	0.6	0.0
Fe	7.3	7.6	9.4	11.8	4.2	10.2	7.8	9.8
Ni	0.0	0.0	0.0	1.0	0.0	0.0	0.0	0.0
Sr	0.0	0.0	0.0	0.0	0.0	0.0	0.0	0.0

Figure 138 - PRB RT4, 25 kV, Spot Size 5.0, Backscattered Electron (BSE).

4.3.11.4 Illinois #6-2 - Deposit Images and Individual Particle Analysis

SEM images of the deposit samples collected from the oxidizing and reducing zones of the BFR burning Illinois #6-2 coal are shown in Figures 141 and 142. In the oxidizing deposit samples, the particle size on the top of the collection probe is larger than that of the bottom. In the reducing zone, particles of the deposit samples from top and bottom of the probe look similar. For the top-oxidizing deposit samples, the particles are a mixture of spherical and irregular shapes; while for the bottom reducing samples, the majority of particles are spherical.

The particles in the top-reducing deposit samples are only slightly larger than those in the top-oxidizing samples. The particles in the bottom-reducing samples are smaller and more dispersed. The RB5 sample is thin and only includes fine particles. For RB5, surface roughness is observed on the sleeve surface. Some of the particles in the reducing deposit samples are layered and quite porous.

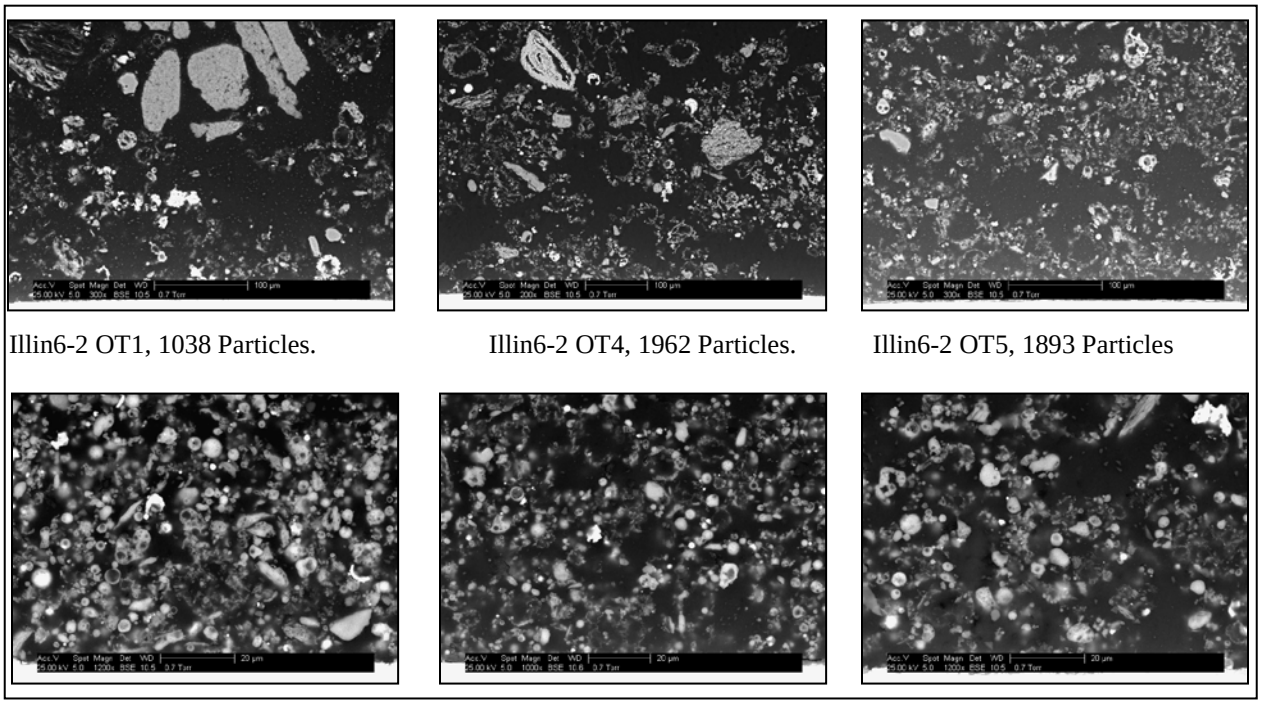

Illin6-2 OT1, 1038 Particles. Illin6-2 OT4, 1962 Particles. Illin6-2 OT5, 1893 Particles

Illin6-2 OB1, 815 Particles. Illin6-2 OB4, 971 Particles. Illin6-2 OB5, 864Particles.

Figure 139 - Backscattered Electron (BSE) Images of Illinois #6-2 Oxidizing Deposit Samples.

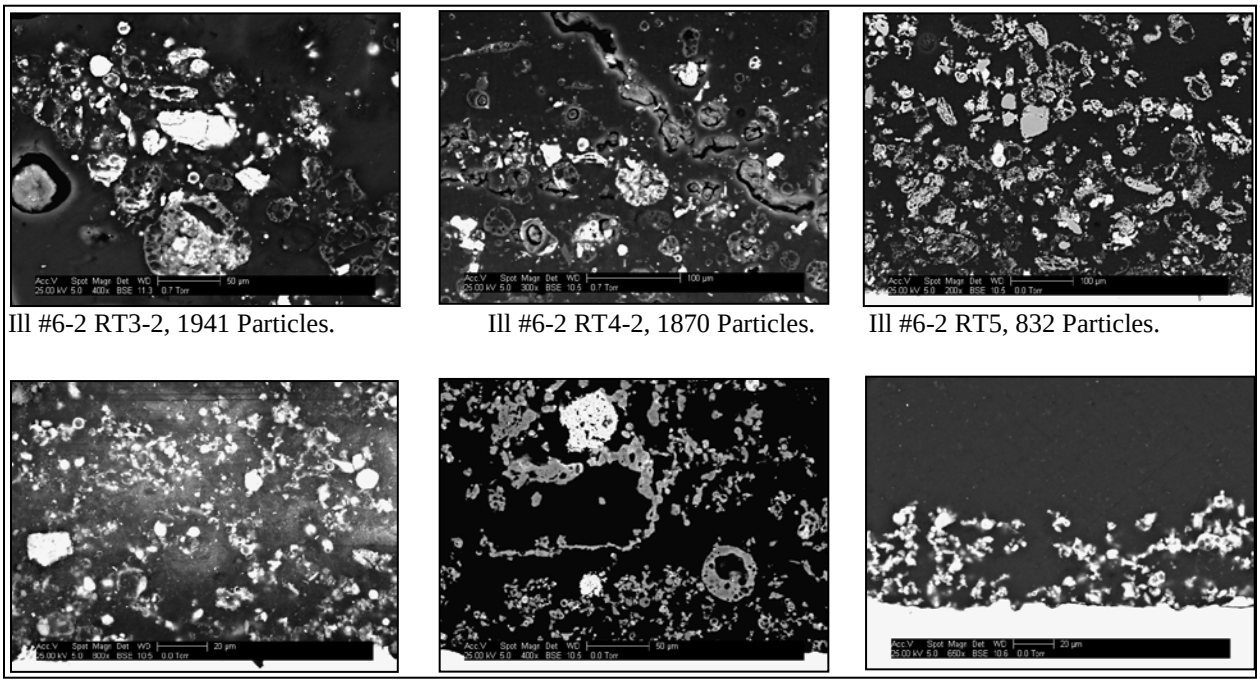

Ill #6-2 RT3-2, 1941 Particles. Ill #6-2 RT4-2, 1870 Particles. Ill #6-2 RT5, 832 Particles.

Ill #6-2 RB3, 543 Particles. Ill #6-2 RB4, 509 Particles. Ill #6-2 RB5, 129 Particles.

Figure 140 - Backscattered Electron (BSE) Images of Illinois #6-2 Reducing Deposit Samples.

Compositions of the individual particles in several deposit samples can be identified in Figures 143-147. Particle A in OB4 is spherical and contains Ca, S, and Fe. The presence of Ca and Fe with S suggests the formation both calcium and iron sulfates. Particle C in OB4 is irregular in shape and consists primarily of Si and O. Particle A in OT4 is relative large and contains primarily Ca, S, and O. Most particles of this composition are small. Particle B in OT4 contains primarily Si, Al, and O but no S.

For the reducing deposit samples, Particle A in RB4 is relatively large and consists primarily of Fe. Most of the other particles in this sample consist primarily of Si, Al, and O. Particle C in RT3 is interesting due to its high Fe and Cr concentrations and irregular shape. This particle is different from Particle A in RB4 that is spherical and contains very little Cr.

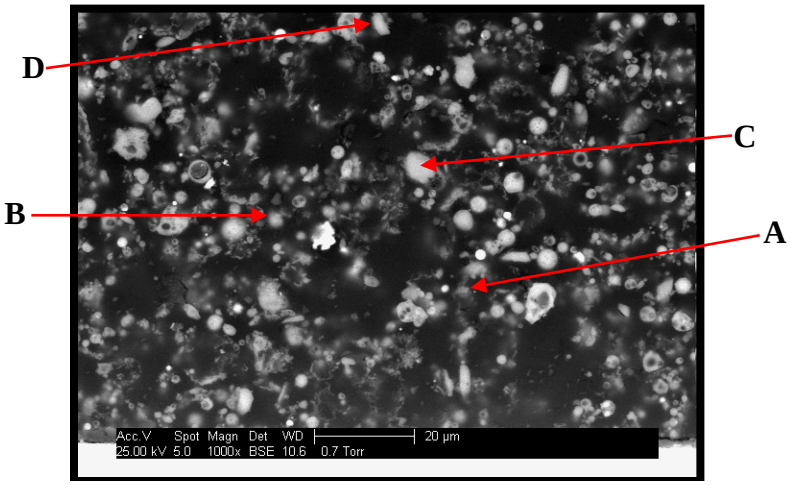

Coal: Illinois #6-2				
Sleeve Location: OXIDIZING BOTTOM #4 (OB4)				
	Label A	Label B	Label C	Label D
Particle No.	555	412	3	241
Area (μm^2)	0.359	3.297	7.391	26.77
O	31.6	12.3	41.2	28.8
Na	1.0	0.0	0.9	0.0
Mg	0.8	0.0	1.0	0.0
Al	3.8	3.8	6.0	9.6
Si	8.9	6.6	30.5	27.5
P	0.0	0.0	0.8	1.2
S	12.7	0.0	1.1	1.4
Cl	0.0	1.2	1.7	2.0
K	1.6	1.2	2.4	3.7
Ca	17.6	1.4	0.9	1.5
Ba	1.3	0.0	0.0	0.0
Ti	0.6	0.9	1.2	0.8
Cr	4.0	3.7	2.8	4.3
Mn	1.0	1.5	0.0	0.0
Fe	13.4	65.3	8.2	17.0
Ni	1.7	2.1	1.2	2.5
Sr	0.0	0.0	0.0	0.0

Figure 141 - Illinois #6-2 OB4, 25 kV, Spot Size 5.0, Backscattered Electron (BSE).

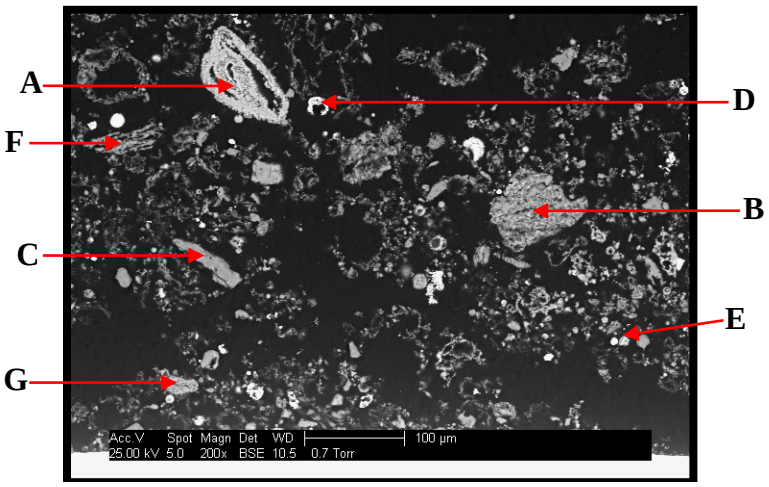

Coal: Illinois #6-2							
Sleeve Location: OXIDIZING TOP #4 (OT4)							
	Label A	Label B	Label C	Label D	Label E	Label F	Label G
Particle No.	76	643	1000	299	1455	471	1080
Area (μm^2)	1608	3158	971.5	224.2	89.84	232.8	1.953
O	26.3	34.0	36.9	26.1	27.0	38.3	27.8
Na	0.0	1.4	6.7	1.1	0.0	1.1	0.0
Mg	0.6	1.1	0.0	0.0	5.0	0.0	0.0
Al	1.4	11.8	11.1	4.6	3.2	8.8	7.1
Si	2.7	33.1	36.2	5.2	6.9	38.6	28.3
P	0.0	0.0	0.0	0.0	0.0	0.0	1.0
S	28.5	0.0	0.0	1.1	13.4	0.8	2.0
Cl	0.0	0.6	0.0	1.1	1.6	0.8	2.9
K	0.0	6.0	2.2	1.2	1.0	4.1	3.4
Ca	34.9	1.2	0.7	1.5	25.7	0.8	2.2
Ba	0.0	0.0	0.0	0.0	1.9	0.0	0.0
Ti	0.7	1.1	0.0	0.8	0.0	1.4	2.0
Cr	1.0	1.4	1.1	1.1	2.8	0.8	3.6
Mn	0.8	0.8	0.6	0.8	1.0	0.0	1.6
Fe	3.1	7.5	4.6	55.3	10.6	4.5	18.1
Ni	0.0	0.0	0.0	0.0	0.0	0.0	0.0
Sr	0.0	0.0	0.0	0.0	0.0	0.0	0.0

Figure 142 - Illinois #6-2 OT4, 25 kV, Spot Size 5.0, Backscattered Electron (BSE).

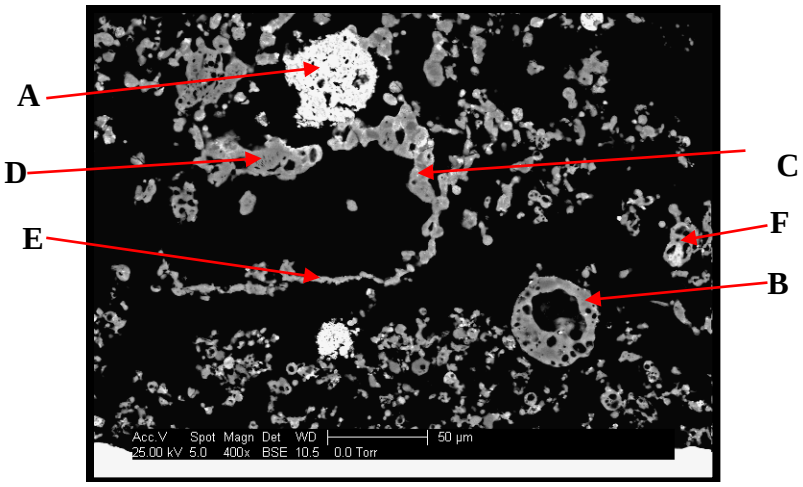

Coal: Illinois #6-2						
Sleeve Location: REDUCING BOTTOM #4 (RB4)						
	Label A	Label B	Label C	Label D	Label E	Label F
Particle No.	23	240	132	150	211	196
Area (μm^2)	1707	182	795.3	282	151.2	206.3
O	19.8	40.4	35.9	43.4	33.5	33.3
Na	1.1	0.0	0.0	1.7	1.7	1.6
Mg	0.0	0.0	0.0	0.0	0.0	1.5
Al	6.5	9.3	10.7	14.8	17.1	15.5
Si	7.7	27.1	18.3	22.2	23.8	24.3
P	0.5	0.0	0.0	0.0	0.5	0.0
S	0.7	0.0	0.0	0.0	0.5	0.0
Cl	0.6	2.1	1.6	2.0	0.9	1.1
K	2.1	5.4	4.6	6.7	6.3	5.7
Ca	0.5	2.5	1.5	1.1	1.4	3.8
Ba	0.0	0.0	0.0	0.0	0.0	0.0
Ti	0.0	0.0	1.0	0.8	1.0	2.7
Cr	0.7	0.0	1.1	0.0	0.9	1.1
Mn	0.0	0.0	0.9	0.0	0.7	0.0
Fe	59.0	13.2	22.9	7.4	11.6	9.4
Ni	1.0	0.0	1.4	0.0	0.0	0.0
Sr	0.0	0.0	0.0	0.0	0.0	0.0

Figure 143 - Illinois #6-2 RB4, 25 kV, Spot Size 5.0, Backscattered Electron (BSE).

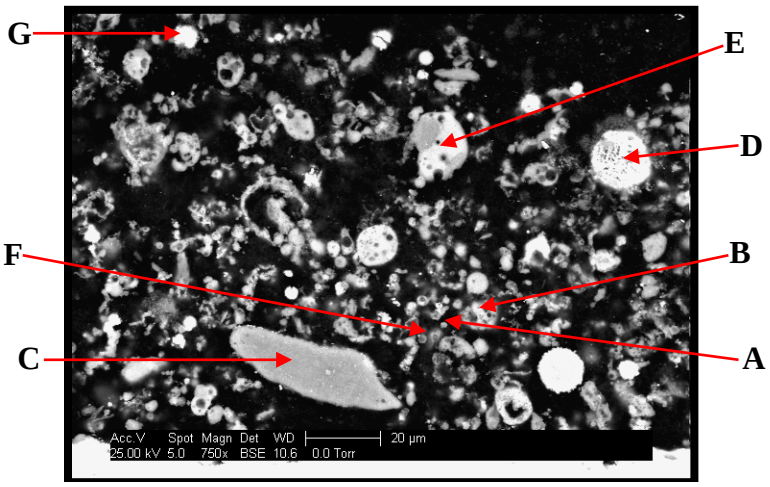

Coal: Illinois #6-2							
Sleeve Location: REDUCING TOP #3 (RT3-1)							
	Label A	Label B	Label C	Label D	Label E	Label F	Label G
Particle No.	353	312	355	113	82	376	10
Area (μm^2)	1.333	5.667	553.3	234.7	224.4	6.667	33.22
O	31.6	24.7	20.5	20.3	44.4	27.4	41.5
Na	0.0	1.8	1.4	1.5	1.5	1.7	1.9
Mg	0.8	3.5	0.0	0.0	0.0	1.0	1.5
Al	1.3	10.7	2.7	7.6	10.4	5.1	3.8
Si	2.3	14.2	4.7	15.2	22.1	6.8	8.5
P	0.0	0.0	0.0	0.0	0.0	0.0	0.0
S	26.1	0.0	0.0	0.9	0.0	14.7	0.0
Cl	1.0	0.0	1.4	1.7	2.8	1.3	3.0
K	0.0	4.0	1.2	2.3	4.5	1.5	1.3
Ca	30.9	1.5	1.0	7.0	5.9	21.3	2.5
Ba	0.0	0.0	0.0	2.7	0.0	1.9	0.0
Ti	0.0	0.0	0.0	0.0	0.0	1.3	3.8
Cr	1.3	0.0	12.3	1.1	0.0	1.4	0.0
Mn	0.0	1.3	1.9	1.0	0.0	1.5	0.0
Fe	4.7	38.3	49.3	38.5	8.5	12.9	32.2
Ni	0.0	0.0	3.5	0.0	0.0	0.0	0.0
Sr	0.0	0.0	0.0	0.0	0.0	0.0	0.0

Figure 144 - Illinois #6-2 RT3-1, 25 kV, Spot Size 5.0, Backscattered Electron (BSE).

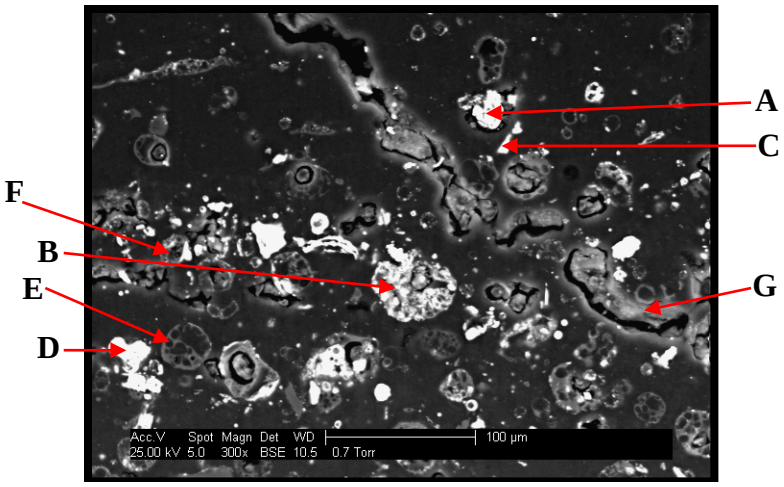

Coal: Illinois #6-2							
Sleeve Location: REDUCING TOP #3 (RT4-2)							
	Label A	Label B	Label C	Label D	Label E	Label F	Label G
Particle No.	83	373	124	602	1545	356	521
Area (μm^2)	343.4	65.1	62.54	612.5	302.9	44.87	83.65
O	24.8	28.4	13.4	17.1	35.5	16.4	15.2
Na	1.1	0.0	0.0	2.4	2.2	0.0	1.4
Mg	1.1	0.0	0.0	1.0	1.9	0.0	1.2
Al	2.4	15.2	0.0	1.3	2.7	9.4	15.6
Si	4.1	26.4	0.0	1.6	4.5	16.9	28.6
P	1.0	0.0	0.0	1.0	2.3	0.0	2.3
S	13.1	3.8	23.6	3.0	17.4	17.2	6.0
Cl	1.0	1.5	0.0	1.3	5.8	1.2	6.5
K	0.6	4.9	0.0	1.1	0.0	1.4	1.8
Ca	40.9	6.7	0.0	0.9	1.8	10.3	1.9
Ba	1.2	0.0	0.0	1.7	5.4	0.0	0.0
Ti	0.5	0.0	0.0	0.5	0.0	0.0	0.8
Cr	1.1	1.4	1.3	1.3	4.9	3.0	4.2
Mn	0.7	0.9	0.0	0.9	1.7	1.4	1.3
Fe	5.4	9.8	60.5	64.2	13.9	21.0	13.0
Ni	0.9	0.9	1.2	0.7	0.0	1.6	0.0
Sr	0.0	0.0	0.0	0.0	0.0	0.0	0.0

Figure 145 - Illinois #6-2 RT4-2, 25 kV, Spot Size 5.0, Backscattered Electron (BSE).

4.3.11.5 Ohio Gatling - Deposit Images and Individual Particle Analysis

SEM images of the deposit samples collected from the top and bottom of the deposition probe in the oxidizing and reducing zones of the BFR burning Gatling are shown in Figures 148 and 149. Particle size of the reducing-top deposit samples is generally larger than that of the bottom-oxidizing samples. A higher number of particles in the top samples are irregular in shape. Several of the images for the top-reducing samples show rounded outlines that appear to have been caused by burnout in the center of the particles.

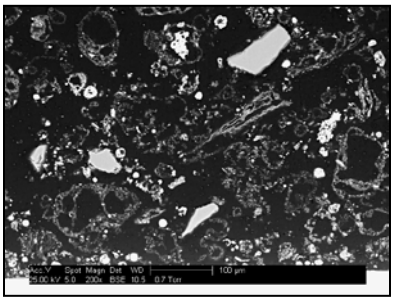

Gatling OT3, 1838 Particles.

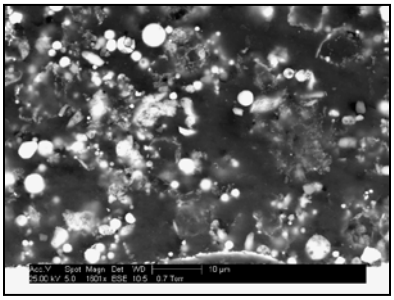

Gatling OB3, 1066 Particles.

Figure 146 - Backscattered Electron (BSE) Images of Gatling Oxidizing Deposit Samples.

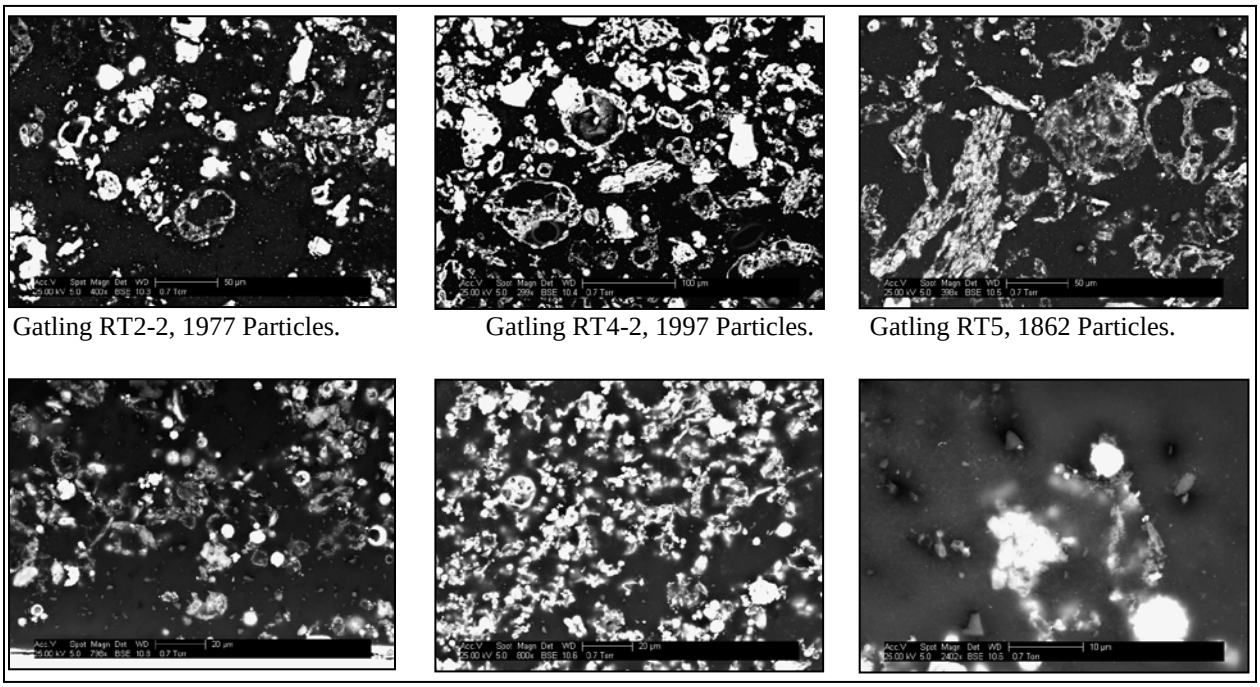

Gatling RT2-2, 1977 Particles. Gatling RT4-2, 1997 Particles. Gatling RT5, 1862 Particles.

Gatling RB2, 1952 Particles. Gatling RB4-2, 1583 Particles. Gatling RB5, 389 Particles.

Figure 147 - Backscattered Electron (BSE) Images of Gatling Reducing Deposit Samples.

The compositions of individual particles can be identified for the Gatling deposit samples shown in Figures 150-152. The Gatling coal produced unique deposit particles not seen from the other coals. Particles B, C, and E in OT3 look similar and contain unusually high Si and O concentrations. Unlike the other coals, no particles in the oxidizing samples contain a high sulfur concentration.

For the reducing RT4-2 sample, Particles A, E, and F are high in S and Fe but contain no Ca. These particles are likely to be iron sulfide. Among the eight coals studied, Gatling has the highest amount of pyritic sulfur in the coal as well as the highest ratio of pyritic to organic sulfur. For the bottom-reducing sample of RB4-2, Particles A, B, and C contain primarily S, Ca, and Fe. Particle G in RB4-2 contains a measureable amount of Na and K as well.

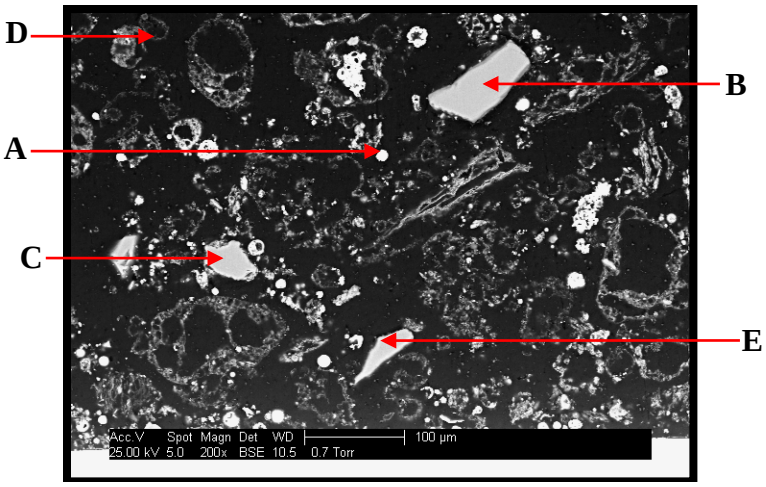

Coal: GATLING					
Sleeve Location: OXIDIZING TOP #3 (OT3)					
	Label A	Label B	Label C	Label D	Label E
Particle No.	393	118	599	1714	580
Area (μm^2)	77.03	3551	1311	0.568	503
O	38.7	34.7	35.2	20.2	34.0
Na	0.0	0.0	0.0	0.0	0.0
Mg	7.0	0.0	0.0	0.0	0.0
Al	0.0	0.8	1.1	3.4	1.7
Si	2.9	60.0	58.0	4.7	60.0
P	0.0	0.0	0.0	0.0	0.0
S	27.5	0.0	0.0	0.0	0.0
Cl	0.0	0.0	0.0	0.0	0.0
K	0.0	0.0	0.0	0.0	0.0
Ca	19.3	0.0	0.0	0.0	0.0
Ba	0.0	0.0	0.0	0.0	0.0
Ti	0.0	0.0	0.0	0.0	0.0
Cr	0.0	0.9	0.9	0.0	0.0
Mn	0.0	0.6	0.7	0.0	1.2
Fe	3.8	2.1	3.3	71.0	3.1
Ni	0.9	0.9	0.8	0.8	0.0
Sr	0.0	0.0	0.0	0.0	0.0

Figure 148 - Gatling OT3, 25 kV, Spot Size 5.0, Backscattered Electron (BSE).

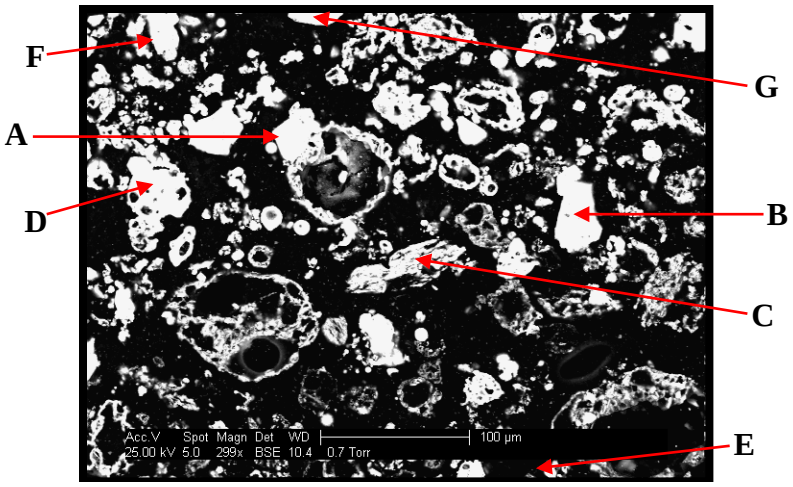

Coal: GATLING							
Sleeve Location: REDUCING TOP #4 (RT4-2)							
	Label A	Label B	Label C	Label D	Label E	Label F	Label G
Particle No.	162	259	323	141	851	49	3
Area (μm^2)	1622	1145	1224	2387	7.071	419.9	1325
O	14.4	37.0	33.1	21.6	6.7	8.8	34.5
Na	0.0	0.0	0.0	0.0	0.0	0.0	0.0
Mg	0.0	0.0	0.0	0.0	0.0	0.0	0.0
Al	12.4	1.6	21.7	15.3	0.0	6.2	1.0
Si	15.8	59.2	36.5	21.1	0.0	5.8	62.5
P	0.0	0.0	0.0	0.0	0.0	0.0	0.0
S	22.7	0.0	0.0	9.9	33.4	29.7	0.0
Cl	0.0	0.0	0.0	0.0	0.0	0.0	0.0
K	0.0	0.0	3.5	2.0	0.0	0.0	0.0
Ca	0.0	0.0	0.0	1.9	0.0	0.0	0.0
Ba	0.0	0.0	0.0	0.0	0.0	0.0	0.0
Ti	0.0	0.0	0.0	0.0	0.0	0.0	0.0
Cr	0.0	0.0	0.0	0.0	0.0	0.0	0.0
Mn	0.0	0.0	0.0	0.0	0.0	0.0	0.0
Fe	34.8	2.2	5.2	28.3	56.2	49.5	2.0
Ni	0.0	0.0	0.0	0.0	0.0	0.0	0.0
Sr	0.0	0.0	0.0	0.0	3.7	0.0	0.0

Figure 149 - Gatling RT4-2, 25 kV, Spot Size 5.0, Backscattered Electron (BSE).

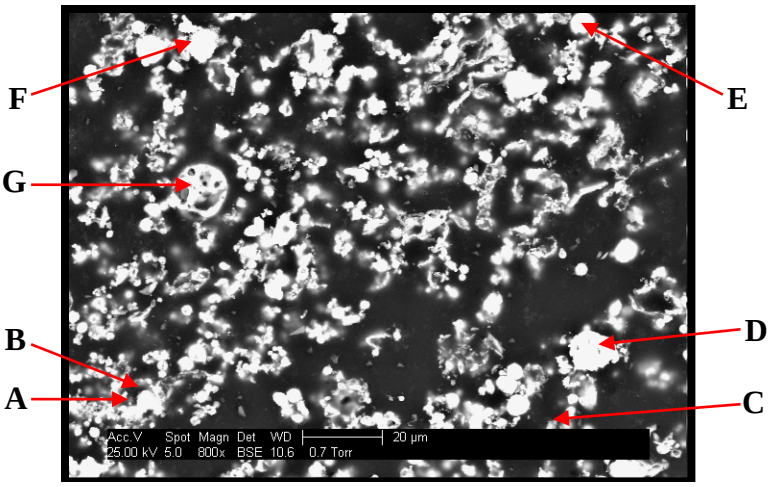

Coal: GATLING							
Sleeve Location: REDUCING BOTTOM #4 (RB4-2)							
	Label A	Label B	Label C	Label D	Label E	Label F	Label G
Particle No.	480	1396	495	383	4	31	206
Area (μm^2)	0.455	8.274	4.773	108.7	124.4	124.3	138.9
O	29.5	33.0	23.9	27.2	34.2	27.5	34.9
Na	0.0	0.0	0.0	0.0	0.0	1.3	1.5
Mg	0.0	0.0	0.0	0.9	0.0	1.4	1.6
Al	6.3	9.1	5.1	5.1	14.0	4.0	17.7
Si	9.2	12.0	7.4	6.3	19.7	5.1	23.6
P	0.0	0.0	0.0	0.0	0.0	1.2	0.0
S	13.3	10.1	16.4	0.0	0.0	1.2	0.0
Cl	0.0	0.0	3.2	0.9	1.7	2.2	1.9
K	0.0	0.0	0.0	0.0	2.2	1.2	3.8
Ca	24.4	22.7	30.4	0.0	2.9	1.2	1.0
Ba	2.8	0.0	0.0	0.0	0.0	0.0	0.0
Ti	0.0	1.0	0.0	0.0	0.9	1.0	1.2
Cr	1.1	0.8	0.0	0.9	1.3	1.2	1.5
Mn	0.0	0.0	1.8	0.0	0.8	0.9	0.9
Fe	12.6	10.2	11.9	57.6	22.4	50.7	10.4
Ni	0.9	1.1	0.0	1.0	0.0	0.0	0.0
Sr	0.0	0.0	0.0	0.0	0.0	0.0	0.0

Figure 150 - Gatling RB4-2, 25 kV, Spot Size 5.0, Backscattered Electron (BSE).

4.3.11.6 Indiana #6 Gibson - Deposit Images and Individual Particle Analysis

Backscattered electron micrographs showing the deposit samples obtained from the top and bottom sleeves of the deposition probe in the oxidizing and reducing zones of the BFR for the Indiana coal are shown in Figures 153 and 154. As with the other coals, the particles on the bottom of the oxidizing sleeve are the smallest and most uniform in size and shape. The images of particles deposited on the top of the reducing sleeves from this coal are different from those of the other coals. There are fewer large irregular particles and less overall population. The deposit samples on the sleeves from the top of the reducing probe appear to have been lost before epoxy mounting. Therefore, only a thin layer of particles and pieces of deposit remained, making the SEM analysis difficult.

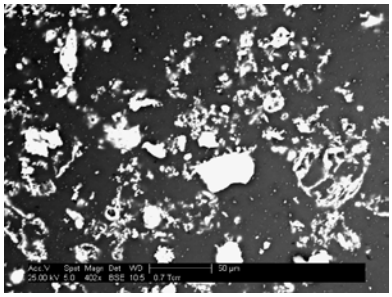

Indiana OT4, 1966 Particles.

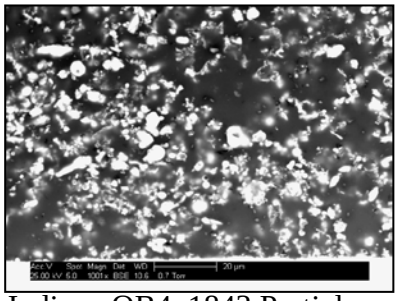

Indiana OB4, 1843 Particles.

Figure 151 - Backscattered Electron (BSE) Images of Indiana Oxidizing Deposit Samples.

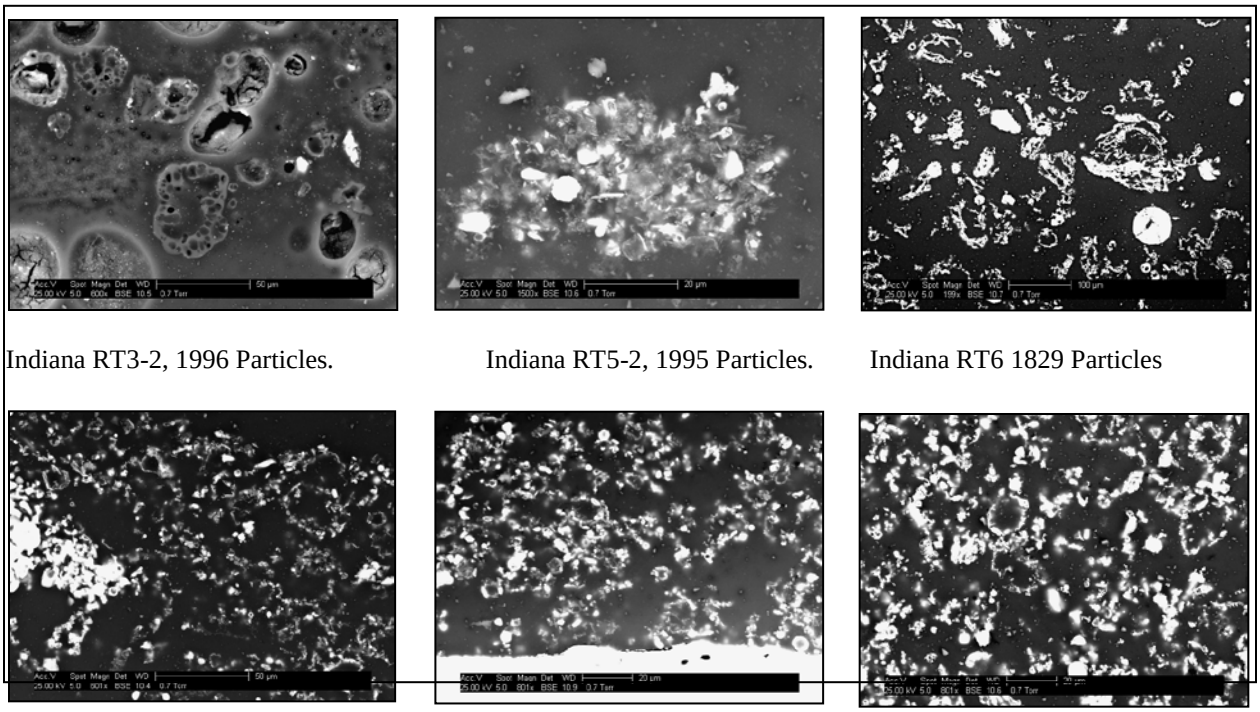

Indiana RT3-2, 1996 Particles. Indiana RT5-2, 1995 Particles. Indiana RT6 1829 Particles

Indiana RB3, 1895 Particles. Indiana RB5, 1947 Particles. Indiana RB6, 1800 Particles.

Figure 152 - Backscattered Electron (BSE) Images of Indiana Reducing Deposit Samples.

Additional SEM images identifying individual particles are shown in Figures 155-159. As with all other coals, examples of sulfur-containing particles, such as Particles A and B in OB4, also contain Fe and Ca; whereas particles that are sulfur-free, such as C and D in OB4, are free of Ca. Therefore, calcium appears to be associated with sulfur. In deposit OT4, Particle D contains a high concentration of Fe but no Cr, suggesting that this particle was not a contaminant from the metal sleeve but was part of the coal ash. For the reducing samples, Particle D in RB3, is representative of most particles, containing 4.5% K along with high concentrations of Si and Al. When the K concentration is high, the Ti concentration is also noticeable. It is possible that K is closely associated with Ti as a complex oxide compound.

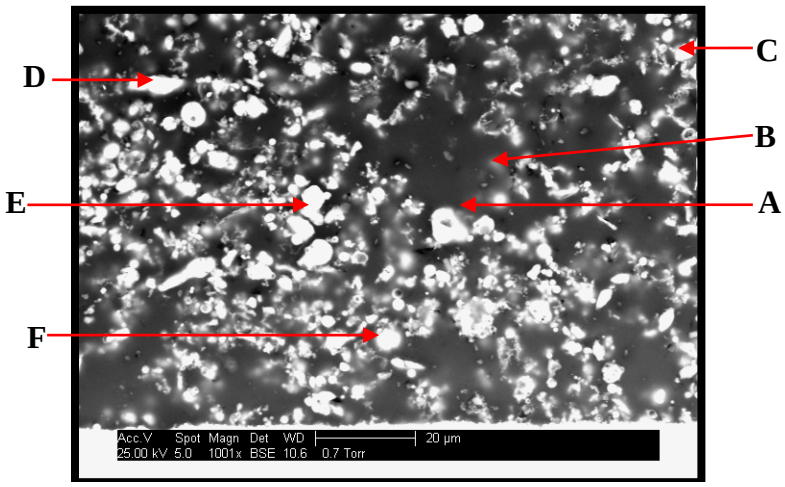

Coal: INDIANA #6						
Sleeve Location: OXIDIZING BOTTOM #4 (OB4)						
	Label A	Label B	Label C	Label D	Label E	Label F
Particle No.	1744	1713	4	151	295	521
Area (μm^2)	0.064	0.178	14.98	27.93	27.44	18.94
O	28.0	28.2	34.8	37.3	23.3	24.2
Na	0.0	0.0	0.0	0.0	0.0	1.6
Mg	0.0	0.0	0.0	0.0	1.0	0.0
Al	16.3	10.3	16.2	5.1	10.2	11.6
Si	21.4	21.3	29.8	42.4	13.0	15.1
P	0.0	0.0	0.0	1.6	0.0	0.0
S	6.8	5.6	0.0	0.0	0.0	0.0
Cl	0.0	1.6	0.0	1.0	1.1	1.7
K	3.8	3.3	4.2	1.2	2.0	2.9
Ca	7.4	6.3	0.0	0.0	0.8	1.4
Ba	0.0	0.0	0.0	0.0	0.0	0.0
Ti	0.0	1.4	0.0	0.8	0.9	0.0
Cr	2.5	3.4	2.0	2.0	2.2	3.8
Mn	0.0	1.0	0.9	0.0	0.0	0.0
Fe	12.0	15.1	10.6	7.4	45.5	35.0
Ni	1.8	2.5	1.5	1.1	0.0	2.7
Sr	0.0	0.0	0.0	0.0	0.0	0.0

Figure 153 - Indiana OB4, 25 kV, Spot Size 5.0, Backscattered Electron (BSE).

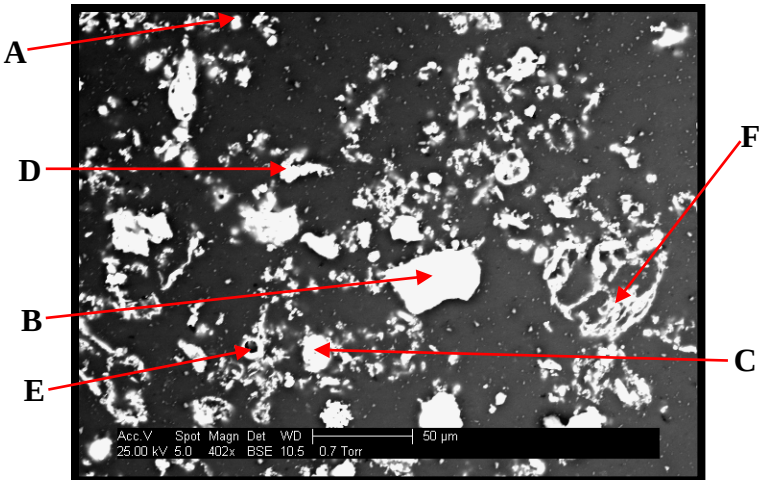

Coal: INDIANA #6						
Sleeve Location: OXIDIZING TOP #4 (OT4)						
	Label A	Label B	Label C	Label D	Label E	Label F
Particle No.	42	332	374	182	349	307
Area (μm^2)	26.22	446	303.2	173.2	162.8	904.3
O	34.0	37.4	19.8	23.9	38.3	33.5
Na	0.0	0.0	1.3	1.3	0.0	2.1
Mg	0.0	0.0	0.8	0.9	2.6	0.0
Al	10.8	0.0	5.8	5.0	12.5	17.3
Si	19.4	59.5	7.2	7.2	20.4	28.3
P	0.0	0.0	1.1	0.0	0.0	0.0
S	12.3	0.0	0.8	0.0	0.0	0.0
Cl	0.0	0.0	1.5	0.0	2.2	2.4
K	2.8	0.0	1.6	1.3	4.5	4.2
Ca	16.9	0.0	0.8	0.0	0.0	0.0
Ba	0.0	0.0	0.0	0.0	0.0	0.0
Ti	0.0	0.0	0.7	0.0	0.0	0.0
Cr	0.0	0.0	0.9	0.0	0.0	0.0
Mn	0.0	0.6	0.9	0.0	0.0	0.0
Fe	3.7	1.9	55.8	59.1	17.8	10.2
Ni	0.0	0.7	0.9	1.1	1.7	2.0
Sr	0.0	0.0	0.0	0.0	0.0	0.0

Figure 154 - Indiana OT4, 25 kV, Spot Size 5.0, Backscattered Electron (BSE).

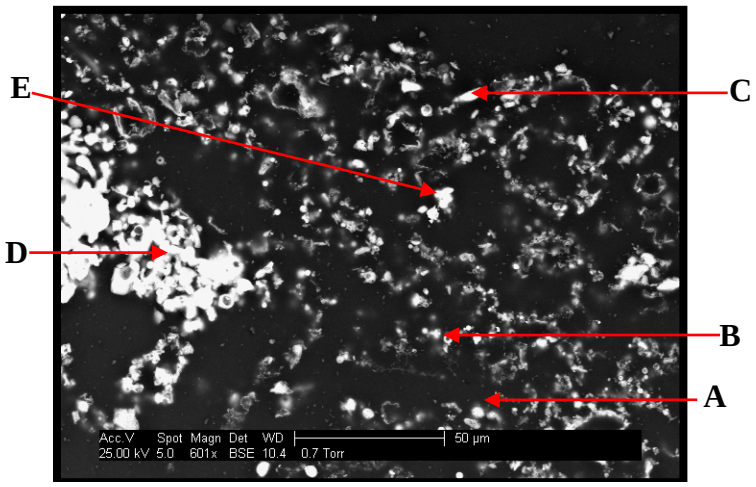

Coal: INDIANA #6					
Sleeve Location: REDUCING BOTTOM #3 (RB3)					
	Label A	Label B	Label C	Label D	Label E
Particle No.	1654	1434	92	286	272
Area (μm^2)	0.095	0.894	24.15	814.5	28.26
O	22.2	21.8	39.0	34.9	15.5
Na	1.5	1.1	0.0	0.0	1.2
Mg	1.2	1.3	0.0	0.0	0.0
Al	8.9	6.9	2.5	13.6	3.5
Si	10.7	8.4	52.5	36.8	5.5
P	1.6	1.6	0.0	0.0	0.8
S	8.9	9.3	0.0	0.0	0.8
Cl	2.5	2.6	0.0	0.0	1.2
K	2.6	1.8	0.0	4.6	1.0
Ca	21.5	28.4	0.0	0.0	1.4
Ba	0.0	0.0	0.0	0.0	0.0
Ti	1.7	1.9	0.0	1.2	0.0
Cr	2.4	3.4	1.0	0.0	0.0
Mn	1.6	1.0	0.7	0.0	0.0
Fe	10.5	8.4	3.4	9.0	69.1
Ni	2.2	2.0	0.9	0.0	0.0
Sr	0.0	0.0	0.0	0.0	0.0

Figure 155 - Indiana RB3, 25 kV, Spot Size 5.0, Backscattered Electron (BSE).

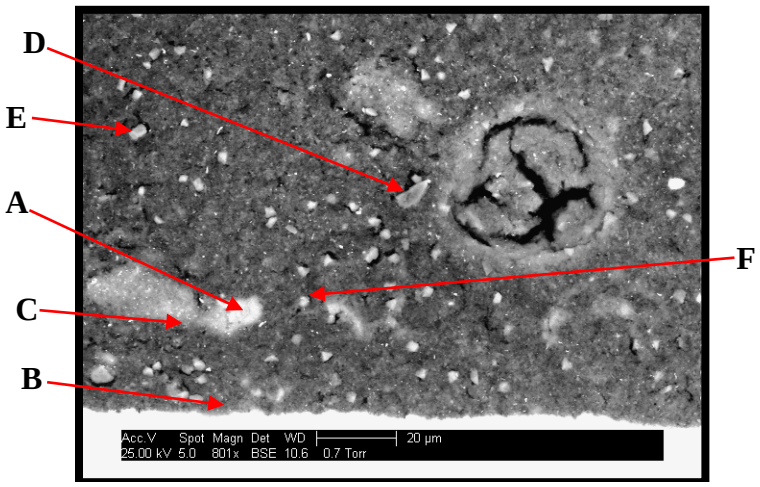

Coal: INDIANA #6						
Sleeve Location: REDUCING TOP #3 (RT3-1)						
	Label A	Label B	Label C	Label D	Label E	Label F
Particle No.	503	659	540	329	1162	499
Area (μm^2)	56.53	0.047	0.136	2.177	6.098	1.851
O	44.7	5.7	6.2	35.3	53.8	26.3
Na	0.0	0.0	0.0	2.6	0.0	2.3
Mg	0.0	0.0	0.0	0.0	0.0	0.0
Al	0.0	0.0	1.5	1.4	0.0	14.7
Si	16.6	7.7	73.6	29.7	12.3	29.8
P	0.0	0.0	0.0	1.6	0.0	0.0
S	0.0	15.8	0.0	1.6	0.0	0.0
Cl	3.1	0.0	0.0	3.3	3.3	1.6
K	0.0	0.0	1.0	0.9	0.0	3.6
Ca	0.0	0.0	0.7	0.8	1.2	0.0
Ba	0.0	0.0	0.0	0.0	0.0	0.0
Ti	0.0	0.0	0.0	0.0	1.5	0.0
Cr	7.3	22.4	3.2	4.8	6.4	3.9
Mn	1.7	1.6	1.2	1.4	1.8	1.4
Fe	23.1	42.7	11.0	14.3	19.7	14.5
Ni	3.6	4.2	1.5	2.2	0.0	1.8
Sr	0.0	0.0	0.0	0.0	0.0	0.0

Figure 156 - Indiana RT3-1, 25 kV, Spot Size 5.0, Backscattered Electron (BSE).

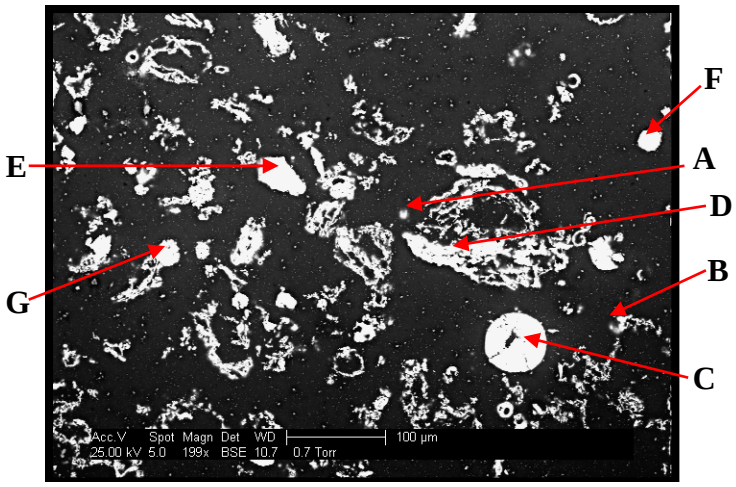

Coal: INDIANA #6							
Sleeve Location: REDUCING TOP #6 (RT6)							
	Label A	Label B	Label C	Label D	Label E	Label F	Label G
Particle No.	387	605	574	428	295	239	460
Area (μm^2)	47.6	9.749	2837	2043	1198	417.9	972.7
O	24.6	19.7	18.2	26.3	38.7	40.6	20.8
Na	0.0	0.0	0.0	0.0	0.0	0.0	0.8
Mg	0.0	0.0	0.0	0.0	0.0	0.0	0.9
Al	0.0	2.5	0.0	8.4	1.5	1.5	7.3
Si	4.5	7.1	1.5	22.4	58.2	53.8	11.1
P	1.4	1.5	0.0	0.0	0.0	0.0	0.0
S	27.0	21.8	0.0	0.0	0.0	0.0	0.0
Cl	1.6	1.7	0.0	0.0	0.0	0.0	0.0
K	0.0	1.7	0.0	2.2	0.0	0.7	1.4
Ca	36.8	33.9	0.0	0.0	0.0	0.5	0.0
Ba	0.0	0.0	0.0	0.0	0.0	0.0	0.0
Ti	0.0	3.3	0.0	2.9	0.0	0.4	0.0
Cr	0.0	1.3	0.0	0.0	0.0	0.5	0.8
Mn	0.0	1.2	0.0	0.0	0.0	0.7	0.7
Fe	2.9	3.3	80.4	37.0	1.5	1.3	56.3
Ni	1.2	0.9	0.0	0.9	0.0	0.0	0.0
Sr	0.0	0.0	0.0	0.0	0.0	0.0	0.0

Figure 157 - Indiana RT6, 25 kV, Spot Size 5.0, Backscattered Electron (BSE).

4.3.11.7 Kentucky #11 - Deposit Images and Individual Particle Analysis

The backscattered electron images of Kentucky deposit samples collected from the top and bottom of the deposition probe in the oxidizing and reducing zones of the BFR are shown in Figures 160 and 161. The general appearances of these deposit particles are consistent with those of the other coals. The particles in the bottom-oxidizing samples are the smallest and most spherical, while those in the top-reducing samples are the largest and most irregular. Many coal particles in the top-reducing samples appear to have been oxidized by a diffusion controlled combustion process, thus creating a skeleton of these particles. The particles in the bottom-oxidizing sample might have melted and coalesced into spheres.

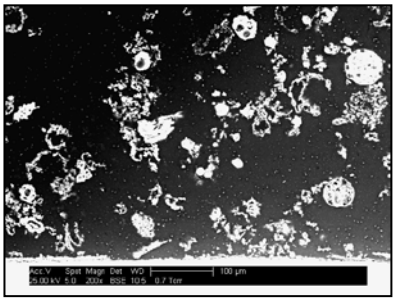

Kentucky OT3, 1352 Particles.

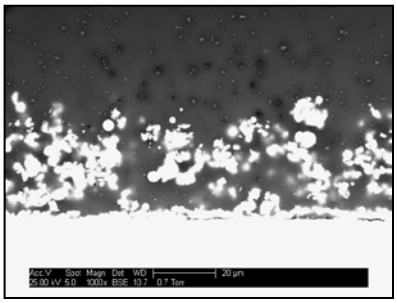

Kentucky OB3, 1538 Particles

Figure 158 - Backscattered Electron (BSE) Images of Kentucky Oxidizing Deposit Samples.

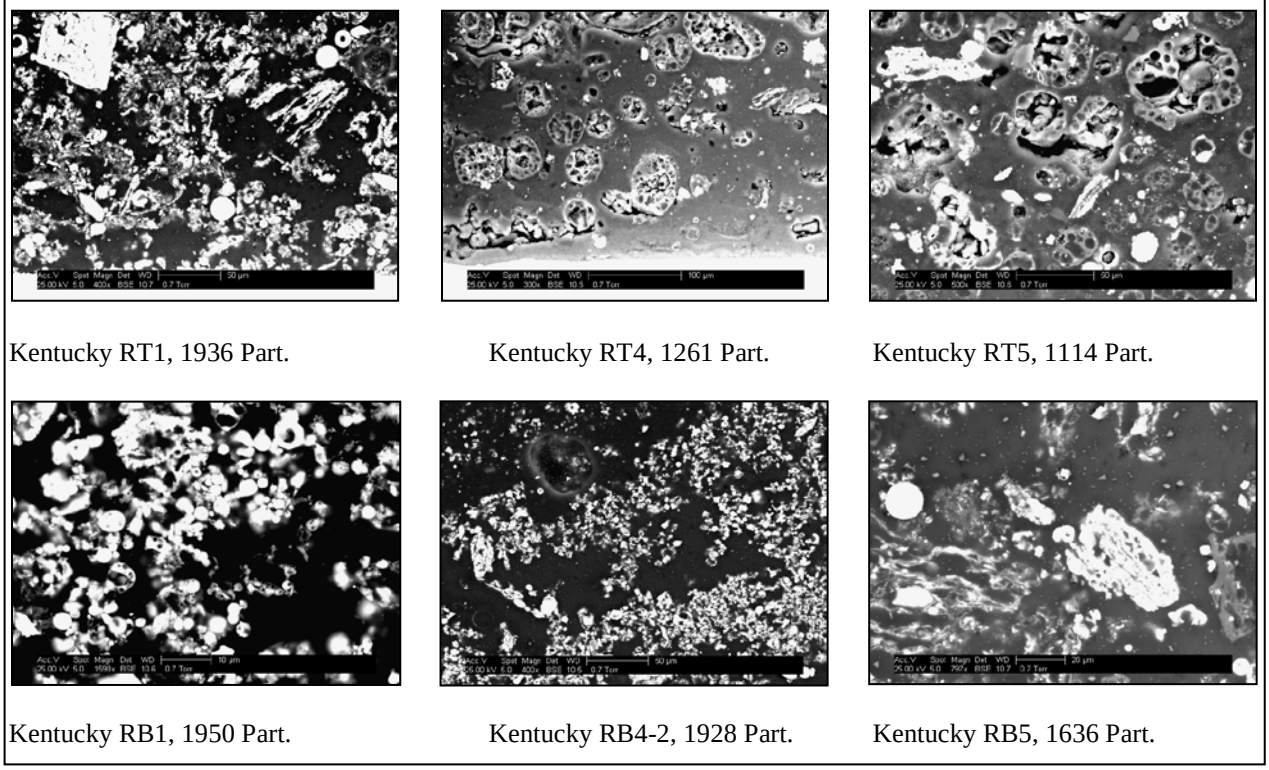

Kentucky RT1, 1936 Part. Kentucky RT4, 1261 Part. Kentucky RT5, 1114 Part.

Kentucky RB1, 1950 Part. Kentucky RB4-2, 1928 Part. Kentucky RB5, 1636 Part.

Figure 159 - Backscattered Electron (BSE) Images of Kentucky Reducing Deposit Samples.

Additional SEM images identifying individual particles for the Kentucky coal deposits are shown in Figures 162-166. The particles in OB3 are similar in shape and composition. The three particles, labeled A, B, and C, consist of a large mass fraction of Si, Al, Fe, and O. These particles also contain measureable amounts of K. Consistent with the other deposit samples, K tends to coexist with Si, Al, and Ti (see also Particle C, RB5 for Kentucky). The K-containing particles do not contain any S. In RB5, the two largest particles, D and C, are very different in shape but contain similar major constituents (i.e., Si, Al, O, and Fe).

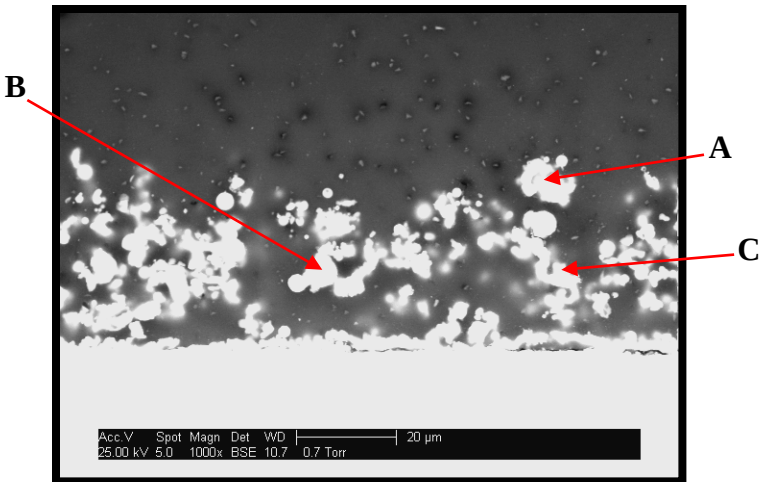

Coal: KENTUCKY #11			
Sleeve Location: OXIDIZING BOTTOM #3 (OB3)			
	Label A	Label B	Label C
Particle No.	5	51	54
Area (μm^2)	63.6546	152.17	75.8276
O	31.4	24.4	23.4
Na	0.0	0.0	0.0
Mg	0.0	0.0	0.0
Al	16.8	7.4	13.9
Si	26.1	21.7	21.2
P	0.0	0.0	0.0
S	0.0	0.0	0.0
Cl	0.0	0.0	0.0
K	4.4	1.7	3.4
Ca	1.5	1.1	1.9
Ba	0.0	0.0	0.0
Ti	1.9	0.0	1.2
Cr	3.4	6.4	6.6
Mn	0.0	1.8	2.0
Fe	13.0	33.8	24.4
Ni	1.7	1.7	1.9
Sr	0.0	0.0	0.0

Figure 160 - Kentucky OB3, 25 kV, Spot Size 5.0, Backscattered Electron (BSE).

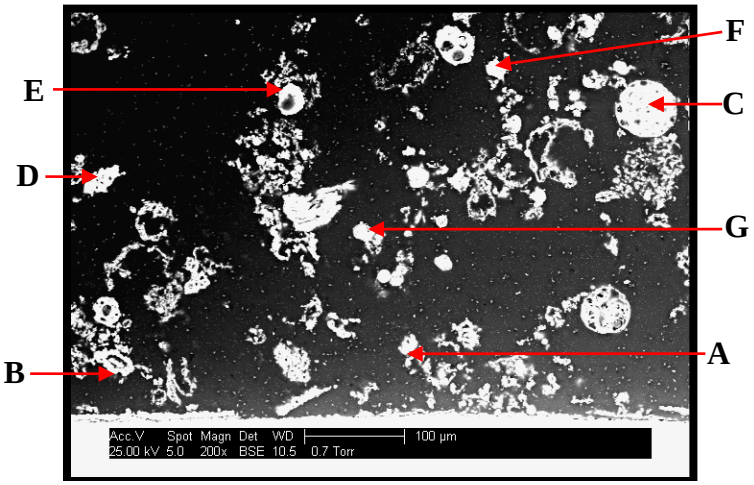

Coal: KENTUCKY #11							
Sleeve Location: OXIDIZING TOP #3 (OT3)							
	Label A	Label B	Label C	Label D	Label E	Label F	Label G
Particle No.	1076	1161	305	514	313	234	684
Area (μm^2)	1.987	14.67	2779	572.8	518.9	352.2	457
O	31.2	17.3	32.5	36.3	26.4	25.7	45.4
Na	0.0	0.0	0.0	0.0	1.0	0.0	0.0
Mg	0.0	0.7	0.0	1.6	1.0	0.9	0.0
Al	0.0	1.4	11.2	2.4	5.8	2.3	3.1
Si	2.5	2.2	26.6	4.9	7.1	5.4	4.3
P	0.0	1.2	0.0	0.0	0.9	0.0	0.0
S	26.4	25.4	0.0	16.5	0.9	0.0	6.0
Cl	0.0	1.6	0.0	2.4	1.6	1.1	5.2
K	0.0	1.1	5.3	0.0	1.4	0.0	0.0
Ca	34.6	30.8	0.0	21.0	1.9	0.8	9.8
Ba	0.0	0.9	0.0	0.0	1.6	0.0	0.0
Ti	0.0	0.8	0.0	0.0	0.6	0.0	0.0
Cr	0.0	3.4	3.0	2.5	1.3	1.3	4.1
Mn	0.0	1.5	0.0	1.8	0.7	0.9	2.0
Fe	5.4	9.8	21.3	8.8	47.4	60.2	18.0
Ni	0.0	2.0	0.0	1.8	0.6	1.3	2.3
Sr	0.0	0.0	0.0	0.0	0.0	0.0	0.0

Figure 161 - Kentucky OT3, 25 kV, Spot Size 5.0, Backscattered Electron (BSE).

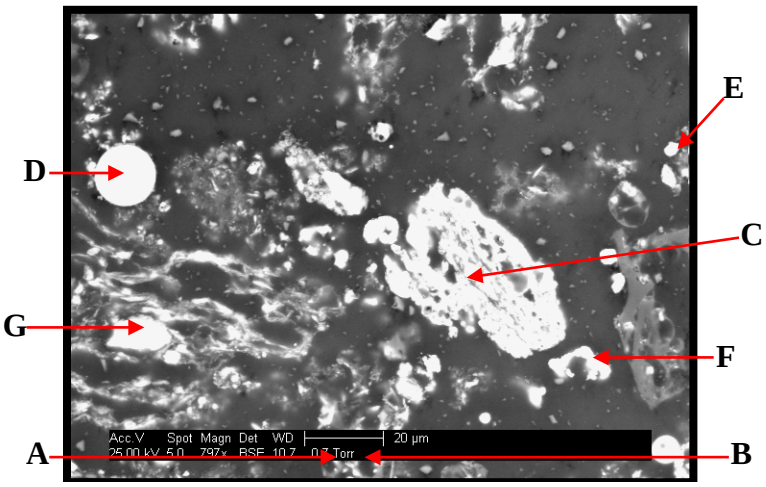

Coal: KENTUCKY #11							
Sleeve Location: REDUCING BOTTOM #5 (RB5)							
	Label A	Label B	Label C	Label D	Label E	Label F	Label G
Particle No.	590	1555	235	148	60	438	346
Area (μm^2)	0.03	28.85	1046	206.4	18.85	44.65	345.1
O	32.6	32.8	30.2	37.5	16.6	35.1	38.3
Na	0.0	0.0	0.0	0.0	1.6	0.0	0.0
Mg	0.0	0.0	1.1	1.3	1.3	0.0	0.0
Al	2.5	3.7	11.6	23.8	3.7	4.3	19.2
Si	4.1	6.1	36.2	26.4	7.1	6.3	23.9
P	0.0	0.0	1.0	0.0	0.9	0.0	0.0
S	19.8	15.6	0.0	0.0	1.3	0.0	0.0
Cl	2.7	2.9	1.0	0.0	2.0	3.6	0.0
K	1.2	0.0	5.8	2.5	1.6	0.0	3.6
Ca	20.2	15.7	0.6	0.0	0.7	0.0	0.0
Ba	0.0	0.0	0.0	0.0	0.0	0.0	0.0
Ti	0.0	0.0	0.8	1.0	0.0	0.0	0.0
Cr	3.9	5.0	1.6	1.3	1.6	4.1	2.4
Mn	0.0	0.0	0.8	0.0	0.0	1.5	0.0
Fe	11.1	15.8	8.2	5.2	61.9	42.5	10.8
Ni	2.0	2.4	1.1	1.0	0.0	2.6	1.8
Sr	0.0	0.0	0.0	0.0	0.0	0.0	0.0

Figure 162 - Kentucky RB5, 25 kV, Spot Size 5.0, Backscattered Electron (BSE).

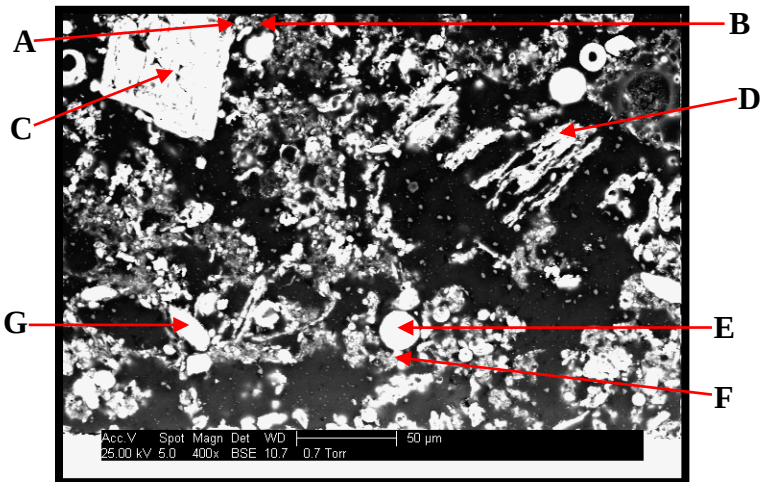

Coal: KENTUCKY #11							
Sleeve Location: REDUCING TOP #1 (RT1)							
	Label A	Label B	Label C	Label D	Label E	Label F	Label G
Particle No.	1093	1102	3	354	747	880	746
Area (μm^2)	1.869	8.067	3587	617.4	900.7	79.65	1032
O	26.1	26.1	24.9	33.8	25.5	22.9	34.6
Na	0.0	0.0	0.9	0.0	0.0	0.0	0.0
Mg	0.0	0.0	0.7	0.0	0.0	0.0	0.0
Al	1.2	2.2	1.9	12.5	8.3	5.2	9.4
Si	1.6	3.5	2.7	29.5	20.6	8.6	38.5
P	0.8	0.0	1.0	0.0	0.0	0.0	0.0
S	27.3	26.4	12.4	0.0	0.0	7.1	0.0
Cl	0.9	0.8	1.2	1.6	0.0	0.0	0.0
K	0.0	0.0	1.0	4.1	1.8	0.0	2.0
Ca	34.5	33.5	43.3	0.8	0.0	10.1	0.0
Ba	0.0	0.0	0.0	1.7	0.0	0.0	0.0
Ti	0.0	0.0	0.8	2.1	0.0	0.0	0.0
Cr	1.2	1.5	1.3	2.4	2.2	4.2	2.5
Mn	1.1	0.0	0.9	1.3	1.0	1.5	0.9
Fe	4.3	5.1	5.6	8.8	38.9	38.1	10.8
Ni	0.9	0.8	1.4	1.4	1.8	2.3	1.3
Sr	0.0	0.0	0.0	0.0	0.0	0.0	0.0

Figure 163 - Kentucky RT1, 25 kV, Spot Size 5.0, Backscattered Electron (BSE).

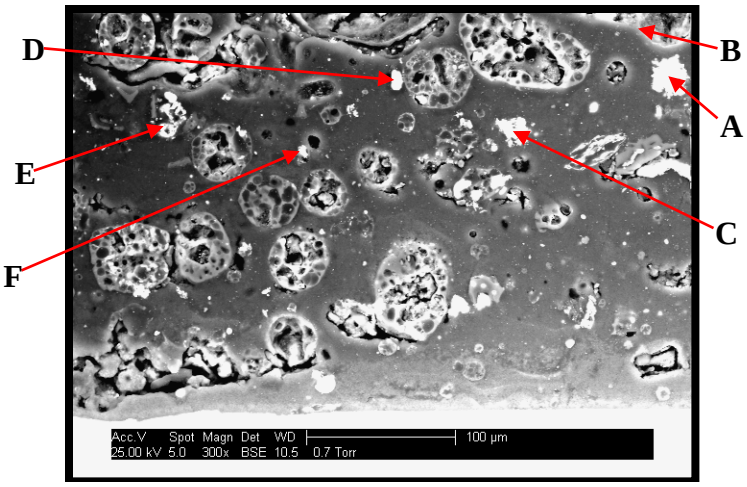

Coal: KENTUCKY #11						
Sleeve Location: REDUCING TOP #4 (RT4)						
	Label A	Label B	Label C	Label D	Label E	Label F
Particle No.	162	991	242	194	220	286
Area (μm^2)	480	2.879	242.8	81.76	94.8	30.02
O	9.4	8.8	14.4	37.3	34.6	34.8
Na	0.0	0.0	0.0	0.0	0.0	0.0
Mg	0.0	0.0	0.0	0.0	0.0	0.0
Al	0.0	0.0	0.0	1.4	12.0	23.4
Si	1.6	0.0	0.0	52.0	35.3	24.3
P	0.0	0.0	0.0	0.0	0.0	0.0
S	32.9	33.8	32.0	0.0	1.6	3.2
Cl	1.6	0.0	0.0	0.0	1.3	0.0
K	0.0	0.0	0.0	0.9	5.0	3.0
Ca	0.0	0.0	0.0	0.5	1.3	0.0
Ba	0.0	0.0	0.0	2.2	0.0	0.0
Ti	0.0	0.0	0.0	0.0	0.0	0.0
Cr	1.2	0.0	0.0	1.2	1.5	2.2
Mn	0.0	0.0	0.0	0.6	0.0	0.0
Fe	53.3	56.0	53.6	3.0	6.2	7.5
Ni	0.0	1.4	0.0	1.0	1.3	1.5
Sr	0.0	0.0	0.0	0.0	0.0	0.0

Figure 164 - Kentucky RT4, 25 kV, Spot Size 5.0, Backscattered Electron (BSE).

4.3.11.8 Pittsburgh #8 - Deposit Images and Individual Particle Analysis

SEM images of the deposit samples collected from the top and bottom of the deposition probe in the reducing and oxidizing zones of the BFR burning the Pittsburgh #8 coal are shown in Figures 167 and 168. The images show that the smallest and most uniform particles are in the bottom oxidizing samples and the largest and most irregular particles are in the top reducing samples. The particles in the bottom oxidizing samples are the least spherical compared to all the other coals tested, thus suggesting minimum melting of the particles. This is consistent with the coal ash analyses that showed the highest T-250 fusion temperature (>2900^{o}F) among the eight coals. Otherwise, the deposit samples of Pittsburgh #8 coal look similar to those of the other coals.

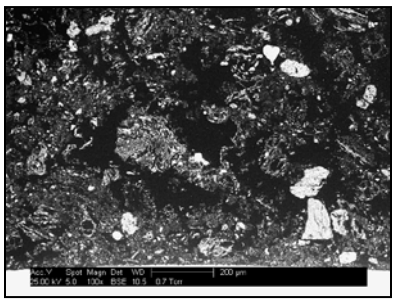

Pitt8 OT5-1, 1998 Particles.

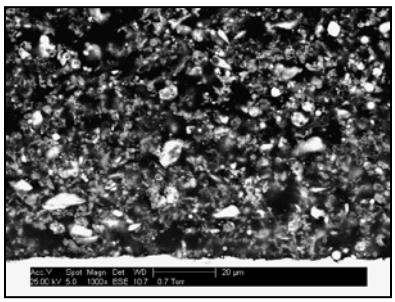

Pitt8 OB1, 1922 Particles.

Figure 165 - Backscattered Electron (BSE) Images of Pittsburgh Oxidizing Deposit Samples.

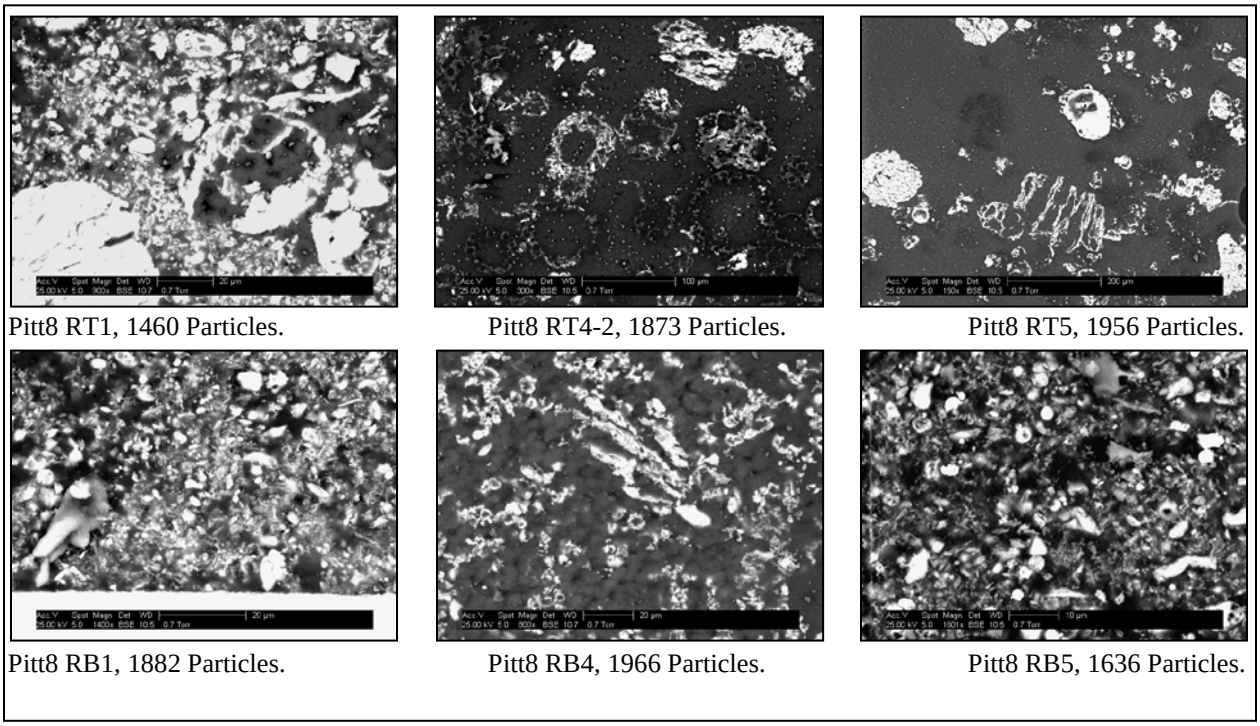

Figure 166 - Backscattered Electron (BSE) Images of Pittsburgh Reducing Deposit Samples.

Additional SEM images identifying the individual particles are shown in Figures 169-172. Most particles in the Pittsburgh 8 deposit samples contain high concentrations of Si, Al, Fe, and O but are absent of any other elements. In addition, these particles are more uniform in composition than those of the other coals. When sulfur is present, Ca is also present. When K is present, there is a tendency to have low or zero S. The Na concentration is often quite low and never exceeds 5%.

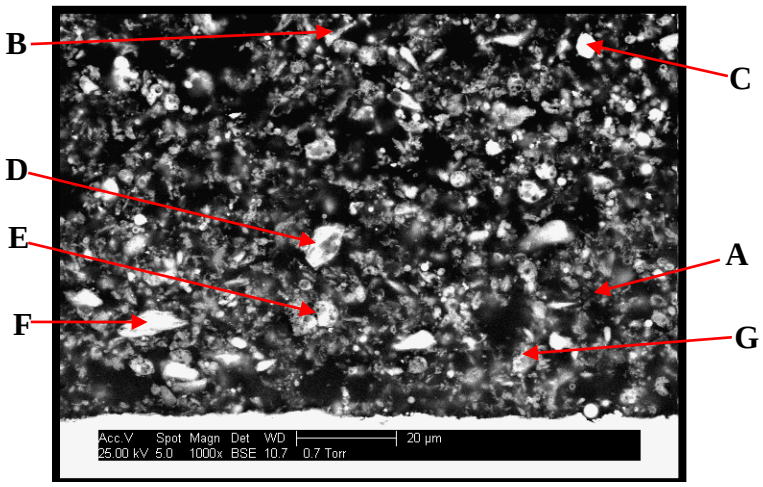

Coal: PITTSBURGH #8							
Sleeve Location: OXIDIZING BOTTOM #1 (OB1)							
	Label A	Label B	Label C	Label D	Label E	Label F	Label G
Particle No.	1883	9	78	460	631	660	1706
Area (μm^2)	0.030	7.32	14.55	29.36	16.87	40.85	110.2
O	22.1	41.6	27.8	33.2	25.1	30.3	27.0
Na	0.0	0.0	1.3	1.3	0.0	0.0	0.0
Mg	0.0	0.0	3.1	1.4	0.0	0.0	0.0
Al	15.9	21.5	4.8	19.2	22.0	18.4	13.7
Si	27.5	24.9	5.4	24.0	27.6	26.2	20.1
P	0.0	0.0	1.1	0.0	0.0	0.0	0.0
S	4.4	0.0	0.7	0.0	0.0	0.0	0.0
Cl	1.7	0.0	0.8	1.1	0.0	0.0	1.9
K	2.3	2.7	0.8	2.8	0.0	3.2	2.4
Ca	5.3	0.0	0.7	0.0	0.0	1.0	1.1
Ba	0.0	0.0	0.0	0.0	0.0	0.0	0.0
Ti	0.0	0.0	0.0	0.7	0.0	1.1	1.4
Cr	3.6	1.8	1.4	2.8	3.9	3.9	7.2
Mn	0.0	0.0	1.1	0.7	0.0	1.0	0.9
Fe	15.0	6.4	49.8	11.3	19.2	13.0	22.4
Ni	2.2	1.0	1.1	1.7	2.3	1.9	1.8
Sr	0.0	0.0	0.0	0.0	0.0	0.0	0.0

Figure 167 - Pittsburgh OB1, 25 kV, Spot Size 5.0, Backscattered Electron (BSE).

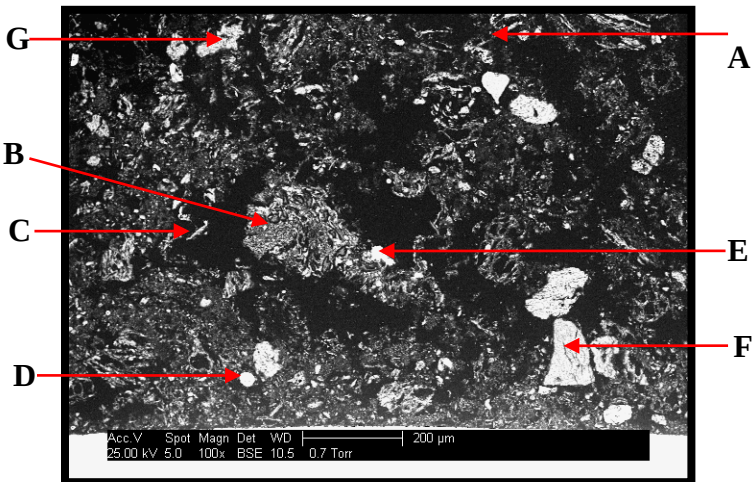

Coal: PITTSBURGH #8							
Sleeve Location: OXIDIZING TOP #5 (OT5-2)							
	Label A	Label B	Label C	Label D	Label E	Label F	Label G
Particle No.	86	877	897	1609	1031	1323	115
Area (μm^2)	79.11	51.86	212.4	669.2	1547	8810	2667
O	29.4	30.4	29.7	24.3	30.7	32.9	32.6
Na	1.1	1.0	0.0	0.7	0.0	0.0	0.0
Mg	1.1	3.5	2.8	2.5	0.0	0.0	0.0
Al	2.5	13.1	3.3	3.0	10.9	27.0	18.5
Si	3.8	7.8	4.2	4.5	16.7	33.2	39.4
P	16.2	0.0	0.0	1.0	0.0	0.0	0.0
S	2.5	18.9	13.7	1.0	0.0	0.0	0.0
Cl	2.8	2.6	1.6	0.0	0.0	0.0	0.0
K	1.2	0.0	0.9	0.7	1.2	1.3	5.4
Ca	33.6	19.7	15.7	0.7	0.0	0.0	0.0
Ba	2.2	0.0	0.0	0.0	0.0	0.0	0.0
Ti	0.0	0.0	1.1	0.0	0.0	0.0	1.5
Cr	1.1	0.0	0.9	1.7	1.1	1.4	0.0
Mn	0.0	0.0	1.2	1.7	0.0	0.7	0.0
Fe	2.4	2.9	24.9	58.0	39.5	3.6	2.7
Ni	0.0	0.0	0.0	0.0	0.0	0.0	0.0
Sr	0.0	0.0	0.0	0.0	0.0	0.0	0.0

Figure 168 - Pittsburgh OT5-2, 25 kV, Spot Size 5.0, Backscattered Electron (BSE).

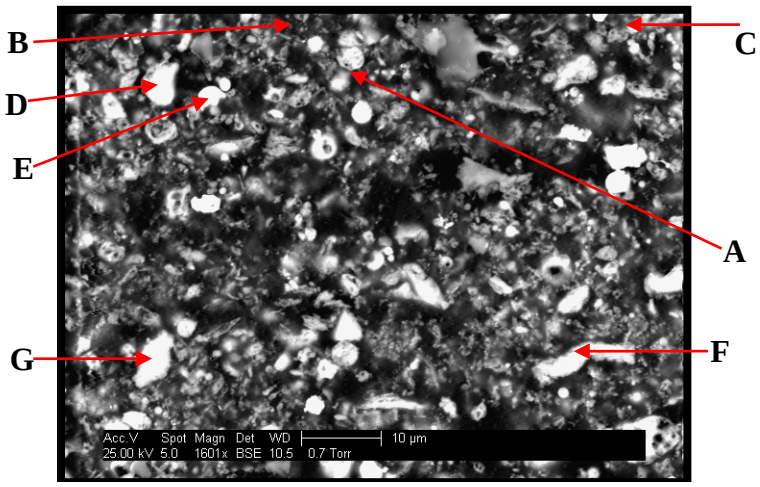

Coal: PITTSBURGH #8							
Sleeve Location: REDUCING BOTTOM #5 (RB5)							
	Label A	Label B	Label C	Label D	Label E	Label F	Label G
Particle No.	1489	35	65	174	263	799	808
Area (μm^2)	0.418	3.055	7.769	16.98	10.59	26.31	23.59
O	38.9	44.5	31.6	39.7	28.4	32.5	31.0
Na	0.0	0.0	1.4	0.0	0.0	0.0	0.0
Mg	0.0	0.0	0.0	0.8	0.0	0.0	0.0
Al	7.7	19.5	24.1	7.5	16.0	19.7	19.9
Si	14.2	20.0	38.5	36.3	24.7	24.1	31.7
P	0.0	3.9	0.0	0.0	0.0	1.5	0.0
S	13.5	0.0	0.0	0.0	0.0	1.5	0.0
Cl	0.0	1.3	0.0	0.9	2.0	2.2	1.5
K	1.2	1.6	0.0	1.6	2.8	2.4	3.4
Ca	17.4	1.3	0.0	0.0	0.0	1.6	0.0
Ba	0.0	0.0	0.0	0.0	0.0	0.0	0.0
Ti	0.9	1.4	0.0	1.6	1.7	2.1	1.5
Cr	1.2	0.9	0.0	0.7	1.8	2.2	2.2
Mn	0.7	0.0	0.0	0.0	1.4	0.0	1.3
Fe	4.3	5.6	4.3	10.8	20.1	8.7	7.6
Ni	0.0	0.0	0.0	0.0	1.1	1.6	0.0
Sr	0.0	0.0	0.0	0.0	0.0	0.0	0.0

Figure 169 - Pittsburgh RB5, 25 kV, Spot Size 5.0, Backscattered Electron (BSE).

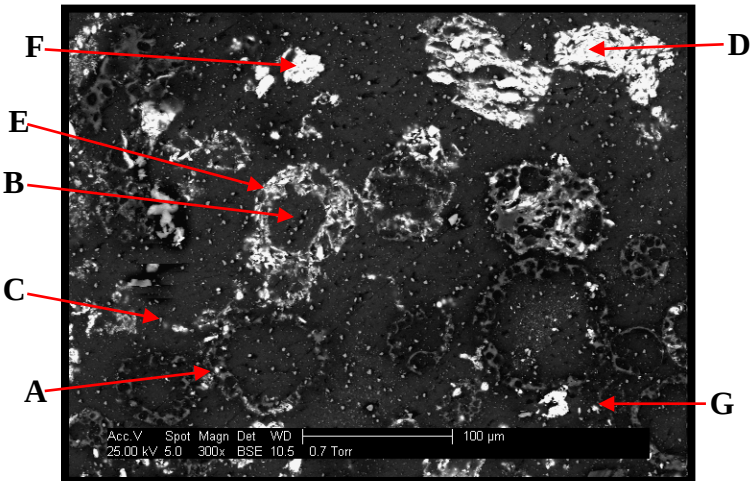

Coal: PITTSBURGH #8							
Sleeve Location: REDUCING TOP #4 (RT4-2)							
	Label A	Label B	Label C	Label D	Label E	Label F	Label G
Particle No.	1352	723	1079	95	536	173	1615
Area (μm^2)	0.168	4.248	2.944	4150	976.0	421.9	12.53
O	12.3	15.4	25.2	28.2	38.0	42.8	31.8
Na	0.0	5.1	5.2	1.1	0.0	0.7	0.6
Mg	0.0	3.7	4.9	1.2	0.0	0.0	1.3
Al	22.6	10.0	6.6	20.2	21.0	12.0	3.9
Si	37.4	12.0	7.5	33.4	28.5	41.3	8.1
P	4.0	5.2	4.4	1.0	0.0	0.0	0.9
S	5.4	4.3	4.2	1.0	0.0	0.0	4.2
Cl	6.9	10.4	12.1	1.8	3.2	0.0	1.3
K	4.3	2.9	2.7	4.2	3.0	1.9	0.0
Ca	0.0	2.6	3.2	0.8	0.0	0.0	43.0
Ba	0.0	2.9	3.0	1.8	0.0	0.0	0.0
Ti	0.0	2.1	2.6	1.3	0.0	0.0	0.0
Cr	0.0	3.3	2.9	0.6	0.0	0.0	0.0
Mn	1.8	2.7	2.2	0.9	1.3	0.0	0.0
Fe	5.4	4.8	5.5	2.5	5.0	1.3	3.6
Ni	0.0	3.5	2.0	0.0	0.0	0.0	1.2
Sr	0.0	9.1	5.7	0.0	0.0	0.0	0.0

Figure 170 - Pittsburgh RT4-2, 25 kV, Spot Size 5.0, Backscattered Electron (BSE).

4.3.12 Ternary Stability Diagrams for Deposit Samples

The construction of ternary stability diagrams can help identify the distribution of particle compositions and sizes in each deposit sample. A ternary diagram also allows for multiple ash elements to be assigned to the axes. Many combinations of axis elements have been investigated and for this study, the sums of Al+Si, S+Ca, and S+Fe were found to be the most important variables. These combinations were chosen because (1) Si and Al were present in almost every particle and (2) both Ca and Fe were closely associated with S.

4.3.12.1 North Dakota Beulah Zap Lignite Ternary Diagrams

A ternary diagram for the Beulah Zap OB3 deposit is shown in Figure 173. The compositional distribution of a total of 1951 particles is plotted in this diagram, with their equivalent spherical diameters indicated by the size of the circle. Towards the Si+Al, S+Ca, and S+Fe axis corners, the particles are highlighted in green, red, and blue, respectively. The vast majority of the particles appear to follow diagonally along the Si+Al (second) axis. Near the Si+Al axis corner, the particles tend to be larger in size.

Figure 173 indicates the presence of three particle groups: (1) the majority of the particles located along the diagonal that contain all five elements, (2) particles containing Al and Si but no S and Ca, and (3) particles containing S, Ca, and Fe but no Si and Al. Only a few particles are present in the second group (~1%) and even fewer in the third group (0.5%). While these particle groups might be considered different condensed phases of the deposit, it is difficult to distinguish the particles within the first group. The large spread of composition in the first group may reflect the natural distribution of coal ash elements in various complex oxide compounds.

The ternary diagram reveals that some deposit particles are rich in S, Ca, and Fe. These particles are likely to be sulfates of Ca and Fe. Particles with the highest Fe+S concentrations tend to be small and spherical, again indicating melting prior to deposition on the probe.

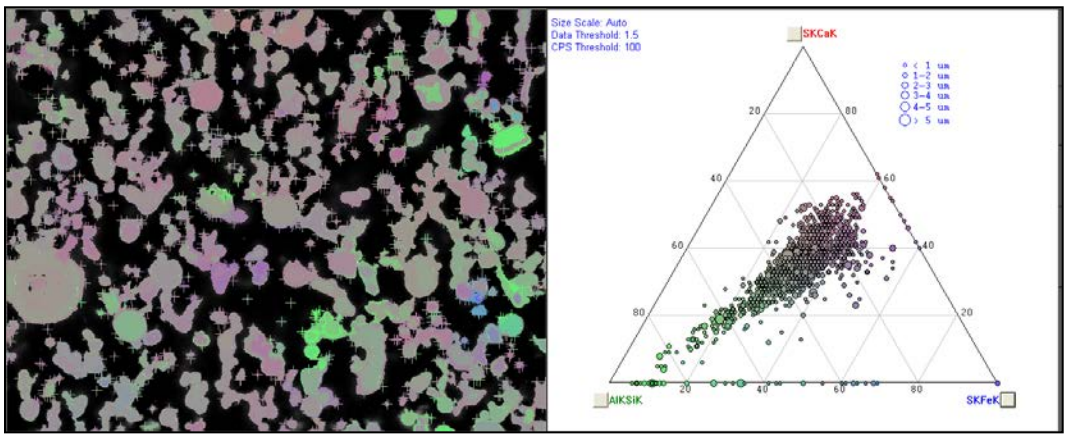

Figure 171 - Beulah Zap OB3 Deposit Particles Distributed on S+Ca, Si+Al, and S+Fe Ternary Diagram.

The Beulah Zap OT3-1 ternary diagram is shown in Figure 174. The result is very similar to OB3 in the distribution of particles. There is however a small number of particles distributed along the left axis and contains no S + Fe. Being a top sleeve sample, the deposit also contains larger ash particles than those on the bottom sleeve. The large particles appear to be mainly Si+Al.

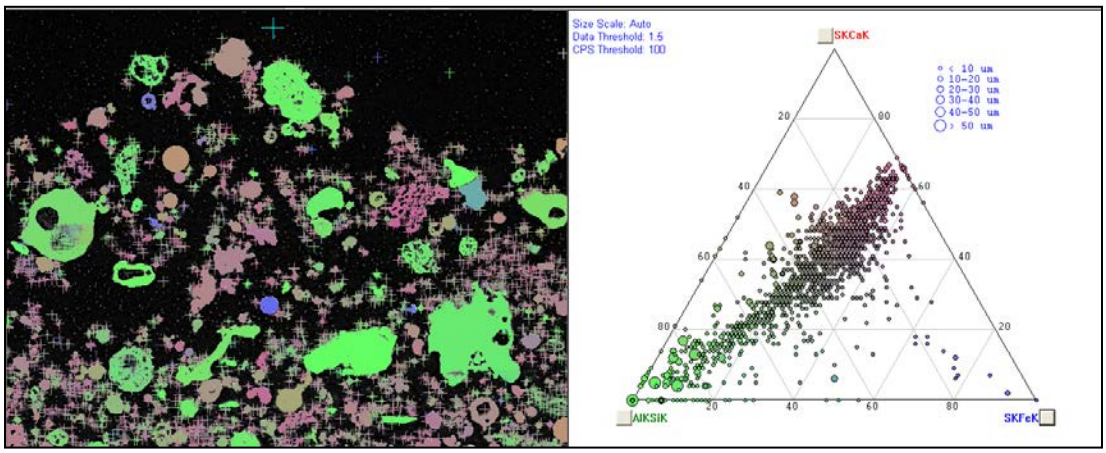

Figure 172 - Beulah Zap OT3-1 Ternary Diagram Measuring S + Ca, Si + Al, and S + Fe.

A ternary diagram for Beulah Zap RB3 is shown in Figure 175. In this sample, the composition is more centered in the diagram, with fewer particles of high S, Ca, and Fe. The final sample, Beulah Zap RT5-2, shows similar trends in Figure 176 as the OT3-1 sample, except for one noticeable difference. There appears to be a greater amount of calcium or less iron in the sample, because the particles are distributed closer to the primary (left) axis of the ternary triangle. Also, there are a greater number of particles that are distributed closer to the Si + Al corner.

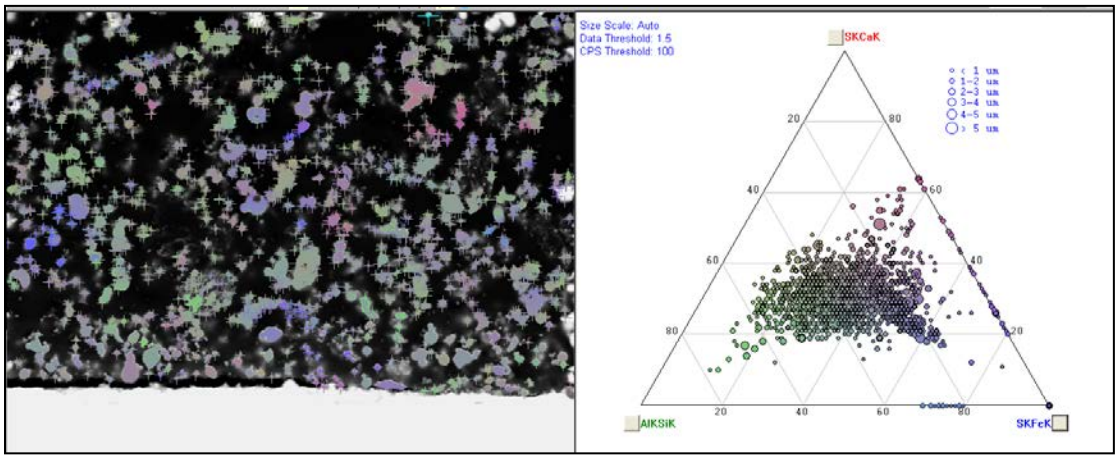

Figure 173 - Beulah Zap RB3 Ternary Diagram Measuring S + Ca, Si + Al, and S + Fe.

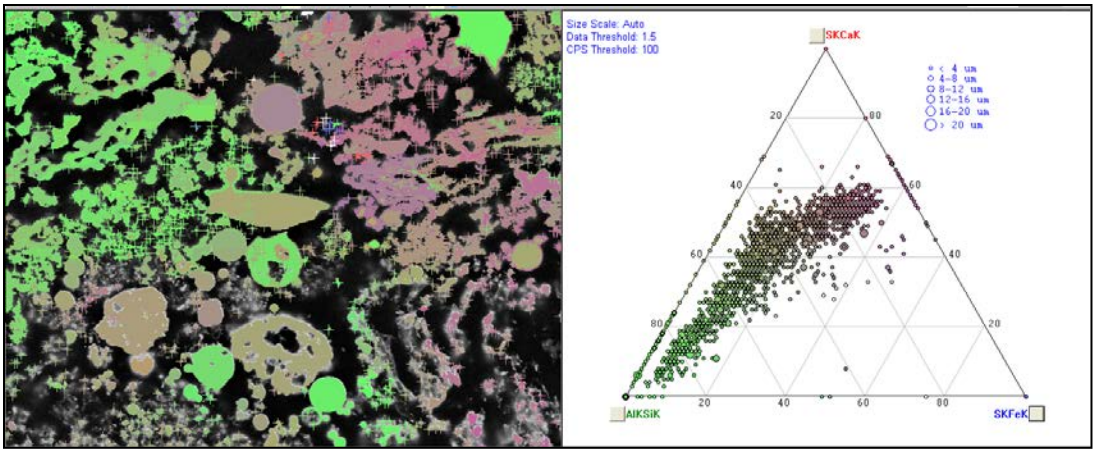

Figure 174 - Beulah Zap RT5-2 Ternary Diagram Measuring S + Ca, Si + Al, and S + Fe.

4.3.12.2 Wyoming Powder River Basin (PRB) Ternary Diagrams

The ternary diagrams for the PRB deposits are found in Figure 177-180. The ternary diagrams for PRB are similar to those for Beulah Zap. These deposits have a relatively larger amount of calcium than the bituminous coals. The top sleeves, both oxidizing and reducing have a greater amount of Si + Al, than the bottom sleeves. As with the other deposits, the larger particles tend to be high in Si + Al.

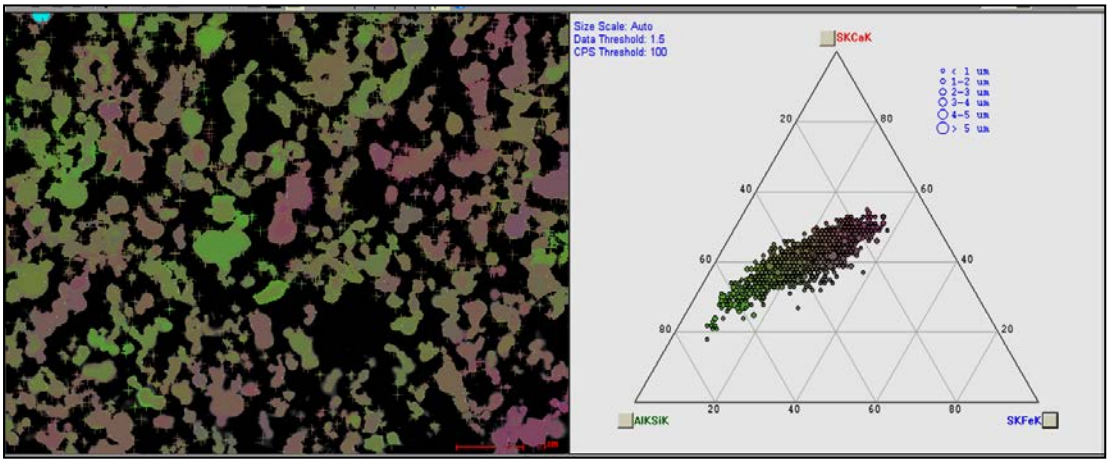

Figure 175 - PRB-1 OB4-2 Ternary Diagram Measuring S + Ca, Si + Al, and S + Fe.

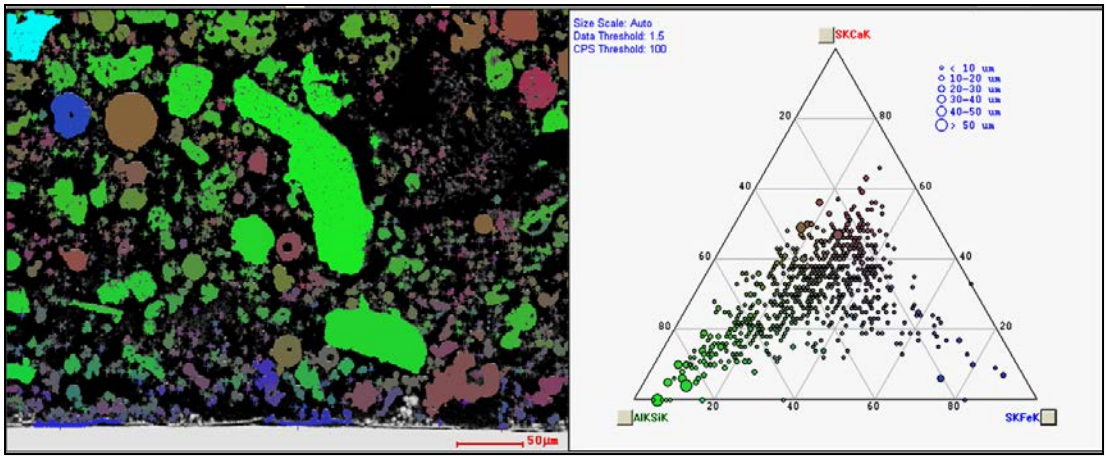

Figure 176 - PRB-1 OT4 Ternary Diagram Measuring S + Ca, Si + Al, and S + Fe.

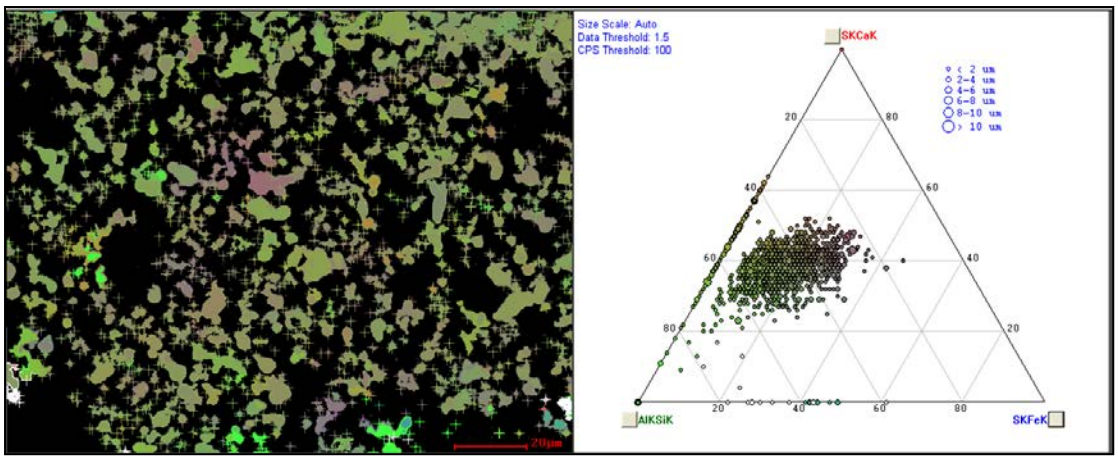

Figure 177 - PRB-1 RB4 Ternary Diagram Measuring S + Ca, Si + Al, and S + Fe.

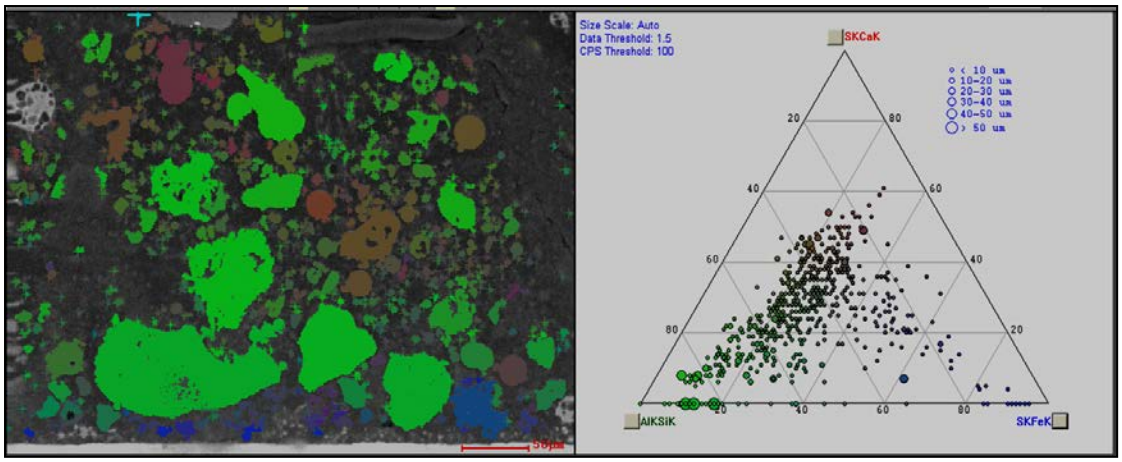

Figure 178 - PRB-1 RT1 Ternary Diagram Measuring S + Ca, Si + Al, and S + Fe.

4.3.12.3 Indiana Particle Ternary Diagrams

The ternary diagrams for the Indiana deposits are found in Figures 181-184. These diagrams are unique because they show the majority of the particles on the bottom of the triangle. This trend suggests that there is very little sulfur and calcium in the Indiana coal. The result is the same for all four measurement locations.

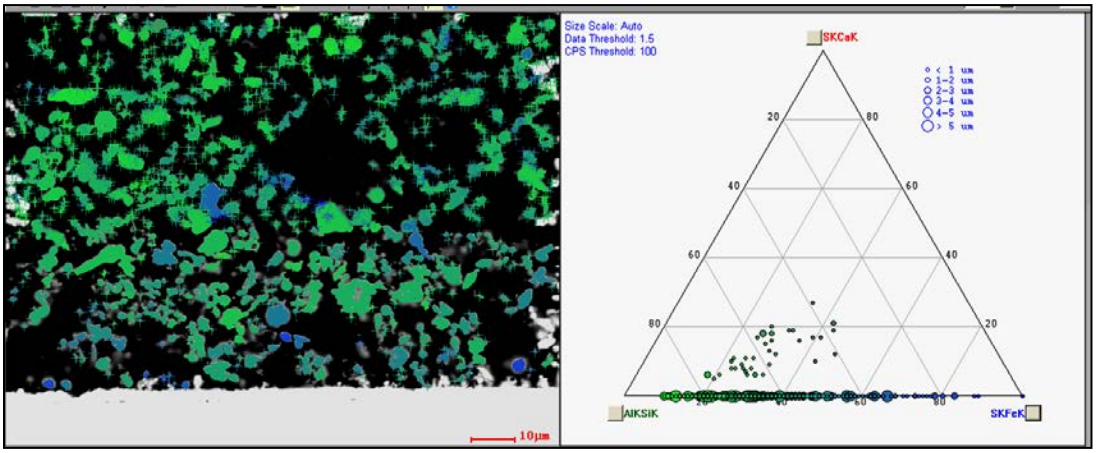

Figure 179 - Indiana OB4 Ternary Diagram Measuring S + Ca, Si + Al, and S + Fe.

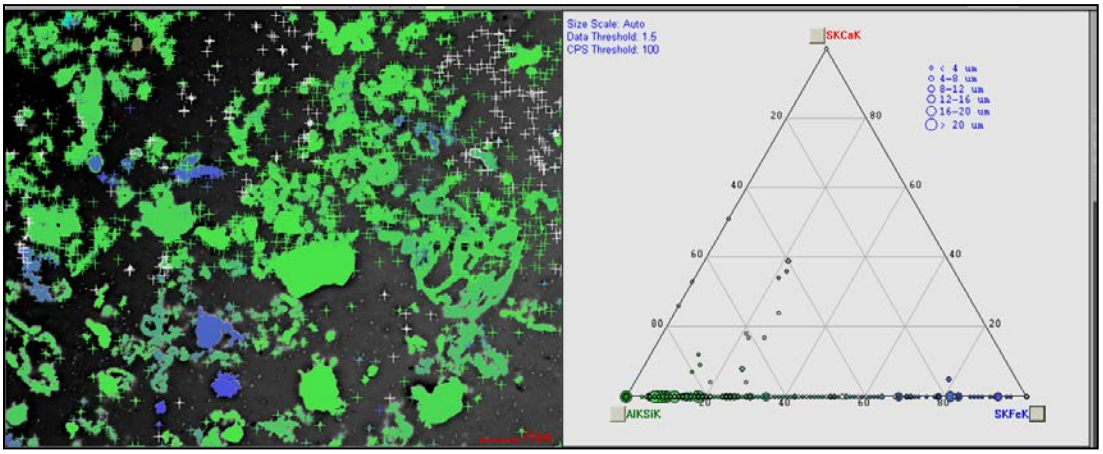

Figure 180 - Indiana OT4 Ternary Diagram Measuring S + Ca, Si + Al, and S + Fe.

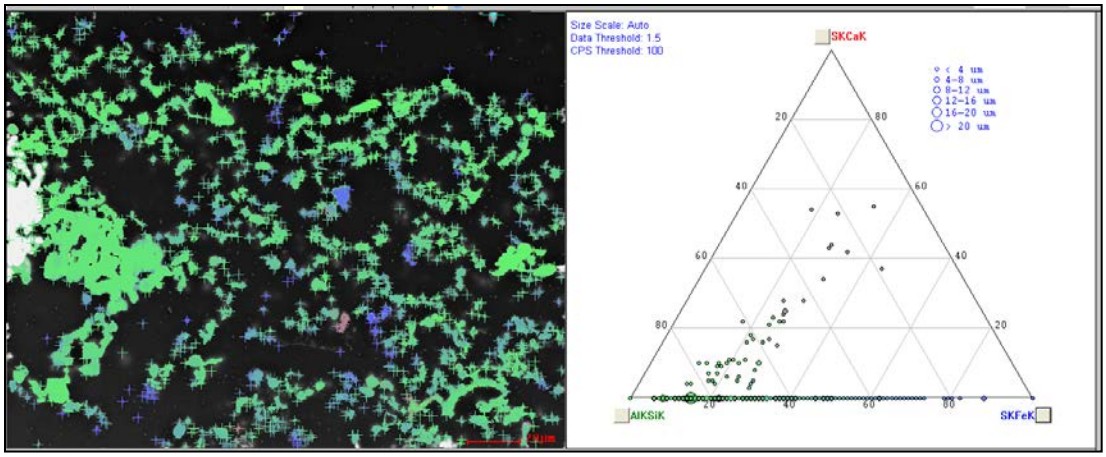

Figure 181 - Indiana RB3 Ternary Diagram Measuring S + Ca, Si + Al, and S + Fe.

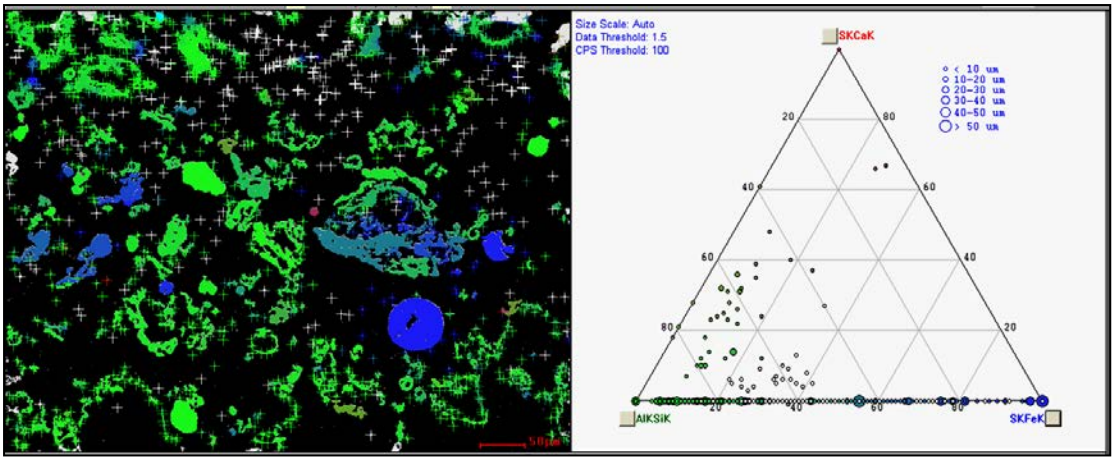

Figure 182 - Indiana RT6 Ternary Diagram Measuring S + Ca, Si + Al, and S + Fe.

4.3.12.4 Gatling Particle Ternary Diagrams

The ternary diagrams for the Gatling deposits are found in Figures 185-188. The backscatter electron image for the OB3 and the OT3 deposits are in black and white because these samples were analyzed using an earlier version of the EDAX Genesis software. The oxidizing-bottom shows most of the particles near the bottom axis with low Ca+S. The other three diagrams show an increased amount of S+Ca, with the highest amount found in the RT2-2 deposit. This deposit also shows a large number of particles near the bottom right corner of the diagram containing a high concentration of S+Fe. A concentration of particles in the S+Fe corner is unique to the Gatling coal. Gatling contains the highest amount of pyritic sulfur among the coals studied.

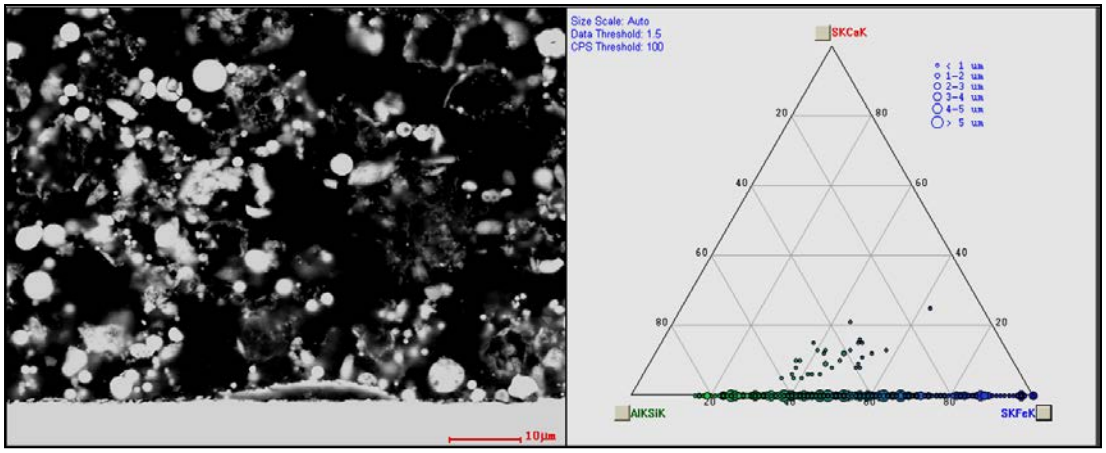

Figure 183 - Gatling OB3 Ternary Diagram Measuring S + Ca, Si + Al, and S + Fe.

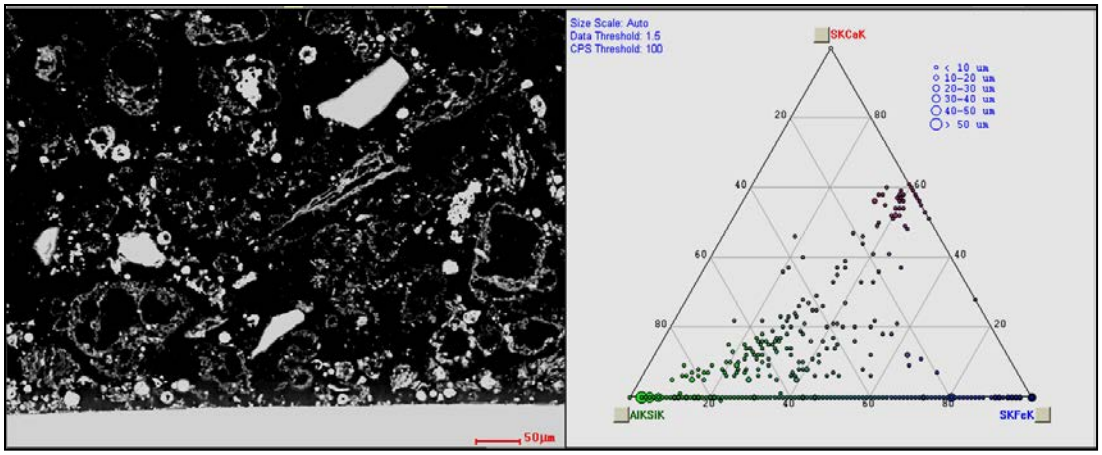

Figure 184 - Gatling OT3 Ternary Diagram Measuring S + Ca, Si + Al, and S + Fe.

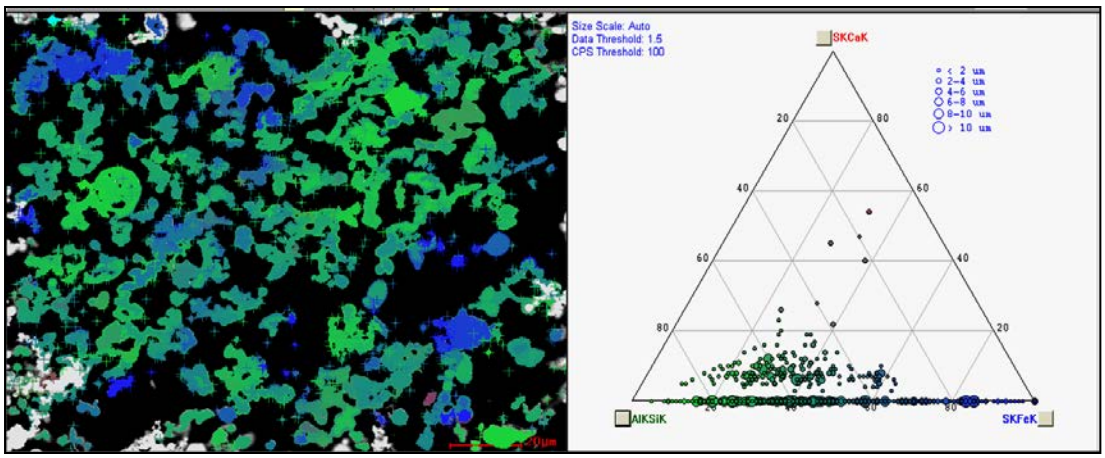

Figure 185 - Gatling RB4-2 Ternary Diagram Measuring S + Ca, Si + Al, and S + Fe.

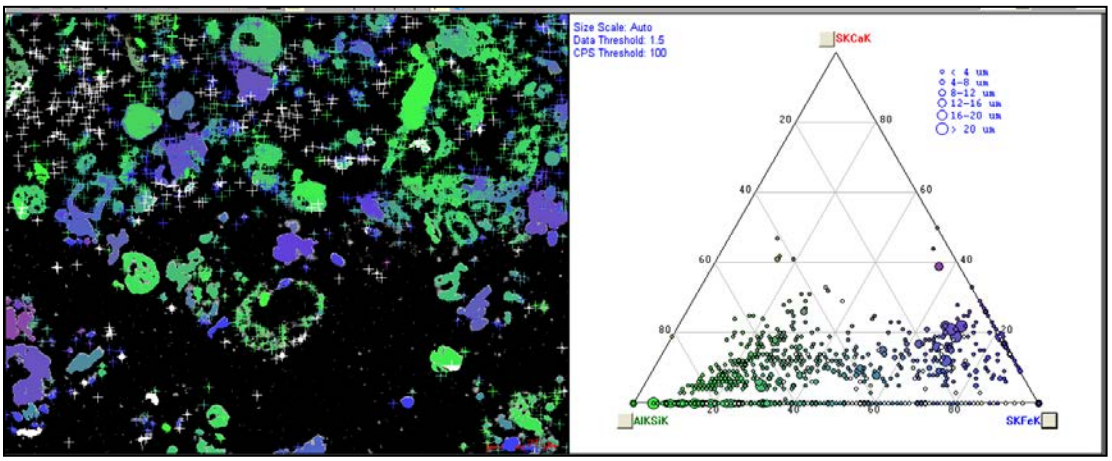

Figure 186 - Gatling RT2-2 Ternary Diagram Measuring S + Ca, Si + Al, and S + Fe.

4.3.12.5Illinois #6-2 Particle Ternary Diagrams

Ternary diagrams for the Illinois #6-2 deposits are found in Figures 189-192. A majority of particles do not contain either sulfur or calcium. The two top deposits have more sulfur than the bottom deposits, which is different from the other bituminous coals. A very small number of particles in the images are in red or blue, indicating high concentrations of Ca+S and Fe+S respectively.

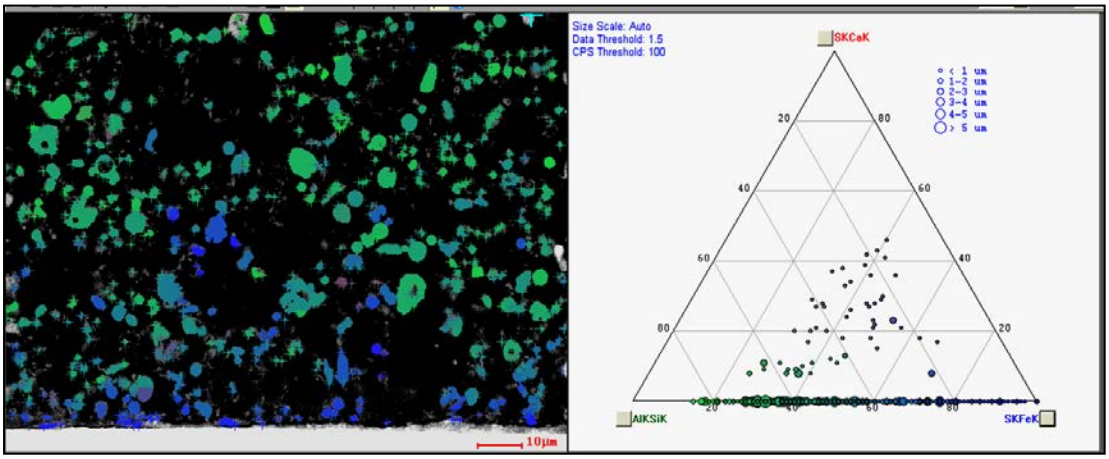

Figure 187 - Illinois #6-2 OB4 Ternary Diagram Measuring S + Ca, Si + Al, and S + Fe.

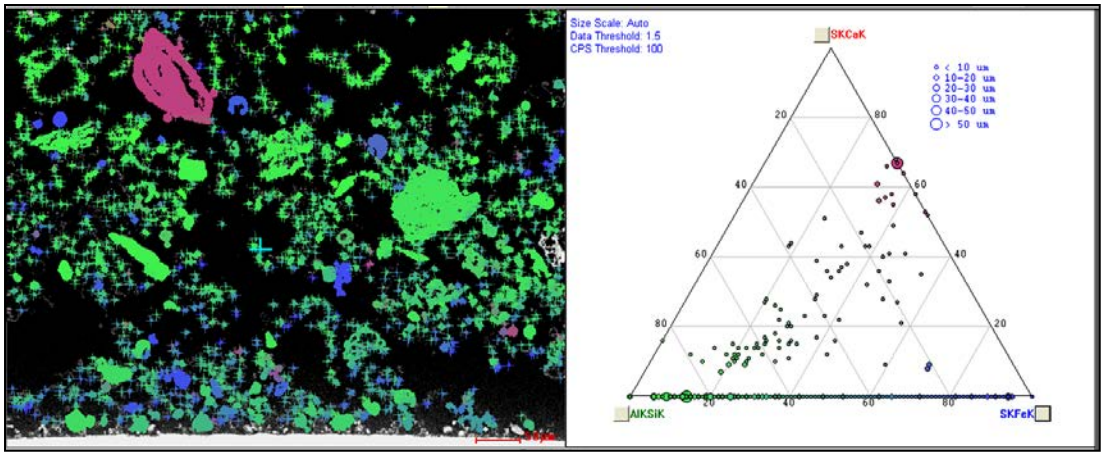

Figure 188 - Illinois #6-2 OT4 Ternary Diagram Measuring S + Ca, Si + Al, and S + Fe.

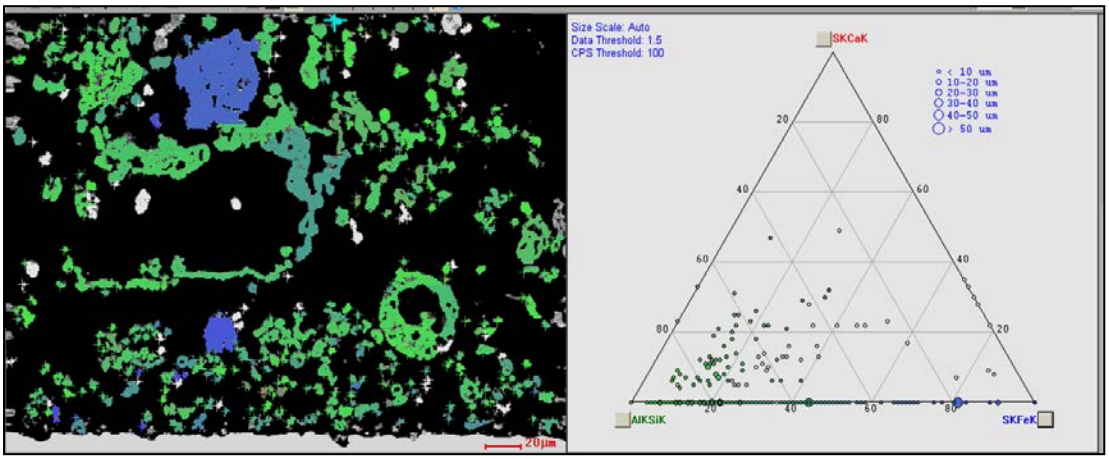

Figure 189 - Illinois #6-2 RB4 Ternary Diagram Measuring S + Ca, Si + Al, and S + Fe.

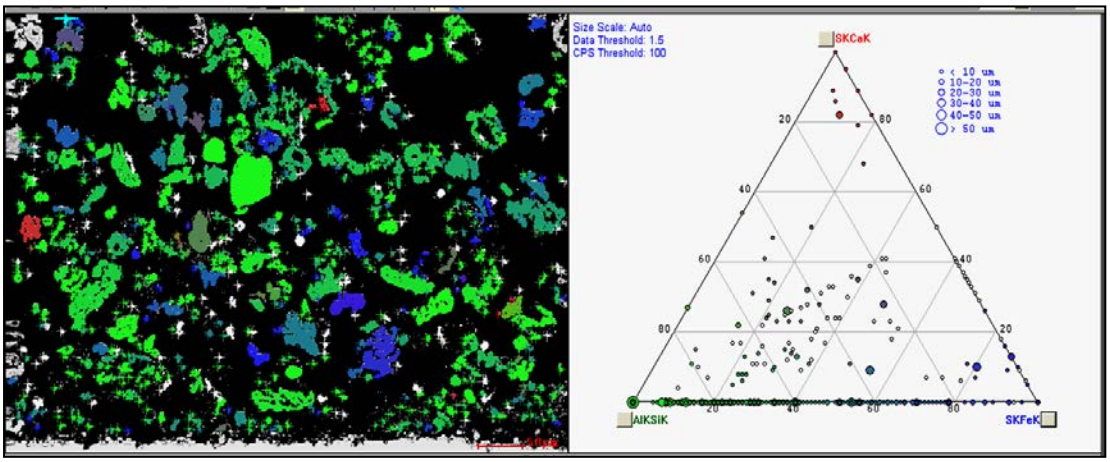

Figure 190 - Illinois #6-2 RT5 Ternary Diagram Measuring S + Ca, Si + Al, and S + Fe.

4.3.12.6 Kentucky Particle Ternary Diagrams

The ternary diagrams for the Kentucky deposits are found Figures 193-196. These diagrams look similar to most of the other bituminous coals, with the majority of particles containing no S+Ca but a large number of particles scattered towards the bottom half of the diagram. The reducing-top ternary diagram is unique in that there are a greater number of particles with large amounts of S+Ca and S+Fe. This appears however to be influenced by one very large particle (red) and several surrounding small particles. This large particle does not appear to be representative of the average composition of this deposit.

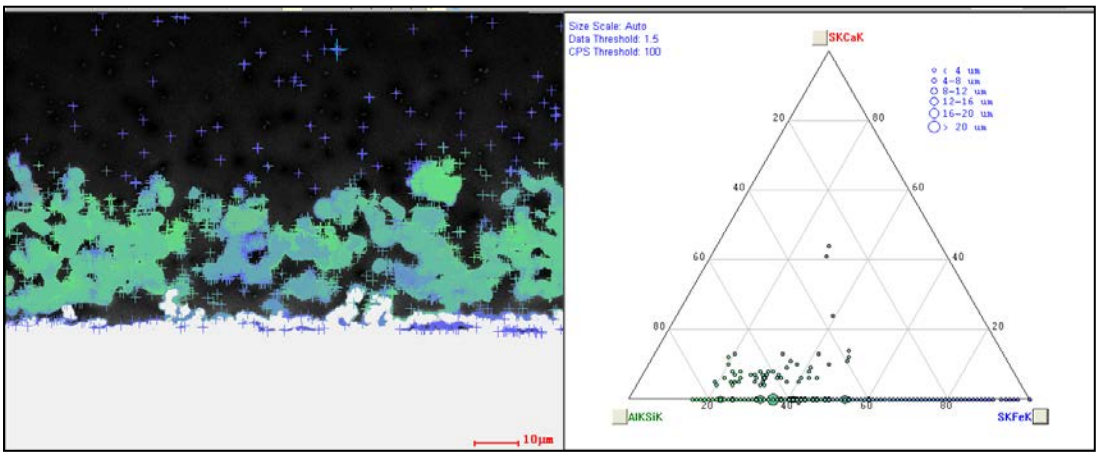

Figure 191 - Kentucky OB3 Ternary Diagram Measuring S + Ca, Si + Al, and S + Fe.

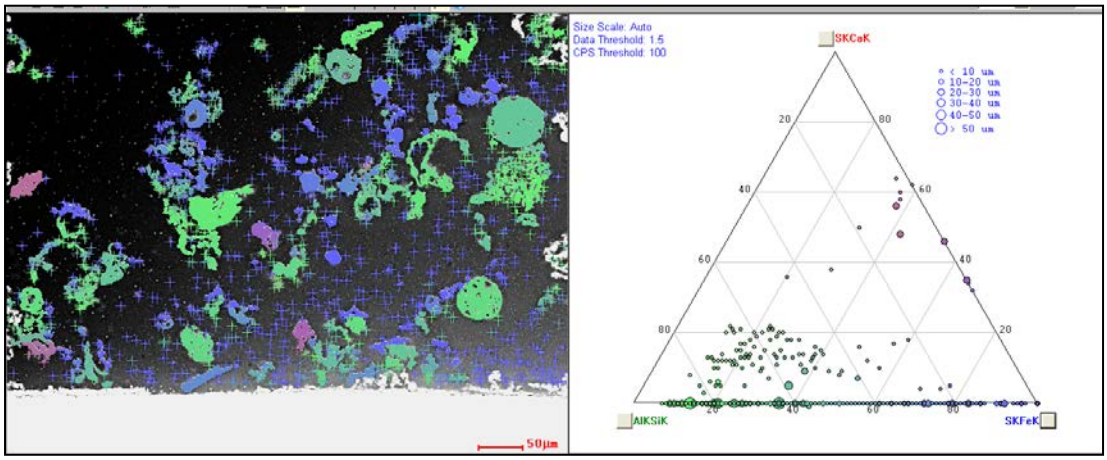

Figure 192 - Kentucky OT3 Ternary Diagram Measuring S + Ca, Si + Al, and S + Fe.

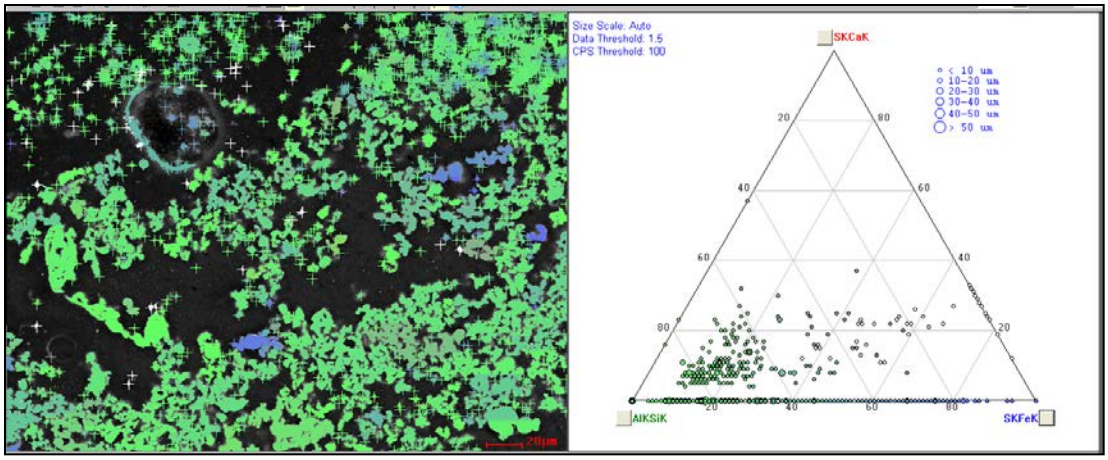

Figure 193 - Kentucky RB4-2 Ternary Diagram Measuring S + Ca, Si + Al, and S + Fe.

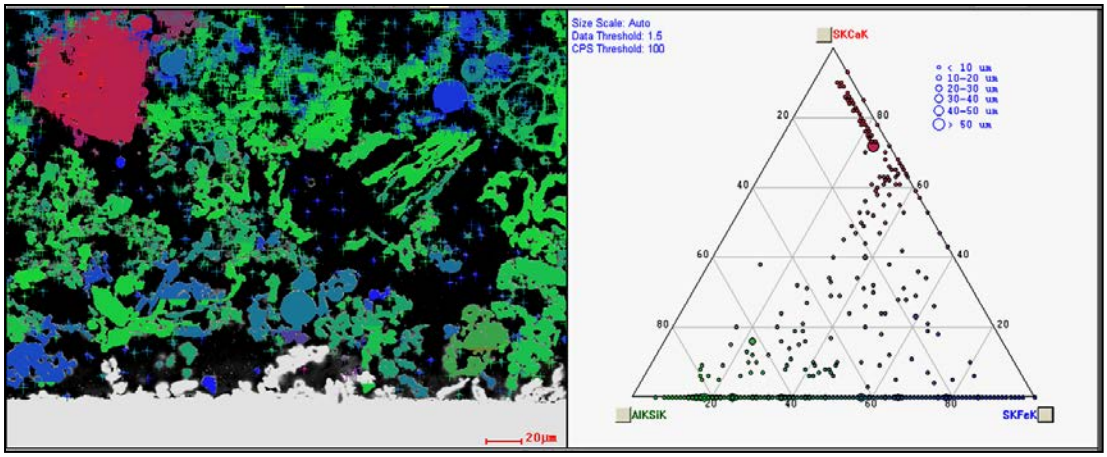

Figure 194 - Kentucky RT1 Ternary Diagram Measuring S + Ca, Si + Al, and S + Fe.

4.3.12.7 Mahoning Particle Ternary Diagrams

The ternary diagrams for the Mahoning deposits are shown in Figures 197-200. The Mahoning deposit is composed of primarily Si, Al, and Fe. The majority of particles are located along the bottom axis, indicating that they contain little S. For those particles with S, the total of Ca+S is typically below 30% and the particles are located in a diagonal as was seen in PRB and Beulah zap. There appears to be little difference between the oxidizing and the reducing regions and between the top and bottom sleeves, except that the OT4 deposit contains a few particles in the Fe+S corner.

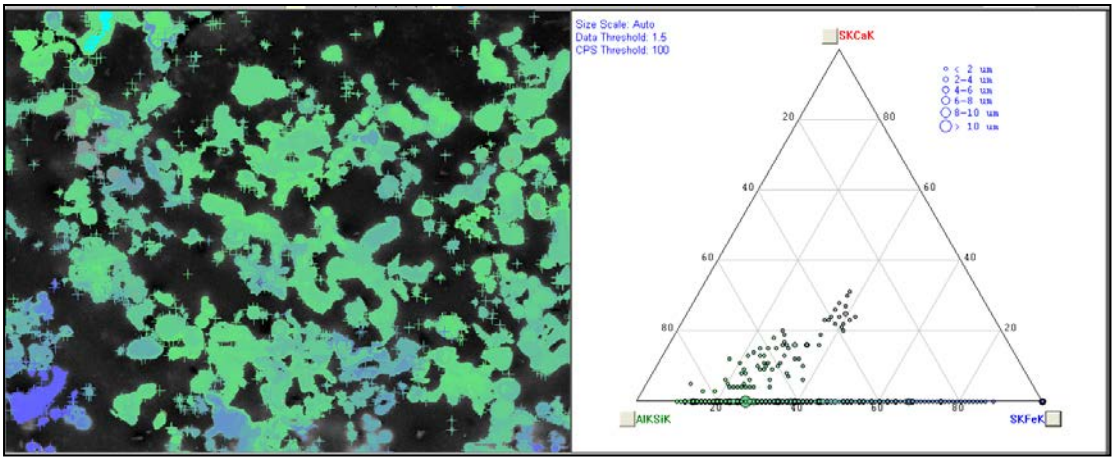

Figure 195 - Mahoning OB1-2 Ternary Diagram Measuring S + Ca, Si + Al, and S + Fe.

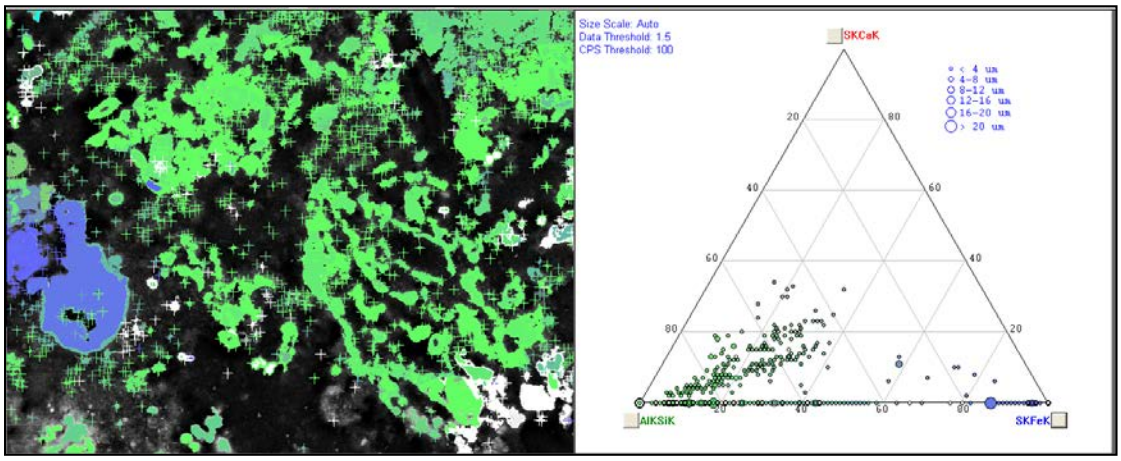

Figure 196 - Mahoning OT4-2 Ternary Diagram Measuring S + Ca, Si + Al, and S + Fe.

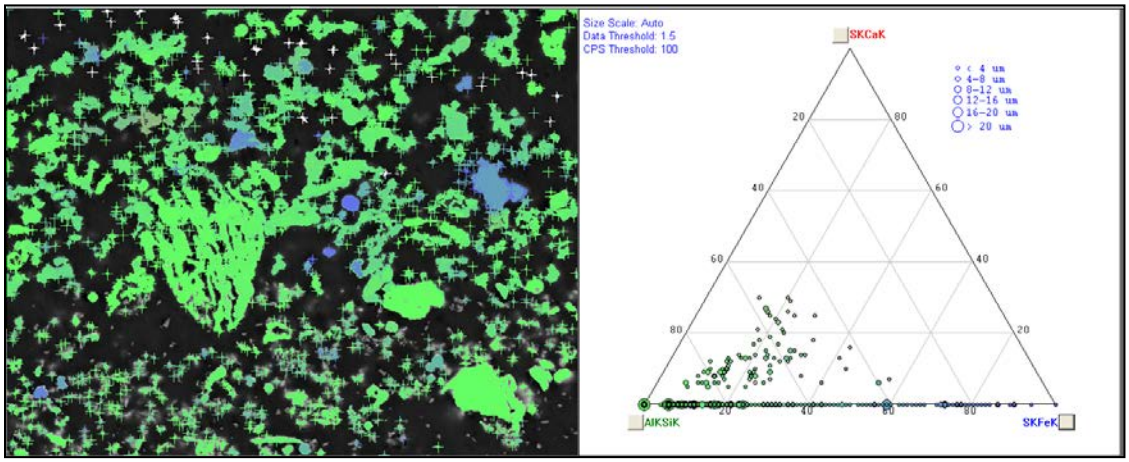

Figure 197 - Mahoning RB3 Ternary Diagram Measuring S + Ca, Si + Al, and S + Fe.

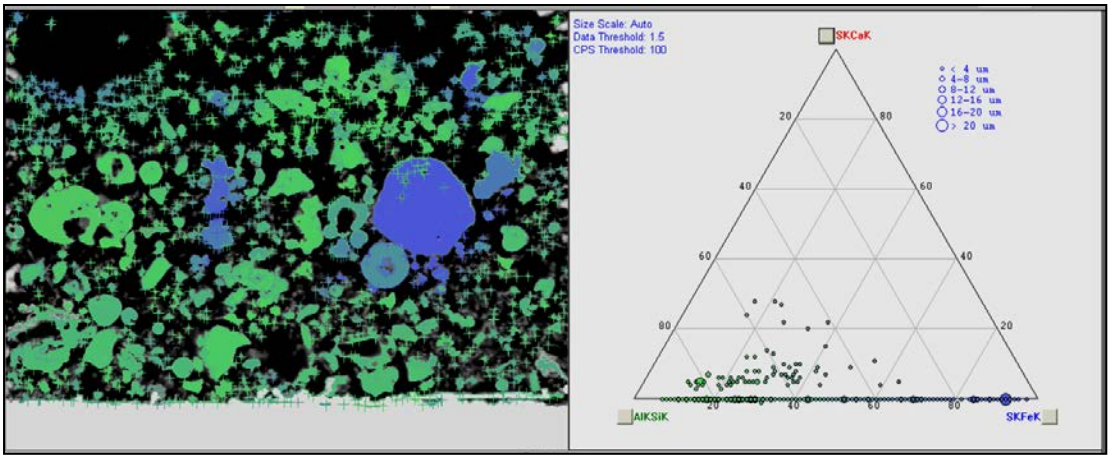

Figure 198 - Mahoning RT3 Ternary Diagram Measuring S + Ca, Si + Al, and S + Fe.

4.3.12.8Pittsburgh Particle Ternary Diagrams

The ternary diagrams for the Pittsburgh deposits are found in Figures 201-204. The Pittsburgh ternary diagrams show most of the particles on the bottom axis of the triangle. The particles that are not on the bottom axis are distributed in a diagonal pattern as was the case for almost all of the particles in the PRB or Beulah Zap coals. These ternary diagrams are most similar to those for the Indiana and Mahoning coals.

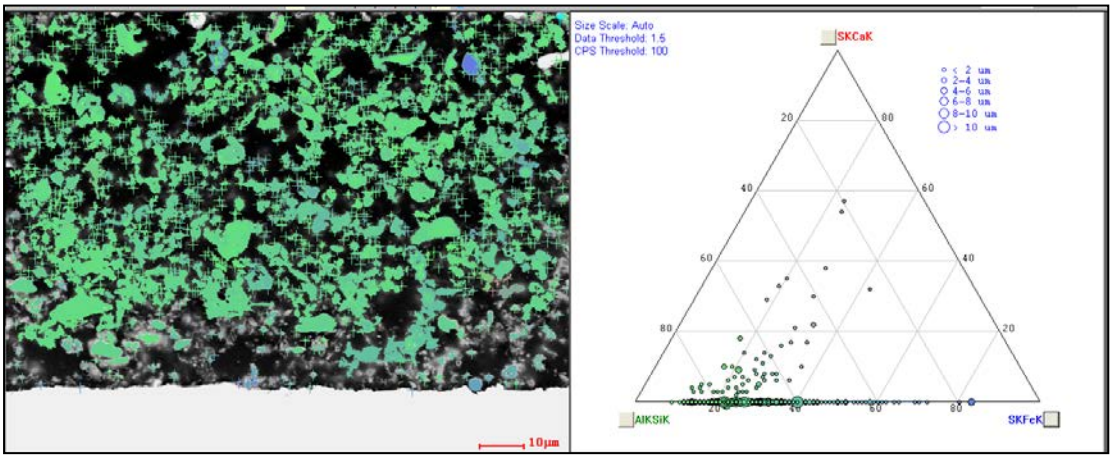

Figure 199 - Pittsburgh OB1 Ternary Diagram Measuring S + Ca, Si + Al, and S + Fe.

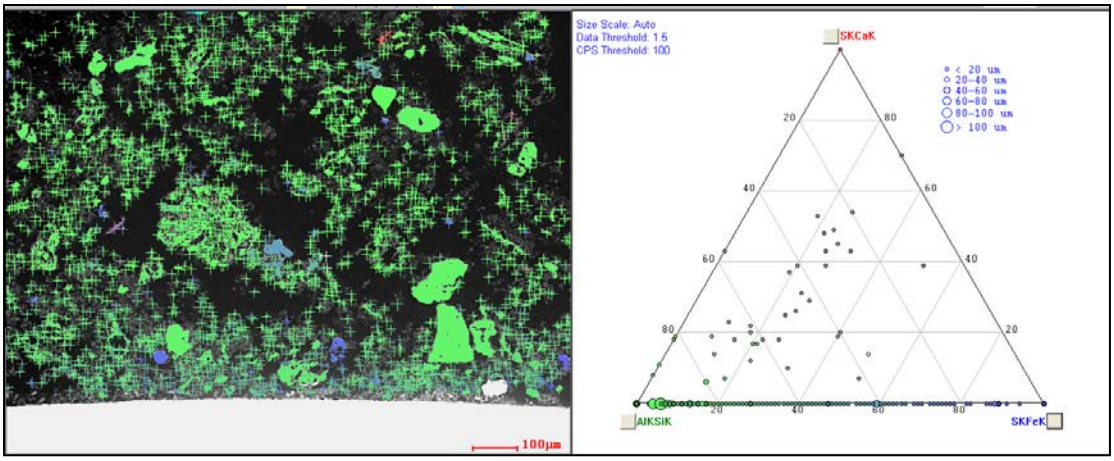

Figure 200 - Pittsburgh OT5-1 Ternary Diagram Measuring S + Ca, Si + Al, and S + Fe.

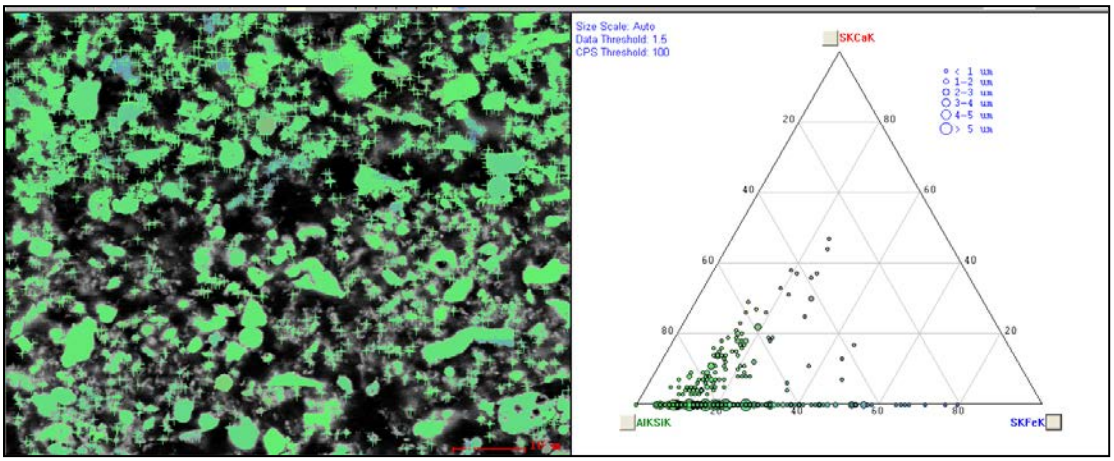

Figure 201 - Pittsburgh RB5 Ternary Diagram Measuring S + Ca, Si + Al, and S + Fe.

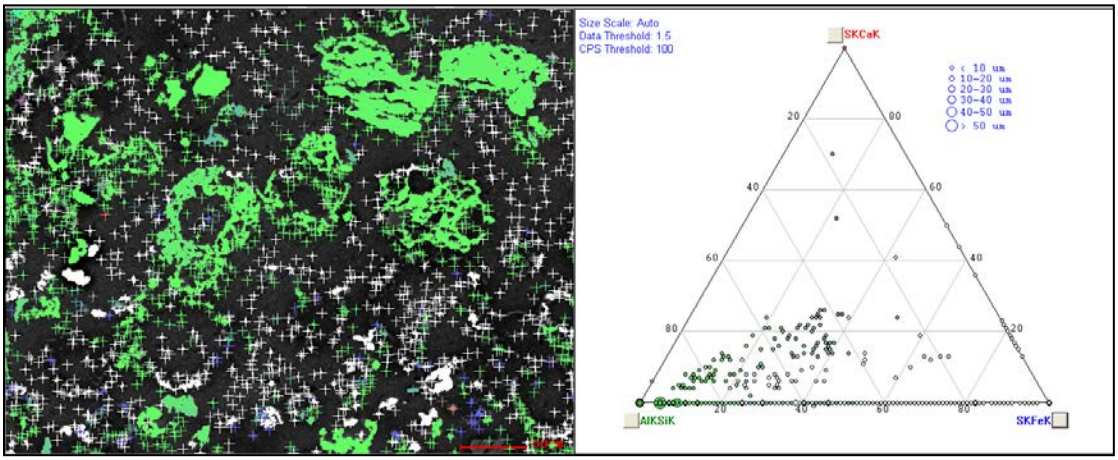

Figure 202 - Pittsburgh RT4-2 Ternary Diagram Measuring S + Ca, Si + Al, and S + Fe.

4.3.12.9 General Observations of Ternary Stability Diagram

The ternary stability diagrams of the deposit samples can be categorized into three groups: (1) Beulah Zap and PRB where the particles were located primarily along a diagonal pattern from the corner of Si+Al to the opposite axis, (2) Indiana, Pittsburgh, and Mahoning where the majority of the particles were present along the bottom axis containing little S and the remainder of particles are distributed in a diagonal pattern, and (3) Illinois #6, Kentucky, and Gatling where most particles were located along the bottom axis but a large number of particles was also spread throughout the bottom center area.

4.3.13 Elemental Enrichment and Depletion in Deposit Samples

The results discussed in the previous sections show that, although elemental compositions of the deposit samples from EDS analyses are generally consistent with those based on the ASTM coal ash analysis, there are often significant differences. This section discusses the differences between the deposit composition of each element and the coal ash analysis. For sulfur and chlorine, a comparison with the coal ultimate analysis and ASTM ash analysis is presented. For the other elements, the composition is compared only to that of the ASTM ash analysis. For each of the elements, the ratio of deposit mass fraction ($Y_{i,EDS}$) to the ASTM ash mass fraction ($Y_{i,ASTM}$) of an element has been used to determine an enrichment factor, E_i as shown by Eq. 11.

$$E_i = \frac{Y_{i,EDS}}{Y_{i,ASTM}} \qquad \text{Eq. 11}$$

4.3.13.1 Sulfur Analysis

The sulfur concentrations determined using EDS for the deposit samples collected from all four probe locations are plotted against the total sulfur content in coal, as shown in Figure 205. The data show that the weight percent of sulfur in the deposit does not correlate well with the weight percent of sulfur in coal. The two low-rank coals on the left are low in sulfur and yet they produced deposits of similar sulfur concentrations to those of the high sulfur coals on the right. The three coals in the middle produced low sulfur deposits.

The highest sulfur contents for the two low-rank coals on the left were found in the deposit samples collected from the bottom of the deposition probe in the oxidizing zone. These deposits are rich in sulfur compared to those of the ASTM coal analyses. The particles on the bottom of the sleeve in the oxidizing zone tend to be small, spherical, and high in Ca. On the contrary, high sulfur concentrations in the deposits from the high sulfur coals were found on the top sleeves in the reducing zone. In addition, these deposits consist of particles with a wide range of sizes, shapes, and high Fe. Pittsburgh #8 and Indiana has medium sulfur contents but low Ca and Fe concentrations. The deposit sulfur contents from these two coals are relatively low. These findings suggest that the amount of sulfur in deposit as well as its location depend primarily on

the amount of Ca and Fe in the coal. Mahoning is a medium sulfur coal and has a relatively high Fe content. However, the sulfur concentration in the Mahoning deposit samples does not seem to follow the trend of those high Fe coals.

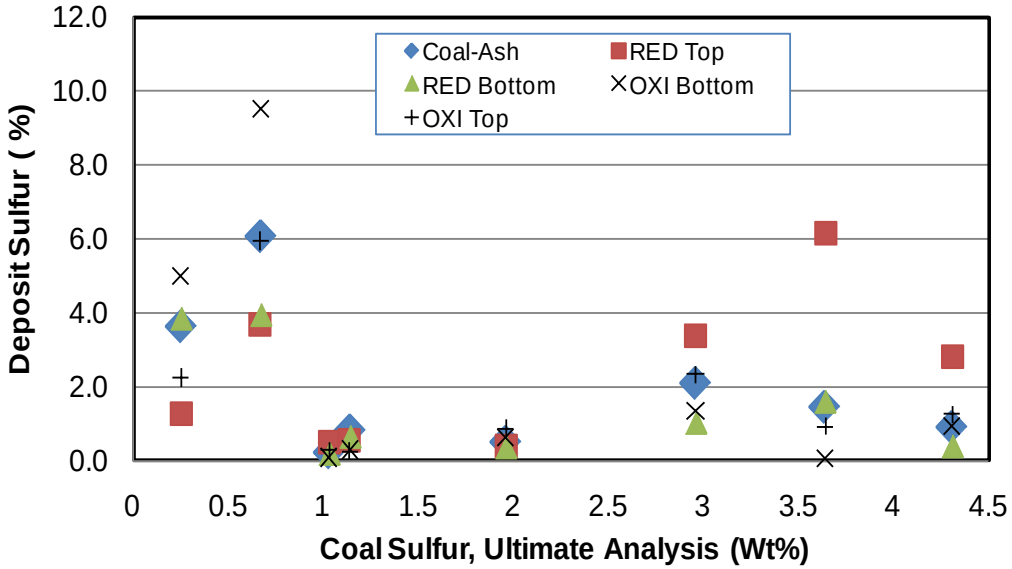

Figure 203 - Weight Percent of Sulfur in Deposits and Coal Ash as a Function of Coal Sulfur Content. The coals in Increasing Sulfur Content from Left to Right: PRB, Beulah Zap, Pittsburgh #8, Indiana, Mahoning, Illinois #6, Kentucky and Gatling.

Figure 206 shows the average deposit sulfur in the oxidizing and reducing zones as a function of the total coal Ca+Fe. The amount of sulfur in a deposit appears to be strongly related to the coal Ca+Fe content. The two data points in the bottom right corner of the graph are for deposits collected from the oxidizing zone of the Kentucky and Gatling tests. These data suggest that high Fe but low Ca coals do not produce high sulfur deposits in the oxidizing regions.

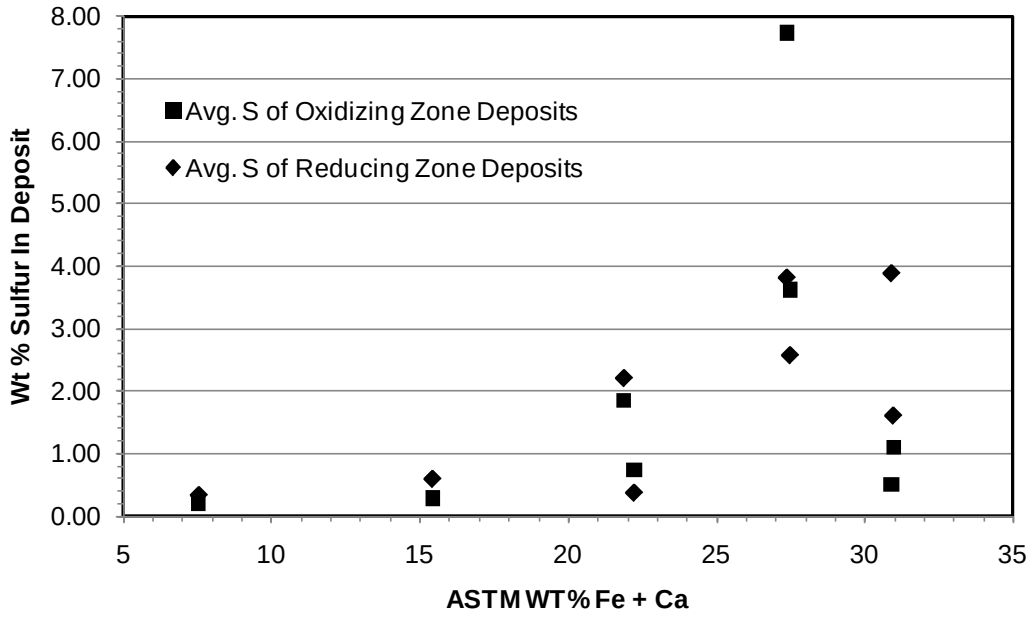

Figure 204 - Average Sulfur in Deposit Samples of Oxidizing and Reducing Zones as a Function of Coal Fe + Ca Content Determined by Standard Ash Analysis.

3.3.13.2. Chlorine Enhancement or Depletion in Deposit Samples

As has been discussed, the chlorine data are complicated by the presence of chlorine in the epoxy and thus is not considered in this analysis.

4.3.14 Particle Cross-Sectional Area

The SEM/EDS software was able to determine the average area of particles captured within an image. Because each image covered only a small fraction of the overall deposit sample, the calculated value may not be fully representative of the actual deposit sample. Results from this analysis are shown in Figures 207 and 208 for the top-sleeve and bottom-sleeve deposits, respectively. The average particle areas range from 9 to 75 μm^2 on the top deposits, while the areas are below 8 square microns in the bottom deposits. More scattering in the particle areas is observed for the top deposits. Clearly, smaller particles deposited preferentially on the bottom of the probes, while particles of various size and shape were on the top. The standard deviation of the particle areas is 39-340 μm^2 for the top deposits and 2.4-31.5 μm^2 for the bottom deposits. Such wide ranges indicate a large variation in the particle sizes.

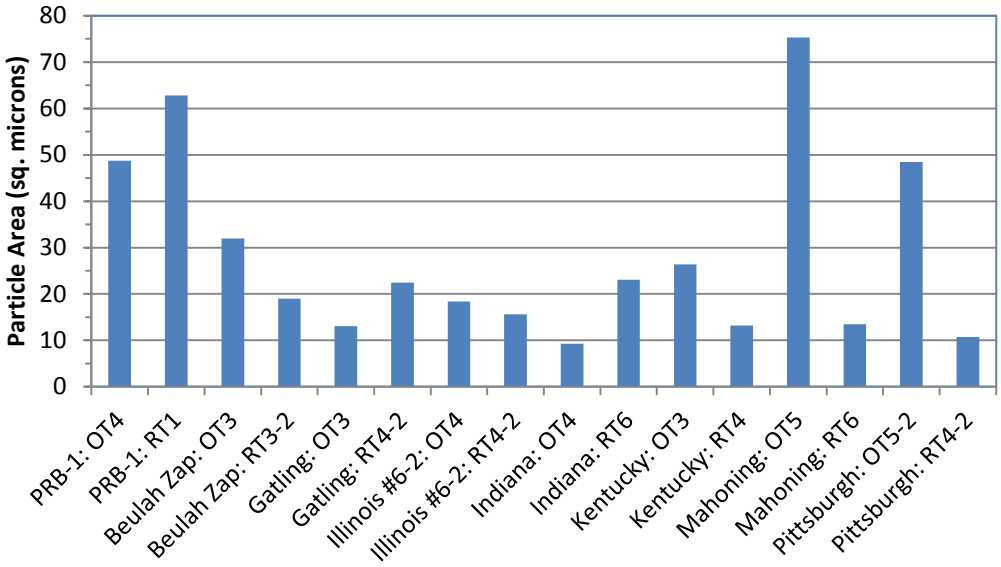

Figure 205 - Mean Particle Cross-Sectional Area for Top-Sleeve Samples.

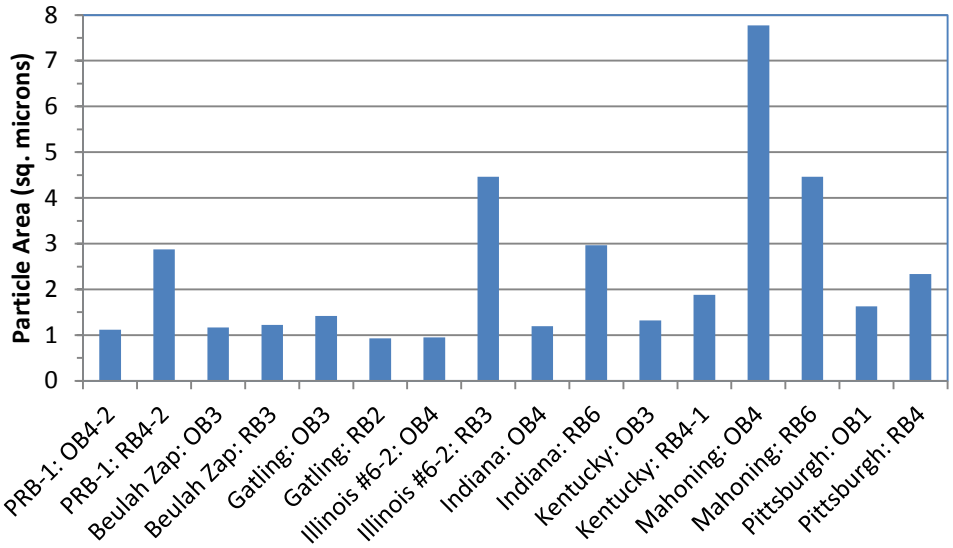

Figure 206 - Mean Particle Cross-Sectional Area for Bottom-Sleeve Samples.

4.4 Task 4 – Laboratory Corrosion Testing

Construction of two new fireside corrosion testing facilities at B&W Research Center in Barberton, OH, was completed in 2009. One of the laboratory facilities was since designated for performing the coal ash corrosion testing under oxidizing-sulfidizing conditions, and the other for furnace-wall corrosion under reducing-sulfidizing conditions. Both facilities are capable of running the planned long-term testing for 1000 hours each. However, the start of the laboratory testing phase (Task 4) was delayed due to an unexpected long approval process mentioned earlier for the workscope change in pilot-scale combustion facility. The approval process has impacted the start of Tasks 2 and 3 on gas and deposit sampling in the BFR and thus inevitably delayed the start of Task 4. As a result, the two fireside furnace facilities were diverted to other testing needs in 2009 for purposes outside of this project. After sufficient combustion information had been generated from the pilot-scale combustion testing facility (BFR) in Tasks 2 and 3, as detailed earlier in this report, the laboratory corrosion testing for Task 4 was commenced in 2010.

Based on the results of gas and deposit analyses in the BFR, a total of twenty one 1000-hour laboratory tests have been designed and performed to date. Among them, eleven tests were conducted to simulate the coal ash corrosion of superheaters in utility boilers burning (1) Black Thunder PRB at 1300^{o}F, (2) Illinois #6 Galatia at 1300^{o}F, (3) Beulah Zap lignite at 1300^{o}F, (4) Mahoning 7A at 1300^{o}F, (5) Indiana #6 Gibson at 1300^{o}F, (6) Ohio Gatling at 1300^{o}F, (7) Kentucky #11 at 1300^{o}F, (8) Pittsburgh #8 at 1300^{o}F, (9) Mahoning 7A at 1400^{o}F, (10) Mahoning 7A at 1200^{o}F, and (11) Mahoning 7A at 1100^{o}F, respectively. The other ten were performed to simulate the lower furnace corrosion in boilers burning (1) Black Thunder PRB at 850^{o}F, (2) Illinois #6 Galatia at 850^{o}F, (3) Beulah Zap lignite at 850^{o}F, (4) Ohio Mahoning 7A at 850^{o}F, (5) Indiana #6 Gibson at 850^{o}F, (6) Ohio Gatling at 850^{o}F, (7) Kentucky #11 at 850^{o}F, (8) Pittsburgh #8 at 850^{o}F, (9) Ohio Mahoning 7A at 950^{o}F, and (10) Ohio Mahoning 7A at 750^{o}F, respectively. Note that the Ohio Mahoning coal is listed multiple times for both the upper and lower furnace tests at different temperatures because it was selected as the model coal to reveal the temperature effect on fireside corrosion. Results of these tests are summarized in the following sections by location (i.e., oxidizing vs. reducing) and coal.

4.4.1 Upper Furnace Testing Under Oxidizing Conditions

4.4.1.1 Oxidizing Test #1 – Black Thunder PRB, 1300^{o}F

The first oxidizing test was performed at 1300^{o}F isothermally for a total of 1000 hours. The simulated coal ash composition is given in Table 29, which reflects the chemistry representative of the actual deposit collected from the BFR on an air-cooled probe discussed in Section 3.3.4.

The coal ash constituents were prepared in a batch process by first grinding each chemical to -80 mesh fineness, then weighing and mixing them to the desired composition. The combined constituents were then well mixed in a V-blender for a minimum of 2 hours.

Table 30 lists the mixed gas composition employed for the Black Thunder PRB test. This composition represents the most realistic conditions measured online from the BFR while burning the PRB coal, as discussed in Section 3.3.

Table 27 - Composition of Simulated Coal Ash Used in Oxidizing Laboratory Test for Black Thunder PRB Coal.

Constituent	Wt.%
Al_2O_3	17. 9
SiO_2	31.8
CaO	21.2
Fe_2O_3	5.1
KOH	0.8
TiO_2	1.2
$MgSO_4$	12.3
$MgSiO_3$	4.2
$Na2SO_4$	5.5

Table 28 - Composition of Mixed Gas Employed in Oxidizing Laboratory Test for Black Thunder PRB Coal.

Constituent	Vol.%[(a)]
CO_2	17
O_2	2.9
SO_2[(b)]	0.02
H_2O[(c)]	12
HCl	-
N_2	68.1

[(a)] Total flow rate of combined gases = 2 liters per minute.
[(b)] Added as 5% SO2 in N2.
[(c)] Added through a micro pump.

A total of thirteen materials, potential suitable for the superheater and reheater applications in advanced boiler systems, were evaluated in the PRB oxidizing test. These materials, consisting of alloys and weld overlays, are listed in Table 31, with detailed compositions given in Appendix D. The compositions of monolithic materials were certified by the alloy vendors, whereas those for the weld overlays were analyzed semi-quantitatively by B&W using SEM/EDS on the actual coating surfaces. It should be mentioned that the number of materials investigated was more than eleven as originally proposed. Reason for the increased number of materials was to extend the range of compositions so that the corrosion modeling work for Task 5 could be better accomplished. Without the additional alloy compositions, accuracy of the predictive equations for coal ash corrosion could suffer.

Duplicate coupons of each material were prepared and included in the test. One of the duplicate coupons was used for dimension loss measurement and the other for metallographic examination. Details of the sample preparation, experimental procedure, and metallographic examination are summarized below.

Each test coupon had an initial dimensions of approximately 1¼" x ¾" x thickness. The weld overlay specimens have been EDM-cut off the substrate to a nominal thickness of 0.070-inches (70 mils), while the monolithic specimens were approximately 1/8" thick. Other key features of the alloy coupons included:

Table 29 - Alloys Evaluated in Black Thunder PRB Oxidizing Laboratory Test.

Material
304H
Super 304H
310HCbN
230
347HFG
347H
72 WO
52 WO
671
740
617
120
800H

- Every dimensional coupon was notched at one corner to help identify the locations of the thickness measurement.
- A certified point micrometer was used to perform a matrix of thickness measurement at 15 predetermined locations on every dimensional coupon. The results were recorded to three decimal places in the logbook along with identification and certification information of the micrometer.
- The dimensional coupons were weighed to three decimal places of a gram using a certified digital balance before and after the test. The results were recorded in the logbook along with the identification and certification information of the balance.
- The coupon were cleaned with a solvent and handled with lint-free gloves.

Following the sample preparations, each test coupon was placed into a 20 ml high purity alumina crucible marked with the specimen ID using a high-temperature marker. The test coupons were positioned vertically in the center of the crucibles. Simulated coal ash was packed into the crucibles and filled to the top edges of the coupons with an approximately 1/16" layer of excess ash powder. The amounts of coal ash were weighed using a certified balance for all crucibles. Attempt was made to ensure about the same amount of coal ash filled in every crucible.

A general description of the test procedures following the placement of the test samples and simulated coal ash in the crucibles are summarized below.

1. Crucibles were loaded into the retort with the test coupons oriented edge-on toward the direction of the gas flow.

2. After the retort was sealed, nitrogen at a flow rate of 2 liters/min was allowed to pass through the system at room temperature.
3. The furnace system was brought to the test temperature under nitrogen.
4. The gas flow rate was checked to verify for tight seal.
5. Flow of the simulated flue gas was initiated and allowed to stabilize for at least 4 hours, followed by the start of test time.
6. At the end of the 1,000 hour test, the simulated flue gas was turned off, and nitrogen flowing at 2 liters/min was initiated while cooling the system to room temperature.
7. After cooling, the crucibles were removed from the retort and placed in a desiccator until the samples were ready to be evaluated.
8. Dimensional coupons were chemically cleaned to remove the simulated coal ash and corrosion products, followed by photographing.
9. The dimensional coupons were reweighed and the results recorded to three decimal places of a gram. The thicknesses of the dimensional coupons were re-measured at the same 15 locations as previously identified.
10. Metallographic coupons were carefully removed from the crucibles to retain as much adhering ash deposit and corrosion product as possible. The ash-covered coupons were then mounted in epoxy under vacuum to cure, followed by dry-cut through a traverse section containing the adhering deposit and scale.
11. The samples were then polished using kerosene (or alcohol) to preserve the integrity of ash deposit on the coupon surfaces. The polished samples were examined using both an optical microscopy and SEM/EDS.

Corrosion rates of the thirteen materials investigated in the PRB oxidizing test were calculated based on the measured weight and thickness losses and are summarized in Figure 209. The red bars represent the rates derived from the weight loss measurements and the blue from the thickness losses. It should be mentioned that weight changes determined by using a digital balance can be extremely accurate. However, weight change measurements do not take into account of the thickness loss from localized corrosion attack and penetration. In comparison, the corrosion rates derived from weight loss data are more representative of the averaged wastage values, whereas those based on thickness loss are of the worst case. A large difference between these two values indicates the presence of significant localized corrosion attack on the materials. From the materials performance standpoint, both the averaged and worst corrosion rates for each alloy are of important from the modeling standpoint. It is also necessary to compare the corrosion rates of a given alloy exposed to different test conditions, i.e., different gas and deposit compositions for different coals, to get a broader perspective of the true behavior of the alloy.

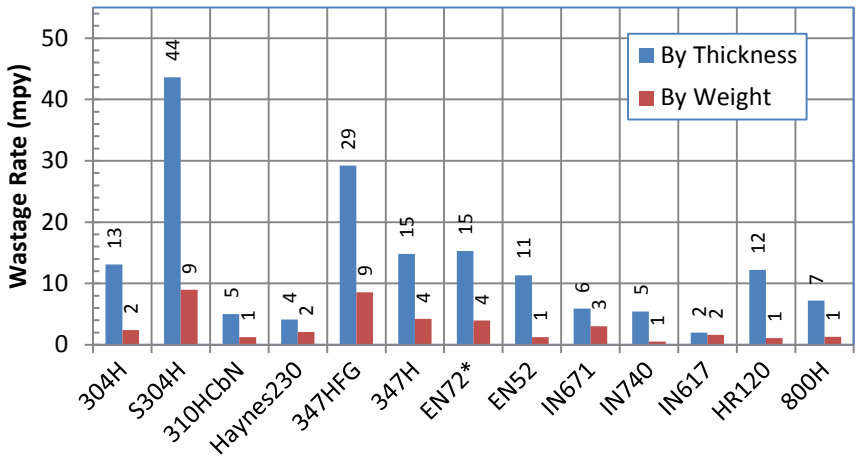

***The corrosion rate of 72 WO from weight loss is likely to be artificially high due to evidence of the ferritic substrate that was not completely removed by EDM before testing.**

Figure 207 - Comparison of Corrosion Rates Calculated from Both Weight Loss and Thickness Loss Data for Different Materials Evaluated in the 1000-Hour WY Black Thunder PRB Oxidizing Test at 1300°F.

4.4.1.2 Oxidizing Test #2 - Illinois #6 Galatia Coal, 1300°F

The second oxidizing test was carried out to simulate the coal ash corrosion of superheaters and reheaters in utility boilers burning Illinois #6 Galatia coal. The test was conducted at 1300°F isothermally for a total of 1000 hours. The simulated coal ash composition is given in Table 32, which represents the actual deposit samples collected from the BFR via an air-cooled probe discussed in Section 3.3.4. The coal ash constituents were prepared in the same batch process as discussed earlier for the PRB coal.

Table 30 - Composition of Simulated Coal Ash Used in Oxidizing Laboratory Test for Illinois #6 Galatia Coal.

Constituent	Wt.%
Al_2O_3	11.1
SiO_2	24.4
CaO	2.2
Fe_2O_3	10.4
KOH	0.7
TiO_2	0.4
$MgSiO_3$	1.0
$Fe_2(SO_4)_3$	17.3
$MgSO_4$	10.0
K_2SO_4	4.8
Na_2SO_4	17.7

Table 33 lists the mixed gas composition employed for the Illinois #6 Galatia test. Again, as discussed in Section 3.3, the composition represents the most realistic combustion conditions

measured online from the BFR while burning the Illinois #6 Galatia coal. Note that this gas composition contains significantly higher amounts of SO_2 and HCl than those for the PRB coal.

Table 31 - Composition of Mixed Gas Employed in Upper Furnace Laboratory Test for Illinois #6 Galatia Coal.

Constituent	Vol.%[(a)]
CO_2	16
O_2	3
SO_2[b]	0.23
H_2O[c]	7
HCl[d]	0.02
N_2	73.8

[a] Total flow rate of combined gases = 2 liters per minute.
[b] Added as 5% SO2 in N2.
[c] Added through a micro pump.
[d] Dissolved in water as a solution.

The material set evaluated in the Galatia oxidizing test is listed in Table 34. Compared to Table 31 for PRB, Alloy 671 was not included in this test and hereafter. Alloy 671 was manufactured by Special Metals many years ago as a bimetallic tubing product. Due to its high cost and low market demand, this product is no longer available commercially. The last two 671 coupons were exhausted in the PRB test, and this material had to be eliminated from future tests of this project. Fortunately, weld overlay EN72 consists of a composition similar to 671 and therefore can adequately replace this alloy. Consequently, a total of twelve materials were investigated in the Illinois #6 Galatia test.

Table 32 - Evaluated in Illinois #6 Galatia Oxidizing Laboratory Test Alloys.

Material
304H
Super 304H
310HCbN
230
347HFG
347H
72 WO
52 WO
740
617
120
800H

The actual alloy and weld overlay compositions are given in Appendix D. Duplicate samples were prepared for each material and included in the test, one for dimensional and weight loss measurement and the other for metallographic examination. The sample preparation and test procedures were identical to those described in Section 3.4.1.1 and thus are not repeated here.

Corrosion rates of the twelve materials investigated in the Galatia oxidizing test were calculated based on the measured weight and thickness losses and are summarized in Figure 210. The red bars represent the rates derived from the simple weight loss measurements and the blue from the thickness losses. Note that these rates are significantly higher than those reported for the PRB coal previously. These results suggest that only weld overlays 72 and 52, potentially Alloy 120 as well, exhibit promises for use in the A-USC boiler system burning the Illinois #6 Galatia coal.

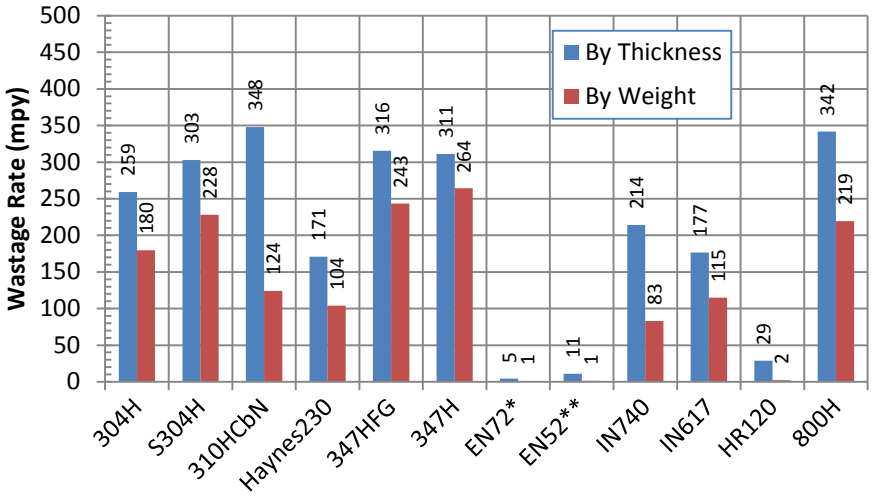

* Coupon was curve in shape. For calculation purpose, it was considered flat.
** Coupon was curve in shape with the OD surface ground flat to facilitate thickness measurement.

Figure 208 - Comparison of Corrosion Rates Calculated from Both Weight Loss and Thickness Loss Data for Different Materials Evaluated in the 1000-Hour Illinois #6 Galatia Oxidizing Test at 1300°F.

4.4.1.3 Oxidizing Test #3 – North Dakota Beulah Zap Lignite, 1300°F

The third oxidizing corrosion test was intended to simulate the coal ash corrosion of superheaters and reheaters in advanced utility boilers burning Beulah Zap lignite coal. The test was conducted at 1300°F isothermally for a total of 1000 hours. The simulated coal ash composition is given in Table 35, which represented the actual deposit samples collected from the BFR via an air-cooled probe discussed in Section 3.3.4. The coal ash constituents were prepared in the same batch process as discussed for the PRB coal.

Table 36 lists the mixed gas composition employed for the ND lignite test. Again, the composition represents the most realistic combustion conditions measured online from the BFR while burning the Beulah Zap lignite coal, as discussed in Section 3.3. Note that this gas composition contained relatively low amounts of SO_2 and HCl compared to those for the Illinois #6 Galatia coal but were comparable to those for the PRB.

Table 33 - Composition of Simulated Coal Ash Used in Oxidizing Laboratory Test for ND Beulah Zap Lignite Coal.

Constituent	Wt.%
Al_2O_3	9.3
SiO_2	24.0
CaO	12.0
Fe_2O_3	3.1
KOH	0.9
TiO_2	0.5
$Fe_2(SO_4)_3$	19.5
$CaSO_4$	0.3
$MgSO_4$	19.5
K_2SO_4	0.4
Na_2SO_4	10.2

Table 34 - Composition of Mixed Gas Employed in Oxidizing Laboratory Test for ND Beulah Zap Lignite Coal.

Constituent	Vol.%[(a)]
CO_2	14
O_2	3
SO_2[b]	0.05
H_2O[c]	12
HCl[d]	0.0002
N_2	70.9

[a] Total flow rate of combined gases = 2 liters per minute.
[b] Added as 5% SO2 in N2.
[c] Added through a micro pump.
[d] Dissolved in water as a solution.

The material set evaluated in the Beulah Zap lignite oxidizing test is listed in Table 37, with the actual alloy and weld overlay compositions given in Appendix D. Similarly, duplicate samples were prepared for each material and included in the test, one for dimensional and weight loss measurement and the other for metallographic examination. The sample preparation and test procedures were identical to those described in Section 3.4.1.1 and are not repeated here.

Corrosion rates of the twelve materials investigated in the Beulah Zap lignite oxidizing test were calculated based on the measured thickness and weight changes and are summarized in Figure 211. The red bars represent the rates derived from the weight loss measurements and the blue from the thickness losses. These corrosion rates are more comparable to those of the PRB coal than the Illinois #6, as expected.

Table 35 - Alloys Evaluated in ND Beulah Zap Lignite Oxidizing Laboratory Test.

Material
304H
Super 304H
310HCbN
230
347HFG
347H
72 WO
52 WO
740
617
120
800H

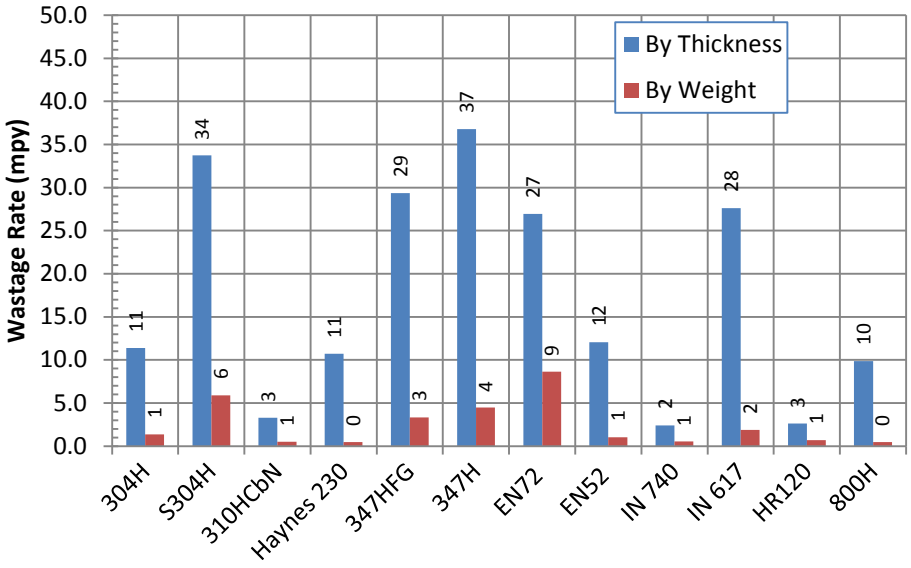

Figure 209 - Comparison of Corrosion Rates Calculated from Both Weight Loss and Thickness Loss Data for Different Materials Evaluated in the 1000-Hour ND Beulah Zap Lignite Oxidizing Test at 1300°F.

4.4.1.4 Oxidizing Test #4 – Ohio Mahoning 7A, 1300°F

The fourth oxidizing corrosion test was performed to simulate the coal ash corrosion of superheaters and reheaters in utility boilers burning Ohio Mahoning 7A coal. The test was conducted at 1300°F isothermally for a total of 1000 hours. The coal ash composition is given in Table 38, which represented the actual deposit samples collected from the BFR via an air-cooled

probe discussed in Section 3.3.4. The coal ash constituents were prepared in the same batch process as discussed for the PRB coal.

Table 36 - Composition of Simulated Coal Ash Used in Oxidizing Laboratory Test for OH Mahoning 7A Coal.

Constituent	Wt.%
Al_2O_3	16.9
SiO_2	22.6
CaO	0.9
Fe_2O_3	7.8
KOH	1.0
TiO_2	0.6
$MgSiO_3$	0.3
$Fe_2(SO_4)_3$	19.8
$MgSO_4$	10.1
K_2SO_4	4.8
Na_2SO_4	15.1

Table 39 lists the mixed gas composition employed for the Mahoning test. Again, as discussed in Section 3.3, the composition represents the most realistic combustion conditions measured online from the BFR while burning the Ohio Mahoning coal. This gas composition contained relatively low concentrations of SO_2 and HCl than those for the Illinois #6 Galatia coal but higher than those for the PRB and lignite.

Table 37 - Composition of Mixed Gas Employed in Upper Furnace Laboratory Test for OH Mahoning 7A Coal.

Constituent	Vol.%[(a)]
CO_2	16
O_2	3
SO_2[b]	0.155
H_2O[c]	9
HCl[d]	0.011
N_2	71.8

[a] Total flow rate of combined gases = 2 liters per minute.
[b] Added as 5% SO2 in N2.
[c] Added through a micro pump.
[d] Dissolved in water as a solution.

The material set evaluated in the Mahoning oxidizing test is listed in Table 40, with the actual alloy and weld overlay compositions given in Appendix D. Again, duplicate samples were prepared for each material and included in the test, one for dimensional and weight loss measurement and the other for metallographic examination. The sample preparation and test procedures were identical to those described in Section 3.4.1.1 and are not repeated here.

Corrosion rates of the twelve materials investigated in the Ohio Mahoning 7A oxidizing test were calculated based on the measured thickness and weight changes and are summarized in Figure 212. The red bars represent the rates derived from the weight loss measurements and the blue from the thickness losses including internal penetrations under the coupon surfaces.

Table 38 - Alloys Evaluated in OH Mahoning 7A Oxidizing Laboratory Test.

Material
304H
Super 304H
310HCbN
230
347HFG
347H
72 WO
52 WO
740
617
120
800H

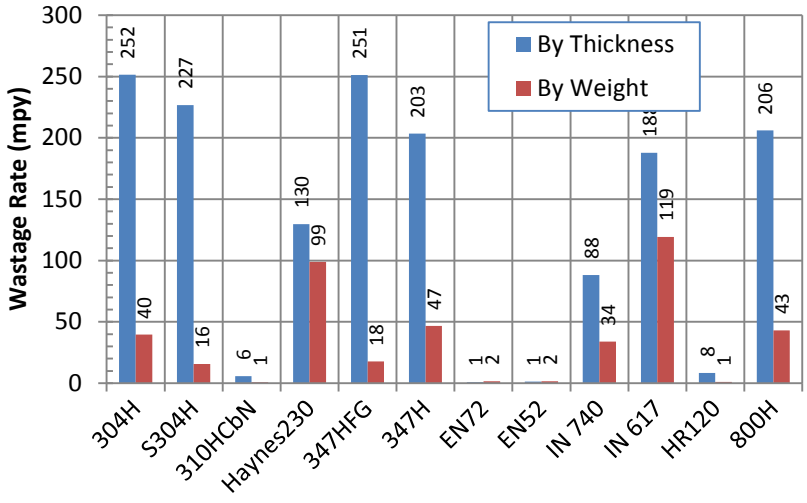

Figure 210 - Comparison of Corrosion Rates Calculated from Both Weight Loss and Thickness Loss Data for Different Materials Evaluated in the 1000-Hour Ohio Mahoning 7A Oxidizing Test at 1300°F.

4.4.1.5 Oxidizing Test #5 – Indiana #6 Gibson, 1300°F

The fifth oxidizing corrosion test was performed to simulate the coal ash corrosion of superheaters and reheaters in utility boilers burning Indiana #6 Gibson coal. The test was conducted at 1300°F isothermally for a total of 1000 hours. The simulated coal ash composition is given in Table 41, which represented the actual deposit samples collected from the BFR via an air-cooled probe discussed in Section 3.3.4. Deposit of the coal ash constituents was prepared in the same batch process as discussed previously for the PRB coal.

Table 39 - Composition of Simulated Coal Ash Used in Oxidizing Laboratory Test for Indiana #6 Gibson Coal.

Constituent	Wt.%
Al_2O_3	12.8
SiO_2	26.6
CaO	1.4
Fe_2O_3	7.5
KOH	1.3
TiO_2	0.6
$Fe_2(SO_4)_3$	17.2
K_2SO_4	12.4
Na_2SO_4	14.2
Na_2O	0.1
K_2CO_3	0.2
Na_2CO_3	5.9

Table 42 lists the mixed gas composition employed for the Indiana #6 test. Again, the composition represented the most realistic combustion conditions measured online from the BFR while burning the Indiana coal, as discussed in Section 3.3. Note that the mixed gas contained 110 ppm (or 0.011% by volume) of HCl due to the coal chlorine content.

Table 40 - Composition of Mixed Gas Employed in Upper Furnace Laboratory Test for Indiana #6 Gibson Coal.

Constituent	Vol.%[(a)]
CO_2	13
O_2	3
SO_2[b]	0.086
H_2O[c]	7.5
HCl[d]	0.011
N_2	76.4

[a] Total flow rate of combined gases = 2 liters per minute.
[b] Added as 5% SO2 in N2.
[c] Added through a micro pump.
[d] Dissolved in water as a solution.

The material set evaluated in the Indiana #6 oxidizing test is listed in Table 43. The actual alloy and weld overlay compositions are given in Appendix D. Again, duplicate samples were prepared for each material and included in the test, one for dimensional and weight loss measurement and the other for metallographic examination. The sample preparation and test procedures were identical to those described in Section 3.4.1.1.

Corrosion rates of the twelve materials investigated in the Indiana #6 Gibson oxidizing test were calculated based on the measured thickness and weight changes and are summarized in Figure 213. The red bars represent the rates derived from the weight loss measurements and the blue from the thickness losses. Note that Alloys 230 and 617, both are considered strong candidates for the A-USC boiler applications due to their high creep strength, exhibited worst corrosion performance in the test.

Table 41 - Alloys Evaluated in Indiana #6 Gibson Oxidizing Laboratory Test.

Material
304H
Super 304H
310HCbN
230
347HFG
347H
72 WO
52 WO
740
617
120
800H

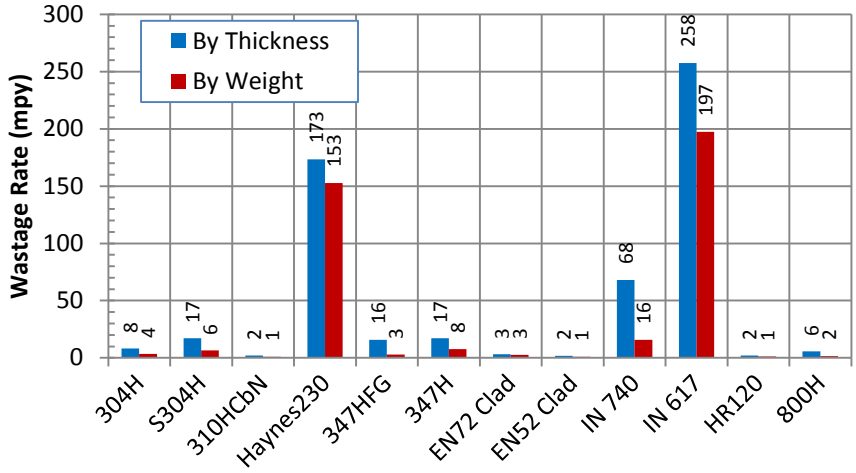

Figure 211 - Comparison of Corrosion Rates Calculated from Both Weight Loss and Thickness Loss Data for Different Materials Evaluated in the 1000-Hour Indiana #6 Gibson Oxidizing Test at 1300°F.

4.4.1.6 Oxidizing Test #6 – Ohio Gatling, 1300°F

The sixth oxidizing corrosion test was performed to simulate the coal ash corrosion of superheaters and reheaters in utility boilers burning high-sulfur Ohio Gatling coal. The test was conducted at 1300°F isothermally for a total of 1000 hours. The simulated coal ash composition is given in Table 44, which represented the actual deposit samples collected from the BFR via an air-cooled probe discussed in Section 3.3.4. Mixture of the coal ash constituents was prepared in the same batch process as discussed previously for the PRB coal.

Table 42 - Composition of Simulated Coal Ash Used in Oxidizing Laboratory Test for Ohio Gatling Coal.

Constituent	Wt.%
Al_2O_3	13.4
SiO_2	21.3
CaO	1.0
Fe_2O_3	13.5
K_2TiO_3	0.9
$Fe_2(SO_4)_3$	17.8
$KAl(SO_4)_2$	0.4
$CaSO_4$	0.1
K_2SO_4	16.8
Na_2SO_4	1.9
$CaCO_3$	2.6
K_2CO_3	0.9
$MgCO_3$	6.3
Na_2CO_3	3.3

Table 45 lists the mixed gas composition employed for the Ohio Gatling test. Again, the composition represented the most realistic combustion conditions measured online from the BFR while burning the Gatling coal, as discussed in Section 3.3. Note that the mixed gas contained 2700 ppm of SO_2 due to the highest coal sulfur content among the eight coals investigated in this study. However, the HCl concentration was only 5 ppm due to a negligible amount of chlorine content in this coal.

The material set evaluated in the Ohio Gatling oxidizing test is listed in Table 46, with the actual alloy and weld overlay compositions given in Appendix D. Again, duplicate samples were prepared for each material and included in the test, one for dimensional and weight loss measurement and the other for metallographic examination. The sample preparation and test procedures were identical to those described in Section 3.4.1.1 and are not repeated here.

Table 43 - Composition of Mixed Gas Employed in Upper Furnace Laboratory Test for Ohio Gatling Coal.

Constituent	Vol.%[(a)]
CO_2	15
O_2	3
SO_2[b]	0.270
H_2O[c]	7
HCl[d]	0.0005
N_2	74.73

[a] Total flow rate of combined gases = 2 liters per minute.
[b] Added as 5% SO2 in N2.
[c] Added through a micro pump.
[d] Dissolved in water as a solution.

Table 44 - Alloys Evaluated in Ohio Gatling Oxidizing Laboratory Test.

Material
304H
Super 304H
310HCbN
230
347HFG
347H
72 WO
52 WO
740
617
120
800H

Corrosion rates of the twelve materials investigated in the Ohio Gatling oxidizing test were calculated based on the measured thickness and weight changes and are summarized in Figure 214. The red bars represent the corrosion rates calculated from simple weight loss measurements and the blue from the thickness losses. Note that the measured corrosion rates, in general, are quite high due to a very high sulfur content in the Ohio Gatling coal.

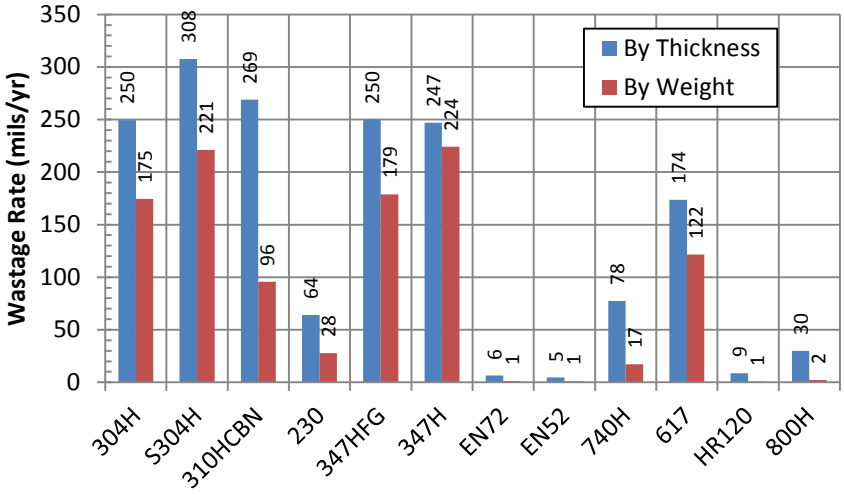

Figure 212 - Comparison of Corrosion Rates Calculated from Both Weight Loss and Thickness Loss Data for Different Materials Evaluated in the 1000-Hour Ohio Gatling Oxidizing Test at 1300°F.

4.4.1.7 Oxidizing Test #7 – Kentucky #11, 1300°F

The seventh oxidizing corrosion test was performed to simulate the coal ash corrosion of superheaters and reheaters in utility boilers burning high-sulfur Kentucky #11 coal. The test was conducted at 1300°F isothermally for a total of 1000 hours. The simulated coal ash composition is given in Table 47, which represented the actual deposit samples collected from the BFR via an air-cooled probe discussed in Section 3.3.4. Mixture of the coal ash constituents was prepared in the same batch process as discussed previously for the PRB coal.

Table 45 - Composition of Simulated Coal Ash Used in Oxidizing Laboratory Test for Kentucky #11 Coal.

Constituent	Wt.%
Al_2O_3	10.5
SiO_2	21.5
CaO	2.8
Fe_2O_3	14.3
KOH	0.6
TiO_2	0.4
$Fe_2(SO_4)_3$	17.6
$CaSO_4$	0.1
K_2SO_4	12.2
$MgSO_4$	9.7
Na_2SO_4	7.1
$MgCO_3$	3.3

Table 48 lists the mixed gas composition employed for the Kentucky coal test. Again, the composition represented the most realistic combustion conditions measured online from the BFR while burning the Kentucky coal, as discussed in Section 3.3. Note that the mixed gas contained

2550 ppm of SO_2 due to a relatively high sulfur content in the coal, while the HCl concentration of 110 ppm was moderate due to its ~0.2% chlorine content.

Table 46 - Composition of Mixed Gas Employed in Upper Furnace Laboratory Test for Kentucky #11 Coal.

Constituent	Vol.%[(a)]
CO_2	16
O_2	3
SO_2[b]	0.255
H_2O[c]	8
HCl[d]	0.011
N_2	72.73

[a] Total flow rate of combined gases = 2 liters per minute.
[b] Added as 5% SO2 in N2.
[c] Added through a micro pump.
[d] Dissolved in water as a solution.

The material set evaluated in the Kentucky #11 oxidizing test is listed in Table 49, with the actual alloy and weld overlay compositions given in Appendix D. Again, duplicate samples were prepared for each material and included in the test, one for dimensional and weight loss measurement and the other for metallographic examination. The sample preparation and test procedures were identical to those described in Section 3.4.1.1 and are not repeated here.

Table 47 - Alloys Evaluated in Kentucky #11 Oxidizing Laboratory Test.

Material
304H
Super 304H
310HCbN
230
347HFG
347H
72 WO
52 WO
740
617
120
800H

Corrosion rates of the twelve materials investigated in the Kentucky #11 oxidizing test were calculated based on the measured thickness and weight changes and are summarized in Figure 215. The red bars represent the corrosion rates calculated from simple weight loss measurements and the blue from the thickness losses.

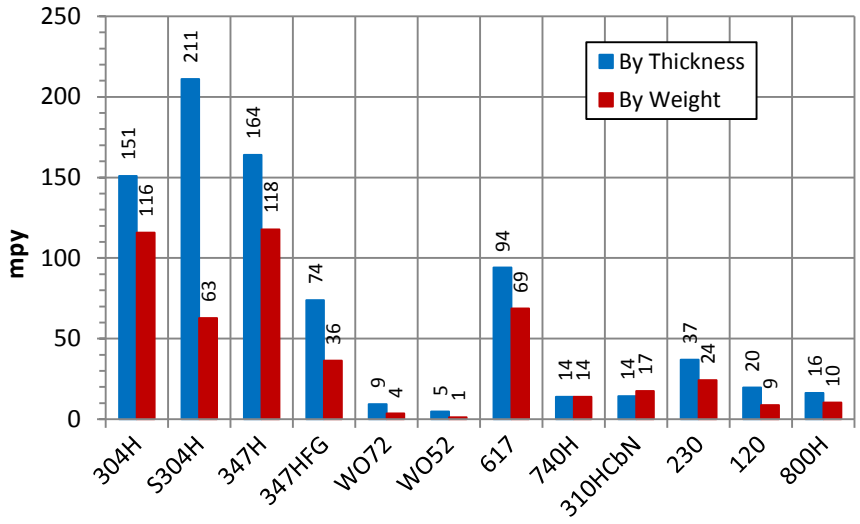

Figure 213 - Comparison of Corrosion Rates Calculated from Both Weight Loss and Thickness Loss Data for Different Materials Evaluated in the 1000-Hour Kentucky #11 Oxidizing Test at 1300°F.

4.4.1.8 Oxidizing Test #8 – Pittsburgh #8, 1300°F

The eighth oxidizing corrosion test was performed to simulate the coal ash corrosion of superheaters and reheaters in utility boilers burning low-sulfur Pittsburgh #8 coal. The test was conducted at 1300°F isothermally for a total of 1000 hours. The simulated coal ash composition is given in Table 50, which represented the actual deposit samples collected from the BFR via an air-cooled probe discussed in Section 3.3.4. Mixture of the coal ash constituents was prepared in the same batch process as discussed previously for the PRB coal. Note that deposit of the Pittsburgh #8 coal consists of a significant amount of metal carbonates.

Table 51 lists the mixed gas composition employed for the Pittsburgh #8 coal test. Again, the composition represented the most realistic combustion conditions measured online from the BFR while burning the Pittsburgh coal, as discussed in Section 3.3. The mixed gas contained only 680 ppm of SO_2 due to a relatively low sulfur content in the coal, while the HCl concentration was negligible due to its very low chlorine content. This coal was relatively more difficult to burn in the pilot-scale combustion facility due to its low volatile content compared to those of the other coals. Therefore, approximately 600 ppm of CO gas was measured by the FTIR in the pilot-scale combustion test at the superheater location and thus included in this laboratory mixed gas.

The material set evaluated in the Pittsburgh #8 oxidizing test is listed in Table 52, with the actual alloy and weld overlay compositions given in Appendix D. Again, duplicate samples were prepared for each material and included in the test, one for dimensional and weight loss measurement and the other for metallographic examination to determine the sub-surface corrosion penetration. The sample preparation and test procedures were identical to those described in Section 3.4.1.1 and are not repeated here.

Table 48 - Composition of Simulated Coal Ash Used in Oxidizing Laboratory Test for Pittsburgh #8 Coal.

Constituent	Wt.%
Al_2O_3	16.8
SiO_2	26.2
Fe_2O_3	6.4
TiO_2	0.7
$Fe_2(SO_4)_3$	5.6
$CaCO_3$	10.5
K_2CO_3	16.5
$MgCO_3$	6.5
Na_2CO_3	11.0

Table 49 - Composition of Mixed Gas Employed in Upper Furnace Laboratory Test for Pittsburgh #8 Coal.

Constituent	Vol.%[(a)]
CO_2	14.5
CO	0.06
O_2	3
SO_2[b]	0.068
H_2O[c]	6.3
HCl[d]	0.0006
N_2	76.1

[a] Total flow rate of combined gases = 2 liters per minute.
[b] Added as 5% SO2 in N2.
[c] Added through a micro pump.
[d] Dissolved in water as a solution.

Table 50 - Alloys Evaluated in Pittsburgh #8 Oxidizing Laboratory Test.

Material
304H
Super 304H
310HCbN
230
347HFG
347H
72 WO
52 WO
740
617
120
800H

Corrosion rates of the twelve materials investigated in the Pittsburgh #8 oxidizing test were calculated based on the measured thickness and weight changes and are summarized in Figure 216. The red bars represent the corrosion rates calculated from simple weight loss measurements and the blue from the thickness losses.

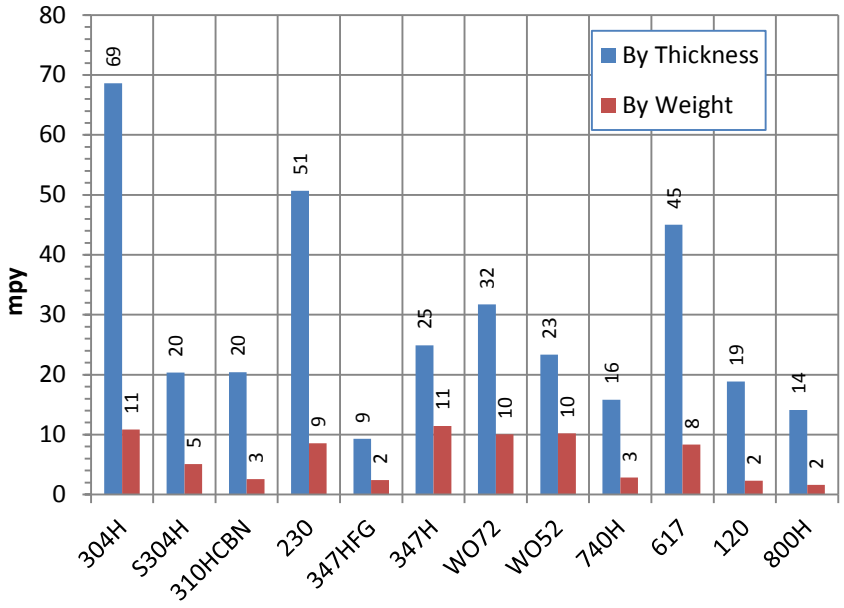

Figure 214 - Comparison of Corrosion Rates Calculated from Both Weight Loss and Thickness Loss Data for Different Materials Evaluated in the 1000-Hour Pittsburgh #8 Oxidizing Test at 1300°F.

4.4.1.9 Oxidizing Test #9 – Ohio Mahoning 7A, 1400°F

The ninth oxidizing corrosion test was performed to simulate the coal ash corrosion of superheaters and reheaters in utility boilers burning Ohio Mahoning 7A coal at a higher temperature. The test was conducted at 1400°F isothermally for a total of 1000 hours. The coal ash composition is given in Table 53, which represented the actual deposit samples collected from the BFR via an air-cooled probe discussed in Section 3.3.4. The coal ash constituents were prepared using the same batch process as discussed for the PRB coal.

Table 51 - Composition of Simulated Coal Ash Used in Oxidizing Laboratory Test for OH Mahoning 7A Coal.

Constituent	Wt.%
Al_2O_3	16.9
SiO_2	22.6
CaO	0.9
Fe_2O_3	7.8
KOH	1.0
TiO_2	0.6
$MgSiO_3$	0.3
$Fe_2(SO_4)_3$	19.8
$MgSO_4$	10.1
K_2SO_4	4.8
Na_2SO_4	15.1

Table 54 lists the mixed gas composition employed for the Mahoning test. Again, as discussed in Section 3.3, the composition represents the most realistic combustion conditions measured online from the BFR while burning the Ohio Mahoning coal. This gas composition contained relatively low concentrations of SO_2 and HCl than those for the Illinois #6 Galatia coal but higher than those for the PRB and lignite.

Table 52 - Composition of Mixed Gas Employed in Upper Furnace Laboratory Test for OH Mahoning 7A Coal.

Constituent	Vol.%[(a)]
CO_2	16
O_2	3
SO_2[b]	0.155
H_2O[c]	9
HCl[d]	0.011
N_2	71.8

[a] Total flow rate of combined gases = 2 liters per minute.
[b] Added as 5% SO2 in N2.
[c] Added through a micro pump.
[d] Dissolved in water as a solution.

The material set evaluated in the Mahoning oxidizing test is listed in Table 55, with the actual alloy and weld overlay compositions given in Appendix D. Again, duplicate samples were prepared for each material and included in the test, one for dimensional and weight loss measurement and the other for metallographic examination. The sample preparation and test procedures were identical to those described in Section 3.4.1.1 and are not repeated here.

Table 53 - Alloys Evaluated in OH Mahoning 7A Oxidizing Laboratory Test.

Material
304H
Super 304H
310HCbN
230
347HFG
347H
72 WO
52 WO
740
617
120
800H

Corrosion rates of the twelve materials investigated in the Ohio Mahoning 7A oxidizing test were calculated based on the measured thickness and weight changes and are summarized in Figure 217. The red bars represent the rates derived from the weight loss measurements and the blue from the thickness losses including internal penetrations under the coupon surfaces.

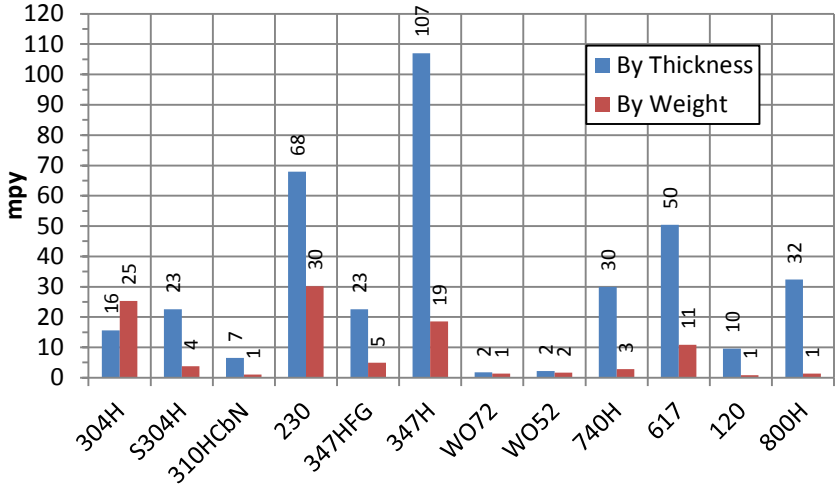

Figure 215 - Comparison of Corrosion Rates Calculated from Both Weight Loss and Thickness Loss Data for Different Materials Evaluated in the 1000-Hour Ohio Mahoning 7A Oxidizing Test at 1400°F.

4.4.1.10 Oxidizing Test #10 – Ohio Mahoning 7A, 1200°F

The tenth oxidizing corrosion test was performed to simulate the coal ash corrosion of superheaters and reheaters in utility boilers burning Ohio Mahoning 7A coal at a lower temperature. The test was conducted at 1200°F isothermally for a total of 1000 hours. The coal ash composition is given in Table 56, which represented the actual deposit samples collected from the BFR via an air-cooled probe discussed in Section 3.3.4. The coal ash constituents were prepared using the same batch process as discussed for the PRB coal.

Table 54 - Composition of Simulated Coal Ash Used in Oxidizing Laboratory Test for OH Mahoning 7A Coal.

Constituent	Wt.%
Al_2O_3	16.9
SiO_2	22.6
CaO	0.9
Fe_2O_3	7.8
KOH	1.0
TiO_2	0.6
$MgSiO_3$	0.3
$Fe_2(SO_4)_3$	19.8
$MgSO_4$	10.1
K_2SO_4	4.8
Na_2SO_4	15.1

Table 57 lists the mixed gas composition employed for the Mahoning test. Again, as discussed in Section 3.3, the composition represents the most realistic combustion conditions measured online from the BFR while burning the Ohio Mahoning coal. This gas composition contained relatively low concentrations of SO_2 and HCl than those for the Illinois #6 Galatia coal but higher than those for the PRB and lignite.

Table 55 - Composition of Mixed Gas Employed in Upper Furnace Laboratory Test for OH Mahoning 7A. Coal

Constituent	Vol.%[(a)]
CO_2	16
O_2	3
SO_2[b]	0.155
H_2O[c]	9
HCl[d]	0.011
N_2	71.8

[a] Total flow rate of combined gases = 2 liters per minute.
[b] Added as 5% SO2 in N2.
[c] Added through a micro pump.
[d] Dissolved in water as a solution.

The material set evaluated in the Mahoning oxidizing test is listed in Table 58, with the actual alloy and weld overlay compositions given in Appendix D. Again, duplicate samples were prepared for each material and included in the test, one for dimensional and weight loss measurement and the other for metallographic examination. The sample preparation and test procedures were identical to those described in Section 3.4.1.1 and are not repeated here.

Table 56 - Alloys Evaluated in OH Mahoning 7A Oxidizing Laboratory Test.

Material
304H
Super 304H
310HCbN
230
347HFG
347H
72 WO
52 WO
740
617
120
800H

Corrosion rates of the twelve materials investigated in the Ohio Mahoning 7A oxidizing test at 1200^{o}F were calculated based on the measured thickness and weight changes and are summarized in Figure 218. The red bars represent the rates derived from the weight loss measurements and the blue from the thickness losses including internal/subsurface penetrations under the coupon surfaces.

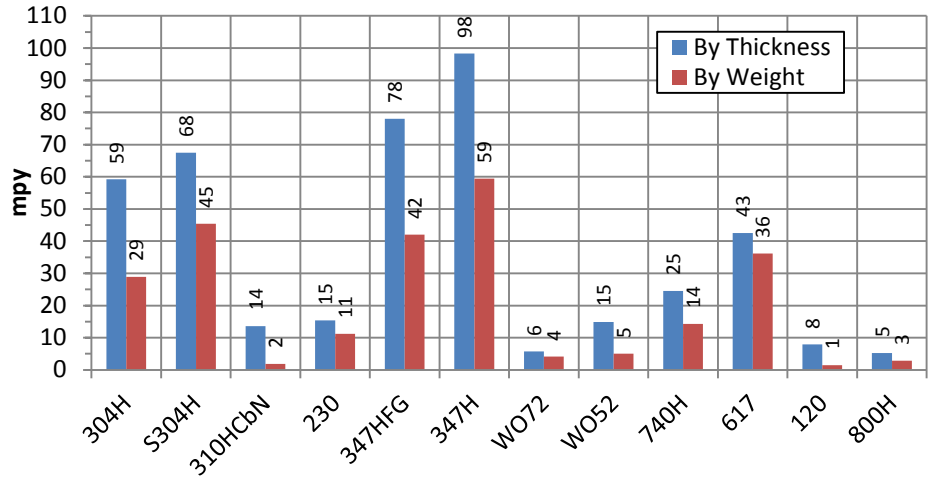

Figure 216 - Comparison of Corrosion Rates Calculated from Both Weight Loss and Thickness Loss Data for Different Materials Evaluated in the 1000-Hour Ohio Mahoning 7A Oxidizing Test at 1200°F.

4.4.1.11 Oxidizing Test #11 – Ohio Mahoning 7A, 1100°F

The eleventh oxidizing corrosion test was performed to simulate the corrosion attack on superheaters and reheaters in utility boilers burning Ohio Mahoning 7A coal at the lower limit of the metal temperatures relevant to coal ash corrosion. The test was conducted at 1100°F isothermally for a total of 1000 hours. The coal ash composition is given in Table 59, which represented the actual deposit samples collected from the BFR via an air-cooled probe discussed in Section 3.3.4. The coal ash constituents were prepared using the same batch process as discussed for the PRB coal.

Table 57 - Composition of Simulated Coal Ash Used in Oxidizing Laboratory Test for OH Mahoning 7A Coal.

Constituent	Wt.%
Al_2O_3	16.9
SiO_2	22.6
CaO	0.9
Fe_2O_3	7.8
KOH	1.0
TiO_2	0.6
$MgSiO_3$	0.3
$Fe_2(SO_4)_3$	19.8
$MgSO_4$	10.1
K_2SO_4	4.8
Na_2SO_4	15.1

Table 60 lists the mixed gas composition employed for the Mahoning test. Again, as discussed in Section 3.3, the composition represents the most realistic combustion conditions measured online from the BFR while burning the Ohio Mahoning coal. This gas composition contained relatively low concentrations of SO_2 and HCl than those for the Illinois #6 Galatia coal but higher than those for the PRB and lignite.

Table 58 - Composition of Mixed Gas Employed in Upper Furnace Laboratory Test for OH Mahoning 7A Coal.

Constituent	Vol.%[(a)]
CO_2	16
O_2	3
SO_2[b]	0.155
H_2O[c]	9
HCl[d]	0.011
N_2	71.8

[a] Total flow rate of combined gases = 2 liters per minute.
[b] Added as 5% SO2 in N2.
[c] Added through a micro pump.
[d] Dissolved in water as a solution.

The material set evaluated in the Mahoning oxidizing test is listed in Table 61, with the actual alloy and weld overlay compositions given in Appendix D. Again, duplicate samples were prepared for each material and included in the test, one for dimensional and weight loss measurement and the other for metallographic examination. The sample preparation and test procedures were identical to those described in Section 3.4.1.1 and are not repeated here.

Table 59 - Alloys Evaluated in OH Mahoning 7A Oxidizing Laboratory Test.

Material
304H
Super 304H
310HCbN
230
347HFG
347H
72 WO
52 WO
740
617
120
800H

Corrosion rates of the twelve materials investigated in the Ohio Mahoning 7A oxidizing test at 1100^{o}F were calculated based on the measured thickness and weight changes and are summarized in Figure 219. The red bars represent the rates derived from the weight loss measurements and the blue from the thickness losses that included the internal/subsurface penetrations under the coupon surfaces.

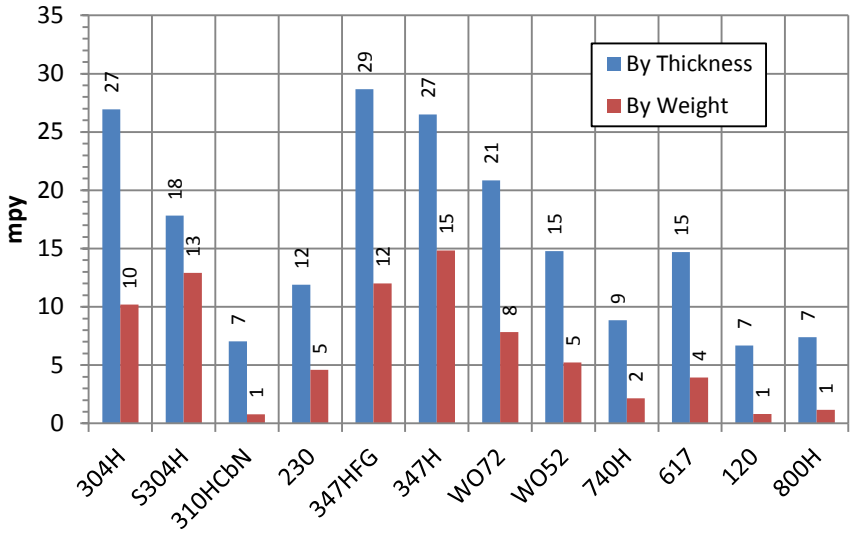

Figure 217 - Comparison of Corrosion Rates Calculated from Both Weight Loss and Thickness Loss Data for Different Materials Evaluated in the 1000-Hour Ohio Mahoning 7A Oxidizing Test at 1100°F.

4.4.1.12 Oxidizing Test #12 – Ohio Mahoning 7A, 1250°F

The twelfth oxidizing corrosion test was performed to simulate the corrosion attack on superheaters and reheaters in utility boilers burning Ohio Mahoning 7A coal at a metal temperature of 1250°F. The test was performed isothermally for a total of 1000 hours. The coal ash composition is given in Table 62, which represented the actual deposit samples collected from the BFR via an air-cooled probe discussed in Section 3.3.4. The coal ash constituents were prepared using the same batch process as discussed for the PRB coal.

Table 60 - Composition of Simulated Coal Ash Used in Oxidizing Laboratory Test for OH Mahoning 7A Coal.

Constituent	Wt.%
Al_2O_3	16.9
SiO_2	22.6
CaO	0.9
Fe_2O_3	7.8
KOH	1.0
TiO_2	0.6
$MgSiO_3$	0.3
$Fe_2(SO_4)_3$	19.8
$MgSO_4$	10.1
K_2SO_4	4.8
Na_2SO_4	15.1

Table 63 lists the mixed gas composition employed for the Mahoning test, which represents the most realistic combustion conditions measured online from the BFR while burning

the Ohio Mahoning coal. This gas composition contained relatively low concentrations of SO_2 and HCl than those for the Illinois #6 Galatia coal but higher than those for the PRB and lignite.

Table 61 - Composition of Mixed Gas Employed in Upper Furnace Laboratory Test for OH Mahoning 7A Coal.

Constituent	Vol.%[(a)]
CO_2	16
O_2	3
SO_2[b]	0.155
H_2O[c]	9
HCl[d]	0.011
N_2	71.8

[a] Total flow rate of combined gases = 2 liters per minute.
[b] Added as 5% SO2 in N2.
[c] Added through a micro pump.
[d] Dissolved in water as a solution.

The material set evaluated in the Mahoning oxidizing test is listed in Table 64, with the actual alloy and weld overlay compositions given in Appendix D. Again, duplicate samples were prepared for each material and included in the test, one for dimensional and weight loss measurement and the other for metallographic examination. The sample preparation and test procedures were identical to those described in Section 3.4.1.1 and are not repeated here.

Table 62 -Alloys Evaluated in OH Mahoning 7A Oxidizing Laboratory Test.

Material
304H
Super 304H
310HCbN
230
347HFG
347H
72 WO
52 WO
740
617
120
800H

Corrosion rates of the twelve materials investigated in the Ohio Mahoning 7A oxidizing test at 1250^{o}F were calculated based on the measured thickness and weight changes and are summarized in Figure 220. The red bars represent the rates derived from the weight loss measurements and the blue from the thickness losses that included the internal/subsurface penetrations under the coupon surfaces.

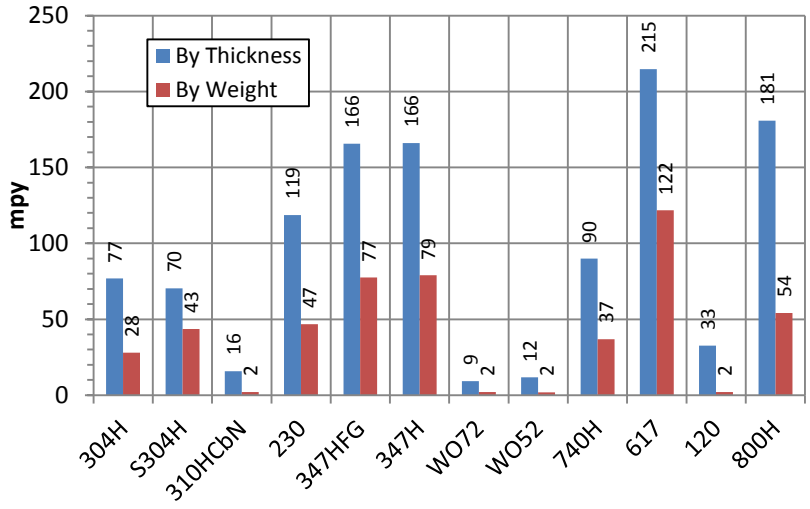

Figure 218 - Comparison of Corrosion Rates Calculated from Both Weight Loss and Thickness Loss Data for Different Materials Evaluated in the 1000-Hour Ohio Mahoning 7A Oxidizing Test at 1250°F.

4.4.1.13 Oxidizing Test #13 – Ohio Mahoning 7A, 1350°F

The thirteenth oxidizing corrosion test was performed to simulate the corrosion attack on superheaters and reheaters in utility boilers burning Ohio Mahoning 7A coal at a metal temperature of 1350°F. The test was performed isothermally for a total of 1000 hours. The coal ash composition is given in Table 65, which represented the actual deposit samples collected from the BFR via an air-cooled probe discussed in Section 3.3.4. The coal ash constituents were prepared using the same batch process as discussed for the PRB coal.

Table 63 - Composition of Simulated Coal Ash Used in Oxidizing Laboratory Test for OH Mahoning 7A Coal.

Constituent	Wt.%
Al_2O_3	16.9
SiO_2	22.6
CaO	0.9
Fe_2O_3	7.8
KOH	1.0
TiO_2	0.6
$MgSiO_3$	0.3
$Fe_2(SO_4)_3$	19.8
$MgSO_4$	10.1
K_2SO_4	4.8
Na_2SO_4	15.1

Table 66 lists the mixed gas composition employed for the Mahoning test, which represents the most realistic combustion conditions measured online from the BFR while burning the Ohio Mahoning coal. This gas composition contained relatively low concentrations of SO_2 and HCl than those for the Illinois #6 Galatia coal but higher than those for the PRB and lignite.

Table 64 - Composition of Mixed Gas Employed in Upper Furnace Laboratory Test for OH Mahoning 7A Coal.

Constituent	Vol.%[(a)]
CO_2	16
O_2	3
SO_2[b]	0.155
H_2O[c]	9
HCl[d]	0.011
N_2	71.8

[a] Total flow rate of combined gases = 2 liters per minute.
[b] Added as 5% SO2 in N2.
[c] Added through a micro pump.
[d] Dissolved in water as a solution.

The material set evaluated in the Mahoning oxidizing test is listed in Table 67, with the actual alloy and weld overlay compositions given in Appendix D. Again, duplicate samples were prepared for each material and included in the test, one for dimensional and weight loss measurement and the other for metallographic examination. The sample preparation and test procedures were identical to those described in Section 3.4.1.1 and are not repeated here.

Table 65 - Alloys Evaluated in OH Mahoning 7A Oxidizing Laboratory Test.

Material
304H
Super 304H
310HCbN
230
347HFG
347H
72 WO
52 WO
740
617
120
800H

Corrosion rates of the twelve materials investigated in the Ohio Mahoning 7A oxidizing test at 1350^{o}F were calculated based on the measured thickness and weight changes and are summarized in Figure 221. The red bars represent the rates derived from the weight loss measurements and the blue from the thickness losses that included the internal/subsurface penetrations under the coupon surfaces.

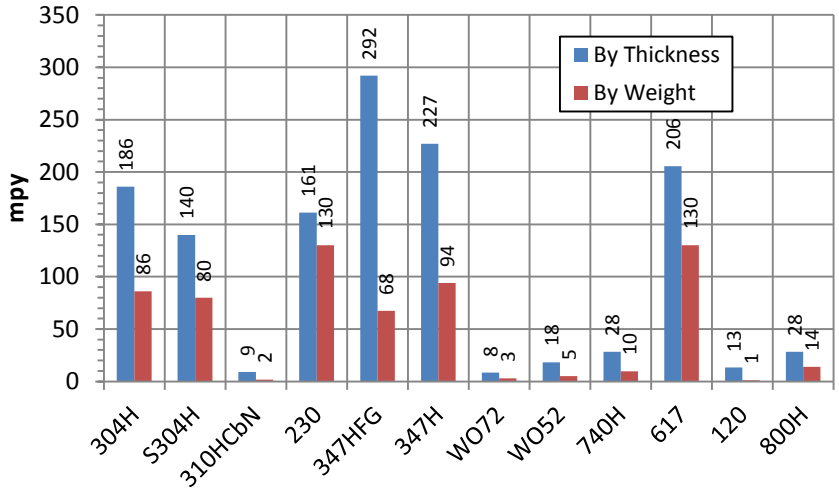

Figure 219 - Comparison of Corrosion Rates Calculated from Both Weight Loss and Thickness Loss Data for Different Materials Evaluated in the 1000-Hour Ohio Mahoning 7A Oxidizing Test at 1350°F.

4.4.1.14 Oxidizing Test #14 – Ohio Mahoning 7A, 1500°F

The fourteenth (and last) oxidizing corrosion test was performed to simulate the corrosion attack on superheaters and reheaters in utility boilers burning Ohio Mahoning 7A coal at a metal temperature of 1500°F. The test was performed isothermally for a total of 1000 hours. The coal ash composition is given in Table 68, which represented the actual deposit samples collected from the BFR via an air-cooled probe discussed in Section 3.3.4. The coal ash constituents were prepared using the same batch process as discussed for the PRB coal.

Table 66 - Composition of Simulated Coal Ash Used in Oxidizing Laboratory Test for OH Mahoning 7A Coal.

Constituent	Wt.%
Al_2O_3	16.9
SiO_2	22.6
CaO	0.9
Fe_2O_3	7.8
KOH	1.0
TiO_2	0.6
$MgSiO_3$	0.3
$Fe_2(SO_4)_3$	19.8
$MgSO_4$	10.1
K_2SO_4	4.8
Na_2SO_4	15.1

Table 69 lists the mixed gas composition employed for the Mahoning test, which represents the most realistic combustion conditions measured online from the BFR while burning the Ohio Mahoning coal. This gas composition contained relatively low concentrations of SO_2 and HCl than those for the Illinois #6 Galatia coal but higher than those for the PRB and lignite.

Table 67 - Composition of Mixed Gas Employed in Upper Furnace Laboratory Test for OH Mahoning 7A Coal.

Constituent	Vol.%[(a)]
CO_2	16
O_2	3
SO_2[b]	0.155
H_2O[c]	9
HCl[d]	0.011
N_2	71.8

[a] Total flow rate of combined gases = 2 liters per minute.
[b] Added as 5% SO2 in N2.
[c] Added through a micro pump.
[d] Dissolved in water as a solution.

The material set evaluated in the Mahoning oxidizing test is listed in Table 70, with the actual alloy and weld overlay compositions given in Appendix D. Again, duplicate samples were prepared for each material and included in the test, one for dimensional and weight loss measurement and the other for metallographic examination. The sample preparation and test procedures were identical to those described in Section 3.4.1.1 and are not repeated here.

Table 68 - Alloys Evaluated in OH Mahoning 7A Oxidizing Laboratory Test.

Material
304H
Super 304H
310HCbN
230
347HFG
347H
72 WO
52 WO
740
617
120
800H

Corrosion rates of the twelve materials investigated in the Ohio Mahoning 7A oxidizing test at 1500^{o}F were calculated based on the measured thickness and weight changes and are summarized in Figure 222. The red bars represent the rates derived from the weight loss measurements and the blue from the thickness losses that included the internal/subsurface penetrations under the coupon surfaces.

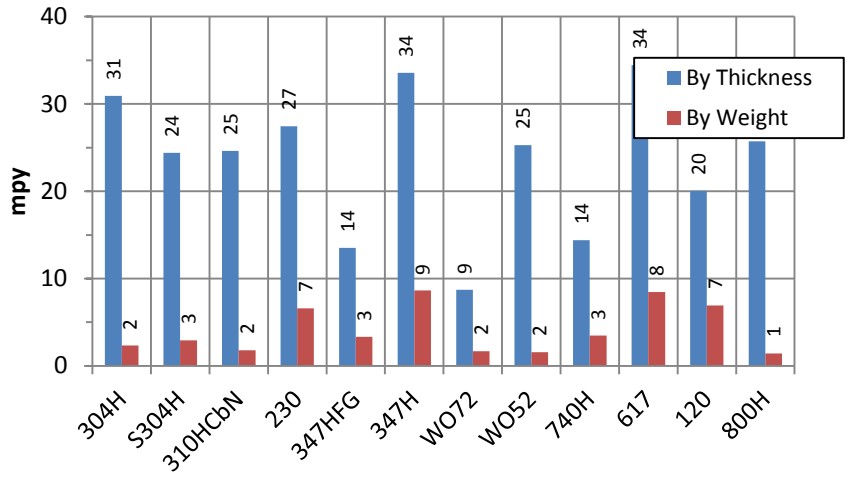

Figure 220 - Comparison of Corrosion Rates Calculated from Both Weight Loss and Thickness Loss Data for Different Materials Evaluated in the 1000-Hour Ohio Mahoning 7A Oxidizing Test at 1500°F.

4.4.2 Lower Furnace Testing Under Reducing Conditions

4.4.2.1 Reducing Test #1 – Black Thunder PRB Coal, 850°F

The test was performed at 850°F isothermally for a total of 1000 hours. The composition of simulated ash deposit is given in Table 71, which represented the actual chemistry of deposit samples collected from the pilot-scale BFR testing via a water-cooled sampling probe discussed in Section 3.3.4.

Table 69 - Composition of Simulated Deposit Used in the Reducing Laboratory Test for Black Thunder PRB Coal.

Constituent	Wt.%
Al_2O_3	17.7
SiO_2	27.9
CaO	22.0
FeO	1.4
Fe_3O_4	1.8
MgO	3.6
TiO_2	0.3
Fe_2O_3	0.4
$MgSiO_3$	1.1
$MgTiO_3$	1.0
$MgCO_3$	1.4
Na_2CO_3	3.7
FeS	1.6
FeS_2	0.1
C	16.0

The deposit generated from combustion of the PRB coal is known to be highly sticky to the furnace walls due to its unique ash composition. When PRB is burned in utility boilers, the use of water jets or water cannons is often necessary to effectively remove the slag buildup from the walls. In preparation of a sticky reducing deposit for this laboratory PRB test, additional chemicals were introduced to the deposit mix to produce a paste-like constituent. Subsequently, the simulated PRB reducing deposit was painted onto the coupon surfaces. Table 72 lists the additional chemicals used and their general purposes.

The deposit chemicals in Tables 71 and 72 were first weighed and mixed together, followed by grinding in an attrition mill to form a colloidal suspension having approximately 60% water and 40% solids. The particle size resulting from the grinding operation was targeted to be less than -325 mesh (i.e., 44 microns). The grinding medium used was either zirconia or alumina beads. Camphor oil was added last in an appropriate amount to achieve a consistency suitable for painting a 1/8-inch layer of deposit onto the test coupons.

Table 70 - Additional Chemicals Required for Making Paste-Like Reducing Deposit.

Ingredient	Purpose	Required Amount	Comment
Naxan AAL	Dispersant	1% by weight of active ingredient(s)	• Alkyl naphthalene sulfonic acid, 50 to 53% active. • This dispersant keeps solids from agglomerating.
Triton X100	Wetting agent	0.05% by weight of active ingredient(s)	• This material is considered 100% active. • This reduces surface tension to inhibit bubble formation.
Camphor Oil	Bonding Agent	A very small amount based on judgment.	• Diminishes the possibility of coating cracking on drying.

Table 73 lists the mixed gas composition employed for the PRB reducing test. Again, the composition represented the realistic conditions measured online from the BFR while burning PRB, as discussed in Section 3.3.

Table 71 - Composition of Mixed Gas Employed in the Lower Furnace Laboratory Test for Black Thunder PRB Coal.

Constituent	Vol.%[(a)]
CO_2	14
CO	3
O_2	1
SO_2[b]	0.012
H_2O[c]	15
H_2S	0.026
H_2	1
HCl	--
N_2	bal.

[a] Total flow rate of combined gases = 2 liter per minute.
[b] Added as 5% SO2 in N2.
[c] Added through a micro pump.

A total of twelve candidate materials for the furnace wall applications in advanced boiler systems were evaluated in the PRB reducing test. The number of materials studied is one more than what was originally proposed. Reason for the added material was again to extend the range of compositions for improved furnace-wall corrosion modeling effort in Task 5.

Duplicate samples were prepared from each material and included in the test. One of the samples was intended for dimensional and weight loss measurement and the other for metallographic examination. Table 74 lists the various materials evaluated in the PRB reducing test. The actual alloy and weld overlay compositions are listed in Appendix D, with the monolithic materials certified by the alloy vendors and weld overlays determined by B&W from SEM/EDS analyses on the actual coating surfaces.

Each test sample had the dimensions of ~1¼" x ¾" x thickness. The clad specimens have been EDM-cut to a nominal thickness of 0.070 inch, while the monolithic specimens were approximately 1/8" thick. Other key features of the samples were identical to those discussed previously for the PRB oxidizing test in Section 3.4.1.1.

Table 72 - Alloys Evaluated in PRB Reducing Laboratory Test.

Material
178A
T2
T11
T22
T23
T9
T91
304H
309H
310H
52 WO
72 WO

Following sample preparation, the specimens were painted with the paste-like deposit mixture to achieve a layer of ~1/8" thick. Each test coupon was then placed into a 20-ml high purity alumina crucible. The crucible/sample/deposit combination was weighed and recorded. The deposit weight was calculated based on the difference between the total weight and weight of the sample and crucible.

The general test procedures for the reducing test are identical to those described previously for the PRB oxidizing test in Section 3.4.1.1.

Figure 223 summarizes the corrosion rates of different alloys and weld overlays calculated from the weight loss and thickness change data after exposure to the 1000-hour PRB reducing test at 850^{o}F. The red bars represent the rates derived from the weight loss measurements and the blue from the thickness losses. As mentioned previously, the corrosion rates derived from weight loss data were more representative of the average values, whereas

those from thickness changes provided the worst case scenarios. A large difference between these two for a given material would suggest the occurrence of localized corrosion attack and/or sub-surface penetration.

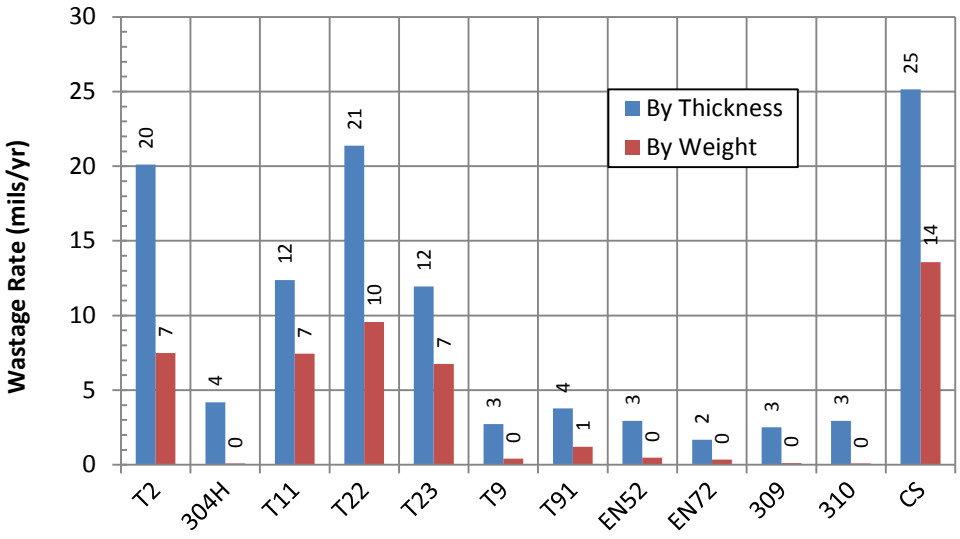

Figure 221 - Comparison of Corrosion Rates Calculated from Weight and Thickness Losses for Different Materials Evaluated in the PRB Reducing Test at 850°F for 1000 Hours.

4.4.2.2 Reducing Test #2 - Illinois #6 Galatia Coal, 850°F

The second laboratory test was completed to simulate the furnace wall corrosion conditions in utility boilers burning Illinois #6 Galatia coal. The test was performed isothermally at 850°F for a total of 1000 hours. The composition of simulated ash deposit is given in Table 75, which represented the actual chemistry of the deposit samples collected from the pilot-scale combustion testing in the BFR via a water-cooled sampling probe discussed in Section 3.3.4.

Unlike the PRB reducing test, the presence of a paste-like deposit constituent was not necessary, as the Galatia ash deposit formed on the furnace walls of utility boilers is not considered sticky. Therefore, a dry deposit mixture was prepared following the same procedures described in Section 3.4.1.1 for the PRB oxidizing test. Similarly, coupons of the test materials were placed in alumina crucibles covered with the dry deposit mixture during the 1000-hour exposure.

Table 76 lists the mixed gas composition employed for the Galatia reducing test. Again, the composition represented the actual conditions measured online from the BFR while burning the Illinois #6 coal. A concentration of 250 ppm of HCl was included in the mixed gas to reflect its presence as measured in the pilot-scale combustion testing.

Table 73 - Composition of Simulated Deposit Used in the Reducing Laboratory Test for Illinois #6 Galatia. Coal

Constituent	Wt.%
Al_2O_3	16.4
SiO_2	36.8
CaO	3.6
FeO	1.5
Fe_2O_3	1.0
KOH	1.0
TiO_2	0.6
Na_2SO_4	4.9
K_2SO_4	4.9
$MgCO_3$	2.0
Na_2CO_3	0.4
FeS	1.0
FeS_2	5.8
NaCl	0.04
KCl	0.06
C	19.9

Table 74 - Composition of Mixed Gas Employed in the Lower Furnace Laboratory Test for Illinois #6 Galatia Coal.

Constituent	Vol.%[(a)]
CO_2	15
CO	1
O_2	0.5
SO_2 [b]	0.16
H_2O[c]	9
H_2S	0.1
H_2	1
HCl[d]	0.025
N_2	73.2

[a] Total flow rate of combined gases = 2 liter per minute.
[b] Added as 5% SO2 in N2.
[c] Added through a micro pump.
[d] Dissolved in water as a solution.

A total of twelve alloys and weld overlays commonly used for the furnace walls of advanced boiler systems were exposed to the Galatia reducing test. The materials are listed in Table 77, with the actual alloy chemistry given in Appendix D. Duplicate samples were prepared from each material and included in the test. One of the samples was used for dimensional and weight loss measurement and the other for metallographic examination. Compositions of the monolithic alloy were certified by the alloy vendors, whereas those of the weld overlays were determined by B&W from SEM/EDS analyses on the actual coating surfaces. The general test procedures for this reducing test were identical to those described in Section 3.4.1.1for the PRB oxidizing test.

Table 75 - Alloys Evaluated in Illinois #6 Galatia Reducing Laboratory Test.

Material
178A
T2
T11
T22
T23
T9
T91
304H
309H
310H
52 WO
72 WO

Figure 224 summarizes the corrosion rates of different alloys and weld overlays calculated from the weight loss and thickness change data after exposure to the 1000-hour Illinois #6 Galatia reducing test at 850°F. The red bars represent the rates derived from the weight loss measurements and the blue from the thickness losses. As mentioned previously, the corrosion rates derived from weight loss data were more representative of the average values, whereas those from thickness changes provided as the worst case. In comparison, these corrosion rates are much higher than those reported for the PRB coal previously.

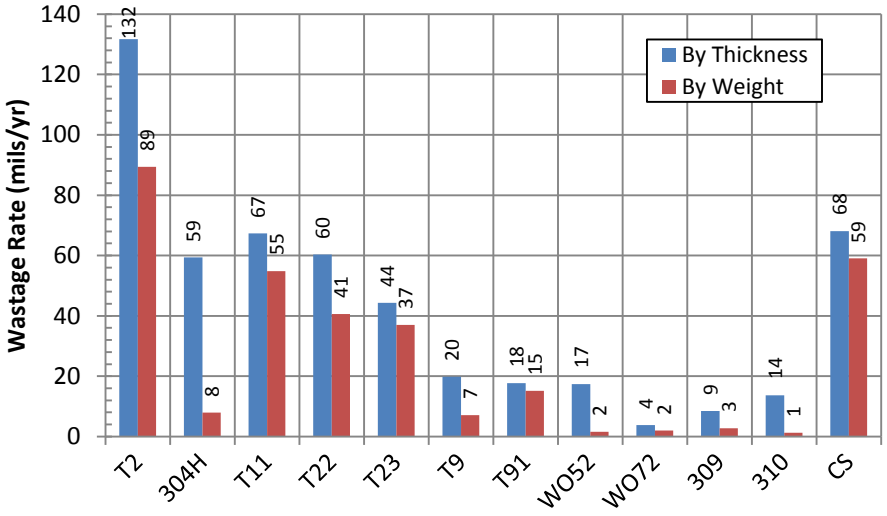

Figure 222 - Comparison of Corrosion Rates Calculated from Weight and Thickness Losses for Different Materials Evaluated in the IL#6 Galatia Reducing Test at 850°F for 1000 Hours.

4.4.2.3 Reducing Test #3 – North Dakota Beulah Zap Lignite Coal, 850°F

The third laboratory test, simulating the furnace wall corrosion conditions in utility boilers burning ND Beulah Zap lignite coal, has been performed. The test was conducted isothermally at 850°F for a total of 1000 hours. The composition of simulated ash deposit is given in Table 78, which represented the actual chemistry of the deposit samples collected from

the pilot-scale combustion testing in the BFR via a water-cooled sampling probe discussed in Section 3.3.4.

A dry deposit mixture was prepared following the same procedures described for the Galatia oxidizing test. Coupons of the test materials were placed in alumina crucibles covered with the dry deposit mixture during the 1000-hour exposure.

Table 76 - Composition of Simulated Deposit Used in the Reducing Laboratory Test for ND Beulah Zap Lignite Coal.

Constituent	Wt.%
Al_2O_3	13.0
SiO_2	23.9
CaO	18.3
FeO	1.7
Fe_2O_3	0.4
Fe_3O_4	1.9
KOH	1.1
TiO_2	0.7
Na_2O	0.1
$MgSiO_3$	3.9
MgO	4.1
$K2CO_3$	0.3
$MgCO_3$	0.2
Na_2CO_3	7.6
FeS	2.7
FeS_2	0.1
NaCl	0.01
KCl	0.02
C	19.9

Table 79 lists the mixed gas composition employed for the Beulah Zap lignite reducing test. Again, the composition represented the actual conditions measured online from the BFR while burning the lignite coal. A low concentration of only 2 ppm of HCl was included in the mixed gas to reflect its low presence as measured from the pilot-scale combustion testing.

A total of twelve alloys and weld overlays commonly used for the furnace walls of advanced boiler systems were exposed to the ND lignite reducing test. The materials are listed in Table 80 with the actual chemistry given in Appendix D. Duplicate samples were prepared from each material and included in the test. One of the samples was used for dimensional and weight loss measurement and the other for metallographic examination. Compositions of the monolithic alloy were certified by the alloy vendors, whereas those of the weld overlays were determined by B&W from SEM/EDS analyses on the actual coating surfaces. The general test procedures for this reducing test were identical to those described in Section 3.4.1.1for the PRB oxidizing test.

Table 77 - Composition of Mixed Gas Employed in the Reducing Laboratory Test for ND Beulah Zap Lignite Coal.

Constituent	Vol.%[(a)]
CO_2	17
CO	2.5
O_2	0.5
SO_2[b]	0.06
H_2O[c]	18
H_2S	0.02
H_2	1
HCl[d]	0.0002
N_2	60.9

[a] Total flow rate of combined gases = 2 liter per minute.
[b] Added as 5% SO2 in N2.
[c] Added through a micro pump.
[d] Dissolved in water as a solution.

Table 78 - Alloys Evaluated in ND Lignite Reducing Laboratory Test.

Material
178A
T2
T11
T22
T23
T9
T91
304H
309H
310H
52 WO
72 WO

Figure 225 summarizes the corrosion rates of different alloys and weld overlays calculated from the weight loss and thickness change data after exposure to the 1000-hour ND Beulah Zap lignite reducing test at 850^{o}F. The red bars represent the corrosion rates derived from the weight loss measurements and the blue from the thickness losses. As mentioned previously, the corrosion rates derived from weight loss data were more representative of the average values, whereas those from thickness changes provided the worst case scenarios.

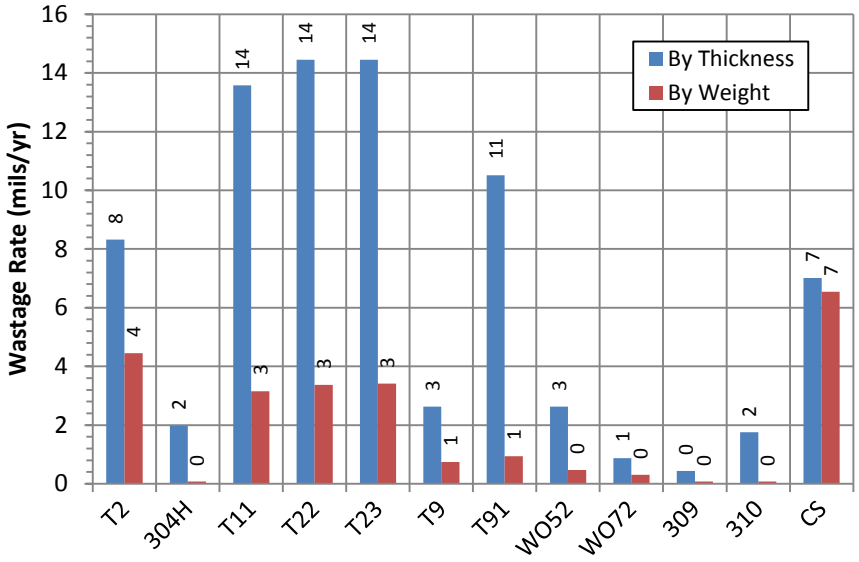

Figure 223 - Comparison of Corrosion Rates Calculated from Weight and Thickness Losses for Different Materials Evaluated in the ND Beulah Zap Lignite Reducing Test at 850°F for 1000 Hours.

4.4.2.4 Reducing Test #4 – Ohio Mahoning 7A Coal, 850°F

The fourth reducing laboratory test, simulating the furnace wall corrosion conditions in utility boilers burning Ohio Mahoning coal, has been completed. The test was performed isothermally at 850°F for a total of 1000 hours. The composition of simulated ash deposit is given in Table 81, which represents the actual chemistry of the deposit samples collected from the pilot-scale combustion testing in the BFR via a water-cooled sampling probe discussed in Section 3.3.4.

A dry deposit mixture was prepared following the same procedures described for the PRB oxidizing test. Coupons of the test materials were placed in alumina crucibles covered with the dry deposit mixture during the 1000-hour exposure.

Table 82 lists the mixed gas composition employed for the Ohio Mahoning reducing test. Again, the composition represented the actual conditions measured in the BFR while burning the lignite coal. A concentration of 100 ppm of HCl was included in the mixed gas to reflect its significant presence as determined by the pilot-scale combustion testing.

Table 79 - Composition of Simulated Deposit Used in the Reducing Laboratory Test for Ohio Mahoning 7A Coal.

Constituent	Wt.%
Al_2O_3	22.5
SiO_2	30.4
CaO	1.2
FeO	2.2
Fe_2O_3	7.6
Fe_3O_4	10.5
KOH	1.6
TiO_2	1.0
Na_2SO_4	0.2
K_2SO_4	1.2
K_2CO_3	0.2
$MgCO_3$	0.7
Na_2CO_3	1.0
C	19.9

Table 80 - Composition of Mixed Gas Employed in the Reducing Laboratory Test for Ohio Mahoning 7A Coal.

Constituent	Vol.%[a]
CO2	15
CO	1.2
O2	0.5
SO2[b]	0.14
H2O[c]	9
H2S	-
H2	1
HCl[d]	0.01
N2	73.2

[a] Total flow rate of combined gases = 2 liter per minute.
[b] Added as 5% SO2 in N2.
[c] Added through a micro pump.
[d] Dissolved in water as a solution.

A total of twelve alloys and weld overlays commonly used for the furnace walls of advanced boiler systems were exposed to the Mahoning reducing test. The materials are listed in Table 83 with the actual chemistry given in Appendix D. Duplicate samples were prepared from each material and included in the test. One of the samples was used for dimensional and weight loss measurements and the other for metallographic examinations. Compositions of the monolithic alloy were certified by the alloy vendors, whereas those of the weld overlays were determined by B&W from SEM/EDS analyses on the actual coating surfaces. The general test procedures for this reducing test are identical to those described previously in Section 3.4.1.1 for the PRB oxidizing test.

Table 81 - Alloys Evaluated in Ohio Mahoning Reducing Laboratory Test.

Material
178A
T2
T11
T22
T23
T9
T91
304H
309H
310H
52 WO
72 WO

Figure 226 summarizes the corrosion rates of different alloys and weld overlays calculated from the weight loss and thickness change data after exposure to the 1000-hour Ohio Mahoning 7A reducing test at 850°F. The red bars represent the rates derived from the weight loss measurements and the blue from the thickness losses. As mentioned previously, the corrosion rates derived from weight loss data are more representative of the average materials performance, whereas those from thickness changes provide the worst case scenarios.

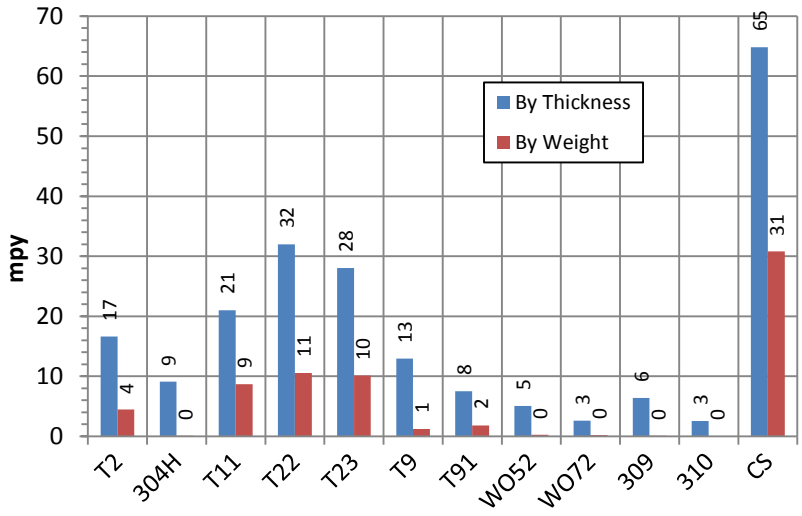

Figure 224 - Comparison of Corrosion Rates Calculated from Weight and Thickness Losses for Different Materials Evaluated in the Ohio Mahoning 7A Reducing Test at 850°F for 1000 Hours.

4.4.2.5 Reducing Test #5 – Indiana #6 Gibson Coal, 850°F

The fifth laboratory test, simulating the furnace wall corrosion conditions in utility boilers burning Indiana #6 Gibson coal, has been completed. The test was performed at 850°F isothermally for a total of 1000 hours. The composition of simulated ash deposit is given in

Table 84, which represented the actual chemistry of the deposit samples collected from the pilot-scale combustion testing in the BFR using a water-cooled sampling probe discussed in Section 3.3.4.

A dry deposit mixture was prepared following the same procedures described for the PRB oxidizing test. Coupons of the test materials were placed in alumina crucibles covered with the dry deposit mixture during the 1000-hour exposure.

Table 85 lists the mixed gas composition employed for the Indiana #6 Gibson reducing test. Again, the composition was design to represent the actual conditions measured in the BFR while burning the lignite coal. A concentration of 100 ppm of HCl was included in the mixed gas to simulate this species measured in the BFR from the pilot-scale combustion testing.

Table 82 - Composition of Simulated Deposit Used in the Reducing Laboratory Test for Indiana #6 Gibson Coal.

Constituent	Wt.%
Al_2O_3	16.8
SiO_2	37.8
CaO	1.9
FeO	1.0
Fe_2O_3	5.2
Fe_3O_4	2.1
KOH	1.7
TiO_2	1.1
$FeSO_4$	5.2
$CaSO_4$	0.1
Na_2SO_4	2.3
K_2SO_4	4.0
$CaCO_3$	0.2
K_2CO_3	0.2
$MgCO_3$	0.8
Na_2CO_3	0.2
NaCl	0.01
KCl	0.01
$FeCl_2$	0.002
C	19.8

A total of twelve alloys and weld overlay coatings commonly used for the furnace walls of advanced boiler systems were exposed to the Indiana #6 reducing test. The materials are listed in Table 86 with the actual chemistry given in Appendix D. Duplicate samples were prepared from each material and included in the test. One of the samples was used for dimensional and weight loss measurement and the other for metallographic examination. Compositions of the monolithic alloys were certified by the alloy vendors, whereas those of the weld overlays were determined by B&W using SEM/EDS analyses on the actual coating surfaces. The general test procedures for this reducing test are identical to those described in Section 3.4.1.1 for the PRB oxidizing test.

Table 83 - Composition of Mixed Gas Employed in the Reducing Laboratory Test for Indiana #6 Gibson Coal.

Constituent	Vol.%[(a)]
CO2	12
CO	2.6
O2	0.5
SO2[b]	0.08
H2O[c]	10
H2S	0.02
H2	1.5
HCl[d]	0.01
N2	73.29

[a] Total flow rate of combined gases = 2 liter per minute.
[b] Added as 5% SO2 in N2.
[c] Added through a micro pump.
[d] Dissolved in water as a solution.

Table 84 - Alloys Evaluated in Indiana #6 Gibson Reducing Laboratory Test.

Material
178A
T2
T11
T22
T23
T9
T91
304H
309H
310H
52 WO
72 WO

Figure 227 summarizes the corrosion rates of different alloys and weld overlays calculated from the weight loss and thickness loss data after exposure to the 1000-hour Ohio Mahoning 7A reducing test at 850^{o}F. The red bars represent the rates derived from the weight loss measurements and the blue from the thickness losses. As mentioned previously, the corrosion rates derived from weight loss data are more representative of the average materials performance, whereas those from thickness changes provide the worst case scenarios.

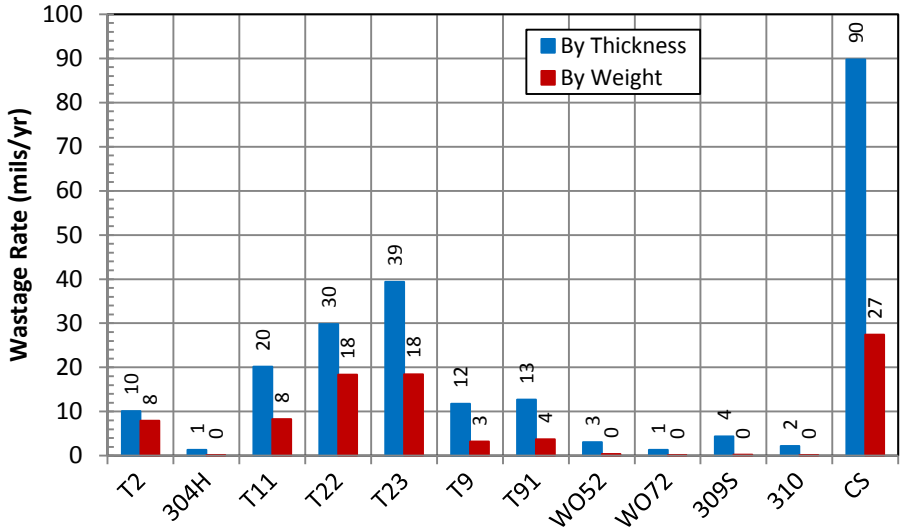

Figure 225 - Comparison of Corrosion Rates Calculated from Weight and Thickness Losses for Different Materials Evaluated in Indiana #6 Gibson Reducing Test at 850°F for 1000 Hours.

4.4.2.6 Reducing Test #6 – Ohio Gatling Coal, 850°F

The sixth laboratory test, simulating the furnace wall corrosion conditions in utility boilers burning Ohio Gatling coal, has been completed. The test was performed isothermally at 850°F for a total of 1000 hours. The composition of simulated ash deposit is given in Table 87, which represents the actual chemistry of the deposit samples collected from the pilot-scale combustion testing in the BFR via a water-cooled sampling probe discussed in Section 3.3.4.

Table 85 - Composition of Simulated Deposit Used in the Reducing Laboratory Test for Ohio Gatling Coal.

Constituent	Wt.%
Al_2O_3	16.2
SiO_2	29.0
K_2TiO_3	0.7
$Fe_2(SO_4)_3$	5.7
$KAl(SO_4)_2$	4.1
$CaSO_4$	0.8
$FeSO_4$	19.7
$CaCO_3$	2.6
Na_2SO_4	0.6
$MgCO_3$	0.6
NaCl	0.005
KCl	0.002
$FeCl_2$	0.02
$FeCl_3$	0.02
C	20.1

A dry deposit mixture was prepared following the same procedures described for the PRB oxidizing test. Coupons of the test materials were placed in alumina crucibles covered with the dry deposit mixture during the 1000-hour exposure.

Table 88 lists the mixed gas composition employed for the Ohio Gatling reducing test. Again, the composition represented the actual conditions measured in the BFR while burning the Gatling coal. A concentration of only 20 ppm of HCl was included in the mixed gas to reflect its minor presence in the flue gas as measured from the pilot-scale combustion testing.

Table 86 - Composition of Mixed Gas Employed in the Reducing Laboratory Test for Ohio Gatling Coal.

Constituent	Vol.%[(a)]
CO2	17
CO	1.7
O2	0.5
SO2[b]	0.29
H2O[c]	10
H2S	0.04
H2	1.0
HCl[d]	0.002
N2	69.5

[a] Total flow rate of combined gases = 2 liter per minute.
[b] Added as 5% SO2 in N2.
[c] Added through a micro pump.
[d] Dissolved in water as a solution.

A total of twelve alloys and weld overlays commonly used for the furnace walls of advanced boiler systems were exposed to the Gatling reducing test. The materials are listed in Table 89, with the actual chemistry given in Appendix D. Duplicate samples were prepared from each material and included in the test. One of the samples was used for dimensional and weight loss measurement and the other for metallographic examination. Compositions of the monolithic alloy were certified by the alloy vendors, whereas those of the weld overlays were determined by B&W using SEM/EDS analyses on the actual coating surfaces. The general test procedures for this reducing test are identical to those described in Section 3.4.1.1 for the PRB oxidizing test.

Figure 228 summarizes the corrosion rates of different alloys and weld overlays calculated from the weight loss and thickness change data after exposure to the 1000-hour Ohio Gatling reducing test at 850^{o}F. The red bars represent the rates derived from the weight loss measurements and the blue from the thickness losses. As mentioned previously, the corrosion rates derived from weight loss data are more representative of the average materials performance, whereas those from thickness changes provide the worst case scenarios.

Table 87 - Alloys Evaluated in Ohio Gatling Reducing Laboratory Test.

Material
178A
T2
T11
T22
T23
T9
T91
304H
309H
310H
52 WO
72 WO

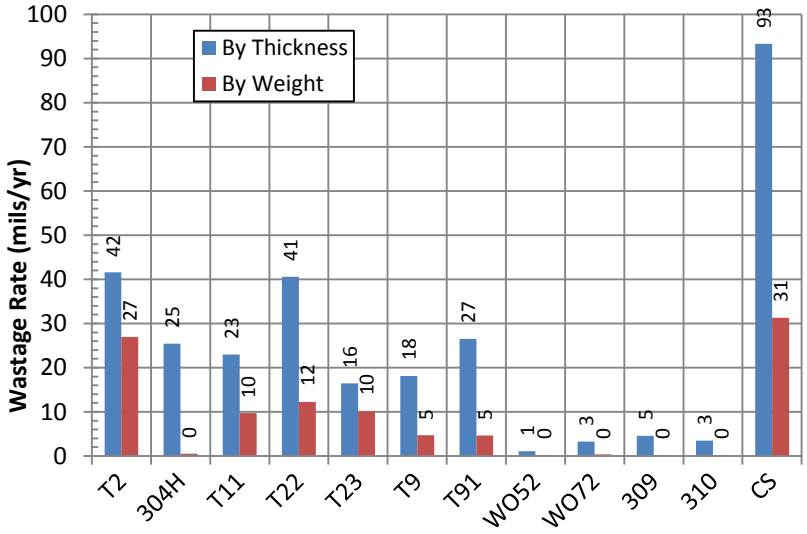

Figure 226 - Comparison of Corrosion Rates Calculated from Weight and Thickness Losses for Different Materials Evaluated in Ohio Gatling Reducing Test at 850°F for 1000 Hours.

4.4.2.7 Reducing Test #7 – Kentucky #11 Coal, 850°F

The seventh laboratory test, simulating the furnace wall corrosion conditions in utility boilers burning Kentucky #11 coal, has been completed. The test was performed isothermally at 850°F for a total of 1000 hours. The composition of simulated ash deposit is given in Table 90, which replicates the actual chemistry of the deposit samples collected from the pilot-scale combustion testing in the BFR via a water-cooled sampling probe discussed in Section 3.3.4.

Table 88 - Composition of Simulated Deposit Used in the Reducing Laboratory Test for Kentucky #11 Coal.

Constituent	Wt.%
Al_2O_3	16.7
SiO_2	34.0
CaO	2.7
FeO	1.1
Fe_2O_3	6.2
Fe_3O_4	3.4
K_2TiO_3	1.9
$FeSO_4$	6.8
$CaCO_3$	0.2
Na_2SO_4	2.2
K_2SO_4	3.4
$MgCO_3$	1.3
Na_2CO_3	0.1
NaCl	0.005
KCl	0.01
$FeCl_2$	0.003
C	20

A dry deposit mixture was prepared following the same procedures described previously for the PRB oxidizing test. Coupons of the test materials were placed in alumina crucibles covered with the dry deposit mixture during the 1000-hour exposure.

Table 91 lists the mixed gas composition employed for the Kentucky #11 reducing test. Again, the composition represented the actual conditions measured in the BFR while burning the Kentucky coal. A concentration of 150 ppm of HCl was included in the mixed gas to reflect its significant presence in the flue gas as measured from the pilot-scale combustion testing.

A total of twelve alloys and weld overlays commonly used for the furnace walls of advanced boiler systems were exposed to the Kentucky #11 reducing test. The materials are listed in Table 92, with the actual chemistry given in Appendix D. Duplicate samples were prepared from each material and included in the test. One of the samples was used for dimensional and weight loss measurement and the other for metallographic examination. Compositions of the monolithic alloys were certified by the alloy vendors, whereas those of the weld overlays were determined by B&W using SEM/EDS analyses on the actual coating surfaces. The general test procedures for this reducing test are identical to those described previously in Section 3.4.1.1 for the PRB oxidizing test.

Table 89 - Composition of Mixed Gas Employed in the Reducing Laboratory Test for Kentucky #11 Coal.

Constituent	Vol.%[(a)]
CO2	16
CO	1.5
O2	0.5
SO2 [b]	0.26
H2O[c]	9.5
H2S	0.01
H2	1.0
HCl[d]	0.015
N2	71.2

[a] Total flow rate of combined gases = 2 liter per minute.
[b] Added as 5% SO2 in N2.
[c] Added through a micro pump.
[d] Dissolved in water as a solution.

Table 90 - Alloys Evaluated in Kentucky #11 Reducing Laboratory Test.

Material
178A
T2
T11
T22
T23
T9
T91
304H
309H
310H
52 WO
72 WO

Figure 229 summarizes the corrosion rates of different alloys and weld overlays calculated from the weight loss and thickness change data after exposure to the 1000-hour Kentucky #11 reducing test at 850^{o}F. The red bars represent the rates derived from the weight loss measurements and the blue from the thickness losses. As mentioned previously, the corrosion rates derived from weight loss data are more representative of the average materials performance, whereas those from thickness changes provide the worst case scenarios.

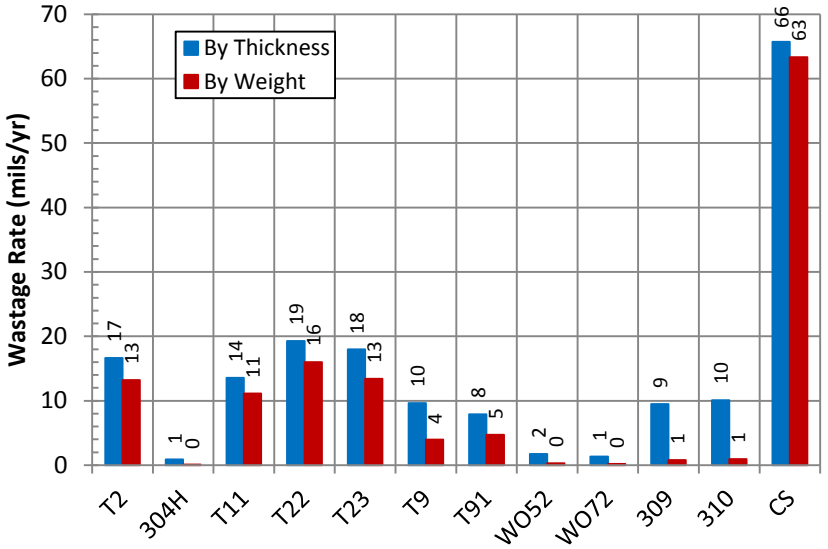

Figure 227 - Comparison of Corrosion Rates Calculated from Weight and Thickness Losses for Different Materials Evaluated in the Kentucky #11 Reducing Test at 850°F for 1000 Hours.

4.4.2.8 Reducing Test #8 – Pittsburgh #8 Coal, 850°F

The eighth laboratory test, simulating the furnace wall corrosion conditions in utility boilers burning Pittsburgh #8 coal, has been completed. The test was performed isothermally at 850°F for a total of 1000 hours. The composition of simulated ash deposit is given in Table 93, which replicates the actual chemistry of the deposit samples collected from the pilot-scale combustion testing in the BFR via a water-cooled sampling probe discussed in Section 3.3.4.

A dry deposit mixture was prepared following the same procedures as described previously for the PRB oxidizing test. Coupons of the test materials were placed in alumina crucibles covered with the dry deposit mixture during the 1000-hour exposure.

Table 94 lists the mixed gas composition employed for the Pittsburgh #8 reducing test. Again, the composition represented the actual conditions measured in the BFR while burning the Pittsburgh coal. A concentration of only 15 ppm of HCl was included in the mixed gas to reflect its negligible presence in the flue gas measured from the pilot-scale combustion testing.

A total of twelve alloys and weld overlays commonly used for the furnace walls of advanced boiler systems were exposed to the Pittsburgh #8 reducing test. The materials are listed in Table 95, with the actual chemistry given in Appendix D. Duplicate samples were prepared from each material and included in the test. One of the samples was used for dimensional and weight loss measurement and the other for metallographic examination to determine the sub-surface corrosion attack. Compositions of the monolithic alloys were certified by the alloy vendors, whereas those of the weld overlays were determined by B&W using SEM/EDS analyses on the actual coating surfaces. The general test procedures for this reducing test are identical to those described previously in Section 3.4.1.1 for the PRB oxidizing test.

Table 91 - Composition of Simulated Deposit Used in the Reducing Laboratory Test for Pittsburgh #8 Coal.

Constituent	Wt.%
Al_2O_3	21.0
SiO_2	39.5
K_2TiO_3	2.0
$FeSO_4$	7.8
$Fe_2(SO_4)_3$	0.2
Na_2SO_4	2.6
K_2SO_4	0.6
$KAl(SO_4)_2$	3.2
$CaSO_4$	1.6
$CaCO_3$	0.6
$MgCO_3$	0.6
NaCl	0.1
KCl	0.1
$FeCl_2$	0.1
$FeCl_3$	0.03
C	20

Table 92 - Composition of Mixed Gas Employed in the Reducing Laboratory Test for Pittsburgh #8 Coal.

Constituent	Vol.%[(a)]
CO2	16
CO	1.5
O2	0.5
SO2 [b]	0.26
H2O[c]	9.5
H2S	0.01
H2	1.0
HCl[d]	0.015
N2	71.2

[a] Total flow rate of combined gases = 2 liter per minute.
[b] Added as 5% SO2 in N2.
[c] Added through a micro pump.
[d] Dissolved in water as a solution.

Figure 230 summarizes the corrosion rates of different alloys and weld overlays calculated from the weight loss and thickness change data after exposure to the 1000-hour Pittsburgh #8 reducing test at 850°F. The red bars represent the rates derived from the weight loss measurements and the blue from the thickness losses. As mentioned previously, the corrosion rates derived from weight loss data are typical of the average materials performance, whereas those from thickness changes provide the worst case scenarios due to localized corrosion attack.

Table 93 - Alloys Evaluated in Pittsburgh #8 Reducing Laboratory Test.

Material
178A
T2
T11
T22
T23
T9
T91
304H
309H
310H
52 WO
72 WO

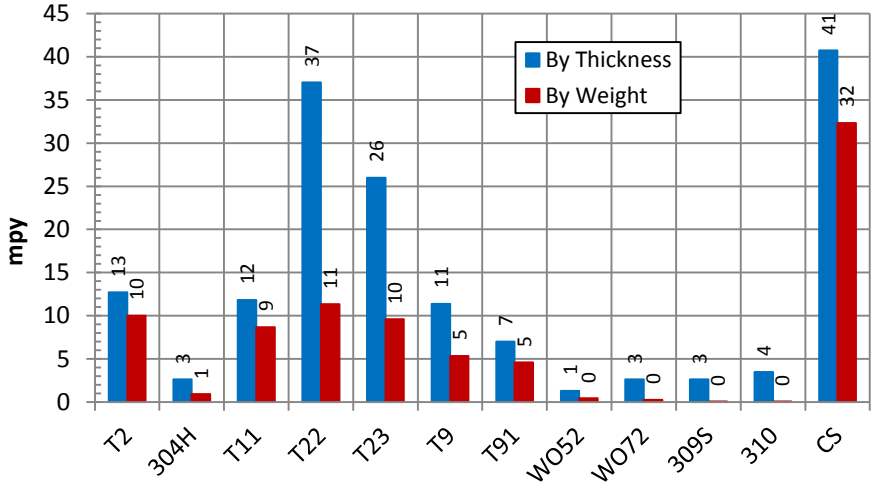

Figure 228 - Comparison of Corrosion Rates Calculated from Weight and Thickness Losses for Different Materials Evaluated in the Pittsburgh #8 Reducing Test at 850°F for 1000 Hours.

4.4.2.9 Reducing Test #9 – Ohio Mahoning 7A Coal, 950°F

The ninth reducing laboratory test, simulating the furnace wall corrosion conditions in utility boilers burning Ohio Mahoning coal at a higher temperature, has been performed. The test was conducted isothermally at 950°F for a total of 1000 hours. The composition of simulated ash deposit is given in Table 96, which represents the actual chemistry of the deposit samples collected from the pilot-scale combustion testing in the BFR via a water-cooled sampling probe discussed in Section 3.3.4.

A dry deposit mixture was prepared following the same procedures as described for the PRB oxidizing test. Coupons of the test materials were placed in alumina crucibles covered with the dry deposit mixture during the 1000-hour exposure. Note that this deposit composition is identical to that used for the fourth reducing test of the same coal at 850°F discussed in Section 3.4.2.4.

Table 94 - Composition of Simulated Deposit Used in the Reducing Laboratory Test for Ohio Mahoning 7A Coal, 950°F.

Constituent	Wt.%
Al_2O_3	22.5
SiO_2	30.4
CaO	1.2
FeO	2.2
Fe_2O_3	7.6
Fe_3O_4	10.5
KOH	1.6
TiO_2	1.0
Na_2SO_4	0.2
K_2SO_4	1.2
K_2CO_3	0.2
$MgCO_3$	0.7
Na_2CO_3	1.0
C	19.9

Table 97 lists the mixed gas composition employed for the Ohio Mahoning reducing test. Again, the composition represented the actual conditions measured in the BFR while burning the Ohio Mahoning coal. A concentration of 100 ppm of HCl was included in the mixed gas to reflect its significant presence as determined by the pilot-scale combustion testing. Again, this gas composition is identical to that used for the fourth reducing test of the same coal at 850°F discussed in Section 3.4.2.4.

Table 95 - Composition of Mixed Gas Employed in the Reducing Laboratory Test for Ohio Mahoning 7A Coal, 950°F.

Constituent	Vol.%[(a)]
CO2	15
CO	1.2
O2	0.5
SO2 [b]	0.14
H2O[c]	9
H2S	-
H2	1
HCl[d]	0.01
N2	73.2

[a] Total flow rate of combined gases = 2 liter per minute.
[b] Added as 5% SO2 in N2.
[c] Added through a micro pump.
[d] Dissolved in water as a solution.

A total of twelve alloys and weld overlays commonly used for the furnace walls of advanced boiler systems were exposed to the Mahoning reducing test. The materials are listed in Table 98 with the actual chemistry given in Appendix D. Duplicate samples were prepared from each material and included in the test. One of the samples was used for dimensional and weight

loss measurements and the other for metallographic examinations to determine the sub-surface corrosion penetration. Compositions of the monolithic alloy were certified by the alloy vendors, whereas those of the weld overlays were determined by B&W from SEM/EDS analyses on the actual coating surfaces. The general test procedures for this reducing test are identical to those described in Section 3.4.1.1 for the PRB oxidizing test.

Table 96 - Alloys Evaluated in Ohio Mahoning Reducing Laboratory Test at 950°F.

Material
178A
T2
T11
T22
T23
T9
T91
304H
309H
310H
52 WO
72 WO

Figure 231 summarizes the corrosion rates of different alloys and weld overlays calculated from the weight loss and thickness change data after exposure to the 1000-hour Ohio Mahoning 7A reducing test at 850°F. The red bars represent the rates derived from the weight loss measurements and the blue from the thickness losses. As mentioned previously, the corrosion rates derived from weight loss data are typical performance of these tested materials, whereas those from thickness changes provide the worst case scenarios due to localized corrosion attack.

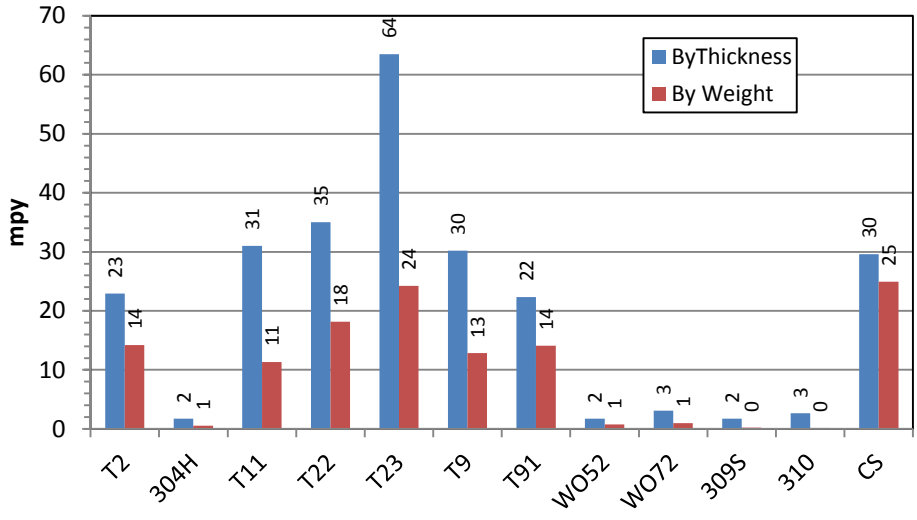

Figure 229 - Comparison of Corrosion Rates Calculated from Weight and Thickness Losses for Different Materials Evaluated in the Ohio Mahoning 7A Reducing Test at 950°F for 1000 Hours.

4.4.2.10 Reducing Test #10 – Ohio Mahoning 7A Coal, 750°F

The tenth reducing laboratory test, simulating the furnace wall corrosion conditions in utility boilers burning Ohio Mahoning coal at a lower temperature, has been performed. The test was conducted isothermally at 750°F for a total of 1000 hours. The composition of simulated ash deposit is given in Table 99, which represents the actual chemistry of the deposit samples collected from the pilot-scale combustion testing in the BFR via a water-cooled sampling probe discussed in Section 3.3.4.

A dry deposit mixture was prepared following the same procedures as described for the PRB oxidizing test. Coupons of the test materials were placed in alumina crucibles covered with the dry deposit mixture during the 1000-hour exposure. Note that this deposit composition is identical to that used for the fourth reducing test of the same coal at 850°F discussed in Section 3.4.2.4.

Table 97 - Composition of Simulated Deposit Used in the Reducing Laboratory Test for Ohio Mahoning 7A Coal, 750°F.

Constituent	Wt.%
Al_2O_3	22.5
SiO_2	30.4
CaO	1.2
FeO	2.2
Fe_2O_3	7.6
Fe_3O_4	10.5
KOH	1.6
TiO_2	1.0
Na_2SO_4	0.2
K_2SO_4	1.2
K_2CO_3	0.2
$MgCO_3$	0.7
Na_2CO_3	1.0
C	19.9

Table 100 lists the mixed gas composition employed for the Ohio Mahoning reducing test. Again, the composition represented the actual conditions measured in the BFR while burning the Ohio Mahoning coal. A concentration of 100 ppm of HCl was mixed in the laboratory gas to reflect its significant presence as determined by the pilot-scale combustion testing. This gas composition is identical to that used for the fourth and ninth reducing tests of the same coal at 850°F and 950°F as discussed in Sections 3.4.2.4 and 3.4.2.9, respectively.

A total of twelve alloys and weld overlays commonly used for the furnace walls of advanced boiler systems were exposed to the Mahoning reducing test. The materials are listed in Table 101 with the actual chemistry given in Appendix D. Duplicate samples were prepared from each material and included in the test. One of the samples was used for dimensional and weight loss measurements and the other for metallographic examinations to determine the sub-

surface corrosion penetration. Compositions of the monolithic alloy were certified by the alloy vendors, whereas those of the weld overlays were determined by B&W from SEM/EDS analyses on the actual coating surfaces. The general test procedures for this reducing test are identical to those described in Section 3.4.1.1 for the PRB oxidizing test.

Table 98 - Composition of Mixed Gas Employed in the Reducing Laboratory Test for Ohio Mahoning 7A Coal, 750°F.

Constituent	Vol.%[(a)]
CO2	15
CO	1.2
O2	0.5
SO2[b]	0.14
H2O[c]	9
H2S	-
H2	1
HCl[d]	0.01
N2	73.2

[a] Total flow rate of combined gases = 2 liter per minute.
[b] Added as 5% SO2 in N2.
[c] Added through a micro pump.
[d] Dissolved in water as a solution.

Table 99 - Alloys Evaluated in Ohio Mahoning Reducing Laboratory Test at 750°F.

Material
178A
T2
T11
T22
T23
T9
T91
304H
309H
310H
52 WO
72 WO

Figure 232 summarizes the corrosion rates of different alloys and weld overlays calculated from the weight loss and thickness change data after exposure to the 1000-hour Ohio Mahoning 7A reducing test at 750°F. The red bars represent the rates derived from the weight loss measurements and the blue from the thickness losses. As mentioned previously, the corrosion rates derived from weight loss data are typical performance of these tested materials, whereas those from thickness changes provide the worst case scenarios due to localized corrosion attack.

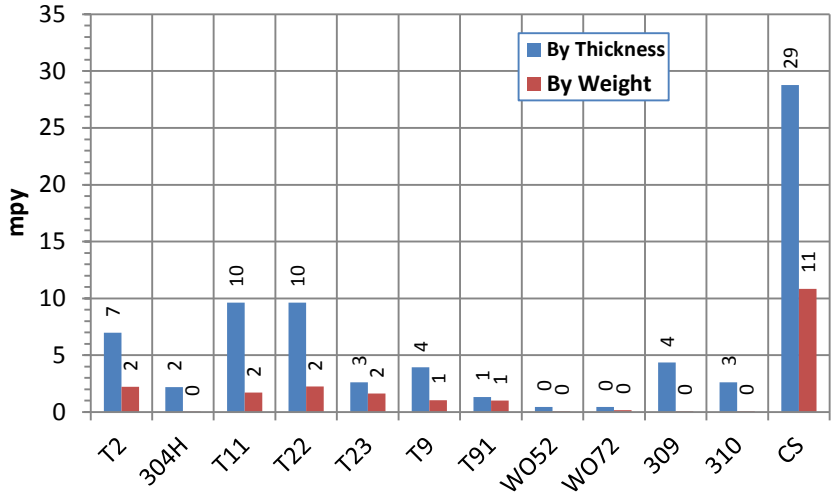

Figure 230 - Comparison of Corrosion Rates Calculated from Weight and Thickness Losses for Different Materials Evaluated in the Ohio Mahoning 7A Reducing Test at 750°F for 1000 Hours.

4.4.3 Long-Term Corrosion Test in HMFR

In addition to the laboratory fireside corrosion tests performed under simulated conditions in furnace retorts, as discussed in Sections 3.4.1 and 3.4.2, it was also desirable to evaluate the corrosion performance of a selected alloy by exposing it to actual combustion environments in a pilot-scale combustor, such as the BFR. Such an attempt is similar to conducting a field test except that the fireside conditions would be reasonably maintained for the entire length of study. Results from the pilot-scale exposure could be used to validate the corrosion data generated from the laboratory tests. As such, the effect from natural fluctuation of the combustion environments in utility boilers on fireside corrosion could be better quantified. However, after careful considerations, it was concluded that the cost of performing such a long-term test in the BFR would be financially prohibitive for the current project. While testing in the BFR was not possible, a smaller combustion facility available at BYU, i.e., Heated Multi-Fuel Reactor (HMFR), may offer the same opportunity for the contemplated long-term corrosion test. The HMFR burns coal at smaller feed rates, and its operation is less labor intensive. It was thus decided that a corrosion test up to 500 hour be performed in the HMFR by exposing a single alloy (304H) to the fireside conditions generated from burning the Indiana #6 Gibson coal.

4.4.3.1 Description of Heated Multi-Fuel Reactor (HMFR)

The HMFR is a down-fired, 10 KW_{th} plug-flow combustor with electrically heated walls. A three dimensional CAD drawing of the reactor is shown in Figure 233. At the center of the reactor, a total of seven cylindrical silicon carbide tubes are stacked vertically. Each tube is 152 mm (6”) in diameter and 609.6 mm (24”) in length, making the total length of the reactor 4,267 mm (168”). Each cylinder section has an access tube attached near the top and bottom of the cylinder, thus allowing access to the combustion process. These access ports are used for gas sampling, fuel delivery, air delivery, and/or deposition probes. Each section is also surrounded by four electric heaters rated to a temperature of 1400^{o}C. Surrounding each tube and heater section are layers of insulation and an outer metal heat shield (not pictured).

Coal is fed using a controlled gravimetric loss-in weight feeder. The feeder uses an auger at a controlled speed to feed coal out of a weighed hopper. The coal falls into a funnel and is entrained into primary air using an eductor. The coal and air travel through a 19 mm diameter tube or fuel lance which injects fuel into the center of the reactor through a 25 mm hole in the side of the HMFR, 152 mm for the top. Primary air and secondary air are inserted into the top of the reactor and flow down toward the exit. The velocity of a fan is controlled in order to pull the exhaust gas from the reactor. The speed is set to produce a slightly positive pressure (less than 0.5 inches of water) at the reactor exit ensuring the entire length of the reactor to be under positive pressure.

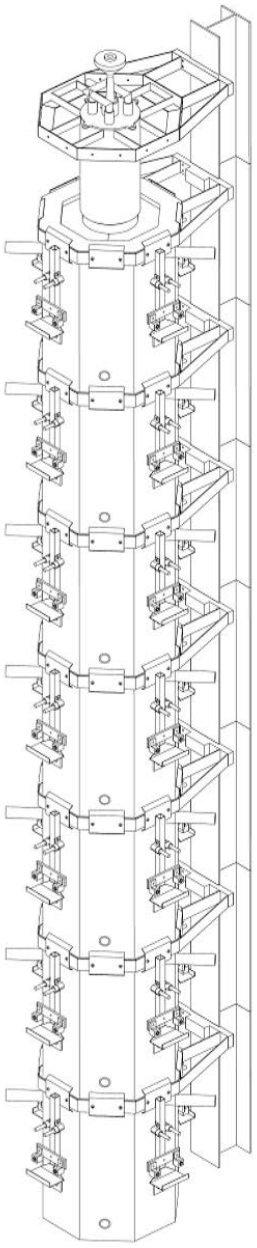

Figure 231 -3D Drawing of Heated Multi-Fuel Reactor (HMFR).

The axial location of the coal feed, gas measurements, and deposit probes are listed in Table 102. The probe sections are numbered 1-7 beginning at the top of the reactor. The fuel lance introduces coal and air into the reactor at 152 mm from the top. Tertiary air is injected at 1,981 mm below the reactor top, approximately in the center allowing time for carbon burnout.

Table 100 - Locations of Coal Feed, Gas Measurements, and Deposition Probes.

Description	Location	Distance From Top (mm)
Fuel Lance – Primary Fuel and Air	1-Top	152
Reducing Zone Gas Sample	2-Bottom	1,067
Reducing Zone Deposition Probe	3-Top	1,372
Tertiary Air Injection	4-Top	1,981
Oxidizing Zone Gas Sample	5-Bottom	2,896
Oxidizing Zone Deposit Probe	6-Top	3,200

Two new deposition probes were built for this corrosion test in HMFR, as shown in Figure 234. The probes were made from stainless steel 304H tubing of 19 mm (0.75”) OD and 0.813 mm (0.032”) wall thickness. The 304H material specifications are shown in Table 103. Each probe was cut in half at center and a step was machined into the tube wall to allow the two pieces to fit tightly together. A small hole was drilled into the tube wall where a thermocouple was located.

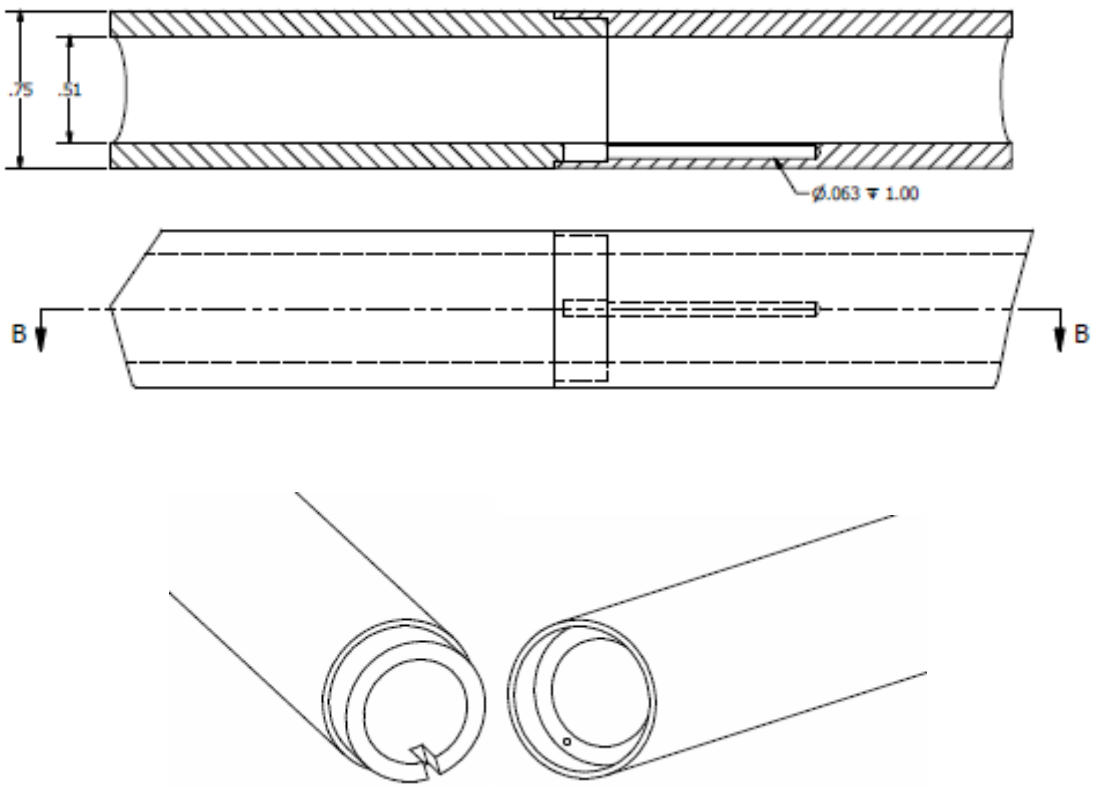

Figure 232 - Drawing of Long Term Corrosion Probe Design.

Table 101 -304H Probe Composition.

	C	Mn	Si	Cr	Ni	P	S	Fe
Wt.%	0.08	2.0	1.0	18-20	8-10.5	0.045	0.03	Bal.

4.4.3.2 Conditions of Long-Term Test in HMFR

The coal and air flow rates controlled at various locations for the long-term corrosion test are shown in Table 104. A total of 450 hours of exposure in the HMFR was achieved over a period of approximately two months. A typical testing day produced 10-14 hours of exposure time. During the test, the gas and probe temperatures were measured. At the end of each test segment, the probes were removed from the HMFR, and the loose deposits were collected on a piece of clean paper by rotating the probes 180 degrees.

Table 102 - Coal and Air Flow Rates Maintained for the HMFR Long Term Test.

Material	Kg/hour
Coal	0.907
Primary Air	6.07
Secondary Air	1.00
Tertiary Air	2.28

Limited gas measurements in the reducing and oxidizing zones of HMFR performed approximately 10 hours into the test with the FTIR and a multi-gas analyzer are summarized in Table 105. Results of these measurements show that the H_2S, SO_2, CO and HCl concentrations in the HMFR were similar to those measured in the BFR while burning the same coal. In the oxidizing zone, the H_2S and COS concentrations fall within the measurement limitations of the FTIR, as discussed previously. Therefore, sulfur was present predominantly as SO_2. The fuel flow rate was found to fluctuate slightly, resulting in the measured O_2 to vary by approximately 1% in the oxidizing zone. The longer the test ran on a given day, the smaller the fluctuation became. Periodically, the oxygen concentration in the HMFR dipped while CO increased. This variation occurred briefly (a couple of seconds) after every 5-10 minutes and was likely caused by fuel building up in the primary feed tube until it was cleared. Improvement was made to minimize this fluctuation for the remaining test.

In the BFR, the gas concentrations varied with the locations of gas measurement in the burner (reducing) zone. The gases were fuel-rich in the center where CO and H_2S concentrations were the highest. Measurements in the reducing region of the HMFR showed comparable CO and H_2S concentrations. The H_2S and CO values measured in the reducing region of the HMFR fall between the maximum and average values measured in the BFR. A small increase in fuel would cause a significant increase in H_2S and CO concentrations in the reducing zone. Because the fuel flow fluctuated constantly by 1-2%, the CO and H_2S concentrations were fluctuated accordingly. The measured CO was typically between 20,000 and 40,000 ppm, and H_2S is typically between 150 and 450 ppm.

Table 103 - Comparison of Selected Gaseous Species Measured in the Reducing and Oxidizing Zones of HMFR and BFR Burning Indiana #6 Coal.

	FTIR						Horiba
	SO_2 (ppm)	SO_3 (ppm)	H_2S (ppm)	COS (ppm)	HCl (ppm)	CO (ppm)	O2 (%)
Oxidizing HMFR	785	18	-76	1	121	481	2.60
Oxidizing BFR	980	29	-10	14.7	111	262	2.44
Reducing HMFR	848	26	196	120	1	29429	N/A
Reducing BFR (avg.)	781	19.6	141	11	91.7	22338	1.21
Reducing BFR (Center)	436	7	423	13	184	39253	0.56

After 20 hours of testing, it was determined that burnout would be improved and therefore the CO concentration would be decreased if the HMFR wall temperature was increased to 1000^{o}C. Consequently, the wall temperature was adjusted. After 35 hours, it was found that the oxidizing probe began to sag slightly at the center as the joint of the two pieces became loose. The sagging led to outward air leakage from the probe, which decreased the local temperatures and prevented the deposit from accumulating on the probe. Consequently, the probe was modified by placing a spring-loaded rod through the ID, thus creating sufficient stiffness between the two sections of the probe.

Periodically, the fuel feed tube plugged, and the test must be temporarily suspended to clean the tube. The plugging was caused by fuel heating, reacting, and depositing within the tube. The fuel plugging would have been avoided if the feed tube had been water-cooled. However, this modification was not made for this test due to time and budget limitations.

The probe temperatures were monitored during the corrosion exposure, as shown in Figure 235 for a period of seven hours (i.e., one day operation). The rapid rise in temperature was observed upon insertion of the corrosion probes into the HMFR at the beginning of the test. The temperature then dropped slowly as the air flow rate was adjusted to bring the probe to the desired temperatures. Over time, deposit was built up on the probe surface, thus causing the tube surface temperature to decrease. During the next 5 hours, the temperatures remained fairly constant, staying within 20-30^{o}C. Small fluctuations during this time were likely caused by the constant build-up and shedding of the deposit on the probe surface. Upon removal of the probes from the HMFR (at ~4 PM), the temperatures of both probes decreased sharply. The process was repeated at the beginning of the next exposure segment.

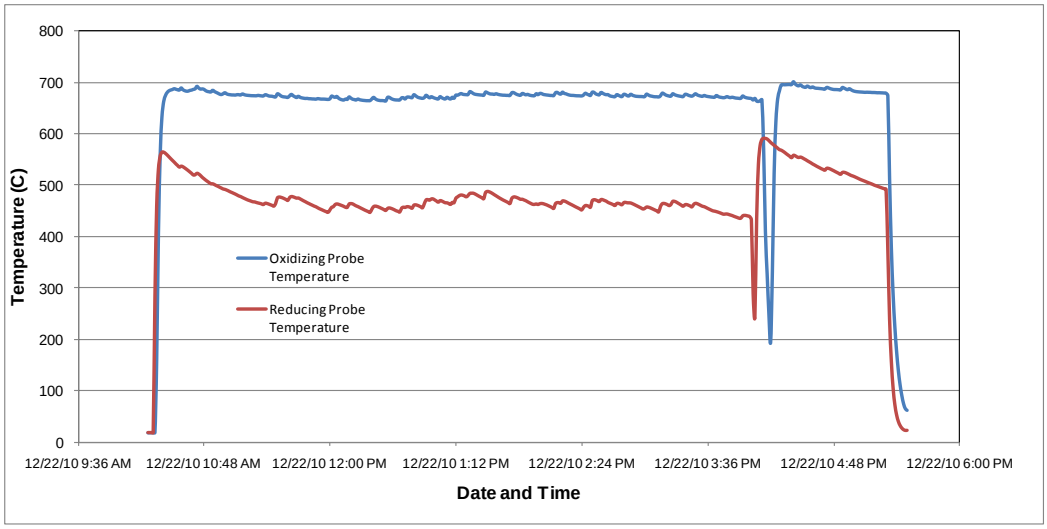

Figure 233 - Temperature Variations on the Reducing and Oxidizing Corrosion Probes.

The probe surface temperatures were better controlled in the HMFR than those in the BFR. This might have been attributed to the lower flow velocities, lower turbulence, and a smaller radiative view factor of the flame in the HMFR.

4.4.3.3 Results of Long-Term Test in HMFR

A picture of the oxidizing probe covered with deposit after 450 hours of exposure is shown in Figure 236. A fluffy brown ash layer with an orange tint is present on top of a black layer. At several locations, the ash has separated from the tube during cooling as a result of a thermal expansion differential between the deposit and probe. The center joint connecting the two parts of the probe body is also visible.

Figure 234 - Photograph of Oxidizing Deposit Probe After 450 Hours of Testing in the HMFR.

A large flake that fell off the oxidizing deposition probe in Figure 236 was broken into two pieces. Each piece was placed on a strip of double-sided conductive carbon tape and attached to a mounting stub for SEM/EDS examinations, one with the deposit side up and the

other with the tube side up. The mounted specimens are shown in Figure 237. An attempt was made to coat the samples with a thin gold conductive layer, but the gold preferentially adhered to the mounting stubs and much less on the specimens. The samples were analyzed using a Phillips XL30 ESEM FEG. The ESEM was operated under a low-vacuum mode to reduce charging of the nonconductive deposit. Backscattered electron images (BSE) were taken from the deposit samples at various magnifications. EDS analyses were also performed on the samples to determine their chemical compositions semi-quantitatively.

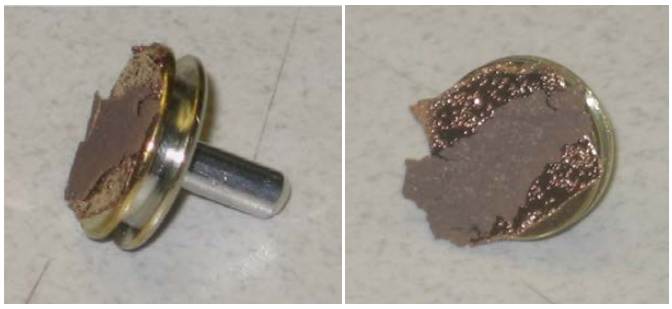

Figure 235 - Photographs of Oxidizing Deposit Flake Mounted on Stubs for SEM/EDS Analyses.

Figure 238 shows a BSE image of the oxidizing deposit on the gas side. The majority of the deposit particles are spherical in shape, with sizes ranging from 0.25-5 μm. The brightness of the particles is relatively uniform, suggesting similar elemental compositions throughout.

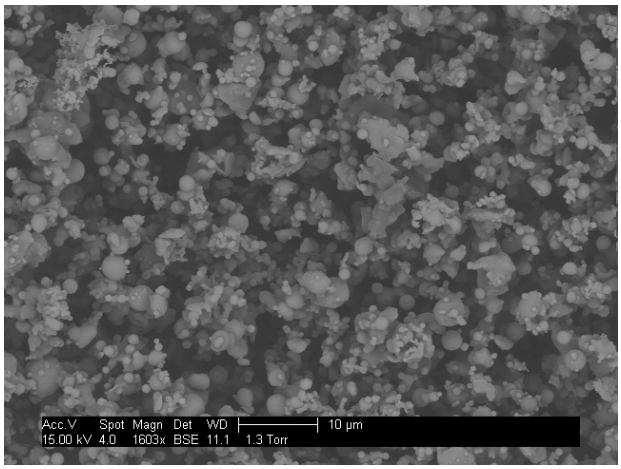

Figure 236 - BSE Image of Surface of Deposit Facing Combustion Gases.

The averaged elemental composition for this oxidizing deposit surface determined from the EDS analysis is summarized in Table 106. This composition is then compared to the results of ash analysis using XRF (per ASTM D-4326 method) for Indiana #6 coal, as shown in Figure 239. The averaged elemental composition of this gas-side deposit appears to be very similar to that of the coal ash analysis. The oxidizing deposit consists primarily of Si, Al, and Fe.

Table 104 - Average Composition of the Oxidizing Deposit Surface Facing the Combustion Gases Wt.%.

C	0.0	P	0.2	Ti	1.8
O	29.9	S	0.1	Cr	0.3
Na	1.1	Cl	0.1	Mn	0.2
Mg	0.9	K	4.2	Fe	10.3
Al	16.7	Ca	1.4	Ni	0.3
Si	29.8	Ba	0.2	Sr	2.6

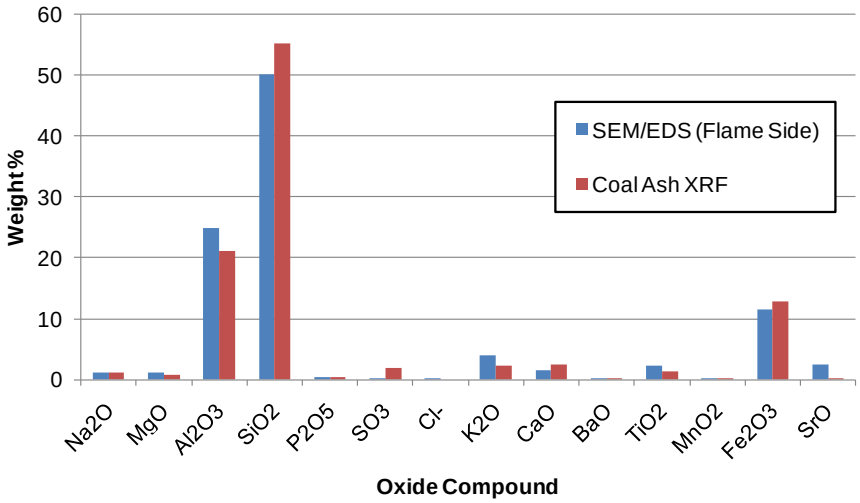

Figure 237 - Averaged Composition of the Oxidizing Deposit Surface on the Gas Side by EDS is Compared to Result of Standard Coal Ash Analysis by XRF for Indiana #6.

Figure 240 shows a BSE image of the deposit surface facing the probe. Two types of particles can be identified, i.e., large flakes on the order of 50-500 μm in length embedded in a matrix of fine spherical particles about 10 μm in diameter. The flakes are relatively bright in intensity, suggesting they are of elements in higher atomic numbers. A higher magnification of the probe-side deposit surface is shown in Figure 241. Results of the EDS analyses revealed that the fine particles in the matrix consist of the same composition as those on the gas side of the deposit.

The compositions determined from the EDS analyses for the small particles and large flakes, shown in Figures 240 and 241, are compared in Table 107. Large differences exist between these two phases. There is little Al and Si in the flakes, while Fe, Cr, Ni and O are abundant. Such a composition suggests that the flakes were part of the scale formed on the 304H probe resulting from fireside corrosion. Elemental compositions for the small spherical particles on both sides of the deposit, the large flakes, and the results of the coal ash analysis are summarized in Figure 242.

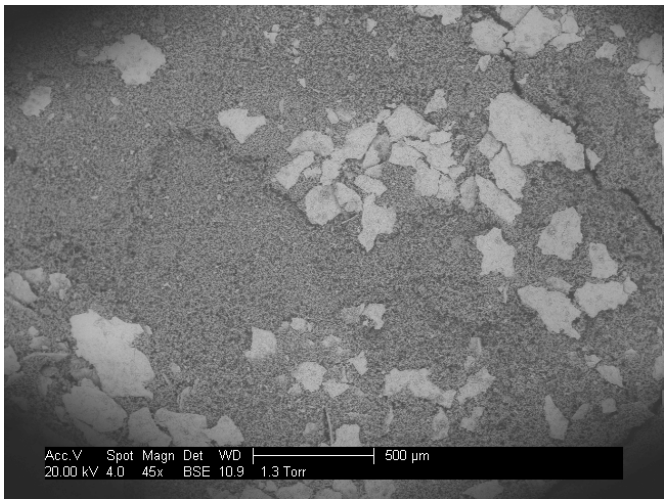

Figure 238 - BSE Image of Probe-Side Deposit Surface Showing Large Flakes Embedded in Ash Matrix.

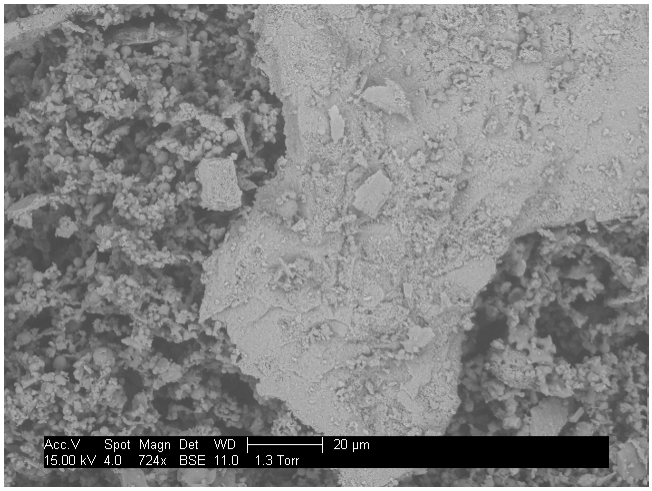

Figure 239 - BSE Image of Probe-Side Deposit Surface Showing Large Flakes Embedded in Ash Matrix.

Table 105 - Average Compositions of Particles and Flakes on Probe-Side of Deposit Wt.%.

	Small Spheres	Flake		Small Spheres	Flake		Small Spheres	Flake
C	0.0	0.3	**P**	0.1	0.6	**Ti**	1.6	0.3
O	30.3	17.2	**S**	0.02	0.6	**Cr**	1.1	25.8
Na	1.3	0.6	**Cl**	0.0	0.4	**Mn**	0.3	1.8
Mg	0.8	0.5	**K**	4.5	0.5	**Fe**	9.9	39.4
Al	16.2	1.9	**Ca**	1.2	0.4	**Ni**	0.5	4.5
Si	29.7	2.7	**Ba**	0.0	0.4	**Sr**	2.4	2.0

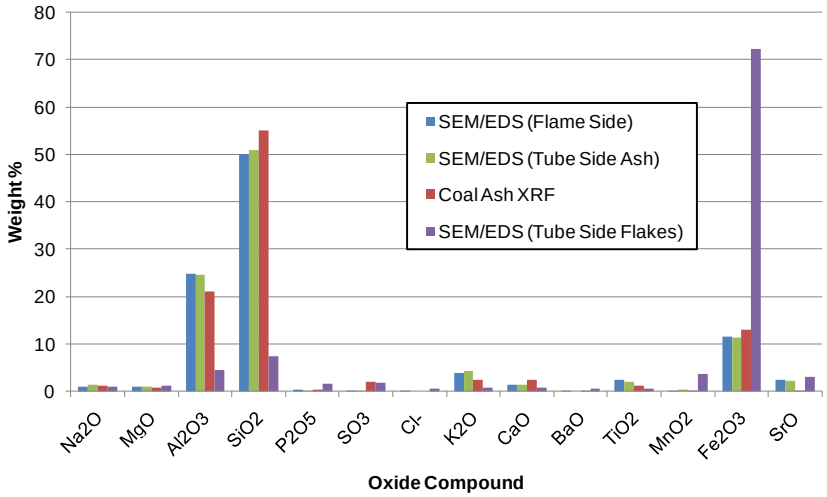

Figure 240 - Comparison of Results for Gas-Side and Probe-Side Oxidizing Deposit Surfaces Analyzed by EDS and Indiana #6 Coal Ash Analysis by XRF.

Each half of the reducing and oxidizing deposition probes was set in epoxy (Struers Epofix resin and hardener). After the epoxy hardened, cross-sectional ring sample, approximately 4-5 mm thick, was cut from each of the probe/epoxy mounts. The cross-sections was then ground and polished down to 1 μm diamond-based slurry compound. No water was used in the entire sample preparation process to preserve the water soluble species present in the deposits. After polishing, the specimens were mounted on stub holders and coated with carbon for SEM/EDS analyses.

A total of four probe locations were examined under SEM/EDS, i.e., the top (leading edge) and bottom (trailing edge) sides of both the reducing and oxidizing probes. For each location, three types of analyses were performed, i.e., (1) backscattered electron images, (2) elemental mapping, and (3) ternary diagrams of particle compositions. The results are summarized below.

Backscattered electron images are a measure of elastically scattered light with the image intensity being a function of atomic number of the element bombarded by the electron beam. The BSE images for the four probe locations are shown in Figures 243-246. The image for the top of the reducing zone, Figure 243, does not include a portion of the probe surface. The dark background of the entire image is epoxy matrix with the lighter regions being embedded ash particles. Most of the particles exhibit a slightly lighter grey than the epoxy, indicating they may be a combination of coal ash and unburned carbon. Most of these particles appear to be hollowed spheres in the size of 20-200 μm. A smaller number of brighter particles also exist, indicating they are of higher atomic numbers than carbon. These particles tend to be smaller in size (less than 20 μm).

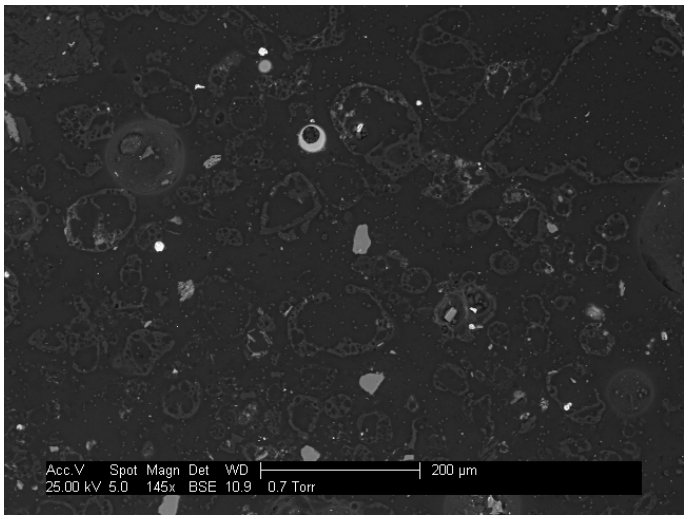

Figure 241 - Cross-Sectional BSE Image of Deposit on Top Surface of Reducing Deposition Probe.

A BSE image of the bottom reducing probe is shown in Figure 244. This image contains portions of the 304H probe surface and bulk of the deposit. The stainless steel probe is located at the top location of the image exhibiting the highest brightness. Three additional layers are present on the stainless steel probe surface. The inner layer, about 5 µm thick, constitutes the thermally grown scale formed as a result of fireside corrosion. The second layer, varied in thickness from 5-20 µm, consists of fine and porous ash particles. The third layer contains loose ash particles distributed in the epoxy.

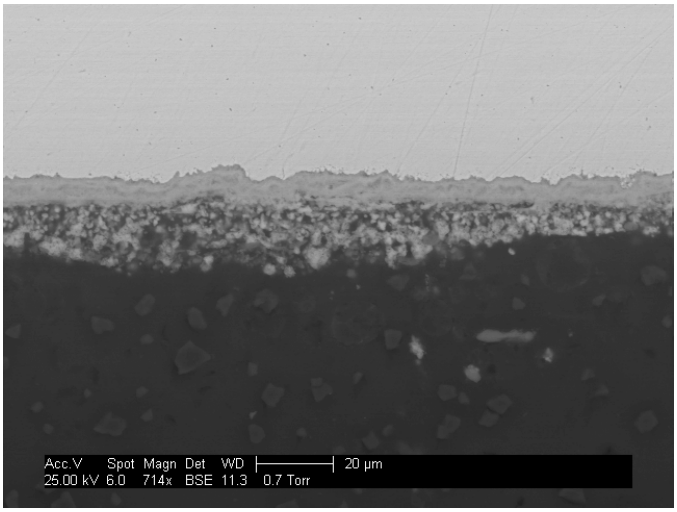

Figure 242 - Cross-Sectional BSE Image of Deposit on Bottom Surface of Reducing Deposition Probe.

A BSE image on the top of the oxidizing probe is shown in Figure 245. This image shows three distinct regions. The metallic probe surface is at the bottom right. The corrosion scale present on the 304H probe surface is about 20 µm thick. Fissures underneath the scale are evident, indicating localized penetration of the corrosion attack. The scale is covered with a thick layer of ash particles distributed in the epoxy. Unlike the reducing probe bottom surface, a

porous layer of adherent deposit between the scale and bulk deposit is absent. Such a deposit layer might have been lost from the frequent removal of the probe from the HMFR during the 450-hour exposure.

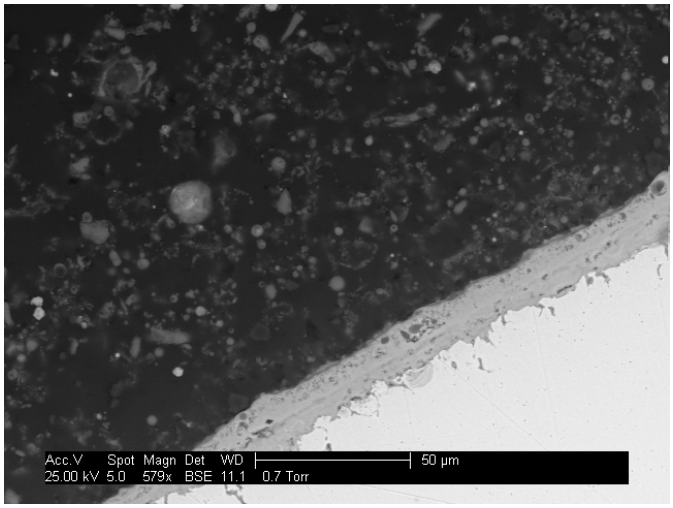

Figure 243 - Cross-Sectional BSE Image of Deposit on Top Surface of Oxidizing Deposition Probe.

Figure 245 shows that the scale thickness formed on 304H is approximately 40 μm. The metal loss could be approximated as half of the scale thickness. Therefore, the corrosion wastage of 304H was ~20 μm after 450 hours of exposure. This wastage translates to ~15 mpy in corrosion rate for 304H in boilers burning the Indiana #6 Gibson coal. Due to the relatively short exposure time, this rate would represent a higher value than those of longer-term testing. However, a corrosion rate of 15 mpy certainly falls in the ballpark of actual performance of 304H superheaters for boilers burning corrosive coals.

The BSE image of the bottom surface of the oxidizing probe is shown in Figure 246. The general features of this image are similar to those of the top surface of the oxidizing probe, except that a portion of the scale has exfoliated from the probe surface. Exfoliation of a portion of the scale is again an indication of the thermal stresses generated from frequent removal of the probes.

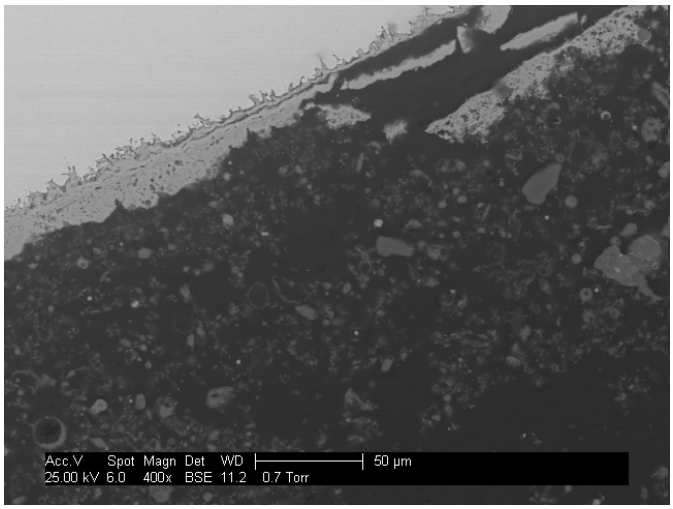

Figure 244 - Cross-Sectional BSE Image of Deposit on Bottom Surface of Oxidizing Deposition Probe.

Elemental mapping is achieved by collecting X-ray florescence generated by the electron beam excitation. X-ray florescence produces photons that are at a unique energy level or wavelength for each element in the sample. The energy level or wavelength of the photon is used to identify the element and the number of photons or photon count at the given energy level is used to determine the concentration of the element. By scanning the electron beam over a region of interest (ROI), a two dimensional map is obtained for each element.

The results of elemental mapping for the reducing top deposit are shown in Figure 247(a)-(r). The first image is the backscattered micrograph showing the location of mapping. The elements mapped are arranged in alphabetical order. The major elements present in the deposit particles are Si, Al, P, and S. On the probe surface, high concentrations of Na, O, and S are observed.

The results of elemental mapping for the reducing bottom deposit are shown in Figures 248(a)-(r), where a portion of the probe is seen at the top. The scale adjacent to the metal is rich in Cr and O. Underneath the scale, higher concentrations of Ni and S are observed. Large particles in the deposit layer are enriched with Al and Si, while the fine particles contain higher amounts of S, Na, and Fe.

The elemental mapping results for the oxidizing top deposit are shown in Figures 249(a)-(r). The scale formed on the probe surface contains high concentrations of Fe, Cr, and Ni. The existence of some Mg in the scale is also evident. In addition, a narrow band of corrosion product, very rich in Cr, is observed in the scale layer. The deposit particles present on the probe surface are rich in Si and Al, with some also rich in calcium. The calcium-rich particles also contain sulfur.

The results of elemental mapping for the oxidizing bottom deposit are shown in Figures 250(a)-(r). The probe surface is located in the upper left corner showing high concentrations of Fe, Ni, and Cr. The scale adjacent to the metal surface is rich in Ni, S, and Cr. In the deposit, the particles that contain a high concentration of Ca are also enriched with S.

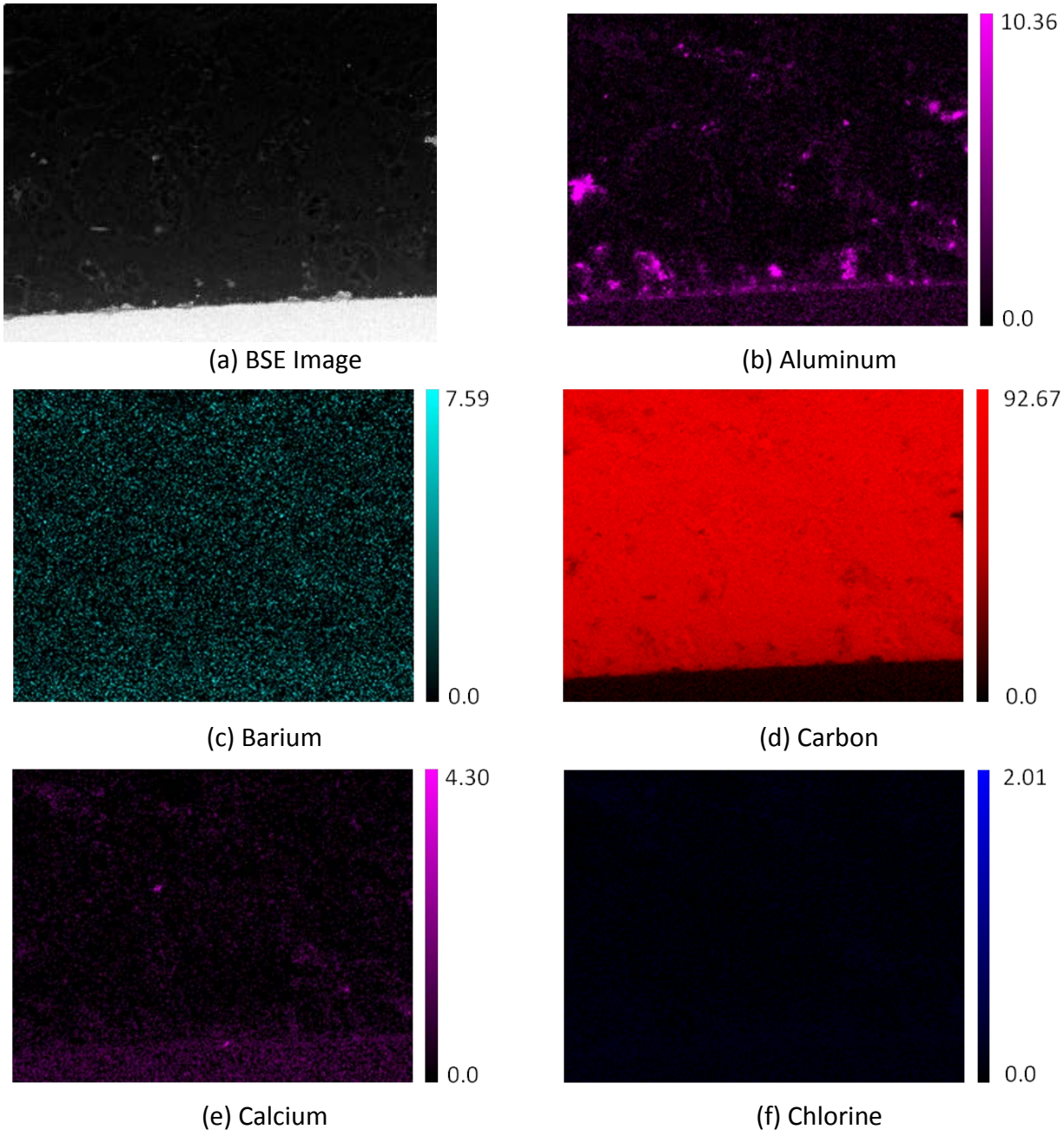

(a) BSE Image (b) Aluminum

(c) Barium (d) Carbon

(e) Calcium (f) Chlorine

Figure 245 (a-f) - EDS Elemental Mapping of Reducing Top Probe Sample.

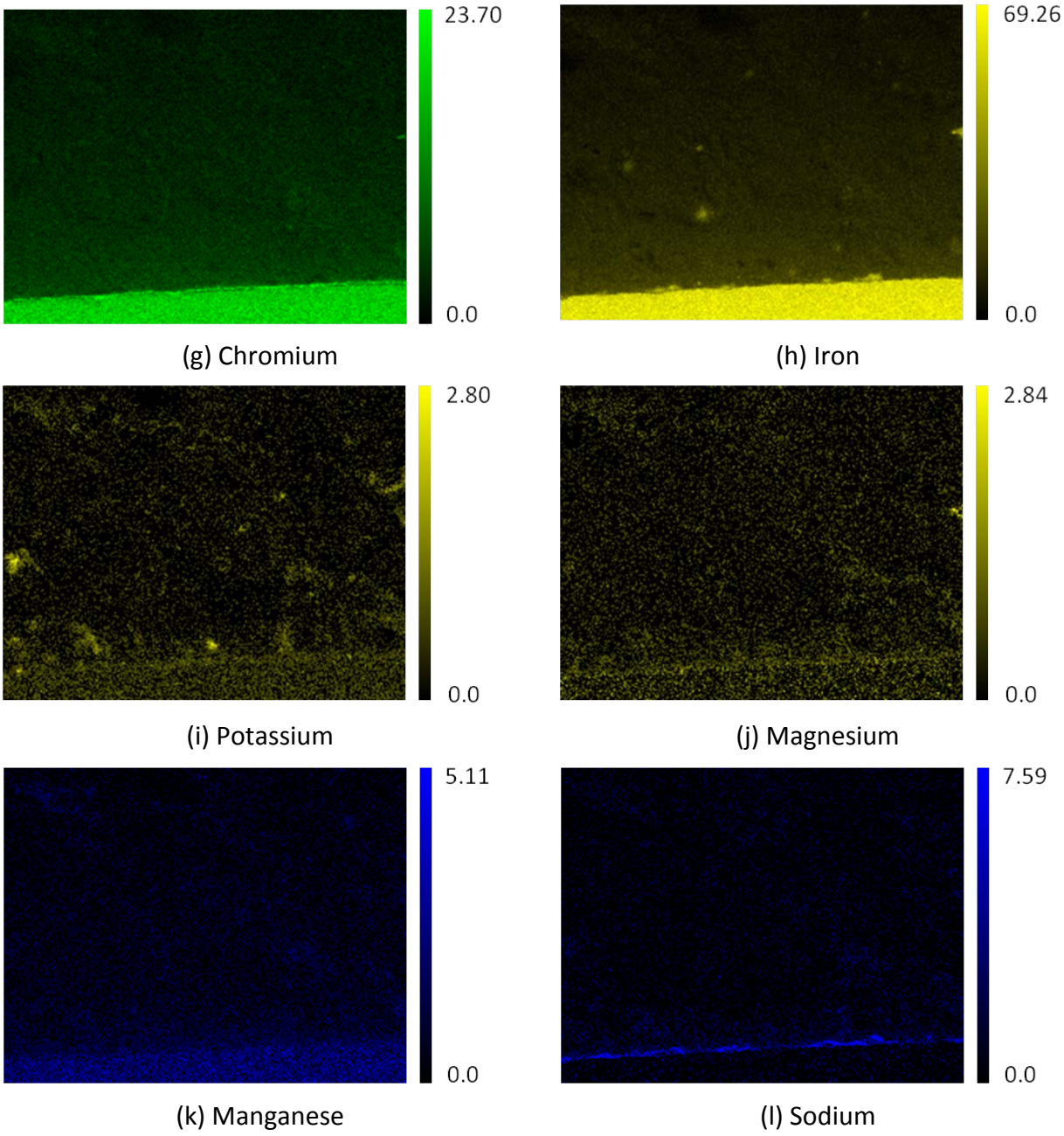

Figure 246 (g-l) - EDS Elemental Mapping of Reducing Top Probe Sample.

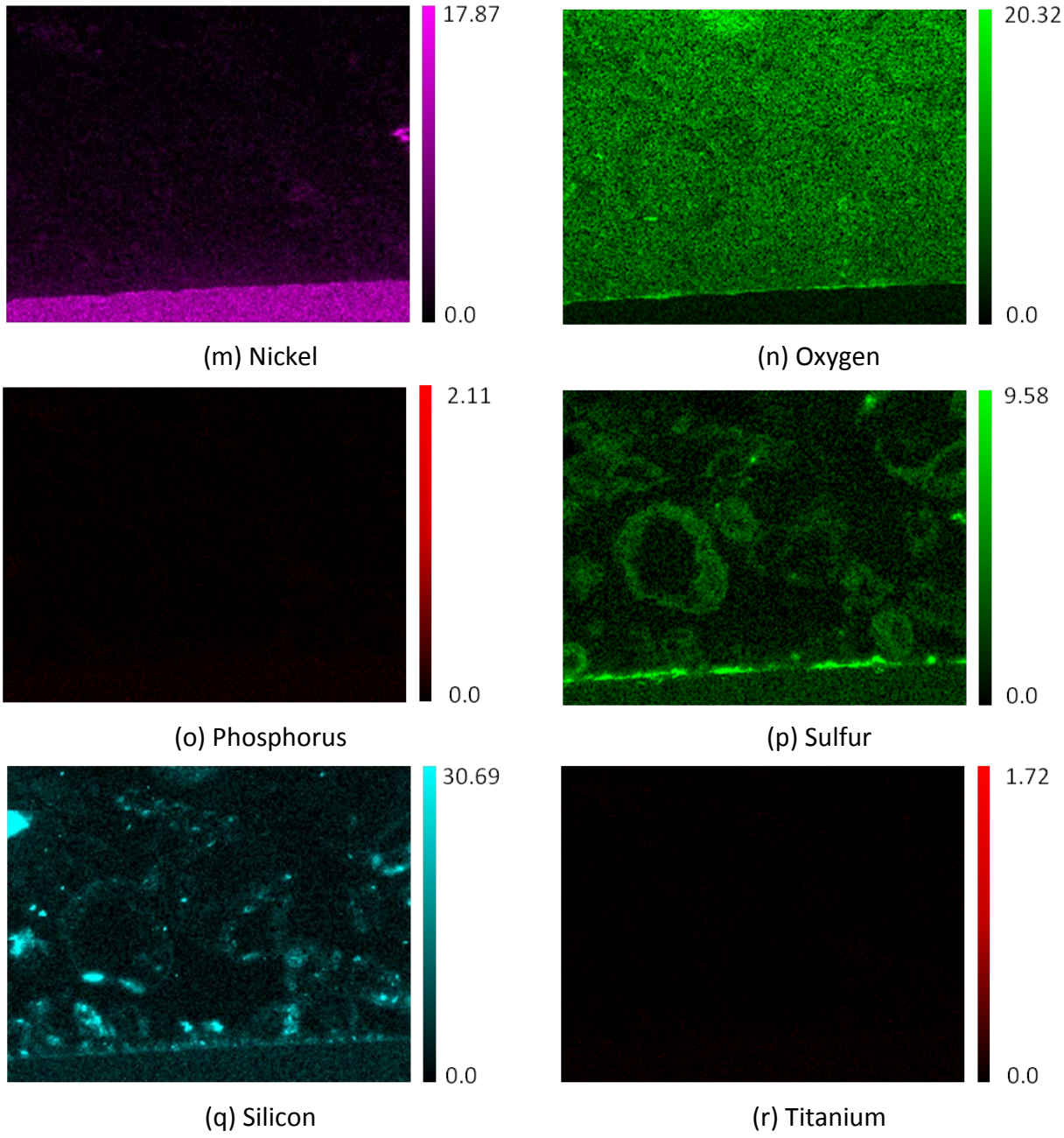

Figure 247 (m-r) - EDS Elemental Mapping of Reducing Top Probe Sample.

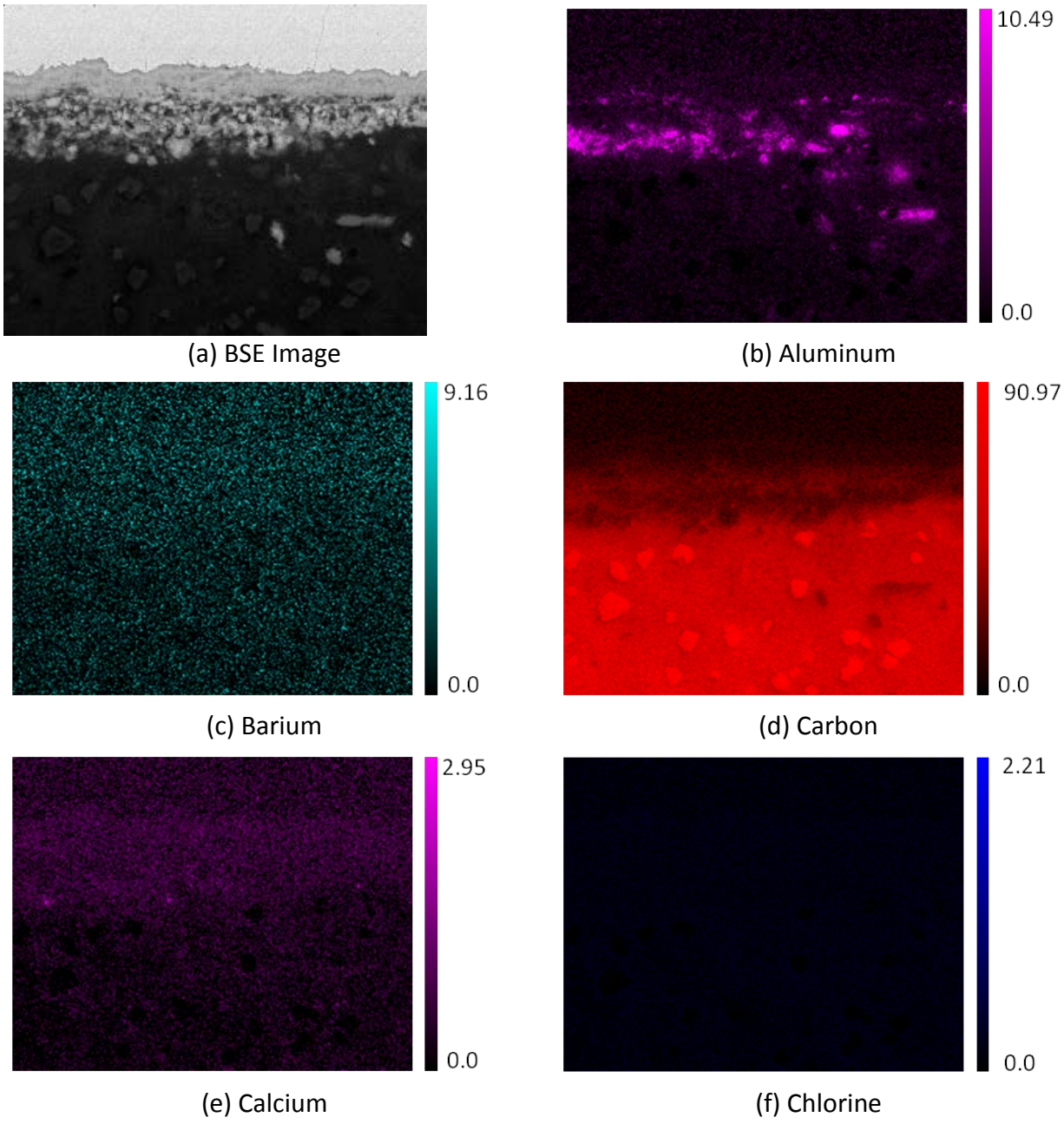

(a) BSE Image (b) Aluminum

(c) Barium (d) Carbon

(e) Calcium (f) Chlorine

Figure 248 (a-f) - EDS Elemental Mapping of Reducing Bottom Probe Sample.

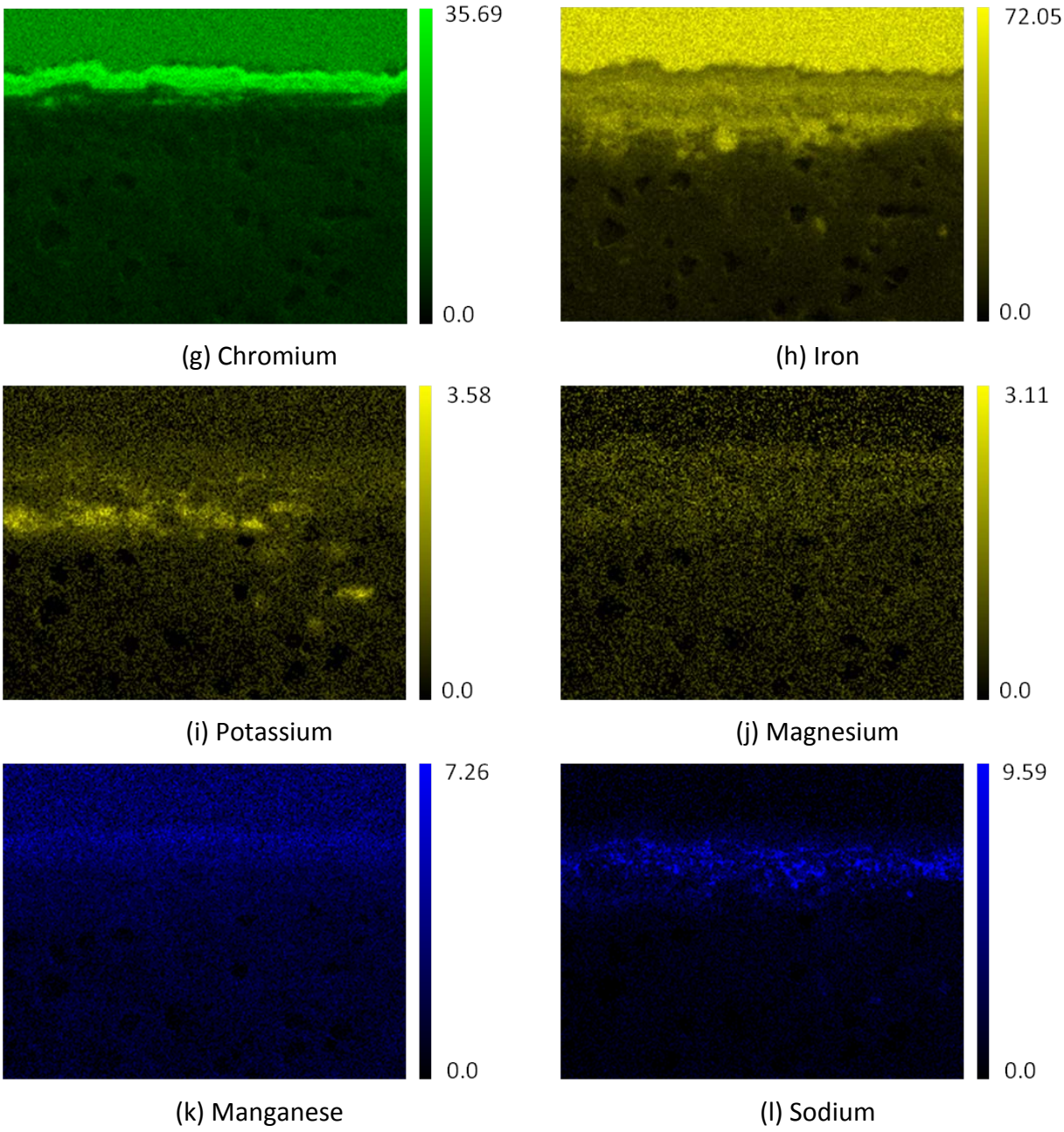

Figure 249 (g-l) - EDS Elemental Mapping of Reducing Bottom Probe Sample.

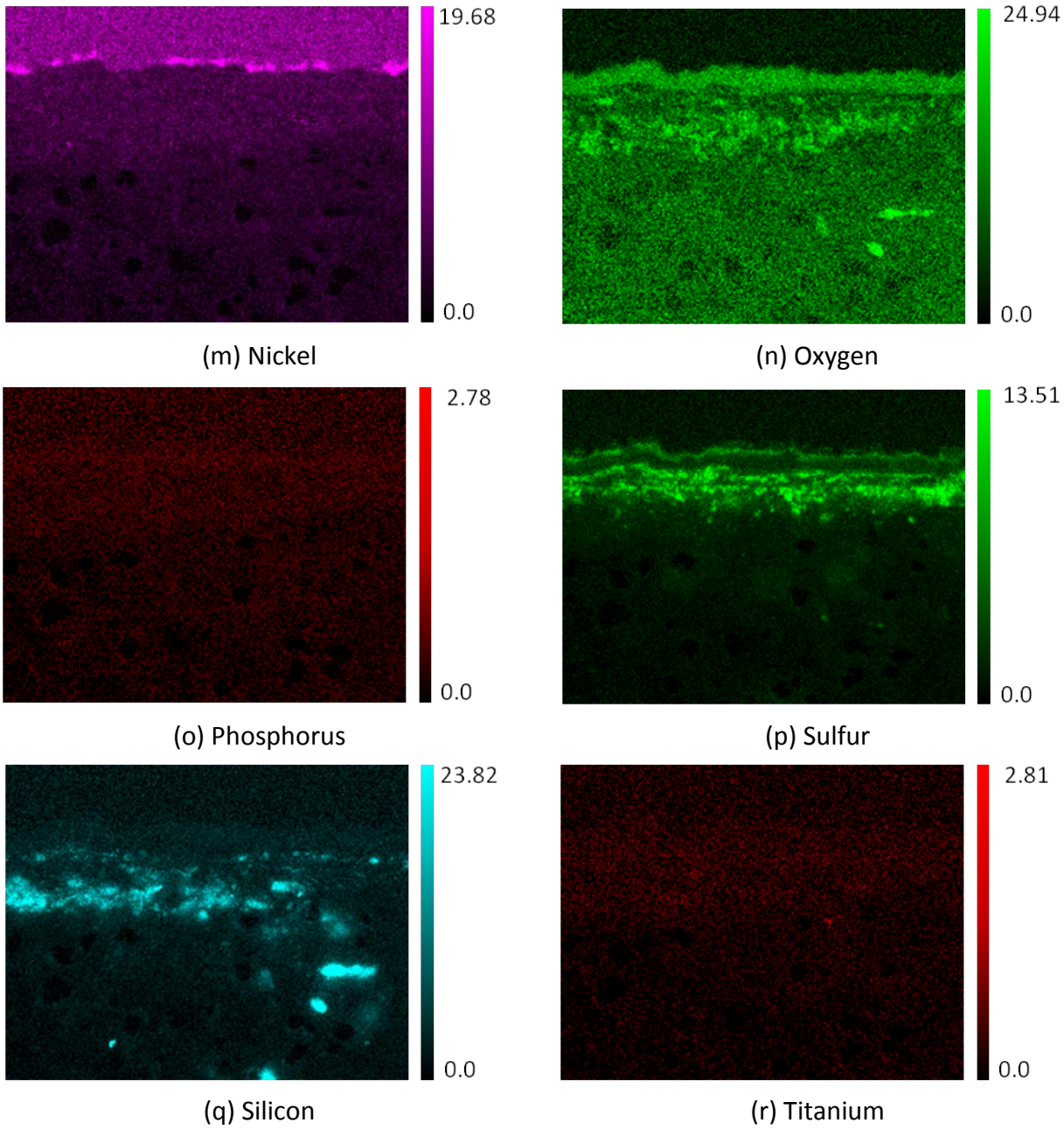

Figure 250 (m-r) - EDS Elemental Mapping of Reducing Bottom Probe Sample.

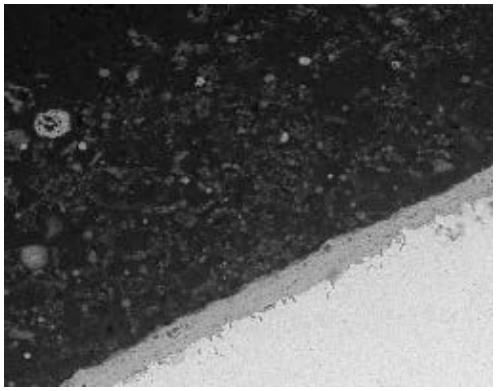

(a) BSE Image

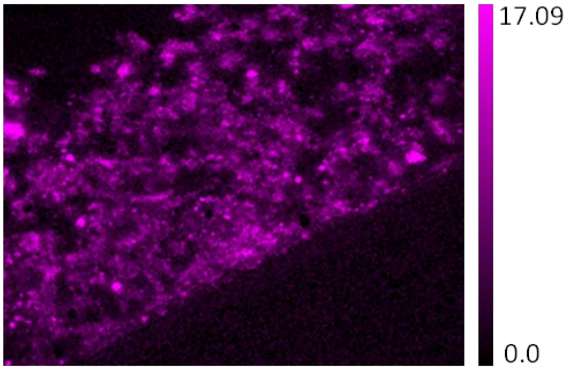

(b) Aluminum

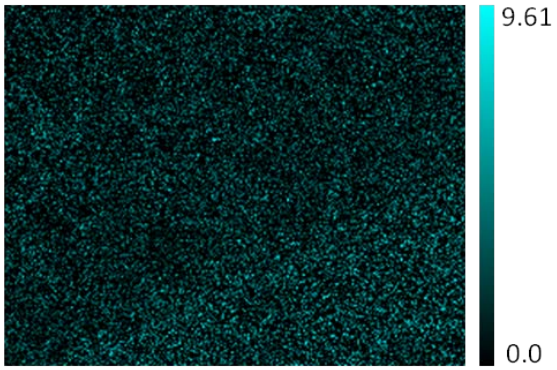

(c) Barium

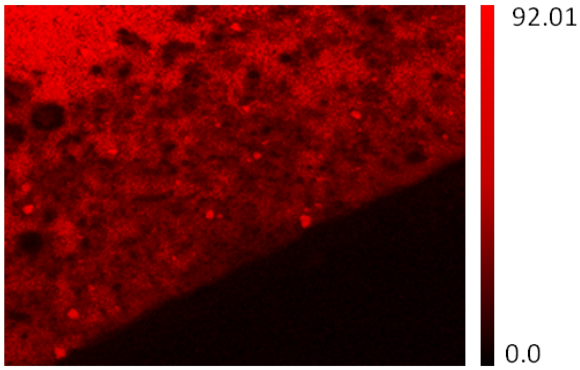

(d) Carbon

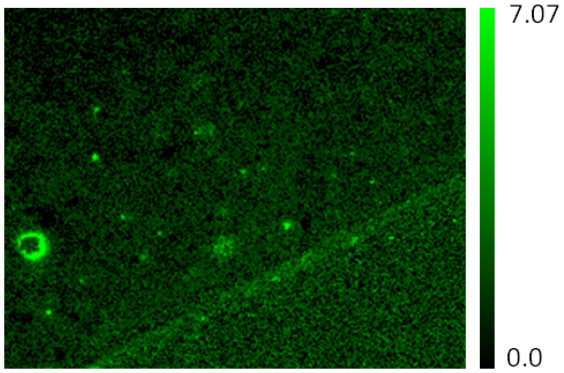

(e) Calcium

(f) Chlorine

Figure 251 (a-f) - EDS Elemental Mapping of Oxidizing Top Probe Sample.

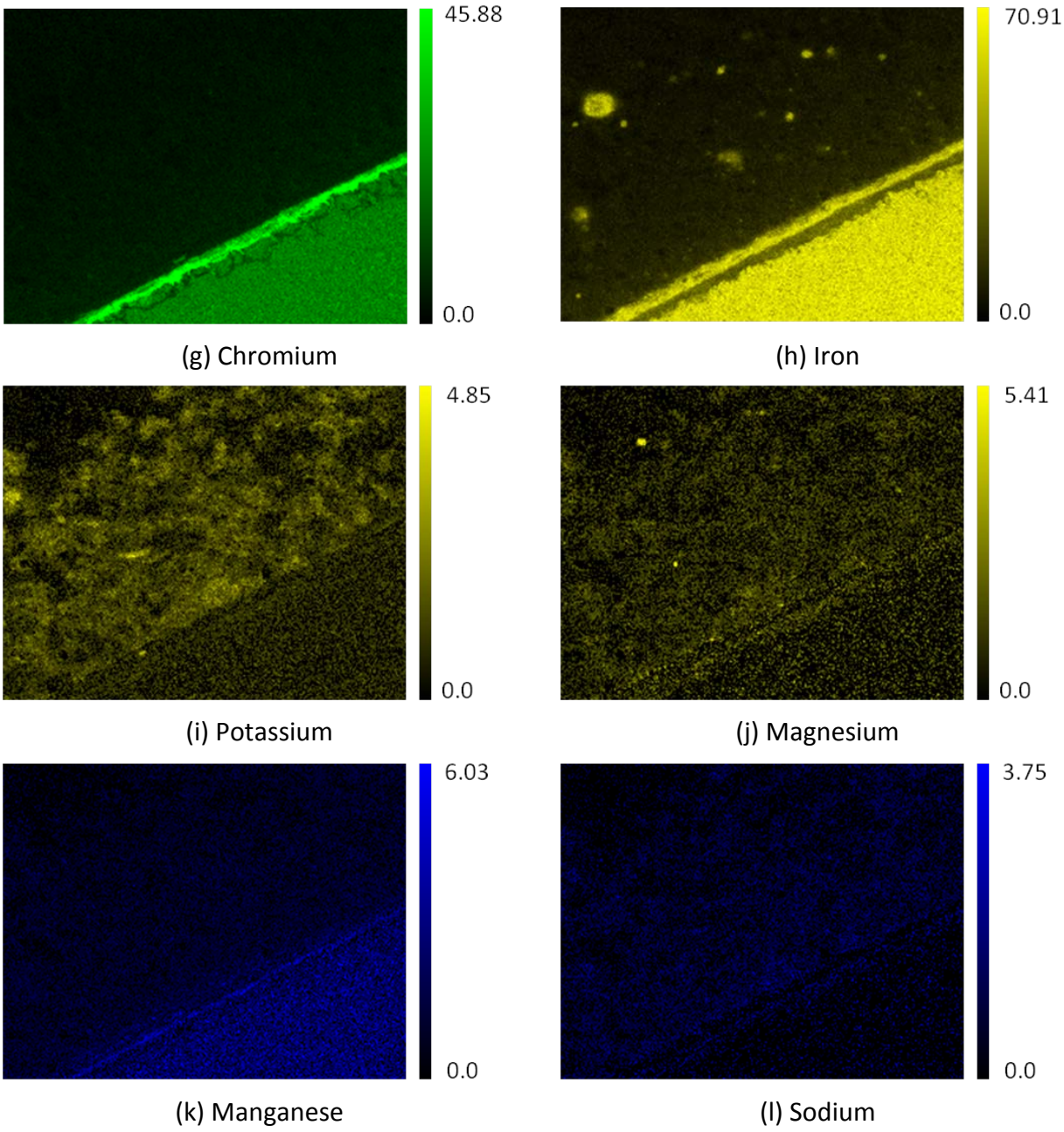

Figure 252 (g-l)- EDS Elemental Mapping of Oxidizing Top Probe Sample.

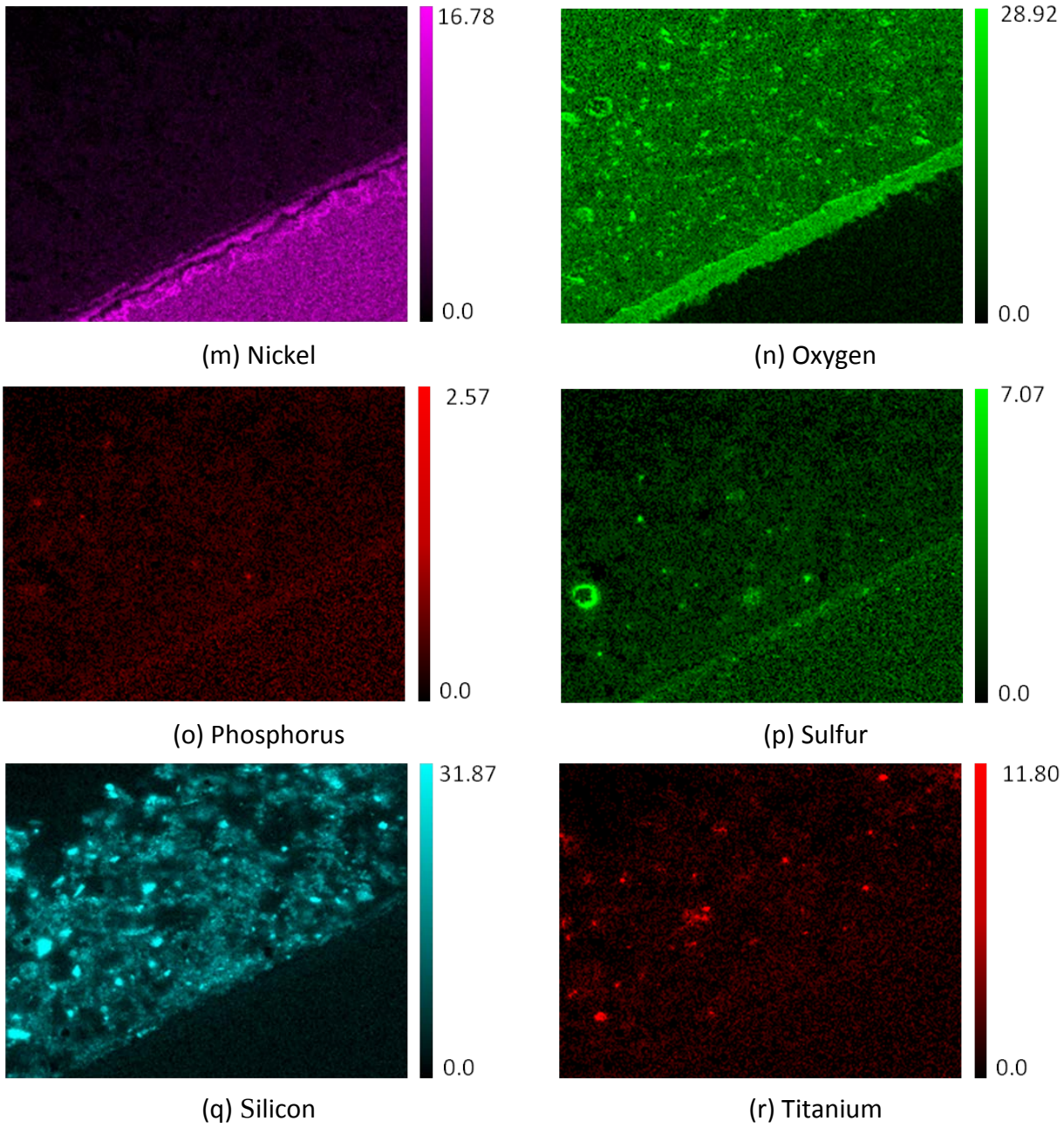

Figure 253 (m-r) - EDS Elemental Mapping of Oxidizing Top Probe Sample.

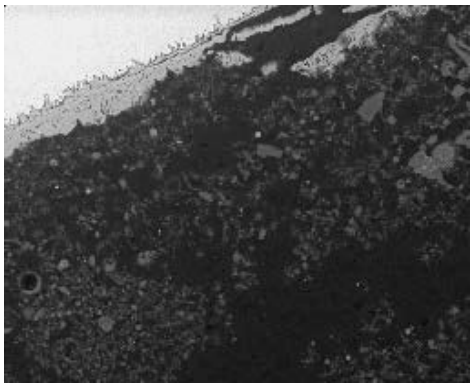

(a) BSE Image

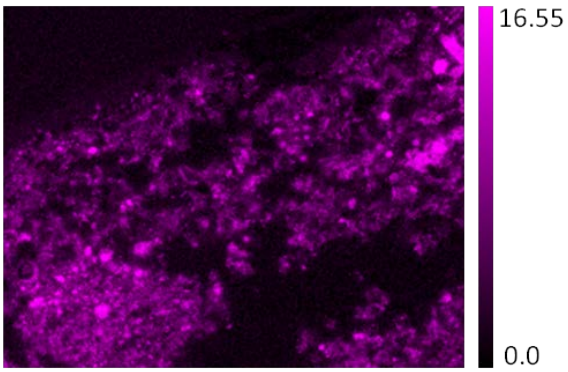

(b) Aluminum

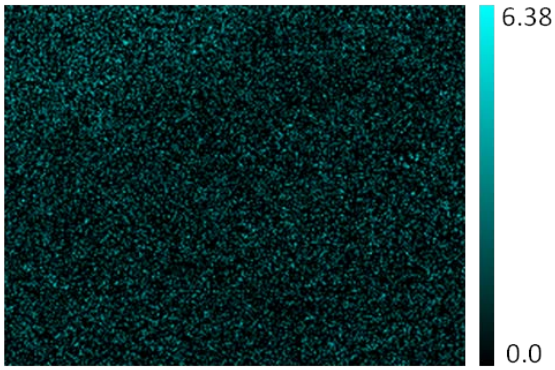

(c) Barium

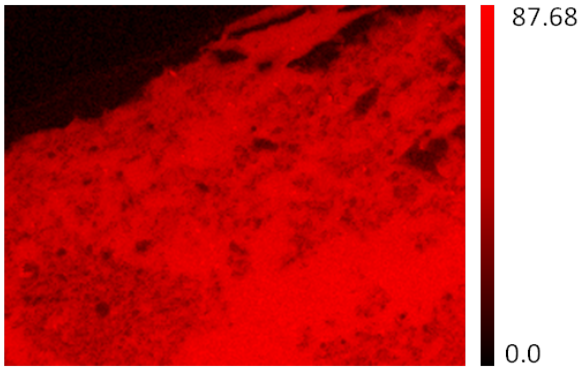

(d) Carbon

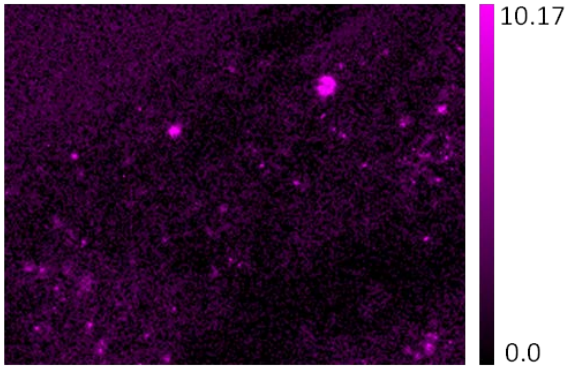

(e) Calcium

(f) Chlorine

Figure 254 (a-f) - EDS Elemental Mapping of Oxidizing Bottom Probe Sample.

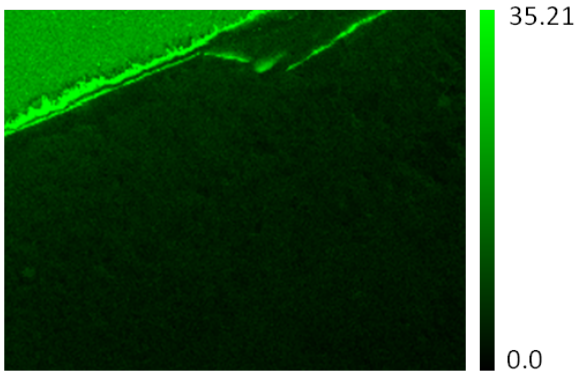

(g) Chromium

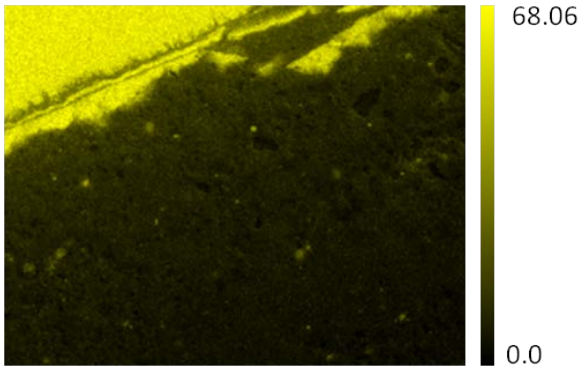

(h) Iron

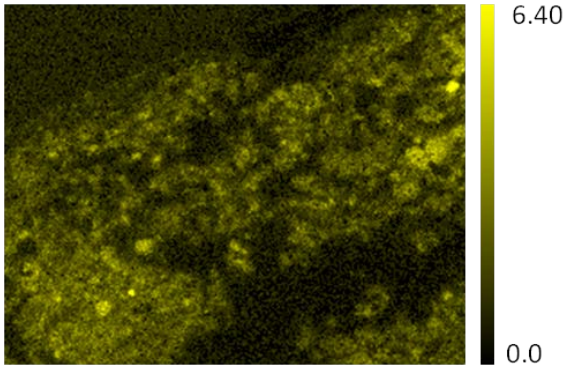

(i) Potassium

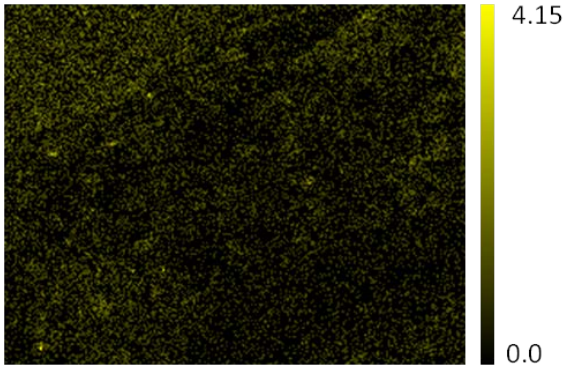

(j) Magnesium

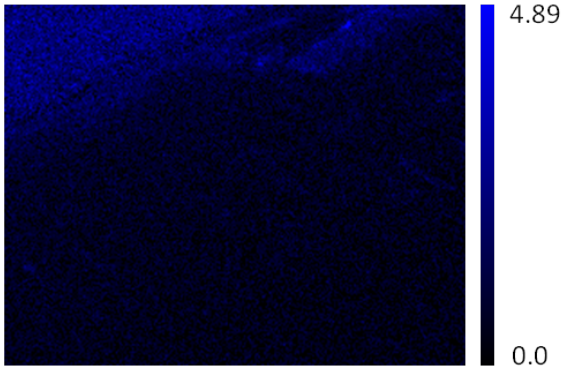

(k) Manganese

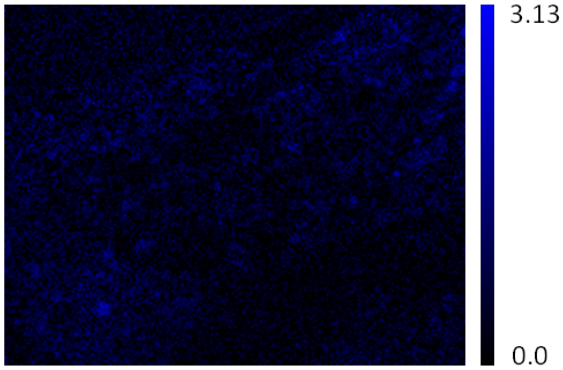

(l) Sodium

Figure 255 (g-l)- EDS Elemental Mapping of Oxidizing Bottom Probe Sample.

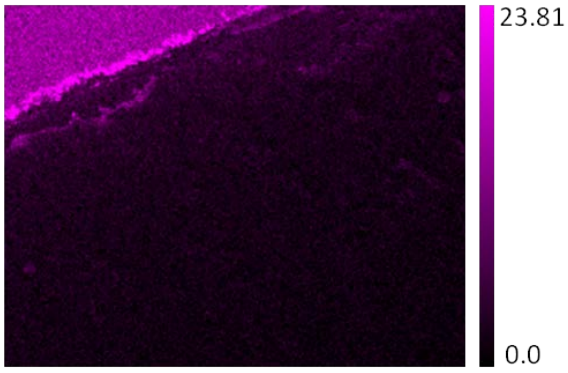

(m) Nickel

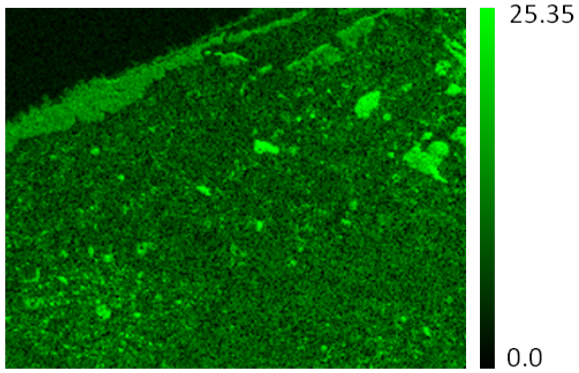

(n) Oxygen

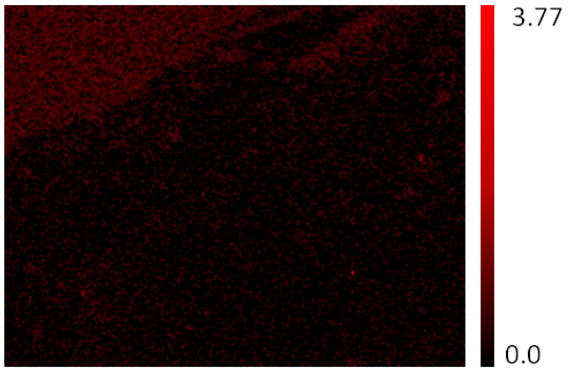

(o) Phosphorus

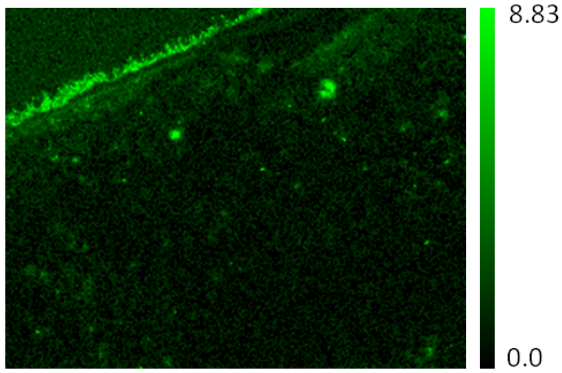

(p) Sulfur

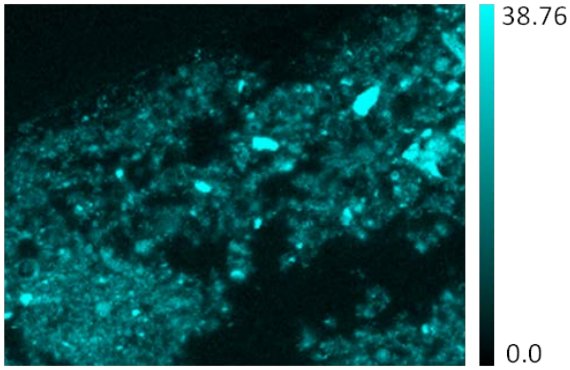

(q) Silicon

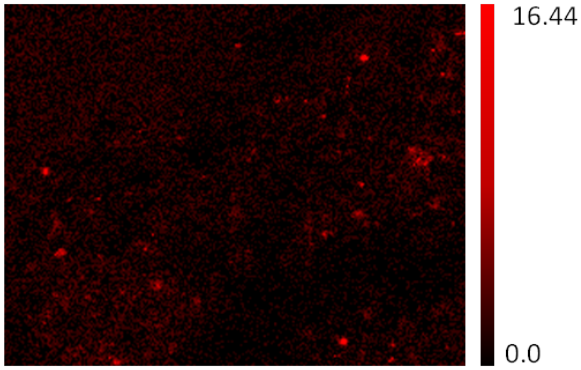

(r) Titanium

Figure 256 (m-r)- EDS Elemental Mapping of Oxidizing Bottom Probe Sample.

Using the backscattered electron images, a threshold intensity was determined for the deposit particles mounted in epoxy. The SEM/EDS software was then used to analyze the individual particles within the measured ROI (region of interest) to produce a composition and equivalent diameter. The diameter is based on a circle with the equivalent area of the particle measured. Ternary diagrams were constructed from the measured elemental compositions for each particle. For each deposit sample, four ternary diagrams have been produced. The elements of interest plotted on the diagrams include: Al, Si, Ca, S, Fe, Cl, and Na.

The ternary diagrams for particles present in the reducing top deposit are shown in Figures 251-254. Figure 251 shows that the concentration of Fe+S is much higher in the particles than that of Ca+S. Such domination is consistent with the results of elemental mapping. Figure 252 shows that the compositions of particles follow a diagonal line towards the middle of the Ca-S axis. This trend indicates that the amounts of Ca and S are present at a nearly 1:1 molar ratio. In Figure 253, the trend of particle compositions based on Fe and S scatters somewhat but follows an average molar ratio of 1:2 for S and Fe. In addition, there are a large number of particles fall on the lower axis, i.e., consisting mostly of Al, Si, and Fe but no sulfur. In Figure 254, a highly scattered grouping of particle compositions is observed in the ternary diagram plotted based on Na and Cl. The average slope in these particles is ≥ 1 in molar ratio for Na and Cl. However, as mentioned previously, the concentration of Cl determined from the cross-sections is not accurate due to the fact that the epoxy material used for mounting contains a significant amount of chlorine. Therefore, in reality, the compositional trend in Figure 254 would be much closer to the lower axis (i.e., higher in Na) than what is shown.

Ternary diagrams for the reducing bottom deposit are given in Figures 255-258. In this deposit sample, Fe is much more abundant than Ca, as shown in Figure 255. However, Figure 256 shows that the amount of Ca compares well with that of S at a nearly1:1 molar ratio. No clear trends can be observed in Figures 257 and 258 when Fe vs. S and Na vs. Cl are plotted in the ternary diagrams.

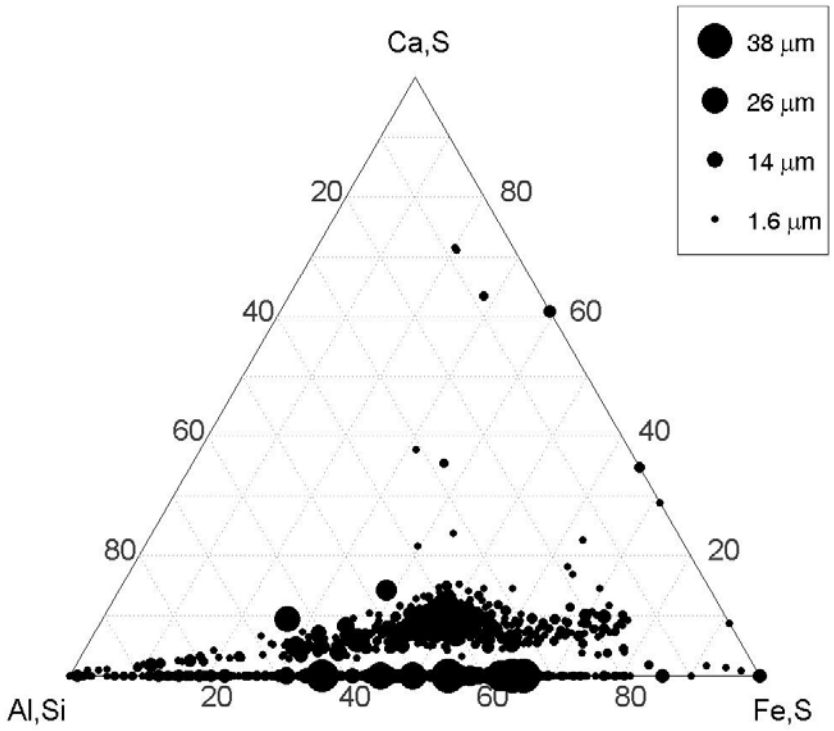

Figure 257 - Ternary Diagram for Reducing Top Probe Sample Based on the Axes of Al/Si, Ca/S, and Fe/S in Molar%.

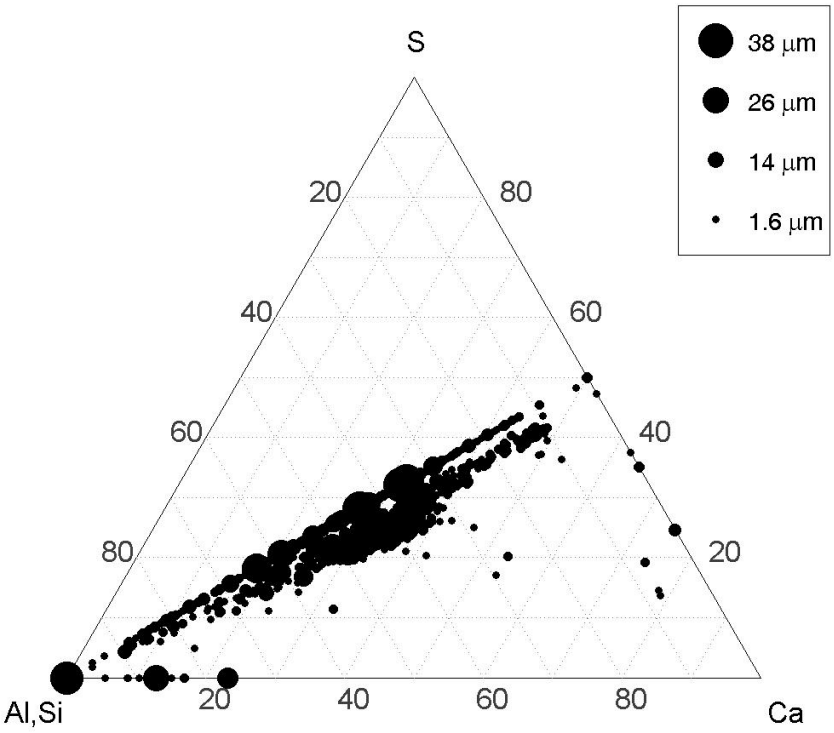

Figure 258 - Ternary Diagram for Reducing Top Probe Sample Based on the Axes of Al/Si, S, and Ca in Molar%..

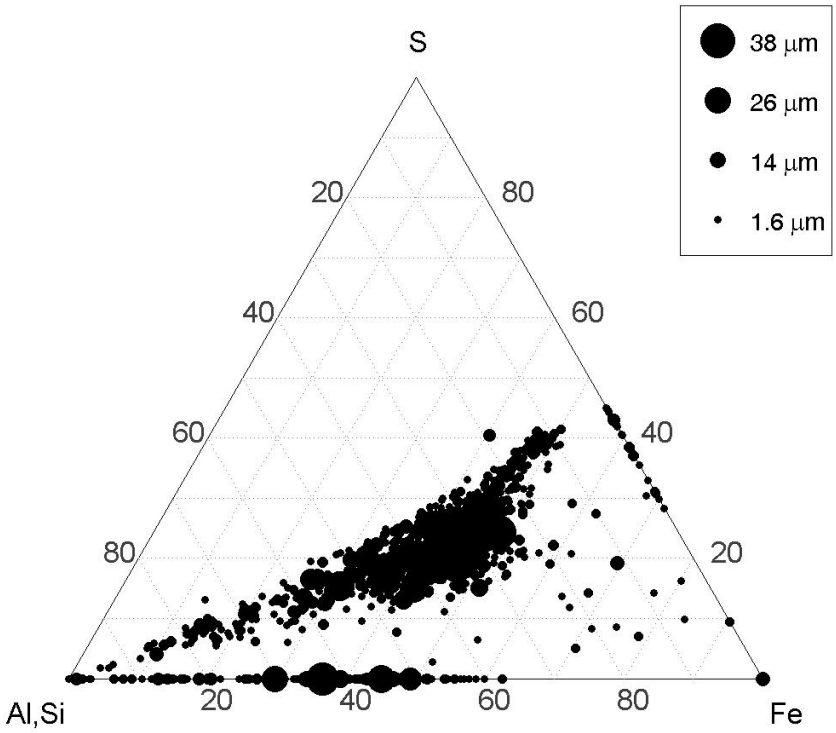

Figure 259 - Ternary Diagram for Reducing Top Probe Sample Based on the Axes of Al/Si, S, and Fe in Molar%.

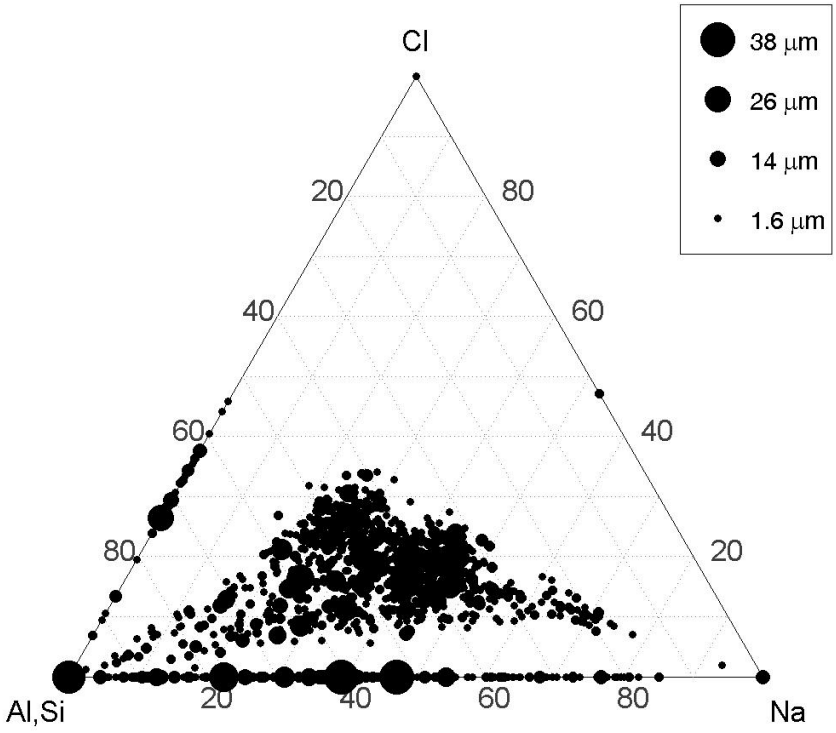

Figure 260 - Ternary Diagram for Reducing Top Probe Sample Based on the Axes of Al/Si, Cl, and Na in Molar%.

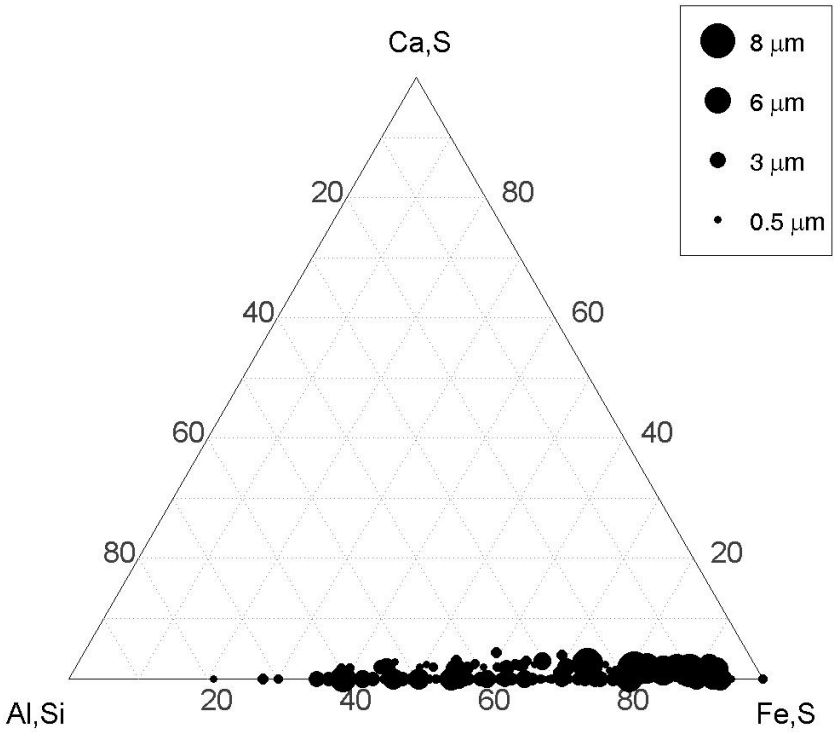

Figure 261 - Ternary Diagram for Reducing Bottom Probe Sample Based on the Axes of Al/Si, Ca/S, and Fe/S in Molar%.

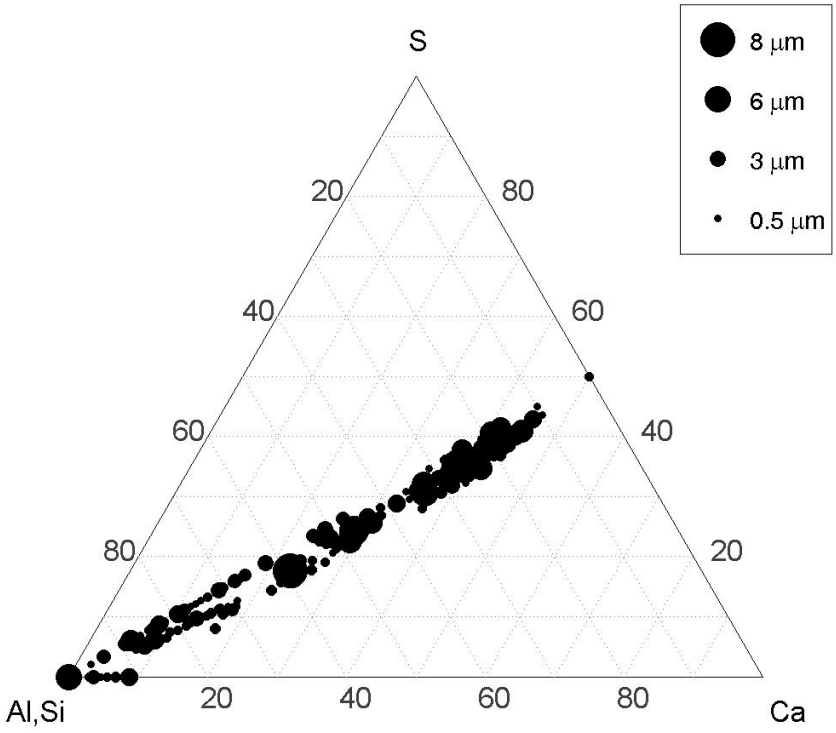

Figure 262 - Ternary Diagram for Reducing Bottom Probe Sample Based on the Axes of Al/Si, S, and Ca in Molar%.

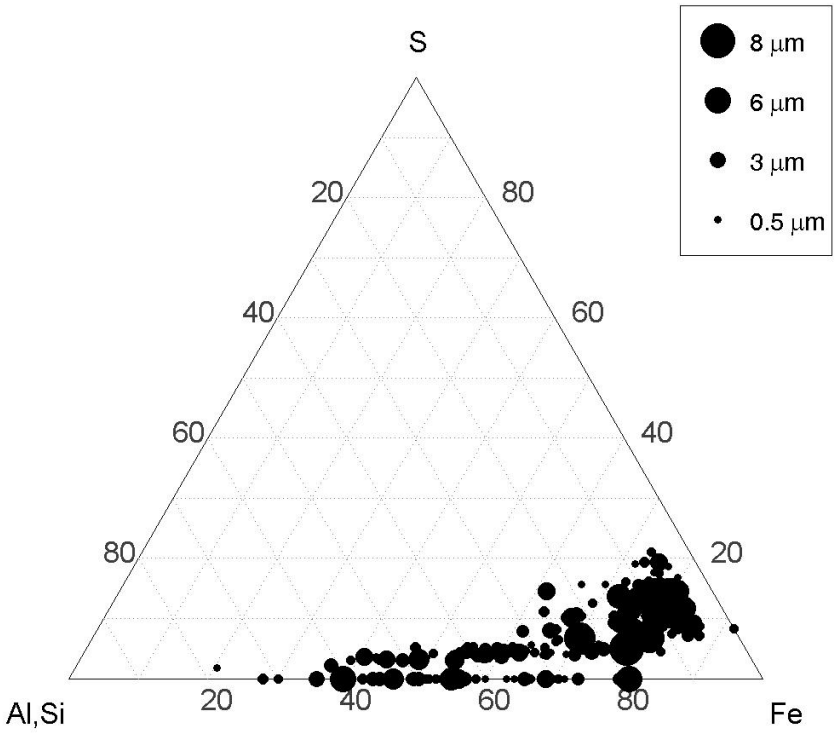

Figure 263 - Ternary Diagram for Reducing Bottom Probe Sample Based on the Axes of Al/Si, S, and Fe in Molar%.

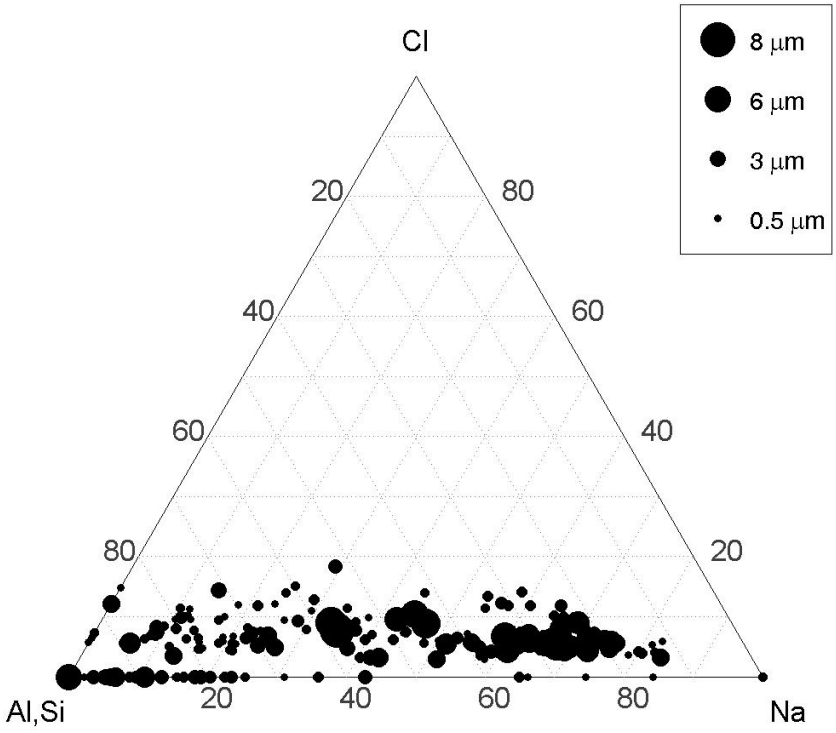

Figure 264 - Ternary Diagram for Reducing Bottom Probe Sample Based on the Axes of Al/Si, Cl, and Na in Molar%.

The ternary diagrams of ash particles for the oxidizing top deposit are shown in Figures 259-262. As with the reducing zone deposits, the particles in Figure 259 contain significantly more Fe than Ca. Figure 260 reveals three groups of particles existing in about equal numbers, i.e., (1) particles that fall on the bottom axis containing no S, (2) particles that follow a diagonal line at a molar ratio of 2:1 for Ca and S, and (3) particles that exhibit a molar ratio of 1:1 for Ca and S. Figure 261 shows that a large number of ash particles contain no sulfur and unlike Ca, Fe does not seem to be associated with S. Figure 261 shows that approximately one third of the particles contain a measurable amount of Na and Cl. Again, as discussed previously, the Cl concentrations determined by EDS are not reliable due to the large amount of chlorine present in the epoxy material used for sample mounting.

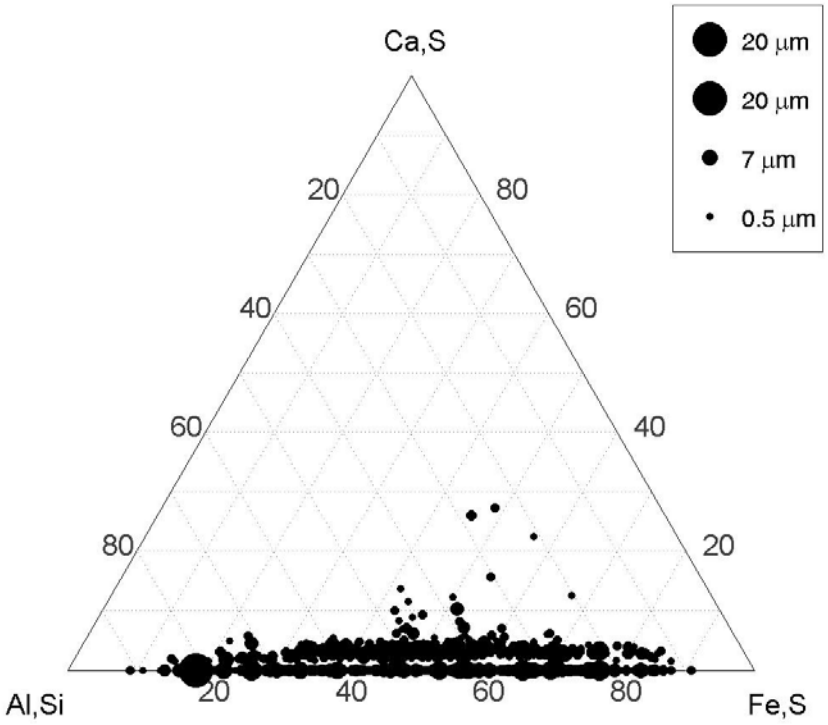

Figure 265 - Ternary Diagram for Oxidizing Top Probe Sample Based on the Axes of Al/Si, Ca/S, and Fe/S in Molar%.

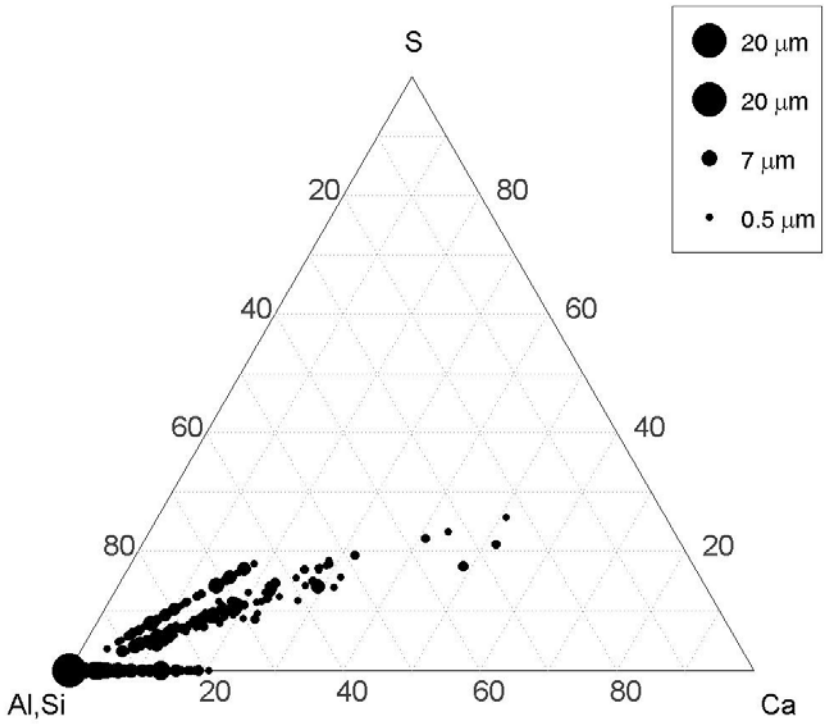

Figure 266 - Ternary Diagram for Oxidizing Top Probe Sample Based on the Axes of Al/Si, S, and Ca in Molar%.

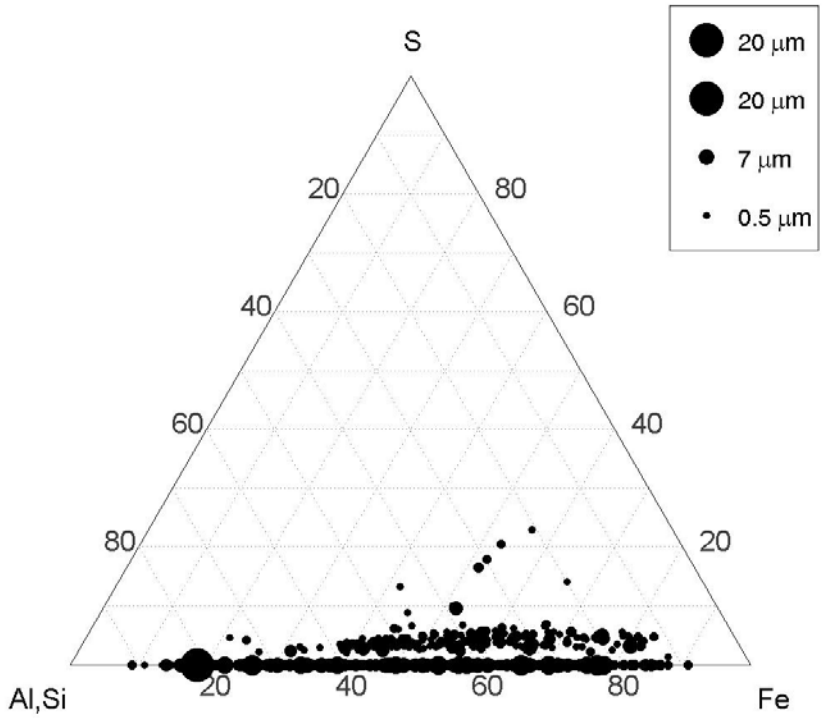

Figure 267 - Ternary Diagram for Oxidizing Top Probe Sample Based on the Axes of Al/Si, S, and Fe in Molar%.

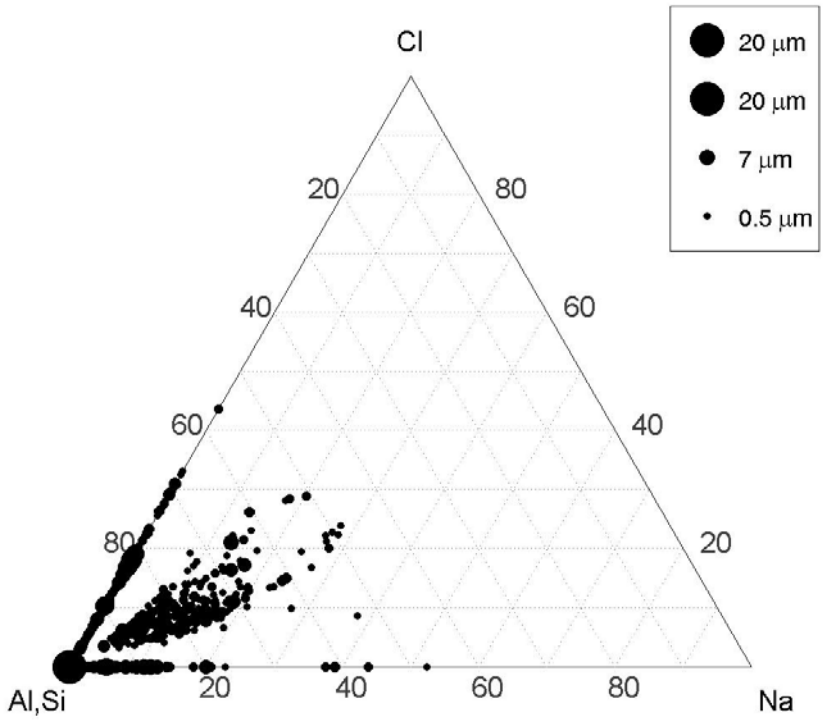

Figure 268 - Ternary Diagram for Oxidizing Top Probe Sample Based on the Axes of Al/Si, Cl, and Na in Molar%.

The ternary diagrams of particles for the oxidizing zone bottom deposit sample are shown in Figures 263-266. These diagrams look very similar to those of oxidizing top deposits. Three groups of particles are again observed in Figure 264, although fewer particles are present along the line at a molar ratio of 1:1 for Ca and S. The Na to Cl ratio is also higher in the oxidizing bottom deposit, shown in Figure 6 compared to the oxidizing top deposit.

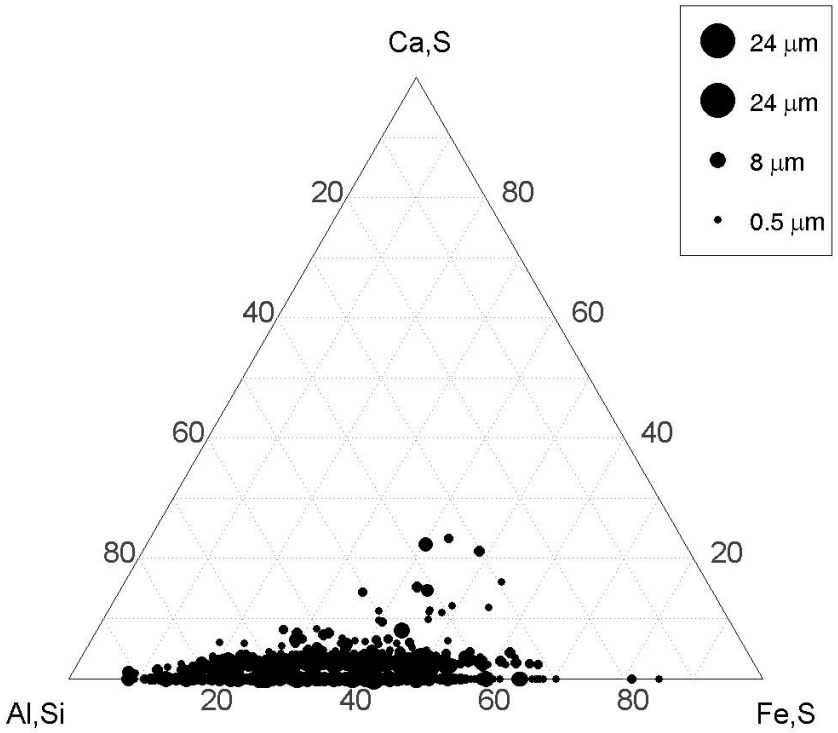

Figure 269 - Ternary Diagram for Oxidizing Bottom Probe Sample Based on the Axes of Al/Si, Ca/S, and Fe/S in Molar%.

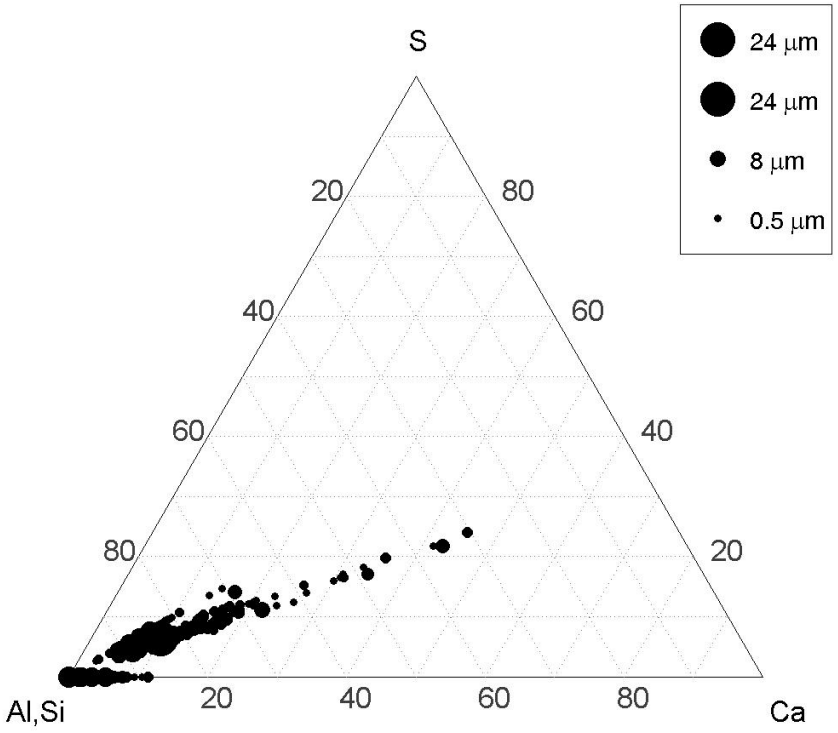

Figure 270 - Ternary Diagram for Oxidizing Bottom Probe Sample Based on the Axes of Al/Si, S, and Ca in Molar%.

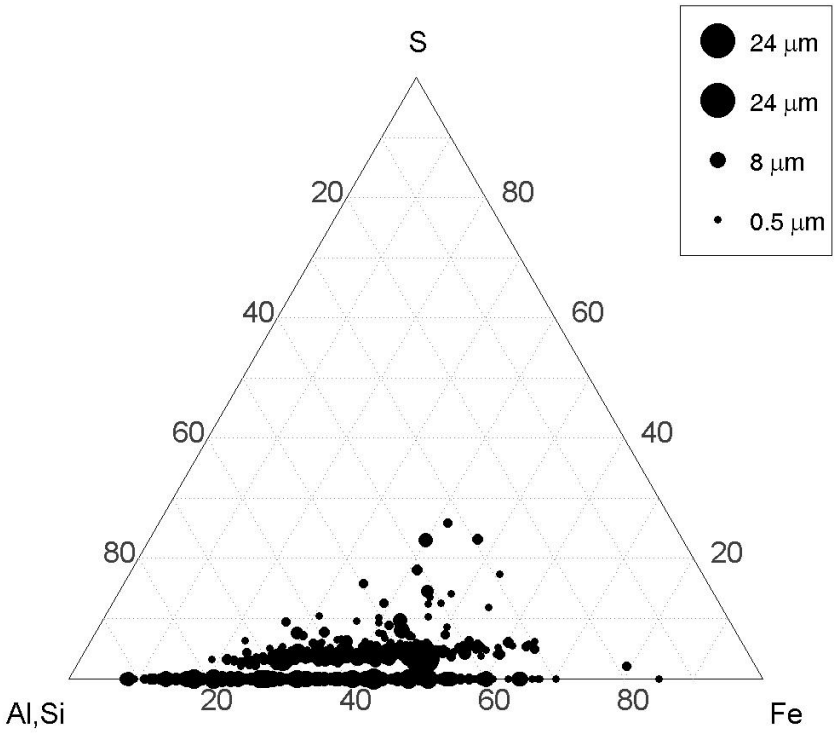

Figure 271 - Ternary Diagram for Oxidizing Bottom Probe Sample Based on the Axes of Al/Si, S, and Fe in Molar%.

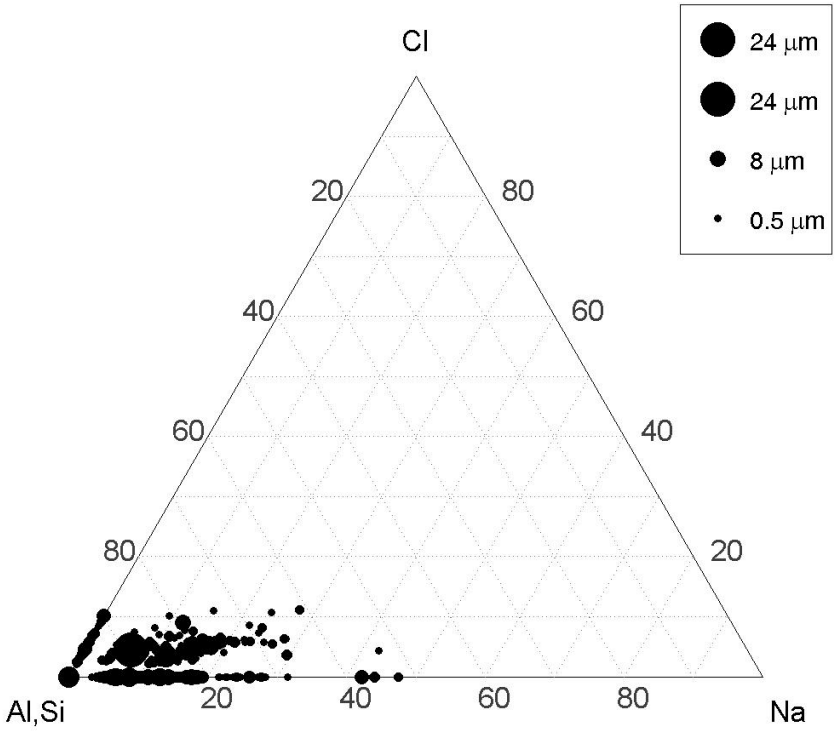

Figure 272 - Ternary Diagram for Oxidizing Bottom Probe Sample Based on the Axes of Al/Si, Cl, and Na in Molar%.

4.5 Task 5 – Corrosion Model Development

As discussed previously, eight different U.S. coals commonly burned in utility boilers, which cover a wide range of chemistry and heating values, were evaluated in the pilot-scale combustion facility, BFR. Analyses were performed on the combustion product gases and deposits for both the low-temperature reducing gas regime (i.e., SR = 0.85) and high-temperature oxidizing gas regime (i.e., SR = 1.15). Following characterizations of the combustion gases and deposits for both regimes, laboratory fireside corrosion tests were conducted on coupons of many candidate alloys and weld overlay coatings for each of the two exposure applications under realistic exposure conditions.

For each corrosion test, duplicate coupons of each candidate alloy and weld overlay were buried in the mixture of simulated deposit relevant to the particular combusted coal. These deposit-covered samples were then exposed isothermally to a flowing mixed gas of composition representative of the specific combustion environment for a period of 1000 hours. The temperatures selected to simulate furnace wall corrosion in the reducing gas (SR = 0.85) were 750-950^{o}F and that for coal ash corrosion in the oxidizing gas (SR = 1.15) were 1100-1500^{o}F. Obviously, differing sets of alloys and coatings were chosen as candidate materials for the two very different boiler environments. The compositions of the candidate alloys and weld overlay coatings for the two temperature regimes are listed in Appendix D. The compositions of both the deposits and combustion gases for each of the different coals at each of the exposure temperatures are discussed in Section 3.4 by test condition and coal. Following the 1000-hour laboratory tests, the coupons from each simulated coal environment were prepared and evaluated separately for both weight loss and thickness loss. The maximum thickness loss was measured by a micrometer and microscopically in cross-section for the maximum depth of subsurface penetration. The weight loss data were used to calculate the average corrosion rate of each sample. Between the two indications of corrosion wastage, the weight change is believed to be more relevant to mechanistic understanding of the corrosion attack of interest, and any large deviations in correlation between the weight-loss measurement and maximum depth of penetration reveals the extent of localized attack for a given sample.

One important aspect of the corrosion tests for both the reducing and oxidizing environments was the complete immersion of each coupon in a particular deposit of the same overall composition as that established by the prior characterization of the actual deposits collected from the BFR. While the laboratory deposit had the same gross composition, it comprised individual reagent-grade chemicals that corresponded to the correct overall composition at equilibrium. The use of reagent-grade chemicals was necessary because many of the deposit compounds expected to exist at equilibrium are not commercially available. The presence of a deposit in a corrosion test plays a vital role in fireside corrosion involving mixed oxidants (oxygen, sulfur, chlorine), especially in combination with a high concentration of an inert diluent gas (i.e., nitrogen from air firing). At the base of a deposit, as a metallic substrate reacts preferentially with one gaseous component (perhaps to form the most thermodynamically stable corrosion product), that reactant is depleted relative to the other oxidant concentrations, thus permitting the formation of a second or third, etc. corrosion product (of perhaps lower stability in the bulk gas phase otherwise). In general, the gas phase at the base of a porous

deposit (because of the absence of local convection) can only be replenished by relatively slow interdiffusion of the dilute, reactive components in the concentrated diluent gas over pores and channels in the deposit. Thus, in general, the gas composition at the base of a porous deposit would not correspond to that for the bulk gas, and thermodynamic calculations using the bulk gas phase composition would not always correctly predict the expected corrosion products. The gas composition locally at the base of a deposit would decide what corrosion products can form on the metal surface.

Another important aspect of the presence of a porous deposit on a reactive metal surface is a sort of "marker motion". Indeed, a porous deposit contacts the substrate irregularly with respect to particle size, shape, and composition. Certainly, the deposit particles are not in intimate physical contact (on an atomic scale) uniformly along the metal/deposit interface. Marker motion has been commonly observed in many classic studies of scaling between a reactive metal and oxidant gas in the absence of a porous deposit; an inert object (traditionally a small inert metal wire) initially attached (welded) to the metal surface is found beneath the scale (at the metal/scale interface) if outward cation diffusion dominates in scale growth at the gas/scale interface. The diffusing cations simply cause the outward grown scale to encompass and eventually bury the inert "marker". Conversely, if dominant anion diffusion results in inward scale growth at the metal/scale interface, an initial surface marker is left at the outer scale/gas interface.

For the growth of scales on Fe and Ni-base alloys at very high temperatures, there is no doubt that any oxide or sulfide corrosion product, which all exhibit dominant outward cation diffusion through the scale lattice, would result in incorporation of the ash particles into the thermally grown scale when a porous deposit is present. As a result, the scale morphology should include embedded deposit particles in such a fashion to yield a very heterogeneous scale in structure and composition. However, in the temperature range of boiler tube operation, such as those employed in this study, the scale growth is no longer simply dominated by outward cation diffusion. The significant change in growth behavior is attributed to the fact that the scale grain size formed at the relatively low boiler tube temperatures is small and diffusion via the grain boundaries becomes the dominant mechanism for scale growth. Consequently, both outward cation diffusion and inward molecular oxidant diffusion over voids can take place simultaneously, especially through different scale layers. For example, steam oxidation of boiler tubes in superheater banks typically leads to the formation of an inner spinel layer and outer magnetite layer. The growth of the spinel layer must be dominated by inward gaseous diffusion of oxidant, such as water vapor, while the growth of the magnetite layer is controlled by outward diffusion of iron ions. Because the scale growth governed by iron ion diffusion requires a counterflow of vacancies, voids are often found at the spinel/magnetite interface. The presence of interfacial voids significantly weakens the adhesion of the outer magnetite layer to the inner layer and is one of the primary reasons responsible for massive scale exfoliation during cooldown.

In general, isothermal scale growth on alloy surfaces by diffusion-limited kinetics would follow a parabolic rate law (i.e., rate slows upon thickening of the scale with time to the power of 0.5). However, industrial experience in such coal-combustion conditions has shown that the kinetics are better approximated by a linear (time-independent) rate. Repeated detachment and

removal of the corrosion product by residual stress created between a thick scale and the underlying metal substrate, as well as thermal stresses from soot blowing and load cycling in boiler operations, contribute importantly to the approximate linear kinetics for the corrosion process. All of the corrosion exposures in the current laboratory study were limited to 1000 hours, with an expectation/assumption of linear kinetics that can be extrapolated to predict the corrosion rates of longer-term boiler operations.

To this date, the role of chlorine in influencing (generally increasing) the corrosion of alloys at such a low temperature as 850^{o}F in a reducing furnace environment has escaped rationalization. However, in several papers by Grabke et al.,[18-20] a mechanism of "active oxidation" was introduced and demonstrated for the high-chloride, oxidizing environment of incinerated municipal refuse at somewhat higher temperatures. A variation of this mechanism ("active sulfidation") is proposed and presented later in Section 3.5.1.2 to explain the effect of chlorine in the attack of low-alloy steels in coal environments of the current studies.

To date, a large amount of corrosion data has been generated from the laboratory fireside corrosion tests performed in Task 4. The available corrosion data are documented in Section 3.4 of this report in the form of bar graphs.

3.5.1 Discussion of Laboratory Corrosion Data for Furnace Wall Corrosion under Reducing Conditions

From the weight-loss corrosion data presented in Section 3.4, detailed inspection revealed that few regular relationships between the coal compositions and the alloy corrosion rates are obvious. On the basis of their low sulfur and chlorine contents, the three coals WY PRB, ND Lignite, and Pitts #8 would be expected to be the least corrosive (in this order). All three coals contain negligible amounts of chlorine. In fact, for the low-Cr ferritic alloys (CS, T2, T11, T22, and T23), the ND Lignite coal was the least corrosive in the reducing tests at 850^{o}F, followed by WY PRB and Pitts #8. To rationalize the observed reversal in expected rates of attack between the relatively higher-sulfur ND Lignite (0.67 wt.%) and lower-sulfur WY PBR (0.25wt.%), one can notice from Table 9 in Section 3.2.3 a noticeable difference in both the amounts of ash and alkali contents between the two coals. The higher-S ND Lignite coal has four times the alkali content in the ash compared to WY PRB (i.e., 3.83% x 8.66% = 0.332 wt.% vs. 1.46% x 5.53% = 0.0807 wt.%). As to be clarified later, the higher alkali content of the ash deposit can apparently lead to the formation of innocuous alkali sulfates (at least at the low temperatures of 750-950^{o}F studied for furnace walls) and thereby tie up some of the sulfur from the aggressive H_2S reactant and consequently reduce the reactivity for that coal.

Coals with high sulfur and chlorine (KY #11 and IL #6) and highest-S but low Cl (OH Gatling) indeed resulted in the worst corrosion for the low-Cr alloys exposed to the 850^{o}F reducing tests, with IL #6 giving the highest rates (by far). Corrosion attack on these alloys and weld overlays by KY #11 and OH Gatling was found comparable. The dominance of corrosion attack by the IL #6 with the highest chlorine content (0.273 wt.%), even though the sulfur content is modest, indicates an important role of chlorine in furnace wall corrosion, at least at this high chlorine concentration. As mentioned, this important role of chloride-induced

accelerated corrosion is shown later to be explained by an "active sulfidation" mechanism. Table 9 indicates little difference in the alkali oxide contents among these three coals at 850°F. For coals with high sulfur content, the previously mentioned advantageous effect of alkali oxides of the ash in trapping sulfur by forming alkali sulfates becomes much less important, perhaps based simply on a stoichiometric argument.

The two coals OH Mahoning 7A and IN #6 Gibson contain intermediate sulfur and chlorine concentrations, but the IN #6 coal with the lower sulfur content was somewhat more aggressive than OH 7A in the corrosion of low-Cr alloys from the 850°F tests. For this comparison, the higher alkali oxide content (a factor of 2) for the lower sulfur IN #6, apparently did not result in a reduction in the corrosion rate. However, the silica ratio of IN #6 Gibson coal ash is higher than that of OH Mahoning 7A. A silica ratio is defined as the ratio of total silica to the sum of silica, hematite, calcia, and magnesia. It is speculated that ash with a higher silica ratio, thus excess large inert particles with a very high melting point, can lead to a more porous deposit layer and allow the corrosive gases to diffuse more easily towards the metal surface. Further evaluation of the potential silica ratio effect on corrosive gas diffusion should be performed.

As anticipated, the corrosion rates of the two ferritic alloys with about 9% Cr, i.e., T9 and T91, were lower than those of the low-Cr ferritic alloys by a factor on the order of 3 or more in the 850°F tests. Likewise, the high alloy compositions used as a weld overlay on furnace walls, including 304H, 309H, 310H, WO52, and WO72, generally exhibited corrosion rates approximately an order of magnitude lower than those of low-Cr alloys at 850°F. However, the two coals (IL #6 and KY #11) with the highest combination of sulfur and chlorine remained the most corrosive for the high-Cr alloys.

Some attention was given to seek correlations with other factors, including the partial pressures of H_2O, the ratios of O_2/H_2 and H_2S/H_2 in the gas phase, and the Fe_2O_3 contents in the coal, but no such correlations were obvious. In a temperature range around 850°F, some literature findings suggest that the relative stabilities of gaseous species, such as SO_2, CO_2, and O_2, would provide little reactivity compared to H_2S, H_2O, and HCl.[21] However, there is every expectation that the overall kinetics of corrosion in this study are governed by solid-state diffusion through the very fine-grained and heterogeneous scale formed on the alloy surface. Molecular dissociation should not contribute significantly to the rate limiting step nor does the diffusion of the gaseous reactant through the porous deposit layer.

4.5.1.1 Microscopic and Analytical Characterization of 850°F Reducing Testing

As discussed in Section 3.4, several alloys intended for use in the low-temperature, reducing-gas furnace wall application were tested at 850°F for 1000 hours. Coupons of these alloys were buried in the presence of the specific coal ash and gas composition with SR = 0.85 relevant to each particular coal. After the corrosion testing, these samples were examined in metallographic cross-section and by elemental analysis. A summary of these observations with remarks about the corrosion mechanism follows.

Alloy T11 (1.3%Cr, 0.5%Mo, bal. Fe) was tested in the OH Gatling environment. This coal has the highest sulfur content (4.31%) but very low Cl, and the deposit contains very high sulfates. The alloy/scale interface and the deposit containing the corrosion product zone for Alloy T11 are shown in Figure 273. The corrosion rate of T11was moderate, about half of those of the fastest corroding Fe-base alloys in the same environment. The microstructure shows that a compact scale, predominant Fe oxide and sulfide of about 10-15 microns thickness, contacts the metal. Residing above this dense oxide is a rather irregular iron sulfide layer of similar thickness. No ash particles are embedded in this compact composite scale. However, isolated (bright) stringers of iron sulfide penetrate to a depth of about 100 microns into the ash deposit over the uniform, adherent scale on the sample. These sulfide stringers are neither uniform nor in a large volume fraction. An “active sulfidation” mechanism (explained in detail shortly) appears to account for this external sulfide penetration into the deposit for Alloy T11, which contributes to a moderate corrosion rate at this temperature.

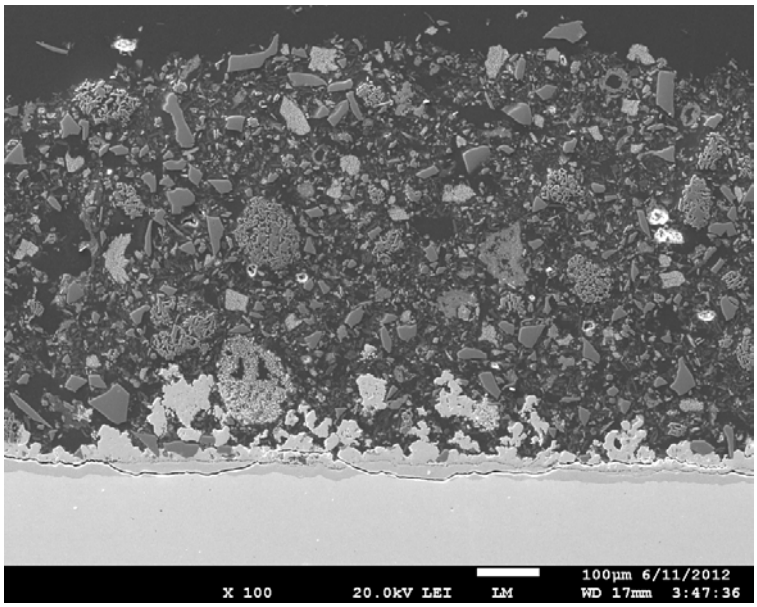

Figure 273 - SEM Micrograph of Corrosion Scale and Portion of Deposit Layer for Alloy T11 after Exposure to OH Gatling Reducing Conditions for 1000 Hours at 850°F.

Alloy T11 (1.3%Cr, 0.5%Mo, bal. Fe) was also exposed to the laboratory environment of IL #6 Galatia coal with medium S but high Cl contents, and the deposit was rich in sulfates. SEM micrographs of differing magnifications shown in Figures 273 and 274 illustrate the extent of external sulfide penetration into the deposit and the bizarre corrosion zone adjacent to the alloy, respectively. The outermost fragmented corrosion product of about 500 microns thickness, as shown in Figure 274, is seen to penetrate and embed the ash deposit. This outermost corrosion product is predominantly iron sulfide, although oxygen is also present, in part from the presence of ash particles. As for the same alloy exposed to lower-chloride OH Gatling shown in Figure 273, the corrosion mechanism could be described to include “active sulfidation” where continuous strings of iron sulfide penetrate the oxide-rich deposit layers. However, for the higher

chloride coal IL #6 Galatia, the depth of penetration of the ash layer by the deposited iron sulfide is a factor of 5 higher.

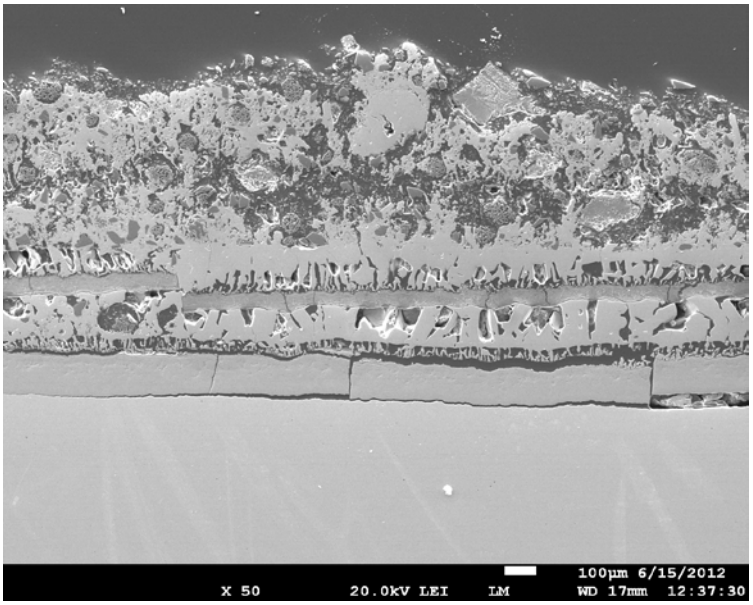

Figure 274 - Lower Magnification SEM Micrograph of Corrosion Scale and Deposit Layer on T11 after Exposure to IL #6 Galatia Reducing Conditions for 1000 Hours at 850°F.

The banded corrosion product for Figure 274 features a compact 100-micron-thick innermost scale containing chromium, iron, oxygen and sulfur, which served as a protective layer at the end of the exposure. The next major layer out from the alloy of about 100 microns thickness (separated by an epoxy-filled gap), is predominantly iron sulfide. A significant amount of porosity exists in this sulfide layer, to the extent that skeletons of individual columnar grains of iron sulfide are obvious. A third thinner layer (about 60 microns) of the corrosion scale again consists primarily of chromium, iron, oxygen and sulfur. This layer probably formed early in the exposure as a temporary protective oxide but was undercut by sulfidation which also occurred below and above this layer. The extreme porosity throughout parts of the compact corrosion product indicates that iron could be transported via volatile species by "Active Sulfidation", both within the scale as well as throughout the external deposit. As will be detailed shortly, this most significant incidence of "active sulfidation" (in combination with a failed initial protective scale) was caused by the IL #6 Galatia coal, with the highest chloride content. The corrosion rates for the low-alloy steels were a factor of about 3 higher than those caused by other high-S coals with lower chloride content. Finally, the outermost layer of fragmented iron sulfide extended about 500 microns into the deposit and is a certain indication of "active sulfidation".

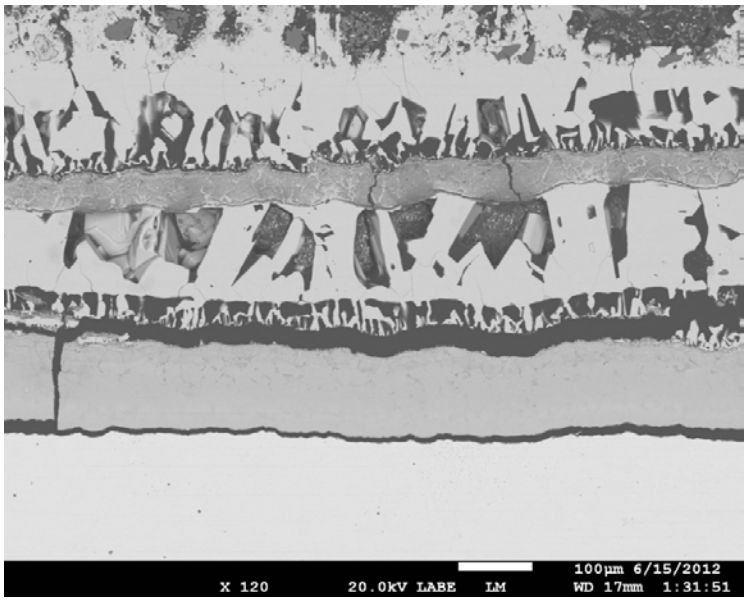

Figure 275 - Higher Magnification SEM Micrograph of Corrosion Scale and Portion of Deposit Layer on T11 after Exposure to IL #6 Galatia Reducing Conditions for 1000 Hours at 850°F.

Alloy T11 (1.3%Cr, 0.5%Mo) was also exposed to the environment of OH Mahoning (medium S and Cl), and the resulting corrosion products are shown in Figure 276. The corrosion rate was rather high (see Section 3.4) but comparable to the other low-alloy steels that were tested. An innermost dense compact layer of about 25 microns is mostly iron oxide with a little sulfur, again probably as sulfide strings spanning in the scale. Above this oxide scale, irregular fragmented Fe sulfide particles traverse into the ash deposit layer for a distance of about 100 microns, embedding the deposit particles. This sulfide layer has spalled from the underlying oxide layer so a gap is filled with mounting epoxy. The reported corrosion rate for Alloy T11 in OH Mahoning was less than one-third of that for the same alloy in IL #6 Galatia but almost identical to that of OH Gatling. The microstructures of Figures 273 and 276 are also rather similar. The corrosion mechanism for the compact scale on this low alloy steel can be described as an oxidation/sulfidation, while again the growth of the irregular sulfide product into the deposit occurs by "active sulfidation."

Alloy 304H (11Ni, 18.8Cr, bal. Fe) was similarly exposed to the OH Gatling (4.31%S, low Cl, but very high sulfates in the deposit) environment. A SEM micrograph of the corrosion zone is shown in Figure 277. Along most of the metal/scale interface, a thin protective chromia-rich scale of about a couple of microns thick had spalled from the alloy, possibly upon cooling. Over some part (about half) of the top of this protective scale, a thicker layer (up to 5 microns thick) of a sulfide of iron and manganese is seen. Perhaps this sulfide was a transient corrosion product formed early in the exposure, which was then undercut by the protective scale. There is no evidence of any sulfide or oxide corrosion products formed in the alloy. Compared to the higher-Cr Alloys 309S and 310, Alloy 304H exhibited a relatively higher corrosion rate, although this rate was still lower than those of the low-alloy steels (including T11 discussed above where the iron sulfide phase extended into the ash deposit). Thus 304H was marginally

protective against sulfidation. The alloys with higher Ni and especially higher Cr provided more protective scales which negated sulfidation.

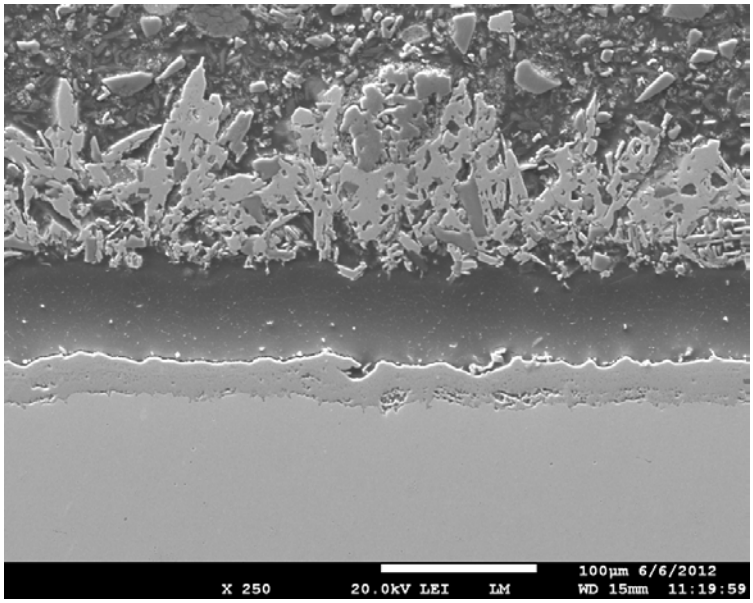

Figure 276 - SEM Micrograph of Corrosion Scale and Portion of Deposit Layer on Alloy T11 after Exposure to OH Mahoning Reducing Conditions for 1000 Hours at 850°F.

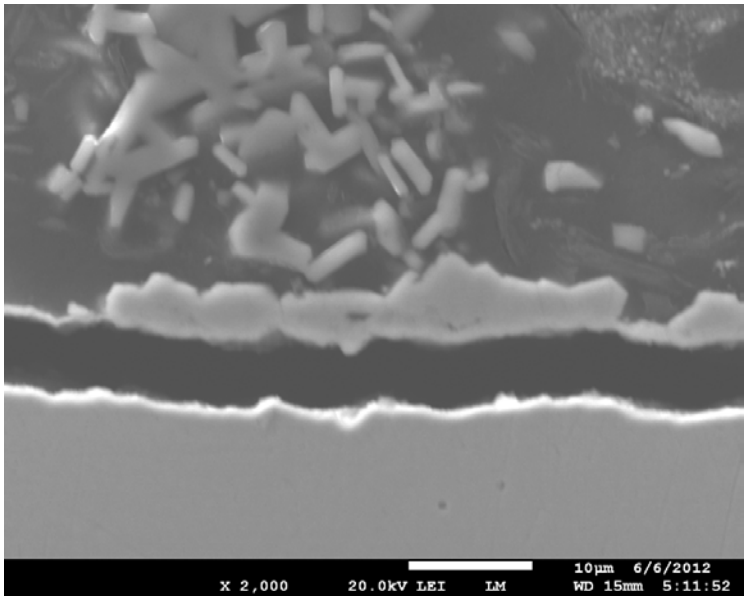

Figure 277 - SEM Micrograph of Corrosion Scale and Portion of Deposit Layer on Alloy 304H after Exposure to OH Gatling Reducing Conditions for 1000 Hours at 850°F.

Alloy 310H (19.4Ni, 25.5Cr, bal. Fe) was exposed to IL #6 Galatia (medium S but high Cl, and very high sulfates in the deposit), and the corrosion products are shown in Figure 278.

The metal/scale interface is quite rough and irregular. However, a couple-micron thick chromium oxide is adherent to the alloy. Above the oxide/deposit interface, a few thicker particles of iron-rich sulfide are seen embedded in the ash deposit. Particles of KCl and NaCl appeared to be present in this deposit. Research at much higher temperature has shown that NaCl contact can lead to cracking of protective oxide films. Perhaps the chloride in the ash deposit, even though its presence is rare, can promote the occasional formation of FeS. The low rate of corrosion for 310H is about the same (perhaps somewhat higher) as for 304 in the same environment, and the corrosion morphologies are also similar.

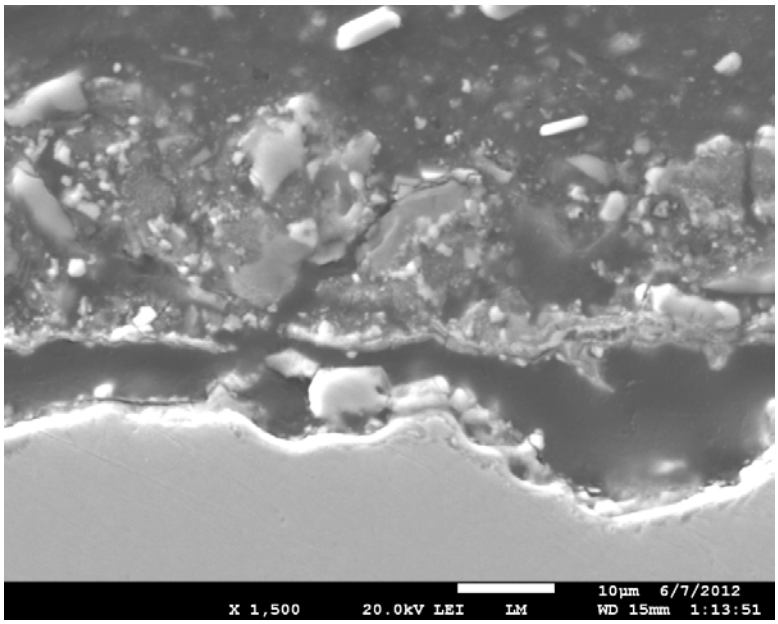

Figure 278 - SEM Micrograph of Corrosion Scale and Portion of Deposit Layer on Alloy 310H after Exposure to IL #6 Gibson Reducing Conditions for 1000 Hours at 850°F.

The Ni-base weld overlay WO 52 (29.6Cr, 12.2Fe, 0.7 Al, bal. Ni) was exposed to the medium-S, high-Cl IL #6 Galatia environment. The corresponding corrosion products are seen in Figure 279. The weight gain shown in Section 3.4 is quite low, but the thickness loss is relatively high, consistent with an irregular attack. The primary adherent scale is a thin chromium oxide which also contains iron and manganese. At some locations, chromium sulfide exists under the oxide scale, and some iron sulfide particles of limited size exist on top of the inner oxide film. Over most of this interface, sulfidation appears to have been controlled by the formation of a protective chromium oxide. However, the Ni-base composition did not show additional advantage over those of the stainless steels.

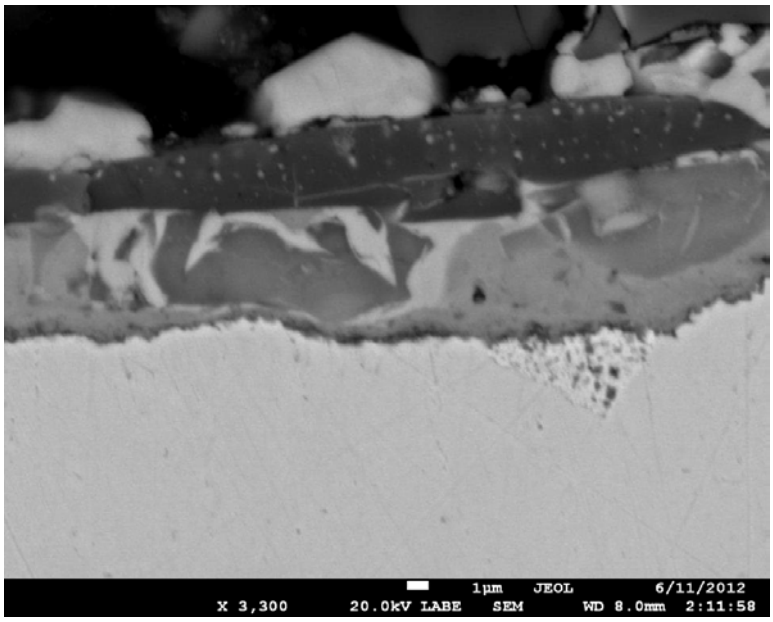

Figure 279 - SEM Micrograph of Corrosion Scale and Portion of Deposit Layer on Ni-Base Weld Overlay WO52 after Exposure to IL #6 Galatia Reducing Conditions for 1000 Hours at 850°F.

4.5.1.2 Corrosion Mechanism for Furnace Wall Corrosion under Reducing Conditions

In the preceding Figures 273-276 for the low-alloy T11, evidence was presented for the growth/penetration of fragmented Fe sulfide particles into the existing porous deposit layer above a reasonably compact adherent sulfide/oxide scale (with the exception of coal IL #6 Galatia, which also had a porous scale layer). With due credit to the previously referenced works of Grabke et al.[18-20] in describing "active oxidation" for oxidizing high-chloride environments, a new mechanism of "active sulfidation" is proposed here to explain the chlorine effect for relatively reducing environments containing both sulfur and chlorine. The mechanism depends upon the short-circuit transport of iron chloride ($FeCl_2$) vapor from a more internal FeS site of higher Fe thermodynamic activity (thus a higher $FeCl_2$ vapor pressure) to a more external site of lower Fe activity (and thus a lower $FeCl_2$ vapor pressure). There the iron chloride vapor is reacted with available hydrogen sulfide to extend the growth of the FeS product. The product HCl gas is returned to the internal site where the cycle repeats. Therefore, at an internal site with higher Fe activity, the following reaction occurs:

$$FeS + 2\ HCl\ (g) = FeCl_2\ (g) + H_2S\ (g) \qquad \text{Eq. 12}$$

The $FeCl_2$ vapor formed by this reaction then diffuses down a gradient in partial pressure farther out into the corrosion product where the Fe activity is lower such that the growth of FeS can be supported by the reverse reaction:

$$FeCl_2\ (v) + H_2S\ (g) = FeS + 2\ HCl\ (g) \qquad \text{Eq. 13}$$

To justify this mechanism of "active sulfidation", the magnitude of the $FeCl_2$ vapor pressure for the given environment and temperature must be adequate, as is demonstrated here. For the reaction at the test temperature of 850°F (727K):

$$Fe + 2\ HCl\ (g) = FeCl_2\ (v) + H_2\ (g) \qquad \text{Eq. 14}$$

From thermodynamic data:

$$\log P_{FeCl_2} = \log \left(\frac{P^2_{HCl}}{P_{H_2}}\right) + \log a_{Fe} - 1.456 \qquad \text{Eq. 15}$$

Upon substitution of the values of laboratory gas composition for IL #6 Galatia, i.e., $P_{H2} = 10^{-2}$ and $P_{HCl} = 2.5 \times 10^{-4}$, and $a_{Fe} = 1$ (maximum value), the calculated log P_{FeCl2} value equals 2.19×10^{-7} atm. or 1.66×10^{-4} torr. While this maximum value for P_{FeCl2} may seem low, the magnitude of the corrosion rate (on a customary comparison) is comparable. As was done by Grabke et al., one needs to compare the maximum possible flux attributable for the given available $FeCl_2$ vapor pressure to that flux required to support the observed corrosion rate. Thus, one needs to calculate the maximum possible flux via evaluation of the Hertz-Knudsen equation,[22,23] which provides the gross flux of a species at equilibrium for a surface exposed to a given vapor pressure, i.e.,

$$P(torr) = 17.14 \times \left(\frac{T}{M}\right)^{\frac{1}{2}} \times G \qquad \text{Eq. 16}$$

where G is the evaporation rate in gms/cm^2-sec, $M_{FeCl_2} = 130.85\ \frac{g}{mole}$, and T = 727K.

For Galatia IL #6, $P_{H2} = 10^{-2}$ atm. and $P_{HCl} = 2.5 \times 10^{-4}$ atm. as implemented in the reducing laboratory test (Section 3.4.2.2),

$$P_{FeCl_2} = 2.19 \times 10^{-7}\ \text{atm.} = 1.66 \times 10^{-4}\ \text{torr}$$

Solving for G,

$$G = 4.1 \times 10^{-6}\ \frac{g}{cm^2 - sec} \qquad \text{Eq. 17}$$

Conversion of units: $1\ \frac{g}{cm^2-sec} = 203\ \frac{g}{cm^2-yr}$

Thus for Fe density of $7.9\ \frac{g}{cm^3} = 1.3 \times 10^{-7}\ \frac{g}{mil^3}$,

$$G = \frac{4.1 \times 10^{-6} \times 203}{1.3 \times 10^{-7}} = 6{,}400\ mpy \qquad \text{Eq. 18}$$

The calculation shows that if the "active sulfidation" mechanism were totally responsible for the corrosion of T11 in the IL #6 Galatia environment, the maximum possible flux of $FeCl_2$ would be capable of producing a corrosion rate of 6,400 mpy, while in fact the observed rates were all lower than 100 mpy. This comparison leads to the conclusion that while the observed

corrosion was limited by a much slower process, certainly due to solid-state diffusion, the calculation indicates that "active sulfidation" can take place and does contribute to the mechanism. For Alloy T11, the corrosion rate in the IL #6 Galatia environment was about a factor of 3 greater than those for other coal environments with high sulfur but lower chlorine. The scale in the Galatia environment had also suffered fracture and an ensuing internal porosity that would also support internal "active sulfidation" to rationalize the occurrence of the highest corrosion rate.

3.5.1.3 Simplified Nonlinear Regression Analysis for Furnace Wall Corrosion under Reducing Condition

Initial modeling of furnace wall corrosion for alloys exposed to the conditions of substoichiometric coal combustion has been performed. A full set of laboratory data generated from the reducing corrosion tests at 850°F is available, despite the fact that the quality of some data is less desirable. The corrosion data of two additional tests, one performed at 750°F and the other at 950°F, are also available. Therefore, the temperature effect can be integrated into the initial corrosion modeling effort. The model proposed by Kung[24] shown in Eq. 19, which relates furnace wall corrosion to the Cr concentration in the alloy, metal temperature, and H_2S concentration in the gas phase, was utilized as a starting point. However, Kung's model did not consider the coal chlorine content in the correlation, as shown here:

$$mpy = \alpha \times e^{-\frac{E_a}{RT}} \times [H_2S]^{\beta} \times \frac{1}{(\mathrm{Cr\%}+\gamma)^{\delta}} \qquad \text{Eq. 19}$$

where *mpy* is the corrosion rate in mils per year, α, β, γ, and δ are constants, and E_a is the activation energy. Depending on the type of alloy being considered, i.e., either a ferritic steel or austenitic steel, the values of E_a in Kung's model were determined to be 15.8 and 19.2 kcal/mole, respectively.

As the first attempt to model furnace wall corrosion for this project, Eq. 19 was simplified by eliminating the constant γ from the equation and the role of chlorine was expressed as a simple multiplier term, i.e.,

$$mpy = \alpha \times exp(-\frac{E_a}{RT}) \times [H_2S]^{\beta} \times \frac{1}{Cr\%^{\delta}} \times [Cl\%]^{\epsilon} \qquad \text{Eq. 20}$$

Taking the natural logarithm on both sides, Eq. 20 becomes

$$ln\,(mpy) = -\frac{E_a}{RT} + \beta \times ln\,[H_2S] - \delta \times ln\,[Cr\%] + \epsilon \times ln\,[Cl\%] \qquad \text{Eq. 21}$$

Because the concentration of H_2S in the gas phase is linearly proportional to the amount of coal sulfur, Eq. 14 can be further modified by replacing [H_2S] with S%, i.e.,

$$ln\ (mpy) = -\frac{E_a}{RT} + \beta\ ln\ (S\%) - \delta\ ln\ (Cr\%) + \epsilon\ ln\ (Cl\%) + constant \quad \text{Eq. 22}$$

Regression analysis was performed to determine the values of the constants in Eq. 22. From the first modeling attempt, the corrosion rate of alloy in mpy can be expressed by Eq. 23.

$$ln\ (CR) = -\frac{18{,}012}{1.987 \times T} + 0.31\ ln\ (S\%) - 0.77\ ln\ (Cr\%) + 0.07\ ln\ (Cl\%) + 14.39 \pm 1.21 \quad \text{Eq. 23}$$

An activation energy of 18 kcal/mole is suggested by Eq. 23, which falls within the values of 15.8 and 19.2 kcal/mole reported previously by Kung for furnace wall corrosion.[24]

3.5.1.4 Extended Nonlinear Regression Analysis for Furnace Wall Corrosion under Reducing Condition

From an empirical standpoint, one would always desire to achieve a correlation of the observed corrosion rates to the alloy composition, especially a correlation that would span the entire range of coals and alloy compositions for the relevant temperature range. Towards that objective, the correlation should be consistent with some presumed approximate mechanism. For the reducing environments of all the eight coals tested over the temperature range of 750-950°F, the corrosion rate would be expected to correlate with the rate of iron sulfidation and oxidation, plus a chloride-dependent contribution via the Active Sulfidation Mechanism. The role of chromium can be perceived as forming protective phases (chromia, iron chromite, nickel chromite, cobalt chromite) which have low diffusion rates and which block some fraction of the surface area to the sulfidation of iron. To the first approximation, the minor alloy contents of other elements (Mo, Si, Al, Ti, Nb, Ta, V, W, and Cu) are not considered important. The usual Arrhenius dependence of temperature is assumed. The most representative measures of the corrosion rates (mpy) are considered to be the weight-loss values (gravimetric data) that are treated here.

For the initial trials, the following expression for corrosion rate has been evaluated by Nonlinear Regression Analysis for all 8 coals and 11 alloy compositions:

$$mpy = A \times e^{\frac{-B}{1.987 \times T}} \times (\%Fe \times \%S)^C \times (1 + D \times \%Cl)^E \times (\%Cr)^F \quad \text{Eq. 24}$$

Therefore,

$$ln(mpy) = ln\ (A) - \frac{B}{1.987 \times T} + C \times ln\ (\%Fe \times \%S) + E \times ln\ (1 + D \times \%Cl) + F \times ln(\%Cr) \quad \text{Eq. 25}$$

where the factor *D* has an arbitrary value introduced to fit best the chloride dependence. The specific form of these expressions was chosen to account for two mpy additive contributions, with the product of (%Fe × %S) describing the sulfidation and the further "triple product" of (%Fe × %S × D%Cl) accounting for some Active Sulfidation. The exact mathematical form of Eq. 24 is indeed limited by the desire to obtain a linear sum of terms in Eq. 25.

Other alloying elements such as Ni, Co, Mo, etc. which are expected to play secondary roles in the corrosion process have not been considered. The Fe and Cr contents of the alloys and the S and Cl contents in the coals were equated to their weight percentages.

After a few iterations, it became clear that the factor related to the alloy Cr content was not suitable for describing the mpy corrosion rate for carbon steel or the low-Cr alloys T11 and T2. Therefore, these alloys were withdrawn from the correlation. Upon this change, the regression analysis for the remaining 10 alloy compositions (covering all 8 coals and Mahoning coal at three temperatures, i.e., 750, 850 and 950^{o}F) provided a value for goodness of fit R^2 = 0.738, although the corrosion rates for the IL#6 coal with the highest Cl content were severely underestimated. This situation was improved by reducing the arbitrarily chosen multiplier factor D for Cl in Eq. 25 from 10 to 5 to 2 and ultimately 1, whereby the derived value for the exponent E was also changed upon fitting the data. At this stage, the regression analysis gave the best fit to the IL#6 corrosion rates, with an improved goodness of fit R^2 = 0.748.

Later in this report, the individual coals are evaluated in terms of a coal corrosion index (CCI) which consists of several factors including the coal alkali and alkaline earth contents which are considered important in deciding what fraction of the sulfur in the coal is released as corrosive H_2S compared to (at low temperature) some innocuous sulfate. Since this consideration was also deemed relevant to furnace wall corrosion, the CCI factor was introduced into the regression analysis expression. Thus, the Cl factor D of Eq. 24 was fixed at one, and the sulfur factor was modified in forming the following revised Regression Analysis Expression:

$$mpy = A \times e^{\frac{-B}{1.987 \times T}} \times (\%Fe)^C \times (\%S)^D \times (1 + \%Cl)^E \times [(\%Ash) \times (CCI \times 100)]^F \times (\%Cr)^G \quad \text{Eq. 26}$$

Therefore,

$$ln(mpy) = ln(A) - \frac{B}{1.987 \times T} + C \times ln(\%Fe) + D \times ln(\%S) + E \times ln(1 + \%Cl) + F \times ln[(\%Ash) \times CCI \times 100] + G \times ln(\%Cr) \quad \text{Eq. 27}$$

whereby in Section 3.5.2.6 for the CCI calculation (to be discussed later), a fraction *y* is used to describe the fraction of the Fe_2O_3 content of the ash which would be converted to iron sulfate upon exposure of the deposit to the combustion gases on the furnace walls at lower metal temperatures.

The evaluation of Eq. 27, with a simple exponential dependence on the coal chlorine content, but with a power dependence also for the CCI values (presented in Section 3.5.2.6) led to the best result, with the highest value for goodness of fit R^2 = 0.778. This result was virtually independent of the fraction f used in evaluating CCI, so that f=0 was adopted for the CCI calculation. Then, according to Eqs. 26 and 27, the alkali and alkaline earth contents of the coal ash is considered to combine with sulfur to form sulfates and thereby remove some sulfur from the H_2S component leading to sulfidation. This evaluation also provided the best prediction for corrosion rates for the highest Cl coal of IL #6 Galatia. When the alloys T1 and T2 were re-

entered into the list of alloys treated by Eqs. 26 and 27, the goodness of fit R^2 was slightly reduced from 0.778 to 0.737. The T1 and T2 alloys have insufficient Cr content to form any significant spinel to block sulfidation as is probably provided by alloys with higher Cr content.

Upon further regression analysis, the expressions in Eqs. 26 and 27 were retained. However, the terms involving Cl and S were removed from the expression for CCI as they were considered to be redundant, and the value for f in CCI was equated to unity. In the absence of the low-Cr alloys (T2 and T11), this regression analysis provided the following values for the fitting parameters: lnA = 25.32, B = -18,745, C = -0.439, D = 0.854, E = 2.03, F = - 0.2031, G = -1.71, and F = -0.987, i.e.,

$$mpy = 9.9 \times 10^{10} \times e^{\frac{-18{,}745}{1.987 \times T}} \times (\%Fe)^{-0.439} \times (\%S)^{0.854} \times (1 + \%Cl)^{2.031} \times [(\%Ash) \times (CCI \times 100)]^{-0.203} \times (\%Cr)^{-1.71} \quad \text{Eq. 28}$$

The resulting Goodness of Fit (i.e., the value of R^2) for Eq. 28 is 0.786, meaning that 78.6% of the corrosion data generated from the laboratory tests for furnace wall corrosion fall within one σ of the standard distribution predicted by Eq. 28. These results are particularly satisfactory because all the exponents for S, Cl, and even (Ash × CCI) are positive, while that for Cr becomes negative. The negative exponent for Fe resulted probably because it was redundantly accounted for in the CCI.

The data of thickness loss for the individual alloys attacked by the various coal combustion environments exhibited much less uniformity than the previously treated data for gravimetric measurements. However, after several iteration attempts, the equations of Eqs. 26 and 27 were again found to best describe the corrosion rates, although the value of R^2 suffered slightly.

4.5.2 Discussion of Laboratory Corrosion Data for Superheater and Reheater Corrosion

The occurrence of fireside corrosion on superheaters at 1300°F can involve an additional particularly aggressive reaction known as "hot corrosion." This type of attack occurs when a liquid oxyanion salt, such as fused alkali sulfate $(Na,K,Mg,Fe)SO_4$, is present in the corrosion layer, especially if the salt should contact and react with the underlying alloy. In fact, the coverage of any part of the alloy or corrosion product by the fused salt isolates the underlying alloy or corrosion product from the bulk gas phase, and creates an interfacial micro-environment that can stabilize other product phases, especially sulfides, that are not stable in the bulk gas phase. A review of the fundamental aspects of hot corrosion has been presented by Rapp and Zhang.[25] Especially for an alloy surface that is buried/coated with an ash deposit of numerous salt components, the deposit itself may have a liquidus temperature below the reaction temperature (1300°F), or else it is also possible that a combination of the deposit with some corrosion product(s) can stabilize the liquid phase, as explained by Luthra and Shores[26] in the explanation for Type II hot corrosion. For example, the eutectic temperature in the Ni-NiS binary system is 746°C (1385°F). The combination of NiS with a multi-cation sulfate in the deposit could result in a liquid phase at 1300°F. The eutectic temperature in the binary K_2SO_4-$MgSO_4$

system is 746°C (1385°F) at 37m/o $MgSO_4$. As will be shown later, the eutectic is 645°C (1208°F) in the ternary Na_2SO_4-K_2SO_4-$MgSO_4$ system.

4.5.2.1 Fundamental Aspects of Hot Corrosion (Coal Ash Corrosion)

Hot corrosion is described as an accelerated oxidation of an alloy at elevated temperatures in contact with a fused salt film. In fact, hot corrosion usually occurs in two stages: an initial "Stage 1" with a slow rate of attack, which is followed by a "Stage 2" rapid attack. During Stage 1, a multi-component alloy is able to avoid direct contact with the fused salt film by the formation of transient oxides which comprise a multi-phase scale of the oxides of all the alloying elements. In simple gaseous oxidation, in the absence of the fused salt film, this transient mixed oxide film may evolve into a thermodynamically favored and more protective oxide, usually based on chromia or a spinel. But in the presence of the adherent fused salt film, the transient oxide may be sufficiently penetrated by the salt until the alloy is contacted. In that case, rapid Stage 2 kinetics begin with direct salt-alloy contact.

The current understanding of hot corrosion, as first advanced by Goebel and Pettit[27] is tied to the reaction of the fused sulfate with the alloy components to form a sulfide phase accompanied by the release of oxide anions as a product of the sulfidation reaction. For example, for pure Ni:

$$4Ni + Na_2SO_4 = NiS + 3NiO + \underline{Na_2O} \qquad \text{Eq. 29}$$

This sulfidation reaction, shielded from the bulk gas phase, causes a significant increase in the local basicity of the melt which could lead to a basic fluxing of the NiO that might otherwise serve as a protective scale. The thermodynamic phase stability diagrams for the Me-S-O systems, where Me is Fe, Ni, Co, Cr, etc. all show that upon metal-salt contact the metal is not stable in contact with a liquid sulfate. Therefore, a sulfidation reaction would occur which could lead to the destruction of the protective scale. This type of sulfidation reaction drastically drops the oxygen activity locally in the fused salt and greatly increases its basicity far from that for equilibrium with the bulk gas phase.

A fused alkali sulfate salt exhibits an acid-base character analogous to the pH of aqueous solutions. In particular, for the equilibrium of

$$Na_2SO_4 = \underline{Na_2O} + SO_3\,(g) \qquad \text{Eq. 30}$$

the Na_2O species can be considered as the basic component and SO_3 as the acidic component. The acid-base character for this fused sulfate with only Na^+ cations can be quantified in terms of the thermodynamic quantity $-\log a_{Na2O}$ where this parameter can be called the basicity of a pure Na_2SO_4 melt. Rapp and Zhang[25] have described how a pair of electrochemical reference electrodes in a pure Na_2SO_4 melt can be used to measure the salt basicity quantitatively, especially in laboratory experimentation.

Any given oxide phase exhibits a certain solubility in a pure Na_2SO_4 melt as both acidic solute(s) and basic solute(s), as reviewed by Rapp and Zhang:[25]

Basic dissolution: $2NiO + \underline{Na_2O} = 2\ \underline{Na_2NiO_2}$ d log $[\underline{NaNiO_2}]$/d -log $(a_{Na2O}) = -\frac{1}{2}$ Eq. 31

Acidic dissolution: $NiO + Na_2SO_4 = \underline{NiSO_4} + \underline{Na_2O}$ d log $[\underline{NiSO_4}]$/d -log $(a_{Na2O}) = +1$ Eq. 32

Basic dissolution: $Cr_2O_3 + 2\ \underline{Na_2O} + 3/2\ O_2\ (g) = 2\ \underline{Na_2CrO_4}$

with d log $[\underline{Na_2CrO_4}]$/d -log $(a_{Na2O}) = -1$, and Eq. 33

d log $[\underline{Na_2CrO_4}]$/d -log $(P_{O2}) = +3/4$ Eq. 33A

Acidic dissolution: $Cr_2O_3 + 3\ Na_2SO_4 = \underline{Cr_2(SO_4)_3} + 3\ \underline{Na_2O}$

with d log $[\underline{Cr_2(SO_4)_3}]$/d -log $(a_{Na2O}) = +3$ Eq. 34

In these expressions, the underlined species indicate different solutes dissolved in the fused salt, and the bracketed terms represent the molar concentrations for the solutes that can be set equal to their thermodynamic activities in dilute solutions. The concentration of the measured solute in equilibrium with its pure oxide is defined as the solubility of the oxide, and this solubility depends upon the melt basicity/acidity (and perhaps the oxygen activity) in the exact manner as outlined here. For some solutes of the oxides of polyvalent transition metals (e.g., Ni, Fe, Cr, Co), the formation of solutes with a cation valence different from the oxide cation also introduces an oxygen partial pressure dependence on the oxide solubility, as shown in Eq. 33 for Cr_2O_3.

A plot of experimentally determined solubilities for many oxides in a pure Na_2SO_4 melt at 1200K (2192°F) at P_{02} = 1 atm. is presented in Figure 274 from Rapp.[28] For a more complex salt, e.g., a sulfate melt consisting of a several cations at a lower temperature (applicable to coal ash corrosion in boilers), a similar sort of plot would be expected, albeit with a different "basicity parameter", and with some shifting in the placement and magnitudes of the specific solutes for the oxide phases.

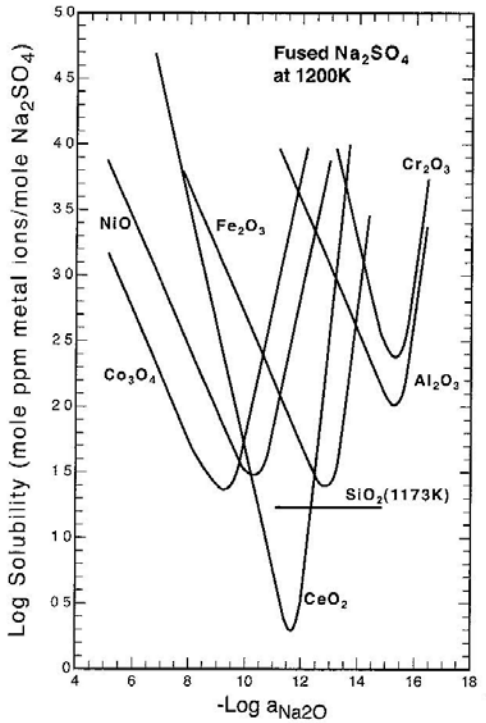

Figure 280 - Compilation of Measured Solubilities for Several Metal Oxides in Pure Fused Na_2SO_4 at 1200K and P_{O2} = 1 atm. (Rapp[23]).

As is the case for the ash deposits in this study, where multiple cations (e.g., K, Na, Mg, Fe, etc.) form the sulfate solution, the use of melt <u>acidity</u> is preferred, which can be defined as log P_{SO3}. As such, analogous solubility expressions for the basic and acidic dissolutions of metal oxides above can be converted to the following reactions involving SO_3:

Basic dissolution: $Fe_2O_3 + M_2SO_4 = 2\ \underline{MFeO_2} + SO_3\,(g)$

$$d \log [\underline{MFeO_2}]/d \log (P_{SO3}) = -½ \qquad \text{Eq. 35}$$

Acidic dissolution: $Fe_2O_3 + 3\ SO_3\,(g) = \underline{Fe_2(SO_4)_3}$

$$d \log [\underline{Fe_2(SO_4)_3}]/d \log (P_{SO3}) = +3 \qquad \text{Eq. 36}$$

Basic dissolution: $Cr_2O_3 + 2\ M_2SO_4 + 3/2\ O_2\,(g) = 2\ \underline{M_2CrO_4} + 2\ SO_3\,(g)$

$$\text{with } d \log [\underline{M_2CrO_4}]/d \log (P_{SO3}) = -1 \text{ and} \qquad \text{Eq. 37}$$

$$d \log [\underline{M_2CrO_4}]/d \log (P_{O2}) = +3/4 \qquad \text{Eq. 37A}$$

Acidic dissolution: $Cr_2O_3 + 3\ SO_3\,(g) = \underline{Cr_2(SO_4)_3}$

$$\text{with } d \log [\underline{Cr_2(SO_4)_3}]/d \log (P_{SO3}) = +3 \qquad \text{Eq. 38}$$

where M represents a solution of multiple cations. Again, the underlined species indicate different solutes dissolved in the fused salt, and the bracketed terms represent the molar concentrations for the solutes that can be set equal to their thermodynamic activities in dilute solutions.

Thus, for the present application at 1300°F, a plot similar to Figure 274, with the acidity parameter of log P_{SO3} as the abscissa replacing –log a_{Na2O}, would be expected to describe the oxide solubilities in these studies.

In fact, Leblanc and Rapp[29] created and demonstrated a reference electrode to measure the acidity (log P_{SO3}) of a mixed cation sulfate melt directly at 690°C (1550°F), corresponding to a synthetic composition of fly-ash condensate with an extremely low liquidus temperature, i.e., 71.2 m/o Na_2SO_4, 17.8 m/o K_2SO_4 and 11 m/o Fe_2SO_4. By the use of this reference electrode to measure quantitatively the melt acidity corresponding to experimentally determined chromia solubilities, the relationship of Eq. 36 was exactly satisfied at 1550°F, and surprisingly, the magnitude for the basic chromia solubility in the mixed sulfate at 1550°F was about an order of magnitude higher than that in pure Na_2SO_4 at 2192°F for the same values of log P_{SO3}. Likewise, the measured value of SiO_2 solubility for the same mixed sulfate at the lower temperature was a factor of almost 3 higher than that for pure Na_2SO_4 at the much higher temperature. From that study,[29] the solubilities of metal oxides can be expected to be quite high in the multi-cation sulfates at the test temperature of 1300°F implemented for this study.

The relationship between oxide solubilities and hot corrosion attack is probably best understood in terms of the "negative solubility gradient" criterion for continuing attack of metals, as introduced by Rapp and Goto.[30] As illustrated schematically in Figure 281, a solute of an oxide in an adherent fused salt film is expected to diffuse out, down a gradient in its solubility, if the oxide solubility is higher at the base (inside) of the salt deposit, and lower farther out in the deposit (toward the gas phase). Because the oxide solubility is decreased upon outward diffusion of the solute, the oxide should precipitate as a non-protective particulate in the salt, and the

inside dissolution and outside precipitation should continue so long as the basicity/acidity (and P_{O2}) gradient is maintained by the dynamics of the corrosion reaction. This continuous dissolution /re-precipitation reaction would eliminate the opportunity for that component to form an adherent protective scale on the metal. On the other hand, an oxide component that experiences a positive solubility gradient with respect to distance in a fused salt film, would simply dissolve locally in accordance with its local solubility but not diffuse out nor suffer re-precipitation due to the fact that the oxide solubility increases towards the gas phase.

According to the solubility plot for several metal oxides in Figure 280, with somewhat different placements for the oxide solubilities in a mixed sulfate melt, one might expect that certain oxide components of a given alloy in a given corrosion environment are subjected to hot corrosion (negative solubility gradient), while the other oxide components are not susceptible (positive solubility gradient). The predictions of this theory were convincingly supported in a study by Otsuka and Rapp[31,32] in which electrochemical probes were attached to the surface on a pre-oxidized pure Ni coupon subjected to hot corrosion (or not) under a film of pure fused sodium sulfate in $O_2/SO_2/SO_3$ at 900°C (1752°F). Whenever the surface basicity probes indicated that the NiO solubility gradient was negative, with basic NiO dissolution following metal sulfidation in this particular case, rapid and continuing hot corrosion occurred. Whenever a positive solubility gradient was indicated in the absence of metal sulfidation, i.e., when the acidic solute and not the basic solute of NiO was stable, no rapid hot corrosion took place. In the case of hot corrosion for pure Ni, the contact of the fused sulfate with the Ni substrate causes sulfidation and a drastic increase in the melt basicity locally (i.e., stabilizing the basic solutes of NiO and a negative solubility gradient).

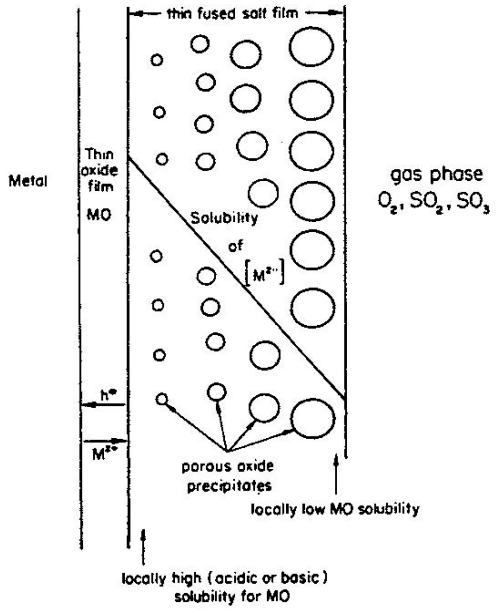

Figure 281 - Re-precipitation of Porous Metal Oxide Supported by a Negative Solubility Gradient in Fused Salt Film (Rapp and Goto[30]).

Other factors are introduced when hot corrosion occurs for a multi-component alloy, since each alloy component has a different placement for its solubility curve on a plot similar to

Figure 280. In particular, Ni and Co are very basic alloy components while Cr and refractory metal components are the most acidic alloy components. Iron has an intermediate acidity or basicity. In fact, a negative concentration gradient as shown in Figure 281 can exist via either basic dissolution or acidic dissolution, causing continuous removal of the metal oxides.

If basic dissolution is dominant in coal combustion environments on superheaters, the solute of Cr_2O_3 would be expected to be Na_2CrO_4 (or perhaps $NaCrO_2$ at very low P_{O2}), while NiO and Fe_3O_4, especially with the occurrence of sulfidation, would be expected to form the basic solutes of $MNiO_2$ and $MFeO_2$, respectively, at the base of the fused salt film. In fact, the Cr component might be expected to act as a buffer, such that by trapping of oxide ions in the chromate formation reaction, the formation of the basic solutes for the oxides for Ni and Fe (which also need to react with oxide ions) can be retarded.[32] According to the usual application of the traditional hot corrosion model, generally a fused deposit is considered to penetrate any initial passivating oxide scale such that upon a sulfidizing reaction involving the salt in direct contact with the underlying metal creates a locally very reducing and basic environment which stabilizes the basic solutes for the oxides of the base metals Ni, Fe, Co and Cr. While the solubility gradients for the basic solutes of NiO, FeO, and CoO experience a negative solubility gradient and therefore a dissolution/reprecipitation sequence, the chromate solute of Cr_2O_3 has a positive gradient, resulting from its strong dependence of P_{O2} according to Eq. 33A.

The hot corrosion model described above was originated to interpret the rapid corrosion of unprotected gas turbine hardware covered with a thin layer of fused alkali sulfate salt at relatively higher metal temperatures, i.e., >900°C (1650°F), rather than for boiler tubes. In addition, no buildup of a thick deposit layer is experienced on the gas turbine hardware. For that application, the metal temperatures are generally high enough to allow the following equilibria to be nearly satisfied on the component surfaces:

$$SO_2\,(g) + ½\,O_2(g) = SO_3\,(g) \qquad \text{Eq. 39}$$

$$SO_2\,(g) + H_2O\,(g) = SO_3\,(g) + H_2\,(g) \qquad \text{Eq. 40}$$

where P_{SO3} is an indication of the salt acidity.

However, for the corrosion of superheater alloys in coal combustion boilers, the conditions are quite different, e.g., the equilibria of Eqs. 39 and 40 are unlikely to be sufficiently catalyzed to establish the equilibrium of P_{SO3} at the much lower temperatures of superheaters. In non-equilibrated coal combustion gases and metal temperature on the order of 1300°F, one might suppose that an initial protective oxide scale, predominantly of the oxides of iron and nickel, covers the surface and excludes a direct contact of any fused salt with the alloy substrate. Likewise, the presence of porous deposit particles might serve to catalyze various chemical reactions, including Eqs. 39 and 40, in the deposit. For these conditions, one might consider that a different hot corrosion attack could occur so long as the surface remains covered by the protective oxide scale.

If the deposit catalyzes the reactions of Eqs. 39 and 40 toward the attainment of local equilibrium, then the base of the deposit may reach a higher local value of P_{SO3} than the exterior

part of the deposit, as shown in Figure 282. In this case, the acidic solutes for more basic oxides (e.g., Fe_2O_3 and NiO) would be stabilized in the presence of a fused salt, and these acidic solutes would experience a negative concentration gradient according to Figure 281, leading to rapid dissolution and reprecipitation of the protective scales. The relative solubility of acidic solutes for Fe_2O_3 and NiO is illustrated in Figure 283. On the other hand, the environment continues to be basic for Cr_2O_3 even with the increased P_{SO3} and therefore, the Cr_2O_3 scale continues to form the basic solute, Na_2CrO_4. As shown in Figure 283, the Cr_2O_3 scale does not suffer a negative solubility gradient through the formation of the basic solute (Na_2CrO_4). Therefore, any loss of protective Cr_2O_3-based scale would not take place from hot corrosion. Although the solubility of Na_2CrO_4 is highly dependent on P_{O2} according to Eq. 36A, a negative concentration gradient cannot be established at any P_{O2} levels. Later in this report, results of the differential scanning calorimetry (DSC) analyses for the deposits of the coal tests indicate that a fused salt phase required for hot corrosion can be formed below 1300°F.

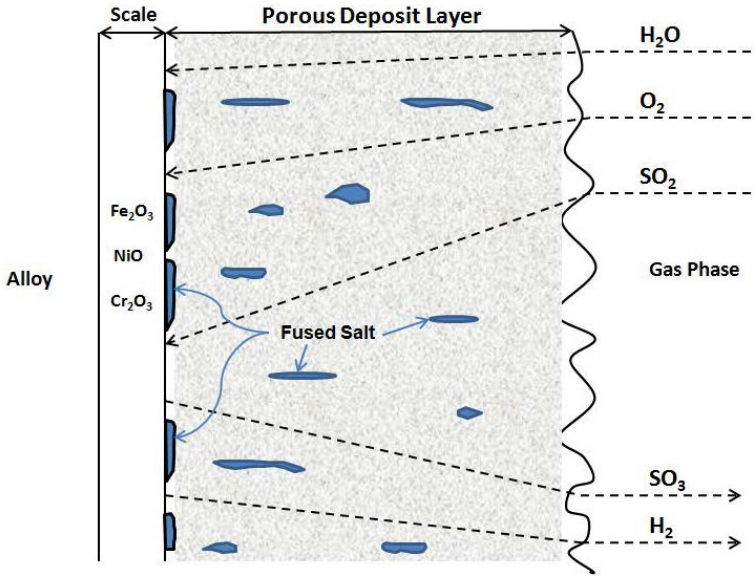

Figure 282 - Catalytic Conversion of SO_2 to SO_3 via Eqs. 38 and 39 in Porous Deposit Layer Producing More Acidic Conditions at the Scale/Deposit Interface than at the Deposit/Gas Interface.

4.5.2.2 Comparative Kinetics Behavior of Alloys in Upper-Furnace Oxidizing Testing

For the corrosion testing of a group of five Fe-Ni-Cr stainless steel alloys (i.e., 304H, S304H, 347H, 310HCbN and 347HFG), with nominally 18 to 25% Cr and higher Fe than Ni, the environments of two coals with highest sulfur contents (IL #6 Galacia and OH Gatling**)** produced the highest corrosion rates (measured either as thickness loss or weight loss), as shown in Section 3.4. However, some exceptional performances were noted. For the two Ni-Fe-Cr alloys of 120 and 800H (with 21% Cr and comparable Ni and Fe), similarly high rates of corrosion attack were experienced in these coal environments. However, in the OH Gatling test, Alloy 800H was attacked at a lower rate; while in the IL #6 Galatia environment, the attack of 800H was exceptionally high. In this instance, one suspects that the high chlorine content of the IL #6 environment may have been important. For the three Ni-base alloys of 230 (high W), 740 (high

Cr and Co) and 617 (high Mo), the corrosion rates were significantly lower for the first two, while those for alloy 617 were high in each of these environments. The two weld overlay compositions with very high Cr contents were reasonably resistant.

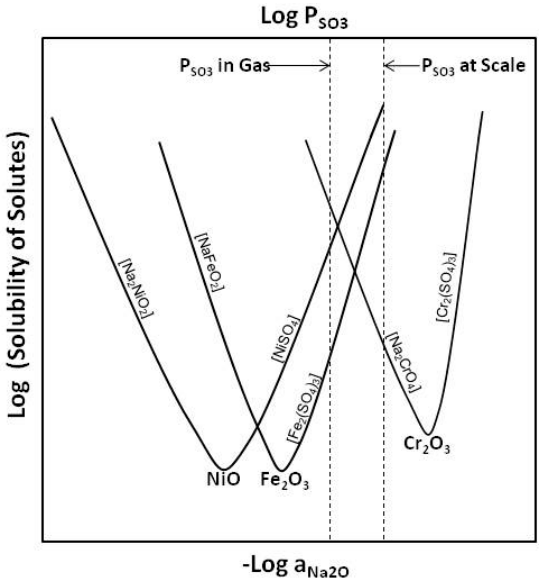

Figure 283 - Illustration of the Formation of Negative Solubility Gradients for Fe_2O_3 and NiO and Positive Solubility Gradient for Cr_2O_3 in the Acidic Fluxing Model Proposed.

The test environment for Kentucky #11, with high sulfur (3.64%) and chlorine (0.199%) contents in the coal, provided remarkably low corrosion attack across the full spectrum of alloys. The alloy 310HCbN behaved especially well. The special properties of this coal and this alloy deserve further investigation.

At the other extreme of the coal environments, the three coals, WY PRB, ND Lignite, and Pitts #8, with their low sulfur and low chlorine contents, generated lower corrosion rates for the group of five austenitic (Fe-Ni-Cr) stainless steels. For the first two coals, Alloy S304H with 3% Cu had about triple the rate of attack as 304H. For this alloy, the Cu addition seems to be deleterious. For this grouping of alloys and environments, Alloy 310HCbN again exhibited the best corrosion resistance. For these three coal environments, the attack of the four Ni-base (Ni-Cr-Fe) alloys was minimal, suggesting the benefit of Ni-base alloys for low-sulfur coals.

For the two coals of OH Mahoning 7A and IN #6 Gibson, which contain medium sulfur and nearly identical chlorine concentrations, the Mahoning 7A coal appeared to be much more aggressive than the IN #6 coal for all five of the Fe-Ni-Cr alloys, with the exception of 310HCbN that exhibited the lowest attack by far. This high-Cr stainless steel seemed to frequently outperform the others in the competitive laboratory testing. For most of the group of Ni-Cr-Fe alloys, the rates of corrosion attack were again high, with the exception of 800H in the IN #6 environment and 120 in both environments. Further microscopic and analytical information may help clarify these significant differences in behavior. Even though both are

considered medium-sulfur coals by ASTM classifications, the sulfur content in Mahoning is nearly twice of that in Gibson.

3.5.2.3 Microscopic and Analytical Characterization of Alloys from Upper-Furnace Oxidizing Testing

In addition to the alloy samples reported above, several other alloys were tested in various gases and deposits and examined after the laboratory corrosion exposures. Figure 284 shows an optical micrograph of the corrosion scale and deposit layer spalled off from a T23 coupon exposed to the combustion environment of OH Gatling coal (very high S but negligible Cl) at 1300°F. The heterogeneous multi-layered scale shown in Figure 284 exhibited little variation in the scale thickness along the test coupon immersed in the crucible filled with simulated deposit. Thus, oxidant diffusion through the porous deposit did not contribute significantly to the rate controlling step or product chemistry, which is consistent with the expectation mentioned previously.

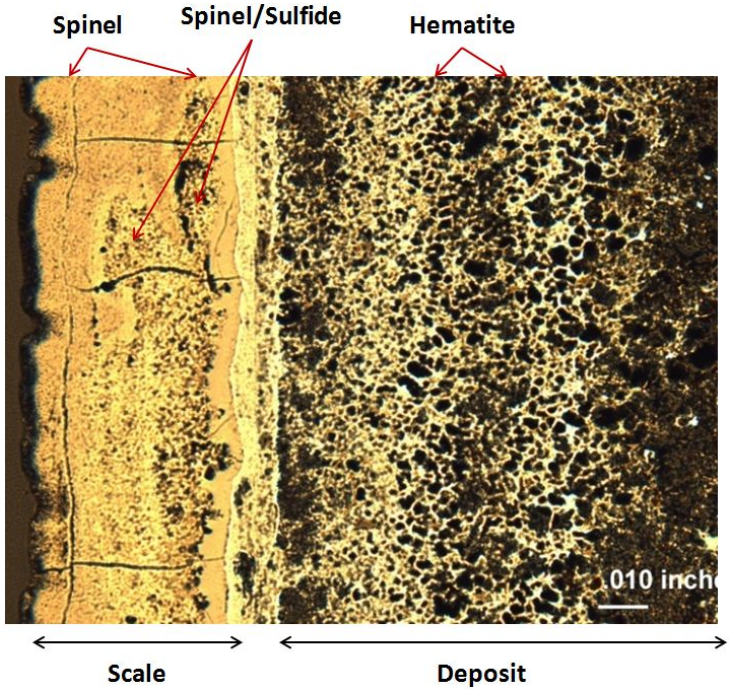

Figure 284 - Optical Micrograph of Corrosion Scale and Portion of Deposit Layer Spalled off from T23 after Exposure to OH Gatling Oxidizing Conditions for 1000 Hours at 1300°F.

The T23 scale exhibited a rather layered and patchy morphology. The dense phase in contact with the metal coupon (metal not shown in the figure) at the left-hand side of the micrograph is about 8-mil thick and is predominantly iron oxide (probably magnetite). Farther out into the scale (toward the right), a similar dense phase is again iron oxide with a thickness of approximately 35-40 microns. The patchy porous parts embedded in this outer scale contain both iron oxide and iron sulfide. The outermost portion of the compact scale is also mostly iron oxide. In this (bright yellow) layer, as well as the stringers intermixed with the particles of the deposit, the presence of potassium is evident. Elemental maps for Fe and Cr indicate a sharp boundary

between the compact corrosion product and the deposit layer, which is also consistent with the maps for K, Si and Al that are all confined to the deposit layer but not in the scale. These characteristics of Figure 284 do not resemble those consistent with hot corrosion, as will be presented shortly for the higher alloy steels.

Generally, farther out in the deposit, above the compact (dark orange) product scale, both potassium and magnesium were found associated with sulfur, likely to be mixed sulfates. Most importantly, in this porous zone of ash deposit, a lacey iron oxide arising from substrate oxidation was present at a distance several times the thickness of the compact scale layer. A zone relatively depleted in sulfur is seen between the top of the compact corrosion scale and sulfate particles farther out in the deposit. The observation of iron oxide far out into and intermixed with the porous ash deposit can only be understood in terms of an "active volatile-chloride-supported oxidation" of iron sulfide at the base of the deposit in contact with the gas phase that also contains HCl molecules.

This proposed Active Sulfide-to-Oxide Mechanism, as originated in the current study, differs in detail from the Active Oxidation Mechanism proposed by Grabke, et al.[20,21] for corrosion of alloys by a much more oxidizing gas in the presence of municipal waste deposits. In that case, the active oxidation mechanism occurred by the formation of volatile $FeCl_2$ from iron oxide (and even condensed $FeCl_2$) at the base of the deposit and the conversion of volatile $FeCl_2$ to iron oxide farther out in the deposit with the release and recycling of molecular chlorine (Cl_2). In the less oxidizing and more sulfidizing environment of the current tests, iron sulfide is seen to exist to the extremity of the compact scale, and this FeS would have a much higher thermodynamic activity for iron than the neighboring iron oxide phase. Therefore the volatile $FeCl_2$ would form from iron sulfide instead of oxide, and would be deposited as a particulate oxide farther out in the deposit. Thus the mixed oxide-sulfide scale on T23 shown in Figure 284 results from reaction of the metal with SO_2 of the gas phase, which is known to form mixed oxide-sulfide scales. If sufficient HCl is present in the gas phase, an "Active Sulfide-to-Oxide Mechanism" involving the reaction of the iron sulfide with HCl to form volatile $FeCl_2$ occurs at the base of the deposit with an oxidation/deposition of iron oxide far out in the deposit with the return of HCl product molecules to the base of the deposit to recycle the reaction. Incidentally, the OH Gatling coal was not (at all) one of the high-chlorine coals, so higher Active Sulfide-to-Oxide rates would be expected for low-alloy steels reacting with coals of higher chlorine content.

A SEM microscopic cross-section of the corrosion product on alloy 309H (12.5Ni, 22.3Cr, Bal. Fe) and the deposit for the OH Gatling coal is shown in Figure 285. The OH Gatling coal has a very high sulfur content (4.31%) and extremely high contents of sulfates of Fe, K, and Mg in the deposit, and the highest SO_2 content in the gas phase. The micrograph and its associated elemental maps show two clearly different types of corrosion behavior.

Over some part of the alloy, a thin protective scale is present (most likely Cr_2O_3), but otherwise there is a pit penetrating into the alloy. The deposit structure and composition over the pit are significantly different from those of the protected area. Sulfur is found concentrated at the base of the pit, along with the alkali elements, likely as a liquid sulfate phase during testing. From the elemental maps, Cr is concentrated in the pit and not outside (above) the pit in the deposit. To the contrary, Fe and Ni are essentially absent in the pit, and the Ni has clearly

migrated into a dense, hemispherical phase in the deposit above the pit. Because the ash deposit already contained a high Fe content, the detection of additional iron in the deposit from the corrosion reaction is more uncertain than the presence of Ni. These characteristics are consistent with the basic fluxing of solutes from the oxides of Ni and Fe and the reprecipitation of these oxides out in the deposit where their solubilities are lower, i.e., negative solubility gradients for these "basic" oxides. A high local salt basicity in the pit could have been generated by the salt penetration of the protective scale, formation of sulfide, and the release of oxide ions into the sulfate salt. Likewise, because the obvious occurrence of the fused salt in the corrosion deposit is localized and not uniform, perhaps a liquid phase was stabilized by the lowering of the liquidus via an interaction of the salt with a corrosion product, perhaps nickel sulfide. The Cr oxide solute must experience a positive solubility gradient in the pit, because there is no evidence for its outward migration.

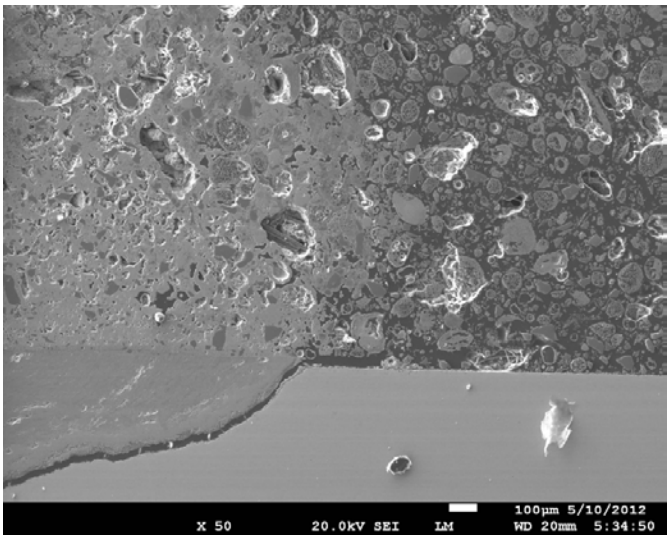

Figure 285 - SEM Micrograph of Corrosion Scale and Portion of Deposit Layer on 309H after Exposure to OH Gatling Oxidizing Conditions for 1000 Hours at 1300°F.

Although the detailed location of the Cr_2O_3 solubility curve is not known under the current test conditions (but it must be far to the right of those for the basic oxides on a plot similar to Figure 280), a basic solute of chromium oxide must have formed locally in the pit. Whether this basic solute is chromate (most likely, especially at this test temperature), or else chromite, is not extremely important because at the much higher oxygen activity in the direction of the bulk gas phase, the chromia solubility gradient would be much higher for basic dissolution. Thus, the oxides of Ni and Fe are dissolved as basic solutes, and in response to negative solubility gradients, these solutes diffuse outward in the fused alkali sulfate into the deposit layer above the pit. These oxides are then re-precipitated as non-protective oxide particles in the sulfate phase. This classic "hot corrosion" behavior meets the expected aspects for this phenomenon. But several points can be raised: (1) To date, a multi-component phase diagram has not been found to support a liquid phase formation for the deposit composition at 1300°F, and indeed a liquid phase is only observed in combination with substrate attack (sulfidation). Therefore, some corrosion product (probably NiS) seems needed to participate in the fusion of the salt for hot corrosion. (2) Alloy 309H has a relatively low Ni content (12.48%)

compared to the other tested corrosion-resistant alloys and a moderately high Cr content (22.3%), a composition that is apparently inadequate to avoid localized hot corrosion for this alloy.

Alloy 310H (19.4Ni, 25.5Cr, Bal. Fe) was another alloy exposed to the laboratory combustion environment of OH Gatling coal for 1000 hours at 1300^{o}F. Figure 286 provides a SEM micrograph of a pit on Alloy 310H. Similar to Alloy 309H of Figure 285, localized hot corrosion attack has also taken place on this alloy. The elemental maps for the elements Ni, Fe and Cr were exactly similar to Alloy 309H of Figure 285, i.e. Ni and Fe were depleted in the pit but found concentrated in the salt phase above the pit, while Cr was left concentrated in the pit.

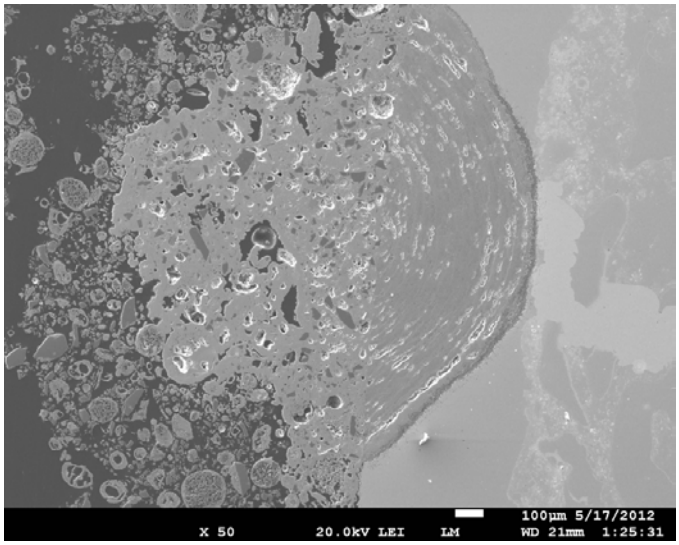

Figure 286 - SEM Micrograph of Localized corrosion Attack on Alloy 310H after Exposure to OH Gatling Oxidizing Conditions for 1000 Hours at 1300^{o}F.

Alloy 304H (11Ni, 18.8Cr, Bal. Fe) was also evaluated in the laboratory OH Gatling coal environment at 1300^{o}F for 1000 hours. In this case, the corrosion kinetics measured at 1300^{o}F had shown a high rate of attack, about the same order of magnitude compared to the medium-S, high-Cl IL #6 Galatia and OH Mahoning coals, see Section 3.4. The SEM micrograph of Figure 287 shows the surface of this alloy, corrosion product, and part of the deposit layer. The elemental maps for the elements of Cr, Fe and Ni and the components for a fused sulfate are again consistent with those for the pitted areas on 309H and 310H attacked by the same environment. In this case, however, none of the 304H surface was protected by a chromia scale, since the entire surface suffered a pitting behavior or general attack. A chromium-rich sulfide lies closest to the metal; but there is only little sulfidation at the alloy grain boundaries. Otherwise, a continuous fused alkali sulfate phase was present throughout the product zone extending up into the deposit. As for the previously described 309H and 310H, Cr was enriched in the sulfate phase in the corrosion product near the metal. Fe and Ni were depleted there, having diffused as basic solutes of their oxides driven by negative gradients in their solubility products into the fused sulfate extending into the overlying deposit. Again, these are classic features of hot corrosion, caused by the high alkali content of the coal ash in combination with an

overall high sulfur content in the coal. Obviously, 304H (18.8 Cr) was inadequate to resist coal ash (hot) corrosion, while 309H (22Cr) and 310H (25Cr) exhibited partial protection. The high rate of corrosion attack of 304H shown in Section 3.4 is consistent with the expectation of hot corrosion.

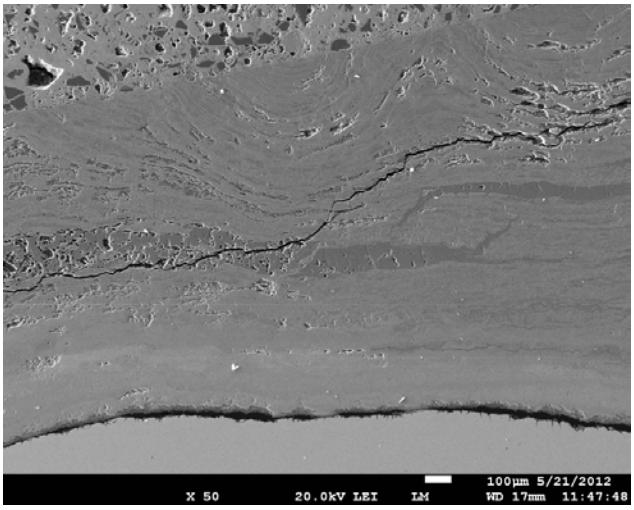

Figure 287 - SEM Micrograph of Corrosion Scale and Portion of Deposit Layer on 304H after Exposure to OH Gatling Oxidizing Conditions for 1000 Hours at 1300°F.

Alloy 310HCbN (20Ni, 25.6Cr, 0.47Nb, Bal. Fe) was exposed to the environment of IL #6 Galatia (2.69% S and 0.273% Cl in coal and high alkali sulfate in deposit) for 1000 hours at 1300°F. The measured data for corrosion rate shown in Section 3.4 indicate the highest thickness loss for any test but a relatively lower weight-loss ranking. The SEM micrograph in Figure 288 documents the alloy morphology with the corroded zone near the surface. Internal sulfidation and oxidation occurred in the metal at the grain boundaries and within the grains. The niobium nitride precipitates have been converted to niobium sulfide and possibly Cr sulfide is formed as well. Perhaps the less stable sulfides that were formed first were later converted to more stable internal oxides close to the metal/scale interface.

Elemental mapping showed again the same characteristics as for 309H and 310H (pitted areas) and general attack as for 304H from the OH Gatling coal test, namely a Cr sulfide-rich scale was present in contact with the alloy and a continuous fused alkali sulfate salt phase existed throughout the corrosion product. Chromium was enriched in this salt phase beneath the deposit. However, both iron and nickel were depleted near the alloy but found concentrated in the salt phase in the deposit layer. Again, the explanation is common to the previous observations, i.e., upon local penetration of an initial (transient) protective scale resulting from an initially acidic gradient, the reaction of the sulfate salt with the metal formed sulfide at the metal/scale interface. The resulting release of oxide ions effected an increase in local basicity such that the basic solutes of NiO and Fe_3O_4, i.e., M_2NiO_2 and $MFeO_2$, respectively, were formed and diffused out in the salt down a negative solubility gradient. These solutes re-precipitated out as non-protective particles of NiO and Fe_3O_4 in the salt phase within the deposit. The basic solute for chromium oxide (probably Na_2CrO_4), in contrast, did not diffuse out because of the positive solubility gradient for the chromate ion resulting from a strong oxygen-pressure dependence for its solubility. Unfortunately, Alloy 310HCbN, which provided exceptional protection for some

other coal environments, suffered severe hot corrosion in the IL #6 Galatia test. In composition, Alloy 310HCbN contains Ni and Cr in amounts identical to 310H that also did not escape localized hot corrosion attack in the similarly corrosive OH Gatling environment.

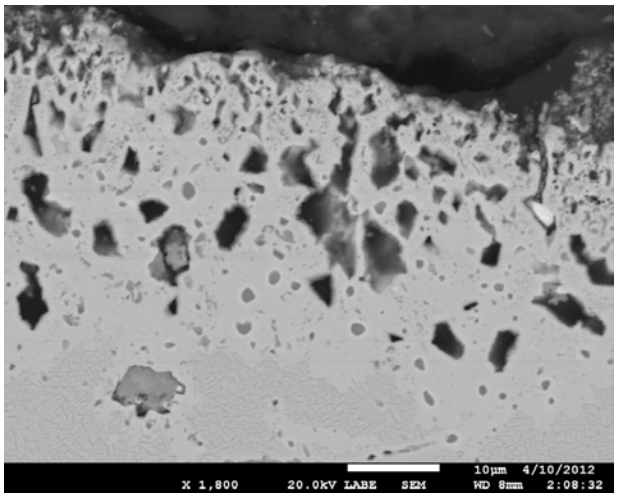

Figure 288 - SEM Micrograph of Alloy, Corrosion Scale and Portion of Deposit Layer for Alloy 310HCbN after Exposure to IL #6 Galatia Oxidizing Conditions for 1000 Hours at 1300°F.

Ferritic T23 (2.2 Cr, 1.5 W, 0.2 Mo, 0.25 V, bal. Fe) was tested in the OH Mahoning 7A environment (1.96% S and 0.198% Cl in coal and high alkali sulfate in deposit) for 1000 hours at 1300°F. Some details of the corrosion zone are shown in Figure 289. Results of elemental mapping showed negligible Cr sulfide particles deep in the metal phase. The corrosion product is predominantly iron oxide, probably magnetite, with Fe-Cr spinel particles in the scale grain boundaries. Indeed, sulfur seems to be present only at the outside of the scale, but continuous sulfide stringers must traverse through the corrosion product to connect this external FeS phase to the metal. In general, there was a clear separation of the dense corrosion product scale and deposit. Copious iron oxide has been deposited into the porous ash deposit as was also seen in Figure 284.

As with the reaction of T23 with OH Gatling of Figure 288, the microstructure is not consistent with hot corrosion that has been demonstrated for the higher alloy steels. Likewise, the porous iron oxide seen in the external deposit in Figure 288 is much less porous than that seen in Figure 284. However, the OH Mahoning coal has about 6 times higher chlorine content than OH Gatling, a fact that would lead to much higher $FeCl_2$ vapor pressure, and therefore a much more dense porous iron oxide product in the deposit. Again, for the reaction illustrated in Figure 289, as for that shown in Figure 284, the low-alloy steel with a sulfide product contacting the gas phase at the base of the deposit, an Active Sulfide-to-Oxide Corrosion Mechanism results in a rapid corrosion rate.

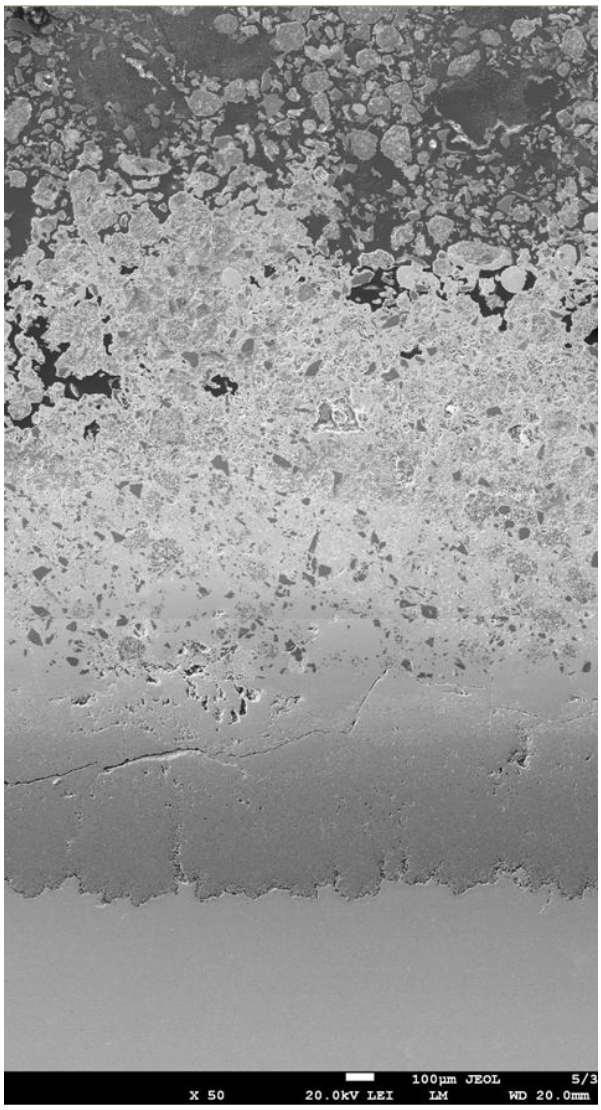

Figure 289 - SEM Micrograph of Corrosion Scale and Portion of Deposit Layer for T23 after Exposure to OH Mahoning 7A Oxidizing Conditions for 1000 Hours at 1300°F.

3.5.2.4 Coal Ash Corrosion Mechanism Operating on Superheaters and Reheaters under Oxidizing Conditions

Before proceeding to a rationalization of the mechanism responsible for fireside corrosion of superheaters and reheaters at 1300°F, one should first explain that the "Active Sulfidation Mechanism", which was so important in describing the chlorine influence in the lower temperature furnace wall corrosion in a reducing/sulfidizing gas, does not contribute in exactly the same way at the higher temperature in the oxidizing/sulfidizing gas. Specifically, only for the low-alloy steels shown in Figures 284 and 289 is FeS present as a secondary corrosion product contacting the gas phase at the base of the deposit. For the 300-series stainless steels and higher alloys at 1300°F, even if sulfides are present at the base of the corrosion product, the sulfides do not contact the gas phase due to the formation of a more protective scale on these higher-Cr alloys. Since the vapor pressure of $FeCl_2$ is proportional to the

thermodynamic activity of Fe as well as the partial pressure of HCl (squared), the vapor pressure of $FeCl_2$ would be too low to support an Active Sulfide-to-Oxide Mechanism (unlike for the low-alloy steels). Consequently, the lacey iron oxide product was not seen in the ash deposit for any of the 300-series and higher alloyed steels, indicating that no FeS product reached the gas phase at the base of the deposit.

Based on extensive examinations by metallography and elemental analyses of many alloy coupons of a wide range of compositions exposed to a wide range of coal chemistries at 1300^{o}F, a pattern of behavior has become obvious, but a detailed understanding proves to be difficult. First, the occurrence of hot corrosion, i.e. the evidence for oxide fluxing in the attack of initial or transient protective scales has been seen for all high-alloy samples, i.e. for all alloy compositions and coal environments, with the possible exception of the very low sulfur WY PRB coal. On the other hand, most high-Cr alloy coupons show some evidence for the formation of protective Cr-rich (probably chromia) scales which may have been only locally penetrated to permit much more rapid hot corrosion attack. In micrographic cross-section, a fused salt phase, generally rich in potassium, magnesium and sodium (and also iron), which supports hot corrosion, is readily obvious as a dense portion of the initial porous deposit above a zone of high attack. Some reacted alloy coupons show several sequential Cr-rich layers where the alloy has been temporarily protected, only to suffer subsequent repeated salt penetration.

The metallography and analytical data are consistent with the accepted mechanism for basic dissolution of the oxides of the more basic alloy components, nickel and iron, with the reprecipitation of these oxides out in the fused salt phase closer to the acidic gas phase (see Section 3.5.2.1). This behavior is consistent with the maintenance of a negative solubility gradient for these basic oxides. In contrast, the solute for chromium oxide, certainly mostly chromate ions, experiences a positive solubility gradient and is therefore concentrated as a solute ion in the zone of rapid attack near the metal/product interface and does not suffer reprecipitation. The origin of the high basicity for the fused sulfate in a highly acidic gas is the formation of sulfides of nickel and iron upon direct reaction with the fused alkali sulfate, such as described by Eq. 28. This sulfide formation necessarily increases the alkali oxide activity of the salt. So at steady state, for all coupons, a competition between passivation (chromia formation) and basic dissolution hot corrosion is occurring, and the imbalance of these two mechanisms decides the corrosion rate. Clearly higher sulfur in the coal, higher ash content, and higher chlorine content (especially for the IL #6 Galatia coal) lead to higher corrosion rates, i.e. minimization of protective scale formation.

For the initial penetration and breakdown of any transient chromia protective scale, a new mechanism has been suggested: acidic fluxing hot corrosion. As described in Figures 282 and 283, chemical thermodynamic equilibrium in the gas phase at 1300^{o}F is certainly not satisfied for coal combustion, although the deposit on the alloy can serve as a catalyzing agent. For these circumstances, the local acidity at the scale/salt interface can be higher than farther out in the deposit towards the gas phase. For these conditions, the iron and nickel solutes in the protective scale could experience a negative solubility gradient and thereby satisfy the condition necessary for acidic dissolution (fluxing), and reprecipitation, leading to penetration/destruction of the initial protective oxide. Once the fused salt makes contact with the underlying alloy to allow the formation of sulfides, the more usual basic fluxing of the oxides of nickel and iron occurs. The

chromium alloy component would suffer some dissolution into the basic salt, but not a continuous loss by fluxing and reprecipitation.

The identification of the aggressive fused salt phase composition is important to the understanding of the corrosion mechanism and its abatement. Figures 290, 291 and 292 are binary phase diagrams for the Na_2SO_4-$Fe_2(SO_4)_3$, Na_2SO_4-$MgSO_4$, and K_2SO_4-$MgSO_4$ systems, respectively. These diagrams indicate liquidus minima at temperatures of about 620°C (1148°F), 660°C (1220°F), and 750°C (1382°F), respectively.

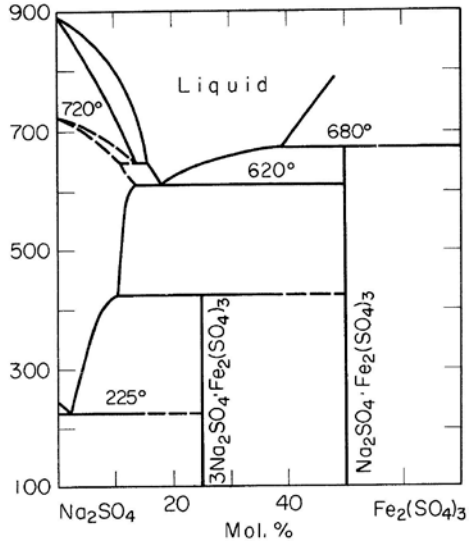

Figure 290 - Na_2SO_4-$Fe_2(SO_4)_3$ Binary Phase Diagram.

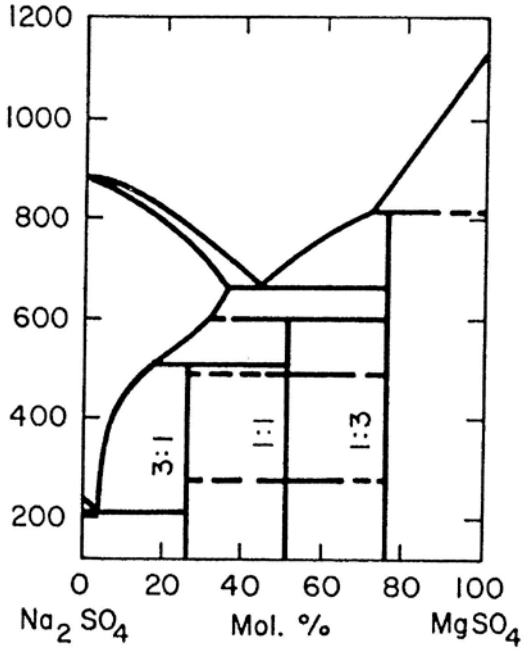

Figure 291 - Na_2SO_4-$MgSO_4$ Binary Phase Diagram.

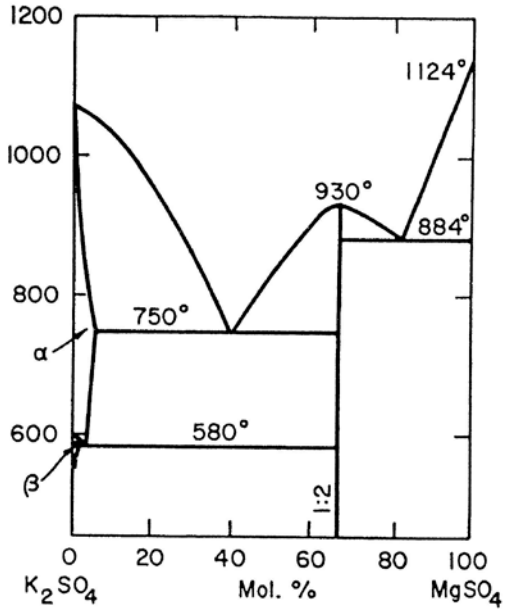

Figure 292 - K_2SO_4-$MgSO_4$ Binary Phase Diagram.

The ternary Na_2SO_4-K_2SO_4-$MgSO_4$ phase diagram shown in Figure 293 indicates two low liquidus compositions: a K_2SO_4-lean minimum at 645°C (1193°F), and a Na_2SO_4-lean minimum at 670°C (1238°F).

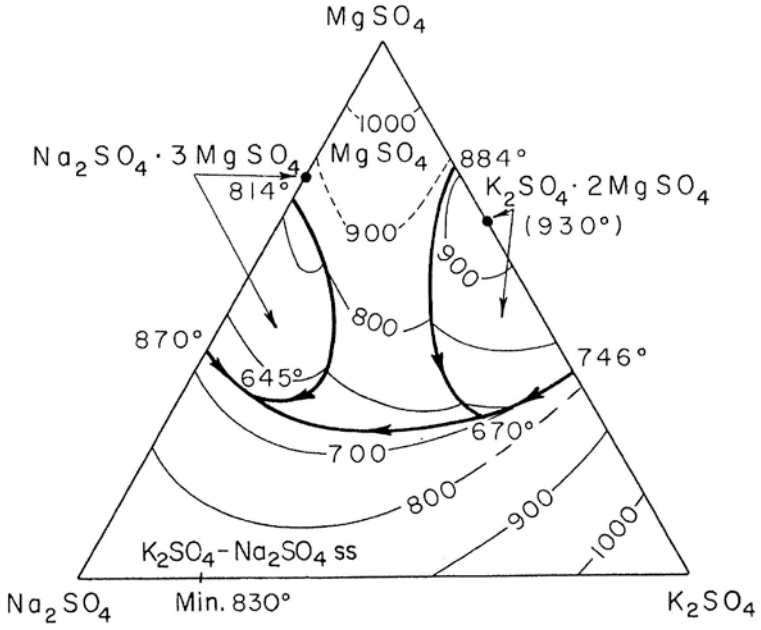

Figure 293 - Na_2SO_4-K_2SO_4-$MgSO_4$ Ternary Phase Diagram.

This phase diagram indicates that a salt containing these three components is capable of forming a liquid phase below 1300°F (704.4°C), a critical requirement for hot corrosion in this testing. Furthermore, the presence of a corrosion product, such as nickel sulfide or nickel sulfate, or especially iron sulfide or iron sulfate would further reduce the liquidus temperature. In the elemental analyses of the corroded coupons, a coupling of the elements Na, K, and Mg are found with sulfur and oxygen in what is known to be the salt phase. Iron is present throughout the deposit, and is certainly a component of the salt phase. Unfortunately, ternary and quaternary phase diagrams involving iron sulfate with the sulfates of sodium, potassium and magnesium are not available.

To test for the presence of a liquid phase in the deposits following corrosion testing for the individual coals, deposit samples selected remote from the corroded coupon (to minimize any influence of corrosion products) were tested for melting phenomena using a Mettler Toledo TGA/DSC 1. Details of the TGA/DSC analyses and results are documented in Appendix E. Each coal deposit composition tested corresponded to that used in the corrosion testing. Duplicate experimental runs were made in a gas phase of composition representative of the respective corrosion test environment. The weight change of the sample, as well its endothermic-exothermic reactions, was investigated. Figure 288 presents an example of the test results for the deposit of the most corrosive deposit of IL #6 Galatia.

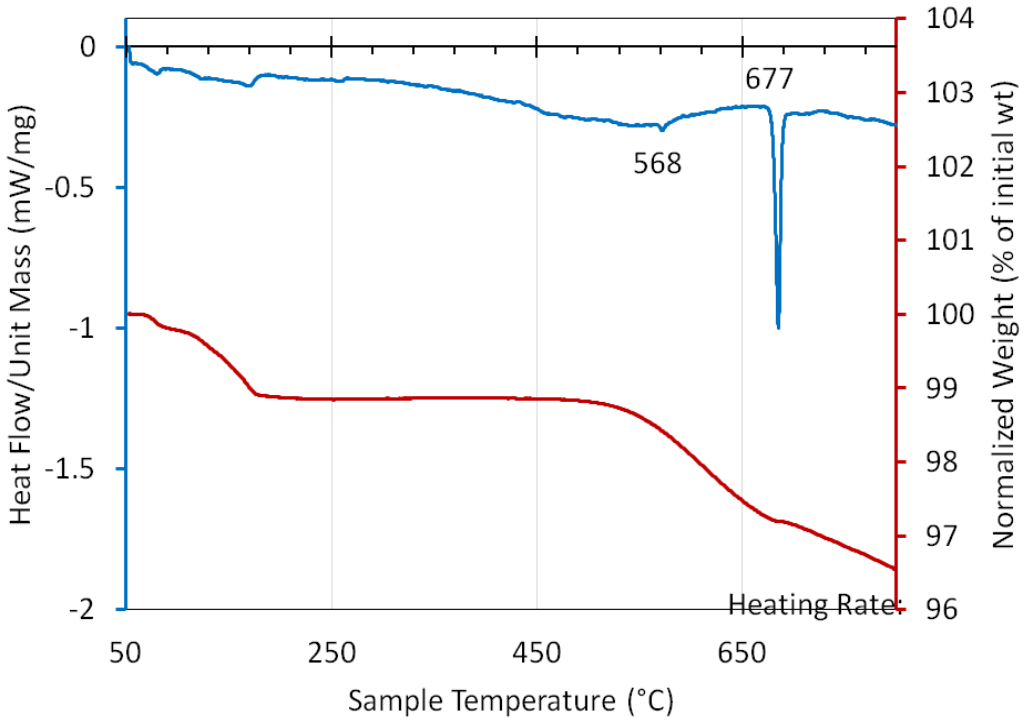

Figure 294 - Results of TGA/DSC Testing of Post-Corrosion Test Deposit for IL #6 Galatia.

A sharp endothermic peak observed at ~677°C (1249°F) lies below the corrosion testing temperature of 704°C (1300°F). A similar sharp endothermic peak at 671°C (1252°F) was seen for the very corrosive OH Mahoning 7A (see Appendix E). For the third most corrosive coal, with a high sulfur composition, OH Gatling, melting initiated at 630°C (1166°F) with a flat peak

(see Appendix E). In contrast, the lowest sulfur content coal WY PRB (0.25 wt.% S) exhibited no melting in the tested temperature range, and the second lowest sulfur coal, ND Lignite (0.67 wt.% S) showed minor melting above 1300°F at around 1364°F. The low sulfur coals Pittsburgh #8 (1.03 wt.% S) and IN #6 (1.14 wt.% S) failed to exhibit clear melting behavior. Thus, while a correlation exists between high-sulfur coals and the corrosion rate, another correlation shows that the high corrosion rate corresponds to a partial melting in the deposit below the corrosion test temperature, clearly consistent with hot corrosion. Coal deposits which did not indicate clear melting via TGA/DSC could still experience hot corrosion (salt melting) if a reaction occurred with some low-melting corrosion product.

Figure 295 provides a compilation for the observed endothermic events for all the coal deposits as recorded by TGA/DSC testing. Almost all the deposits indicated some minor melting at a temperature 570°C (1058°F), which surely involves a molten phase containing $Fe_2(SO_4)_3$, for which the necessary multi-component phase diagram is not available. Otherwise, two of the most corrosive deposits gave the largest, most distinct peaks, at a temperature of around 675°C (1247°F), probably indicating that a larger volume of liquid involving $MgSO_4$ was formed. Another very corrosive coal, OH Gatling, initiated second melting at 630°C (1166°F). The detailed TGA/DSC testing results are summarized in Appendix E.

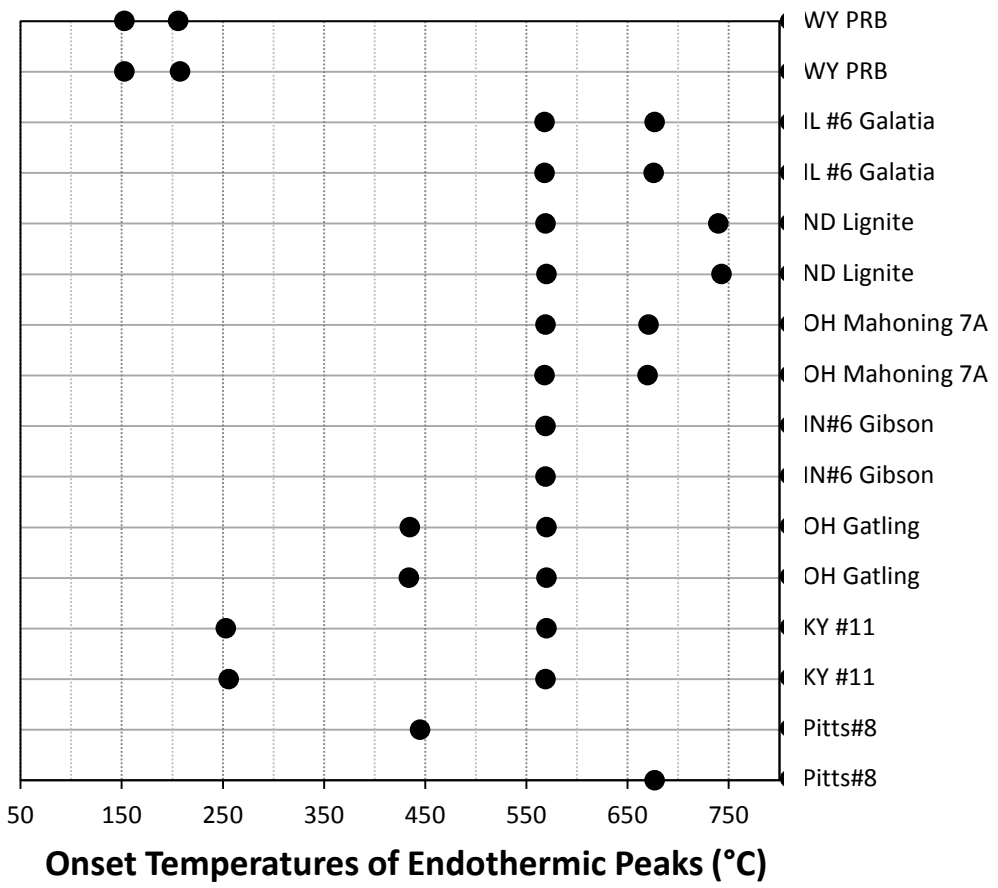

Figure 295 - Summary of Clearly Defined Endothermic Peaks Observed by TGA/DSC Experiments for Different Coals Studied.

In the absence of the required quaternary phase diagram (i.e., including ferric sulfate), the ash composition (wt.%) values from Table 32 for the IL #6 Galatia deposit, namely Na_2SO_4=17.7wt.%, K_2SO_4=4.8%, and $MgSO_4$=10.0%, correspond to the mole fractions of approximately Na_2SO_4= 0.48, K_2SO_4= 0.14 and $MgSO_4$= 0.38. For this composition, the ternary phase diagram of Figure 286 gives a liquidus of around 750C (1382F), but this temperature would certainly be reduced below 1300°F with the inclusion of $Fe_2(SO_4)_3$ that is abundant in the deposit. Upon consideration of the 17.31 wt.% $Fe_2(SO_4)_3$ content for IL #6 from Table 32, the quaternary composition becomes Na_2SO_4=0.34 mole fraction, K_2SO_4=0.12, $MgSO_4$=0.31, and $Fe_2(SO_4)_3$=0.18. The highly corrosive IL #6 Galatia coal had a high original ash content of 10.45 wt.%.

For the second most corrosive coal, OH Mahoning 7A, the deposit sulfate composition from Table 38 corresponds to the quaternary composition of approximately Na_2SO_4=0.41 molar fraction, K_2SO_4=0.11, $MgSO_4$=0.29 and $Fe_2(SO_4)_3$=0.19, actually rather similar to IL #6 Galatia. The highly corrosive OH Mahoning 7A coal had a relatively high original ash content of 9.92 wt.%.

For the third most corrosive coal, OH Gatling, the deposit sulfate composition from Table 44 corresponds to the quaternary composition of approximately Na_2SO_4=0.09 mole fraction, K_2SO_4=0.63, $MgSO_4$~0, and $Fe_2(SO_4)_3$=0.29, significantly different from the other two coal deposits and practically a binary potassium-iron sulfate. The highly corrosive OH Gatling coal had the highest original ash content of 11.34 wt.%. Clearly a need exists for multi-component phase diagrams including the ferric sulfate component to identify more exactly the corrosive fused salt composition.

3.5.2.5 Modeling of Coal Ash Corrosion for Superheaters/Reheaters under Oxidizing Conditions Based on Acidic and Basic Dissolution of Fused Salt

Initial modeling of the coal ash corrosion for superheaters and reheaters was performed. As a first attempt, the following derivations for a predictive equation that relates the coal ash corrosion rate to alloy composition and coal sulfur content during the Stage 1 acidic hot corrosion attack is attempted, i.e., the attack governed by the acidic fluxing of the initially protective basic oxides, such as Fe_2O_3 and NiO, formed during the early stage of hot corrosion, as described by Figures 282 and 283. The impact of coal chlorine on coal ash corrosion is not considered in these derivations at this time.

For the Stage 1 acidic dissolution of Fe_2O_3 in Eq. 36, the concentration of dissolved solute in fused salt can be expressed as a function of partial pressure of SO_3, i.e.,

$$[Fe(SO_4)_{3/2}]^2 \propto P(SO_3)^3$$

or $$[Fe(SO_4)_{3/2}] \propto P(SO_3)^{3/2} \quad \text{Eq. 41}$$

Note that Eq. 40 does not require the concentration of $Fe(SO_4)_{3/2}$ to be in equilibrium with the partial pressure of SO_3. In fact, such an equilibrium is unlikely to attain at the typical

temperatures of boiler tubes. Rather, the correlation of Eq. 40 suggests that the concentration of dissolved Fe_2O_3 is in proportion to the local partial pressure of SO_3, which is a reasonable assumption even without equilibrium.

Similarly, for the acidic dissolution of NiO in Eq. 32, the concentration of dissolved solute in fused salt can be expressed by the following equation:

$$[NiSO_4] \propto P(SO_3) \qquad \text{Eq. 42}$$

On the other hand, basic dissolution continues to dominate the loss of Cr_2O_3, as described by Figure 283. Therefore, the concentration of dissolved Cr_2O_3 in Eq. 37 can be expressed by the following equation:

$$[M_xCrO_4]^2 \propto P(SO_3)^{-2} \times P(O_2)^{3/2}$$

or $$[M_xCrO_4] \propto P(SO_3)^{-1} \times P(O_2)^{3/4} \qquad \text{Eq. 43}$$

where x = 1 for Mg and Ca
x = 2 for Na and K

The formation of SO_3 via Eqs. 39 and 40 can be expressed in terms of the partial pressures of O_2, H_2O, and H_2. Again, the partial pressure of SO_3 should be in proportion to these reactant species, even though equilibrium may not be attained.

$$P(SO_3) \propto P(SO_2) \times P(O_2)^{1/2} \qquad \text{Eq. 44}$$

$$P(SO_3) \propto P(SO_2) \times P(H_2O) \times P(H_2)^{-1} \qquad \text{Eq. 45}$$

Combine Eqs. 41 and 44:

$$[Fe(SO_4)_{3/2}] \propto P(SO_2)^{3/2} \times P(O_2)^{3/4} \qquad \text{Eq. 46}$$

Combine Eqs. 42 and 44:

$$[NiSO_4] \propto P(SO_2) \times P(O_2)^{1/2} \qquad \text{Eq. 47}$$

Combine Eqs. 43 and 44:

$$[M_xCrO_4] \propto P(SO_2)^{-1} \times P(O_2)^{1/4} \qquad \text{Eq. 48}$$

Note that the values of both $P(SO_2)$ and $P(O_2)$ are known, as these gases were employed in the fireside corrosion tests.

Assuming the coal ash corrosion rate in mils per year (*mpy*) of alloys is proportional to the total loss of Ni+Fe+Cr:

$$mpy = A \times X_{Ni} \times P(SO_2) \times P(O_2)^{1/2} + B \cdot X_{Fe} \times P(SO_2)^{3/2} \times P(O_2)^{3/4} + C \times (D - X_{Cr}) \times (P(SO_2)^{-1} \times P(O_2)^{1/4}) + E \quad \text{Eq. 49}$$

where A, B, C, D, and E are constants, and the value of D is a function of X_{Cr}.

The possible functions for D include:

$$D = F \times \exp(G \times X_{Cr}) \quad \text{Eq. 50}$$

$$D = F' \times G'(1 - X_{Cr}) \quad \text{Eq. 51}$$

At a stoichiometric ratio of 1.15 implemented for the oxidizing (upper furnace) tests,

$$P(SO_2, \text{ppmv}) = 697.2 \times S \text{ (wt.\% in coal)} \quad \text{Eq. 52}$$

or $$P(SO_2, \%) = 0.6972 \times S \text{ (wt.\% in coal)} \quad \text{Eq. 53}$$

Combine Eqs. 49 and 53,

$$mpy = A \cdot X_{Ni} \times [S] \times P(O_2)^{1/2} + B \times X_{Fe} \times [S]^{3/2} \times P(O_2)^{3/4} + C \times (D - X_{Cr}) \times ([S]^{-1} \times P(O_2)^{1/4}) + E \quad \text{Eq. 54}$$

Because $P(O_2) \approx 3\%$ for all oxidizing laboratory tests, Eq. 54 can be further simplified, i.e.,

$$mpy = A \times X_{Ni} \times [S] + B \times X_{Fe} \cdot [S]^{3/2} + C \times (D - X_{Cr}) \times [S]^{-1} + E \quad \text{Eq. 55}$$

or $$mpy = A \times X_{Ni} \times [S] + B \times X_{Fe} \times [S]^{3/2} - C \times X_{Cr} \times [S]^{-1} + F \times [S]^{-1} + E \quad \text{Eq. 56}$$

where A, B, C, F, and E are constants.

Regression analysis was performed to determine the values of the constants shown in Eq. 56. To simplify the model at this time, only the corrosion rates of alloys obtained from the laboratory test conditions simulating four low-Cl coals, i.e. PRB, Lignite, Gatling, and Pittsburgh #8, were used in this analysis. The sulfur contents of these four coals differed considerably, ranging from 0.25% to 4.32% S. The compositions of the exposed alloys, especially in the Fe, Ni, and Cr concentrations, also varied significantly. As the first attempt, the corrosion rates of alloys can be expressed by Eq. 57.

$$mpy = 2.35 \times X_{Ni} \times [S] + 27.35 \times X_{Fe} \times [S]^{3/2} + 0.23 \times X_{Cr} \times [S]^{-1} + 1.21 \times [S]^{-1} - 4.27 \pm 31.56 \quad \text{Eq. 57}$$

where [S] is the sulfur wt.% in coal and X is the weight fraction of elements in the alloy.

During the Stage 2 hot corrosion attack after the scale is penetrated, the following derivation for a predictive equation that correlates the corrosion rate with alloy composition and coal sulfur content was also attempted. During this stage, the attack is governed by basic dissolution of the oxides, such as Fe_2O_3 and NiO, at the scale/metal interface by fused salt. The impact of coal chlorine on coal ash corrosion is again not considered in this derivation.

For the basic dissolution of Fe_2O_3 in Eq. 35, the concentration of dissolved solute in fused salt can be expressed as a function of partial pressure of SO_3, i.e.,

$$[MFeO_2]^2 \propto P(SO_3)^{-1}$$

or $$[MFeO_2] \propto P(SO_3)^{-1/2} \quad \text{Eq. 58}$$

As mentioned previously, Eq. 58 does not require the concentration of $MFeO_2$ to be in equilibrium with the partial pressure of SO_3. In fact, such equilibria are unlikely to attain at the typical temperatures of boiler tubes. Rather, the correlation of Eq. 58 suggests that the concentration of dissolved Fe_2O_3 is in proportion to the local partial pressure of SO_3, which is a reasonable assumption even without equilibrium.

For NiO, the basic dissolution in fused sulfate salt can be expressed by the following reaction:

$$NiO + M_2SO_4 = \underline{M_2NiO_2} + SO_3\,(g) \quad \text{Eq. 59}$$

Thus, the concentration of M_2NiO_2 solute can be expressed as in proportion to the partial pressure of SO_3, i.e.,

$$[M_2NiO_2] \propto P(SO_3)^{-1} \quad \text{Eq. 60}$$

On the other hand, because of the acidic nature of Cr_2O_3, basic dissolution continues to dominate the loss of this oxide. Hence, the concentration of dissolved Cr_2O_3 in Eq. 43 is still valid.

As mentioned previously, the partial pressure of SO_3 is described in Eqs. 43 and 44.

Combining Eqs. 44 and 58:

$$[MFeO_2] \propto P(SO_2)^{-1/2} \times P(O_2)^{-1/4} \quad \text{Eq. 61}$$

Combining Eqs. 44 and 60:

$$[M_2NiO_2] \propto P(SO_2)^{-1} \times P(O_2)^{-1/2} \quad \text{Eq. 62}$$

Again, the values of both $P(SO_2)$ and $P(O_2)$ for Eqs. 61 and 62 are those employed in the fireside corrosion tests. The solute concentration of M_2CrO_4 as a function of $P(SO_2)$ and $P(O_2)$ from the basic dissolution of Cr_2O_3 remains the same as that described in Eq. 48.

Assuming the coal ash corrosion rate (CR) of alloys is proportional to the total loss of Ni + Fe + Cr:

$$mpy = A \times X_{Ni} \times P(SO_2)^{-1} \times P(O_2)^{-1/2} + B \times X_{Fe} \times P(SO_2)^{-1/2} \times P(O_2)^{-1/4} + C \times (D - X_{Cr}) \times (P(SO_2)^{-1} \times P(O_2)^{1/4}) + E \quad \text{Eq. 63}$$

where A, B, C, D, and E are constants.

Combine Eqs. 53 and 63,

$$mpy = A \times X_{Ni} \times [S]^{-1} \times P(O_2)^{-1/2} + B \times X_{Fe} \times [S]^{-1/2} \times P(O_2)^{-1/4} + C \times (D - X_{Cr}) \times ([S]^{-1} \times P(O_2)^{1/4}) + E \quad \text{Eq. 64}$$

Since $P(O_2) \approx 3\%$ for all oxidizing laboratory tests, Eq. 63 can be further simplified:

$$mpy = A \times X_{Ni} \times [S]^{-1} + B \times X_{Fe} \times [S]^{-1/2} + C \times (D - X_{Cr}) \times [S]^{-1} + E \quad \text{Eq. 65}$$

or $$mpy = A \times X_{Ni} \times [S]^{-1} + B \times X_{Fe} \times [S]^{-1/2} - C \times X_{Cr} \times [S]^{-1} + F \times [S]^{-1} + E \quad \text{Eq. 66}$$

where A, B, C, F, and E are constants.

3.5.2.6 Empirical Treatment of Corrosion Modeling for Coal Ash Corrosion of Superheaters/Reheaters under Oxidizing Conditions

Based on the available binary and ternary phase diagrams, which were presented in Figures 291-293, as well as the DSC results in Figures 294 and 295, clearly a fused sulfate phase involving iron and a combination of the alkali metals (Na + K) plus the alkaline earth Mg, as well as sulfur, are responsible for the high corrosion rates of high-alloy steels at 1300° F. On this basis, the corrosion rates might be empirically related to a combined amount (on a molar basis) of these components as presented in the ultimate analyses of the coal ash, as well as the weight percent of the coal ash in the proximate analysis, as presented previously in Table 9. Since the components iron, alkalis, and sulfur are individually required, a schematic sulfation reaction might be represented as

$$M + \tfrac{1}{2} S_2 (g) + 2 O_2 (g) = M(SO_4) \quad \text{Eq. 67}$$

where M represents divalent cations and the oxygen activity was nominally the same for all the oxidizing tests at 1300°F.

Equation 66 implicitly assumes that each of the ash components Na, K, Mg and Fe have equal probabilities in contributing to sulfate formation. Based on Eq. 67, a Coal Corrosivity Index (CCI) to rank the corrosivity of the coals might be defined as follows:

$$CCI = [ash] \times \frac{[S]}{32} \times \{2 \times \frac{[Na_2O]_f}{62} + 2 \times \frac{[K_2O]_f}{94} + \frac{[MgO]_f}{40} + 2 \times y \times \frac{[Fe_2O_3]_f}{160}\} \quad \text{Eq. 68}$$

where the ash components have been normalized relative to their molecular weights. Both [ash] and [S] are in 100×wt.% from a coal analysis on the basis of 100g coal, and $[Na_2O]_f$, $[K_2O]_f$, $[MgO]_f$, and $[Fe_2O_3]_f$ are the fractions of these oxides in the coal ash determined by the ash analysis. It is desirable to simply use the values of 100×wt.% for all species in the calculation by adding a multiplier to the CCI in Eq. 68. Thus

$$CCI \times 100 = [ash] \times 3.125 \times [S] \times \{3.23 \times [Na_2O] + 2.13 \times [K_2O] + 2.48 \times [MgO] + 1.25 \times y \times [Fe_2O_3]\} \quad \text{Eq. 69}$$

where the brackets denote the indicated components of the ash, now also in 100×wt.%, and y is the variable fraction of the Fe_2O_3 ash component that is considered to form sulfate. Again, Eq. 69 is on the basis of 100g coal.

Because thermodynamically iron has a lower tendency to sulfation compared to the alkali and alkaline earth components, the full weighting factor for iron oxide content is probably exaggerated. In contrast, one might suppose that as little as none of the Fe_2O_3 from the ash is needed to stabilize the fused sulfate. This assumption is not completely baseless, because the alloys all contain a high iron (or nickel) component which would be oxidized upon exposure to form at least a transient Fe_2O_3 (or NiO) phase which could sulfate in contact with the environment.

Equation 69 has been evaluated to provide the following CCI values ($x10^2$) for the eight coals assuming y = 0, 0.3, 0.7 and 1.0. The rankings of the coals and their calculated CCI values are presented here. For y=0, i.e. assuming no provision for Fe_2O_3 content in influencing a liquid sulfate formation: #1-2: OH Gatling (880) and Kentucky (878); #3: IL #6-1(826); #4: Beulah Zap (515); #5: Mahoning (353); #6-7: Indiana Gibson (289) and Pittsburgh #8 (282); and #8: PRB-1 (77). These values are listed in Table 105.

A comparison of these calculated rankings and values of CCI (excluding Fe_2O_3) for these eight coals with the observed corrosion kinetics (calculated from both weight loss and thickness loss), as given in Section 3.4, is difficult because of irregularity in the kinetics values. However, if one directs attention to only the 300-series steels (304H, S304H, 310HCbN, 347HFG, and 347H), the coal corrosivity can be quantitatively ranked as follows: #**1:** IL #6, #**2-3:** OH Gatling and OH Mahoning, #**4:** Kentucky #11, #**5-6:** Pittsburgh #8 and IN #6 Gibson, and #**7-8:** Beulah Zap Lignite and PRB-1. According to the preceding calculations of CCI using Eq. 69, the CCI values and rankings for these coals seem to have inflated the corrosivity of Kentucky and Beulah Zap Lignite and underestimated the corrosivity of IL #6 and Mahoning, incidentally the coals with high chlorine contents.

To return to the apparent problem of the excessive weighting for the Fe_2O_3 content of the ash, one notes that for OH Gatling, the moles of iron in the ash exceed by a factor of 7.4 the moles of (divalent) alkali and by a factor or 3.9 the moles of sulfur in the coal. For the high-Fe_2O_3 KY #11 coal, these ratios are 4.5 and 4.3. Therefore, it is obvious that not all the iron from the ash is converted to sulfate, although some iron sulfate is certainly required to lower the liquidus temperature below 1300^{o}F. To further assess the participation of Fe_2O_3 in the ash to the corrosivity of the coal, calculations of CCI were made for the value of y (in Eq. 69) equal to 0.3, 0.7 and 1.0. The resulting CCI values and the associated ranking calculated for the coals are also provided in Table 105. As seen in the table, the values for the variable y higher than 0.3 make no difference in the rankings of the coals. On the other hand, the assumption of y = 0.3 causes a reversal in the rankings between OH Mahoning (from 5 to 4) and ND Beulah Zap (from 4 to 5) which agrees better with the experimental observations. In fact, a value for y lower than 0.3 (perhaps 0.1) would provide this desired reversal in the ranking. At this stage in the empirical development, the Eq. 69 does not predict that IL #6 Galatia is the most corrosive coal.

Whether the role of chlorine in the high-temperature corrosion of the high-alloy steels is understood mechanistically or not, chlorine is known to increase corrosion rates. Therefore a factor is needed to predict the influence of chlorine. If a term of 10×[Cl] is added to the CCI function of Eq. 69, where again the brackets represent the weight percent in the ash, the assumption of y = 0 provides the following CCI values and rankings: #**1:** IL #6 (1215), #**2:** Kentucky #11 (1083), #**3:** OH Gatling (919), #**4:** OH Mahoning (552), #**5:** Beulah Lignite (516), #**6:** IN #6 Gibson (501), #**7:** Pittsburgh #8 (287), and #**8:** PRB-1 (78). With the exceptions that Kentucky #11 and Beulah Zap Lignite are somewhat overrated, this revised Eq. 69 provides a reasonable agreement with the experimentally observed rankings of the eight coals.

Table 106 - Coal Corrosivity Index (CCI×100) Determined for the Eight Coals Studied.

Parameter	Ill. #6, 2009	PRB, 2009	Beulah Zap	Mahoning 7A	Indiana #6	Gatling	Pitt #8	Kentucky #11
Visual Ranking →	1	8	7	3	6	2	5	4
CCI x 100 = [Ash] x [S]/32 x (2[Na2O]/62 + 2[K2O]/94 + [MgO]/40.3 + 2y[Fe2O3]/160) where y=0	826	77	515	353	289	880	282	878
CCI Ranking	3	8	4	5	6	1	7	2
CCI x 100 = [Ash] x [S]/32 x (2[Na2O]/62 + 2[K2O]/94 + [MgO]/40.3 + 2y[Fe2O3]/160) where y=0.3	1307	85	566	819	414	2503	366	1819
CCI Ranking	3	8	5	4	6	1	7	2
CCI x 100 = [Ash] x [S]/32 x (2[Na2O]/62 + 2[K2O]/94 + [MgO]/40.3 + 2y[Fe2O3]/160) where y=0.7	1948	97	633	1441	580	4666	477	3074
CCI Ranking	3	8	5	4	6	1	7	2
CCI x 100 = [Ash] x [S]/32 x (2[Na2O]/62 + 2[K2O]/94 + [MgO]/40.3 + 2y[Fe2O3]/160) where y=1.0	2429	106	684	1907	704	6289	561	4016
CCI Ranking	3	8	5	4	6	1	7	2
CCI x 100 = [Ash] x [S]/32 x (2[Na2O]/62 + 2[K2O]/94 + [MgO]/40.3 + 2y[Fe2O3]/160) + 10(Cl) where y=0	1215	78	516	552	501	919	287	1083
CCI Ranking	1	8	5	4	6	3	7	2
CCI x 100 = [Ash] x [S]/32 x (2[Na2O]/62 + 2[K2O]/94 + [MgO]/40.3 + 2y[Fe2O3]/160) + 10(Cl) where y=0.3	1696	87	567	1018	626	2541	370	2025
CCI Ranking	3	8	6	4	5	1	7	2
CCI x 100 = [Ash] x [S]/32 x (2[Na2O]/62 + 2[K2O]/94 + [MgO]/40.3 + 2y[Fe2O3]/160) + 10(Cl) where y=0.7	2338	98	634	1640	792	4705	482	3280
CCI Ranking	3	8	6	4	5	1	7	2
CCI x 100 = [Ash] x [S]/32 x (2[Na2O]/62 + 2[K2O]/94 + [MgO]/40.3 + 2y[Fe2O3]/160) + 10(Cl) where y=1.0	2819	107	685	2106	916	6327	565	4222
CCI Ranking	3	8	6	4	5	1	7	2

4.5.2.3 Role of Alloy Components in Resistance to High-Temperature Superheater and Reheater Corrosion

In general, materials intended for service at high temperatures where creep property becomes a major consideration are comprised of iron, nickel and chromium, along with other strength-enhancing elements intended to form precipitates and/or otherwise solid solution in the alloys. Nickel is often required to stabilize the creep-resistant face-centered-cubic lattice structure, while chromium (typically greater than 20 wt.%) is generally needed to provide corrosion resistance. While such alloy compositions represent the general pattern, one can expect that, for a specific application with a given range of high temperatures and corrosion conditions, some alloy compositions with adequate mechanical properties would be better than the others from the corrosion standpoint. In the laboratory experimentation reported here, alloys with a wide range of composition were tested at 1300^{o}F in the presence of representative ash deposits and combustion gases for a variety of eight different coals. Appendix D summarizes the compositions of all alloys and weld overlays tested in this study, among which the major components of Fe, Ni, and Cr for ten materials are listed in Table 106. These materials are arranged with the most Fe-rich alloys at top and the most Ni-rich alloys at the bottom. Comments drawn from the corrosion rate data are also given in the table.

Table 107 - Major Component Percentages for Eight Alloys Tested at 1300°F.

Alloy	Fe, wt.%	Ni, wt.%	Cr, wt.%	Others, wt.%	Comments
347H	68.4	10.4	17.7	0.35 Cu	Poor resistance generally, especially in IL #6 Galatia, OH Mahoning 7A, and OH Gatling
304H	68	11	18.8		Comparable poor resistance to 347H
310HCbN	52.3	20	25.6	0.47 Nb, 0.24 N	Irregular behavior: poor in IL #6 Galatia and OH Gatling; good in OH Mahoning 7A and KY #11
800H	44	32.7	21	0.45 Al, 0.32 Ti	Good resistance except for IL #6 (high Cl) and OH Mahoning
120	34.7	37.3	25	0.61 Nb	Best overall resistance for all coals
WO52	12.2	56.3	29.6		Best overall resistance for all coals
740H	1.02	49.45	24.3	19.6 Co	Better resistance than alloys with higher Ni contents
WO72	10.6	47.2	41.2		Best overall resistance for all coals
617	0.76	53.2	25	9.38 Mo	Fair resistance but generally worse than 230
230	1.25	59.5	21.3	14.9 W	Fair resistance except for IN #6 Gibson and Pitts. #8

A definitive selection/preference of one alloy above the others is difficult because of variations in the relative corrosion rates from one coal to the other. Therefore, discussion on the role of alloying components must be qualitative at a best effort.

The alloys suffered from hot corrosion attack at 1300°F, specifically fluxing and re-precipitation, either by localized pitting or more uniformly over the surface. The higher the number of corrosion pits and/or more scale penetration, the higher the observed corrosion rate. In general, while chromium has a reputation for providing the needed corrosion resistance, it seemed to play a double positive role in this study. First, portions of alloys that resisted localized pitting or general attack from hot corrosion were protected by a chromia (or perhaps spinel) protective scale beneath the ash deposit. Secondly, as discussed by Rapp and Otsuka,[31] in the presence of hot corrosion and basic fluxing, chromium buffers the extent of basicity and thereby the basic solubility gradient in the fused salt phase by complexing with the oxide ions in the formation of chromate ions. In fact, alloys with (even marginally) higher Cr content provided superior corrosion resistance across the range of coal composition in this study. Alloy 120, with 25% Cr and essentially equal parts of Fe and Ni, was the best monolithic material for essentially all of the laboratory corrosion tests. The presence of 0.61% Nb in Alloy 120 would have reduced the formation of $Cr_{23}C_6$, thus "freeing" more Cr for the needed corrosion resistance.

Perhaps the second best overall corrosion resistance (but significantly worse than Alloy 120) was exhibited by Alloy 740H (with 24.3% Cr and 19.6% Co). Specifically, this Co-rich Ni-based alloy performed better than the high-Fe alloys in the laboratory environments with high chlorine contents. As discussed previously and shown in Figure 289, the exposure of low-Cr ferritic steel T23 to the OH Gatling resulted in the deposition of porous iron oxide throughout a significant part of the deposit layer by the Active Sulfide-to-Oxide Mechanism, supported by the transport of $FeCl_2$ vapor, even for a coal with a very low Cl content. In general, then, one might fear that even for austenitic Fe-base alloys with about 20% Cr, the Active Sulfide-to-Oxide Mechanism might still play a role and lead to accelerated corrosion. While such alloys (347H and 304H, with the highest Fe and lowest Cr) suffered rapid corrosion in high-Cl coal environments, evidence for any Active Sulfide-to-Oxide Mechanism was not clearly identified from the metallographic examinations at relatively low magnifications. However, the formation of minute sulfide phase in the scale in contact with the gas phase could have occurred.

Alloy 310HCbN (25.6Cr, 20Ni and 52.3Fe) exhibited irregular behavior, i.e., rapid corrosion in IL #6 Galatia and OH Gatling but exceptional resistance to OH Mahoning 7A and Kentucky #11. Likewise, Alloy 230 with the highest Ni content but only 21.3Cr behaved better

that the highest Fe-base alloys (347H, 304H and 310HCbN) in the corrosive coals IL #6 Galatia and OH Gatling but suffered worse corrosion for IN #6 Gibson and Pitts #8. Alloy 800H with 21% Cr, 44% Fe, and 32.7% Ni performed poorly in the two most corrosive coals of IL #6 Galatia and OH Mahoning 7A but was relatively resistant to the other coal environments. In principle, the high refractory metal contents for Alloy 617 (9.4% Mo) and Alloy 230 (14.9W) would behave like Cr in complexing oxide ions and buffering the fused salt basicity. However, judging by the measured corrosion rates, these acidic components appeared to have reacted preferentially with fused salt to accelerate the corrosion attack, perhaps during Stage 2 (basic) hot corrosion.

In summary, the relatively high-Fe but low-Cr alloys, 347H and 304H, performed the worst in the most corrosive coal environments, although no apparent Active Sulfide-to-Oxide Mechanism was identified. The medium Fe-content alloys 310HCbN and 800H exhibited irregular behavior but were generally sensitive to a high chlorine content environment. The most corrosion-resistant alloy across the assortment of coal environments (by far) was Alloy 120 with 25% Cr and equal amounts of Fe and Ni. The Ni-based alloys became less resistant as the Ni content increased compared to Alloy 120. Clearly, a little extra Cr content in the alloy was beneficial in limiting corrosion in these coal environments.

4.5.2.4 Chlorine-Containing Volatile Species Produced from HCl Reacting with Cr_2O_3 Scale at 1300°F (977K)

All laboratory studies and field experiences indicate that increasing the Cl content in coal is deleterious to any alloy exposed to coal combustion environments at high temperatures. In addition, increasing Cr content in the alloy generally increases its corrosion resistance. The impact of chlorine and chromium contents on fireside corrosion has also clearly been demonstrated by the corrosion data generated from this project. However, no meaningful amount of chlorine has ever been found in the corrosion products or deposits on alloys after exposure to laboratory or field conditions. The lack of condensed chlorine-bearing compounds suggests that chlorine must attack the metal predominately via the formation of volatile species. As discussed previously, the active Sulfide-to-Oxide Corrosion Mechanism involving the formation of $FeCl_2$ vapor serves to explain the high corrosion rates for low-alloy steels and lower-grade stainless steels. Another hypothesis is that Cl may react with Cr to accelerate the loss of material. Therefore, an attempt to evaluate the volatile species from Cl and Cr and the corresponding corrosion mechanism operating under the coal combustion environments of interest was made here.

Ebbinghaus[33] provided fundamental thermodynamic data for gaseous species involving chromium in complex environments including oxygen, chlorine, and hydrogen, which are relevant to the alloys of high Cr contents in this study. Specifically, for the oxidizing environment investigated by Ebbinghaus that consisted of P_{O2}=0.10 atm, P_{HCl}=0.01 atm, and P_{H2O}=0.10 atm. at 1300°F (977K), the three dominant vapor species were found to yield the vapor pressures as follows: $P(CrO_2Cl(OH)) = 4x10^{-6}$ atm, $P(CrO_2Cl_2)=10^{-6}$ atm, and $P(CrO_2(OH)_2)=8x10^{-7}$ atm.

The formation of such complex vapor species can be described by the following reactions, respectively:

$Cr_2O_3 + 2\ HCl\ (g) + 3/2\ O_2\ (g) = 2\ CrO_2Cl(OH)\ (v)$ Eq. 70

i.e., $P(CrO_2Cl(OH)) \propto P_{HCl} \times P_{O_2}^{3/4}$

$Cr_2O_3 + 4\ HCl\ (g) + 3/2\ O_2(g) = 2\ CrO_2Cl_2\ (g) + 2\ H_2O\ (g)$ Eq. 71

i.e., $P(CrO_2Cl_2) \propto \frac{P_{HCl}^2 \times P_{O_2}^{3/4}}{P_{H_2O}}$

$Cr_2O_3 + 2\ H_2O\ (g)\ + 3/2\ O_2\ (g) = 2\ CrO_2(OH)_2\ (g)$ Eq. 72

i.e., $P(CrO_2(OH)_2) \propto P_{H_2O} \times P_{O_2}^{3/4}$

Upon adjusting the vapor pressures for the Cr-bearing volatiles quoted above to the oxidizing test conditions of high-Cl IL #6 Galatia coal, namely P_{O2}=0.03 atm, P_{H2O}= 0.07 atm, and P_{HCl}=0.0002 atm, the partial pressures of these dominant volatile species become:

$P(CrO_2Cl(OH)) = 9.2\times10^{-9}$ atm.

$P(CrO_2Cl_2) = 1.8\times10^{-10}$ atm.

$P(CrO_2(OH)_2) = 1.3\times10^{-7}$ atm.

These values indicate that all of the major Cr-bearing Cr vapor species resulting from reactions between HCl and Cr_2O_3 have rather low partial pressures, and that the dominant species of $CrO_2(OH)_2$ does not even contain chlorine. In addition, the above calculations are based on the IL #6 coal containing the highest Cl content of the eight coals investigated, thus producing the highest HCl concentration in the bulk gas phase. Clearly, the concentration of HCl (and O_2) at the base of the deposit where Eqs. 70-72 take place would be much lower, thus leading to even lower partial pressures for the Cr-bearing vapors than what are calculated above. As a result, the destruction and removal of any protective Cr_2O_3-rich scale in contact with the gas phase via the formation of Cl-containing volatiles does not seem feasible.

4.5.2.5 Role of Chlorine in Coal in the Attack of Cr-Bearing Alloys

The calculations presented above indicate that Cr_2O_3 (and even a spinel phase with high Cr_2O_3 activity) is so stable that it cannot be volatilized even in contact with the combustion gases of IL Galatia #6, the coal with the highest Cl content in this study. Thus, further examinations of a Cr product of lower thermodynamic stability, i.e. CrS, in the presence of the gas phase was performed. The two possibilities are (1) the formation of CrS at the interface between the scale and deposit in contact with the gas phase (although thermodynamically CrS would be highly unstable in the oxidizing environments containing excess oxygen) and (2) the formation of CrS near the alloy/scale interface (where it would be thermodynamically stable) and therefore does not contact the gas phase directly.

According to the first premise, the reaction can be described by Eq. 73 as follows:

$$CrS + 2\,HCl\,(g) + 3/2\,O_2\,(g) = CrCl_2\,(g) + H_2O\,(g) + SO_2\,(g) \qquad \text{Eq. 73}$$

Applying the oxidizing test condition of IL #6 Galatia coal consisting of P(O2) = 0.03 atm., $P(H_2O)$ = 0.07 atm., and $P(SO_2)$ = 0.0023 atm. (based on the assumption of zero resistance for gas diffusion in the deposit layer), the partial pressure of $CrCl_2$ (g) at 1300°F was calculated to be $2.73\times10^{+17}$ atm. using available thermodynamic data.[34] Such a high theoretical equilibrium partial pressure of $CrCl_2$ reflects the extreme instability of CrS upon exposure to an oxidizing condition. Obviously, such a high value of partial pressure is not attainable realistically. However, it does reveal that any CrS formed on the scale as a corrosion product can react with HCl (and O_2) rapidly to form $CrCl_2$ vapor if direct contact between CrS and the oxidizing gas phase is allowed.

Equation 74 describes the second premise contemplated:

$$CrS + 2HCl\,(g) = CrCl_2\,(g) + H_2S\,(g) \qquad \text{Eq.74}$$

The reaction of Eq. 74 assumes the condition at the scale/metal interface being reducing and sulfidizing and HCl can arrive at the interface via molecular diffusion through the defects of otherwise protective scale, such as grain boundaries, microcracks, and pores. Because HCl consists of only one atom of H and Cl each, with the size of H being negligible, its overall molecular size is essentially that of a single Cl ion. The size of this ion would be relatively small compared to most of the other gases employed in the oxidizing laboratory tests containing multiple atoms. Therefore, the reaction of Eq. 74 to generate $CrCl_2$ vapor at the scale/metal interface would be feasible. The same scenario could be applied to the molecular diffusion of other hydrogen-bearing gaseous species, such as H_2O and H_2S, even though the valence of these ions is -2.

Based on the available thermodynamic data[34] and assuming an equal amount of $CrCl_2$(g) and H_2S(g) formed from Eq. 74, a partial pressure of $1.6\text{x}10^{-7}$ atm. is estimated for $CrCl_2$ at 1300°F under the test condition of IL #6 Galatia coal containing 0.0002 atm. HCl. If the partial pressure of H_2S in Eq. 74 is further reduced (perhaps significantly) because of subsequent sulfidation of H_2S with other alloying elements, the partial pressure of $CrCl_2$(g) would be easily increased to a level that becomes significant for evaporation and metal loss. However, due to the relatively large molecular size, the outward diffusion of $CrCl_2$ vapor must be facilitated by the presence of significant defects in the scale. Of course, the potentially high partial pressure of $CrCl_2$ (and H_2S) generated at the scale/alloy interface could damage the scale locally and allow the outward diffusion to proceed rather quickly.

Either the reaction of Eq. 73 or Eq. 74 would explain the accelerated corrosion attack on high-Cr alloys exposed to coal combustion environments containing chlorine. Both mechanisms involve the formation of CrS as a corrosion product from coal sulfur as well as HCl gas from coal chlorine. As $CrCl_2$(g) diffuses outward to a region where the partial pressure of oxygen is sufficiently high, it would be oxidized to form non-protective Cr_2O_3 precipitates and release

chlorine as HCl. This HCl may return to the scale/deposit interface (even with some escaping to the scale/alloy interface) to sustain the cycling vaporization process. Further analysis is justified to determine which cycling reaction is more dominant in the corrosion attack involving chlorine, although the second mechanism in Eq. 74 appears to be more likely, which is supported by the porous morphology shown in Figure 282 at the metal surface of 310HCbN after exposure to the IL#6 Galatia test conditions.

4.5.2.6 Nonlinear Regression Analysis for Superheater/Reheater Corrosion under Oxidizing Conditions

From the preceding treatment of regression analysis of corrosion rates for furnace walls in reducing conditions (see Section 3.5.1.4), the formulations attempted have described two mechanisms deemed to be operative: (1) sulfidation/oxidation in the absence of chlorine in coal and (2) an Active Sulfidation Mechanism resulting from chlorine in coal. Only the elements of iron and chromium from the alloys and sulfur and chlorine from the coals were considered in the predictive expression.

To construct an equivalent formulation of regression analysis for the fireside corrosion of superheaters and reheaters under oxidizing conditions is much more complicated and challenging. Under these conditions, the dominant mechanism for rapid corrosion was, in part, "Hot Corrosion", comprising a local dissolution of the protective oxide film by a thin fused salt phase in or under the porous deposit and the subsequent reprecipitation of this oxide as non-protective particles in the salt phase. Much of the quantitative knowledge of the acid-base nature for complex sulfate salts and the oxides of the alloy components is lacking, although some general qualitative understanding is available. Likewise, the acidic hot corrosion mechanism, i.e., Stage 1 Hot Corrosion, was expected to operate at the start of the exposure prior to penetration of the protective scale, as shown in Figures 282 and 283, followed by the more aggressive basic fluxing hot corrosion mechanism, i.e., Stage 2 Hot Corrosion, after scale penetration. Furthermore, the presence of fused salt might not cover all sample surfaces uniformly for a given set of alloy and exposure condition. The scale composition might also vary significantly, with some areas lean in Cr but rich in Fe and/or Ni. Consequently, the attack is believed to occur locally after some "incubation" time during which the acidic fluxing hot corrosion mechanism (Stage 1 Hot Corrosion) is accelerated locally at these Cr-lean areas. Because the corrosion data were only collected after 1000 hours, any attempt at a regression analysis must be considered more empirical than the preceding treatment for furnace wall corrosion.

The following expression describes the initial attempt for the fireside corrosion of the superheater and reheater. A Gaussian function is used to describe the corrosion rate that exhibits the behavior of a bell-shaped curve as a function of temperature, i.e.,

$$f(Gaussian) = a \times e^{-\left(\frac{(x-b)^2}{2\times c^2}\right)} + d \qquad \text{Eq. 75}$$

where x is the variable that represents the metal temperature T here, and a, b, c, and d are constants for the bell-shaped curve of a given alloy.

For modeling of the superheater and reheater corrosion, the most important constant that needs to be determined from the regression analysis is perhaps the value of *a*, which represents the height of the bell-shaped curve and is a strong function of coal chemistry and alloy composition. Many variables in a selected coal and alloy can affect the value *a*, which include the Fe and Cr concentrations in the alloys as well as the S, Cl, and ash contents in coal. In addition, the alloying elements can behave either acidic or basic in fused sulfate upon oxidation. Therefore, their roles are also included for consideration in determining the value *a*.

Combining the Gaussian function with all the variables considered for *a*, the following equation is proposed for corrosion modeling:

$$mpy = [A \times (\%Fe)^B \times (\%S)^C \times (1 + \alpha \times \%Cl)^D \times (CCI \times 100)^E \times (\%Cr)^F \times (total\ acidic\ elements)^G \times (total\ basic\ elements)^H] \times f(Gaussian) \quad \text{Eq. 76}$$

where *A*-*H* are constants required to define the value of *a*, *f(Gaussian)* is the Gaussian function used here to describe the bell-shape curve for the corrosion rates of superheaters and reheaters as a function of temperature, and α in the Cl term is an arbitrary value to best fit the chloride dependence. The total acidic elements comprised the sum of the molar percentages of Mo+Al+Ti+Ta+V+W+Si in the alloy (excluding Cr). Likewise, the total basic components comprised the total molar percentages of Ni+Fe+Co+Cu in the alloy. Although Cr is an acidic alloying element, it plays the most important role in resisting high-temperature corrosion and therefore is separated out as a standalone term from the other acidic elements for a special treatment in the regression analysis.

By taking the natural logarithm on both sides of Eq. 76,

$$ln(mpy) = ln(A) + B \times ln(\%Fe) + C \times ln(\%S) + D \times ln(1 + \alpha \times \%Cl) + E \times ln(\mathrm{CCI} \times 100) + F \times ln(\%Cr) + G \times ln(total\ acidic\ elements) + H \times ln(total\ basic\ elements) - \frac{(T-b)^2}{2 \times c^2} \quad \text{Eq. 77}$$

Because of the large differences in molecular weights among the elements involved in Eq. 77, the use of molar percentages was thought, in principle, to be desired. However, alloy and coal compositions are always reported in weight percent, and converting these values to molar percents can be tedious and time consuming for many. Therefore, the preference of using molar percentages is not reinforced here in this study. Consequently, the use of weight percent for the nonlinear regression analysis was carried out.

Numerous iterations of the nonlinear regression analysis under various scenarios have been performed. The goal of the analysis is to generate a set of best parameters/constants for Eq. 77 with the maximum "Goodness of Fit" using the laboratory corrosion data generated from Task 4. Because of a large number of independent variables involved, the goodness of fit is not expected to be high.

Based on the current modeling **e**ffort for superheater/reheater corrosion, a best-fit predictive corrosion equation has been obtained, as shown in Eq. 78.

$$mpy = 1 \times 10^{31} \times (Fe\ wt.\%)^{-0.53} \times (S\ wt.\%)^{2.3} \times (1 + Cl\ wt.\%)^{2.2} \times (CCI \times 100)^{-0.9} \times (Cr\ wt.\%)^{-7.8} \times (total\ acidic\ elements)^{-0.9} \times (total\ basic\ elements)^{-8.8} \times e^{-\frac{T-975}{2\times45^2}} \pm 3.6 \quad \text{Eq. 78}$$

where α is assumed to be 1 for the Cl function and y=1.0 for the CCI function.

The Goodness of Fit (i.e., the value of R^2) for Eq. 78 is 0.587, indicating that 58.7% of the laboratory corrosion data fall within one sigma (σ) of the mean of the predicted corrosion rates. The exponent for the Fe wt.% function is negative despite the fact that the corrosion rate is expected to increase with increasing Fe wt.% in the alloy. A negative exponent is likely attributed to the inclusion of the CCI term in which the Fe_2O_3 wt.% in the deposit has been considered. In other words, iron in the alloy would form Fe_2O_3 first upon exposure to the oxidizing coal combustion environments. The Fe_2O_3 would behave as if it were part of the deposit constituent, some of which may convert to $Fe_2(SO_4)_3$. Since plentiful amounts of Fe_2O_3 and $Fe_2(SO_4)_3$ are already present in the deposit, the apparent effect of Fe wt.% in the alloy might have already been accounted for by the CCI function. Another possible explanation is that Fe_2O_3 is a basic oxide, which is capable of neutralizing the basicity (or acidity) of the fused salt during Stage 1 Hot Corrosion prior to scale penetration. As discussed previously, the fused salt at the scale/deposit interface during Stage 1 Hot Corrosion would be relatively acidic due to the formation of SO_3, as illustrated in Figure 283. With the acidic dissolution of Fe_2O_3, which reduces the partial pressure of SO_3 at the scale/deposit interface according to Eq. 36, the salt becomes less acidic and thus results in a reduced concentration gradient according to Figure 281.

As mentioned earlier, given the large number of variables involved in the nonlinear regression analysis, a relatively low Goodness of Fit is expected. Further to the challenge, the bell-shaped curves of the corrosion rates for different alloys were generated at different temperatures under the test environments for only one coal, i.e., OH Mahoning 7A. These bell-shaped curves of different alloys were then assumed to be applicable to those of different coal environments. Obviously, such an assumption is far from ideal because the peak temperature and peak width of the bell-shaped curve for each alloy would change with the coal combustion environment. Without additional testing performed for the alloys under the other coal environments, this assumption was made but has inevitably contributed to the low Goodness of Fit observed significantly. To perform the regression analysis adequately, the corrosion rates of these alloys need to be generated from a laboratory study under the different coal environments as a function of temperature. Only with such additional corrosion data, coal-specific values of *b* and *c* in the Gaussian expression could be determined for the different coals under investigation and consequently, the Goodness of Fit for Eq. 78 would be significantly improved.

5 REFERENCES:

1. J. J. Renton, "*Coal Structure*", Chapter 7, Mineral Matter in Coal, 1982.

2. R. J. Gray and G. F. Moore, "*Burning the Sub-Bituminous Coals of Montana and Wyoming in Large Utility Boilers*", ASME Paper No. 74-WA/FU-1, New York, November 1974.

3. Babcock & Wilcox, "Steam", Chapter 20, *Fuel Ash Effects on Boiler Design and Operation*, 40th Edition, 1992.

4. W. A. Nazeer, "*Species and Temperature Measurements in a Pulverized Coal Controlled Profile with Natural Gas Reburning*." Master's Thesis, Brigham Young University, 1997.

5. W. Leuckel, "*Swirl Intensities, Swirl Types, and Energy Losses of Different Swirl Generating Devices*", IFRF-Doc. No. G02/a/16, Ijmuiden, 1967.

6. B. Damstedt, J. Pederson, D. Hansen, T. Knighton, J. Jones, C. Christensen, L. Baxter, and D. Tree, "*Biomass Cofiring Impacts on Flame Structure and Emissions*," Proceedings of the Combustion Institute, V 31 II, Proceeding of the Combustion Institute – Thirty-First International Symposium on Combustion, 2007b, p 2813-2820.

7. D. R. Tree and A. W. Clark, "*Advanced Reburning Measurements of Temperature and Species in a Pulverized Coal Flame*," Fuel, Vol. 79, pp 1687 – 1695, 2000.

8. W. A. Nazeer, R. E. Jackson, J. A. Peart, and D. R. Tree, "*Detailed Measurements in a Pulverized Coal Flame with Reburning*," Fuel, Vol. 78:6 pp 689-699, 1999.

9. L. M. Pickett, R. E. Jackson, and D. R. Tree "*LDA Measurements in a Pulverized Coal Flame at Three Swirl Ratios*," Combustion Science and Technology, V 143, pp. 79, 1999.

10. L. M. Pickett, R. E. Jackson, and D. R. Tree "*LDA Measurements in a Pulverized Coal Flame at Three Swirl Ratios*," Combustion Science and Technology, V 143, pp. 79, 1999.

11. M. F. Modest, "*Radiative Heat Transfer*," Second Edition. California: Academic Press, 2003.

12. B. Damstedt, "*Structure of Nitrogen Chemistry in Coal, Biomass, and Cofiring Low-NO_X Flames*," Brigham Young University, Ph.D. Dissertation, 2007.

13. S. S. Lokare, J. D. Dunaway, D. Moulton, D. Rogers, D. R. Tree, and L. L. Baxter, "*Investigation of Ash Deposition Rates for a Suite of Biomass Fuels and Fuel Blends*," Energy & Fuels; 20(3); 1008-1014, 2006.

14. T. A. Reeder, D. R. Tree, and S. C. Kung, "*Sulfur Evolution in a Pilot Scale Combustion Facility Burning Pulverized Coal Under Staged Conditions*," The 35th International Technical Conference on Clean Coal and Fuel Systems, June 6-10, Clearwater, Florida, 2010.

15. W. H. Gibb, "*The Nature of Chlorine in Coal and Its Behavior during Combustion*," Corrosion Resistant Materials for Coal Conversion Systems, Ed. D. B. Meadowcroft and M. I. Manning, Ch. 2, 25-45. London: Applied Science Publishers, 1983.

16. F. Clarke and C. W. Morris, "*Combustion Aspects of Furnace Wall Corrosion*," Corrosion Resistant Materials for Coal Conversion Systems, Ed. D. B. Meadowcroft and M. I. Manning, Ch. 3, 47-63. London: Applied Science Publishers, 1983.

17. L. L. Baxter, Personal Communication, 2010.

18. E. Reese and H. J. Grabke, Werkstoffe und Korrosion, 43, (1992), 547-57.

19. M. Spiegel and H. J. Grabke, Materials and Corrosion, 46, (1995), 121-131.

20. H.J. Grabke, E. Reese and M. Spiegel, Molten Salt Forum, Vol. 5-6, (1998), 405-11.

21. H. J. Grabke, "*Kinetics of Interfacial Reactions of Gases on Metals and Oxides*", Proceedings of International Conference on High Temperature Corrosion, NACE (1980), pp. 287-94.

22. M. Knudsen, Ann. Physik., Vol. 29, (1909), p. 179.

23. H. Hertz, Ann. Physik., Vol. 17, (1882), p. 177.

24. S. C. Kung, "*Prediction of Corrosion Rate for Alloys Exposed to Reducing/Sulfidizing Combustion Gases*," Materials Performance, vol. 36, No. 12, pp.36-40, December 1997.

25. R. A. Rapp and Y. S. Zhang, "*Fundamental Studies of Hot Corrosion of Materials*", J. Metals, 1994, vol. 46, pp. 47-55.

26. K. L. Luthra and D. A. Shores, J. Electrochemical Soc., 1980, vol. 127, pp. 2202-10.

27. J. A. Goebel and F. S. Petit, Metall. Trans. 1970, vol.1, pp. 1943-54.

28. R. A. Rapp. Metall. and Mater. Transactions A, 2000, vol. 31A, pp. 2105-18.

29. P. Leblanc and R. A. Rapp, J. Electrochem. Soc.1993, vol. 140, pp. L31-32; ibid. vol. 140, pp. L41-43.

30. R. A. Rapp and K. S. Goto, "*The Hot Corrosion of Metals by Molten Salts*", Molten Salts II, R. Selman and J. Braunstein, Eds., Electrochem. Soc., Princeton (1979) p.159.

31. N. Otsuka and R. A. Rapp, J. Electrochem. Soc., 1990, vol. 137, pp. 46-52.

32. R. A. Rapp and H. N. Otsuka, "*The Role of Chromium in the Hot Corrosion of Metals*", Electrochemical Transactions, (2008).

33. B. B. Ebbinghaus, Combustion and Flame, vol. 101, (1995), pp. 311-338.

34. HSC Chemistry for Windows, Ver. 5.1, Outokumpu, Finland, 2002.

6 CONCULSIONS AND RECOMMENDATIONS

The gas and deposit compositions in the lower furnace of boilers burning eight U.S. coals in staged combustion were characterized in a comprehensive pilot-scale combustion study. These coals contained a wide range of sulfur and chlorine concentrations, constituents which are important to better understanding of furnace wall corrosion. The low-NO_x combustion environments were then implemented in a series of 1000-hour laboratory corrosion tests to evaluate the materials performance of different furnace-wall alloys and weld overlays.

Results of the laboratory tests indicate that a dual-layered scale is formed on the metal surface from simultaneous oxidation/sulfidation due to the presence of sulfur in coal. However, a new corrosion mechanism, "Active Sulfidation," was identified and clarified here to account for the additional attack from coal chlorine in staged coal combustion. The mechanism involves the conversion of FeS in the corrosion scale to $FeCl_2$ vapor by reacting with HCl in the gas phase. Once formed, the $FeCl_2$ vapor diffuses into the porous deposit layer on top of the scale, followed by re-formation of FeS to form sulfide whiskers. Such a $FeCl_2$-assisted corrosion process can significantly accelerate the rate of sulfidation attack. Apparently, the contribution of Active Sulfidation to furnace wall corrosion would be supported by the chlorine content in coal. Such a correlation is consistent with the coal corrosivity observed from this study, especially for low-alloy ferritic steels. When the Cr concentration is increased sufficiently in the alloy, a more protective scale can be produced on the surface upon exposure to the low-NO_x combustion environments, which effectively minimizes the formation of FeS in the scale and decreases the activity of Fe in this sulfide. Consequently, the gas phase transport of $FeCl_2$ vapor by the proposed Active Sulfidation Mechanism is reduced.

The test results from the furnace wall corrosion study indicate that Grade 9 and Grade 91 steels with nearly 9% Cr outperformed the lower-Cr ferritic steels significantly under the low-NO_x combustion conditions employed in this study. The attack of stainless steels and nickel-based weld overlays was governed by oxidation/sulfidation without noticeable contribution from Active Sulfidation. When both the sulfur and chlorine contents in coal are low, the Active Sulfidation Mechanism is also minimized. The proposed mechanism has effectively elucidated and demonstrated the synergistic corrosion attack on furnace walls from staged combustion of coals containing both sulfur and chlorine.

Pilot-scale combustion testing and long-term laboratory corrosion studies have also been performed to determine the corrosion performance of superheater and reheater alloys exposed to the combustion gases of the eight U.S. coals. For the combustion tests, the coals were burned under the conditions of the same heat input to the pilot-scale combustor and 3% excess oxygen in the combustion gases. Similar to the furnace wall corrosion study, extensive online measurements of the combustion gas species were again performed. In addition, deposit samples were collected and analyzed. Information generated from the online gas measurements and deposit analyses allowed the combustion environments adjacent to the superheaters and reheaters of utility boilers burning a wide range of U.S. coals to be well characterized. The gas and deposit compositions were then simulated in a series of 1000-hour laboratory corrosion tests in which the corrosion performance of different alloys and weld overlays was evaluated at 704^{o}C (1300^{o}F).

For OH Mahoning 7A coal, the corrosion test was repeated at additional temperatures, ranging from 1100 to 1500^{o}F (593 to 816^{o}C).

Based on the results of this study, two major, and perhaps competing, corrosion mechanisms have been discovered to operate on the superheaters and reheaters of utility boilers burning coals containing sulfur and/or chloride as impurities. These mechanisms consist of (1) hot corrosion from the presence of a fused salt and (2) the newly proposed Active Sulfide-to-Oxide Corrosion Mechanism involving the formation and cycling reactions of volatile $FeCl_2$. The dominance of one of the two mechanisms is decided by a number of factors, including the relative sulfur and chloride contents in the coal and the ability of an alloy to form a protective scale. Chromium appears to be the most important alloying element in determining the type of scale formed on the alloy surface. At a higher Cr concentration, a more corrosion-resistant chromia scale is formed upon exposure to the coal combustion gases, which prevents the formation of FeS in the scale and thus averts the initiation of rapid corrosion attack via the Active Sulfide-to-Oxide Corrosion Mechanism.

A protective chromia scale can also extend the slower rate of attack from acidic fluxing and re-precipitation in Stage 1 Hot Corrosion prior to local penetration of the scale, thus delaying the more severe attack of Stage 2 Hot Corrosion. On the other hand, when insufficient Cr is present in the alloys, the scale formed is predominantly less-resistant spinel, resulting in rapid corrosion attack by the Active Sulfide-to-Oxide Mechanism in HCl-bearing combustion gases. Even under the conditions in which the partial pressure of HCl is too low to initiate the Active Sulfide-to-Oxide Mechanism, the formation of a spinel scale on an alloy can suffer early penetration by the fused salt during Stage 1 Hot Corrosion, thus subjecting the alloy to a high rate of attack via the basic fluxing and re-precipitation of Stage 2 Hot Corrosion.

For fireside corrosion on superheaters and reheaters, the original project workscope specified one coal (OH Mahoning 7A) to be evaluated at different temperatures, whereas the other seven coals were investigated only at 1300^{o}F (704^{o}C). Such a scope was based on the assumption that the corrosion behaviors of different alloys would be similar in all coal combustion environments. However, as a result of many new findings from this study, it became clear that different corrosion mechanisms operate on different alloys, and the dominant mechanism varies with temperature. Consequently, it is imperative to determine the corrosion behaviors of alloys at different temperatures for each of the eight coal environments. Such data are needed to properly perform modeling of the fireside corrosion for superheater and reheater alloys. It is recommended that such data be generated in future laboratory studies.

7 PUBLICATIONS

A total of eleven technical papers have been published in different journals and/or presented at various international conferences during the performance period of this project. This number of written publications, excluding verbal presentations only, far exceeded the commitment as part of the project deliverables. The publications are:

(1) S. C. Kung, "High-Temperature Corrosion Mechanisms for Iron and Nickel-Based Alloys Exposed to Sulfur and Chlorine-Containing Environments," accepted for publication in the March 2015 issue of CORROSION Journal.

(2) S. C. Kung, "Further Understanding of Furnace Wall Corrosion in Coal-Fired Boilers," CORROSION, Vol. 70 (7), pp. 749-763, 2014. Link to NACE Special Press Release: http://www.nace.org/Newsroom/Press-Releases/New-study-may-enable-improved-materials-selection-for-corrosion-prone-coal-fired-boiler-tubes/

(3) S. C. Kung, "Comparison of Coal-Ash Corrosion of Alloys Exposed to Advanced Air-Coal and Oxy-Coal Combustion Environments," Proc. 7th International A-USC Materials Conference, ASM, January 2014.

(4) C. K. Stimpson, D. R. Brunner, T. A. Reeder, D. R. Tree, R. F. DeVault, and S. C. Kung, "*Analysis of Sulfur in Deposits Collected from the Reducing and Oxidizing Zones of the BFR Burning Eight Coals*," 2012 Spring Technical Meeting of the Western States Section of the Combustion Institute, March 2012.

(5) S. Chamberlain, T. A. Reeder, D. R. Brunner, D. R. Tree, and S. C. Kung, "*Sulfur and Chlorine Gas Species Measurements for a suite of Nine Coals in a Staged Pulverized Coal Reactor*," 2012 Spring Technical Meeting of the Western States Section of the Combustion Institute, March 2012.

(6) S. C. Kung, "*Measurement of Corrosive Gaseous Species in Staged Coal Combustion*," Oxidation of Metals, Vol. 77, pp. 289-304, 2012.

(7) S. C. Kung, "*Online Gas Measurements in a Pilot-Scale Combustion Facility for Fireside Corrosion Study*," Proc. 6th Int'l Conf. on Advances in Materials Technology for Fossil Power Plants, eds. D. Gandy, J. Shingledecker, and R. Viswanathan, pp. 268-287, March 2011.

(8) D. Brunner, D. R. Tree, R F. DeVault, and S. C. Kung**, "***Coal Deposit Composition and Morphology In Reducing and Oxidizing Conditions*," 36th International Technical Conference on Clean Coal & Fuel Systems, Clearwater, FL, 2011.

(9) S. C. Kung, "*Fireside Corrosion Environments in Coal-Fired Utility Boilers,*" 2010 DOE Fossil Energy Materials Conference, Pittsburgh, PA, 2010.

(10) T. Reeder, D. Brunner, C. Stimpson, K. Hill, B. Roper, D. R. Tree, and S. C. Kung, "*Sulfur Evolution in a Pilot-scale Combustion Facility Burning Pulverized Coal under Staged Conditions*," 35th International Technical Conference on Clean Coal & Fuel Systems, Clearwater, FL, 2010.

(11) T. Reeder, David Brunner, C. Stimpson, K. Hill, B. Roper, D. R. Tree, and S. C. Kung, "*Deposit and Gas Phase Corrosion Potential of Three Coals Under Oxidizing and Reducing Conditions*," ASME International Mechanical Engineering Congress and Exposition, Lake Buena Vista, FL, 2009.

8 PRODUCT AND TECHNOLOGY TRANSFER

None.

9 APPENDICES

See attachments.

9.1 Appendix A - Proximate, Ultimate, and Ash Analyses on Eight Model Coals Selected

Proximate and Ultimate Analyses of Illinois #6 Galatia Coal

Proximate Analysis			
	As Received wt%	**Moisture Free wt%**	**MAF Basis wt%**
Moisture	5.40	N/A	N/A
Ash	8.65	9.14	N/A
Volatile Matter	35.68	37.72	41.51
Fixed Carbon	50.27	53.14	58.49
Total	100.00	100.00	100.00
Ultimate Analysis			
Moisture	5.40	N/A	N/A
Hydrogen	3.74	3.95	4.35
Carbon	70.16	74.16	81.62
Nitrogen	1.04	1.10	1.21
Sulfur	2.69	2.84	3.13
Oxygen	8.32	8.81	9.69
Ash	8.65	9.14	N/A
Total	100.00	100.00	100.00
Chloride		0.3892	
Heating Value, Btu/lb	12575	13293	14630

Ash Analysis of Illinois #6 Galatia Coal

Silicon Dioxide, % as SiO2	48.12
Aluminum Oxide, % as Al2O3	19.65
Iron Oxide, % as Fe2O3	17.64
Calcium Oxide, % as CaO	4.28
Magnesium Oxide, % as MgO	0.95
Sodium Oxide, % as Na2O	1.08
Potassium Oxide, % as K2O	2.59
Titanium Dioxide, % as TiO2	1.05
Manganese Dioxide, % as MnO2	0.07
Phosphorus Pentoxide, % as P2O5	0.08
Strontium Oxide, % as SrO	0.03
Barium Oxide, % as BaO	0.05
Sulfur Trioxide, % as SO3	4.41
Alkalies as Na20	2.79
Base to Acid Ratio	0.39
Silica Ratio	0.68
T250, ^{0}F	2429

Proximate and Ultimate Analyses of Pulverized WY PRB Black Thunder Coal

Proximate Analysis			
	As Received wt%	**Moisture Free wt%**	**MAF Basis wt%**
Moisture	24.59	N/A	N/A
Ash	5.14	6.82	N/A
Volatile Matter	37.00	49.07	52.66
Fixed Carbon	33.27	44.11	47.34
Total	100.00	100.00	100.00
Ultimate Analysis			
Moisture	24.59	N/A	N/A
Hydrogen	2.55	3.38	3.63
Carbon	54.75	72.60	77.91
Nitrogen	0.83	1.10	1.18
Sulfur	0.25	0.33	0.35
Oxygen	11.89	15.77	16.93
Ash	5.14	6.82	N/A
Total	100.00	100.00	100.00
Chloride		0.0012	
Heating Value, Btu/lb	9156	12142	13031

Ash Analysis of Pulverized WY PRB Black Thunder Coal

Silicon Dioxide, % as SiO2	36.04
Aluminum Oxide, % as Al2O3	16.84
Iron Oxide, % as Fe2O3	5.86
Calcium Oxide, % as CaO	21.61
Magnesium Oxide, % as MgO	5.06
Sodium Oxide, % as Na2O	1.69
Potassium Oxide, % as K2O	0.50
Titanium Dioxide, % as TiO2	1.32
Manganese Dioxide, % as MnO2	0.02
Phosphorus Pentoxide, % as P2O5	1.00
Strontium Oxide, % as SrO	0.35
Barium Oxide, % as BaO	0.62
Sulfur Trioxide, % as SO3	9.09
Alkalies as Na20	2.02
Base to Acid Ratio	0.64
Silica Ratio	0.53
T250, ^{0}F	2228

Proximate and Ultimate Analyses of Pulverized ND Beulah-Zap Lignite Coal

Proximate Analysis			
	As Received wt%	**Moisture Free wt%**	**MAF Basis wt%**
Moisture	27.33	N/A	N/A
Ash	8.66	11.92	N/A
Volatile Matter	33.77	46.47	52.76
Fixed Carbon	30.24	41.61	47.24
Total	100.00	100.00	100.00
Ultimate Analysis			
Moisture	27.33	N/A	N/A
Hydrogen	2.03	2.79	3.17
Carbon	46.56	64.07	72.74
Nitrogen	0.86	1.18	1.34
Sulfur	0.67	0.92	1.04
Oxygen	13.89	19.12	21.71
Ash	8.66	11.92	N/A
Total	100.00	100.00	100.00
Chloride		0.001	
Heating Value, Btu/lb	7792	10772	12173

Ash Analysis of Pulverized ND Beulah-Zap Lignite Coal

Silicon Dioxide, % as SiO2	32.25
Aluminum Oxide, % as Al2O3	12.23
Iron Oxide, % as Fe2O3	7.45
Calcium Oxide, % as CaO	19.91
Magnesium Oxide, % as MgO	6.47
Sodium Oxide, % as Na2O	3.29
Potassium Oxide, % as K2O	0.82
Titanium Dioxide, % as TiO2	0.65
Manganese Dioxide, % as MnO2	0.08
Phosphorus Pentoxide, % as P2O5	0.27
Strontium Oxide, % as SrO	0.64
Barium Oxide, % as BaO	0.73
Sulfur Trioxide, % as SO3	15.21
Alkalies as Na20	3.83
Base to Acid Ratio	0.84
Silica Ratio	0.49
T250, ^{0}F	2130

Proximate and Ultimate Analyses of Pulverized OH Mahoning 7A Coal

Proximate Analysis			
	As Received wt%	**Moisture Free wt%**	**MAF Basis wt%**
Moisture	2.22	N/A	N/A
Ash	9.92	10.15	N/A
Volatile Matter	40.79	41.72	46.43
Fixed Carbon	47.07	48.13	53.57
Total	100.00	100.00	100.00
Ultimate Analysis			
Moisture	2.22	N/A	N/A
Hydrogen	4.18	4.27	4.75
Carbon	74.67	76.37	85.00
Nitrogen	0.93	0.95	1.06
Sulfur	1.96	2.00	2.23
Oxygen	6.12	6.26	6.96
Ash	9.92	10.15	N/A
Total	100.00	100.00	100.00
Chloride		0.1989	
Heating Value, Btu/lb	13404	13708	15257

Ash Analysis of Pulverized OH Mahoning 7A Coal

Silicon Dioxide, % as SiO2	42.65
Aluminum Oxide, % as Al2O3	29.07
Iron Oxide, % as Fe2O3	20.45
Calcium Oxide, % as CaO	1.76
Magnesium Oxide, % as MgO	0.52
Sodium Oxide, % as Na2O	0.34
Potassium Oxide, % as K2O	1.61
Titanium Dioxide, % as TiO2	1.41
Manganese Dioxide, % as MnO2	0.00
Phosphorus Pentoxide, % as P2O5	0.76
Strontium Oxide, % as SrO	0.12
Barium Oxide, % as BaO	0.07
Sulfur Trioxide, % as SO3	1.24
Alkalies as Na20	1.40
Base to Acid Ratio	0.34
Silica Ratio	0.65
T250, ^{0}F	2497

Proximate and Ultimate Analyses of Pulverized Indiana #6 Coal

Proximate Analysis			
	As Received wt%	**Moisture Free wt%**	**MAF Basis wt%**
Moisture	7.25	N/A	N/A
Ash	7.20	7.76	N/A
Volatile Matter	30.87	33.28	36.08
Fixed Carbon	54.68	58.95	63.92
Total	100.00	100.00	100.00
Ultimate Analysis			
Moisture	7.25	N/A	N/A
Hydrogen	4.02	4.33	4.70
Carbon	69.48	74.91	81.22
Nitrogen	1.36	1.47	1.59
Sulfur	1.14	1.23	1.33
Oxygen	9.55	10.30	11.16
Ash	7.20	7.76	N/A
Total	100.00	100.00	100.00
Chloride		0.2121	
Heating Value, Btu/lb	12400	13369	14494

Ash Analysis of Pulverized Indiana #6 Coal

Silicon Dioxide, % as SiO2	55.14
Aluminum Oxide, % as Al2O3	21.10
Iron Oxide, % as Fe2O3	12.93
Calcium Oxide, % as CaO	2.48
Magnesium Oxide, % as MgO	0.86
Sodium Oxide, % as Na2O	1.25
Potassium Oxide, % as K2O	2.40
Titanium Dioxide, % as TiO2	1.30
Manganese Dioxide, % as MnO2	0.03
Phosphorus Pentoxide, % as P2O5	0.35
Strontium Oxide, % as SrO	0.08
Barium Oxide, % as BaO	0.06
Sulfur Trioxide, % as SO3	2.02
Alkalies as Na20	2.83
Base to Acid Ratio	0.26
Silica Ratio	0.77
T250, ^{0}F	2624

Proximate and Ultimate Analyses of Pulverized OH Gatling Coal

Proximate Analysis			
	As Received wt%	**Moisture Free wt%**	**MAF Basis wt%**
Moisture	3.77	N/A	N/A
Ash	11.34	11.78	N/A
Volatile Matter	40.73	42.33	47.98
Fixed Carbon	44.16	45.89	52.02
Total	100.00	100.00	100.00
Ultimate Analysis			
Moisture	3.77	N/A	N/A
Hydrogen	4.07	4.23	4.79
Carbon	67.11	69.74	79.05
Nitrogen	0.94	0.98	1.11
Sulfur	4.31	4.48	5.08
Oxygen	8.46	8.79	9.97
Ash	11.34	11.78	N/A
Total	100.00	100.00	100.00
Chloride		0.0387	
Heating Value, Btu/lb	12191	12669	14361

Ash Analysis of Pulverized OH Gatling Coal

Silicon Dioxide, % as SiO2	40.35
Aluminum Oxide, % as Al2O3	22.56
Iron Oxide, % as Fe2O3	28.33
Calcium Oxide, % as CaO	2.62
Magnesium Oxide, % as MgO	0.69
Sodium Oxide, % as Na2O	0.41
Potassium Oxide, % as K2O	1.28
Titanium Dioxide, % as TiO2	1.04
Manganese Dioxide, % as MnO2	0.05
Phosphorus Pentoxide, % as P2O5	0.22
Strontium Oxide, % as SrO	0.09
Barium Oxide, % as BaO	0.11
Sulfur Trioxide, % as SO3	2.25
Alkalies as Na20	1.25
Base to Acid Ratio	0.52
Silica Ratio	0.56
T250, ^{0}F	2295

Proximate and Ultimate Analyses of Pulverized Kentucky #11 Coal

Proximate Analysis			
	As Received wt%	**Moisture Free wt%**	**MAF Basis wt%**
Moisture	3.39	N/A	N/A
Ash	8.46	8.76	N/A
Volatile Matter	36.97	38.27	41.94
Fixed Carbon	70.89	73.38	80.42
Total	100.00	100.00	100.00
Ultimate Analysis			
Moisture	3.39	N/A	N/A
Hydrogen	4.34	4.49	4.92
Carbon	70.89	73.38	80.42
Nitrogen	1.23	1.27	1.40
Sulfur	3.64	3.77	4.13
Oxygen	8.05	8.33	9.13
Ash	8.46	8.76	N/A
Total	100.00	100.00	100.00
Chloride		0.2057	
Heating Value, Btu/lb	12905	13358	14640

Ash Analysis of Pulverized Kentucky #11 Coal

Silicon Dioxide, % as SiO2	41.70
Aluminum Oxide, % as Al2O3	18.40
Iron Oxide, % as Fe2O3	26.09
Calcium Oxide, % as CaO	4.80
Magnesium Oxide, % as MgO	0.90
Sodium Oxide, % as Na2O	0.53
Potassium Oxide, % as K2O	2.43
Titanium Dioxide, % as TiO2	0.96
Manganese Dioxide, % as MnO2	0.03
Phosphorus Pentoxide, % as P2O5	0.31
Strontium Oxide, % as SrO	0.05
Barium Oxide, % as BaO	0.18
Sulfur Trioxide, % as SO3	3.62
Alkalies as Na20	2.13
Base to Acid Ratio	0.57
Silica Ratio	0.57
T250, ^{0}F	2263

Proximate and Ultimate Analyses of Pulverized Pittsburgh #8 Coal

Proximate Analysis			
	As Received wt%	**Moisture Free wt%**	**MAF Basis wt%**
Moisture	1.05	N/A	N/A
Ash	10.45	10.56	N/A
Volatile Matter	18.61	18.81	21.03
Fixed Carbon	69.89	70.63	78.97
Total	100.00	100.00	100.00
Ultimate Analysis			
Moisture	1.05	N/A	N/A
Hydrogen	3.86	3.90	4.36
Carbon	77.37	78.19	87.42
Nitrogen	1.44	1.46	1.63
Sulfur	1.03	1.04	1.16
Oxygen	4.80	4.85	5.42
Ash	10.45	10.56	N/A
Total	100.00	100.00	100.00
Chloride		0.0045	
Heating Value, Btu/lb	13715	13861	15497

Ash Analysis of Pulverized Pittsburgh #8 Coal

Silicon Dioxide, % as SiO2	56.77
Aluminum Oxide, % as Al2O3	29.28
Iron Oxide, % as Fe2O3	6.63
Calcium Oxide, % as CaO	0.90
Magnesium Oxide, % as MgO	0.56
Sodium Oxide, % as Na2O	0.65
Potassium Oxide, % as K2O	2.30
Titanium Dioxide, % as TiO2	1.53
Manganese Dioxide, % as MnO2	0.05
Phosphorus Pentoxide, % as P2O5	0.56
Strontium Oxide, % as SrO	0.12
Barium Oxide, % as BaO	0.12
Sulfur Trioxide, % as SO3	0.53
Alkalies as Na20	2.17
Base to Acid Ratio	0.13
Silica Ratio	0.88
T250, ^{0}F	> 2900

9.2 Appendix B - Chemical Analyses of Probe Deposit Samples Collected from the BFR Burning Eight Model Coals

Sample Description: Furnace Probe Deposit, Illinois #6, Galatia, Oxidizing, Top, Position 4

REPORT of ANALYSIS
(Powdered X-ray Semi-quantitative)

Sum before normalization:	95.50%
Normalised to:	100.00%
Sample type:	Pressed powder
Correction applied for medium:	No
Correction applied for film:	None
Used Compound list:	OXIDES
Results database:	iq+ 4kw 27mm
LECO Carbon	0.32
LOI	0.32

Analyte	Compound	Weight %	As Received Weight %	LECO S as SO3
<As>	As2O3	Fixed	-	
Na	Na2O	1.12	1.11	
Mg	MgO	0.90	0.89	
Al	Al2O3	20.99	20.92	
Si	SiO2	47.23	47.08	
P	P2O5	0.10	0.10	
S	SO3	2.67	2.66	2.88
K	K2O	2.05	2.04	
Ca	CaO	4.09	4.08	
Ti	TiO2	0.78	0.77	
Cr	Cr2O3	0.07	0.07	
Mn	MnO	0.05	0.05	
Fe	Fe2O3	19.68	19.62	
Co	Co3O4	0.02	0.02	
Ni	NiO	0.01	0.01	
Cu	CuO	0.02	0.02	
Zn	ZnO	0.04	0.04	
Rb	Rb2O	0.02	0.02	
Sr	SrO	0.10	0.09	
Y	Y2O3	0.00	0.00	
Ce	CeO2	0.03	0.03	
Pb	PbO	0.02	0.02	
U	U3O8	0.03	0.03	
Total		100.00		

Notes:
1. This analysis represents specifically the sample submitted.
2. Sample results reported on an as received weight basis.
3. Oxide analysis by X-ray fluorescence spectrometry using PANalytical IQ+ Quantification program.
4. This report may not be reproduced except in its entirety.

Sample Description: Furnace Probe Deposit, Illinois #6, Galatia, Reducing, Top, Position 4

REPORT of ANALYSIS

(Powdered X-ray Semi-quantitative)

Sum before normalization:	69.30%
Normalised to:	100.00%
Sample type:	Pressed powder
Correction applied for medium:	Yes
Correction applied for film:	1.00
Used Compound list:	OXIDES
LECO Carbon	26.95
LOI	26.95

Analyte	Compound	Weight % (%)	As Received Weight %
Na	Na2O	2.76	2.01
Mg	MgO	1.17	0.86
Al	Al2O3	18.52	13.53
Si	SiO2	41.85	30.57
P	P2O5	0.96	0.70
S	SO3	15.90	11.62
K	K2O	3.95	2.88
Ca	CaO	3.98	2.91
Ti	TiO2	0.70	0.51
Cr	Cr2O3	0.11	0.08
Mn	MnO	0.05	0.03
Fe	Fe2O3	9.69	7.07
Ni	NiO	0.07	0.05
Cu	CuO	0.07	0.05
Zn	ZnO	0.19	0.14
Cl	Cl	0.05	0.04
	Total	100.00	

Notes:
1. This analysis represents specifically the sample submitted.
2. Sample results reported on an as received weight basis.
3. Oxide analysis by X-ray fluorescence spectrometry using PANalytical IQ+ Quantification program.
4. This report may not be reproduced except in its entirety.

Sample Description: Furnace Probe Deposit, PRB, Black Thunder, Oxidizing, Top, Position 3

REPORT of ANALYSIS
(Powdered X-ray Semi-quantitative)

Sum before normalization:	77.60%
Normalised to:	100.00%
Sample type:	Pressed powder
Correction applied for medium:	No
Correction applied for film:	None
Used Compound list:	OXIDES
Results database:	iq+ 4kw 27mm
LECO Carbon	1.08
LOI	1.08

Analyte	Compound	Weight %	As Received Weight %
Na	Na2O	2.36	2.34
Mg	MgO	4.71	4.66
Al	Al2O3	17.84	17.64
Si	SiO2	32.52	32.17
P	P2O5	1.53	1.52
S	SO3	11.15	11.03
K	K2O	0.59	0.59
Ca	CaO	21.16	20.93
Ti	TiO2	1.31	1.30
Cr	Cr2O3	0.12	0.11
Mn	MnO	0.08	0.08
Fe	Fe2O3	5.37	5.31
Ni	NiO	0.02	0.02
Cu	CuO	0.03	0.03
Zn	ZnO	0.34	0.34
Sr	SrO	0.10	0.10
Zr	ZrO2	0.03	0.03
Ba	BaO	0.75	0.74
	Total	100.00	

Notes:
1. This analysis represents specifically the sample submitted.
2. Sample results reported on an as received weight basis.
3. Oxide analysis by X-ray fluorescence spectrometry using PANalytical IQ+ Quantification program.
4. This report may not be reproduced except in its entirety.

Sample Description: Furnace Probe Deposit, PRB, Black Thunder, Reducing, Top, Position 3

REPORT of ANALYSIS
(Powdered X-ray Semi-quantitative)

Sum before normalization:	67.70%
Normalised to:	100.00%
Sample type:	Pressed powder
Correction applied for medium:	No
Correction applied for film:	None
Used Compound list:	OXIDES
Results database:	iq+ 4kw 27mm
LECO Carbon	16.00
LOI	16.00

Analyte	Compound	Weight %	As Received Weight %
Na	Na2O	2.46	2.06
Mg	MgO	5.92	4.97
Al	Al2O3	20.28	17.04
Si	SiO2	32.78	27.53
P	P2O5	1.50	1.26
S	SO3	1.79	1.50
K	K2O	0.31	0.26
Ca	CaO	25.19	21.16
Ti	TiO2	1.60	1.34
Cr	Cr2O3	0.09	0.08
Mn	MnO	0.03	0.03
Fe	Fe2O3	7.67	6.44
Ni	NiO	0.05	0.04
Cu	CuO	0.03	0.03
Zn	ZnO	0.03	0.02
Ga	Ga2O3	0.01	0.01
Sr	SrO	0.13	0.10
Zr	ZrO2	0.04	0.04
Ba	BaO	0.10	0.08
Total		100.00	

Notes:
1. This analysis represents specifically the sample submitted.
2. Sample results reported on an as received weight basis.
3. Oxide analysis by X-ray fluorescence spectrometry using PANalytical IQ+ Quantification program.
4. This report may not be reproduced except in its entirety.

Sample Description: Furnace Probe Deposit, Beulah-Zap Lignite, Oxidizing, Top, Position 4

REPORT of ANALYSIS
(Powdered X-ray Semi-quantitative)

Sum before normalization:	85.70%
Normalised to:	100.00%
Sample type:	Pressed powder
Correction applied for medium:	No
Correction applied for film:	None
Used Compound list:	OXIDES
Results database:	iq+ 4kw 27mm
LECO Carbon	0.05
LOI	3.25

Analyte	Compound	Weight %	As Received Weight %
Na	Na2O	2.95	2.85
Mg	MgO	4.30	4.16
Al	Al2O3	12.34	11.94
Si	SiO2	31.74	30.71
P	P2O5	0.28	0.27
S	SO3	20.32	19.66
K	K2O	0.97	0.94
Ca	CaO	16.43	15.90
Ti	TiO2	0.69	0.67
Cr	Cr2O3	0.03	0.03
Mn	MnO	0.06	0.06
Fe	Fe2O3	9.24	8.94
Cu	CuO	0.04	0.04
Zn	ZnO	0.08	0.08
Sr	SrO	0.27	0.26
Zr	ZrO2	0.02	0.02
Ag	Ag2O	0.02	0.02
Cd	CdO	0.09	0.09
Sb	Sb2O3	0.03	0.03
Ba	BaO	0.11	0.10
Cl	Cl	0.01	0.01
	Total	100.00	

Notes:
1. This analysis represents specifically the sample submitted.
2. Sample results reported on an as received weight basis.
3. Oxide analysis by X-ray fluorescence spectrometry using PANalytical IQ+ Quantification program.
4. This report may not be reproduced except in its entirety.

Sample Description: Furnace Probe Deposit, Beulah-Zap Lignite, Reducing, Top, Position 4

REPORT of ANALYSIS
(Powdered X-ray Semi-quantitative)

Sum before normalization:	85.30%
Normalised to:	100.00%
Sample type:	Pressed powder
Correction applied for medium:	No
Correction applied for film:	None
Used Compound list:	OXIDES
Results database:	iq+ 4kw 27mm
LECO Carbon	1.02
LOI	2.15

Analyte	Compound	Weight %	As Received Weight %
Na	Na2O	5.72	5.60
Mg	MgO	7.29	7.13
Al	Al2O3	16.27	15.92
Si	SiO2	32.95	32.24
P	P2O5	0.37	0.36
S	SO3	3.12	3.06
K	K2O	1.30	1.27
Ca	CaO	22.95	22.45
Ti	TiO2	0.85	0.83
Cr	Cr2O3	0.05	0.05
Mn	MnO	0.06	0.06
Fe	Fe2O3	8.39	8.21
Ni	NiO	0.02	0.02
Cu	CuO	0.04	0.04
Zn	ZnO	0.09	0.09
Ga	Ga2O3	0.01	0.01
As	As2O3	0.01	0.01
Rb	Rb2O	0.02	0.01
Sr	SrO	0.37	0.36
Ba	BaO	0.13	0.12
Cl	Cl	0.02	0.02
	Total	100.00	

Notes:
1. This analysis represents specifically the sample submitted.
2. Sample results reported on an as received weight basis.
3. Oxide analysis by X-ray fluorescence spectrometry using PANalytical IQ+ Quantification program.
4. This report may not be reproduced except in its entirety.

Sample Description: Furnace Probe Deposit, Mahoning 7A, Oxidizing, Top, Position 3

REPORT of ANALYSIS
(Powdered X-ray Semi-quantitative)

Sum before normalization:	80.20%
Normalised to:	100.00%
Sample type:	Pressed powder
Correction applied for medium:	No
Correction applied for film:	None
Used Compound list:	OXIDES
LECO Carbon	0.45
LOI	0.45

Analyte	Compound	Weight %	As Received Weight %
Na	Na2O	0.625	0.62
Mg	MgO	0.553	0.55
Al	Al2O3	32.467	32.32
Si	SiO2	43.793	43.60
P	P2O5	0.821	0.82
S	SO3	1.635	1.63
K	K2O	1.644	1.64
Ca	CaO	1.702	1.69
Ti	TiO2	1.190	1.18
Cr	Cr2O3	0.369	0.37
Mn	MnO	0.075	0.07
Fe	Fe2O3	14.912	14.84
Ni	NiO	0.021	0.02
Cu	CuO	0.056	0.06
Zn	ZnO	0.023	0.02
As	As2O3	0.056	0.06
Sr	SrO	0.028	0.03
Pb	PbO	0.031	0.03
	Total	100.00	

Notes:
1. This analysis represents specifically the sample submitted.
2. Sample results reported on an as received weight basis.
3. Oxide analysis by X-ray fluorescence spectrometry using PANalytical IQ+ Quantification program.
4. This report may not be reproduced except in its entirety.

Sample Description: Furnace Probe Deposit, Mahoning 7A, Reducing, Top, Position 4

REPORT of ANALYSIS
(Powdered X-ray Semi-quantitative)

Sum before normalization:	96.70%
Normalised to:	100.00%
Sample type:	Pressed powder
Correction applied for medium:	No
Correction applied for film:	None
Used Compound list:	OXIDES
LECO Carbon	2.14%
LOI	2.14

Analyte	Compound	Weight %	As Received Weight %
Na	Na2O	0.758	0.74
Pb	PbO	0.031	0.03
Mg	MgO	0.424	0.41
Al	Al2O3	27.512	26.92
Si	SiO2	37.270	36.47
P	P2O5	0.847	0.83
S	SO3	0.784	0.77
K	K2O	2.369	2.32
Ca	CaO	1.426	1.40
Ti	TiO2	1.143	1.12
Cr	Cr2O3	0.861	0.84
Mn	MnO	0.151	0.15
Fe	Fe2O3	25.507	24.96
Co	Co3O4	0.032	0.03
Ni	NiO	0.192	0.19
Cu	CuO	0.092	0.09
Zn	ZnO	0.255	0.25
Ga	Ga2O3	0.029	0.03
Ge	GeO2	0.063	0.06
As	As2O3	0.012	0.01
Rb	Rb2O	0.012	0.01
Sr	SrO	0.070	0.07
Y	Y2O3	0.005	0.00
Zr	ZrO2	0.027	0.03
Mo	MoO3	0.049	0.05
Ba	BaO	0.040	0.04
Ce	CeO2	0.041	0.04
Total		100.00	97.86

Notes:
1. This analysis represents specifically the sample submitted.
2. Sample results reported on an as received weight basis.
3. Oxide analysis by X-ray fluorescence spectrometry using PANalytical IQ+ Quantification program.
4. This report may not be reproduced except in its entirety.

Sample Description: Furnace Probe Deposit, Indiana #6, Gibson, Oxidizing, Top, Position 3

REPORT of ANALYSIS
(Powdered X-ray Semi-quantitative)

Sum before normalization:	83.10%
Normalised to:	100.00%
Sample type:	Pressed powder
Correction applied for medium:	No
Correction applied for film:	None
Used Compound list:	OXIDES
LECO Carbon	0.07
LOI	0.07

Analyte	Compound	Weight % (%)	As Received Weight %
Na	Na2O	1.15	1.15
Mg	MgO	0.88	0.88
Al	Al2O3	24.46	24.45
Si	SiO2	50.77	50.73
P	P2O5	0.47	0.47
S	SO3	1.39	1.39
K	K2O	2.31	2.31
Ca	CaO	2.64	2.64
Ti	TiO2	1.11	1.11
Cr	Cr2O3	0.17	0.17
Mn	MnO	0.09	0.09
Fe	Fe2O3	14.31	14.30
Zn	ZnO	0.04	0.04
Sr	SrO	0.05	0.05
Pb	PbO	0.15	0.15
	Total	100.00	

Notes:
1. This analysis represents specifically the sample submitted.
2. Sample results reported on an as received weight basis.
3. Oxide analysis by X-ray fluorescence spectrometry using PANalytical IQ+ Quantification program.
4. This report may not be reproduced except in its entirety.

Sample Description: Furnace Probe Deposit, Indiana #6, Gibson, Reducing, Top, Position 4

REPORT of ANALYSIS
(Powdered X-ray Semi-quantitative)

Sum before normalization:	58.80%
Normalised to:	100.00%
Sample type:	Pressed powder
Correction applied for medium:	No
Correction applied for film:	None
Used Compound list:	OXIDES
LECO Carbon	26.91
LOI	26.91

Analyte	Compound	Weight % (%)	As Received Weight %
Na	Na2O	1.39	1.01
Mg	MgO	0.45	0.33
Al	Al2O3	20.98	15.33
Si	SiO2	47.27	34.55
P	P2O5	0.35	0.25
S	SO3	6.85	5.01
K	K2O	4.27	3.12
Ca	CaO	2.54	1.86
Ti	TiO2	1.33	0.97
Cr	Cr2O3	0.12	0.09
Mn	MnO	0.03	0.02
Fe	Fe2O3	13.55	9.91
Ni	NiO	0.05	0.03
Cu	CuO	0.04	0.03
Zn	ZnO	0.36	0.26
Ge	GeO2	0.15	0.11
As	As2O3	0.04	0.03
Sr	SrO	0.02	0.01
Zr	ZrO2	0.05	0.04
Ce	CeO2	0.05	0.04
Pb	PbO	0.09	0.07
Cl	Cl	0.02	0.01
Total		100.00	

Notes:
1. This analysis represents specifically the sample submitted.
2. Sample results reported on an as received weight basis.
3. Oxide analysis by X-ray fluorescence spectrometry using PANalytical IQ+ Quantification program.
4. This report may not be reproduced except in its entirety.

Sample Description: Furnace Probe Deposit, Gatling Mine Coal, Oxidizing, Top, Position 4

REPORT of ANALYSIS

(Powdered X-ray Semi-quantitative)

Sum before normalization:	97.50%
Normalised to:	100.00%
Sample type:	Pressed powder
Correction applied for medium:	No
Correction applied for film:	None
Used Compound list:	OXIDES
Results database:	iq+ 4kw 27mm
LECO Carbon	0.21
LOI	0.21

Analyte	Compound	Weight %	As Received Weight %	LECO S as SO3
Na	Na2O	0.35	0.35	
Mg	MgO	0.38	0.38	
Al	Al2O3	24.95	24.90	
Si	SiO2	39.67	39.58	
P	P2O5	0.15	0.15	
S	SO3	2.50	2.49	3.86
K	K2O	2.14	2.14	
Ca	CaO	2.02	2.01	
Ti	TiO2	0.77	0.77	
Mn	MnO	0.05	0.05	
Fe	Fe2O3	26.10	26.04	
Ni	NiO	0.05	0.04	
Cu	CuO	0.16	0.16	
Zn	ZnO	0.38	0.38	
Ge	GeO2	0.01	0.01	
Rb	Rb2O	0.00	0.00	
Sr	SrO	0.04	0.04	
Y	Y2O3	0.01	0.00	
Zr	ZrO2	0.02	0.01	
Ag	Ag2O	0.07	0.06	
Cd	CdO	0.08	0.08	
Ce	CeO2	0.06	0.05	
Pb	PbO	0.06	0.06	
Cl	Cl	0.01	0.01	
Total		100.00		

Notes:
1. This analysis represents specifically the sample submitted.
2. Sample results reported on an as received weight basis.
3. Oxide analysis by X-ray fluorescence spectrometry using PANalytical IQ+ Quantification program.
4. This report may not be reproduced except in its entirety.

Sample Description: Furnace Probe Deposit, Gatling Mine Coal, Reducing, Top, Position 3

REPORT of ANALYSIS

(Powdered X-ray Semi-quantitative)

Sum before normalization:	59.40%
Normalised to:	100.00%
Sample type:	Pressed powder
Correction applied for medium:	No
Correction applied for film:	None
Used Compound list:	OXIDES
Results database:	iq+ 4kw 27mm
LECO Carbon	30.79
LOI	30.79

Analyte	Compound	Weight %	As Received Weight %	LECO S as SO3
Na	Na2O	0.32	0.22	
Mg	MgO	0.32	0.22	
Al	Al2O3	21.09	14.59	
Si	SiO2	35.77	24.76	
P	P2O5	0.19	0.13	
S	SO3	21.54	14.91	19.47
K	K2O	1.45	1.01	
Ca	CaO	2.19	1.52	
Ti	TiO2	0.78	0.54	
Cr	Cr2O3	0.08	0.06	
Mn	MnO	0.03	0.02	
Fe	Fe2O3	15.61	10.81	
Ni	NiO	0.44	0.30	
Zn	ZnO	0.11	0.08	
Sr	SrO	0.02	0.01	
Pb	PbO	0.02	0.02	
Cl	Cl	0.04	0.03	

Total	100.00

Notes:
1. This analysis represents specifically the sample submitted.
2. Sample results reported on an as received weight basis.
3. Oxide analysis by X-ray fluorescence spectrometry using PANalytical IQ+ Quantification program.
4. This report may not be reproduced except in its entirety.

Sample Description: Furnace Probe Deposit, Kentucky #11, Oxidizing, Top, Position 4

REPORT of ANALYSIS

(Powdered X-ray Semi-quantitative)

Sum before normalization:	95.90%
Normalised to:	100.00%
Sample type:	Pressed powder
Correction applied for medium:	No
Correction applied for film:	None
Used Compound list:	OXIDES

LOI	0.84
LECO Carbon	0.08
LECO S as SO3	4.7

Analyte	Compound	Weight %	As Received Weight %
Na	Na2O	0.53	0.53
Mg	MgO	0.84	0.83
Al	Al2O3	18.66	18.50
Si	SiO2	38.04	37.72
P	P2O5	0.53	0.53
S	SO3	4.62	4.58
K	K2O	1.93	1.91
Ca	CaO	5.03	4.99
Ti	TiO2	0.66	0.66
Cr	Cr2O3	0.44	0.44
Mn	MnO	0.08	0.08
Fe	Fe2O3	26.56	26.34
Ni	NiO	0.07	0.07
Cu	CuO	0.21	0.21
Zn	ZnO	0.78	0.78
Rb	Rb2O	0.01	0.01
Sr	SrO	0.02	0.02
Zr	ZrO2	0.02	0.02
Ag	Ag2O	0.19	0.18
Cd	CdO	0.70	0.69
Ba	BaO	0.08	0.08
Total		100.00	100.00

Notes:

1. This analysis represents specifically the sample submitted.
2. Sample results reported on an as received weight basis.
3. Oxide analysis by X-ray fluorescence spectrometry using PANalytical IQ+ Quantification program.
4. "Overlap" indicates interfering elements are present. The percent analyte could not be estimated.
5. This report may not be reproduced except in its entirety.

Sample Description: Furnace Probe Deposit, Kentucky #11, Reducing, Bottom, Position 3

REPORT of ANALYSIS
(Powdered X-ray Semi-quantitative)

Sum before normalization:	70.20%
Normalised to:	100.00%
Sample type:	Pressed powder
Correction applied for medium:	No
Correction applied for film:	None
Used Compound list:	OXIDES

LOI		15.1	
LECO Carbon		15.6	
LECO Sulfur as SO3		6.3	As Received
Analyte	Compound	Weight %	Weight %
Na	Na2O	1.22	1.03
Mg	MgO	0.77	0.66
Al	Al2O3	20.55	17.45
Si	SiO2	41.79	35.49
P	P2O5	0.28	0.24
S	SO3	7.83	6.65
K	K2O	3.52	2.99
Ca	CaO	3.51	2.98
Ti	TiO2	1.07	0.91
Cr	Cr2O3	0.44	0.37
Mn	MnO	0.06	0.05
Fe	Fe2O3	17.90	15.21
Ni	NiO	0.14	0.12
Cu	CuO	0.04	0.04
Zn	ZnO	0.75	0.63
Ge	GeO2	0.06	0.05
As	As2O3	0.02	0.01
Rb	Rb2O	0.01	0.01
Sr	SrO	0.02	0.01
Zr	ZrO2	0.01	0.01
Cl	Cl	0.01	0.01
Total		100.00	100.00

Notes:
1. This analysis represents specifically the sample submitted.
2. Sample results reported on an as received weight basis.
3. Oxide analysis by X-ray fluorescence spectrometry using PANalytical IQ+ Quantification program.
4. "Overlap" indicates interfering elements are present. The percent analyte could not be estimated.
5. This report may not be reproduced except in its entirety.

Sample Description: Furnace Probe Deposit, Pittsburgh #8, Oxidizing, Top, Position 3

REPORT of ANALYSIS

(Powdered X-ray Semi-quantitative)

Sum before normalization:	80.20%
Normalised to:	100.00%
Sample type:	Pressed powder
Correction applied for medium:	Yes
Correction applied for film:	1.00
Used Compound list:	OXIDES
LOI	2.63
LECO C	2.1

Analyte	Compound	Weight %	As Received Weight %
Na	Na2O	1.04	1.01
Mg	MgO	0.51	0.49
Al	Al2O3	30.77	29.96
Si	SiO2	47.87	46.61
P	P2O5	1.39	1.35
S	SO3	0.54	0.53
K	K2O	1.81	1.77
Ca	CaO	0.96	0.93
Ti	TiO2	1.34	1.30
Cr	Cr2O3	1.06	1.03
Mn	MnO	0.11	0.11
Fe	Fe2O3	12.20	11.88
Co	Co3O4	0.02	0.02
Ni	NiO	0.13	0.13
Cu	CuO	0.03	0.03
Zn	ZnO	0.03	0.03
Ga	Ga2O3	0.01	0.01
As	As2O3	0.01	0.01
Rb	Rb2O	0.01	0.01
Sr	SrO	0.05	0.05
Zr	ZrO2	0.03	0.03
Ba	BaO	0.05	0.05
Ce	CeO2	0.04	0.04
Pb	PbO	0.02	0.02
Total		100.00	100.00

Notes:
1. This analysis represents specifically the sample submitted.
2. Sample results reported on an as received weight basis.
3. Oxide analysis by X-ray fluorescence spectrometry using PANalytical IQ+ Quantification program.
4. "Overlap" indicates interfering elements are present. The percent analyte could not be estimated.
5. This report may not be reproduced except in its entirety.

Sample Description: Furnace Probe Deposit, Pittsburgh #8, Reducing, Top, Position 3

REPORT of ANALYSIS

(Powdered X-ray Semi-quantitative)

Sum before normalization:	43.00%
Normalised to:	100.00%
Sample type:	Pressed powder
Correction applied for medium:	Yes
Correction applied for film:	1.00
Used Compound list:	OXIDES

LOI		71.96	
LECO C		59.1	
LECO S		1.5	As Received
Analyte	Compound	Weight %	Weight %
Mg	MgO	0.44	0.12
Al	Al2O3	22.81	6.40
Si	SiO2	42.54	11.93
P	P2O5	1.90	0.53
S	SO3	13.70	3.84
K	K2O	2.48	0.70
Ca	CaO	1.41	0.40
Ti	TiO2	1.96	0.55
Cr	Cr2O3	0.09	0.03
Fe	Fe2O3	11.93	3.35
Ni	NiO	0.08	0.02
Cu	CuO	0.04	0.01
Zn	ZnO	0.33	0.09
Ga	Ga2O3	0.02	0.01
Ge	GeO2	0.01	0.00
As	As2O3	0.07	0.02
Rb	Rb2O	0.01	0.00
Sr	SrO	0.07	0.02
Y	Y2O3	0.01	0.00
Zr	ZrO2	0.03	0.01
Pb	PbO	0.07	0.02
Total		100.00	100.00

Notes:
1. This analysis represents specifically the sample submitted.
2. Sample results reported on an as received weight basis.
3. Oxide analysis by X-ray fluorescence spectrometry using PANalytical IQ+ Quantification program.
4. "Overlap" indicates interfering elements are present. The percent analyte could not be estimated.
5. This report may not be reproduced except in its entirety.

9.3 Appendix C - X-ray Diffraction Phase Identification Analyses on Deposit Samples Collected from Coal Combustion

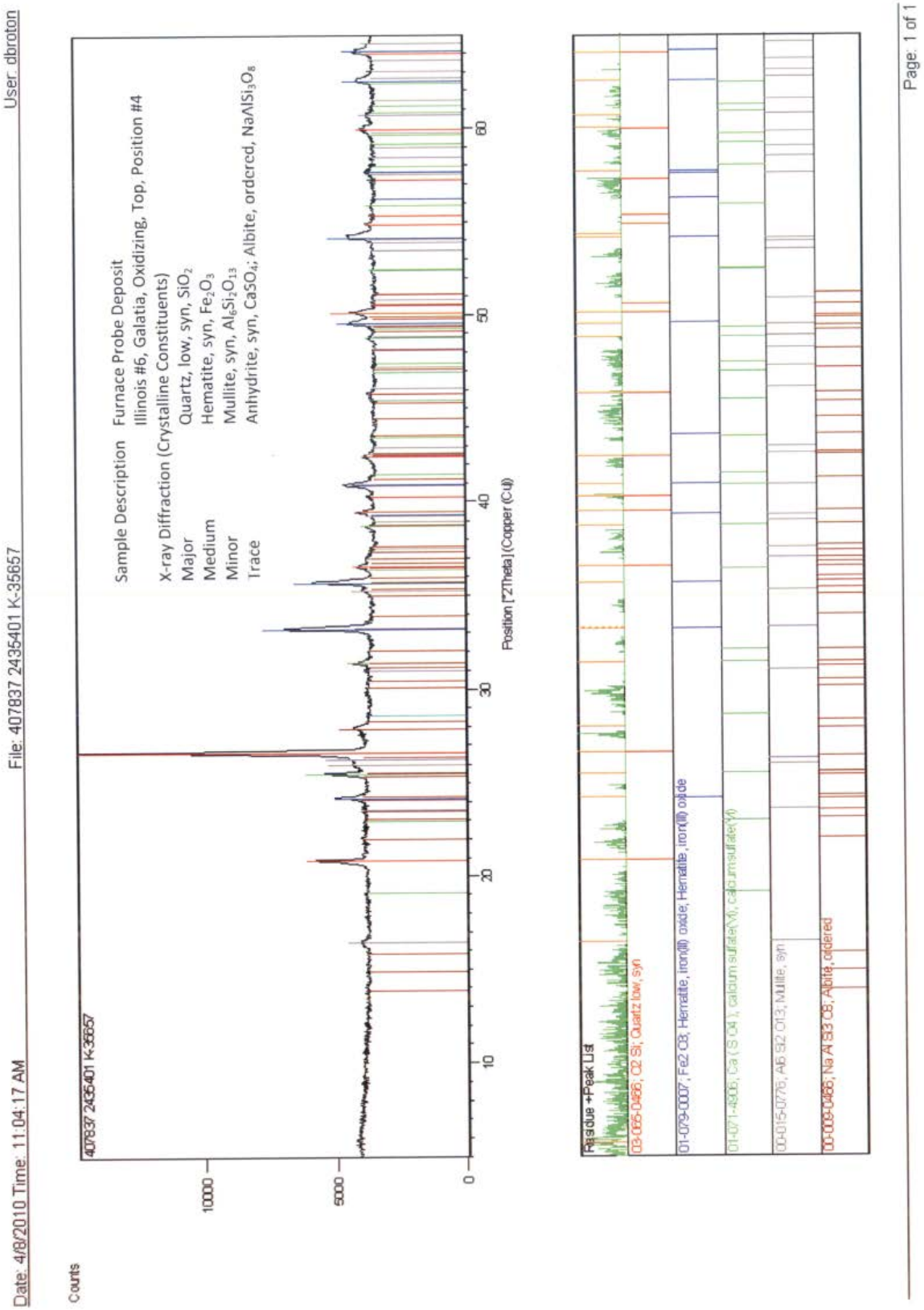
Date: 4/8/2010 Time: 11:04:17 AM
File: 407837 2435401 K-35657
User: dbroton
Counts
10000
5000
0
407837 2435401 K-35657
Sample Description Furnace Probe Deposit
Illinois #6, Galatia, Oxidizing, Top, Position #4
X-ray Diffraction (Crystalline Constituents)
Major Quartz, low, syn, SiO2
Medium Hematite, syn, Fe2O3
Minor Mullite, syn, Al6Si2O13
Trace Anhydrite, syn, CaSO4; Albite, ordered, NaAlSi3O8
0
10
20
30
40
50
60
Position [°2Theta] (Copper (Cu))
Residue +Peak List
03-065-0466; O2 Si; Quartz low, syn
01-079-0007; Fe2 O3; Hematite, iron(III) oxide; Hematite, iron(III) oxide
01-071-4806; Ca (S O4); calcium sulfate(VI); calcium sulfate(VI)
00-015-0776; Al6 Si2 O13; Mullite, syn
00-009-0466; Na Al Si3 O8; Albite, ordered
Page: 1 of 1

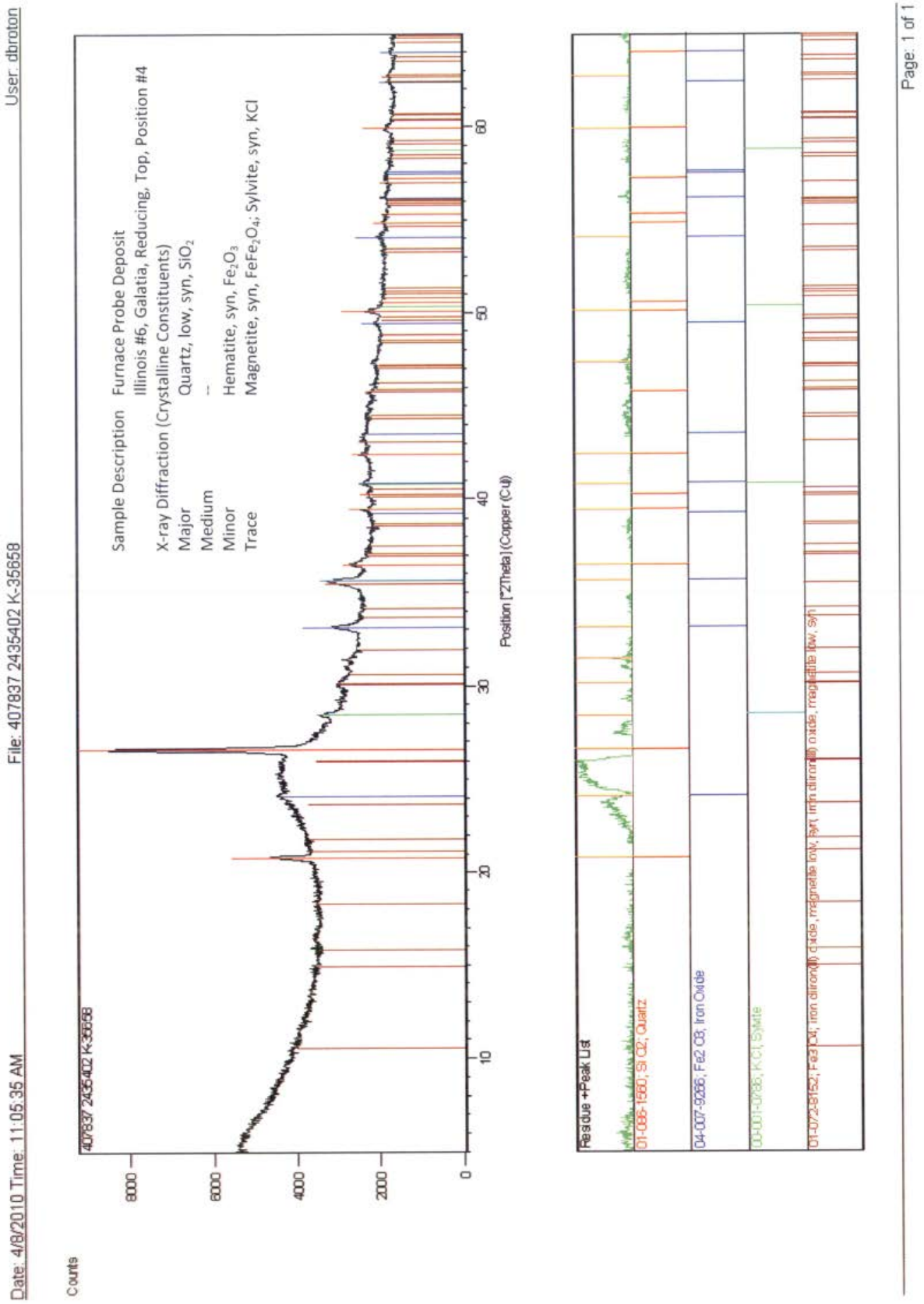
Date: 4/8/2010 Time: 11:05:35 AM
File: 407837 2435402 K-35658
User: dbroton
Counts
8000
6000
4000
2000
0
407837 2435402 K-35658
Sample Description Furnace Probe Deposit
Illinois #6, Galatia, Reducing, Top, Position #4
X-ray Diffraction (Crystalline Constituents)
Major Quartz, low, syn, SiO2
Medium --
Minor Hematite, syn, Fe2O3
Trace Magnetite, syn, FeFe2O4; Sylvite, syn, KCl
10
20
30
40
50
60
Position [°2Theta] (Copper (Cu))
Residue +Peak List
01-086-1560; Si O2; Quartz
04-007-9286; Fe2 O3; Iron Oxide
00-001-0786; K Cl; Sylvite
01-072-8152; Fe3 O4; iron diiron(III) oxide, magnetite low, syn; iron diiron(III) oxide, magnetite (low, syn)
Page: 1 of 1

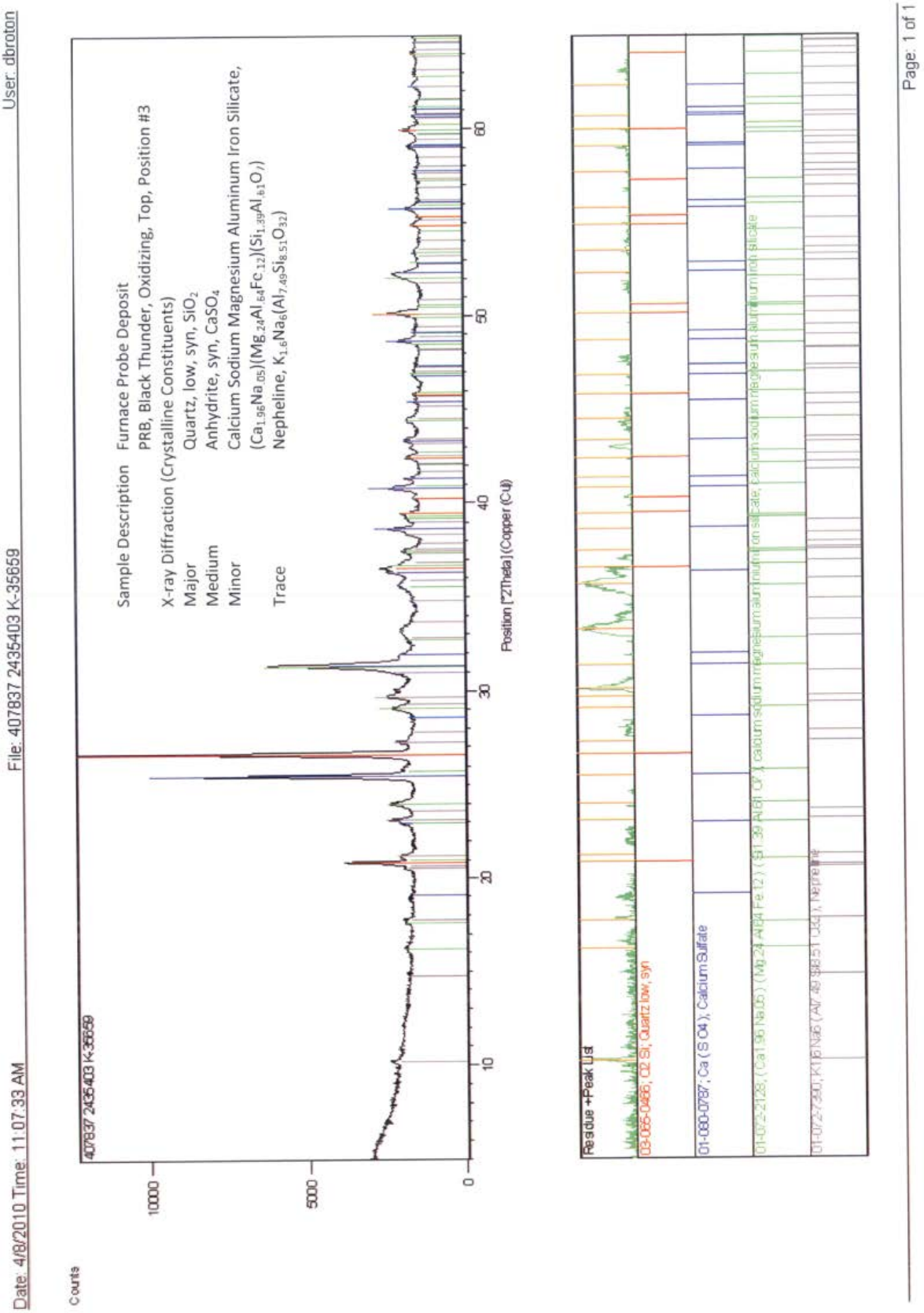
Date: 4/8/2010 Time: 11:07:33 AM
File: 407837 2435403 K-35659
User: dbroton
Sample Description Furnace Probe Deposit
PRB, Black Thunder, Oxidizing, Top, Position #3
X-ray Diffraction (Crystalline Constituents)
Major Quartz, low, syn, SiO2
Medium Anhydrite, syn, CaSO4
Minor Calcium Sodium Magnesium Aluminum Iron Silicate, (Ca1.96Na0.05)(Mg.24Al.64Fe.12)(Si1.39Al.61O7)
Trace Nepheline, K1.6Na6(Al7.49Si8.51O32)
407837 2435403 K-35659
Counts
Position [°2Theta] (Copper (Cu))
Residue +Peak List
03-065-0426; Ca2 Si; Quartz low, syn
01-080-0797; Ca (S O4); Calcium Sulfate
Page: 1 of 1

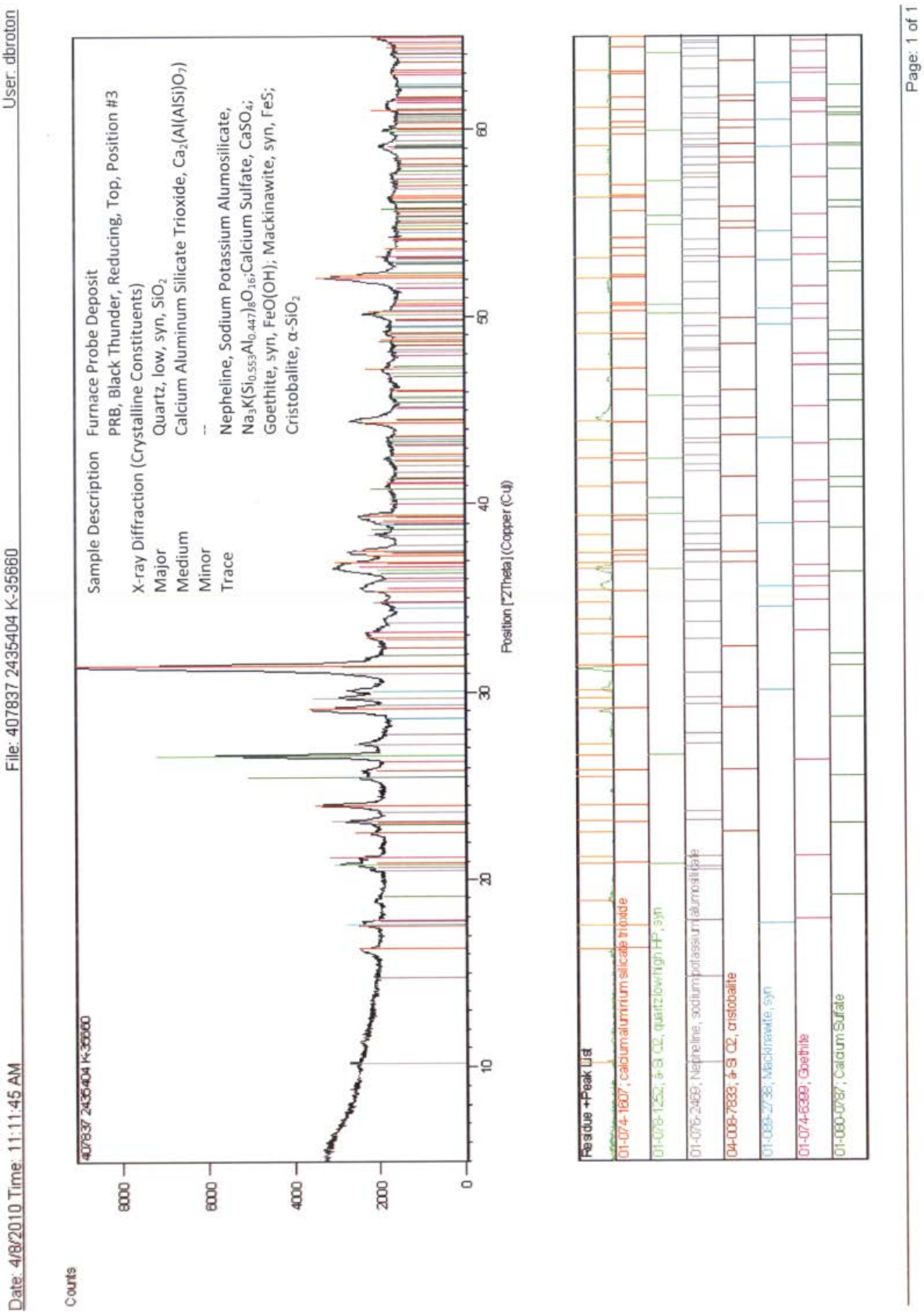
Date: 4/8/2010 Time: 11:11:45 AM
File: 407837 2435404 K-35660
User: dbroton
Counts
407837 2435404 K-35660
Sample Description
Furnace Probe Deposit
PRB, Black Thunder, Reducing, Top, Position #3
X-ray Diffraction (Crystalline Constituents)
Major
Quartz, low, syn, SiO2
Medium
Calcium Aluminum Silicate Trioxide, Ca2(Al(AlSi)O7)
Minor
--
Trace
Nepheline, Sodium Potassium Alumosilicate, Na3K(Si0.553Al0.447)8O16;Calcium Sulfate, CaSO4; Goethite, syn, FeO(OH); Mackinawite, syn, FeS; Cristobalite, α-SiO2
8000
6000
4000
2000
0
10
20
30
40
50
60
Position [°2Theta] (Copper (Cu))
Residue +Peak List
01-074-1607; calcium aluminum silicate trioxide
01-078-1252; α-SiO2; quartz low high HP, syn
01-075-2469; Nepheline, sodium potassium aluminosilicate
04-009-7933; α-SiO2; cristobalite
01-083-2736; Mackinawite, syn
01-074-6399; Goethite
01-080-0787; Calcium Sulfate
Page: 1 of 1

Date: 11/18/2009 Time: 11:36:02 AM File: 407837 2463001 K-35634 User: dbroton

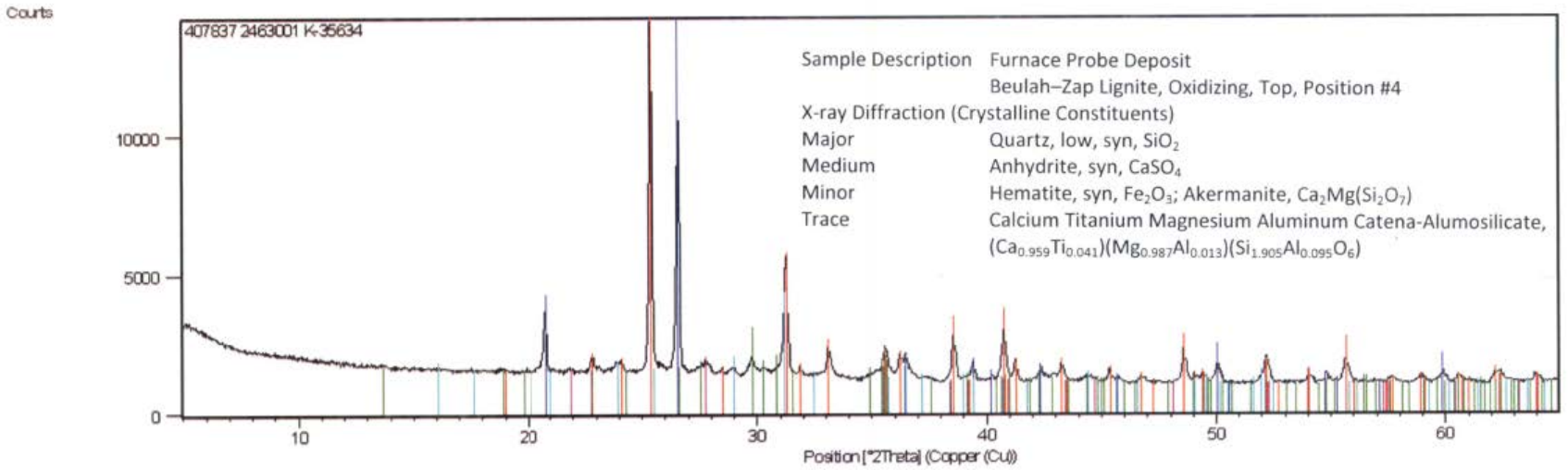

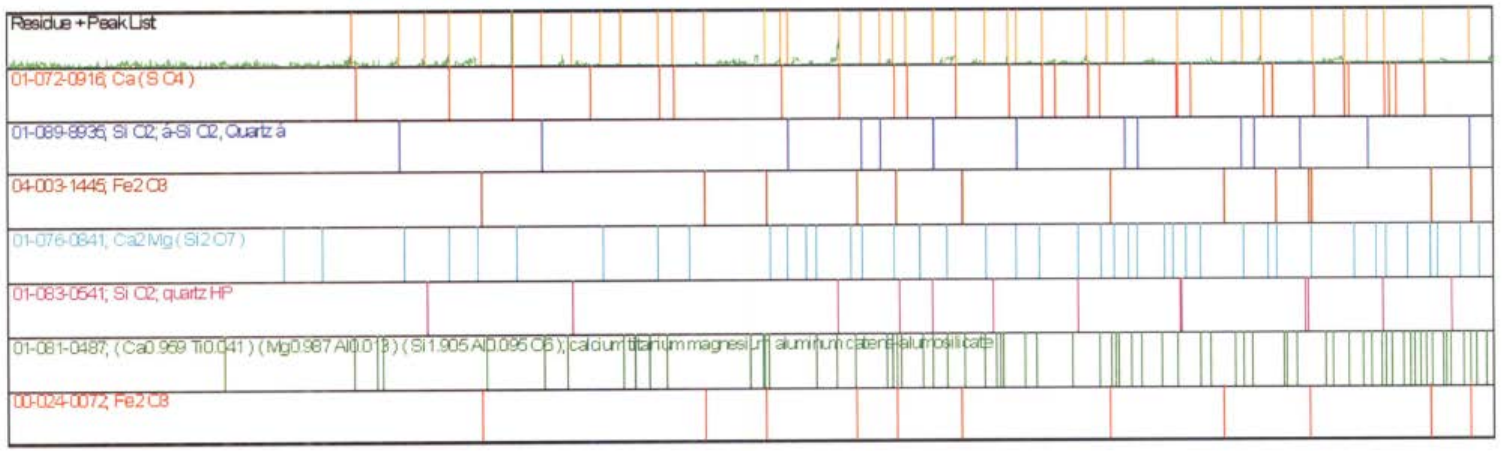

Page: 1 of 1

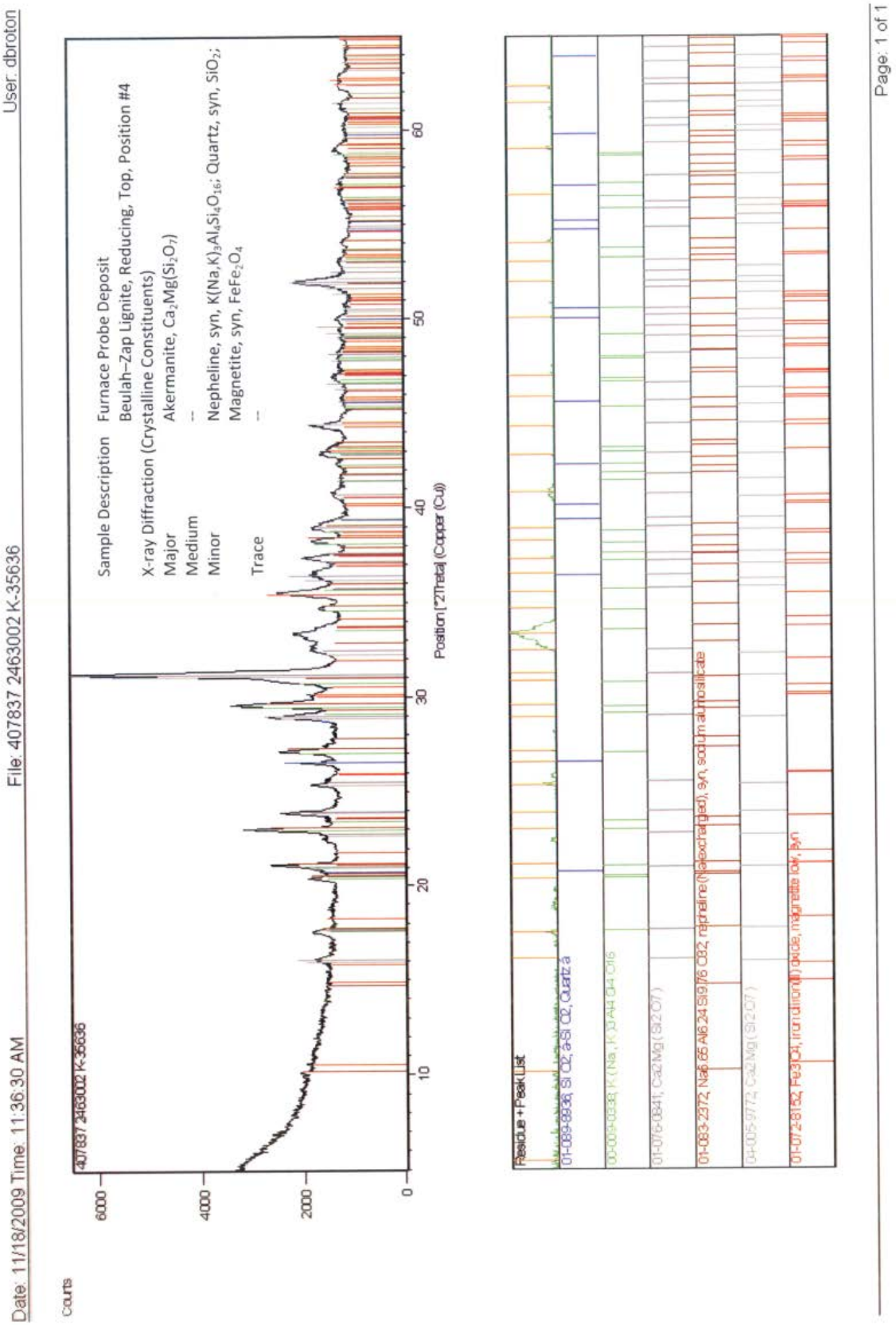
Date: 11/18/2009 Time: 11:36:30 AM
File: 407837 2463002 K-35636
User: dbroton
Counts
6000
4000
2000
0
407837 2463002 K-35636
Sample Description Furnace Probe Deposit
Beulah–Zap Lignite, Reducing, Top, Position #4
X-ray Diffraction (Crystalline Constituents)
Major Akermanite, $Ca_2Mg(Si_2O_7)$
Medium --
Minor Nepheline, syn, $K(Na,K)_3Al_4Si_4O_{16}$; Quartz, syn, SiO_2;
Magnetite, syn, $FeFe_2O_4$
Trace --
10
20
30
40
50
60
Position [°2Theta] (Copper (Cu))
Residue + Peak List
01-089-8936; Si O2; a-Si O2; Quartz a
00-004-0838; K (Na, K) Al4 Si4 O16
01-076-0841; Ca2 Mg (Si2 O7)
01-083-2372; Na6.66 Al6.24 Si9.76 O32; nepheline, (Na-exchanged), syn, sodium aluminosilicate
01-075-9772; Ca2 Mg (Si2 O7)
01-072-8152; Fe3 O4; iron (II,III) oxide, magnetite low, syn
Page: 1 of 1

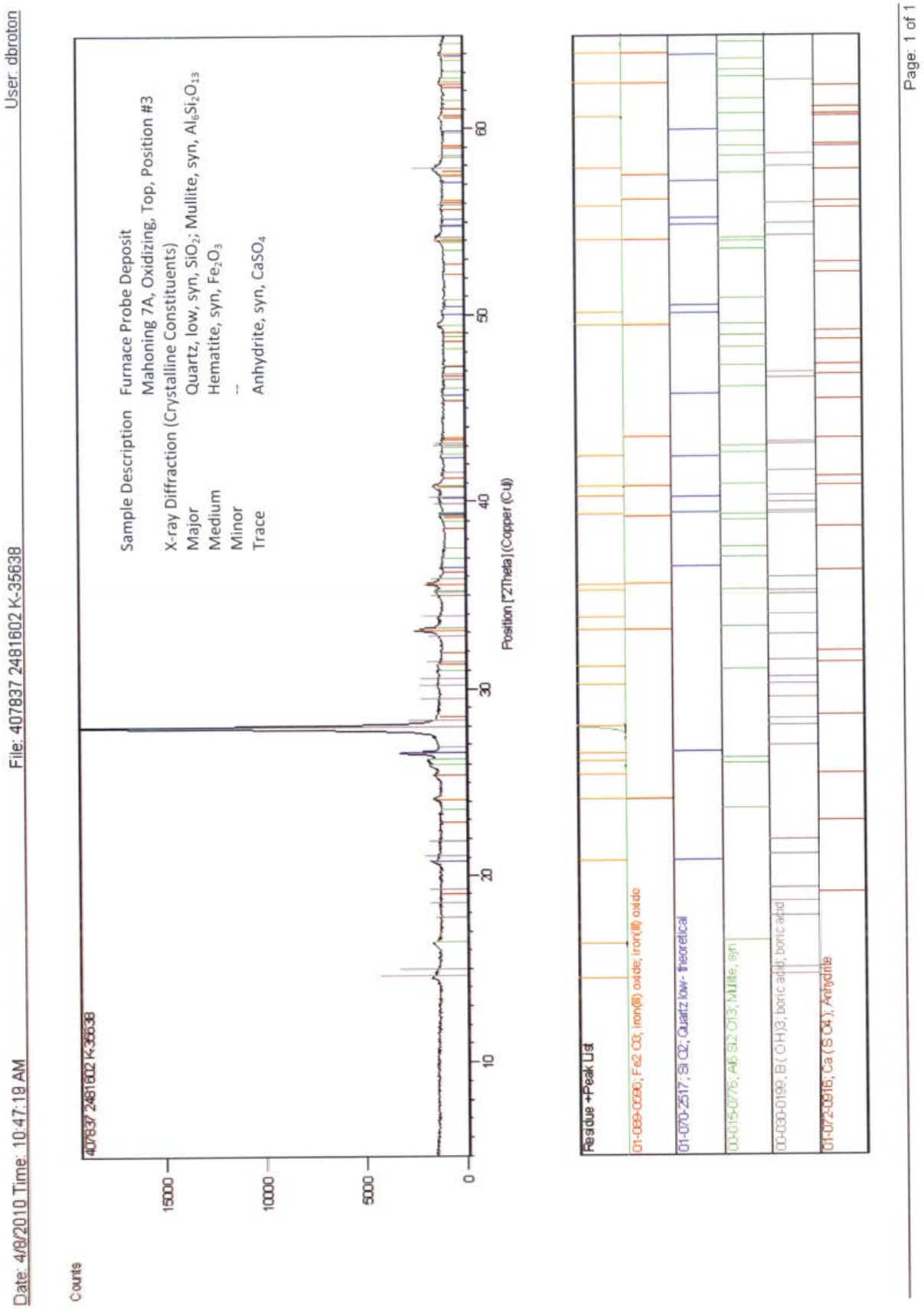
Date: 4/8/2010 Time: 10:47:19 AM
File: 407837 2481602 K-35638
User: dbroton
Counts
407837 2481602 K-35638
Sample Description Furnace Probe Deposit
Mahoning 7A, Oxidizing, Top, Position #3
X-ray Diffraction (Crystalline Constituents)
Major Quartz, low, syn, SiO2; Mullite, syn, Al6Si2O13
Medium Hematite, syn, Fe2O3
Minor --
Trace Anhydrite, syn, CaSO4
Position [°2Theta] (Copper (Cu))
Residue +Peak List
01-089-0596; Fe2 O3; Iron(III) oxide; iron(III) oxide
01-070-2517; Si O2; Quartz low - Theoretical
00-015-0776; Al6 Si2 O13; Mullite, syn
00-030-0199; B (O H)3; boric acid; boric acid
01-072-0916; Ca (S O4); Anhydrite
Page: 1 of 1

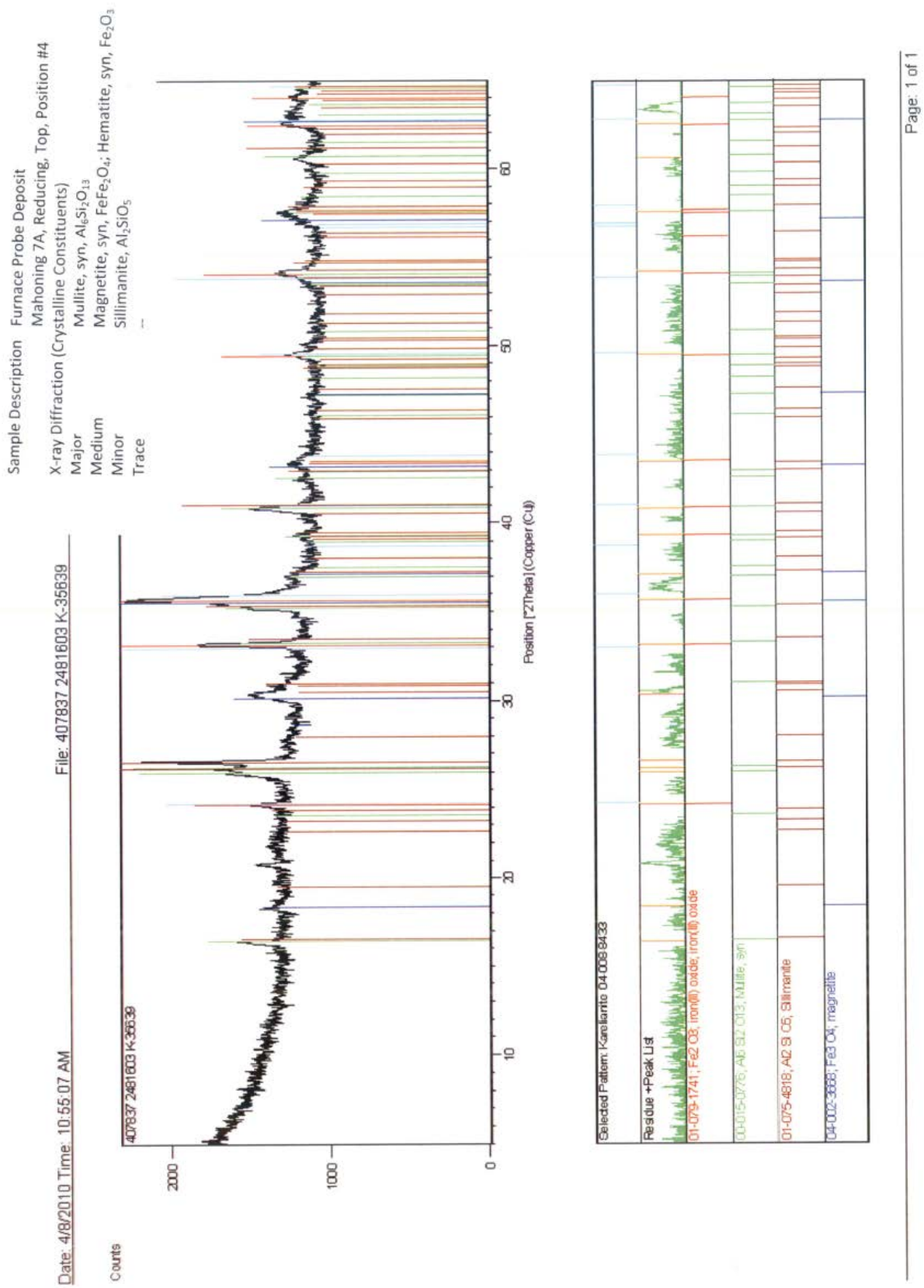
Sample Description Furnace Probe Deposit
Mahoning 7A, Reducing, Top, Position #4
X-ray Diffraction (Crystalline Constituents)
Major Mullite, syn, $Al_6Si_2O_{13}$
Medium Magnetite, syn, $FeFe_2O_4$; Hematite, syn, Fe_2O_3
Minor Sillimanite, Al_2SiO_5
Trace --
File: 407837 2481603 K-35639
Date: 4/8/2010 Time: 10:55:07 AM
Counts
407837 2481603 K-35639
2000
1000
0
10
20
30
40
50
60
Position [°2Theta] (Copper (Cu))
Selected Pattern: Kanellanite 04 008 8433
Residue +Peak List
01-079-1741; Fe2 O3; Iron(III) oxide; Iron(III) oxide
00-015-0776; Al6 Si2 O13; Mullite, syn
01-075-4818; Al2 Si O5; Sillimanite
04-002-3668; Fe3 O4; magnetite
Page: 1 of 1

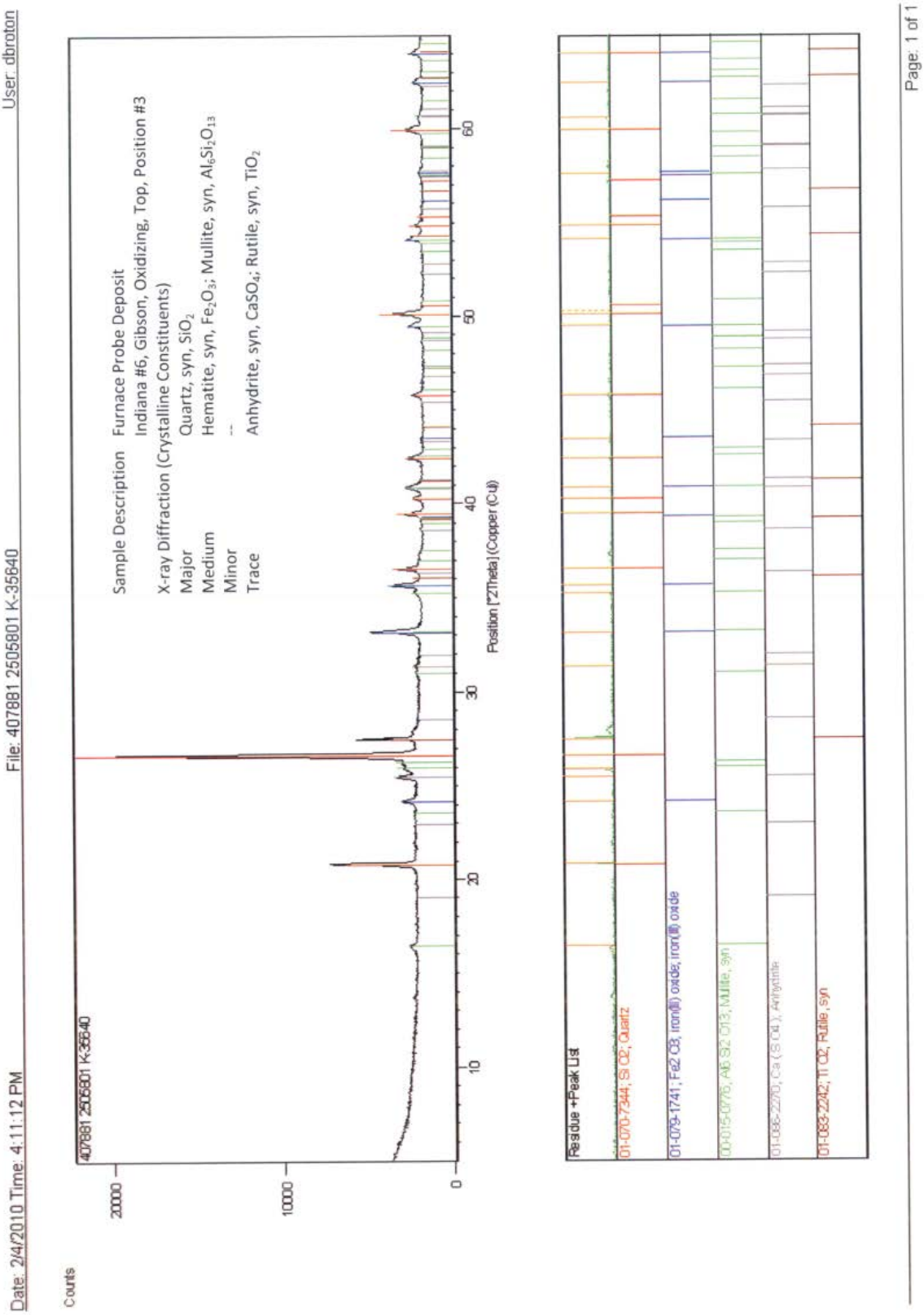
Date: 2/4/2010 Time: 4:11:12 PM
File: 407881 2505801 K-35640
User: dbroton
Counts
20000
10000
0
407881 2505801 K-35640
Sample Description Furnace Probe Deposit
Indiana #6, Gibson, Oxidizing, Top, Position #3
X-ray Diffraction (Crystalline Constituents)
Major Quartz, syn, SiO2
Medium Hematite, syn, Fe2O3; Mullite, syn, Al6Si2O13
Minor --
Trace Anhydrite, syn, CaSO4; Rutile, syn, TiO2
10
20
30
40
50
60
Position [°2Theta] (Copper (Cu))
Residue +Peak List
01-070-7344; Si O2; Quartz
01-079-1741; Fe2 O3; iron(III) oxide; iron(III) oxide
00-015-0776; Al6 Si2 O13; Mullite, syn
01-086-2390; Ca (S O4); Anhydrite
01-089-2242; Ti O2; Rutile, syn
Page: 1 of 1

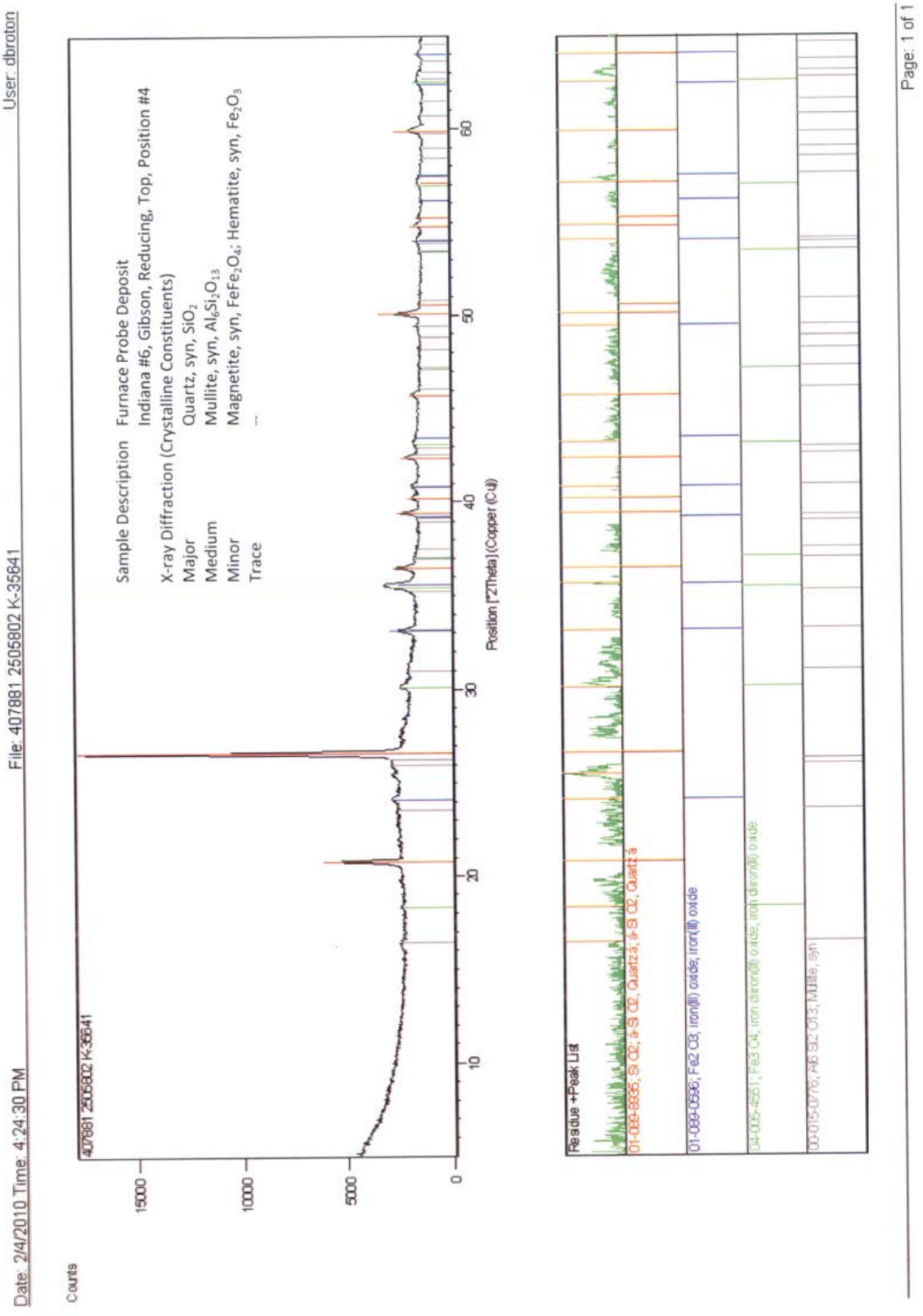
Date: 2/4/2010 Time: 4:24:30 PM
File: 407881 2505802 K-35641
User: dbroton
Counts
407881 2505802 K-35641
Sample Description Furnace Probe Deposit
Indiana #6, Gibson, Reducing, Top, Position #4
X-ray Diffraction (Crystalline Constituents)
Major Quartz, syn, SiO2
Medium Mullite, syn, Al6Si2O13
Minor Magnetite, syn, FeFe2O4; Hematite, syn, Fe2O3
Trace --
Position [°2Theta] (Copper (Cu))
Residue +Peak List
01-089-8936; Si O2; a-Si O2; Quartz a
01-089-0596; Fe2 O3; iron(III) oxide
04-005-4551; Fe3 O4; iron dioxide; iron dironIII) oxide
00-015-0776; Al6 Si2 O13; Mullite, syn
Page: 1 of 1

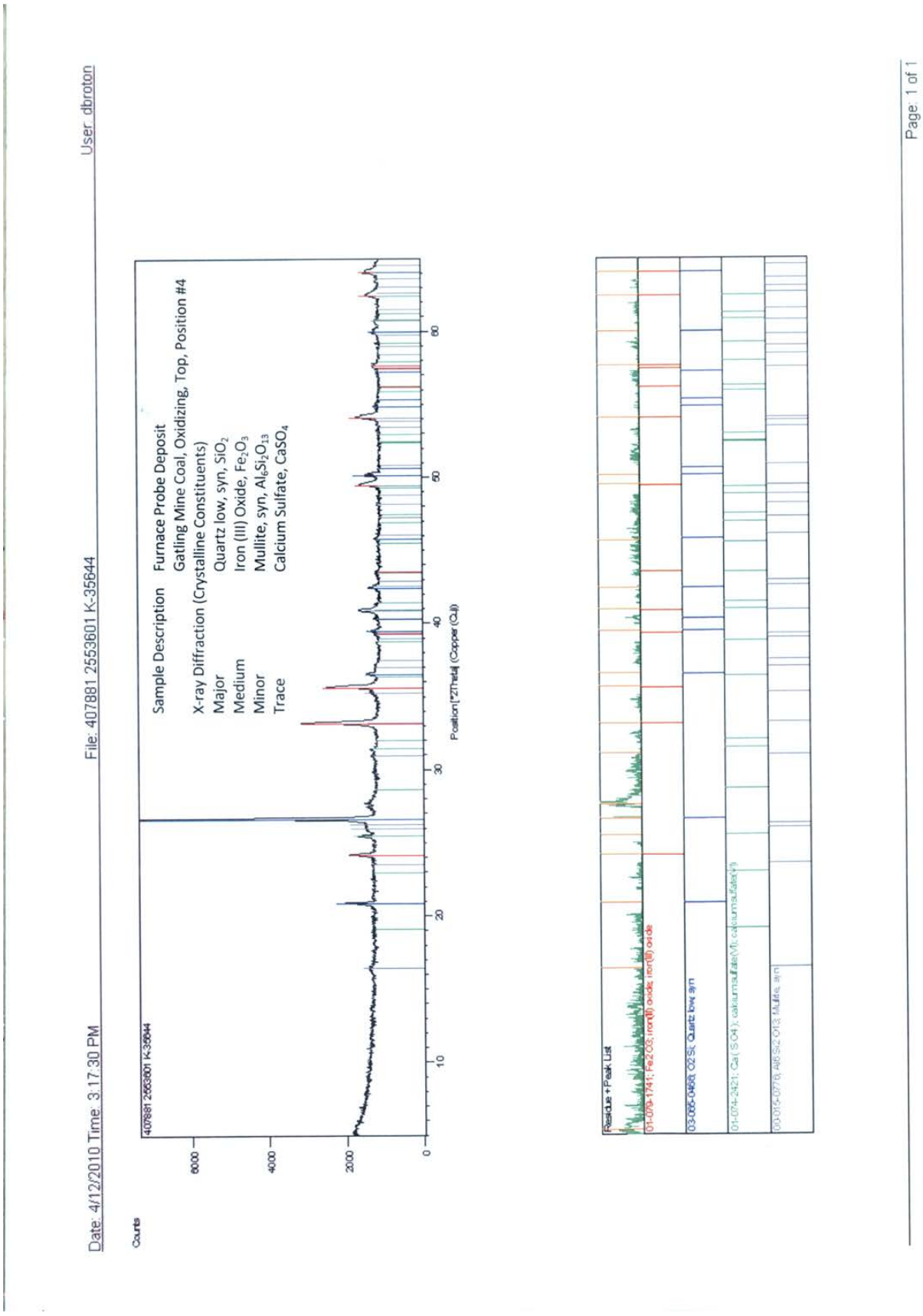
Date: 4/12/2010 Time: 3:17:30 PM
File: 407881 2553601 K-35644
User: dbroton
Sample Description Furnace Probe Deposit
Gatling Mine Coal, Oxidizing, Top, Position #4
X-ray Diffraction (Crystalline Constituents)
Major Quartz low, syn, SiO2
Medium Iron (III) Oxide, Fe2O3
Minor Mullite, syn, Al6Si2O13
Trace Calcium Sulfate, CaSO4
Counts
Position [°2Theta] (Copper (Cu))
Residue + Peak List
Page: 1 of 1

Date: 4/12/2010 Time: 3:17:47 PM
File: 407881 2553602 K-35645
User: dbroton
Sample Description
Furnace Probe Deposit
Gatling Mine Coal, Reducing, Top, Position #3
X-ray Diffraction (Crystalline Constituents)
Major
Quartz low, syn, SiO2
Medium
Iron (III) Oxide, Fe2O3
Minor
Mullite, syn, Al2(Al2.8Si1.2)O9.6
Trace
Pyrrhotite 4C, Fe7S8; Calcium Magnesium bis(catena-Silicate), CaMg(SiO3)2
407881 2553602 K-35645
Counts
Position [°2Theta] (Copper (Cu))
Residue + Peak List
Page: 1 of 1

9.4 Appendix D – Alloy and Weld Overlay Compositions Evaluated in Task 4, Laboratory Fireside Corrosion Testing

Alloys Evaluated for Coal Ash Corrosion

Compositions of Monolithic Alloys Certified by Vendors and Weld Overlays Analyzed with SEM/EDS on Coating Surfaces (Weld overlays are highlighted in yellow)

	304H	S304H	310HCbN	230	347HFG	347H	72	52	671	740	617	120	800H
Ni	11	8.73	19.97	59.5	11.98	10.42	47.2	56.3	50.7	49.45	53.2	37.3	32.7
Cr	18.83	18.68	25.61	21.31	18.4	17.67	>41.2	29.6	48.19	24.31	22.63	25.1	21.0
Fe	Bal	67.6	Bal	1.25	Bal	68.4	10.6	12.2	0.078	1.02	0.76	34.7	Bal.
Mo		0.32	-	1.28	-	0.24	0.07	0.03	0.034	0.52	9.38	0.27	-
Co		0.14	-	0.14	-	< 0.1	0.02	0.003	0.23	19.63	12.33	0.10	-
C	0.05	0.084	0.05	0.088	0.09	0.045	0.023	0.029	0.047	0.034	0.06	0.06	0.08
N		0.11	0.24		-	-				-	-	0.20	-
B		-	-	0.005	-	-	-	-	0.002	-	0.002	-	-
Mn	1.8	0.8	1.18	0.51	1.46	1.84	0.11	0.29	-	-	0.02	0.71	0.80
Si	0.45	0.14	0.36	0.45	0.41	0.44	0.16	0.2	0.018	0.45	0.15	0.48	0.59
Al	-	-	-	0.44	-	-	0.14	0.7	0.27	0.75	1.15	0.059	0.45
Ti	-	-	-	-	-	-	0.44	0.53	0.37	1.58	0.27	-	0.31
Nb	-	0.52	0.47	0.053	-	-				1.83	-	0.61	-
Nb+Ta	-	-	-	-	0.9	-	0.02	0.02	-	-	-	-	-
V	-	<0.1	-	0.011	-	-	0.02	0.02	0.008	-	-	-	-
W	-		-	14.93	-	-	ND	ND	0.002	-	-	0.10	-
Cu	-	2.78	-	-	-	0.35	0.03	0.02	0.002		0.05	-	0.11
P	0.01	-	0.015	-	0.027	0.026	-	-	-	-	-	-	-
S	0.013	-	-	-	0.001	0.003	-	-	-	-	0.001	-	<0.002
Other	-	-	-	-	-	-	-	0.058	-	-	-	-	-

Alloys Evaluated for Furnace Wall Corrosion

Compositions of Monolithic Materials Certified by Vendors and Weld Overlays Analyzed with SEM/EDS on Coating Surfaces
(Weld overlays are highlighted in yellow)

	T2	304H	T11	T22	T23	F9	F91	52	72	309H	310H	A179/ 178A
Ni		11	0.04	0.13			0.14	56.3	47.2	12.48	19.37	0.02
Cr	0.56	18.83	1.29	2.41	2.18	8.92	8.15	29.6	>41.2	22.34	25.45	0.03
Fe		Bal	BAL	Bal	Bal	Bal	Bal	12.2	10.6	Bal	Bal	Bal
Mo	0.46		0.52	0.96	0.21	0.97	0.91	0.03	0.07	0.09	0.40	0.01
Co				-				0.003	0.02			
C	0.12	0.05	0.07	0.15	0.084	0.110	0.11	0.029	0.023	0.05	0.04	0.09
N				-	0.0076	0.013	0.044					
B				-	0.001			-	-			
Mn	0.56	1.8	0.47	0.5	0.50	0.37	0.39	0.29	0.11	1.62	1.63	0.34
Si	0.20	0.45	0.59	0.23	0.25	0.73	0.27	0.2	0.16	0.31	0.63	0.01
Al		-	0.019	0.021	0.027	0.009	0.017	0.7	0.14			0.052
Ti		-		0.001			0.002	0.53	0.44			
Nb		-		-	0.034		0.095					
Nb+Ta		-		-				0.02	0.02			
V		-	0.001	0.013	0.25	0.03	0.21	0.02	0.02			
W		-		-	1.46			ND	ND			
Cu		-	0.06	0.19		0.19	0.25	0.02	0.03	0.40	0.17	0.02
P	0.011	0.01	0.018	0.008	0.009	0.016	0.014	-	-	0.023	0.021	0.015
S	0.002	0.013	0.009	0.013	<0.001	0.006	0.004	-	-	0.003	0.0004	0.008
Other		-	0.007 Sn			0.011 Sn	0.020 Sn	0.058	-			0.004 Sn

9.5 Appendix E – TGA/DSC Study on Deposit Samples Analyzed after Exposure to 1000-Hour Laboratory Corrosion Tests

9.5.1 INTRODUCTION

Thermal analysis is analysis of transitions, chemical reactions, and other properties as a function of temperature, heating rate, and atmosphere. Thermogravimetric analysis (TGA) is measurement of the **mass** of a sample under a controlled atmosphere and temperature program. Events such as evaporation, pyrolysis, calcination, and sulfation can all be observed through changes in mass of a sample. Differential scanning calorimetry (DSC) is the measurement of **heat flow** into or out of a sample by comparison (hence the "differential" in the method name) to an empty sample holder in the same furnace. "Scanning" refers to the ability of a DSC instrument to maintain a constant predetermined heating rate or temperature program. DSC experiments can identify the endothermic or exothermic nature of an event, and provide a measure of the heat or energy involved as well as the temperature at which it occurs, such as a melting point. However, a DSC instrument does not provide the mass change associated with the event.

In recent times instruments combining mass and heat flow measurements as a function of time or sample temperature (TGA/DSC) have become available. These conveniently allow simultaneous determination of mass and energy changes as a function of sample temperature where previously two separate experiments would have been required.

In this work synthetic ash samples were analyzed in a TGA/DSC instrument to provide insight into the ash behavior at elevated temperatures. This brief report presents the experimental methods used and the resulting TGA/DSC data. Details of the synthetic ash composition and interpretation of the data is outside the scope of this report.

9.5.2 EQUIPMENT AND METHODS

9.5.2.1 Mettler-Toledo TGA/DSC 1

The instrument used in this work was a Mettler Toledo TGA/DSC 1 with a high temperature furnace (up to 1600°C/2900°F). Platinum crucibles (30 μL, with lid) were used for holding the samples as it was determined during method development that alumina crucibles could leach molten components of the ash samples and result in the crucible sticking to the crucible holder.

Two platinum crucibles were used in each experiment. One would hold the sample and the other remained empty as a reference for the DSC measurement. Both sat inside the TGA/DSC furnace on a crucible holder connected to the precision balance of the instrument. In the holder beneath each crucible are 3 thermocouple junctions (6 total) connected in such a way as to provide a differential temperature measurement between the reference and sample crucibles. This signal is scaled during calibration to provide the heat flow signal.

The furnace has a separate temperature sensor in the furnace wall. During instrument calibration various pure metal melting point standards are tested so that correlations between the measured furnace temperature and the known sample temperature (given by the onset of melting detected by the differential temperature sensor) can be developed. Additional correlations developed by repeating the calibration at three different heating rates allow correction for changes in heating rate during experiments. More detail is available in the instrument hardware and software manuals if required. An additional calibration using the heat of fusion of indium is

used to calibrate the heat flow signal. Table 1 shows the literature values of the calibration standards with the tolerance allowed during the Mettler Toledo's calibration procedure.

Table 1 - Calibration values for the melting of metal standards.

Calibration Substance	Standard Calibration Values (and Tolerance – METTLER TOLEDO specifications)
Indium	Melting Point: 156.6°C (±1.5°C) Heat of Fusion: -28.5 J/g (±15%)
Zinc	Melting Point: 419.5°C (±2.0°C)
Aluminum	Melting Point: 660.3°C (±2.5°C)
Gold	Melting Point: 1064.2°C (±3.0°C)

Once the calibration procedure is completed (in an atmosphere of air) the resulting correlations are used so that the instrument can report to the user the sample and reference temperatures, mass, and heat flow from the directly measured furnace temperature, sample-reference differential temperature.

The instrument software (STAR^e) includes corrections for a number of changes which may be made from calibration to experiment, including changes to crucible type and size, and furnace atmosphere. Since the simulated flue gas (a mixture of N_2, CO_2, O_2, and SO_2) used in this work was not part of the library of pure gases in the software, and accounting for it by direct calibration for each different mixture was not feasible due to time constraints, a test was conducted with extremes of mixture composition (such as highest CO_2 concentration) to determine the temperature measurement error associated with treating all tests in the calibration correlations as being conducted in N_2. The results of this test are shown in Figure 1, and indicated that sample temperature error was within 5°C of the actual temperature. This was outside the range of the manufacturer tolerances, but deemed acceptable for this work.

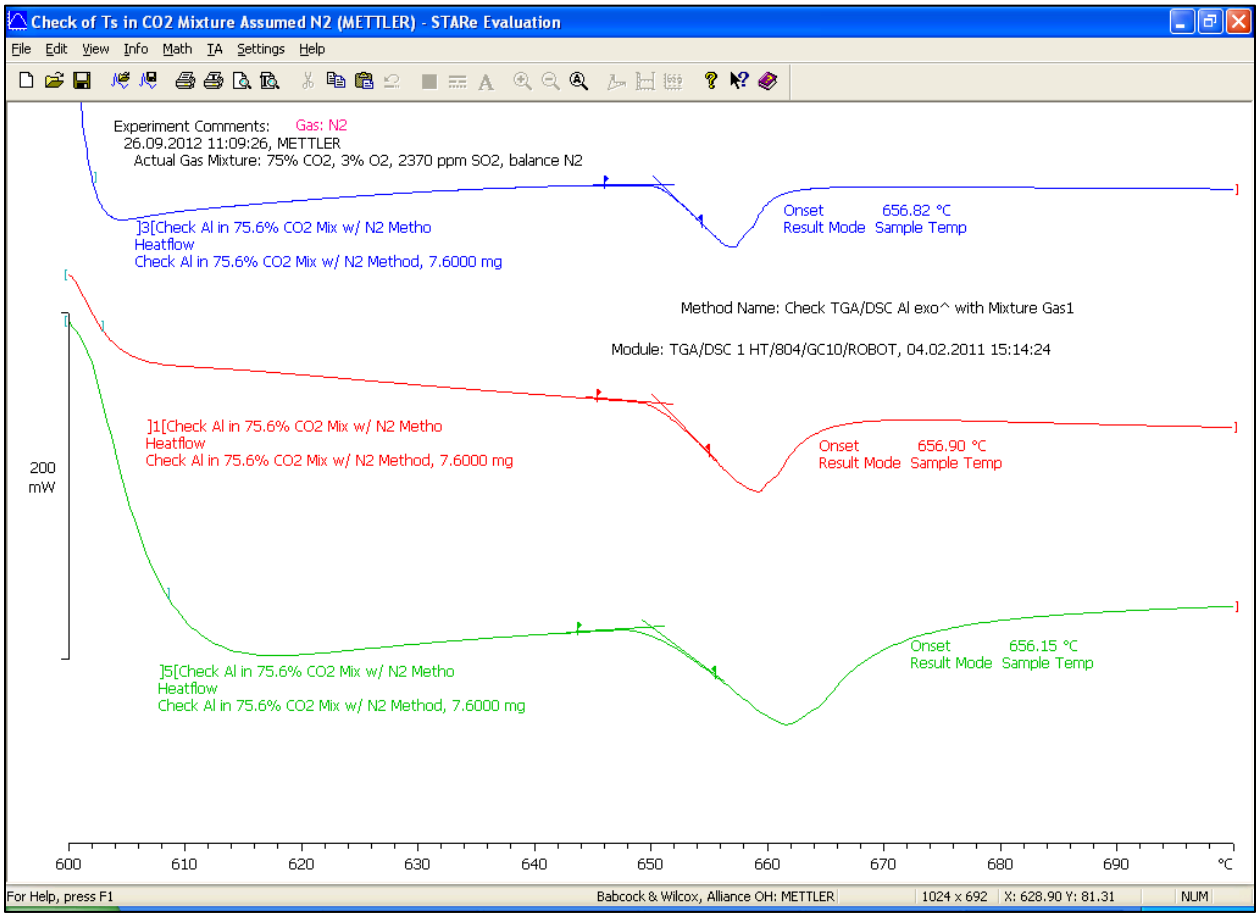

Figure 1 – Results of calibration checks in a high CO_2 gas mixture assuming 100% N_2 in the furnace. Heating rates were 5°C/min (blue), 10°C/min (red), 20°C/min (green). The aluminum melting onset temperatures were 656.82, 656.90, and 656.15°C, respectively (all within 5°C of the specified temperature of 660.3°C).

The tolerance for the heat flow calibration standard in Table 1 is relatively high (±15%). This is due to the limited number (6) of thermocouple junctions in the differential temperature sensor/crucible holder. In a traditional DSC instrument in excess of 50 or even 100 junctions is typical, but these sensors are not capable of high temperature operation and hence this high temperature instrument was supplied with a more robust sensor with limited accuracy. For this reason the heat flow data in this work are probably best treated as semi-quantitative.

The temperature program used in this work (with one or two exceptions identified below) consisted of 12 minutes at 50°C, a ramp from 50 to 1000°C at 5°C/min, followed by a 10 minute hold at 1000°C. It is the "reference temperature" (defined as the temperature at the sample position in the empty crucible) that is controlled to the temperature program. When an exothermic event occurs the sample temperature exceeds the reference temperature, and vice versa for an endothermic event.

Prior to each run in a different gas mixture a "blank" run was conducted. This is the same as a conventional test, but with no sample in the sample crucible. The mass and heat flow signals from this run are then subtracted from the mass and heat flow signals of all subsequent runs to correct for changes in furnace gas buoyancy, and crucible heat capacity. As is normal practice

for calibration checks where only the onset temperature is of interest, the data in Figure 1 was not blank-corrected. This explains some of the floating baseline behavior, but even for blank-corrected data some movement of the heat flow baseline is normal due to changes in heat capacity with temperature. Usually enthalpy measurements conducted on DSC data are done by integration of a peak in the heat flow signal relative to the local baseline rather than zero.

Table 2 presents a list of a number of physical transitions that can be observed with DSC measurements and how they appear in the heat flow signal. The heat flow sign convention used in this work is that negative heat flow corresponds to endothermic events.

Table 2 - Various physical transitions observed in heat flow data.

Physical Transitions	Appearance in Heat Flow Data
Fusion / Melting	Endothermic Peak
Crystalline Transition	Endothermic or Exothermic Peak
Crystallization	Exothermic Peak
Vaporization	Endothermic Peak
Sublimation	Endothermic Peak
Adsorption	Exothermic Peak
Absorption	Endothermic Peak
Curie Point Transition	Endothermic Peak
Glass Transition	Baseline Shift
Liquid Crystal Transition	Endothermic Peak
Heat Capacity	Baseline Shift

9.5.2.2 Gas Mixing Controls

The gas mixtures used in this work were prepared by passing pure gases (CO_2, N_2, and O_2) and one gas mixture (SO_2 in N_2) through 4 individual mass flow controllers followed by a mixing manifold. Since the mass flow controllers used were designated “calibrate before use”, prior to each test the actual mass flow through each mass flow controller was verified using a primary flow standard.

The TGA/DSC mass balance required a constant purge flow of N_2 (through a 5^{th} mass flow controller), which is ultimately vented into the furnace upstream of the sample crucible. This N_2 was therefore accounted for in calculating the composition of the furnace gas.

The desired composition for the gases was to match the percentage of CO_2, SO_2, and O_2 used in the fireside lab testing. N_2 was used to make up the balance, substituting for other gases used in the fireside lab, but not used here (such as H_2O, CO, Ar, etc.).

9.5.2.3 Experiment Procedure

The following procedure was generally followed for each sample:

- Perform balance adjustment / internal calibration
- Set and check flows of gas mixture components through each mass flow controller

- Set up TGA to perform blank run and two runs on the selected sample (fresh samples were used for each run)
- Weigh in crucibles using TGA
- Using analytical balance put 15-20 mg in each sample crucible
- Weigh in sample masses with TGA
- Start experiments
- After runs complete, export data to spreadsheet template for data analysis

9.5.2.4 Data Analysis

The data from the TGA/DSC 1 (time, mass, sample temperature, reference temperature, and heat flow) were exported to Microsoft Excel. Heat flow at any instant was normalized by the current mass to give mW/mg, and then this data and sample weight were plotted versus sample temperature.

For any clearly defined peaks in the normalized heat flow data the onset temperature was labeled on the plots. Onset temperature is defined as the temperature where a tangent to the local baseline and tangent to the melting peak intersect. Such tangents are visible on the melting peaks in Figure 1.

9.5.3 RESULTS AND OBSERVATIONS

9.5.3.1 Samples and Experiments

Table 3 shows the test names for each sample, the name of the experiments in the TGA instrument database, sample masses, and any comments on unusual experiment conditions. The "Post" in the experiment names indicates that these synthetic ash samples had previously been exposed to simulated flue gas in the fireside test facility for an extended period.

Table 3 - Test names and sample sizes with comments on any unusual conditions.

Test ID	Sample Mass (mg)	Comments
WY PRB	17.3	
	16.4	
IL #6 Galatia	17.3	
	19.2	
ND Lignite	16.1	
	17.3	
OH Mahoning 7A	16.8	
	20.9	
IN #6 Gibson	15.7	
	19.0	
OH Gatling	18.4	
	20.1	
KY #11	18.1	
	17.3	
Pitts #8	19.1	
	17.8	
	16.9	2nd repeat to confirm data
	19.2	Increased heating rate to 10°C/min
	16.6	Substituted CO_2 with N_2

9.5.3.2 Gas Mixtures

Table 4 shows the gas mixtures used in the experiments (volume percentages) with the error in the flow relative to the desired composition (the error is expressed as a percentage of the desired flow rate).

Table 4 - Gas compositions used in the experiments.

	Actual Composition (%)				% Error from Desired Composition			
Coal Test ID	**CO_2**	**SO_2**	**O_2**	**N_2**	**CO_2**	**SO_2**	**O_2**	**N_2**
WY PRB	17.00	0.0200	2.93	80.05	0%	0%	1%	0%
	17.00	0.0200	2.93	80.05	0%	0%	1%	0%
IL #6 Galatia	16.02	0.2305	2.97	80.79	0%	0%	-1%	0%
	16.02	0.2305	2.97	80.79	0%	0%	-1%	0%
ND Lignite	14.04	0.0460	3.00	82.91	0%	2%	0%	0%
	14.04	0.0460	3.00	82.91	0%	2%	0%	0%
OH Mahoning 7A	16.04	0.1561	2.95	80.86	0%	1%	-2%	0%
	16.04	0.1561	2.95	80.86	0%	1%	-2%	0%
IN#6 Gibson	13.11	0.0893	2.98	83.82	1%	-1%	-1%	0%
	13.11	0.0893	2.98	83.82	1%	-1%	-1%	0%
OH Gatling	74.75	0.2729	2.97	22.00	0%	1%	-1%	0%
	74.75	0.2729	2.97	22.00	0%	1%	-1%	0%
KY #11	16.19	0.2592	3.00	80.55	1%	0%	0%	0%
	16.19	0.2592	3.00	80.55	1%	0%	0%	0%
Pitts#8	14.59	0.0695	3.07	82.27	1%	2%	2%	0%
	14.59	0.0695	3.07	82.27	1%	2%	2%	0%
	14.67	0.0700	2.91	82.35	1%	3%	-3%	0%
	14.67	0.0700	2.91	82.35	1%	3%	-3%	0%
	0.00	0.0698	2.90	97.03	-100%	3%	-3%	18%

9.5.3.3 TGA/DSC Data

Figure 2 provides a summary of the onset temperatures for any clearly defined endothermic peaks observed in the TGA/DSC data for all the experiments. Figures 3-12 show the TGA/DSC data, with onset temperatures labeled. The axes limits and/or ranges are matched to facilitate comparison.

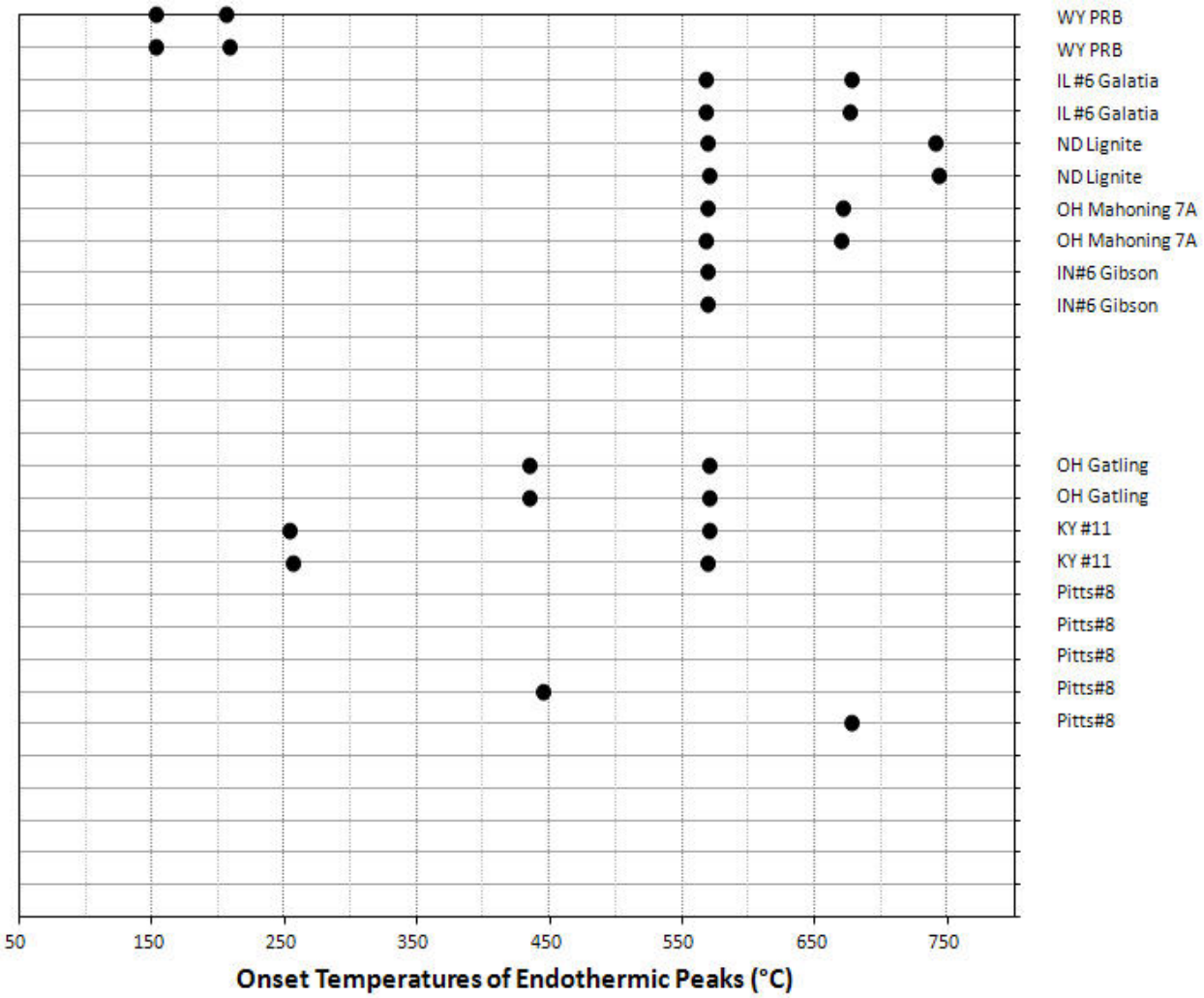

Figure 2 – Summary of locations of clearly defined endothermic peaks observed in the experiments.

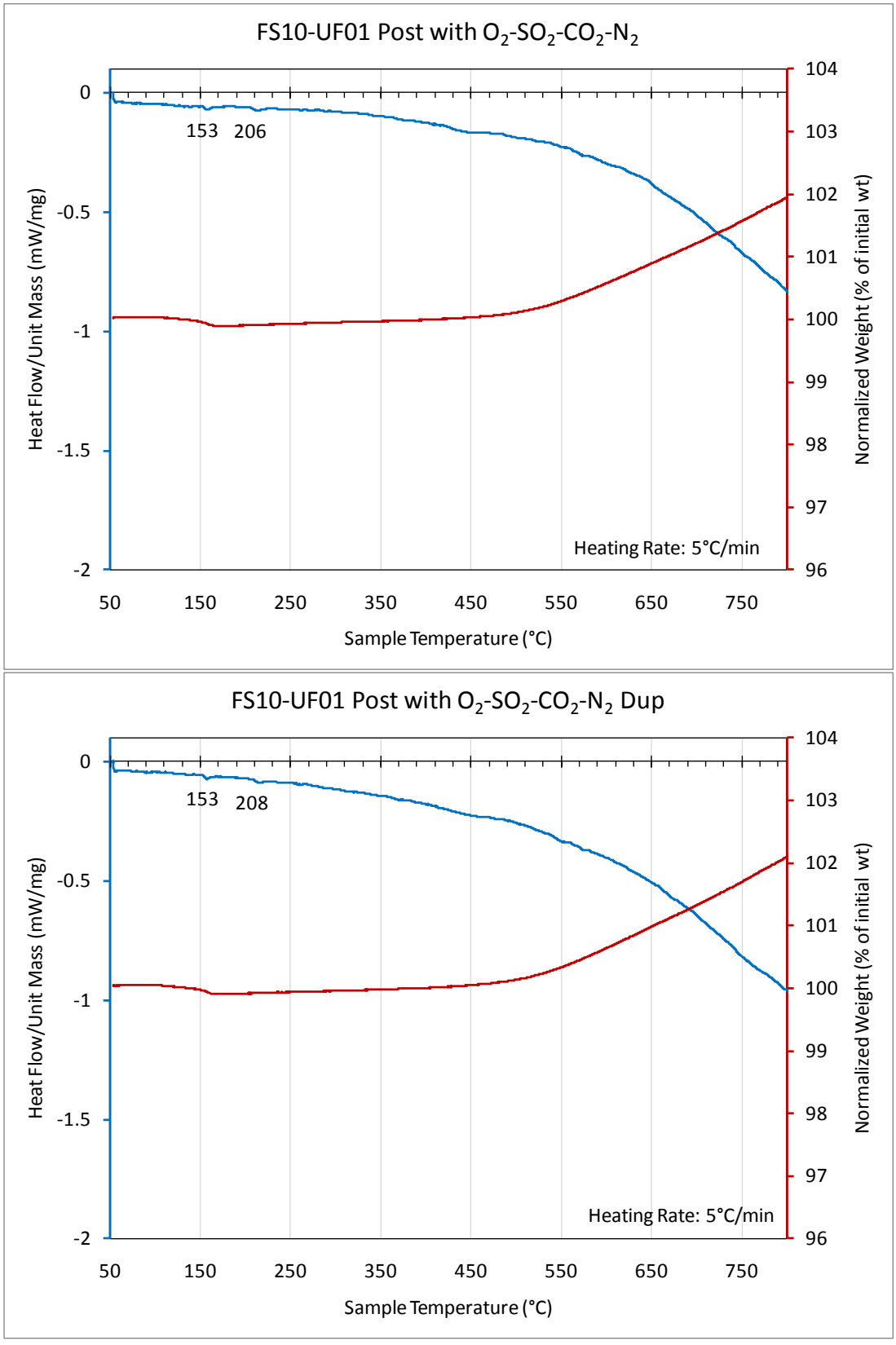

Figure 3 – TGA/DSC data for WY PRB coal.

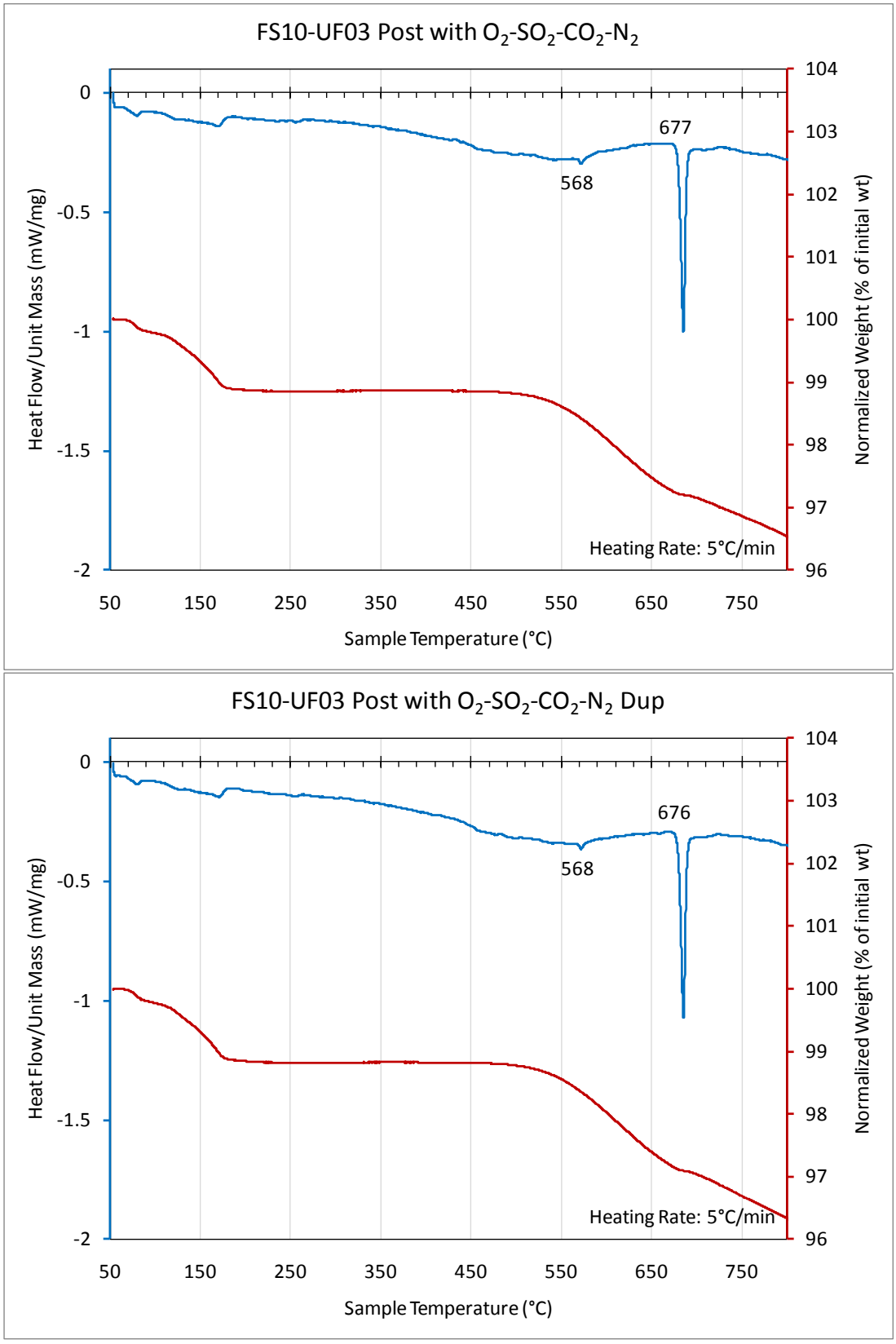

Figure 4 – TGA/DSC data for IL #6 Galatia coal.

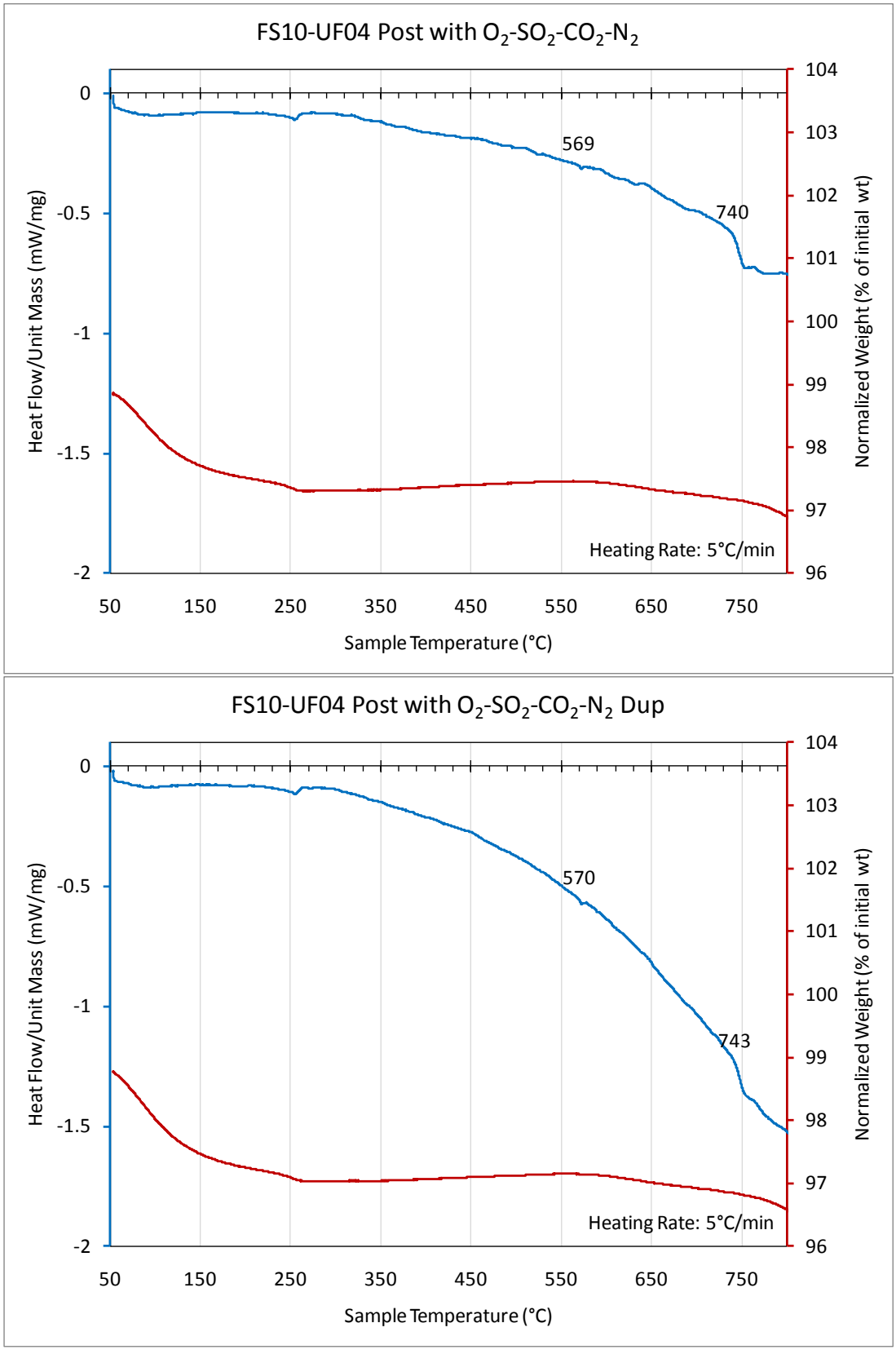

Figure 5 – TGA/DSC data for ND Lignite coal.

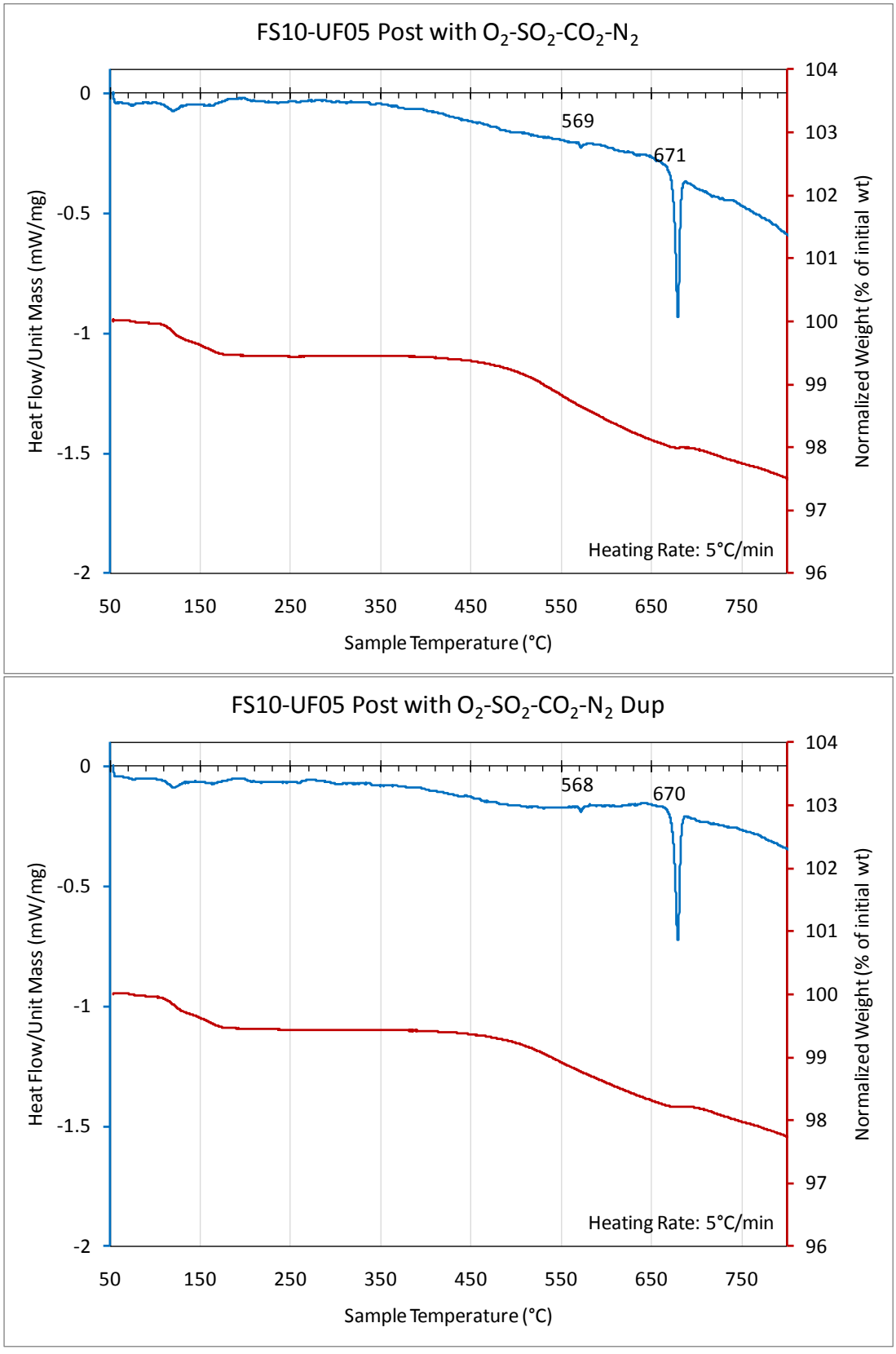

Figure 6 – TGA/DSC data OH Mahoning 7A coal.

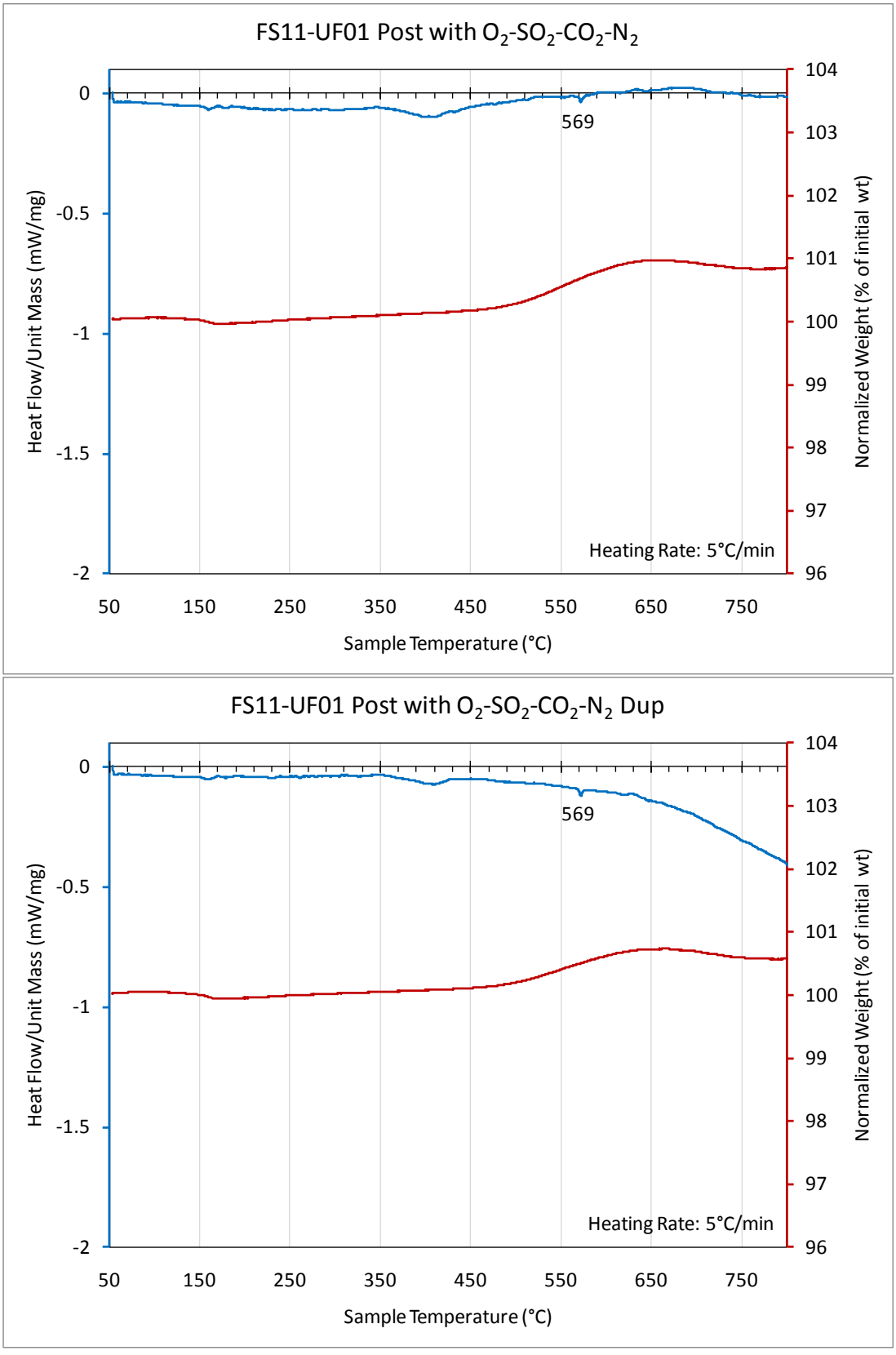

Figure 7 – TGA/DSC data IN #6 Gibson coal.

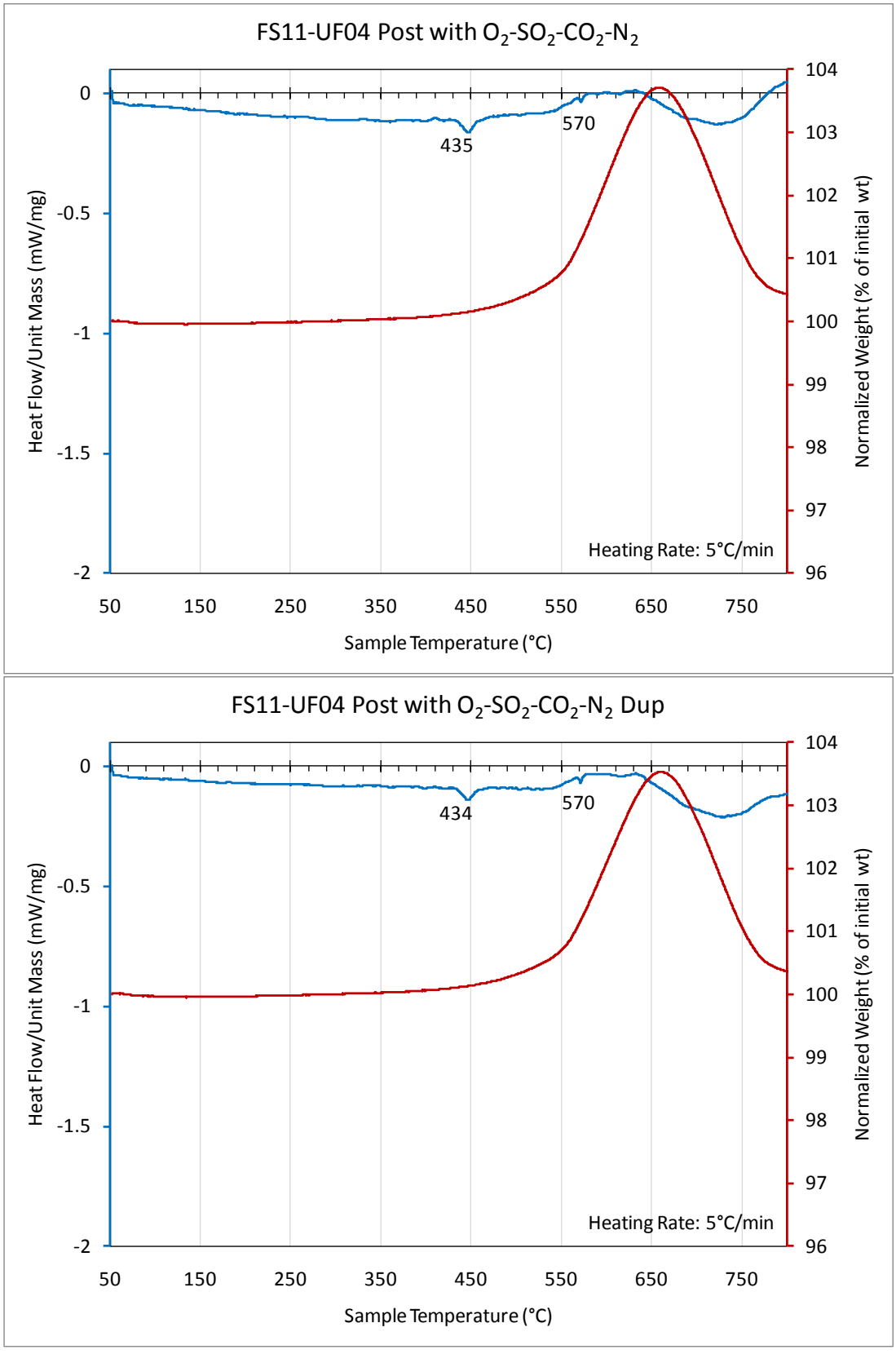

Figure 8 – TGA/DSC data for OH Gatling coal.

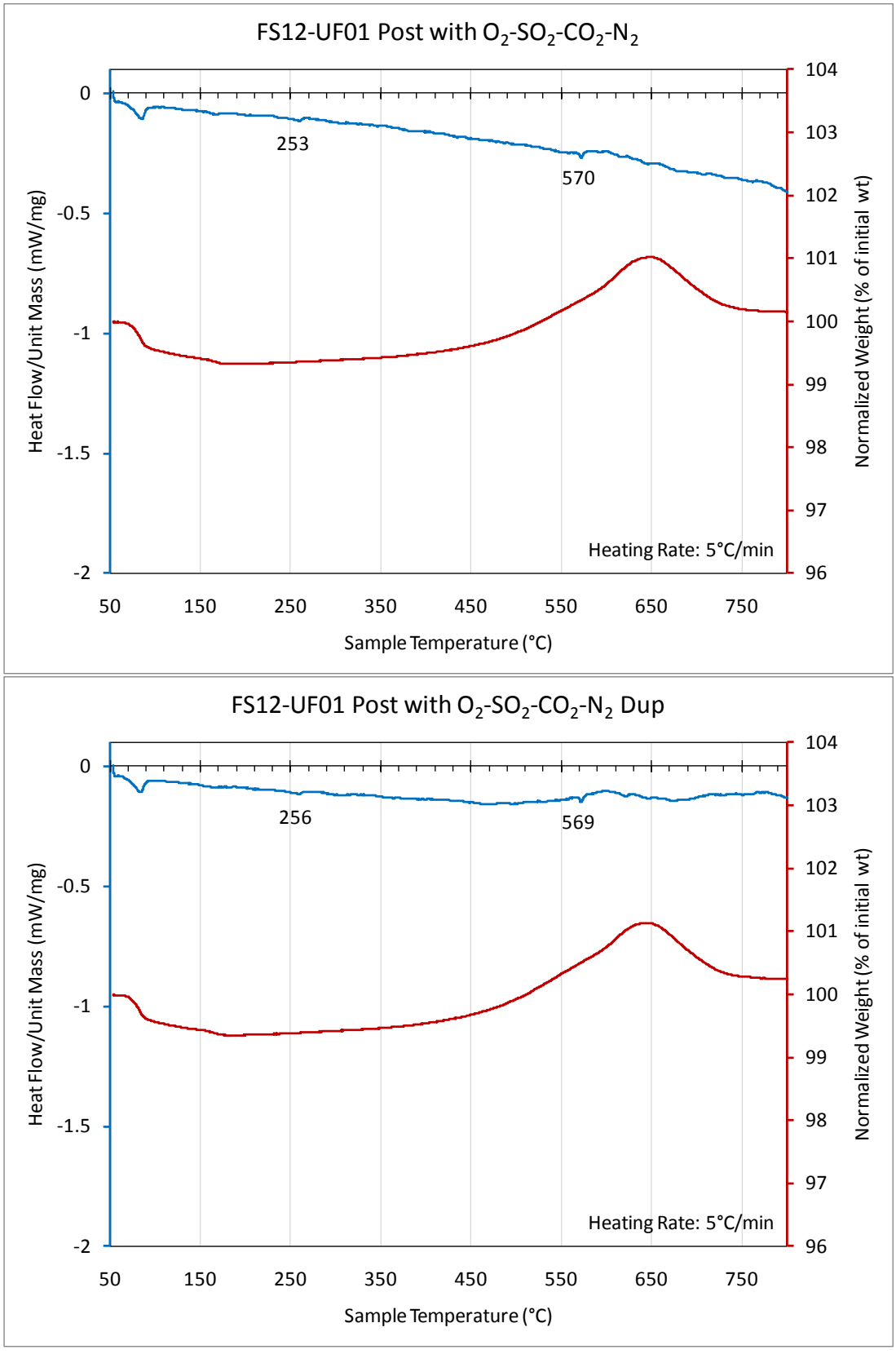

Figure 9 – TGA/DSC data for KY #11 coal.

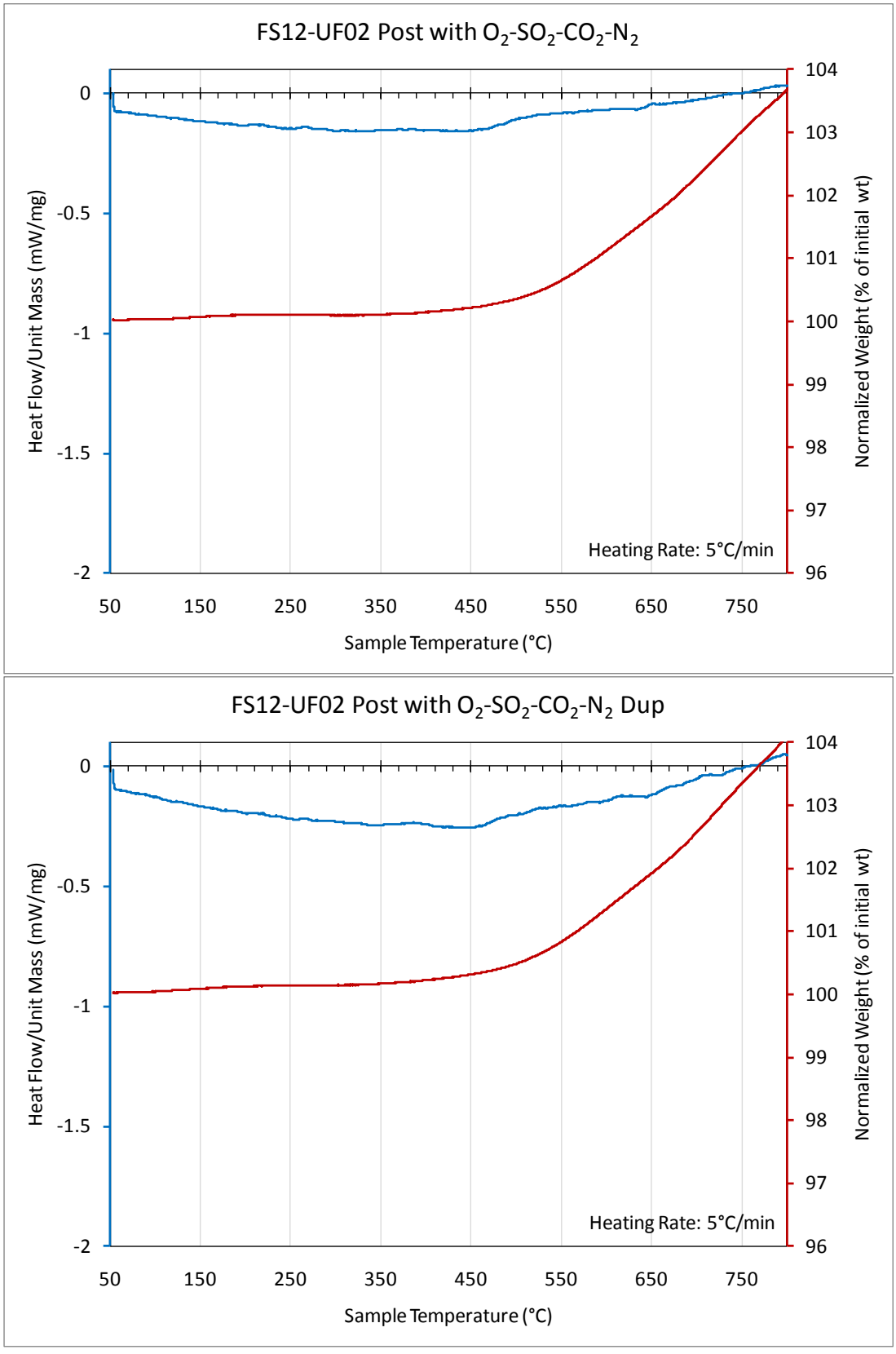

Figure 10 – TGA/DSC data for Pitts #8 coal.

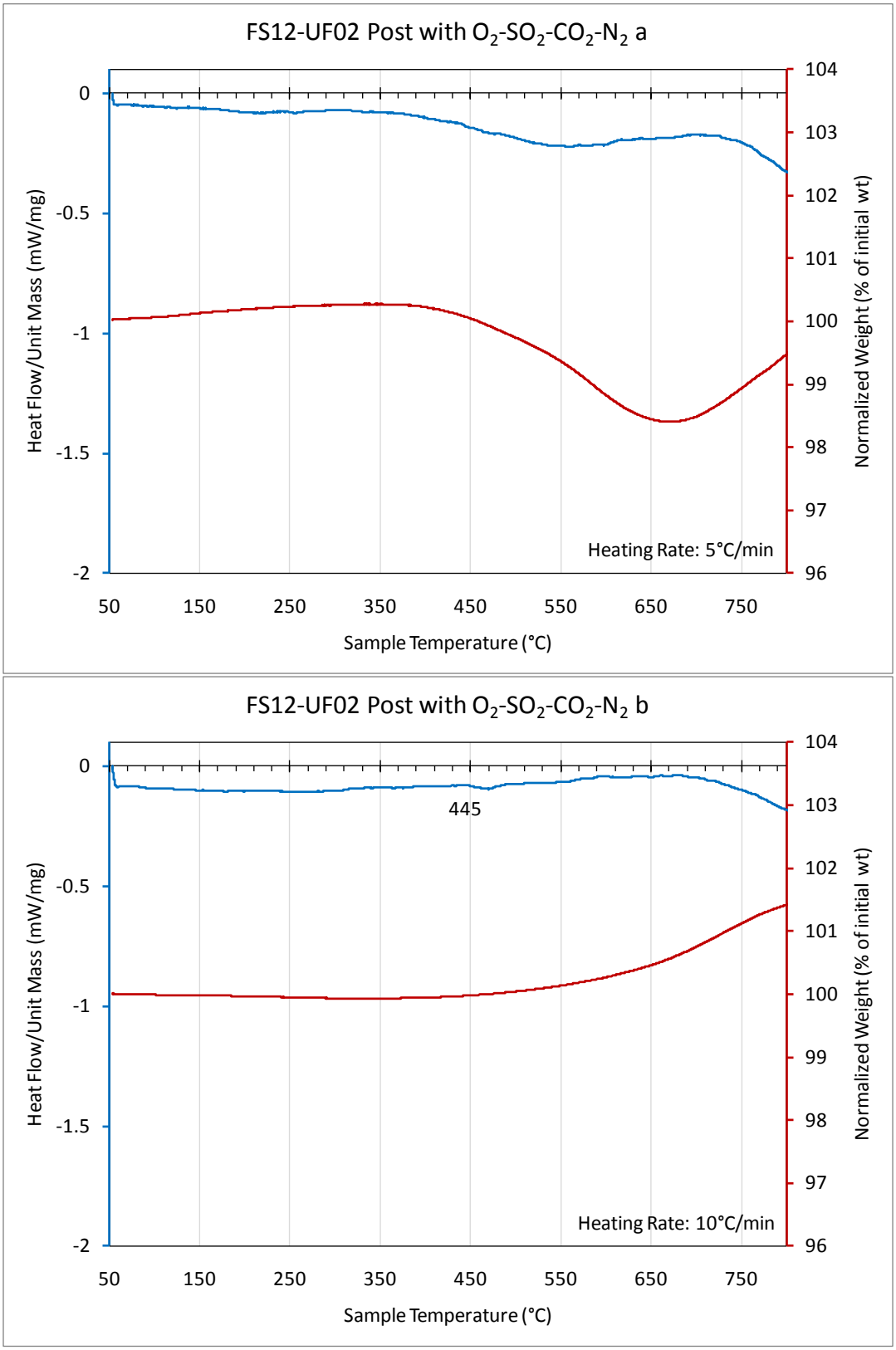

Figure 11 – TGA/DSC data for Pitts #8 coal, repeats at 5°C/min (top) and 10°C/min (bottom) to confirm absence of sharp endothermic peaks in this atmosphere. Compare to Figure 12.

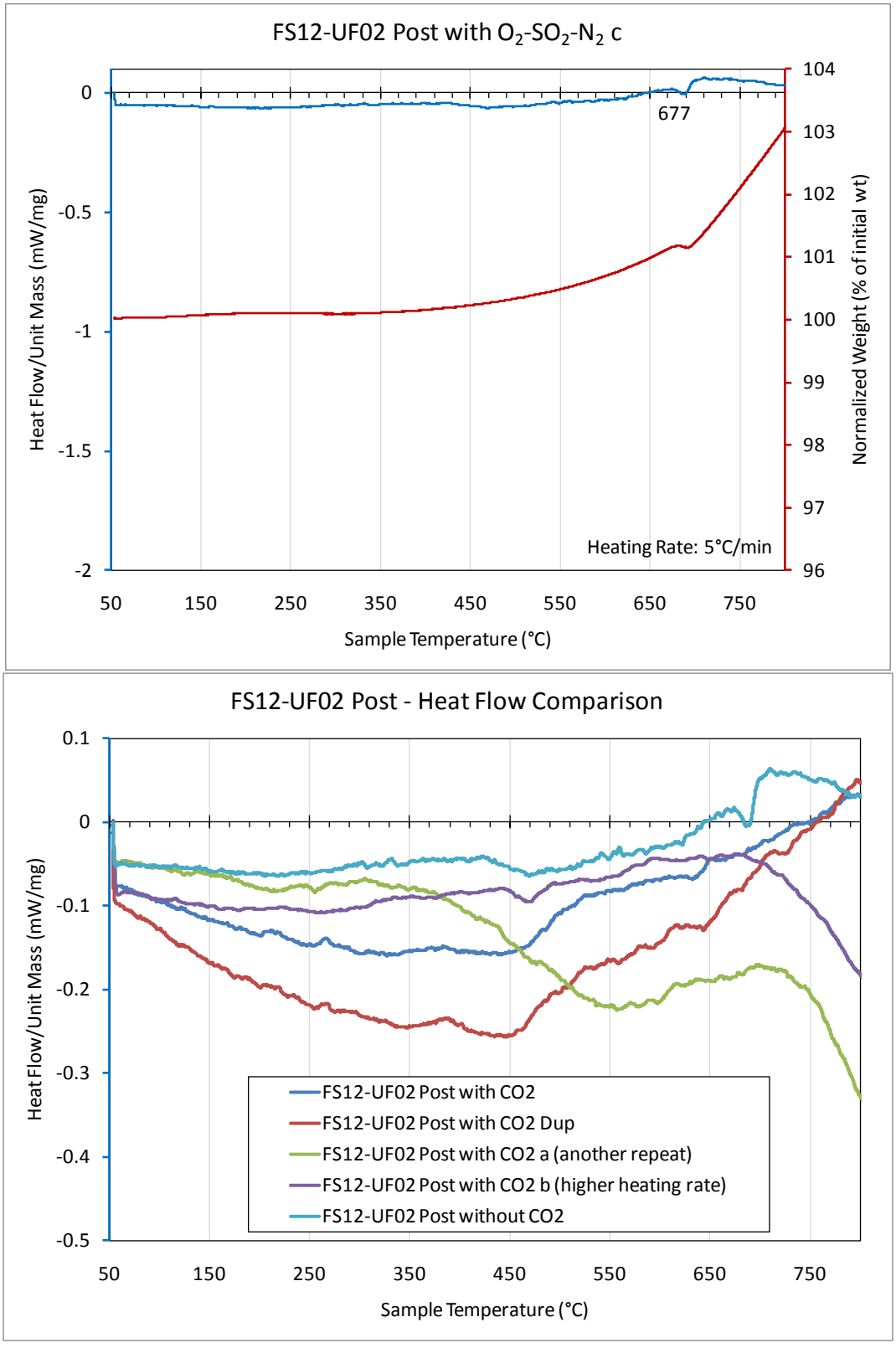

Figure 12 – Top: TGA/DSC data for Pitts #8 coal obtained without CO_2 in the gas mixture. Bottom: Heat flow data for all Pitts #8 experiments showing that only the run without CO_2 exhibited a sharp peak.

9.5.4 INSTRUMENT LIST

Instruments used for the TGA/DSC analysis consisted of as follows:

- Mass flow controller – balance protective gas (N_2): BWRC# 0-2006-0018
- Mass flow controller – furnace N_2: BWRC# 0-2006-0017
- Mass flow controller – furnace O_2: BWRC# 0-2006-0020
- Mass flow controller – furnace SO_2 in N_2: BWRC# 0-2006-0016
- Mass flow controller – furnace CO_2: BWRC# 0-2006-0015
- Primary flow standard for mass flow controller verification: BWRC# 0-2012-0208
- Mettler Toledo TGA/DSC 1 – BWRC# 0-2011-0009
- Analytical balance: BWRC# 0-2003-0001